Proceedings of the XII Finnish Mechanics Days

Suomen XII mekaniikkapäivien esitelmät

Edited by R. Kouhia, J. Mäkinen, S. Pajunen and T. Saksala

RAKENTEIDEN MEKANIIKAN SEURA R.Y.
FINNISH ASSOCIATION FOR STRUCTURAL MECHANICS

JÄSENET 1.1.2015 **MEMBERS**

HENKILÖJÄSENET	198
OPISKELIJAJÄSENET	38
YHTEISÖJÄSENET:	

A-Insinöörit Oy
ELOMATIC Consulting and Eng. Oy
Ramboll Finland Oy
Ins. tsto Pontek Oy
Konecranes Oyj
Konecranes Finland Oy
Process Flow Ltd Oy
Pöyry Finland Oy
Sweco Rakennetekniikka Oy
RIL ry
Suomalainen Insinööritoimisto SITO Oy
Aalto-yliopisto/Meritekniikka

OSOITE: http://rmseura.tkk.fi/
Rakenteiden Mekaniikan Seura ry
Rakentajanaukio 4 A, 02150 Espoo
PL 12100, 00076 Aalto

Finnish Association for Structural Mechanics
P.O. Box 12100, FI-00076 Aalto, Finland.

Proceedings of the XII Finnish Mechanics Days

Suomen XII mekaniikkapäivien esitelmät

Edited by R. Kouhia, J. Mäkinen, S. Pajunen and T. Saksala

RAKENTEIDEN MEKANIIKAN SEURA R.Y.
FINNISH ASSOCIATION FOR STRUCTURAL MECHANICS

XII Finnish Mechanics Days – XII Suomen Mekaniikkapäivät

Local organizing committee

Hannu Ahlstedt, TTY
Erkki Ahola, VTT
Markku Heinisuo, TTY
Arttu Kalliovalkama, FS Dynamics Oy
Lauri Kettunen, TTY
Reijo Kouhia, TTY
Tim Länsivaara, TTY
Jari Mäkinen, TTY
Pentti Saarenrinne, TTY
Ilpo Vattulainen, TTY
Arto Vento, Sandvik Mining and Construction Oy

RAKENTEIDEN MEKANIIKAN SEURA R.Y.
FINNISH ASSOCIATION FOR STRUCTURAL MECHANICS

ISBN 978-952-93-5608-9 (printed)
ISBN 978-952-93-5609-6 (PDF)

Picaset Oy
Helsinki 2015

Finland

Preface

This book contains the papers of lectures presented at the XII Finnish Mechanics Days conference held at the Tampere Congress & Culture Centre Puistotorni on 4-5 June 2015 and hosted by Tampere University of Technology.

The first Mechanics Days were held in Oulu 33 years ago in 1982. The conference has been organized every three years since then. The objective of this conference is to stimulate and promote research and applications within the area of solid mechanics, fluid mechanics and mathematical problems related to mechanics. The conference provides a forum for researchers, designers, teachers and other professionals to network, discuss and share ideas and information.

Sincere thanks go to all of the authors and participants for making the XII Finnish mechanics days a stimulating conference. This conference book contains 59 papers, including papers of four plenary speakers invited: Professor Anders Eriksson, KTH, Sweden, Professor Gordan Jenenic, University of Rijeka, Croatia, Professor Ignacio Romero, Universidad Politecnica de Madrid, Spain and Professor Tarmo Soomere, Tallinn University of Technology, Estonia. Finally, we thank all the sponsors: A-Insinöörit, EDR&Medeso, ETI Products, Federation of Finnish Learned Societies, FEMdata, Finnish Association of Civil Engineers RIL, Pressus Oy, Rambøll Finland Oy and Vertex Systems, whose support was indispensable for the organisation of this conference.

Just before finalizing this book we received a message of the untimely death of Professor Emeritus Juhani Koski. We remember Juhani as a kind and helpful colleague and friend and we will dedicate this book to his memory.

Tampere, May 2015

Editors

Juhani Koski in memoriam

17.2.1947 – 14.5.2015

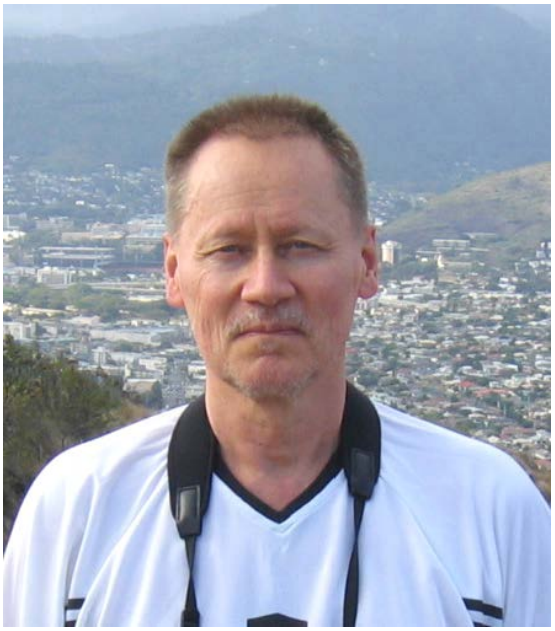

Table of contents

Multibody Dynamics:

Numeeriset Menetelmät – Numerical Methods:

Teoreettinen Mekaniikka – Theoretical Mechanics:

Finite Element Methods:

Optimointi – Optimization:

Palkkiteoria – Beam Theory:

Jäämekaniikka – Ice Mechanics:

Matemaattiset Menetelmät – Mathematical Methods:

Mallit ja Analyysit – Models and Analyses:

Kokeellinen mekaniikka – Experimental Mechanics:

Seismic & Soil Mechanics:

Mallintaminen & Modelling:

Materiaalimallit & Material Models:

Isogeometric Analysis:

Proceedings of the XII Finnish Mechanics Days
R. Kouhia, J. Mäkinen, S. Pajunen and T. Saksala (Eds.)

(All kinds of) instabilities in structural membranes

Anders Eriksson

KTH Mechanics, Osquars backe 18, SE-10044 Stockholm, Sweden, anderi@kth.se

Summary. Many classes of optimized structures can exhibit instability phenomena, related to large displacements, material effects, loading or contact conditions. Numerical treatment of these structures needs sophisticated simulation algorithms for the evaluation and interpretation of instabilities. The contribution will discuss methods for such simulations, in a general FEM-based context. The presentation will use as main example the response of thin closed membranes to applied pressure loads, from gas or fluid. The special aspects of displacement-dependent loading on a flexible structure will be discussed, as will their consequences for stability conclusions. Main results will be formulated on how the stability conclusions depend on what is considered as the control variable for the load, where, for instance, gas pressure or injected gas amount will give different conclusions for balloon-like structures. Aspects will be given on the direct and indirect stability effects from wrinkling in the thin membrane material, and how these effects can be described in the simulations.

Key words: Instability; large deflections; pressure load; simulations; parameter dependence; wrinkling.

Introduction

Many classes of optimized structures are prone to exhibit instability phenomena, related to large displacements, material effects, loading or contact conditions. General aspects of, primarily, geometric instabilities are discussed in classical works like [22], but also often in the context of finite element simulations.

The presentation examplifies the problem class by discussing very thin membranes, loaded by internal over-pressures, from gas or fluid. A large variety of thin three-dimensional inflatable structures are used in several engineering and medical contexts, [10, 11, 14], representing significantly different length scales. These situations are both geometrically non-linear due to finite deformations and materially non-linear through the constitutive relationship. Analytical results can be obtained for several simple geometries, [13, 20]. Numerical treatment of more or less general situations are also available in literature, [1, 2]. The main conclusions below are, however, also valid for other classes of optimized structures.

Basic formulation

Numerical treatment of instability affected structures, in a general FEM-based context, needs sophisticated simulation algorithms for the evaluation and interpretation of results obtained. First, a reliable finite element formulation is needed, which is not overly sensitive to, e.g., the scaling of the problem. For thin membranes, shell models have been shown to be less reliable, due to large rotations, the aspect ratios of the elements, and the stiffness differences in membrane and bending action. Rotation-free shell elements suggested by many researchers are described and compared in [8]. In the present work, simulations of the loading process have been based purely on the membrane behavior. The mechanical model is thereby one of local plane stress conditions, but in a 3-dimensional setting. When discretizing a structural model, triangular elements with linear kinematic assumptions are used, disregarding the bending stiffness, [6].

It is further assumed that hyper-elastic material models can be used for the formulation of the internal energy during large strain situations. Several formulations are available, each with a number of free parameters for accurate description of a particular material. The relations between constitutive parameters in a material model significantly affects the response of simulated membranes, [6, 15]. The material can show an instability at certain stress states, [9, and many others]. A recent study discussed the stability of hyper-elastic material models in a situation of bi-axial stresses, [7], showing that a two-parameter Mooney-Rivlin model [12, 19] can give non-intuitive instabilities for certain bi-axial membrane states.

The kinematic assumptions and the material model are used to formulate the structural internal forces

$$\boldsymbol{f} = \boldsymbol{f}(\boldsymbol{u}) \tag{1}$$

with $\boldsymbol{u}$ the global structural displacement components. Similar expressions give the the tangent stiffness matrix.

Pressure loading

The loading on a pressurized membrane comes from one-sided gas or fluid over-pressures, with significant differences in their formulations. Where an over-pressure from gas ψ is uniform over all elements, giving the structural external force vector $\boldsymbol{p} = \boldsymbol{p}(\boldsymbol{u}, \psi)$, a hydro-static pressure is linearly varying over a subset of elements. Assuming gravity in the global negative z direction, the pressure on an element surface is described by $\psi(z) = \rho g(z_{\text{fluid}} - z)$ for $z \leq z_{\text{fluid}}$, with ρ the fluid density, g the gravitational acceleration, and z_{fluid} the fluid surface level. Consistent nodal loads representing the discontinuous linear pressure variation give a vector of external forces $\boldsymbol{p} = \boldsymbol{p}(\boldsymbol{u}, z_{\text{fluid}})$. In either case, the external forces are described by a primary load control variable

$$\boldsymbol{p} = \boldsymbol{p}(\boldsymbol{u}, \gamma) \tag{2}$$

It is noted that the structural loads are follower forces dependent on current displacements. They are commonly conservative, giving a symmetric tangential stiffness matrix.

Symmetry

Membranes, as most classes of optimized structures, often possess a high degree of symmetry in their geometries. Typically, the response to pressure loading respects these symmetry aspects, at least when moderate loading levels are considered. In many cases, however, instabilities lead to symmetry-breaking secondary response paths for the structure, [17]. In these cases, the kinematic formulation of the model must allow the non-symmetric response aspects, or these are easily hidden in the simulations. The symmetry in the structure, and also in its discretized model can have significant effects on the obtained results, and in their interpretation.

Simulation algorithms

For a quasi-static formulation, the discretized equilibrium between external and internal forces demands solutions $(\boldsymbol{u}, \gamma)$ satisfying the structural residual equilibrium equations:

$$\boldsymbol{F}(\boldsymbol{u}, \gamma) \equiv \boldsymbol{f}(\boldsymbol{u}) - \boldsymbol{p}(\boldsymbol{u}, \gamma) = \boldsymbol{0} \tag{3}$$

where $\boldsymbol{F}$, $\boldsymbol{f}$, $\boldsymbol{p}$, and $\boldsymbol{u}$ are of dimension N_u, and γ is the load control parameter. With one free parameter, this system gives solutions in the form of one-dimensional curve segments. The differential relation corresponding to Eq. (3) is:

$$\delta\boldsymbol{F} = (\boldsymbol{K} - \boldsymbol{K}_p)\,\delta\boldsymbol{u} - \delta\gamma\frac{\partial\,\boldsymbol{p}}{\partial\,\gamma} \tag{4}$$

which gives a tangent stiffness matrix containing a load-dependent term, [21]. Important properties of an evaluated equilibrium configuration are described by this matrix.

The response to loading must be evaluated as load-displacement paths, where an equilibrium path is represented by a sequence of equilibrium configurations. Different forms of instabilities are often found along these paths. These must be seen as main aspects of the structural response, and should be detected and classified.

Parameter dependence

For the membranes, a key issue for the simulation algorithms is thereby the analysis of the parameter dependence in a simulated response, in particular the interesting solution points. For this, specially designed algorithms can introduce augmenting variables, representing a parameterization of the structure or the loading, and then solve the equilibrium problem, and its corresponding stability properties in the higher-dimensional space. The generalized path-following algorithm used in the present work is discussed in [3, 4], with a linear step-wise parameterization and regulation [5].

Instability

The most prominent instability phenomena in thin membranes are related to the geometric non-linearity, with significant configuration changes. These will often lead to limit points with respect to a considered loading parameter. Bifurcations, for instance giving symmetry-breaking deformation modes can also occur in the loading process. Special solution states of particular interest are thereby turning points in any interesting parameter, and states where the degree of instability of the equilibrium changes, i.e., where the tangent stiffness matrix has a zero eigenvalue, [3].

Wrinkling

In the analysis of thin pressurized membranes, wrinkling of the material under compressive stresses is a common result. This phenomenon, which does not allow a detailed modelling with finite-sized elements, can be reasonably handled by relaxed energy formulations, [18], which in essence disregard all compressive stress components. The wrinkling of parts of a membrane leads to direct as well as indirect stability effects in the results.

Contacts

In particular in biological contexts, thin membranes often interact with mechanically stiffer surroundings. Recent work, [16], has studied how the response of a pressurized cylindrical membrane is constrained by stiff or soft foundations. For a general FEM-based simulation, penalty formulations are preferred, but a conclusion is that at least third order penalty forces must be used, in order to avoid strong discontinuities in stiffness.

Control variables

The displacement-dependent loading on a flexible structure demands special attention. Technically, the follower forces affect the equilibrium formulation of the problem, demanding new aspects in the solution algorithm. In addition, the setting of the problem demands new methods to interpret the obtained results. An important discussion is related to how the stability conclusions depend on what is considered as the control variable for the loading. It is in [6] noted that the instability can be related to either the internal over-pressure or to the amount of gas introduced in a gas-pressurized closed membrane. A model for the inflation of a closed membrane must therefore pay attention to the precise mechanism for the introduction of the pressure loading.

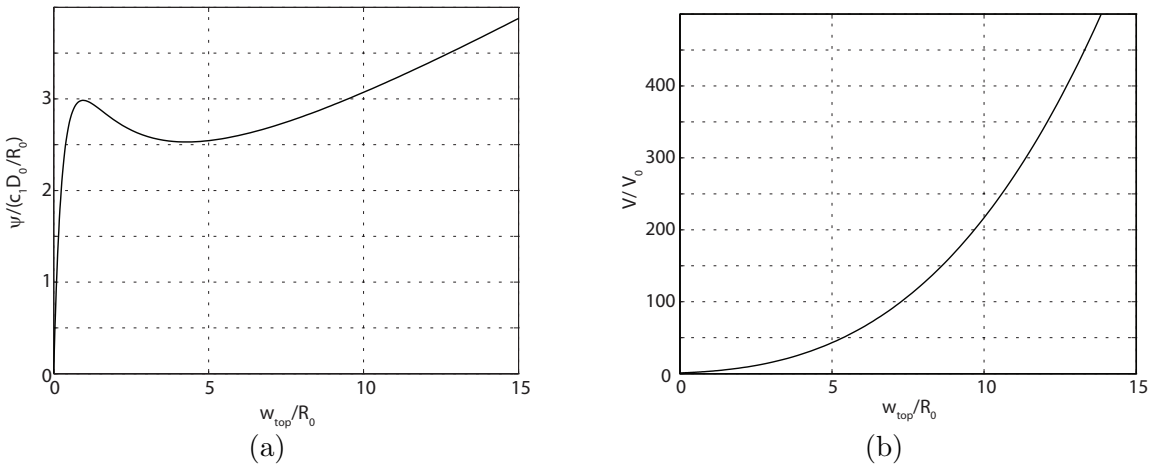

(a) (b)

Figure 1. Gas-pressurized sphere. Non-dimensional vertical displacement of top node in model, related to non-dimensional pressure in (a), and to non-dimensional enclosed volume in (b).

Numerical example

Several circular, spherical and cylindrical membranes have been simulated, when subjected to gas or fluid loading, affected by pre-stretching and with rigid or flexible substrates restricting the deformation. Only results from the spherical membrane of radius $R_0 = 10\,\text{mm}$ are presented here. The membrane had an initial thickness of $D_0 = 0.01\,\text{mm}$. Material data were chosen as $c_1 = 0.1920\,\text{MPa}$, $c_2 = 0.1c_1$ in an invariant-based Mooney-Rivlin model for strain energy $W = c_1(I_1(\boldsymbol{C}) - 3) + c_2(I_2(\boldsymbol{C}) - 3)$ with $\boldsymbol{C}$ the strain tensor. Gravity acceleration was $g = 9.81\,\text{m/s}^2$.

The element mesh used was based on successive refinements of a 20-face regular icosahedron, arriving at a 5120 element model. Almost minimal supports were introduced around the lowest node, creating a model of 7678 active d.o.f.s. Additional contacts were disabled for the results below.

For gas loading, the sphere will expand radially with an increasing injected amount of gas. The equilibrium path will show two limit points with respect to the pressure variable, Fig. 1(a), but the expansion will be monotonous and stable with respect to the injected volume, Fig. 1(b). The membrane will not show any wrinkling at any positive pressure, but the whole structure will be wrinkled and computationally not reachable for any negative pressures, corresponding to a volume lower than the initial V_0 (calculated for the faceted model).

For fluid loading, the response is highly dependent on the fluid density ρ. For a relatively high density, $\rho = 10^{-6}\,\text{kg/mm}^3$, related to the non-dimensional parameter $(\rho g R_0^2)/(\mu D_0)$, the deformation will deviate from spherical due to the variation of internal over-pressure, which is visible as another relation between top point displacement and enclosed volume, Fig. 2(a) An enclosed volume lower than the initial V_0 can be simulated, as not all the computational elements will enter wrinkling at the same loading. Figure 2(b) shows the deformed membrane, and a coloring of the wrinkling regions at a volume of $0.825\,V_0$, where almost 23% of elements are wrinkled. Simulations were continued, without significant numerical problems down to a volume of $0.6\,V_0$, when top point deflection $w_{\text{top}} = -1.660\,R_0$, and 28% of elements are wrinkled. It is noted that the support conditions assumed are of major importance for the results.

Concluding remarks

Hyper-elastic thin membranes show several forms of instabilities when pressurized. Limit points with respect to the pressure variable are commonly detected, in particular when hyper-elastic material models with low hardening are considered. Bifurcations, often related to symmetry-breaking secondary paths are common, when fluid-loading is considered. Wrinkling, commonly defined from compressive principal stresses in some regions of a structure, often occurs. A re-

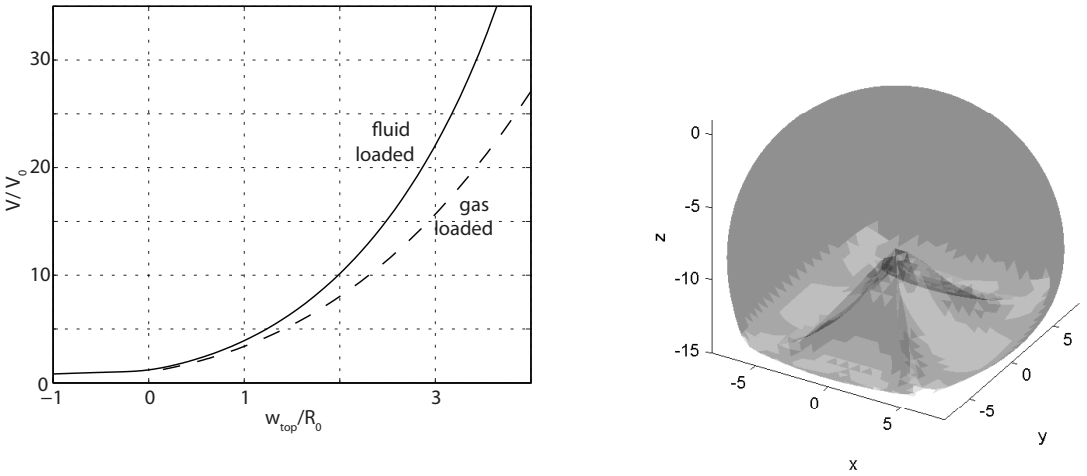

(a) (b)

Figure 2. Fluid-pressurized sphere. (a) Non-dimensional vertical displacement of top node in model, related to non-dimensional enclosed volume, with a comparison to Fig. 1(b); (b) Deformed membrane and wrinkling extent for an equilibrium solution with $V = 0.825\,V_0$.

duced stiffness in the compressed direction can then be modelled by relaxed energy expressions, where details of the wrinkling are disregarded and only the effects on a mid-surface described. Wrinkling has both local and global stability effects which must be considered. The hyper-elastic model itself can also, under some conditions related to the modelling of the acting loads, lead to a non-uniqueness in response. The instability effects and conclusions in the simulations are often significantly dependent on the discretization used, and in particular the mesh of finite elements. The instability conditions are difficult to introduce in common optimization algorithms, but constraint path following can show the boundaries of a feasible design domain related to instability conditions.

Acknowledgements

The work presented represents joint efforts within our group. Primarily, the important contributions by Costin Pacoste, Arne Nordmark, Amit Patil and Yang Zhou are acknowledged.

References

[1] D. T. Berry and H. T. Y. Yang. Formulation and experimental verification of a pneumatic finite element. *International Journal for Numerical Methods in Engineering*, 39:1097–1114, 1996.

[2] J. Bonet, R. D. Wood, J. Mahaney, and P. Heywood. Finite element analysis of air supported membrane structures. *Computer Methods in Applied Mechanics and Engineering*, 190:579–595, 2000.

[3] A. Eriksson. Equilibrium subsets for multi-parametric structural analysis. *Computer Methods in Applied Mechanics and Engineering*, 140:305–327, 1997.

[4] A. Eriksson. Structural instability analyses based on generalised path-following. *Computer Methods in Applied Mechanics and Engineering*, 156:45–74, 1998.

[5] A. Eriksson and R. Kouhia. On step size adjustments in structural continuation problems. *Computers and Structures*, 55:495–506, 1995.

[6] A. Eriksson and A. Nordmark. Instability of hyper-elastic balloon-shaped space membranes under pressure loads. *Computer Methods in Applied Mechanics and Engineering*, 237–240:118–129, 2012.

[7] A. Eriksson and A. Nordmark. Non-unique response of Mooney-Rivlin model in bi-axial membrane stress. *Computers and Structures*, 144:12–22, 2014.

[8] M. Gärdsback and G. Tibert. A comparison of rotation-free triangular shell elements for unstructured meshes. *Computer Methods in Applied Mechanics and Engineering*, 196:5001–5015, 2007.

[9] R. Hill and J.W. Hutchinson. Bifurcation phenomena in the plane tension test. *Journal of the Mechanics and Physics of Solids*, 23:239–264, 1975.

[10] D. K. Liang, D. Z. Yang, M. Qi, and W. Q. Wang. Finite element analysis of the implantation of a balloon-expandable stent in a stenosed artery. *International Journal of Cardiology*, 104:314–318, 2005.

[11] J. A. Main, S. W. Peterson, and A. M. Strauss. Load-deflection behavior of space-based inflatable fabric beams. *Journal for Aerospace Engineering*, 7:225–238, 1994.

[12] M. Mooney. A theory of large elastic deformation. *Journal of Applied Physics*, 11:582–592, 1940.

[13] A. Needleman. Inflation of spherical rubber balloons. *International Journal of Solids and Structures*, 13:409–421, 1977.

[14] M. Pagitz and S. Pellegrino. Maximally stable lobed balloons. *International Journal of Solids and Structures*, 47:1496–1507, 2010.

[15] A. Patil and A. Dasgupta. Finite inflation of an initially stretched hyperelastic circular membrane. *European Journal of Mechanics, A/Solids*, 41:28–36, 2013.

[16] A. Patil, A. Nordmark, and A. Eriksson. Free and constrained inflation of a pre-stretched cylindrical membrane. *Proceedings of the Royal Society A*, 470:20140282, 2014.

[17] A. Patil, A. Nordmark, and A. Eriksson. Instability investigation on fluid-loaded pre-stretched cylindrical membranes. *Proceedings of the Royal Society A*, 471:20150016, 2015.

[18] A.C. Pipkin. The relaxed energy density for isotropic elastic membranes. *IMA Journal of Applied Mathematics*, 36:85–99, 1986.

[19] R.S. Rivlin. Large elastic deformations of isotropic materials. IV. Further developments of the general theory. *Philosophical Transactions of the Royal Society of London*, A 241:379–397, 1948.

[20] J. Rodríguez and J. Merodio. A new derivation of the bifurcation conditions of inflated cylindrical membranes of elastic material under axial loading. Application to aneurysm formation. *Mechanics Research Communications*, 38:203–210, 2011.

[21] T. Rumpel and K. Schweizerhof. Volume-dependent pressure loading and its influence on the stability of structures. *International Journal for Numerical Methods in Engineering*, 56:211–238, 2003.

[22] J. M. T. Thompson and G. W. Hunt. *Elastic Instability Phenomena*. Wiley, Chichester, 1984.

Proceedings of the XII Finnish Mechanics Days
R. Kouhia, J. Mäkinen, S. Pajunen and T. Saksala (Eds.)

Finite elements on non-linear manifolds of rotations or complete motion – relationships between objectivity, helicoidal interpolation and fixed-pole approach

Gordan Jelenić

University of Rijeka, Faculty of Civil Engineering, R. Matejčić 3, Rijeka, gordan.jelenic@uniri.hr

Summary. Finite-element implementation of mechanical problems defined on non-linar manifolds requires particular attention, since some of the important physical properties of equilibrium or motion are not necessarily automatically inherited from the underlying continuous governing equations. Here we review some of the features of the so-called objective, helicoidal and fixed-pole approaches and show that there exist interesting similarities between them even though their development has been motivated by clearly different demands. More detail is presented for the configuration space formed by a product of a three-dimensional vector space and a three-parametric orthogonal differential manifold as well as the non-linear non-orthogonal six-parametric differential manifold of complete motion.

Key words: objectivity, configuration-dependent interpolation, helicoidal interpolation, linked interpolation, fixed-pole approach, 3D rotation group, 6D group of complete motion

Introduction

The geometrically exact 3D beam theory developed by Simo in 1985 [1] along with its original finite-element implementation in 1986 [2] makes perhaps one of the most well-known excursions into applications of numerical techniques, the finite-element method in particular, to mechanical problems defined on non-linear manifolds. The non-linearity of the problem domain here shows up as a consequence of non-linearity of the manifold of 3D rotations – the special orthogonal Lie group. Other examples naturally include higher-dimensional cases of the Cosserat (or micropolar) continuum theory, such as shells with drilling rotations [3] or a 3D micro-polar continuum [4], but also more sophisticated implementations of the 1D (beam) theory defined on a complete six-parametric Lie group of complete motion [5, 6].

Special care need be exercised in the process of interpolation of the degrees of freedom that belong to the non-linear part of the configuration space lest one may end up in a numerical procedure that fails to inherit the important physical property of objectivity of the solution with respect to the frame of reference of the observer. A possible solution has been presented in [7] involving a configuration-dependent interpolation for the rotational degrees of freedom, but a number of alternative procedures have been suggested also, e.g. [8, 9].

A perhaps not so well-known relationship exists, however, between the interpolation for the rotational degrees of freedom presented in [7] and the so-called helicoidal interpolation given in [10], which was originally devised with a completely different objective in mind - to provide a solution which is independent of the choice of the beam reference axis. It turns out, interestingly, that so long as we limit our attention to two-node beam elements, the interpolation for the rotational degrees of freedom in these two sources turns out to be the same. On the other hand, the helicoidal interpolation appears to be more sophisticated in that it also produces a more elaborate, and in many senses beneficial, configuration-dependent interpolation for the

displacement field which, incidentally, turns out to be identical to that utilised for interpolation of the rotational field.

An attempt to generalise the helicoidal interpolation to beam elements with arbitrary number of nodes has been made in [11], but there clearly appears to remain present both a need and a potential for further development of the procedure proposed. The idea to apply the interpolation of the rotational field from [7] (which has been developed for a general n-node element) to the displacement field comes as very natural, but a closer inspection reveals that this is not necssarily so. The principal obstacle appears to lie in a conflict between the demands to secure the exact solution of a linear problem [12] and the solution independent of the position of the reference axis [10]. Intrestingly, this conflict disappears precisely and exclusively for the two-node elements, thus effectively asserting that the helicoidal interpolation is a genuinely two-noded interpolational concept.

The helicoidal interpolation also has links with the so-called fixed-pole approach [5]. Nonetheless, there is no limitation to two-node intepolation in the fixed-pole concept while, in contrast to the helicoidal interpolation, objectivity of the formulation is not provided unless specifically taken care of [13, 14]. The fixed-pole concept also provides a very natural setting for development of conservative and group-motion preserving energy-dissipative time-stepping schemes in implicit non-linear dynamics, where simultaneous conservation of both global momenta and energy is, if needed, much more easily attained than in the standard 'moving-pole' approaches.

Also, the fixed-pole concept effectively re-expresses governing equations of a problem in a fully non-linear manifold inhabited by the complete motion, where translations and rotations are only the specifically defined parts of a new six-dimensional motion parameter. This poses certain practical problems, as we end up in having to work with non-standard problem unknowns, which are not straightforward to relate to the standard displacements and rotations present in the existing finite elements. Also, they are awkward to utilise to define even relatively simple support conditions and an attempt to exploit its benefits, while by-passing its short-comings has been made in [13], where the standard degrees of freedom have been re-introduced at the nodal level. Again, objectivity of a finite-element implementation is not automatically guaranteed in the fixed-pole approach and an algorithm which enforces it may be devised in analogy with the procedure given in [7]. This follows as a consequence of the fact that the six-parametric group of complete motion is also a Lie group, and the governing equations of the problem defined on this group take a strikingly parallel form to those defining the kinematic and constitutive equations as well as the equations of motion for the rotational part in the 'moving-pole' approaches [14].

Brief outline of 3D geometrically exact beam theory and its original FE implementation

The geometrically exact 3D beam theory provided by Simo in 1985 [1] makes one of the milestones in the development of the non-linear finite-element method by introducing a non-linear manifold, composed of a three-dimensional vector space of displacements and a three-parametric Lie group of the rotation tensors as the configuration space. To present it briefly, for a beam of length L in free flight the weak form of the power-balance law reads $\int_0^L \left[(\mathbf{v}' + \widehat{\mathbf{r}'}\mathbf{w}) \cdot \mathbf{n} + \mathbf{w}' \cdot \mathbf{m}\right] dx + \int_0^L \left(\mathbf{v} \cdot \dot{\mathbf{k}} + \mathbf{w} \cdot \dot{\boldsymbol{\pi}}\right) dx = 0$, where $\mathbf{n}$ and $\mathbf{m}$ are vectors of spatial stress and stress-couple resultants, $\mathbf{k} = A\rho\mathbf{v}$ and $\boldsymbol{\pi} = \boldsymbol{\Lambda}\mathbf{J}_\rho\boldsymbol{\Lambda}^{\mathrm{t}}\mathbf{w}$ are the vectors of specific momentum and angular momentum with respect to the beam reference axis at a cross-section, $\mathbf{r}$ and $\boldsymbol{\Lambda}$ are the position vector of the reference line and the orientation tensor of the principal axes of the cross-section with respect to their position in the reference state, which belong to a non-linear configuration space composed of a three-dimensional vector space $\mathcal{R}^3$ and the three-parametric special orthogonal group $SO(3)$. A dot and a dash in the power-balance equation indicate differentiation with respect to time t and the beam-length parameter x, a superimposed hat indicates a cross-product operator, $\mathbf{v} = \dot{\mathbf{r}}$ and $\mathbf{w}$ (for which $\widehat{\mathbf{w}} = \boldsymbol{\Lambda}^{\mathbf{t}}\dot{\boldsymbol{\Lambda}}$) are the velocity and the angular velocity vectors, A and ρ

are the cross-sectional area and density of the material, and $\mathbf{J}_\rho$ is the tensor of cross-sectional moments of inertia.

Originally [2], only the velocity fields in the power-balance equation have been interpolated using Lagrangian polynomials $I^{\mathrm{i}}(x)$ via $\mathbf{v}(x) = \sum_{i=1}^{N} I^{\mathrm{i}}(x)\mathbf{v}_{\mathrm{i}}$ and $\mathbf{w}(x) = \sum_{i=1}^{N} I^{\mathrm{i}}(x)\mathbf{w}_{\mathrm{i}}$. For arbitrary nodal velocities, this has resulted in the nodal balance $\mathbf{g}^{\mathrm{i}} \equiv \mathbf{q}^{\mathrm{i}}_{\mathrm{i}} + \mathbf{q}^{\mathrm{i}}_{\mathrm{m}} = \mathbf{0}$ at any node $i = 1, \ldots, N$ with the nodal internal and inertial force vectors $\mathbf{q}^{\mathrm{i}}_{\mathrm{i}}$ and $\mathbf{q}^{\mathrm{i}}_{\mathrm{m}}$ as

$$\mathbf{q}^{\mathrm{i}}_{\mathrm{i}} = \int_{\mathbf{0}}^{\mathbf{L}} \begin{bmatrix} I^{\mathrm{i}\prime}\mathbf{I} & \mathbf{0} \\ -I^{\mathrm{i}}\widehat{\mathbf{r}'} & I^{\mathrm{i}\prime}\mathbf{I} \end{bmatrix} \begin{Bmatrix} \mathbf{n} \\ \mathbf{m} \end{Bmatrix} dx \qquad \text{and} \qquad \mathbf{q}^{\mathrm{i}}_{\mathrm{m}} = \int_{\mathbf{0}}^{\mathbf{L}} I^{\mathrm{i}} \begin{Bmatrix} \dot{\mathbf{k}} \\ \dot{\boldsymbol{\pi}} \end{Bmatrix} dx. \tag{1}$$

The system of non-linear equations $\mathbf{g}^{\mathrm{i}} \equiv \mathbf{q}^{\mathrm{i}}_{\mathrm{i}} + \mathbf{q}^{\mathrm{i}}_{\mathrm{m}} = \mathbf{0}$ (for $i = 1, \ldots, N$) may now be solved for the kinematic unknowns $\mathbf{r}(x)$ and $\boldsymbol{\Lambda}(x)$ using the Newton–Raphson solution procedure in which the linear part of the changes in these unknowns $\Delta\mathbf{r}$ and $\Delta\boldsymbol{\vartheta}$ (emerging from $\Delta\boldsymbol{\Lambda} = \widehat{\Delta\boldsymbol{\vartheta}}\boldsymbol{\Lambda}$) may be interpolated in the same manner as $\mathbf{v}(x)$ and $\mathbf{w}(x)$ [2].

Note that this interpolation (along with a suitable time-stepping procedure) is sufficient to completely define the dynamic problem, too, even though in [15] additional interpolations are also provided for the incremental rotations, angular velocities and accelerations, in conjunction with the Newmark time-integration scheme. In any case, however, this approach, as well as a variety of related approaches, turn out to be incapable of algorithmic preservation of the important mechanical property of objectivity of the solution with respect to the choice of the observer, also implying a solution which ceases to be strain-invariant with respect to a rigid-body motion.

Objective finite-element interpolation of 3D rotations

In the objective formulation for geometrically exact higher–order beam elements [7] the position vector of the beam reference axis is taken to coincide with the line of centroids and has been interpolated in a standard Lagrangian manner. The rotations, in contrast, have been interpolated very differently: the rotation matrix $\boldsymbol{\Lambda}(x)$ has been *multiplicatively* decomposed into a part constant for the whole beam and rigidly attached to a node I ($\boldsymbol{\Lambda}_I$) and the part due to a *local* rotation $\boldsymbol{\Psi}^l$ with respect to that orientation as $\boldsymbol{\Lambda}(x) = \boldsymbol{\Lambda}_I \exp\hat{\boldsymbol{\Psi}}^l(x)$, where $\exp\hat{\boldsymbol{\Psi}}^l = \mathbf{I} + \alpha\hat{\boldsymbol{\Psi}}^l + \beta(\hat{\boldsymbol{\Psi}}^l)^2$, $\alpha = \sin\Psi^l/\Psi^l$ and $\beta = (1-\cos\Psi^l)/(\Psi^l)^2$. The local rotation $\boldsymbol{\Psi}^l(x)$ is next interpolated in the standard Lagrangian way, where the local nodal rotations $\boldsymbol{\Psi}^l_i$ are extracted from $\exp\hat{\boldsymbol{\Psi}}^l_i = \boldsymbol{\Lambda}_I^T\boldsymbol{\Lambda}_i$.
The Newton–Raphson increment $\Delta\boldsymbol{\vartheta}$ has been found in the form $\Delta\boldsymbol{\vartheta} = \sum_{i=1}^{N}\mathbf{N}^i(\boldsymbol{\Lambda})\Delta\boldsymbol{\vartheta}_i$ with

$$\mathbf{N}^i = \sum_{j=1}^{N}\sum_{k=1}^{N}\Delta^{ij}_k\boldsymbol{\Lambda}_I\left\{\delta_{Ik}\left[\mathbf{I} - \mathbf{H}(\boldsymbol{\Psi}^l)\sum_{m=1}^{N} I_m\mathbf{H}^{-1}(\boldsymbol{\Psi}^l_m)\right] + \mathbf{H}(\boldsymbol{\Psi}^l)I_k\mathbf{H}^{-1}(\boldsymbol{\Psi}^l_j)\right\}\boldsymbol{\Lambda}_I^T \tag{2}$$

and $\mathbf{H}(\boldsymbol{\Psi}^l) = \mathbf{I} + \beta\hat{\boldsymbol{\Psi}}^l + \gamma(\hat{\boldsymbol{\Psi}}^l)^2$, $\gamma = \dfrac{\Psi^l - \sin\Psi^l}{(\Psi^l)^3}$, $\Delta^{ij}_k = 1$ for $i = j = k$ and $\Delta^{ij}_k = 0$ otherwise.

Helicoidal interpolation

The helicoidal interpolation [10] follows from a requirement that the finite-element solution should be invariant to the choice of the beam reference axis and consistent with the configuration space, in particular with $SO(3)$ and its core properties of orthogonality and unimodularity.

The FE solution will be invariant to the choice of the beam reference axis if the position vector and the rotation tensor are interpolated using the same interpolation functions [10, 11]. The simplest example of this, of course, is the standard Lagrangian interpolation for both fields

(i.e. $\mathbf{r}(x) = \sum_{i=1}^{N} I_i(x)\mathbf{r}_i$ and $\mathbf{\Lambda}(x) = \sum_{i=1}^{N} I_i(x)\mathbf{\Lambda}_i$) but, in the case of the rotation tensor, this interpolation is clearly inconsistent with the rotation group, since such a $\mathbf{\Lambda}(x)$ is neither orthogonal nor unimodular. To satisfy group consistence, Borri and Bottasso [10] have assumed a deformed configuration in a form of spatial helix originating from a constant distribution of the translational and the rotational strain measures along the beam and in this way derived an alternative interpolation of the type

$$\mathbf{r}(x_1) = \sum_{i=1}^{2} \mathbf{N}_i \mathbf{r}_i \qquad \text{and} \qquad \mathbf{\Lambda}(x_1) = \sum_{i=1}^{2} \mathbf{N}_i \mathbf{\Lambda}_i \;\; \Rightarrow \;\; \Delta\boldsymbol{\vartheta}(x_1) = \sum_{i=1}^{2} \mathbf{N}_i \Delta\boldsymbol{\vartheta}_i, \tag{3}$$

with the generalised interpolation functions $\mathbf{N}_i$ *identical to those given earlier*. It is important to emphasise, however, that the proposed helicoidal interpolation *makes sense only for two–noded elements*. For the cases of (uncoupled) constant bending and shearing (as well as, of course, constant axial force and torsional moment) this interpolation provides exact solution irrespective of the amount of loading and deformation.

If we attempted to apply this result to a higher–order element by simply substituting N for 2 in $(3)_1$, we would realise that the exact result, even in the limit case of the analysis becoming linear, cannot be achieved anymore. Still, such a solution is quite legitimate and in [11] it has been analysed numerically. To analyse the linear solution, it is instructive to isolate the linear part of the generalised interpolation $\mathbf{N}^i = I_i(\mathbf{I} + \widehat{\boldsymbol{\psi} - \boldsymbol{\psi}_i}/2)$ [11] and compare it to the interpolation representing the exact linear solution $\mathbf{N}^i = I_i(\mathbf{I} + \widehat{\boldsymbol{\psi} - \boldsymbol{\psi}_i}/N)$ [12].

The very close similarity between these results suggests that the original helicoidal interpolation may be generalised to higher order elements by applying a modification to the generalised interpolation $\mathbf{N}_i$ used for the interpolation of the positions. This avenue has been also pursued in [11]. It has to be noted that in this way the interpolation for the position vector again becomes different from the interpolation for the rotations thus spoiling the original requirement which the interpolation sought should provide, i.e. invariance of the solution with respect to the choice of the beam reference axis.

Fixed-pole approach

In [5] Bottasso and Borri thoroughly investigated the idea of replacing the stress-couple resultant $\mathbf{m}$ and the specific angular momentum $\boldsymbol{\pi}$ at the beam reference axis with another stress-couple resultant $\bar{\mathbf{m}}$ and specific angular momentum $\bar{\boldsymbol{\pi}}$, defined with respect to a unique point for the whole structure - the fixed pole, i.e. $\bar{\mathbf{m}} = \mathbf{r} \times \mathbf{n} + \mathbf{m}$ and $\bar{\boldsymbol{\pi}} = \mathbf{r} \times \mathbf{k} + \boldsymbol{\pi}$ if the origin of the spatial co-ordiante system is taken for the fixed pole. Substituting this into the earlier power-balance equation results in $\int_0^L (\bar{\mathbf{v}}' \cdot \mathbf{n} + \mathbf{w}' \cdot \bar{\mathbf{m}})\, dx + \int_0^L \left(\bar{\mathbf{v}} \cdot \dot{\mathbf{k}} + \mathbf{w} \cdot \dot{\bar{\boldsymbol{\pi}}}\right) dx = 0$, where $\bar{\mathbf{v}} = \mathbf{v} + \mathbf{r} \times \mathbf{w}$ is the velocity vector as seen by an observer rigidly attached to the frame rotating with the cross-section. Further, they defined six-dimensional fixed-pole velocity, stress-resultant and specific momentum vectors as

$$\boldsymbol{\omega} = \begin{Bmatrix} \bar{\mathbf{v}} \\ \mathbf{w} \end{Bmatrix}, \quad \mathbf{s} = \begin{Bmatrix} \mathbf{n} \\ \bar{\mathbf{m}} \end{Bmatrix}, \quad \mathbf{p} = \begin{Bmatrix} \mathbf{k} \\ \bar{\boldsymbol{\pi}} \end{Bmatrix}. \tag{4}$$

Choosing to interpolate $\boldsymbol{\omega}(x)$, an alternative nodal balance $\bar{\mathbf{g}}^{\mathrm{i}} \equiv \bar{\mathbf{q}}^{\mathrm{i}}_{\mathrm{i}} + \bar{\mathbf{q}}^{\mathrm{i}}_{\mathrm{m}} = \mathbf{0}$ is obtained with the following corresponding six-dimensional nodal internal and inertial force vectors

$$\bar{\mathbf{q}}^{\mathrm{i}}_{\mathrm{i}} = \int_0^L I^{\mathrm{i}\prime} \mathbf{s}\, dx \qquad \text{and} \qquad \bar{\mathbf{q}}^{\mathrm{i}}_{\mathrm{m}} = \int_0^{\mathrm{L}} I^{\mathrm{i}} \dot{\mathbf{p}}\, dx. \tag{5}$$

This result is interesting in its own right as it obviously by-passes the anomalous presence of shape-functions in the internal force vector, which are known to be responsible for shear locking. Additional consequence is that this set-up leads to a relatively simple satisfaction of the energy

and momentum conservation properties in discrete non-linear 3D beam dynamics without the need to re-parametrise the rotation field using tangent-scaled rotations as in [16].

The most striking of all, however, is the relationship between $\mathbf{w}$ and $\boldsymbol{\omega}$, which are not only the elements of a three-dimensional and a six-dimensional vector space, but are in fact elements of the vector spaces which are topologically equivalent to the three-dimensional Lie algebra of skew-symmetric tensors $so(3)$ and the six-dimensional Lie algebra of tensors of the form $\widetilde{\boldsymbol{\omega}} = \begin{bmatrix} \widehat{\mathbf{w}} & \widehat{\mathbf{v}} \\ \mathbf{0} & \widehat{\mathbf{w}} \end{bmatrix}$, which in [5] Bottasso in Borri have named $sr(6)$. Exponentiation of the elements of these algebras, of course, results in the corresponding elements of Lie groups, the Lie group $SO(3)$ of rotation tensors $\boldsymbol{\Lambda}$ and $SR(6)$, the so-called *Lie group of rigid motions* $\mathbf{C} = \begin{bmatrix} \boldsymbol{\Lambda} & \widehat{\mathbf{r}}\boldsymbol{\Lambda} \\ \mathbf{0} & \boldsymbol{\Lambda} \end{bmatrix}$. The system of non-linear equations may now be solved for the complete motion $\mathbf{C}$ using the Newton–Raphson solution procedure in which the linear part of the change in this unknown $\Delta\boldsymbol{\varsigma}$ (emerging from $\Delta\mathbf{C} = \widetilde{\Delta\boldsymbol{\varsigma}}\mathbf{C}$) may be interpolated in the same manner as $\boldsymbol{\omega}$ [14]. The parallels between the elements of $SO(3)$ and the elements of $SR(6)$ were investigated thoroughly in [5] where it was shown that the complete problem of motion of a 3D beam may be made mathematically equivalent to the problem of rotational motion of the 3D beam.

These results have been re-derived in detail in [14], where special emphasis has been placed onto objectivity of the formulations defined on $SR(6)$ which, owing to the parallels with the non-linear manifold $SO(3)$, naturally must suffer from the same short-comings. A remarkably similar result is obtained for the generalised interpolation that should be applied to $\Delta\boldsymbol{\varsigma}$ to provide the objective finite-element solution. The configuration tensor $\mathbf{C}(x)$ has been *multiplicatively* decomposed into a part constant for the whole beam and defined at a node I ($\mathbf{C}_I$) and the part due to a *local* configurational change $\boldsymbol{\Phi}^l$ with respect to that configuration as $\mathbf{C}(x) = \mathbf{C}_I \exp\tilde{\boldsymbol{\Phi}}^l(x)$ (see [5, 14] for details on exponentiation in $SR(6)$). The local configurational change $\boldsymbol{\Phi}^l(x)$ (which consists of the upper part $\mathbf{P}^\mathbf{l}$ and the lower part $\boldsymbol{\Psi}^l$) is next interpolated in the standard Lagrangian way, where the local nodal configurational changes $\boldsymbol{\Phi}^l_i$ are extracted from $\exp\tilde{\boldsymbol{\Phi}}^l_i = \mathbf{C}_I^{-1}\mathbf{C}_i$. It follows that $\Delta\boldsymbol{\varsigma} = \sum_{i=1}^N \mathbf{J}^i(\mathbf{C})\Delta\boldsymbol{\varsigma}_i$ with

$$\mathbf{J}^i = \sum_{j=1}^{N}\sum_{k=1}^{N}\Delta_k^{ij}\boldsymbol{C}_I\left\{\delta_{Ik}\left[\mathbf{I} - \mathbf{X}(\boldsymbol{\Phi}^l)\sum_{m=1}^{N} I_m\mathbf{X}^{-1}(\boldsymbol{\Phi}^l_m)\right] + \mathbf{X}(\boldsymbol{\Phi}^l)I_k\mathbf{X}^{-1}(\boldsymbol{\Phi}^l_j)\right\}\boldsymbol{C}_I^{-1}. \tag{6}$$

where $\mathbf{X}(\boldsymbol{\Phi}^l) = \begin{bmatrix} \mathbf{H}(\boldsymbol{\Psi}^\mathbf{l}) & \mathbf{B}(\mathbf{P}^\mathbf{l}, \boldsymbol{\Psi}^\mathbf{l}) \\ \mathbf{0} & \mathbf{H}(\boldsymbol{\Psi}^\mathbf{l}) \end{bmatrix}$, $\mathbf{B}(\mathbf{P}^l, \boldsymbol{\Psi}^l) = \beta\widehat{\mathbf{P}^l} + \frac{\alpha-2\beta}{\psi^2}\left(\mathbf{P}^l\cdot\boldsymbol{\Psi}^l\right)\widehat{\boldsymbol{\Psi}^l} + \frac{\beta-3\gamma}{\psi^2}\left(\mathbf{P}^l\cdot\boldsymbol{\Psi}^l\right)\widehat{\boldsymbol{\Psi}^l}^2 + \gamma\left(\widehat{\boldsymbol{\Psi}^l}\widehat{\mathbf{P}^l} + \widehat{\mathbf{P}^l}\widehat{\boldsymbol{\Psi}^l}\right)$.

Conclusions

The so-called objective, helicoidal and fixed-pole interpolations are reviewed and shown to possess many interesting similarities despite the fact that they have been developed with quite different demands in mind. The well-known equivalence between the rotational part of the mechanical problem of motion of a 3D flexible beam defined on $SO(3)$ and the complete motion defined on $SR(6)$ is shown to extend to the issue of objectivity of the finite-element solution with respect to the position of an observer allowing for a completely corresponding solution process.

Acknowledgements

Finanacial supports provided by the Croatian Science Foundation under the research project No. IP-11-2013-1631 *Configuration-dependent approximation in finite-element analysis of structures* and the University of Rijeka under the ongoing research programme No. 13.05.1.3.06 *Testing of slender spatial beam structures with emphasis on model validation* are gratefully acknowledged.

References

[1] J.C. Simo. A finite strain beam formulation. The three-dimensional dynamic problem. Part I. *Computer Methods in Applied Mechanics and Engineering*, 49:55-70, 1985.

[2] J.C. Simo and L. Vu-Quoc. A three-dimensional finite-strain rod model. Part II: Computational Aspects. *Computer Methods in Applied Mechanics and Engineering*, 58:79-116, 1986.

[3] A. Ibrahimbegović. Stress resultant geometrically nonlinear shell theory with drilling rotations – Part I. A consistent formulation. *Computer Methods in Applied Mechanics and Engineering*, 118(3-4):265–284, 1994.

[4] T. Merlini and M. Morandini. The helicoidal modeling in computational finite elasticity. Part I: Variational formulation. *International Journal of Solids and Structures*, 41(18-19):5351–5381, 2004.

[5] C. Bottasso and M. Borri. Integrating finite rotations. *Computer Methods in Applied Mechanics and Engineering*, 164:307-331, 1998.

[6] V. Sonneville, A. Cardona and O. Brüls. Geometrically exact beam finite element formulated on the special Euclidean group. *Computer Methods in Applied Mechanics and Engineering*, 268:451–474, 2014.

[7] G. Jelenić and M.A. Crisfield. Geometrically exact 3D beam theory: implementation of a strain-invariant finite element for statics and dynamics. *Computer Methods in Applied Mechanics and Engineering*, 171(1-2:141–171, 1999.

[8] P. Betsch and P. Steinmann. Frame-indifferent beam finite elements based upon the geometrically exact beam theory. *International Journal for Numerical Methods in Engineering* 54(12:1775–1788, 2002.

[9] D. Zupan and M. Saje. Finite-element formulation of geometrically exact three-dimensional beam theories based on interpolation of strain measures. *Computer Methods in Applied Mechanics and Engineering*, 192(49-50):5209–5248, 2003.

[10] M. Borri and C. Bottasso. An intrinsic beam model based on a helicoidal approximation — Part I: Formulation. *International Journal for Numerical Methods in Engineering* 37:2267-2289, 1994.

[11] E. Papa Dukić, G. Jelenić and M. Gaćeša. Configuration-dependent interpolation in higher-order 2D beam finite elements. *Finite Elements in Analysis and Design*, 78:47–61, 2014.

[12] G. Jelenić and E. Papa. Exact solution of 3D Timoshenko beam problem using linked interpolation of arbitrary order. *Archive of Applied Mechanics*, 81(2):171–183, 2011.

[13] M. Gaćeša and G.Jelenić. Modified fixed-pole approach in geometrically exact spatial beam finite elements. *Finite Elements in Analysis and Design*, 99:39–48, 2015.

[14] Gaćeša, M. *Fixed-pole concept in 3D beam finite elements – relationship to standard approaches and analysis of different interpolations.* Doctoral Thesis. University of Rijeka, 2015.

[15] J.C. Simo and L. Vu-Quoc. On the dynamics in space of rods undergoing large motions – a geometrically exact approach. *Computer Methods in Applied Mechanics and Engineering*, 66:125-161, 1988.

[16] J.C. Simo, N. Tarnow and M. Doblare, Non-linear dynamics of three-dimensional rods: Exact energy and momentum conserving algorithms. *International Journal for Numerical Methods in Engineering* 38(9):1431-1473, 1995.

Proceedings of the XII Finnish Mechanics Days
R. Kouhia, J. Mäkinen, S. Pajunen and T. Saksala (Eds.)

A stabilized, meshless method for the simulation of strongly coupled fluids and nonlinear solids

I. Romero

Technical University of Madrid, José Gutiérrez Abascal, 2, 28006 Madrid, Spain
IMDEA Materials Institute, Eric Kandel 2, 28906 - Getafe, Madrid, Spain
ignacio.romero@{upm.es,imdea.org}

Introduction

Strongly coupled fluid/solid interaction (FSI) problems arise in many important applications of Engineering. For example, in biomechanics, blood exerts a pressure on the wall of the heart which, reciprocally, distorts the flow. Also, aerodynamical forces bend and twist rotating blades in wind generators, and the later generate vortices behind the generators. In manufacturing, for instance, it is important to assess the interaction forces between a molten polymer and the molt employed for shaping it. In all these cases, the coupling between solid and fluid parts goes in both directions, and when studied numerically, the motions of the fluid and solid parts cannot be decoupled if accurate predictions are to be obtained.

Numerical methods for strongly coupled fluid and solids are fairly complex. A common approach consists in using standard solid and fluid solvers, independently, and define an interface that transfers forces between them (see, e.g., [1]). This kind of staggered solutions have the advantage of re-using existing, optimized codes for each of the parts, but are not guaranteed to be stable. These considerations have motivated the development of *monolithic* solutions to FSI problems. There is a fundamental difficulty in this approach, and it is based on the kinematic descriptions employed to approximate solid and fluid problems. In the first case, Lagrangian methods are required to trace the history of each material particle; in the latter, Eulerian method are more appropriate because they avoid the mesh distortions that would inevitably would result if the motion of each individual fluid particle had to be followed.

Although Arbitrary Lagrangian-Eulerian (ALE) formulations alleviate some of the problems associated with mesh distortion [2], we present next a novel formulation base on a purely Lagrangian description of both the solid and the fluid domain. This choice makes trivial the solution of the solid part, and addresses the problems derived from the mesh distortion in the fluid by avoiding it altogether, employing a meshless Galerkin method. More specifically, we use a Galerkin method with *local maximum entropy* functions [3] and improve its stability, for the incompressible fluid, by using a stabilization technique introduced by Douglas and Wang [4]. The outcome is a method that addresses all the major difficulties of simulating strongly coupled FSI problems, and shows promise to solve very complex situations.

Numerical method

We summarize the main ingredients of the numerical method proposed, starting from the initial boundary value problem we aim to solve, and outlying the choices made for its approximation

Problem description

The balance equations that describe the motion of fluids and solids are identical. For any body occupying a set $\mathcal{B}_0 \in \mathbb{R}^3$ in its reference configuration, a motion taking place on a time interval $[0, T]$ is a map $\boldsymbol{\varphi} : \mathcal{B}_0 \times [0, T] \to \mathbb{R}^3$, with $\boldsymbol{\varphi}_t(\cdot) = \boldsymbol{\varphi}(\cdot, t)$, defining the current placement $\boldsymbol{\varphi}_t(\mathcal{B}_0) = \mathcal{B}_t$, and with tangent map $\boldsymbol{F} = D\boldsymbol{\varphi}$ of determinant $J = \det(\boldsymbol{F})$. The balance of linear momentum, or equilibrium equation, is

$$\operatorname{div} \boldsymbol{\sigma} + \boldsymbol{f} = \rho \boldsymbol{a} \ , \tag{1}$$

where $\boldsymbol{\sigma}$ is Cauchy's stress, $\boldsymbol{f}$ is the body force, ρ the density, and $\boldsymbol{a} = \ddot{\boldsymbol{\varphi}} \circ \boldsymbol{\varphi}^{-1}$ the spatial acceleration. The only difference between solids and fluids is the constitutive law. Whereas solids might have complex relations between $\boldsymbol{\sigma}$ and the history of $\boldsymbol{F}$, incompressible newtonian fluids, the only type we consider, satisfy

$$\boldsymbol{\sigma} = 2\mu \ \operatorname{grad}^s \boldsymbol{v} - p\boldsymbol{I} \ , \qquad \operatorname{div} \boldsymbol{v} = 0 \ , \tag{2}$$

with μ, the dynamic viscosity, $\boldsymbol{v} = \dot{\boldsymbol{\varphi}} \circ \boldsymbol{\varphi}^{-1}$, the spatial velocity, and p, the pressure. The problem we are interested in solving is finding the deformation $\boldsymbol{\varphi}$ of all interacting solids and fluids, for all time, given an initial value $\boldsymbol{\varphi}_0$, initial velocity $\dot{\boldsymbol{\varphi}}_0$ and known external forces.

Approximation spaces

For all solids and fluids analyzed, we propose to employ a Galerkin discretization. In it, the main unknown field, the motion is approximated with a linear combination of known functions. In our case, we select a finite nodal set $\mathcal{N} = \{X_\alpha\}$ of points in $\mathcal{B}_0$ and functions $\phi^\alpha : \mathcal{B}_0 \to \mathbb{R}$ built only from the information of the nodal set. These *meshless* approximation functions are chosen to be optimal in the sense of locality and information entropy as defined in [3], and we approximate

$$\begin{aligned} \boldsymbol{\varphi}(\boldsymbol{X}, t) &\approx \boldsymbol{\varphi}^h(\boldsymbol{X}, t) = \sum_\alpha \phi^\alpha(\boldsymbol{X}) \boldsymbol{\varphi}_\alpha(t) \ , \\ \boldsymbol{v}(\boldsymbol{X}, t) &\approx \boldsymbol{v}^h(\boldsymbol{X}, t) = (\sum_\alpha \phi^\alpha(\boldsymbol{X}) \boldsymbol{V}_\alpha(t)) \circ (\boldsymbol{\varphi}^h(\boldsymbol{X}))^{-1} \ . \end{aligned} \tag{3}$$

Local maximum entropy entropy (*max-ent*) functions do not have an analytic expression. They can be computed, as well as their derivatives, at any point of the domain as the solution of a convex optimization problem. This makes them more expensive to calculate than other meshless functions, but they possess very attractive numerical properties, like for example a weak Kronecker-delta property on the boundary which greatly simplifies the imposition of essential boundary conditions.

Numerical method

The numerical method employed to approximate the dynamic equilibrium of any solid is completely standard (except for the choice of approximation space). Indeed, *max-ent* approximation functions seem to be locking-free and a standard Galerkin discretization of the governing equations suffices to obtain accurate solutions of elastic and inelastic models.

For fluids, however, the incompressibility constraint makes standard formulations unstable and some kind of stabilization must be employed. We advocate the use of the *absolutely stabilized formulation* of [4]. In this formulation, for a given time increment $\Delta t = t_{n+1} - t_n$, we seek for $\boldsymbol{\varphi}^h_{n+1}$ and P^h_{n+1} such that, with $p_{n+1} = P^h_{n+1} \circ (\boldsymbol{\varphi}^h_{n+1})^{-1}, \boldsymbol{v}_{n+1} = \boldsymbol{V}^h_{n+1} \circ (\boldsymbol{\varphi}^h_{n+1})^{-1}$ and $(\boldsymbol{\varphi}^h_{n+1} - \boldsymbol{\varphi}^h_n)/\Delta t = \boldsymbol{V}^h_{n+1}$,

$$\begin{aligned} \int_{\mathcal{B}_t} \rho \frac{\boldsymbol{v}_{n+1} - \boldsymbol{v}_n}{\Delta t} \cdot \boldsymbol{w} \, \mathrm{d}v + \int_{\mathcal{B}_t} 2\mu \ \operatorname{grad}^s \boldsymbol{v}_{n+1} \cdot \boldsymbol{w} \, \mathrm{d}v - \int_{\mathcal{B}_t} p_{n+1} \operatorname{div} \boldsymbol{w} \, \mathrm{d}v \\ + \int_{\mathcal{B}_t} q \operatorname{div} \boldsymbol{v}_{n+1} \, \mathrm{d}v + \mathrm{ST} = (\boldsymbol{f}_{n+1}, \boldsymbol{w})_t \end{aligned} \tag{4}$$

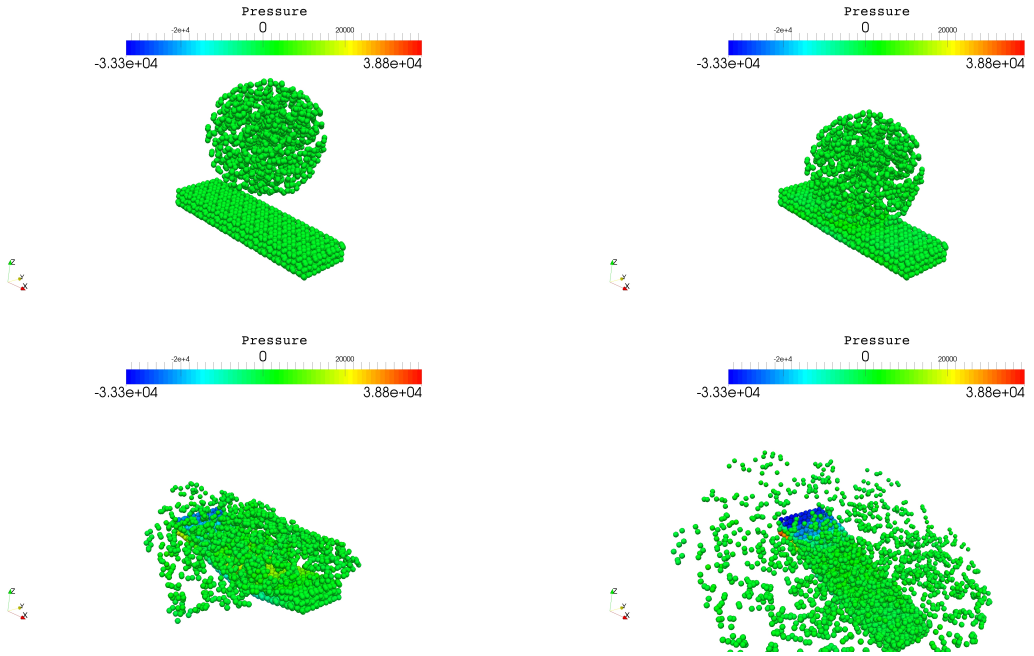

Figure 1. Fluid splashing on elastic plate

for all $\boldsymbol{W}^h = \boldsymbol{w} \circ (\boldsymbol{\varphi}^h)$ and $Q^h = q \circ (\boldsymbol{\varphi}^h)$. The the stabilization term is

$$\mathrm{ST} = \int_{\mathcal{B}_t} \tau(-2\mu \operatorname{div} \operatorname{grad}^s \boldsymbol{v}_{n+1} + \operatorname{grad} p_{n+1} - \boldsymbol{f}_{n+1})(-2\mu \operatorname{div} \operatorname{grad}^s \boldsymbol{w} + \operatorname{grad} q)\, \mathrm{d}v, \qquad (5)$$

where the stabilization parameter τ has dimensions of time and is chosen to be identical to that in stabilized finite elements (cf, e.g., [1]).

Simulations

The method outline heretofore allows to simulate in a unified way interactions between solids and fluids. For example, figure 1 shows four instants of the impact calculation between a fluid sphere of radius 1, density $\rho = 1000$ and dynamic viscosity $\mu = 10$ against a hyperelastic plate of dimensions $3 \times 1 \times 0.3$ with a Neohookean constitutive model of constants $\lambda = 0, \mu = 5 \cdot 10^6$. To model the contact between the two media, a simple point-to-point repulsion algorithm has been implemented.

The figures of this purely academic example illustrate that the method can encompass very large distortions in both the fluid and the solid, without any special modification. Even though in this simple example the solid material is purely elastic, no modification would have to be made in order to include inelastic effects in its behavior.

In a second example, depicted in figure 2, a dam breaks releasing all the contained fluid. This well-documented benchmark has been studied both numerically and experimentally [5], and serves as a testbed to assess the ability of a method to simulate fluids with large distortions.

Closure

A unified approach to solve complex fluid/solid interaction problems has been presented. The formulation is purely Lagrangian, so the interaction and the treatment of free surfaces is trivial. To avoid all the issues associated with using mesh-based methods when the mesh reaches high distortions, a meshless approach has been followed. In particular, local *max-ent* functions have been chosen due to the ease with which essential boundary conditions can be imposed. A final

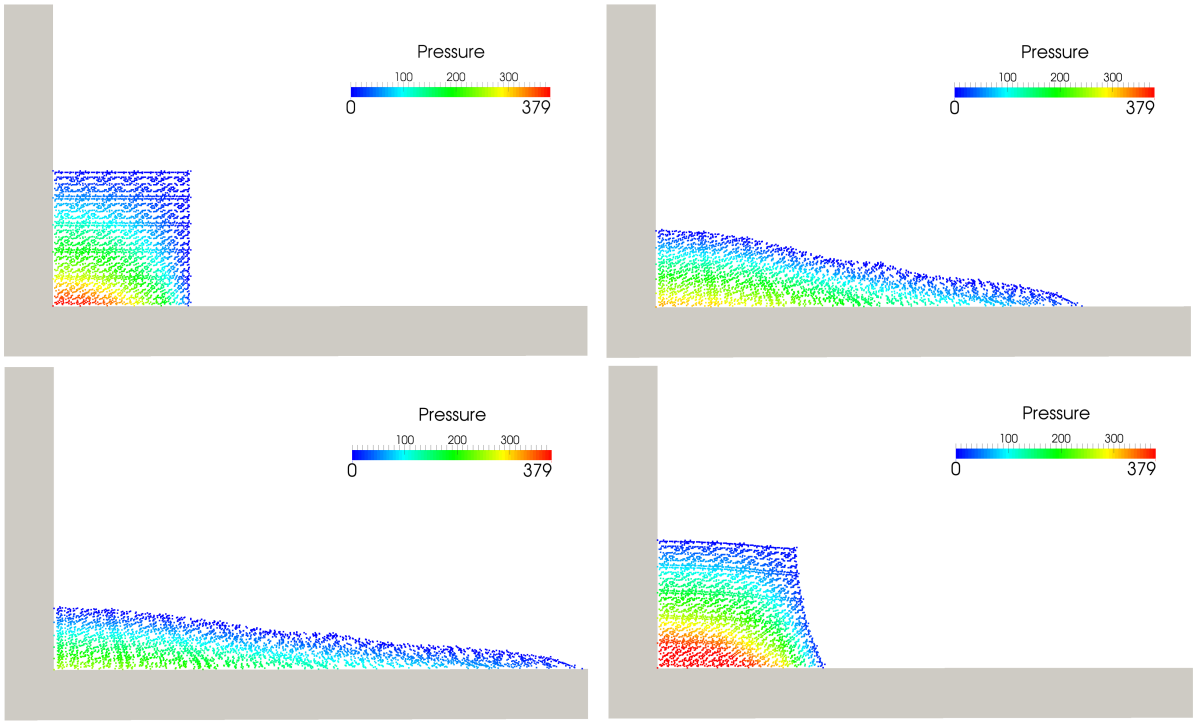

Figure 2. Dam breaking

ingredient of the framework is the stabilization of the fluid equations to deal with the instabilities arising from the incompressibility constraint. An *absolutely stabilized* formulation was employed that guaranteed the stability of the method even in the nonlinear range.

References

[1] Axel Gerstenberger and Wolfgang A Wall. An eXtended Finite Element Method/Lagrange multiplier based approach for fluid–structure interaction. *Computer Methods in Applied Mechanics and Engineering*, 197(19-20):1699–1714, March 2008.

[2] J Donea, A Huerta, and J P Ponthot. Arbitrary Lagrangian-Eulerian methods. In E Stein, R de Borst, and T J R Hughes, editors, *Encyclopedia of Computational Mechanics*. John Wiley & Sons, 2004.

[3] M Arroyo and M Ortiz. Local maximum-entropy approximation schemes: a seamless bridge between finite elements and meshfree methods. *International Journal for Numerical Methods in Engineering*, 65:2167–2202, 2006.

[4] J Douglas and J Wang. An Absolutely Stabilized Finite-Element Method for the Stokes Problem. *Mathematics of Computation*, 52(186):495–508, April 1989.

[5] J C Martin and W J Moyce. Part IV. An Experimental Study of the Collapse of Liquid Columns on a Rigid Horizontal Plane. *Philosophical Transactions of the Royal Society of London. Series A, Mathematical and Physical Sciences*, 244(882):312–324, March 1952.

Proceedings of the XII Finnish Mechanics Days
R. Kouhia, J. Mäkinen, S. Pajunen and T. Saksala (Eds.)

Challenges of climatic changes for coastal engineering

Tarmo Soomere
Estonian Academy of Sciences and Institute of Cybernetics at Tallinn University of Technology, Estonia

Summary. This lecture will focus on recently identified changes in wind and wave properties over the Baltic Sea basin that may considerably affect processes of all kind in the nearshore, coastal floodings etc., and also impact inland constructions. Along with common parameters characterising climatic changes (such as air or water temperature, extension in the ice cover, changes in the precipitation etc.), many dynamical features are strongly determined by wind direction. The related changes to the extreme water levels and associated coastal floodings, wave properties and the level of exposure of the nearshore area to various hydrodynamic loads may have substantial consequences for the course of coastal processes, safety issues and engineering activities. The changes that involve alteration of the wind properties may lead to drastic impact on the entire ecosystem. For example, irregular inflows of oxygen-rich North Sea water (that support life in the deeper layers of the Baltic Sea) have almost stopped since 1980s eventually because of changes in the air pressure and wind patterns.

I make an attempt to consolidate results of recent studies into wave properties and the course of coastal processes in the Baltic Sea in the light of the resulting challenges for various coastal engineering issues. The existing instrumental measurements since the 1970s, several numerical reconstructions of wave field and re-analysis of the longest visually observed wave data since the 1940s reveal rich patterns of spatio-temporal variations, mostly on a decadal scale, in the wave heights and propagation directions in various part of the Baltic Sea. The consequences of these variations include modifications in the pattern of alongshore sediment transport, alterations of the locations of substantial wave-induced set-up (and potential extreme water levels), and the loss of stability of certain sedimentary coastal segments. A likely reason behind many of these changes may be a major shift in the atmospheric forcing: an abrupt turn in the geostrophic air flow over the southern Baltic Sea by about 40 degrees since the 1980s. The implications of this turn extend to the latitudes of the Gulf of Finland where the sea-level air flow also exhibits extensive fluctuations.

Proceedings of the XII Finnish Mechanics Days
R. Kouhia, J. Mäkinen, S. Pajunen and T. Saksala (Eds.)

The effects of initial moisture on damp problems of a timber framed wall construction – a numerical approach

Filip Fedorik[1], Mikko Malaska[2]

(1) Structural Engineering and Construction Technology, University of Oulu, P.O.Box 4200, FI-90014, Oulu, Finland, fedorikfilip@gmail.com
(2) Structural Engineering and Construction Technology, University of Oulu, P.O.Box 4200, FI-90014, Oulu, Finland, mikko.malaska@oulu.fi

Summary. The presented study deals with simulation of thermal and moisture transfer in timber element located above foundation of a timber-framed family house. The bottom location of a building represents sensitive component for damp problem. Providing careful attention to each structural element, especially at the initiation of the construction, to protect it against redundant moisture to ensure sustainability of the structure and health indoor environment form integral part of the design. Moisture content at any element of the building might significantly effects the life-span of the structure.

Key words: heat and mass transfer, numerical simulation, mould index, foundation

Introduction

Effort towards energy efficiency in building engineering supports a creativity of designers to provide new construction techniques and procedures to ensure maximal thermal resistance of the structures and health indoor environment [4]. The present policy is to promote low-energy high-closure housing [12]. Building practises attempts to control structural contamination by mould spores, preventing of moisture build-up and absorption, or design guidelines. The excellent thermal performance of current buildings brings another phenomena along that should be considered in the design. High air tightness causes less heat outflow which leads to the lowering energy costs but it might effect moisture conditions in the envelope and cause favourable environment for mould growth initiation. One of the most threatened locations for moisture problems is at the bottom of the buildings, especially between foundations and the envelope [7]. In the case, the structural elements are not carefully protected against ambient moisture the saturation level might significantly influence properties of the subjected materials and effect future behaviour of the structural elements and reduce the life-span of the building. Especially in the case of timber-framed houses the damp problem increases considering sensitivity of wooden materials from the point of view of suitable bio-base for mould growth. This is why it might be beneficial to control the physical conditions of the structural elements before and while constructing the building [1].

The presented study simulates thermal and moisture conditions of a bottom timber plate installed above foundation in the cases where the timber is initially fully saturated and dry. For achieving limits of the humidity conditions in the timber the analysis is performed in its radial and longitudinal direction. The analysed structure is illustrated at the Figure 1. The temperature and relative humidity data are taken at corners of the bottom timber plate (points 1-4 at Figure 1.) and in its entire cross-section. Then, the obtained results are applied in a mould growth risk model [5-6, 9-11].

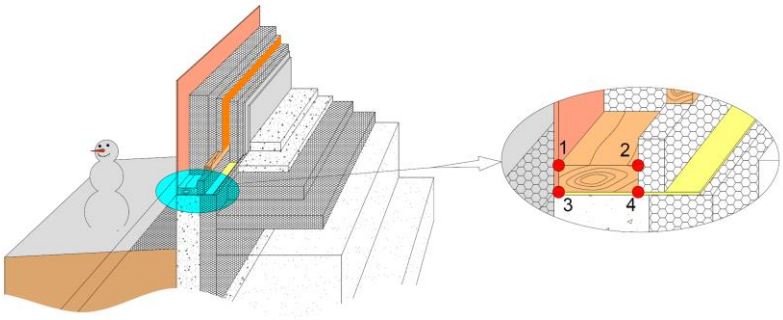

Figure 1. Structure of foundation and location of analysed points

Numerical model and boundary conditions

Two-dimensional numerical models were created in Wufi®2D representing structure of a foundation of a single family timber-framed house. The Wufi program uses finite volumes method for realistic calculation of the transient coupled one- and two-dimensional heat and mass transfer problems [3]. Wufi material library is used for material properties definition of each applied element. The simulations suggest outdoor conditions without effect of standing water and/or snow. The indoor conditions within the model that simulates foundation of the complex structure are defined according to EN 13788.

The presented study analyses effect of weather conditions on initially fully saturated and dry bottom timber plate in the foundation model. The simulation was performed for a time period from 1.1.2014 to 11.1.2015. The weather data, representing the outdoor conditions for the numerical model, were measured by weather station located in Hiukkavaara/Oulu/Finland. The temperature and relative humidity conditions in the period are illustrated at the Figure 2 below:

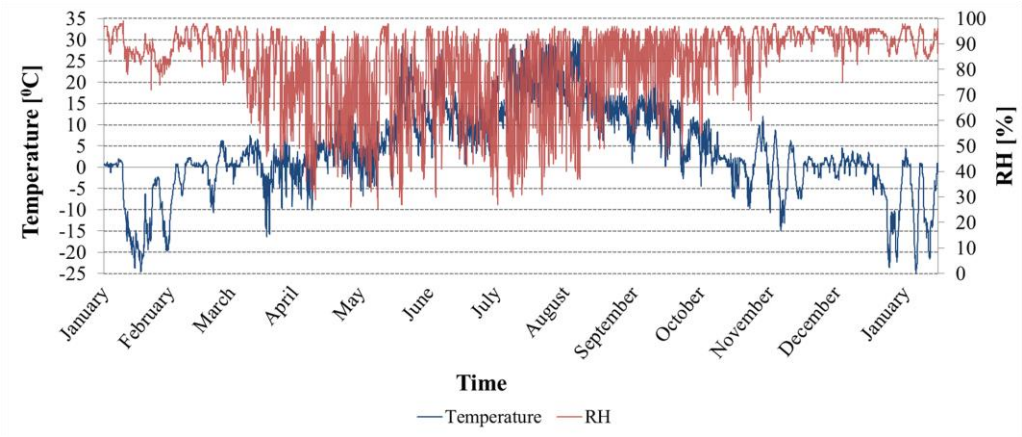

Figure 2. Weather conditions during analysed period

Mould growth

Specific combinations of temperature and relative humidity promote mould growing which may lead to allergic reactions and other health issues of the inhabitants [5], and which may also influence the behaviour and properties of the structural elements [8]. Numerous studies present mathematical models expressing the risk of mould growth based on environmental factors [9]. The boundary between favourable and unfavourable conditions for mould growth initiation was defined [2, 5, 6, 9-11]. Its graphical expression is illustrated at the Figure 3:

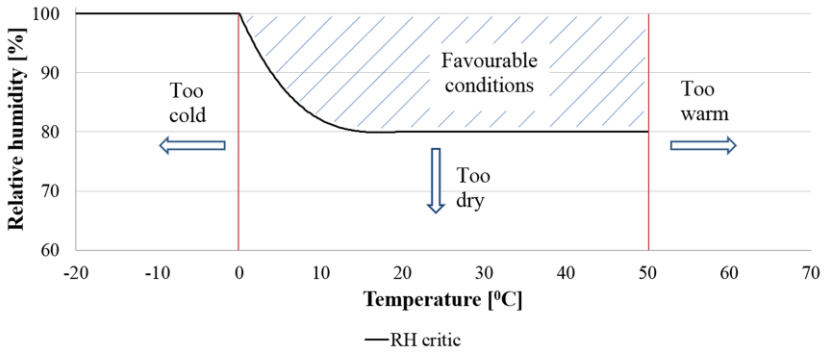

Figure 3. Graphical expression of critical relative humidity for mould growth initiation

The mathematical models defining the mould growth risk are based on the relation between temperature and relative humidity in an exposed time. It is based on long-term laboratory tests or on-site measurements [5, 6].

The following figure (Figure 4) illustrates mutual relation between temperature and relative humidity at each time-step of the solution of outdoor conditions. It can be seen that inconsiderable amount of the conditions are in the favourable area for mould growth initiation.

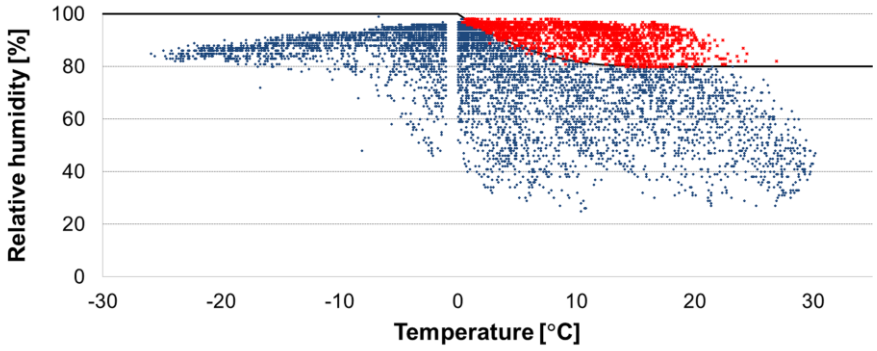

Figure 4. Favourable and unfavourable conditions for mould growth initiation

Results and discussion

The relative humidity conditions in the bottom horizontal timber plate is shown at the Figure 5. In the case the timber is initially fully saturated the drying process progresses very slowly. Hence, the relative humidity might lead to the favourable conditions for mould growth. The

humidity in the initially dried timber copies the trend of the outdoor humidity. If the characteristics for the longitudinal moisture diffusion in the timber is applied the relative humidity trend achieves larger differences. This is caused by ability of quicker drying and absorption of the humidity in the material.

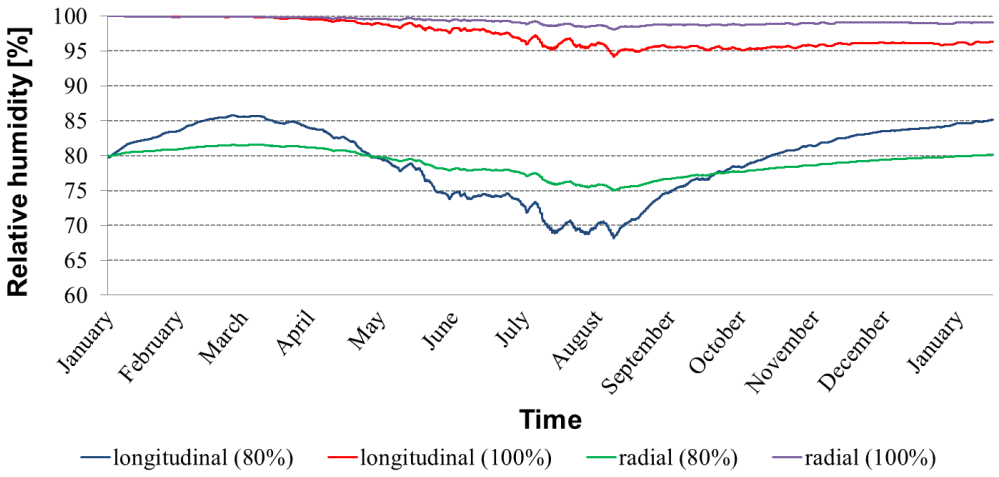

Figure 5. Relative humidity in timber during analysed period

Statistical expression of the conditions in the favourable environment for mould growth at the corners of the timber are shown in the Table 1. The initially fully saturated cases achieve high percentage of the favourable conditions for mould growth during the analysed period. Although, there is an assumption the higher water vapour diffusion resistance factor of cross grain (radial) direction of the timber would cause slowing-down the drying process it achieves slightly less conditions in the favourable area for mould growth. However, the full saturation at the beginning of the analysis, regardless direction of grains causes high water content in the timber that might lead to the mould growing and significant reducing of the life-span of the structure. The least amount of conditions in the favourable environment for mould growth is in the case of the initially dried timber. This is caused by lower relative humidity in ambient and inside of the timber which leads to the conditions located outside the favourable conditions for mould growth initiation.

Table 1 Environmental conditions promoting mould growth in corners of timber

location / case	left-up [%]	left-down [%]	right-up [%]	right-down [%]
longitudinal (80%)	9.57	10.01	1.28	7.99
longitudinal (100%)	26.75	30.39	80.98	73.54
radial (80%)	12.48	14.34	0.14	15.85
radial (100%)	20.03	23.03	71.09	70.83

Preliminary estimation for mould growth initiation represented by the mould index is shown at the Figure 6. It can be seen the lowest risk for mould growth initiation is on the left (exterior) side of the timber. This is caused by negative temperature values during the simulation period which prevents the biological processes to initiate. On the other hand, the right side of the timber is subjected to an extended drying process of the material, which might be critical from the point of view of the mould growth initiation.

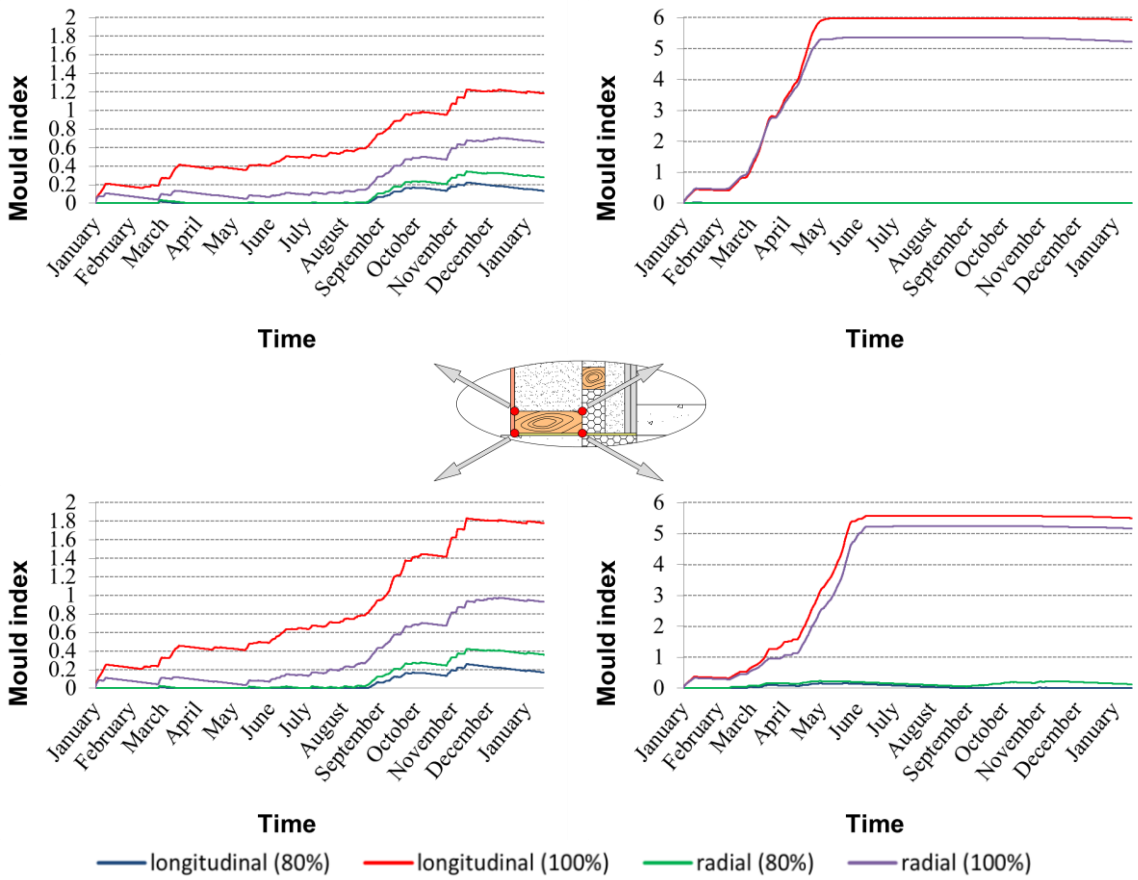

Figure 6. Mould index at corners of timber

In the case of the initially fully saturated timber the mould index achieves values which might estimate high risk for mould growth initiation. It might be beneficial being cautious and provide substantial care of the structural material during the entire construction and the life-span of the structure to prevent water and vapour content in the material.

Conclusion

The presented study shows advantages of the numerical analysis in practical problems, i.e. building physics problems. The Wufi®2D software was applied to simulate heat and mass transfer of multi-layer structure representing foundation of timber-framed house. Effect of the initial saturation of the bottom timber plate located above foundation was analysed depending on grain direction. The initial water content in the building material might lead to a damp problem and significantly effect durability and life-span of the structural elements or the building. It is important to provide careful attention to each structural element at any time of the construction to protect it against redundant moisture to ensure sustainability of the structure and health indoor environment.

References

[1] Fedorik F., Illikainen K., HAM and Mould Growth Analysis of a Wooden Wall, *International Journal of Stustainable Built Environment (IJSBE)*, ISSN: 2212-6090, 2013

[2] Hukka A., Viitanen, H.A., A mathematical model of mould growth on wooden material, Wood Science and Technology, 33, 475-485, 1999

[3] Künzel H.M., Simultaneous Heat and Moisture Transport in Building Components, One- and two- dimensional calculation using simple parameters, Fraunhofer IRB Verlag Suttgart, ISBN: 3-8167-4103-7, 1995

[4] Mudarri D., Fish W.J., Public Health and Economic Impact of Dampness and Mold, *Indoor Air Journal*, 17, 226-235, 2007

[5] Ojanen T., Peuhkuri R., Viitanen H., Lähdesmäki K., Vinha J., Salminen K., Classification of material sensitivity - New approach for mould growth modeling, Paper at the *9th Nordic Symposium on Building Physics - NSB 2011*, Tampere, Finland, 2011

[6] Peuhkuri R., Viitanen H., Ojanen T., Modelling of Mould Growth in Building Envelopes, paper *Porto 2007* Working meeting

[7] Pirinen J., Building Inspections in Finland – Fighting Against the Moulds, Moisture and Mould Programme, *Nordic Building Physic Symposium*, 2011

[8] Singh J., Fungal Problems in Historic Buildings, *Journal of Architectural Conservation*, 6(1), 17-37, doi: 10.1080/13556207.2000.10785259, 2014

[9] Viitanen H., Toratti T., Makkonen L., Peuhkuri R., Ojanen T., Ruokolainen L., Räisänen J., Towards modelling of decay risk of wooden materials, Published online: 9 June 2010

[10] Viitanen H., Vinha J., Salminen K., Ojanen T., Peuhkuri R., Paajanen L., Lähdesmäki K., Moisture and Bio-deterioration Risk of building Materials and Structures, *Journal of Building Physics*, vol. 33, no. 3, doi: 10.1177/1744259109343511, 2010

[11] Vinha J., Laukkarinen A., Mäkitalo M, Nurmi S., Huttunen P., Pakkanen T., Kero P., Manelius E., Lahdensivu J., Köliö A., Lähdesmäki K., Piironen J., Kuhno V., Pirinen M., Aaltonen A., Suonketo J., Jokisalo J., Teriö O., Koskenvesa A., Palolahti T., Effects of Climate Change and Increasing of Thermal Insulation on Moisture Performance of Envelope Assemblies and Energy Consumption of Buildings, Research report 159, Tampere University of Technology, Department of Civil Engineering, Structural Engineering, 2013

[12] Euro 2010, Directive 2010/31/EU on the energy performance of buildings, 2010

Suomen XII mekaniikkapäivien esitelmät
R. Kouhia, J. Mäkinen, S. Pajunen ja T. Saksala (toim.)

Numeerisen virtauslaskennan käyttö tuulikuormien määrittämisessä

Juha Soini ja Jussi Jalkanen

Sweco Rakennetekniikka Oy, Hatanpään valtatie 11, 33100 Tampere
juha.soini@sweco.fi ja jussi.jalkanen@sweco.fi

Tiivistelmä. Artikkelissa esitellään numeerisen virtauslaskennan käyttömahdollisuuksia rakennusten tuulikuormien määrittämisessä. Aluksi on käyty läpi tuulikuormiin vaikuttavia tekijöitä. Artikkelissa sovelluskohteina ovat olleet Silsoen kuutio ja Helsingin Olympiastadionin päätykatsomoiden katokset.

Avainsanat: tuulikuormat, CFD, tuulitekniikka

Johdanto

Tuulikuormat ovat merkittävässä roolissa etenkin rakennuksen jäykistysjärjestelmän suunnittelussa ja mitoituksessa. Tavallisesti tuulikuormat määritetään normeissa esitetyillä erilaisiin kokeellisesti määritettyihin ja taulukoituihin arvoihin perustuvilla menetelmillä, jotka pätevät ainoastaan rajoitetulle joukolle perustapauksia. Monimutkaisemmissa tapauksissa tuulikuormia ei voi määrittää suoraan normeissa esitetyillä menetelmillä.

Tuulikuormien tutkimus ja tuulitekniikka (wind engineering) on perustunut lähes täysin tuulitunneleissa pienoismalleille tehtyihin mittauksiin. Viime vuosina tapahtunut laskentamenetelmien ja tietokoneiden laskentakapasiteetin kehitys on laajentanut numeerisen virtauslaskennan (computational fluid dynamics, CFD) käyttömahdollisuuksia yleisesti virtaustekniikan sovellutuksissa ja siten myös tuulikuormien analysoinnissa.

Työssä keskitytään osa-alueisiin, joiden vaikutusten arviointiin CFD-laskentaa voidaan hyödyntää. Kokonaiskuvan hahmottamiseksi tehdään myös lyhyt katsaus koko prosessiin, jonka mukaan tuulikuormat määräytyvät. Davenportin tuulikuormitusketjun (Kuva 1) mukaisesti tuulikuormien määrittämisessä on tärkeää kiinnittää huomiota kaikkiin prosessin vaiheisiin. Yksittäisen osa-alueen tarkempi analysointi ei tavallisesti johda oleellisesti tarkempaan lopputulokseen. Kaiken kaikkiaan aihealue on poikkitieteellinen ja haastava.

Tuulikuormista

Rakenteen suunnittelussa käytettävä tuulikuorma tulisi valita siten, että sen ylittymisen todennäköisyys rakennuksen suunniteltuna käyttöaikana on riittävän pieni. Suomessakin suunnitteluohjeena käytettävän eurokoodin mukaan suunnittelussa lähtökohtana oleva tuulikuorma ylittyy keskimäärin kerran 50 vuodessa, [3]. Rakenteen kestävyyden näkökulmasta

ollaan siis kiinnostuneita hyvin harvoin toistuvista kovista myrskyistä. Tuulikuormitusnormeissa esitetyt menetelmät mallintavat laaja-alaisiin ja melko pitkäkestoisiin myrskyihin liittyviä tuulikuormia. Paikallisten meteorologisten ilmiöiden kuten ukkosmyrskyjen aiheuttamien tuulikuormien laskentaan ei anneta tuulikuormitusnormeissa erillisiä ohjeita.

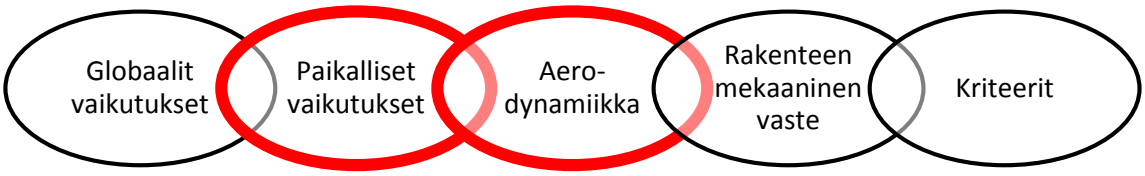

Kuva 1. Davenportin tuulikuormitusketju, johon on korostettu lenkit, joiden vaikutuksien arviointiin voidaan hyödyntää virtauslaskentaa.

Tuulikuorman suuruuteen vaikuttavat seuraavat tekijät: (i) rakennuspaikan globaali tuulisuus, (ii) maanpinnanmuodot, (iii) ympäröivät rakennukset, (iv) maaston pinnankarheus, (v) kuormitusalueen pinta-ala ja (vi) rakennuksen dynaamiset ominaisuudet. Rakennuspaikan maantieteellisestä sijainnista riippuva globaali tuulisuus sisältää alueen pitkän aikavälin säätilastoihin perustuvan ns. tuulennopeuden perusarvon (Suomessa 21 m/s). Maan pinnanmuodot, kuten mäet, vaikuttavat tuulen nopeusprofiiliin. Ympäröivät rakennukset toisaalta suojaavat tuulelta, mutta lähellä sijaitseva ympäristöään selvästi korkeampi rakennus voi myös kasvattaa viereisten rakennusten tuulikuormaa. Maanpinnan rosoisuudella on merkittävä vaikutus tuulikuormaan. Sileässä maastossa (esim. meren läheisyydessä) tuulen nopeus maanpinnan lähellä on suurempi kuin rosoisemmassa maastossa (esim. kaupungeissa). Toisaalta maanpinnan rosoisuus kasvattaa turbulenssin intensiteettiä eli tekee tuulesta puuskaisempaa. Kuormitetun pinta-alan kasvaessa siihen kohdistuva tuulikuorma ei kasva yhtä nopeasti, koska suuren pinnan eri osissa pintapaineen ääriarvot eivät esiinny yhtä aikaa.

Mitoituksessa käytettävä tuulikuorman arvo perustuu tuulenpuuskan aiheuttamaan pintapaineeseen. Tuulenpuuskassa vaikuttava tuulen nopeus määritetään korottamalla 10 minuutin keskimääräistä tarkasteltavalla korkeudella vaikuttavaa tuulen nopeutta puuskakertoimella. Puuskakerroin määritetään huippuarvokertoimen ja tuulen turbulenssin intensiteetin perusteella. Puuskakerroin on maaston pinnankarheudesta riippuen noin 1,4 - 2,0.

Rakenteita mitoitettaessa käsitellään tyypillisesti suurinta tuulenpainetta. Tämän lisäksi hoikilla rakenteilla on kiinnitettävä huomiota aeroelastisiin ilmiöihin ja tuulen herättämään värähtelyyn. Nämä ilmiöt voivat tulla mitoittaviksi alhaisillakin tuulennopeuksilla.

Virtauslaskenta tuulitekniikassa

Virtausta hallitsevien epälineaaristen osittaisdifferentiaaliyhtälöiden eli ns. Navier-Stokes –yhtälöiden advektiotermit käyttäytyvät hyvin epälineaarisesti ja tekevät numeerisesta ratkaisusta hankalaa. Laskentatyön vähentämiseksi virtauksen turbulenttisuus voidaan huomioida keskiarvottamalla yhtälöt (Reynolds-averaged Navier-Stokes, RANS), jolloin yhtälöihin tulee kuitenkin uusia tuntemattomia (Reynoldsin jännitykset). Ongelman ratkaisemiseksi tarvitaan turbulenssimalli eli lisäyhtälöt, jotka ovat kytköksissä RANS-yhtälöiden kanssa. Turbulenssimallit perustuvat osittain kokeisiin, eikä ole olemassa yhtä turbulenssimallia, joka antaisi hyviä tuloksia kaikissa virtaustapauksissa.

Vaihtoehtoinen turbulentin virtauksen laskentatapa on suurten pyörteiden simulointi (large eddy simulation, LES). Siinä kontrollitilavuutta suuremmat pyörteet lasketaan tarkasti ja

pienemmille pyörteille käytetään turbulenssimallia. Menetelmällä todellista virtausta pystytään kuvaamaan yleensä selvästi tarkemmin kuin RANS-laskennalla, mutta se vaatii aina kolmiulotteisen ja transientin analyysin ollen siten hyvin laskentaintensiivinen. LES ei ole vielä nykyään realistinen vaihtoehto useimmissa käytännön virtaustehtävissä.

Tuulitekniikan virtaustehtävissä on seuraavia erityispiirteitä: i) rakenteen kohtaava virtaus on valmiiksi voimakkaasti turbulenttia ja sisältää paljon erikokoisia pyörteitä, ii) Reynoldsin luku on hyvin suuri ja virtaus voidaan olettaa yleensä aina turbulentiksi, iii) ilmakehän rajakerros voidaan olettaa termisesti neutraaliksi, koska kovissa tuulissa mekaaninen turbulenssi dominoi, iv) maaston pinnankarheus on mittakaavaltaan hyvin suurta verrattuna moniin muihin virtaustehtäviin, v) rakennukset ovat massiivisia (bluff body) ja sisältävät teräviä nurkkia. Tyypillisiä tuulitekniikassa ilmeneviä virtaustilanteita ovat puolestaan: vi) virtauksen törmääminen seinään, vii) virtauksen irtoaminen ja viii) uudelleen kiinnittyminen.

Virtauslaskentaohjelmistoissa pinnankarheus mallinnetaan ekvivalenttisena hiekanjyväkarheutena, mikä aiheuttaa ongelmia tuulitekniikan sovelluskohteissa. Tyypillisen kaupunkialueen maanpinnan rosoisuus $z_0 = 0{,}3$ m on ekvivalenttiseksi hiekanjyväkarheudeksi muutettuna yli 8 m. Ensimmäisen laskentapisteen etäisyys maanpinnasta tulisi olla vähintään hiekanjyväkarheuden suuruinen, mutta toisaalta hyvien tulosten saavuttamiseksi laskentaverkon pitää olla huomattavasti tätä tiheämpi. Lisäksi valitun turbulenssimallin tulisi kyetä säilyttämään haluttu nopeusprofiili sekä turbulenssisuureiden (turbulenssin kineettinen energia ja sen dissipaatio) profiilit virtaussuunnassa muuttumattomina tyhjässä laskenta-alueessa. Pinnankarheuden mallintamista ja profiilien säilymistä on käsitelty tarkemmin lähteessä [1].

Silsoen kuution painekertoimien määrittäminen

Numeerisen virtauslaskennan käyttökelpoisuuden selvittämiseksi sitä on aluksi sovellettu yksinkertaiseen ja hyvin dokumentoituun Silsoen kuutioon, [4]. Täyden mittakaavan kokeita varten rakennettu sivumitaltaan 6 metrinen kuutio on sijoitettu käännettävälle alustalle. Maasto rakennuksen ympärillä on suhteellisen tasaista vastaten parhaiten eurokoodin maastoluokkaa 1. Vaikka kuutio vaikuttaakin geometrialtaan varsin yksinkertaiselta todellisiin rakennuksiin verrattuna, ilmenee siinä olennaisimmat tuulitekniikan virtaustekniset erityispiirteet.

Stationaarissa RANS-laskennassa turbulenssimallina on käytetty SST k-ω –mallia lähteen [6] mukaan muokatuilla paremmin tuulitekniikkaan soveltuvilla parametreilla. Advektiotermin diskretointiin on käytetty tarkkuudeltaan toisen kertaluvun menetelmää ja seinämänkäsittelyksi on valittu automaattinen seinämäfunktio. Laskentaohjelmistona käytettiin Ansys CFX 15.0 ja rakenteellisessa laskentaverkossa oli 1,8 miljoonaa kontrollitilavuutta. Laskenta on tehty myös tiheämmällä (8,3 milj.) ja harvemmalla (0,8 milj.) verkolla. Täyttä riippumattomuutta laskentaverkosta ei saavutettu, mutta tästä aiheutuva virhe arvioitiin pieneksi verrattuna turbulenssimallista aiheutuviin virheisiin.

Tulosten voidaan todeta vastaavan hyvin kirjallisuudessa esitettyjä laskennallisia arvoja (Kuva 2). Taulukossa 1 on vertailtu painekertoimia tuulieurokoodin [3] mukaisissa lohkoissa A-I. Taulukossa asteluvut tarkoittavat tuulen suuntaa siten, että 0° vastaa kohtisuoraan kuution seinään puhaltavaa tuulta. Tuloksista nähdään, että eurokoodin arvot ovat itseisarvoltaan suurempia tuulitunnelikokeiden [5] tuloksiin ja tämän tutkimuksen CFD-analyysin tuloksiin verrattuna lukuun ottamatta lohkoa I (katon alavirranpuoleinen puolikas), jossa eurokoodin mukaan vaikuttaisi selvästi pienempi alipaine.

Tunnetusti virtauslaskennalla saadaan tarkimpia tuloksia tuulenpuoleiselle seinälle, katon ja sivuseinien tulosten erotessa eniten kokeellisista arvoista. Eroavaisuudet esimerkiksi katon tuloksissa johtunevat enimmäkseen käytetyn turbulenssimallin virheistä virtauksen irtoamis- ja uudelleenkiinnittymisalueilla.

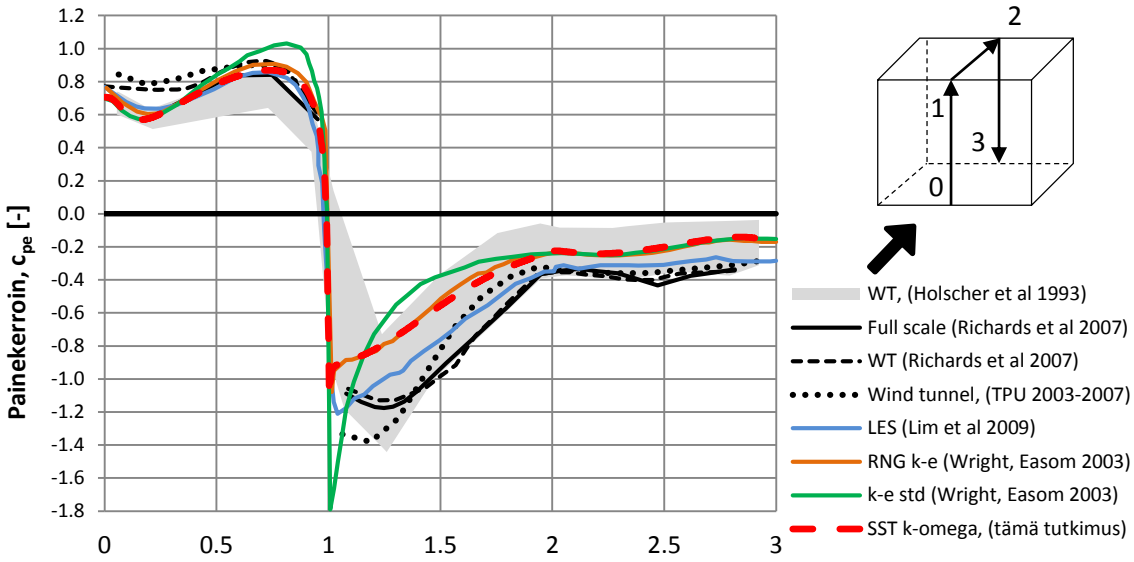

Kuva 2. Silsoen kuution painekertoimet ja vertailu kirjallisuudesta esitettyihin tuloksiin [2].

Taulukko 1. Silsoen kuution painekertoimet tuulilohkoittain (negatiivinen arvo alipainetta).

Lohko	A	B	D	E	F	G	H	I
Lohkon suhteellinen ala [%]	20	80	100	100	2,5	5	40	50
CFD, SST k-ω, 0°	-0,76	-0,45	0,58	-0,21	-1,01	-0,94	-0,73	-0,35
TPU tuulitunneli [5], 0°	-1,10	-0,69	0,70	-0,35	-1,51	-1,36	-1,14	-0,47
CFD, SST k-ω, 45°	-0,34	-0,38	0,34	-0,37	-1,70	-1,13	-0,47	-0,42
TPU tuulitunneli, 45°	-0,47	-0,54	0,33	-0,52	-1,20	-1,28	-0,63	-0,50
EN 1991-1-4 [3]	-1,20	-0,80	0,80	-0,50	-1,80	-1,20	-0,70	-0,20/+0,20
CFD, SST k-ω, -45° - 45°	-0,76	-0,45	0,58	-0,37	-1,70	-1,13	-0,73	-0,42
TPU tuulitunneli, -45° - 45°	-1,10	-0,73	0,70	-0,52	-1,74	-1,43	-1,14	-0,50

Helsingin Olympiastadionin tuulikuormien arviointi

Varsinaisena sovelluskohteena työssä on ollut Helsingin Olympiastadionin uudet teräskatokset. Peruskorjauksen yhteydessä kaarteiden katsomot katetaan ja näiden katoksien alustavassa rakennesuunnittelussa on käytetty virtauslaskennalla määritettyjä tuulikuormia. Lopullisia rakennesuunnittelussa käytettäviä tuulikuormia varten tehdään pienoismalleilla mittauksia Aalto-yliopiston tuulitekniikkatunnelissa.

Katoksen geometria on melko virtaviivainen, jolloin ajan suhteen keskimääräisen virtauksen aiheuttamat pintapaineet ovat suhteellisen pieniä ja tuulen puuskaisuudesta johtuvan tuulikuorman merkitys on tavanomaista suurempi. Koko tutkittava rakenne on lisäksi kattoa, missä tapahtuu virtauksen irtoamista. Siten Olympiastadionin katokset ovat lähtökohdiltaan hankalia analysoitavia virtauslaskennan näkökulmasta.

Tarkasteltavia tuulen suuntia on kaikkiaan 12 kpl. Painekertoimen määrittämisessä referenssipaineena on käytetty katoksen korkeudella vaikuttavan tuulen dynaamista painetta ja referenssipinta-alana katoksen ala- ja yläpinnan vaakatasoon projisoitujen alojen keskiarvoa.

Laskennassa käytettiin samaa ohjelmaa, turbulenssimallia ja laskenta-asetuksia kuin Silsoen kuutiolle. Rakenteettomassa laskentaverkossa oli 11,6 miljoonaa kontrollitilavuutta, joista noin 60 % katoksen rajakerrostihennyksessä. Laskentaverkon riippumattomuustarkastelua ei tehty laskentakapasiteetista aiheutuneiden rajoitusten vuoksi. Täydellistä konvergenssia ei saavutettu, vaan tuloksiin jäi pientä jaksottaista heiluntaa. Laskentaa jatkettiin transienttina muutama aika-askel, jolloin residuaalit laskivat heti lähes kahdella dekadilla. Todennäköisesti jollakin alueella on transientteja virtausilmiöitä, eikä stationaari analyysi siksi konvergoi täysin. Stationaarin analyysin pintapaineiden heilahtelun amplitudi oli kuitenkin suhteellisen pientä.

Kuvassa 3 on vertailtu tuulitunnelikokeilla ja virtauslaskennalla määritettyä pohjoiskaarteen katoksen keskimääräistä nettopainekerrointa. Kuvaajista nähdään, että kun tuuli kohdistuu kentän puolelta pohjoiskatokseen (suunnat 79° - 259°), ovat kokeellisesti ja laskennallisesti saadut keskimääräiset nettopainekertoimet lähellä toisiaan. Jos tuuli osuu katokseen suoraan (289° - 49°), on tulosten ero huomattavasti suurempi, virtauslaskennalla saatujen painekertoimien ollessa selvästi suurempia.

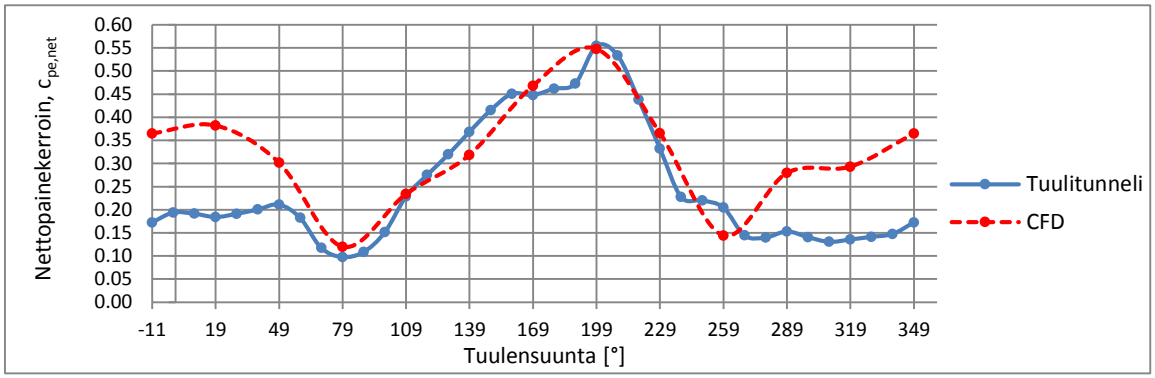

Kuva 3. Pohjoiskaarteen katoksen keskimääräinen nettopainekerroin eri tuulen suunnilla. Positiivinen arvo tarkoittaa ylöspäin suuntautuvaa kuormaa. Suunta 0°on pohjoisesta etelään.

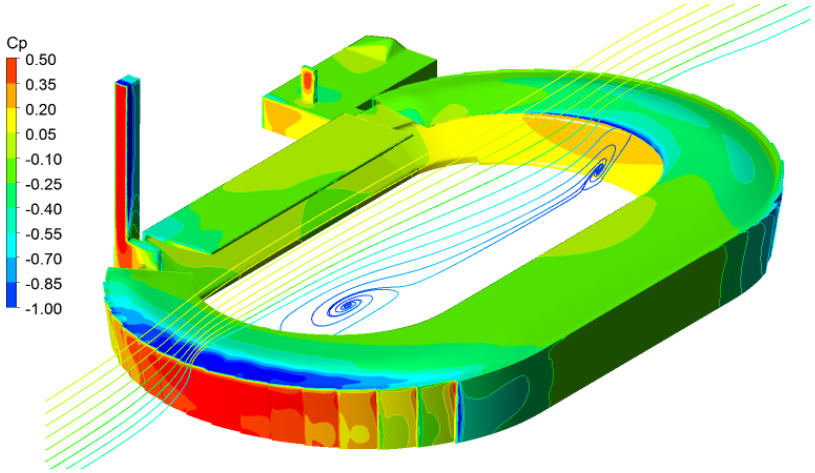

Kuva 4. Painekertoimen jakauma ja stadionin keskilinjalle piirretyt virtaviivat (tuuli 169°).

Katoksen lopullisen tuulikuorman määrittämiseen ei riitä pelkkien keskimääräisten pintapainekertoimien määrittäminen, vaan sen lisäksi täytyy huomioida tuulen puuskaisuuden ja rakenteen dynaamisuuden vaikutus. Puuskakertoimen määrittämisessä voidaan hyödyntää

normeissa annetun turbulenssin intensiteetin sijaan virtausanalyysilla laskettua arvoa, joka tulisi ottaa laskentamallista alueelta, joka on ylävirran puolella analysoitavan kohdan lähistöllä. Tällä tavalla tuulen puuskaisuuden vaikutukset saadaan huomioitua karkealla tasolla. Tämä yksinkertainen menetelmä ei kuitenkaan huomio oikein esim. toisesta rakennuksesta jaksollisesti irtoavien pyörteiden vanaan aiheutuvaa voimakasta turbulenttisuutta. Tällaisen vanavärähtelyn tarkempi huomiointi vaatisi transientin analyysin.

Yhteenveto

Artikkelissa on esitelty rakennusten tuulikuormien suuruuteen vaikuttavat tekijät sekä käsitelty erityispiirteitä, jotka liittyvät virtauslaskennan soveltamiseen tuulikuormien määrittämisessä. Virtauslaskenta tarjoaa pienoismalleilla tehtyjen tuulitunnelikokeiden rinnalle uusia mielenkiintoisia mahdollisuuksia.

Nykyään käytettävissä oleva laskentakapasiteetti rajoittaa yhä virtauslaskennan käyttömahdollisuuksia. Vaikka tutkimuksissa LES-laskentaan perustuvilla ajasta riippuvilla analyyseillä on saatu lupaavia tuloksia, työssä havaittiin, että edelleen käytännön suunnittelukäytössä stationaarit RANS-laskentaan perustuvat analyysit ovat realistinen vaihtoehto tuulitekniikan sovellutuksissa. Virtauslaskentaa voidaan hyödyntää esimerkiksi maanpinnanmuotojen vaikutuksen ja maaston pinnankarheuden muutoksen arvioinnissa tai keskimääräisten pintapainekertoimien määrittämisessä. Tuulen puuskaisuuden vaikutusta voidaan huomioida karkeasti turbulenssin kineettisen energian perusteella.

Virtauslaskentaohjelmistot ovat kehittyneet yhä helppokäyttöisemmiksi. Virtauslaskennan yhteydessä on kuitenkin erityisen voimakkaasti korostettava analysoijan omaa virtausteknistä osaamista ja tulosten luotettavuuden arvioinnin tärkeyttä. Analyysejä on helppo tehdä, mutta todellisuuden kanssa yhtä pitävien tulosten saaminen on jo paljon haastavampaa.

Viitteet

[1] Blocken, B., Stathopoulos, T., Carmeliet, J. CFD simulation of the atmospheric boundary layer: wall function problems. Atmospheric Environment 41(2007), pp. 238-252. doi: http://dx.doi.org/10.1016/j.atmosenv.2006.08.019

[2] Dagnew, A. Computational Evaluation of Wind Loads on Low- and High-Rise Buildings. Dissertation. Florida 2012. Florida International University. 226 p. http://digitalcommons.fiu.edu/etd/802/

[3] EN 1991-1-4. Eurokoodi 1: Rakenteiden kuormat. Osa 1-4: Yleiset kuormat – tuulikuormat. Brussels 2011. CEN. 157 s. + liitt. 96 s.

[4] Irtaza, H., Beale, R.G., Godley, M.H.R., Jameel, A. Comparison of wind pressure measurements on Silsoe experimental building from full-scale observation, wind-tunnel experiments and various CFD techniques. International Journal of Engineering, Science and Technology 5(2013)1, pp. 28-41. doi: http://dx.doi.org/10.4314/ijest.v5i1.3

[5] Wind pressure database of Tokyo Polytechnic University. [WWW]. [viitattu: 23.3.2015]. http://www.wind.arch.t-kougei.ac.jp/system/eng /contents/code/tpu

[6] Yang, W., Quan, Y., Jin, X., Tamura, Y., Gu, M. Influence of equilibrium atmosphere boundary layer and turbulence parameter on wind loads of low-rise buildings. Journal of Wind Engineering and Industrial Aerodynamics 96(2008)10-11, pp. 2080-2092. doi: 10.1016/j.jweia.2008.02.014

Suomen XII mekaniikkapäivien esitelmät
R. Kouhia, J. Mäkinen, S. Pajunen and T. Saksala (toim.)

Teräsristikon paarteiden liitoksen vapaan välin leikkausvoiman arviointi

Teemu Tiainen[1] ja Markku Heinisuo[1]

(1)Tampereen teknillinen yliopisto, PL 600, 33101 Tampere,
teemu.tiainen@tut.fi, markku.heinisuo@tut.fi

Tiivistelmä. Teräksisten putkiristikoiden suunnittelussa käytetään tyypillisesti verrattain yksinkertaisia rakennemalleja, joista ei välttämättä saada kaikkea suunnittelustandardien laskentakaavojen edellyttämiä voimasuureita. Näin on laita esimerkiksi käytettäessä klassista ristikkoteoriaa ja vapaavälisiä liitoksia. Kyseisen vapaan välin leikkausvoima tulisi tuntea, jotta kaikki standardin edellyttämät tarkastukset voidaan tehdä. Tätä voimaa ei valitettavasti kuitenkaan saada mallista suoraan. Tästä syystä käsillä olevassa artikkelissa esitellään yksinkertainen tapa arvioida vapaan välin leikkausvoimaa.

Avainsanat: putkiristikko, liitosmitoitus

Johdanto

Eräänä osana teräksisen putkiristikon suunnittelua on liitosten kestävyyden varmistaminen erilaisia vauriomuotoja vastaan. Liitoksen kestävyyden arviointi on haastava tehtävä, joka käytännössä edellyttäisi järeän 3D-elementtimenetelmämallin käyttöä. Kuitenkin tavanomaisimpia vauriomuotoja silmällä pitäen suunnittelustandardeihin on sisällytetty joitakin yksinkertaisia laskentakaavoja. Esimerkiksi Eurokoodien teräsrakenteiden liitoksia käsittelevä osa EN 1993-1-8 [5] esittää putkiristikon vapaaväliselle liitokselle neljä murtumismuotoa, joita vastaavien kestävyyksien riittävyys suunnittelijan tulee tarkastaa.

Näistä muodoista paarteen normaalivoimakestävyys vapaan välin leikkausvoima huomioon otettuna on nyt erityistarkastelun kohteena. Tämä kestävyys lasketaan kaavalla

$$N_{0,gap,Rd} = \frac{\left(A_0 - A_{v0}\right) f_{y0} + A_{v0} f_{y0} \sqrt{1 - \left(\frac{V_{Ed}}{V_{pl,Rd}}\right)^2}}{\gamma_{M5}} \tag{1}$$

missä f_{y0} on paarteen materiaalin myötöraja, γ_{M5} osavarmuuskerroin, A_0 paarteen poikkileikkauksen pinta-ala, A_{v0} paarteen leikkausala, V_{Ed} paarteessa vapaassa välissä vallitseva leikkausvoima, $V_{pl,Rd}$ paarteen vapaan välin leikkauskestävyys, joka puolestaan lasketaan kaavalla

$$V_{pl,Rd} = \frac{A_{v0} f_{y0}}{\sqrt{3}\gamma_{M5}} \tag{2}$$

Kestävyyden laskemiseksi on tarpeen tuntea vapaassa välissä vallitseva leikkausvoima V_{Ed}. Useimmiten käytetyistä sauva- tai palkkielementtejä hyödyntävistä elementtimentelmämalleista (kuva 1) tätä leikkausvoimaa ei kuitenkaan suoraan saada selville, vaan se pitää laskea sauvavoimien perusteella jälkikäsittelynä [3].

Systemaattinen tapa saada välin leikkausvoima selville on käyttää mallia, jossa mainitussa välissä on oma elementtinsä (kuva 2). Tämän kaltaisia malleja voidaan muodostaa monin eri tavoin ja näitä tapoja käsitellään lähteessä [1]. Syy, miksi kuvan 2 mallia ei juurikaan käytetä,

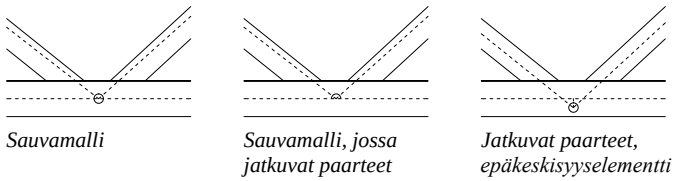

Kuva 1. Yleisesti käytettyjä tapoja muodostaa ristikon elementtimenetelmämalli.

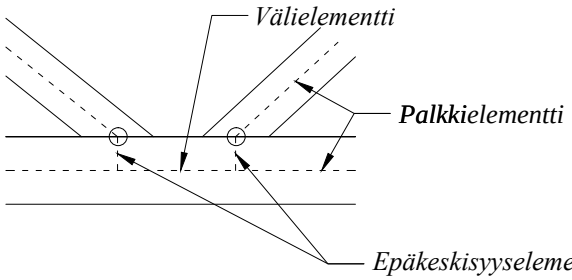

Kuva 2. Liitosalueiden mallintaminen siten, että kullakin uumasauvalla on oma epäkeskisyyselementtinsä ja vapaassa välissä oma elementtinsä.

lienee yksinkertaisesti se, että mallin kasaaminen manuaalisesti on jonkin verran tavanomaisia malleja työläämpää eikä analyysiohjelmissa ole tähän tarkoitukseen valmiita automaattisia toimintoja.

Toinen syy miksi monimutkaisempaa mallia ei aina voida tai haluta käyttää on optimointi. Optimoinnissa rakenneanalyysimallista halutaan saada mahdollisimman kevyt, ettei ongelma ja siten laskenta-aika paisu tolkuttomaksi. Esimerkiksi Melan [2] esittämässä ristikon topologiaoptimoinnin sekalukuformuloinnissa tehtävän muuttujien määrä tuntuvasti kasvaa, jos yritetään käyttää muunlaista mallia kuin nivelpäisisistä sauvoista koostuvaa.

Leikkausvoima saadaan ratkaistua mainitusti myös uumasauvojen sauvavoimista [3], mutta tämäkään tapa ei ole ongelmattomasti yhdistettävissä mainittuun optimointiformulointiin. Muuta ratkaisua yllä kuvattuun leikkausvoimaongelmaan ei kirjoittajien käsityksen mukaan ole kirjallisuudessa esitetty, josta syystä tässä artikkelissa esitellään verrattain yksinkertainen malli, jolla ongelma voidaan tyydyttävällä tavalla ratkaista. Mallin toimintaa on lisäksi havainnollistettu ja varmennettu muutamin esimerkkilaskelmin.

Malli

Tarkastellaan kuvaa 3. Koko ristikko voidaan ajatella palkkina, jonka jänneväli on L, ja sille voidaan määrittää leikkausvoimapinta $Q(x)$.

Yksinkertaisen menettelyn idea on valita tästä kuvitteellisen palkin leikkausvoimapinnasta x_i-koordinaatin kohdalta paarteessa liitoksessa i vaikuttava leikkausvoima kaavan

$$V_{Ed}^{i} = |Q\left(x_i\right)| \tag{3}$$

ja kuvan 4 mukaisesti.

Etenkin ulkoisesti staattisesti määrättyihin ristikoihin, joita kattoristikot monesti tapaavat olla, voidaan menettelyä soveltaa helposti mielivaltaiselle kuormalle $q(x)$. Tällöin kattoristikon tapauksessa eri kuormitusyhdistelyille saadaan laskettua omat paarteen liitosten leikkausvoima-arviot.

Esimerkkilaskelmat

Arvioidaksemme esitetyn menettelyn kelvollisuutta ja arvion paikkansa pitävyyttä tarkastellaan kuvan 5 ristikkoa, joka on mallinnettu kuvan 2 periaatteen mukaisesti yleisesti käytetyin *Euler-*

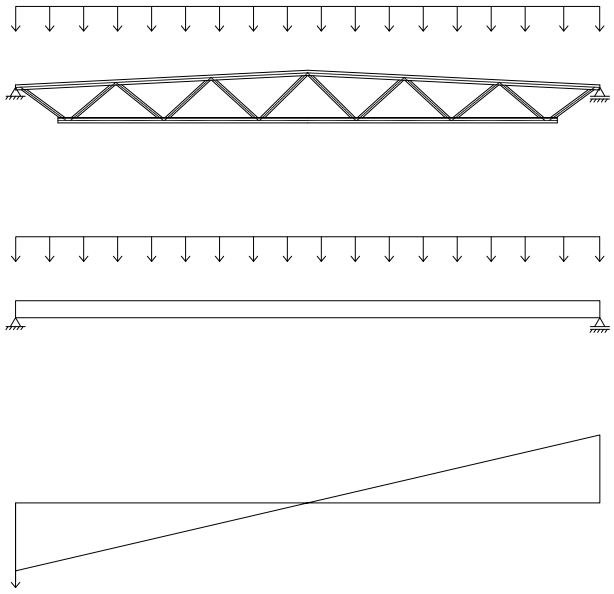

Kuva 3. Ristikko voidaan ajatella palkkina, jolle puolestaan voidaan laskea leikkausvoimapinta.

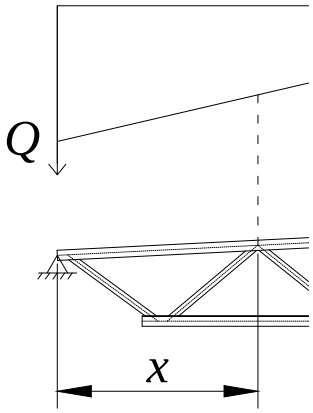

Kuva 4. Liitoksessa vallitseva leikkausvoima luetaan ”globaalista” leikkausvoimapinnasta.

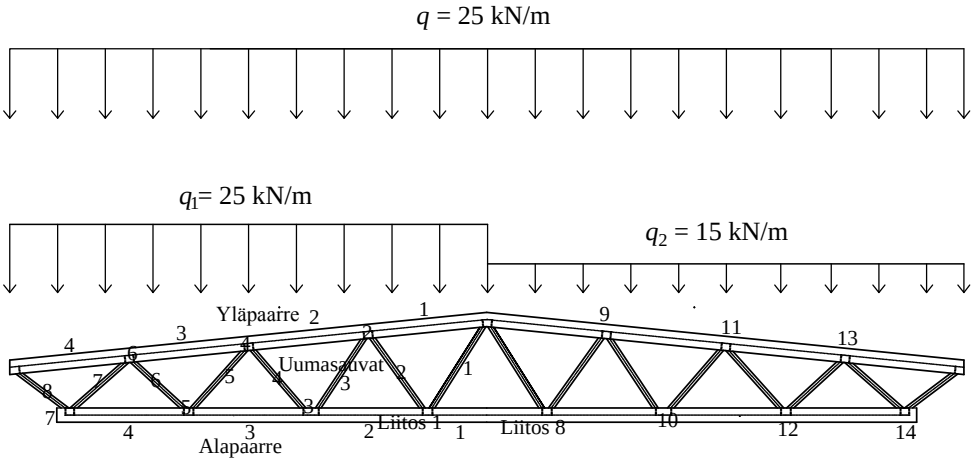

Kuva 5. Esimerkkiristikko kuormineen.

Bernoulli-palkkielementein siten, että epäkeskisyyselementit ovat lähes ideaalisen jäykkiä ja uumasauvat liittyvät epäkeskisyyselementteihin nivelisesti. Koska liitoksen välialueessa on oma elementtinsä, saadaan kyseisen alueen leikkausvoima suoraan tästä mallista.

Ristikon jänneväli on 36 metriä, ensimmäisessä kuormitusyhdistelyssä kuorma tasainen 25 kN/m ja toisessa kuormitusyhditelyssä toisella lappeella 25 kN/m ja toisella 15 kN/m. Ristikko on tasan jaoteltu K-liitoksinen neliöputkista hitsaamalla koottu ristikko, jonka profiilivalinnat nähdään taulukossa 1. Elementtien leikkausvoimapinnat molemmissa kuormitusyhdistelytapauksissa nähdään kuvassa 6. Huomataan, että leikattaessa ristikko kahtia K-liitoksen kohdalta enin osa leikkausvoimasta kulkeutuu liitoksessa olevan paarteen kautta ja verrattain pieni osa vastakkaisen paarteen kautta.

Taulukko 1. Sauvojen poikkileikkaukset. Sauvanumerointi kuvan 5 mukaan.

Sauva	Koko [mm]
Yläpaarre	180x10
Alapaarre	160x6
Uumasauva 1	60x3
Uumasauva 2	70x3
Uumasauva 3	90x3
Uumasauva 4	70x3
Uumasauva 5	110x4
Uumasauva 6	80x3
Uumasauva 7	140x5
Uumasauva 8	140x5

Esitetyn arviointitekniikan käyttämiseksi tulee laskea leikkausvoimapinta $Q(x)$. Tasaisen kuormituksen tapauksessa käyttäen lähteen [4, sivu 183] merkkisääntöä saadaan

$$Q_1(x) = \frac{qL}{2} - qx \tag{4}$$

ja kahden kuormituksen tapauksessa

$$Q_2(x) = \frac{3q_1L}{8} + \frac{q_2L}{8} - q_1x - (q_2 - q_1) < x - \frac{L}{2} > \tag{5}$$

missä kärkisuljemerkintä tarkoittaa *Macaulay*-funktiota

$$f(x) =< x - \frac{L}{2} >= \begin{cases} x - \frac{L}{2}, & \text{kun } x - \frac{L}{2} \geq 0 \\ 0, & \text{muussa tapauksessa} \end{cases}$$

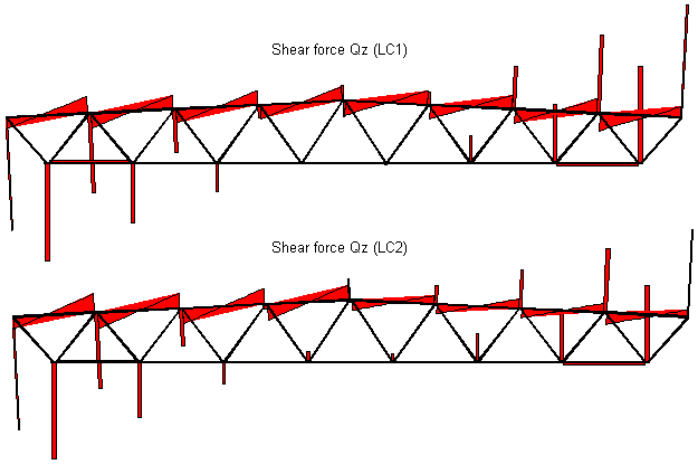

Kuva 6. Leikkausvoimapinnat koko ristikoille elementtimenetelmällä.

Taulukossa 2 nähdään vertailu arvioidun ja FEM-mallista saadun leikkausvoiman välillä ristikon K-liitoksissa virheineen, kun tarkkana ratkaisuna pidetään FEM-mallista saatua leikkausvoiman arvoa. Elementtimenetelmän tarjoamana ratkaisuna valitaan itseisarvoltaan suurin elementissä esiintyvä leikkausvoiman arvo ja esitetyn mallin mukaiseen arvioon tarvittavana liitoksen x-koordinaattina liitoksen keskikohdan koordinaattia.

Taulukko 2. Vertailu. Leikkausvoiman itseisarvot K-liitosten vapaissa väleissä laskettuna elementtimenetelmällä ja esitetyllä mallilla.

	Mitoitusleikkausvoima V_{Ed}					
	Kuormitus 1			Kuormitus 2		
Liitos	FEM	Arvio	Virhe [%]	FEM	Arvio	Virhe [%]
Liitos 1	4.01	56.25	1304.2	33.02	11.25	-65.9
Liitos 2	50.08	112.50	124.6	64.30	67.50	5.0
Liitos 3	108.04	168.75	56.2	99.54	123.75	24.3
Liitos 4	165.23	225.00	36.2	135.75	180.00	32.6
Liitos 5	227.90	281.25	23.4	175.25	236.25	34.8
Liitos 6	303.58	337.50	11.2	223.10	292.50	31.1
Liitos 7	375.17	393.75	5.0	266.73	348.75	30.7
Liitos 8	4.01	56.25	1304.2	39.43	78.75	99.7
Liitos 9	50.07	112.50	124.7	15.83	112.50	610.7
Liitos 10	108.04	168.75	56.2	73.32	146.25	99.5
Liitos 11	165.19	225.00	36.2	128.59	180.00	40.0
Liitos 12	227.90	281.25	23.4	189.39	213.75	12.9
Liitos 13	303.51	337.50	11.2	262.57	247.50	-5.7
Liitos 14	375.17	393.75	5.0	333.53	281.25	-15.7
Keskiarvo	-	-	223.0	-	-	79.2

Ehdotetun menettelyn keskimääräinen virhe on melko suuri. Symmetrisessä kuormitustapauksessa ristikon keskialueella (liitokset 1 ja 8) esiintyy jopa yli kymmenkertaisia leikkausvoiman arvoja verrokkiin nähden. Kuitenkin on syytä huomata, että paarteet ovat verrattain järeitä profiileja ja yleensä koko ristikon matkalla samaa profiilia. Tällöin niiden leikkauskestävyys on suuri, jolloin kaavan 1 perusteella normaalivoimakestävyyden aleneminen leikkausvoiman takia jää pieneksi, jos leikkausvoimakin on pieni. Uloimpien liitoksien (liitokset 6, 7, 13 ja 14), joissa leikkausvoimalla ylipäänsä voidaan katsoa olevan mitoituksen kannalta merkitystä, osalta ar-

vion voidaan katsoa olevan riittävän tarkka liitoksen mitoitukseen. Näissä liitoksissa sauvojen normaalivoima- ja taivutusmomenttitarkasteluissa kestäväksi osoittautuvan ristikon paarteen leikkausvoimakestävyys saattaa jopa ylittyä. Huomattavaa on, että symmetrisessä kuormitustilanteessa arvio oli aina suurempi kuin oikea leikkausvoima, kun taas epäsymmetrisessä tilanteessa virheen suuntaa ei voida päätellä.

Päätelmät

Tässä esityksessä ehdotetaan yksinkertaista menettelyä leikkausvoiman määrittämiseksi putkiristikon vapaavälisessä liitoksessa. Ristikolle lasketaan globaali leikkausvoimapinta, josta saatavaa leikkausvoiman arvoa tarkasteltavan liitoksen kohdalla käytetään liitoksen mitoitukseen. Menettely vaikuttaisi esimerkkien perusteella olevan riittävän tarkka liitosten mitoittamisen apuna tavanomaisessa insinöörityössä ja se on sovellettavissa myös optimointimenettelyn yhteyteen.

Viitteet

[1] H. Boel. *Buckling Length Factors of Hollow Section Members in Lattice Girders.* Master's thesis, Eindhoven university of technology, 2010.

[2] K. Mela. *Mixed-Variable Formulations for Truss Topology Optimization.* Väitöskirja, Tampereen teknillinen yliopisto, 2013.

[3] Ruukki. *Rakenneputket.* Rautaruukki Oyj, 2013.

[4] T. Salmi. *Statiikka.* Pressus Oy, 2001.

[5] Suomen Standardisoimisliitto. *SFS EN-1993-1-8. Eurocode 3: Teräsrakenteiden suunnittelu. Osa 1-8: Liitosten suunnittelu*, 2006.

Suomen XII mekaniikkapäivien esitelmät
R. Kouhia, J. Mäkinen, S. Pajunen ja T. Saksala (toim.)

Seismiset analyysimenetelmät rakennesuunnittelussa

Jyri Tuori ja Jussi Jalkanen

Sweco Rakennetekniikka Oy, Hatanpään valtatie 11, 33100 Tampere
jyri.tuori@sweco.fi ja jussi.jalkanen@sweco.fi

Tiivistelmä. Tässä artikkelissa käsitellään seismisessä rakennesuunnittelussa käytettäviä analyysimenetelmiä. Tarkastelun kohteena ovat korvausvoima-, vastespektri-, PushOver- ja aikahistoriamenetelmä. Näitä menetelmiä on sovellettu teräsrunkoiseen esimerkkirakenteeseen.

Avainsanat: Maanjäristys, korvausvoima, vastespektri, PushOver, aikahistoria

Johdanto

Maanjäristys on luonteeltaan selvästi erilainen kuormitus verrattuna tuuli- tai lumikuormaan, ja siten maanjäristysmitoituksen suunnittelukriteerit poikkeavat lähtökohdiltaan totutuista. Isoja maanjäristyksiä tapahtuu harvoin, mutta niissä rakenteiden kuormat kasvavat erittäin suuriksi. Tämän seurauksena siirtymät ovat suuria ja rakenteisiin syntyy pysyviä muodonmuutoksia.

Tässä esityksessä tarkastellut numeeriset analyysimenetelmät muodostavat vain yhden osan maanjäristysmitoituksesta, sillä muita vähintään yhtä tärkeitä osa-alueita ovat alkuvaiheen konseptisuunnittelu ja detaljien suunnittelu. Myös oikea seismisyyden tason (seismic hazard) määrittely on tärkeätä, mutta se ei kuulu rakennesuunnittelijan tehtäviin.

Maanjäristyksiä tapahtuu jatkuvasti ympäri maapalloa tyypillisesti mannerlaattojen seismisesti aktiivisilla reuna-alueilla. Suomessa maanjäristykset ovat pieniä ja seismistä mitoitusta tarvitaan lähinnä sellaisissa erikoistapauksissa kuin ydinvoimalat. Monet kotimaiset vientiyritykset myyvät kuitenkin tuotteitaan maanjäristysherkille seuduille ja tämän takia Suomessakin tarvitaan maanjäristysmitoituksen osaamista.

Maanjäristysmitoitus

Rakennusten seismisessä suunnittelussa voidaan erottaa kolme eri osa-aluetta, jotka yhdessä muodostavat varautumisen maanjäristyksen mahdollisuuteen: Konseptisuunnittelu, maanjäristysvoimien laskenta ja yksityiskohtien suunnittelu. Maanjäristysmitoitus ei siis käsitä vain seismistä rakenneanalyysiä ja rakenteen mitoittamista tästä tuleville rasituksille, vaan myös tarkoituksenmukaisen rakennesysteemin valinnan, jotta rasitukset jäisivät lähtökohtaisesti pieniksi, ja detaljien suunnittelun, jotta riittävä sitkeys olisi mahdollista saavuttaa.

Voimakkaassa maanjäristyksessä rakenteiden siirtymät kasvavat väistämättä hyvin suuriksi. Tällöin tavanomaisia rakenteita ei kannata suunnitella kestämään kimmoisena maanjäristyksiä, vaan on järkevämpää sallia pysyvien muodonmuutosten syntyminen. Suunnittelunormien taustalla olevan kapasiteettisuunnittelun periaatteiden mukaisesti rakenteen sallitaan muodostaa ennalta valittu myötömekanismi, jossa maanjäristyksen energia dissipoituu plastisoituvissa osissa lämmöksi. Tällöin lähtökohtaisesti hyväksytään se, että voimakkaassa maanjäristyksessä rakennus vaurioituu pahoin, mutta se ei saa kuitenkaan sortua. Voi olla halvempaa purkaa vaurioitunut rakennus pois ja rakentaa tilalle uusi kuin korjata vauriot.

Valtaosa maanjäristysmitoituksesta tehdään käyttäen lineaarisia analyysimenetelmiä, vaikka kyseessä on hyvin epälineaarinen ilmiö. Yksinkertaisissa tapauksissa käytetään korvausvoimamenetelmää ja muissa vastespektrimenetelmää. Suunnittelustandardeissa esitetään keinot kiihtyvyysspektrin muokkaamiseksi muotoon, joka ottaa huomioon rakenteen epälineaarisen käyttäytymisen (kuva 1).

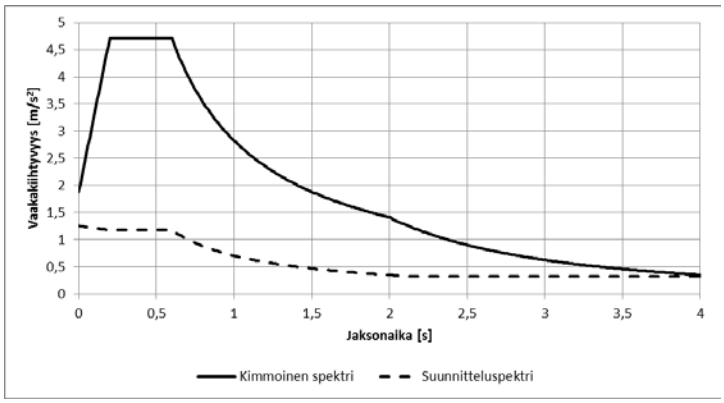

Kuva 1. Artikkelin rakenteen EN 1998-1[1] mukainen vaakavastespektri, joka kuvaa maanjäristyksen rakenteelle aiheuttamia kiihtyvyyksiä.

Seismiset analyysimenetelmät

Korvausvoimamenetelmä

Yksinkertaisin seisminen analyysimenetelmä on korvausvoimamenetelmä. Tavoite on korvata dynamiikan tehtävä staattisella kuormitusjakaumalla, joka saa aikaan maanjäristyksen aiheuttaman suurimman siirtymätilan. Jos rakenteen merkitsevin ominaismuoto kuvaisi tarkasti rakenteen vastetta maanjäristyksessä, tuottaisi korvausvoimamenetelmä tarkkoja tuloksia. Jos useammat muodot osallistuvat oleellisesti vasteeseen, heikkenee tuloksien tarkkuus.

Ominaismuotoon $\boldsymbol{\varphi}$ liittyvä staattinen korvausvoima saadaan kaavalla

$$F_{s,i} = m_s \, S_a(T) \frac{m_i \varphi_i}{\sum m_j \varphi_j}, \tag{1}$$

missä m_s on kokonaismassa, m_i vapausasteen i massa ja $S_a(T)$ ominaisvärähdysaikaan T liittyvä kiihtyvyysspektrin arvo.

Vastespektrimenetelmä

Vastespektrimenetelmä on nykyään eniten käytetty seisminen analyysimenetelmä monimutkaisemmilla rakenteilla. Siinä rakenteen ominaismuotoja $\boldsymbol{\varphi}_i$ $(\boldsymbol{\varphi}_i^T \boldsymbol{M} \boldsymbol{\varphi}_i = 1, \forall\, i)$

vastaavien ominaisvärähdysaikojen T_i ja osallistumiskertoimien Γ_i perusteella saadaan kutakin ominaismuotoa vastaava staattinen voimajakauma $\boldsymbol{F}_i$ kaavalla

$$\boldsymbol{F}_i = \Gamma_i \boldsymbol{M} \boldsymbol{\varphi}_i S_a(T_i) \,, \tag{2}$$

jossa $\boldsymbol{M}$ on massamatriisi. Osallistumiskertoimet voidaan puolestaan laskea kaavalla

$$\Gamma_i = \boldsymbol{\varphi}_i^T \boldsymbol{M} \boldsymbol{l} \,, \tag{3}$$

jossa $\boldsymbol{l}$ on siirtymävektori, kun alusta saa ykkössiirtymän maanjäristyksen suunnassa.

Menetelmän myötä tulokset saadaan jokaiselle muodolle erikseen. Yleensä muodoilla on vaihe-eroa, joten tulosten suora summaaminen yhteen tuottaisi liian suuria tuloksia. Yhdistelyyn on kehitetty useita tilastollisia menetelmiä, joista yleisimmin käytetty on CQC (complete qudratic combination). Yhdistelyn jälkeen rakenne ei ole enää tasapainossa, joten yhdistely tulee suorittaa erikseen jokaiselle tarvittavalle suureelle erikseen. Yhdistelyn seurauksena normaali- ja leikkausvoiman sekä taivutusmomentin rasituskuviot eivät enää vastaa sitä, mihin on totuttu statiikan tehtävässä.

PushOver-menetelmä

Epälineaarisen statiikan analyysin ja vastespektrin käyttö voidaan yhdistää PushOver-menetelmässä, jolloin pystytään ottamaan huomioon rakenneosien plastisoituminen maanjäristyksessä. Menetelmästä on käytössä useita eri variaatioita, mutta periaatteessa kaikissa niissä määritetään rakenteelle ekvivalentti epälineaarinen yhden vapausasteen värähtelijä. Tällä mallilla ratkaistaan maanjäristyksessä syntyvä vaakasiirtymä, joka muunnetaan takaisin alkuperäisen FE-mallin siirtymätilaksi ja sitä vastaavaksi rasituksiksi.

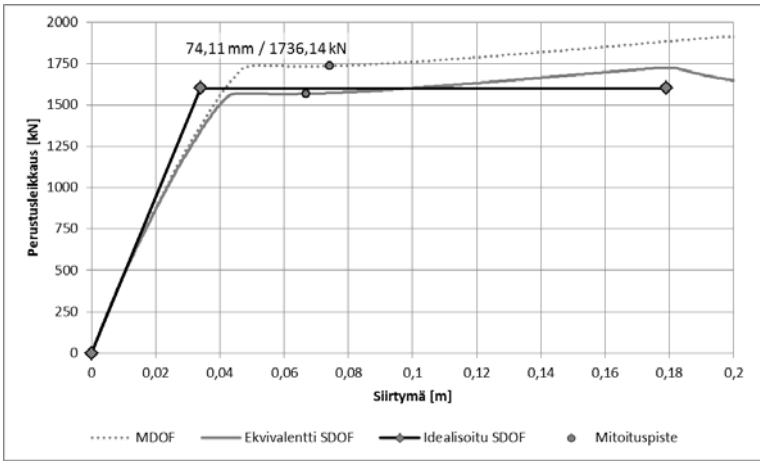

Kuva 2. Vaakakuormitus huipun siirtymän funktiona PushOver-menetelmässä esimerkkirakenteelle. MDOF-käyrä saadaan FE-mallin epälineaarisesta statiikan analyysistä. Ekvivalentti SDOF-käyrä saadaan eurokoodin [1] N2-menetelmässä skaalaamalla MDOF-käyrästä. Bi-lineaarisen idealisoidun SDOF-käyrä ja ekvivalentin SDOF-käyrä vastaavat samaa muodonmuutosenergiaa. Mitoituspiste määräytyy kuvan 3 tavoitesiirtymän perusteella.

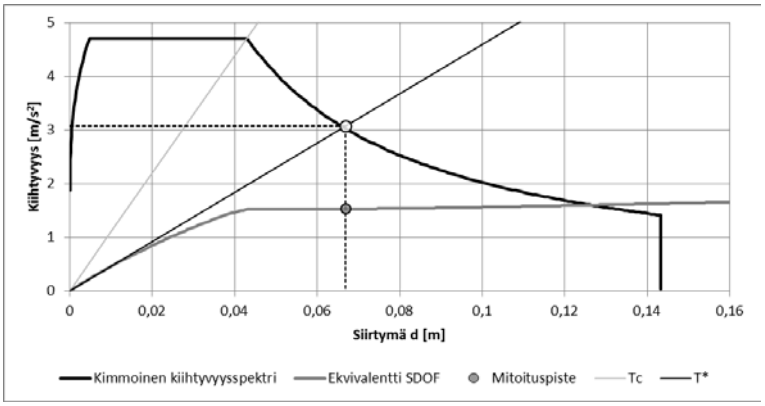

Kuva 3. PushOver tavoitesiirtymän määritys esimerkkirakenteelle. Kimmoinen spektri on esitetty koordinaatistossa, missä jaksonaikaa vastaa origon kautta kulkeva suora. T* on yhden vapausasteen värähtelijän jaksonaika, jonka perusteella löydetään ekvivalentin mallin tavoitesiirtymä.

Aluksi PushOver-menetelmässä kasvatetaan askeleittain poikittaista kuormitusta epälineaarisessa statiikan analyysissä kunnes rakenne saavuttaa myötömekanismin. Rakennuksen huipulta valitun tarkkailusolmun siirtymän ja kuorman välistä epälineaarista yhteyttä sanotaan PushOver-käyräksi (kuva 2). Tehdyn analyysin perusteella tiedetään kutakin siirtymäarvoa vastaava rasitusjakauma. Tässä esityksessä on käytetty eurokoodin [1] N2-menetelmää ja sen mukaisesti kahta eri kuormitusta: vakio kiihtyvyyttä sekä lineaarisesti ylöspäin kasvavaa kiihtyvyyttä. Muita yleisesti käytettyjä menetelmiä ovat siirtymäkerroin ja kapasiteettispektri menetelmä [3]. Kiihtyvyys-siirtymä –spektrin (kuva 3) avulla määritetään rakenteelle siirtymä, jonka täysin kimmoisena säilyvä idealisoitu rakenne kokisi.

Monimuotoisissa epäsäännöllisissä rakenteissa PushOver-menetelmässä tehtyjen yksinkertaistuksien myötä rakenteeseen kohdistuva vääntö ei vastaa todellisuutta. Näiden rakenteiden analysointiin on kehitetty parempia menetelmiä.[2]

Aikahistoriamenetelmä

Aikahistoriamenetelmän idea on ratkaista sopivaa aikaintegrointimenetelmää käyttäen rakenteen vaste, kun maaperän kiihtyvyyshistoria tunnetaan. Kiihtyvyyshistoriaksi voidaan valita rakennuksen sijaintipaikan läheltä mitattu todellinen tai keinotekoinen kiihtyvyys ajan funktiona. Herätteiden taajuussisältö sovitetaan vastaamaan suunnittelustandardissa vaadittua kimmoista spektriä. Sovitetun herätteen lisäksi voidaan käyttää keinotekoisia herätteitä. Suoraviivaisin ja todenmukaisin menetelmä on epälineaarinen dynamiikan analyysi, mutta se on samalla myös laskennallisesti kaikkein raskain.

Aikahistoriamenetelmässä ei synny samanlaista eri muotojen tulosten yhdistelyongelmaa kuin vastespektrimenetelmän yhteydessä. Toisaalta tulokseksi saadaan iso joukko eri aika-askelien tuloksia, eikä yksiselitteistä yhtä voimajakaumaa. Aikahistoriamenetelmässä tulee käyttää riittävän pientä aika-askelta, mikä nostaa sen laskennallista hintaa. Kiihtyvyyshistorioita tarvitaan useita, jotta mahdollisesti tulevaisuudessa sattuvan maanjäristyksen vaikutukset tulisivat varmuudella otetuksi huomioon. Näiden haasteiden takia aikahistoriamenetelmä ei ole rakenteiden käytännön maanjäristysmitoituksessa vielä yleisesti käytössä, mutta mahdollisuudet sen soveltamiseen paranevat tietokoneiden laskentakapasiteetin parantuessa.

Esimerkkirakenne

Seismisten analyysimenetelmien ominaisuuksia on vertailtu kuvan 4 mukaisella symmetrisellä teräsrakenteella. Kuvitteellinen rakennus sijaitsee Luoteis-Turkissa, missä kallioperän vaakakiihtyvyys (PGA-arvo) on 0,167g. Kiihtyvyysspektri (kuva 1) on muodostettu standardin EN 1998-1-1:2005 perusteella olettaen spektrin tyypiksi 1, maaperäluokaksi C, tärkeyskertoimeksi $\gamma_I = 1{,}0$ ja käyttäytymiskertoimeksi keskeisiä vinositeitä vastaava $q = 4$.

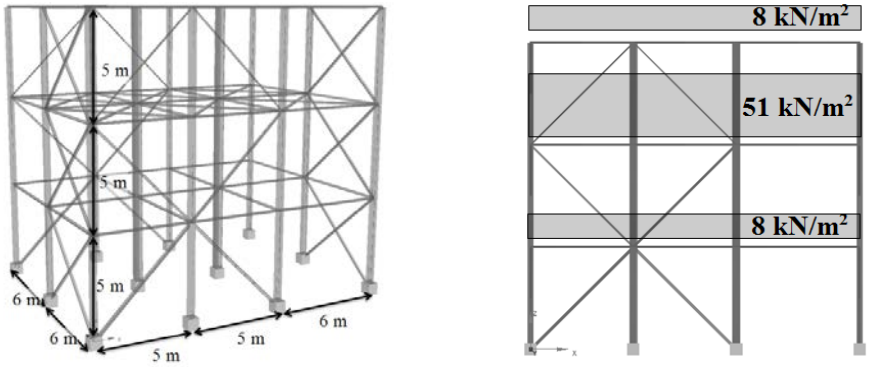

Kuva 4. Teräsrakenteen mitat ja tasojen kuormat (oma paino + hyötykuorma).

Ominaisarvotehtävän perusteella saadut jaksonajat ja seismisen massan osallistuminen eri ominaismuotoihin on esitetty taulukossa 1. Symmetrisellä rakennuksella on selkeät erilliset päämuodot X- ja Y-suuntaan.

Korvausvoima- ja vastespektrimenetelmissä oli mukana X-suunnassa vain puristussiteet ja Y-suunnassa sekä puristus- että vetositeet. Tutkitussa kuormitustapauksessa on otettu huomioon maanjäristysvoimien lisäksi oma paino ja hyötykuorma $1{,}0D + 1{,}0L + 1{,}0E_x + 0{,}3E_Y$.

Taulukko 1. Rakenteen jaksonajat ja massan osallistuminen eri muotoihin.

Muoto	*Jaksonaika [s]*	*Ux [%]*	*Uy [%]*	*Uz [%]*
1	0,904	1,2	96,0	0,0
2	**0,778**	**95,8**	1,3	0,0
3	0,536	0,1	0,0	0,0
4	0,333	0,0	0,6	0,0
		97,0	**97,4**	**0,0**

PushOver- ja aikahistoriamenetelmissä on käytössä epälineaarinen rakennemalli, missä huomioidaan suuret siirtymät ja myötölujittumaton kimmoplastinen materiaalimalli. Epälineaarisen mallin työtä lisää huomattavasti siteille mallinnettavan alkuhäiriöt, jotka mahdollistavat siteiden todellisen käyttäytymisen syklisessä kuormituksessa. Lineaarisessa mallissa siteiden nurjahtaminen otetaan huomioon käyttämällä vain vetositeitä.

Aikahistoriamenetelmässä on valittu viisi Turkista mitattua todellista aikahistoriaa, jotka on sovitettu vastaamaan kuvan 1 mukaista spektriä välillä 0,5 s – 1,3 s. Sovitus on suoritettu SeismoSoftin SeismoMatch ohjelmalla ja rakenneanalyysit SeismoStruct ohjelmalla.

Lineaaristen analyysien tulokset ovat merkittävästi pienempiä kuin tarkempien epälineaaristen menetelmien (kuva 5). Eurokoodin [1] suosittelema käyttäytymiskertoimen q arvo 4 näyttäisi olevan liian optimistinen esimerkkitapauksessa, sillä rakenteen vaste aikahistoriamenetelmässä on lähes kimmoinen. Kuvasta 3 nähdään, että kimmoisen ja todellisen rakenteen suhde on 1,8. Jos tätä kerrointa sovellettaisiin vasteenmuokkaustekijänä q, saataisiin lineaarisilla analyyseillä yhtenäisempiä tuloksia.

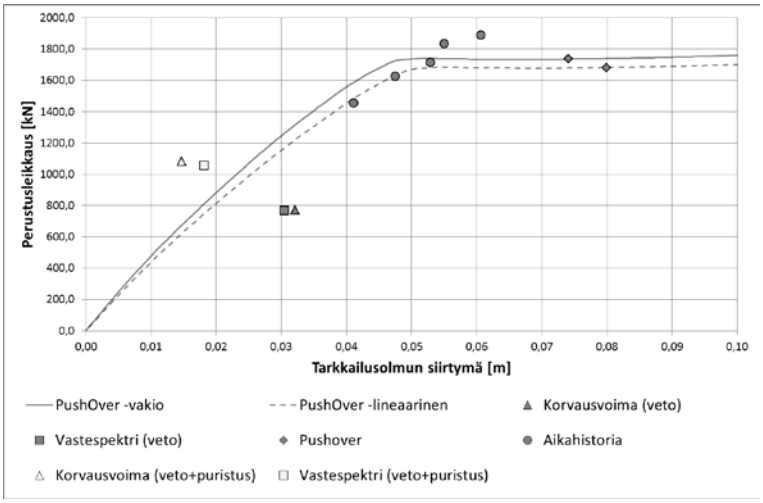

Kuva 5. Rakenteelle kohdistuva perustusleikkaus eri analyysimenetelmillä.

Yhteenveto

Seisminen rakennesuunnittelu on monivaiheinen prosessi aina esisuunnittelusta detaljeihin asti. Vaikka analyysimenetelmät ovat vain yksi vaihe seismistä rakennesuunnittelua, niiden oikea soveltaminen luo perustan onnistuneelle lopputulokselle.

Tässä työssä on esitelty neljä yleistä seismistä analyysimenetelmää sekä sovellettu niitä symmetriseen keskeisillä vinositeillä jäykistettyyn teräsrakenteeseen.

Viitteet

[1] EN 1998-1:2005, Eurocode 8: Design of structures for earthquake resistance. Part 1: General rules, seismic actions and rules for buildings.

[2] C. Bhatt, R.Bento *Estimating Torsional Demands In Plan Irregular Buildings Using Pushover Procedures Coupled With Linear Dynamic Response Spectrum Analysis*, 6th European Workshop on the seismic behaviour of Irregular and Complex Structures, Haifa, Israel, 12–13 September 2011.

[3] N.D. Lagaros, M. Fragiadakis, *Evaluation of ASCE-41, ATC-40 and N2 static pushover methods based on optimally designed buildings*, Soil Dynamics and Earthquake Engineering, Vol. 31, 2011, pp. 77-90.

[4] J. Tuori, *Seismiset Analyysimenetelmät Rakennesuunnittelussa*, diplomityö, Tampereen teknillinen yliopisto, 2015.

Proceedings of the XII Finnish Mechanics Days
R. Kouhia, J. Mäkinen, S. Pajunen and T. Saksala (Eds.)

Nonsingular fracture mechanics within generalized continua

S. Mahmoud Mousavi[1], and Juha Paavola[1]

[(1)]Department of Civil and Structural Engineering, Aalto University, Box 12100, FI 00076 Aalto, Finland, mahmoud.mousavi@aalto.fi, juha.paavola@aalto.fi

Summary. Dislocations can be used as macro elements to achieve the elastic model of material weakened by cracks. Here, the dislocation-based fracture mechanics will be introduced and applied for the analysis of materials within generalized continuum mechanics. The motivation for this study is the fact that the singularity of the dislocation is regularized within generalized frameworks such as nonlocal and gradient elasticity. Consequently, it is expected that the crack which is modelled through the convolution of the dislocations will also have nonsingular stress fields.

Key words: Dislocation, fracture, generalized continua, nonsingular

Introduction on generalized continua

In classical continuum mechanics, the particles are idealized as point masses and the elastic continuum is understood as a collection of particles with only three translational degrees of freedom. Due to the lack of intrinsic length scale in classical elasticity theories, such as linear or nonlinear elasticity and plasticity, they represent scale-free continuum theories. In order to analyse the behaviour of structures with different sizes from micro to macro, a more general theory is needed to account for scale effects. The generalized continuum theories enrich the classical theories with additional material characteristic lengths in order to describe the scale effects resulting from the microstructures. The generalized continuum elasticity theory, namely Cosserat or micropolar, were introduced at the beginning of the nineteenth century first by the Cosserat brothers in which a particle is identified by its position vector and its micro-rotation vector (six degrees of freedom). Nonlocal elasticity is one of the extensions of the classical one which was introduced to explain the material behaviour at nanoscale. This theory considers the inner structure of materials and takes into account long-range (nonlocal) interactions. Another simplified extension of the classical theory of elasticity is called gradient elasticity, which can be related to nonlocal elasticity.

Gradient elasticity

Gradient elasticity is a generalization of linear elasticity which includes higher-order terms to account for microstructural effects. Within strain gradient elasticity, the strain energy depends on the elastic strain, and higher order strain tensors defined as spatial gradients either of the displacement field, or of the strain field [3]. Due to the gradient terms, it contains additional coefficients with the dimension of a length, which are called gradient coefficients. To study dislocations, an incompatible strain gradient elasticity should be employed.

Nonlocal elasticity

In this Section, we briefly present the basic ideas and equations of nonlocal elasticity of Helmholtz type. In the theory of nonlocal elasticity (e.g., [1, 2]), the so-called nonlocal stress tensor t_{ij} is defined at any point $\boldsymbol{x}$ of the analyzed domain of volume V as

$$t_{ij}(\boldsymbol{x}) = \int_V \alpha(|\boldsymbol{x}-\boldsymbol{y}|)\sigma_{ij}(\boldsymbol{y})\,\mathrm{d}V(\boldsymbol{y})\,, \tag{1}$$

where $\alpha(|\boldsymbol{x}-\boldsymbol{y}|)$ is a nonlocal kernel and σ_{ij} is the stress tensor of classical isotropic elasticity defined at the point $\boldsymbol{y} \in V$ as

$$\sigma_{ij}(\boldsymbol{y}) = \lambda\,\delta_{ij}e_{kk}(\boldsymbol{y}) + 2\mu e_{ij}(\boldsymbol{y})\,, \tag{2}$$

where λ, μ are the Lamé constants, δ_{ij} is the Kronecker delta and e_{ij} denotes the classical elastic strain tensor, which is the symmetric part of the classical elastic distortion tensor

$$e_{ij} = \frac{1}{2}\big(\beta_{ij} + \beta_{ji}\big)\,. \tag{3}$$

We employ a comma to indicate partial derivative with respect to rectangular coordinates x_j, i.e. $t_{ij,j} = \frac{\partial t_{ij}}{\partial x_j}$.

Dislocation-based fracture mechanics within generalized continua: A nonsingular theory

A dislocation is a line defect which give rise to elastic and plastic distortion. The dislocation density of a single dislocation can be convolved with a so-called distribution function, so that the boundary conditions of the crack-faces are satisfied. The unknown distribution function is to be determined using the appropriate boundary conditions. Using such distribution of the dislocations, the stress field of the cracked material is derived.

The dislocation-based fracture or distributed dislocation technique (DDT) is rather well/known in classical elasticity. Here, we will focus on its application to present nonsingular models of cracks in generalized continuum mechanics.

Mousavi and Lazar [6] applied DDT for nonlocal elasticity and derived nonsingular nonlocal stress fields for cracks, while this theory does not give any nonlocal strain. In other words, within this framework, the strain is still singular and the crack opening is identical to the classical one. The nonlocal elasticity has also been applied to anisotropic materials. A nonlocal dislocation-based fracture mechanics of anisotropic materials results in a nonsingular fracture theory [5]. It is to be noted that the boundary conditions in nonlocal elasticity are as simple as classical elasticity.

In contrast to nonlocal elasticity, gradient elasticity includes non-classical boundary conditions. Consequently, it is more complicated to establish a nonsingular gradient elastic fracture theory. Once the non-classical boundary conditions are neglected, an approximate solution is obtained which results in nonsingular stress and strain fields [7, 8]. Recently, an exact gradient elastic formulation considering the non-classical boundary conditions are presented by Mousavi and Aifantis [4]. This study deals with the cracks of mode III. It is noticed that higher order gradient theories contribute to regularization of stress and higher-order stress (hyper-stress) tensors.

An interesting aspect of the dislocation-based fracture mechanics is its ability to model crack tip plasticity. The dislocations are source of incompatibility and give rise to plastic distortion. Accordingly, it is possible to model cracks with dislocation and capture the crack tip plasticity, without any assumption of cohesive fracture zone (Such as Barenblatt's fracture theory).

Conclusion

Dislocations play a key role in fracture and plasticity of crystalline materials. In line with this observation, within continuum mechanics of crystalline materials, the dislocations are interpreted as the building blocks of cracks in fracture mechanics and also are denoted as the carriers of plasticity. In this regard, a unified dislocation-based theory for plasticity and fracture is an ambitious long-standing goal. Special forms of generalized continua, including nonlocal and gradient elasticity, success in the regularization of classical singularities of the dislocations. Consequently, by convolution of nonsingular dislocations, a nonsingular fracture theory is developed.

Acknowledgements

It is a pleasure for SMM to acknowledge the invited visits and fruitful discussions with Prof. Markus Lazar (Darmstadt University of Technology), Prof. Alexander M. Korsunsky (University of Oxford) and Prof. Elias C. Aifantis (Aristotle University of Thesaloniki).

References

[1] A.C. Eringen. On differential equations of nonlocal elasticity and solutions of screw dislocation and surface waves. *Journal of Applied Physics*, 54:4703–4710, 1983.

[2] A.C. Eringen. Nonlocal continuum field theories. *New York Springer*, 2002.

[3] R.D. Mindlin. Micro-structure in linear elasticity. *Archive for Rational Mechanics and Analysis*, 16:51–78, 1964.

[4] S.M. Mousavi and E.C. Aifantis. A note on dislocation-based mode III gradient elastic fracture mechanics. *Journal of the Mechanical Behavior of Materials*, 2015.

[5] S.M. Mousavi and A.M. Korsunsky. Non-singular fracture theory within nonlocal anisotropic elasticity. *in preparation*, 2015.

[6] S.M. Mousavi and M. Lazar. Distributed dislocation technique for cracks based on nonsingular dislocations in nonlocal elasticity of helmholtz type. *Engineering Fracture Mechanics*, 136:79–95, 2015.

[7] S.M. Mousavi, J. Paavola, and D. Baroudi. Cracks in strain gradient elasticity-distributed dislocation technique. *Procedia Materials Science*, 3:77–82, 2014.

[8] S.M. Mousavi, J. Paavola, and D. Baroudi. Distributed nonsingular dislocation technique for cracks in strain gradient elasticity. *Journal of the Mechanical Behavior of Materials*, 23: 47–58, 2014.

Proceedings of the XII Finnish Mechanics Days
R. Kouhia, J. Mäkinen, S. Pajunen and T. Saksala (Eds.)

Continuum damage mechanics without the variable damage *D*

Kari Santaoja

Department of Applied Mechanics, Aalto University, P.O. Box 14300, FI-00076 Aalto, Finland

Summary. Based on Eshelby's inclusion problem a constitutive equation is derived for spherical voids in a matrix material also showing Hookean deformation is derived. A modified postulate of strain equivalence with the effective stress concept is used to introduce the effective stress tensor. The relation between the effective stress tensor and the stress tensor is derived. A simple tube example is applied to show, that the effective stress tensor describes the stress state between the voids and is therefore the driving force for the dislocation glide, for example. The specific Gibbs energy for a 2D material having rectilinear non-interacting microcracks is given.

Keywords: damage, effective stress, damage effect tensor, specific Gibbs free energy for a microcracked medium

Introduction

For commercial reasons the capability of structures to carry loads is being exploited ever more effectively. Thus it is becoming increasingly important to understand how materials behave under high loading.

Damage mechanics describes the weakening of materials due to the formation of distributed flaws in the material. It is therefore a potential tool for fulfilling the requirement to predict the response of materials under high loadings. Despite the huge amount of progress made in damage mechanics since the pioneering work by Kachanov [4] in 1958, the toolset for engineers still does not include this approach because of the limited quality of models for damage. The reason for this is that too often damage is described by a variable D (scalar or tensor) without linking it to the micro-mechanisms of materials.

The present paper focuses on micro mechanisms of materials and derives material models for damaged materials that are strongly based on events in nature. As a special case, materials containing voids or microcracks are studied. The derived constitutive equations do not have a variable damage D but they are built on physics based quantities such as the void volume fraction f and the microcrack densities Q^r.

Spherical voids in the Hookean matrix material

Eshelby [3] studied the elastic field in a Hookean material containing an ellipsoidal inclusion. As a special case he determined the value for the complementary strain-energy density w^c of a material containing "a volume fraction f " of inhomogeneous spheres. For the purpose of this work the inhomogeneous spheres are "replaced" by spherical cavities, as shown in Figure 1. This is done by assuming that the values for the elastic constants for the cavities vanish. Based on the work by Eshelby [3], the specific Gibbs energy for a Hookean material with spherical voids $g^{de}(\boldsymbol{\sigma}, f)$ takes the following appearance [5, Eq. (26.6)]:

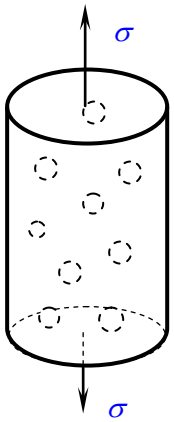

Figure. 1. Porous material.

$$g^{de}(\boldsymbol{\sigma}, f) = \frac{1}{2\rho_0}\left[\frac{1}{3(3\lambda + 2\mu)}(1 + \underline{A}\, f)\left[\mathbf{1}:\boldsymbol{\sigma}\right]^2 + \frac{1}{2\mu}\left(1 + \underline{B}\, f\right)\mathbf{s}:\mathbf{s}\right] \quad (1)$$

where $\boldsymbol{\sigma}$ is the stress tensor, f is the void volume fraction, ρ_0 is the density, $\mathbf{1}$ is the second-order identity tensor [5, Def. (2.26)], $\mathbf{s}$ is the deviatoric stress tensor and where [5, Defs (26.2)]

$$\underline{A} = \frac{6\mu + 3\lambda}{4\mu} \qquad \text{and} \qquad \underline{B} = \frac{15(1-\nu)}{7 - 5\nu}\,. \quad (2)$$

In Expressions (1) and (2) the notations λ and μ are the Lamé elastic constants [5, Def. (21.3)].

For the present study the material model is written in the following format:

$$g(\boldsymbol{\sigma}, f\ldots, T) = g^{de}(\boldsymbol{\sigma}, f) + g^{rest}(\ldots, T)\,. \quad (3)$$

The specific Gibbs free energy $g^{rest}(\ldots, T)$ is out of the scope of the present study.

According to [5, Eqs (26.7)] the state equations take the following appearances:

$$\boldsymbol{\varepsilon} - \boldsymbol{\varepsilon}^i = \rho_0 \frac{\partial g(\boldsymbol{\sigma}, f, \ldots, T)}{\partial \boldsymbol{\sigma}} = \frac{\partial g^{de}(\boldsymbol{\sigma}, f)}{\partial \boldsymbol{\sigma}}, \qquad \text{and} \qquad e = \rho_0 \frac{\partial g^{de}(\boldsymbol{\sigma}, f)}{\partial f}\,, \quad (4)$$

where $\boldsymbol{\varepsilon}$ is the strain tensor, $\boldsymbol{\varepsilon}^i$ is the inelastic strain tensor, T is the absolute temperature and e is the internal force related to the void volume fraction f. Substitution of Expression (1) into State Equation $(4)_1$ gives

$$\boldsymbol{\varepsilon} - \boldsymbol{\varepsilon}^i = \frac{1}{3(3\lambda + 2\mu)}(1 + \underline{A}\, f)\,\mathbf{1}\mathbf{1}:\boldsymbol{\sigma} + \frac{1}{2\mu}\left(1 + \underline{B}\, f\right)(\mathbf{I}^s - \tfrac{1}{3}\mathbf{1}\mathbf{1}):\boldsymbol{\sigma}\,. \quad (5)$$

where $\mathbf{I}^s$ is the fourth-order symmetric identity tensor [5, Def. (2.37)]. Expression (5) can be written in the form

$$\boldsymbol{\varepsilon} - \boldsymbol{\varepsilon}^i = \tilde{\mathbf{S}}(f):\boldsymbol{\sigma} = [\mathbf{S} + \mathbf{S}^d(f)]:\boldsymbol{\sigma}\,, \quad (6)$$

where $\tilde{\mathbf{S}}(f)$ is the effective compliance tensor, $\mathbf{S}$ is the compliance tensor for a Hookean material and $\mathbf{S}^d(f)$ is the compliance tensor due to damage. The latter two tensors are

$$\mathbf{S} = \frac{1}{3(3\lambda + 2\mu)}\mathbf{1}\mathbf{1} + \frac{1}{2\mu}(\mathbf{I}^s - \tfrac{1}{3}\mathbf{1}\mathbf{1}) \quad (7)$$

and

$$\mathbf{S}^d(f) = \frac{\underline{A}\, f}{3(3\lambda + 2\mu)}\,\mathbf{1}\mathbf{1}:\boldsymbol{\sigma} + \frac{\underline{B}\, f}{2\mu}(\mathbf{I}^s - \tfrac{1}{3}\mathbf{1}\mathbf{1})\,, \quad (8)$$

Based on Expressions (6), the following can be written:

$$\boldsymbol{\varepsilon}^e = \mathbf{S}:\boldsymbol{\sigma} \qquad \text{and} \qquad \boldsymbol{\varepsilon}^d := \mathbf{S}:\boldsymbol{\sigma} \qquad \Rightarrow \qquad \boldsymbol{\varepsilon} - \boldsymbol{\varepsilon}^i = \boldsymbol{\varepsilon}^e + \boldsymbol{\varepsilon}^d\,. \quad (9)$$

In Expressions (9) the notations $\boldsymbol{\varepsilon}^e$ and $\boldsymbol{\varepsilon}^d$ stand for the elastic strain tensor and the damage strain tensor, respectively. The effective compliance tensor $\tilde{\mathbf{S}}(f)$ may not be separable into two terms and therefore the damage-elastic strain tensor $\boldsymbol{\varepsilon}^{de}$ is defined to be

$$\boldsymbol{\varepsilon}^{de} := \tilde{\mathbf{S}}(f):\boldsymbol{\sigma}\,, \qquad \text{which with Eq. (6) gives} \qquad \boldsymbol{\varepsilon}^{de} = \boldsymbol{\varepsilon} - \boldsymbol{\varepsilon}^{i}\ . \tag{10}$$

Damage description by the postulate of strain equivalence with the effective stress concept

The postulate of damage-elastic strain equivalence with the effective stress concept was introduced by Chaboche [2, p. 19]. Here the definition of the effective stress tensor $\tilde{\boldsymbol{\sigma}}$ by Chaboche is extended for a non-linear material response as follows: If the virgin (undamaged) material obeys the following constitutive equation:

$$\boldsymbol{\sigma} = f_2(\boldsymbol{\varepsilon}^{de}, \text{Virgin})\ , \tag{11}$$

then the effective stress tensor $\tilde{\boldsymbol{\sigma}}$ is defined by

$$\tilde{\boldsymbol{\sigma}} = f_2(\boldsymbol{\varepsilon}^{de}, \text{Damaged})\ . \tag{12}$$

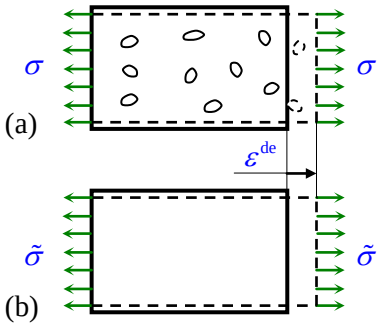

Figure. 2. Postulate of strain equivalence with the effective stress concept.

The message of this postulate is given in Figure 2. It is important to note that Material Models (11) and (12) have an identical functional appearance. Determination of the function f_2 may be difficult in practice, since damage can occur immediately after loading and no loaded virgin state, within which to determine the function f_2, exists. Such problems are not studied here.

Here the elastic response of the virgin (un-voided / uncracked / undamaged) material is assumed to obey Hooke's law. Thus, the constitutive equation for a (undamaged) Hookean material corresponding to Material Model (11) takes the following appearance:

$$\boldsymbol{\sigma} = \mathbf{C}:\boldsymbol{\varepsilon}^{e} \quad \text{or} \quad \boldsymbol{\sigma} = \mathbf{C}:\boldsymbol{\varepsilon}^{de} \quad \text{for a virgin material}\,. \tag{13}$$

Equation $(13)_2$ can be written, since in a virgin material no damage exists and therefore the damage-elastic strain tensor $\boldsymbol{\varepsilon}^{de}$ equals the elastic strain tensor $\boldsymbol{\varepsilon}^{e}$. The fourth-order tensor $\mathbf{C}$ is the constitutive tensor for a Hookean material. Comparison of Expressions (11) and (12) with Material Model (13) gives

$$\tilde{\boldsymbol{\sigma}} = \mathbf{C}:\boldsymbol{\varepsilon}^{de} \quad \text{~~for a damaged material~~}\ . \tag{14}$$

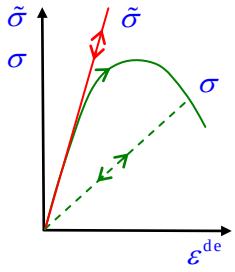

Figure. 3. Stress $\boldsymbol{\sigma}$ and the effective stress $\tilde{\boldsymbol{\sigma}}$ vs. damage-elastic strain ε^{de} curves.

Comparison of Expressions (11) and (12) with the Expressions (13) and (14) shows that in the definition of for the effective stress tensor $\tilde{\boldsymbol{\sigma}}$ the term "for a damaged material" is struck out. The reason to struck out the term "for a damaged material" is that Definition (14) also holds for a case where the amount of damage is negligible, i.e. for a virgin material. In such a case the value of the effective stress tensor $\tilde{\boldsymbol{\sigma}}$ equals that of the stress tensor $\boldsymbol{\sigma}$.

According to Expression (14), the relationship between the effective stress $\tilde{\sigma}$ and the damage-elastic strain ε^{de} is linear. This is shown in Figure 3. It is important to note that the relationship between the effective stress $\tilde{\sigma}$ and the damage-elastic strain ε^{de} is also linear in the case of damage evolution. Figure 3 allows to compare the behaviour of the effective stress $\tilde{\sigma}$ with the stress σ.

Role of the effective stress tensor $\tilde{\boldsymbol{\sigma}}$

A rod under tensile load N, shown in Figure 4(a), is studied. The rod is assumed to have non-interacting voids. The material between the voids is linear elastic. The material of the rod is simplified by concentrating all the voids around the centre line of the rod. This means that the

rod is modelled as a tube sketched in Figure 4(b). Thus, in the model the wall is continuous matter where no voids exist.

The area of the wall of the cross section of the tube is denoted by A^{m} (where the "m" refers to the matrix material). Figure 4(b) gives

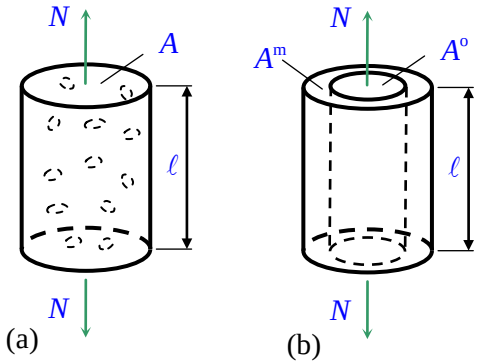

Figure. 4. (a) Rod with voids is modelled as a (b) tube with continuous matter.

$$\frac{N}{A^{\mathrm{m}}} = E\,\varepsilon^{\mathrm{de}} \ . \tag{15}$$

In the uniaxial case the definition for the effective stress $\tilde{\sigma}$ is assumed to take the following form:

$$\tilde{\sigma} := \frac{N}{A^{\mathrm{m}}} \ . \tag{16}$$

Substituting of Definition (16) into Equation (15) yields

$$\tilde{\sigma} = E\,\varepsilon^{\mathrm{de}} \ . \tag{17}$$

Expression (17) equals the uniaxial form of Definition (14). Thus, the effective stress tensor $\tilde{\boldsymbol{\sigma}}$ can be interpreted to be a measure of the stress state in the matrix material between the voids. It is important to notice that the effective stress tensor $\tilde{\boldsymbol{\sigma}}$ does not describe the microscopic local variation of the stress state between the voids instead, it deals with an averaged microscopic quantity.

Relation between the effective stress tensor $\tilde{\boldsymbol{\sigma}}$ and the stress tensor $\boldsymbol{\sigma}$

The postulate of strain equivalence with the effective stress concept gave Expression (14) which with Equation $(10)_2$ takes the following appearance:

$$\tilde{\boldsymbol{\sigma}} = \mathbf{C}:(\boldsymbol{\varepsilon} - \boldsymbol{\varepsilon}^{\mathrm{i}}) \ . \tag{18}$$

Equation (6) is recalled. It is

$$\boldsymbol{\varepsilon} - \boldsymbol{\varepsilon}^{\mathrm{i}} = \tilde{\mathbf{S}}(f):\boldsymbol{\sigma} \ . \tag{19}$$

Substitution of Equation (19) into Equation (18) gives

$$\tilde{\boldsymbol{\sigma}} = \mathbf{C}:\tilde{\mathbf{S}}:\boldsymbol{\sigma} \qquad \Rightarrow \qquad \tilde{\boldsymbol{\sigma}} = \mathbf{M}:\boldsymbol{\sigma}\,, \qquad \mathbf{M} := \mathbf{C}:\tilde{\mathbf{S}} \ . \tag{20}$$

The quantity f is dropped out in Equations (20) to show that Equations (20) are also valid for a microcracked material, for example. The notation $\mathbf{M}$ stands for the damage effect tensor. Equation (6), i.e. $\tilde{\mathbf{S}} = \mathbf{S} + \mathbf{S}^{\mathrm{d}}$, allows Definition $(20)_3$ to take the following appearances:

$$\mathbf{M} := \mathbf{C}:\tilde{\mathbf{S}} = \mathbf{C}:(\mathbf{S} + \mathbf{S}^{\mathrm{d}}) = \mathbf{I}^{\mathrm{s}} + \mathbf{C}:\mathbf{S}^{\mathrm{d}} \ , \tag{21}$$

where the fact that $\mathbf{C}:\mathbf{S} = \mathbf{I}^{\mathrm{s}}$ is exploited.

Specific Gibbs free energy g^{de} for a two-dimensional microcracked medium

Based on stress intensity factors K_{I}, K_{II} and K_{III}, Basista [1] derived an expression of the specific Gibbs free energy g^{de} for a Hookean material with rectilinear non-interacting microcracks in a two-dimensional body. The author [4] enhanced this expression and gave it in the following appearance for the plane stress:

$$g^{\mathrm{de}}(\sigma,Q^r) = \frac{1}{2\rho_0}\left[\frac{1}{3(3\lambda+2\mu)}[\mathbf{1}:\boldsymbol{\sigma}]^2 + \frac{1}{2\mu}\mathbf{s}:\mathbf{s}\right] + \frac{\pi h}{E}\sum_{r=1}^{M} Q^r (a^r)^2 \times \left\{ \vec{n}^r\cdot\boldsymbol{\sigma}\cdot\boldsymbol{\sigma}\cdot\vec{n}^r - [1-H(\vec{n}^r\cdot\boldsymbol{\sigma}\cdot\vec{n}^r)](\vec{n}^r\cdot\boldsymbol{\sigma}\cdot\vec{n}^r)^2 \right\}, \tag{22}$$

where h is the thickness of the two-dimensional body and M is the number of microcrack groups. In each group the sizes and orientations of the microcracks are equal. The quantity a^r is the length of the microcrack and the unit normal vector for the microcrack surface is denoted by $\vec{n}^r$, as shown in Figure 5. The microcrack densities are defined to be

$$Q^r := m^r / (\rho_0 V^{\mathrm{rve}}), \tag{23}$$

where m^r is the number of microcracks within the r'th microcrack group and V^{rve} is the volume of the representative volume element.

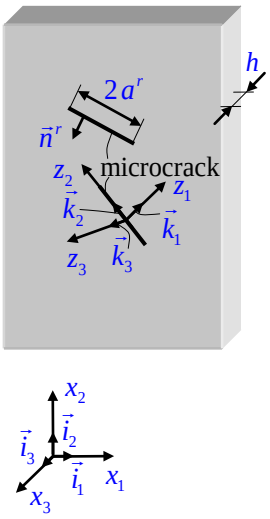

Figure 5. Microcracks in a 2D body.

Eq. (22) has three major enhancements to the original one proposed by Basista [1].

First, microcracks are collected into groups containing microcracks of the same size and orientation. The introduction of microcrack groups is of course only an approximation given that the size and orientation of microcracks can be randomly distributed. However, microcrack groups make computation faster and the approximation error can be neglected by increasing the number of microcrack groups.

The second enhancement involves the introduction of microcrack densities Q^r, which enter into the formulation of continuum thermodynamics as internal variables. The strong physical foundation of these internal variables makes them more attractive quantities for damage mechanics than variable damage D (scalar, vector or tensor), the physical background of which is sometimes unclear.

The third enhancement involves the Heaviside function $H(\vec{n}^r\cdot\boldsymbol{\sigma}\cdot\vec{n}^r)$. Basista [1] wrote his expression for the specific Gibbs free energy only for tension. The author introduced the Heaviside function $H(\vec{n}^r\cdot\boldsymbol{\sigma}\cdot\vec{n}^r)$ for extending the work by Basista [1] for compression. The Heaviside function $H(\vec{n}^r\cdot\boldsymbol{\sigma}\cdot\vec{n}^r)$ prevents the microcrack surfaces from penetrating each other under compression, as sketched in Figure 6.

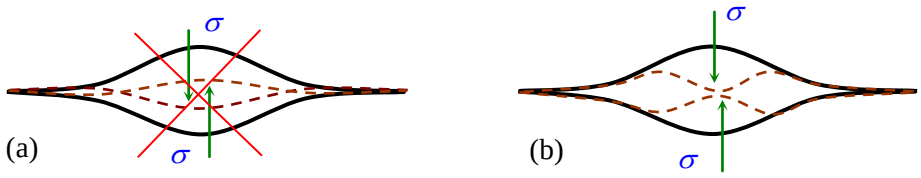

Figure. 6. (a) Surfaces of a microcrack penetrate each other. (b) Penetration is prevented by the Heaviside function $H(\vec{n}^r\cdot\boldsymbol{\sigma}\cdot\vec{n}^r)$.

Substituting Model (22) into Equation $(4)_1$ and taking Expression $(9)_3$ into account yields

$$\boldsymbol{\varepsilon} - \boldsymbol{\varepsilon}^{\mathrm{i}} = \boldsymbol{\varepsilon}^{\mathrm{e}} + \boldsymbol{\varepsilon}^{\mathrm{d}}, \qquad \text{where} \qquad \boldsymbol{\varepsilon}^{\mathrm{e}} = \mathbf{S}:\boldsymbol{\sigma} \tag{24}$$

and

$$\boldsymbol{\varepsilon}^{\mathrm{d}} = \frac{\pi h}{E}\sum_{r=1}^{M} Q^r (a^r)^2 \left\{ \vec{n}^r\boldsymbol{\sigma}\cdot\vec{n}^r + \vec{n}^r\cdot\boldsymbol{\sigma}\,\vec{n}^r - [1-H(\vec{n}^r\cdot\boldsymbol{\sigma}\cdot\vec{n}^r)][2\,\vec{n}^r\,\vec{n}^r(\vec{n}^r\cdot\boldsymbol{\sigma}\cdot\vec{n}^r)\right\}. \tag{25}$$

Expressions $(24)_2$ and (25) show that the effective compliance tensor $\tilde{\mathbf{S}}$ can be derived. Thus, based on Equations (6) and (20) the effective stress tensor $\tilde{\boldsymbol{\sigma}}$ can be obtained for a Hookean material with rectilinear non-interacting microcracks in a two-dimensional body.

Discussion and conclusions

Based on Eshelby's inclusion problem [3], a Hookean material with spherical non-interacting voids was investigated. A stress-strain relation and the necessary compliance tensors as a function of the material porosity f and the elasticity constants of the matrix material were derived. The standard notation, which expresses the stress-strain relation for brittle damaging materials by the elastic strain tensor $\boldsymbol{\varepsilon}^{\mathrm{e}}$, was replaced by the damage-elastic strain tensor $\boldsymbol{\varepsilon}^{\mathrm{de}}$. Hookean material with non-interacting spherical voids was shown to support this concept.

A modified postulate of strain equivalence with the effective stress $\tilde{\boldsymbol{\sigma}}$ concept was expressed. The different relations of the stress tensor $\boldsymbol{\sigma}$ and the effective stress tensor $\tilde{\boldsymbol{\sigma}}$ in terms of the damage-elastic strain tensor $\boldsymbol{\varepsilon}^{\mathrm{de}}$ were shown. The role of the effective stress tensor $\tilde{\boldsymbol{\sigma}}$ was evaluated by a simple uniaxial tube example. The example showed that the effective stress tensor $\tilde{\boldsymbol{\sigma}}$ can be interpreted to be related to the averaged stress between the voids.

The expressions obtained from the problem of non-interacting voids in the Hookean materials were used for derivation of an analytical expression between the damage effect tensor $\tilde{\boldsymbol{\sigma}}$ and the stress tensor $\boldsymbol{\sigma}$. This expression reads: $\tilde{\boldsymbol{\sigma}} = \mathbf{M} : \boldsymbol{\sigma}$, where $\mathbf{M}$ is the damage effect tensor.

Evaluation of the non-interacting rectilinear microcracks embedded by a Hookean matrix material is based on the work by Basista [1]. The expression for the specific Gibbs free energy g^{de} for a Hookean body with non-interacting rectilinear microcracks by Basista was enhanced in three different ways:

First, microcracks were collected into groups containing microcracks of the same size and orientation. Microcrack groups make computation faster.

The second enhancement involved the introduction of microcrack densities Q^r, which entered into the formulation of continuum thermodynamics as internal variables. The strong physical foundation of these internal variables makes them more attractive quantities for damage mechanics than variable damage D (scalar, vector or tensor), the physical background of which is sometimes unclear.

The third enhancement involved the Heaviside function $H(\vec{n}^r \cdot \boldsymbol{\sigma} \cdot \vec{n}^r)$. Basista [1] wrote his expression for the specific Gibbs free energy only for tension. The author introduced the Heaviside function $H(\vec{n}^r \cdot \boldsymbol{\sigma} \cdot \vec{n}^r)$ to extend the work by Basista [1] for compression.

References

[1] M. Basista. *Micromechanics of Damage in Brittle Solids*. In: Skrzypek J.J., Ganczarski A.W., editors. Anisotropic Behaviour of Damaged Materials. Springer Verlag; Berlin, Germany, 221-258, 2003

[2] J.-L. Chaboche. *Description thermodynamique et phénoménologique de la viscoplasticité cyclique avec endommagement*. Office National d'Etudes et de Recherches Aérospatiales, Chatillon, France, Publication no. 1978-3. (In French)

[3] J.D. Eshelby. *The determination of the elastic field of an ellipsoidal inclusion, and related problems*. Proceedings of the Royal Society of London, A241, 376-396, 1957

[4] K. Santaoja. Thermodynamic formulation of a material model for microcracking applied to creep damage, ECF20, 20th European Conference on Fracture, Procedia Materials Science, Elsevier, Vol. 3, 1179-1184, 2014

[5] K. Santaoja. Lecture Notes on Continuum Thermodynamics. Taras, Espoo, Finland, 2014.

Proceedings of the XII Finnish Mechanics Days
R. Kouhia, J. Mäkinen, S. Pajunen and T. Saksala (Eds.)

An anisotropic continuum damage model for concrete

Saba Tahaei Yaghoubi[1], Juha Hartikainen[1], Kari Kolari[2], and Reijo Kouhia[3]

[1]Aalto University, Department of Civil and Structural Engineering
P.O. Box 12100, 00076 Aalto, Finland
[2]VTT, P.O. Box 1806, 02044 VTT, Finland
[3]Tampere University of Technology, Department of Mechanical Engng and Industrial Systems
P.O. Box 589, 33101 Tampere, Finland
saba.tahaei@aalto.fi, juha.hartikainen@aalto.fi, kari.kolari@vtt.fi, reijo.kouhia@tut.fi

Summary. In this paper, a thermodynamic formulation for modelling anisotropic damage of elastic-brittle materials based on Ottosen's 4-parameter failure surface is proposed. The model is developed by using proper expressions for Gibb's free energy and the complementary form of the dissipation potential. The formulation predicts the basic characteristic behaviour of concrete well and results in a realistic shape for the damage surface.

Key words: damage, elastic-brittle material, the spesific Gibb's free energy, dissipation potential, Ottosen's 4-parameter criterion

Introduction

Concrete is a composite material composed mainly of water, aggregate and cement. It has relatively high compressive strength, but it has a low tensile strength, which is usually between 5-10% of the compressive strength.

A myriad of models have been proposed to model the mechanical behaviour of concrete. Earlier investigations have mainly focused in formulating the form of the ultimate failure surface in a way similar to the yield function of plasticity (e.g. [12], [21],[3], [11], [6], [17]). These models did not always take a proper account of the gradual degradation process prior to failure.

Recently, continuum damage mechanics is videly used for modelling the brittle behaviour of materials. The scalar damage variable which was first introduced by Kachanov [8] has been applied by several authors due to the simplicity of application together with plasticity, e.g. [10], [7],[13], [19]. Studies such as [5], [2] and [20] have proposed a mixed plasticity anisotropic damage model for concrete using higher order damage tensors.

Ottosen's four parameter criterion

In 1977, Ottosen proposed a failure surface for concrete which contains the three stress invariants and is capable of capturing the essential features of concrete's behaviour [14, 15, 16]. The failure criterion has four adjustable parameters and has the form

$$A\frac{J_2}{\sigma_\mathrm{c}} + \Lambda\sqrt{J_2} + BI_1 - \sigma_\mathrm{c} = 0, \tag{1}$$

where σ_c is the uniaxial compressive strength, $I_1 = \mathrm{tr}\boldsymbol{\sigma}$ the first invariant of the stress tensor and $J_2 = \frac{1}{2}\boldsymbol{s} : \boldsymbol{s}$ the second invariant of the deviatoric stress tensor $\boldsymbol{s} = \boldsymbol{\sigma} - \sigma_\mathrm{m}\boldsymbol{I}$, where σ_m is

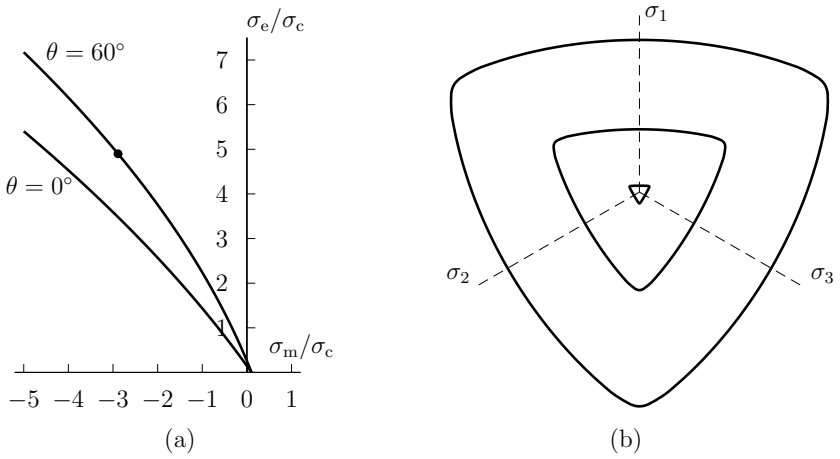

Figure 1. Ottosen's 4-parameter failure surface: (a) compressive and tensile meridian lines and (b) shape on the deviatoric plane when $\sigma_m = 0, \sigma_m = -\sigma_c$ and $\sigma_m = -2.887\sigma_c$, strength ratios are $\sigma_t/\sigma_c = 0.1$, and $\sigma_{bc}/\sigma_c = 1.16$. $\sigma_e = \sqrt{3J_2}$ is the effective stress.

the mean normal stress $\sigma_m = \frac{1}{3}I_1$. Furthermore, the shape of the failure surface in the deviatoric plane is determined by the function $\Lambda = \Lambda(\theta)$ as

$$\Lambda = \begin{cases} k_1 \cos[\frac{1}{3}\arccos(k_2 \cos 3\theta)] & \text{if} \quad \cos 3\theta \geq 0 \\ k_1 \cos[\frac{1}{3}\pi - \frac{1}{3}\arccos(-k_2 \cos 3\theta)] & \text{if} \quad \cos 3\theta \leq 0 \end{cases} . \tag{2}$$

The Lode angle θ in the deviatoric plane can be expressed in terms of the deviatoric invariants as

$$\cos 3\theta = \frac{3\sqrt{3}}{2}\frac{J_3}{J_2^{3/2}}, \tag{3}$$

where $J_3 = \det \boldsymbol{s}$ is the third invariant of the deviatoric stress tensor. Determination of the dimensionless parameters A and B, the size factor k_1 and the shape factor k_2 requires four tests, see [14, 16]. Shape of the failure surface is illustrated in Figure 1 in the meridian and deviatoric planes.

Present model

Constitutive theory

The constitutive equations of the model are derived by using the second principle of thermodynamics and associated thermodynamic potentials. Considering isothermal elastic damaging material with small deformations the reversible behaviour of material is captured by the specific Gibb's free energy

$$\psi^c = \psi^c(\boldsymbol{\sigma}, \boldsymbol{D}, \kappa) \tag{4}$$

which is defined by the stress tensor $\boldsymbol{\sigma}$, the second order damage tensor $\boldsymbol{D}$ and the scalar variable κ that characterises the internal state of the material.

The second principle of thermodynamics is represented by the Clausius-Duhem inequality in the form

$$\gamma \geq 0, \quad \gamma = \rho_0 \dot{\psi}^c - \dot{\boldsymbol{\sigma}} : \boldsymbol{\varepsilon} = \left(\rho_0 \frac{\partial \psi^c}{\partial \boldsymbol{\sigma}} - \boldsymbol{\varepsilon}\right) : \dot{\boldsymbol{\sigma}} + \boldsymbol{Y} : \dot{\boldsymbol{D}} - K\dot{\kappa}, \tag{5}$$

where γ is the power of dissipation and

$$\boldsymbol{Y} = \rho_0 \frac{\partial \psi^c}{\partial \boldsymbol{D}} \quad \text{and} \quad K = -\rho_0 \frac{\partial \psi^c}{\partial \kappa} \tag{6}$$

are thermodynamic forces dual to the rates $\dot{\boldsymbol{D}}$ and $\dot{\kappa}$, respectively [18]. Density of the material is denoted by ρ_0.

The irreversible material behaviour is described through the dissipation potential

$$\varphi = \varphi(\boldsymbol{Y}, K; \boldsymbol{\sigma}) \tag{7}$$

as a function of the dissipation variables $\boldsymbol{Y}$ and K. The dissipation potential is a non-smooth monotonic and subdifferentiable function from a linear space into $\bar{\mathbb{R}} = \mathbb{R} \cup \{+\infty\}$. It determines the power of dissipation such that

$$\gamma \equiv \boldsymbol{B}_Y : \boldsymbol{Y} + B_K K, \quad (\boldsymbol{B}_Y, B_K) \in \partial\varphi(\boldsymbol{Y}, K; \boldsymbol{\sigma}), \tag{8}$$

where $\boldsymbol{B}_Y$ and B_K are the components of the subgradient of $\varphi(\boldsymbol{Y}, K; \boldsymbol{\sigma})$ and $\partial\varphi(\boldsymbol{Y}, K; \boldsymbol{\sigma})$ is the subdifferential set of all subgradients [4].

Combining definition of γ in equations (5) and (8) results in equation

$$\left(\rho_0 \frac{\partial \psi^{\mathrm{c}}}{\partial \boldsymbol{\sigma}} - \boldsymbol{\varepsilon}\right) : \dot{\boldsymbol{\sigma}} + \left(\dot{\boldsymbol{D}} - \boldsymbol{B}_Y\right) : \boldsymbol{Y} + \left(-\dot{\kappa} - B_K\right) K = 0. \tag{9}$$

If the bracketed coefficients in equation (9) tend to zero, the equation holds for arbitrary $\dot{\boldsymbol{\sigma}}$, $\boldsymbol{Y}$ and K, and the following general constitutive equations are obtained

$$\boldsymbol{\varepsilon} = \rho_0 \frac{\partial \psi^{\mathrm{c}}}{\partial \boldsymbol{\sigma}}, \qquad \dot{\boldsymbol{D}} = \boldsymbol{B}_Y, \qquad \dot{\kappa} = -B_K. \tag{10}$$

Specific model

The specific Gibb's free energy function is formulated by using the representation theory of tensorial functions, which states that a scalar isotropic function depending on two symmetric second order tensors can be expressed by a combination of the invariants belonging to the integity basis

$$\left\{\operatorname{tr}\boldsymbol{\sigma}, \operatorname{tr}(\boldsymbol{\sigma}^2), \operatorname{tr}(\boldsymbol{\sigma}^3), \operatorname{tr}\boldsymbol{D}, \operatorname{tr}(\boldsymbol{D}^2), \operatorname{tr}(\boldsymbol{D}^3), \operatorname{tr}(\boldsymbol{\sigma}\boldsymbol{D}), \operatorname{tr}(\boldsymbol{\sigma}\boldsymbol{D}^2), \operatorname{tr}(\boldsymbol{\sigma}^2\boldsymbol{D}), \operatorname{tr}(\boldsymbol{\sigma}^2\boldsymbol{D}^2)\right\}. \tag{11}$$

Assuming no crack interaction, only the linear terms in $\boldsymbol{D}$ are retained [1]. Furthermore, restricting to linear elasticity, only the linear and quadratic invariants of the stress tensor are included. Hence, the specific Gibb's free energy function describing the isothermal elastic behaviour of material with a reduction effect due to damage can be formulated as

$$\rho_0\psi^{\mathrm{c}}(\boldsymbol{\sigma}, \boldsymbol{D}, \kappa) = \frac{1+\nu}{2E}\left[\operatorname{tr}\boldsymbol{\sigma}^2 + \operatorname{tr}(\boldsymbol{\sigma}^2\boldsymbol{D}\right] - \frac{\nu}{2E}(1 + \tfrac{1}{3}\operatorname{tr}\boldsymbol{D})(\operatorname{tr}\boldsymbol{\sigma})^2 + \psi^{\mathrm{c},\kappa}(\kappa), \tag{12}$$

where ν and E stand for Poisson's ratio and elastic modulus, respectively. The function $\psi^{\mathrm{c},\kappa}(\kappa)$ denotes the damage hardening part of the specific Gibb's free energy. It should be noticed that in the case of isotropic damage, $\boldsymbol{D} = D\boldsymbol{I}$, where D is a scalar damage variable, and the model reduces into the form

$$\rho_0\psi^{\mathrm{c}} = (1+D)\left[\frac{1+\nu}{2E}\operatorname{tr}\boldsymbol{\sigma}^2 - \frac{\nu}{2E}(\operatorname{tr}\boldsymbol{\sigma})^2\right] + \psi^{\mathrm{c},\kappa}(\kappa). \tag{13}$$

The dissipation potential is defined by the non-smooth indicator function $\mathrm{I}_\Sigma = \mathrm{I}_\Sigma(\boldsymbol{Y}, K; \boldsymbol{\sigma})$ [4] such that

$$\varphi(\boldsymbol{Y}, K; \boldsymbol{\sigma}) = \mathrm{I}_\Sigma(\boldsymbol{Y}, K; \boldsymbol{\sigma}), \quad \mathrm{I}_\Sigma(\boldsymbol{Y}, K; \boldsymbol{\sigma}) = \begin{cases} 0 & \text{if } (\boldsymbol{Y}, K) \in \Sigma \\ +\infty & \text{if } (\boldsymbol{Y}, K) \notin \Sigma \end{cases}, \tag{14}$$

where

$$\Sigma = \{(\boldsymbol{Y}, K) | f(\boldsymbol{Y}, K; \boldsymbol{\sigma}) \leq 0\} \tag{15}$$

is a convex set of admissible thermodynamic force $\boldsymbol{Y}$ and hardening variable K defined by the damage surface

$$f(\boldsymbol{Y}, K; \boldsymbol{\sigma}) = \frac{A\tilde{J}_2}{\sigma_{c0}} + \Lambda\sqrt{\tilde{J}_2} + BI_1 - (\sigma_{c0} + K) = 0, \tag{16}$$

where σ_{c0} denotes the initial elastic limit in uniaxial compression. The damage surface (16) is obtained by reformulating the deviatoric invariants of the Ottosen's 4-parameter failure surface in terms of the thermodynamic force $\boldsymbol{Y}$, hardening variable K, and stress $\boldsymbol{\sigma}$ as

$$\tilde{J}_2 = \frac{1}{1+\nu}\left[E \operatorname{tr} \boldsymbol{Y} - \tfrac{1}{6}(1-2\nu)(\operatorname{tr}\boldsymbol{\sigma})^2\right], \tag{17}$$

$$\tilde{J}_3 = \frac{2}{3(1+\nu)}\left\{E\left[\operatorname{tr}(\boldsymbol{\sigma}\boldsymbol{Y}) - \operatorname{tr}\boldsymbol{\sigma}\operatorname{tr}\boldsymbol{Y}\right] + \tfrac{1}{9}(1-2\nu)(\operatorname{tr}\boldsymbol{\sigma})^3\right\}. \tag{18}$$

The subdifferential of φ is defined by the set

$$\partial\varphi(\boldsymbol{Y}, K; \boldsymbol{\sigma}) = \begin{cases} \{(\boldsymbol{B}_Y, B_K)\}, & \text{if } (\boldsymbol{Y}, K) \in \Sigma, \\ \emptyset, & \text{if } (\boldsymbol{Y}, K) \notin \Sigma, \end{cases} \tag{19}$$

where $\boldsymbol{B}_Y$ and B_K are the components of the subgradient which is zero in the interior of the damage surface and equals to the the normal of the damage surface at point $(\boldsymbol{Y}, K)$ such that

$$(\boldsymbol{B}_Y, B_K) = \begin{cases} (\boldsymbol{0}, 0), & \text{if } f(\boldsymbol{Y}, K_\alpha; \boldsymbol{\sigma}) < 0, \\ \left(\dot{\lambda}\dfrac{\partial f}{\partial \boldsymbol{Y}}, \dot{\lambda}\dfrac{\partial f}{\partial K}\right),\ \dot{\lambda} \geq 0, & \text{if } f(\boldsymbol{Y}, K_\alpha; \boldsymbol{\sigma}) = 0. \end{cases} \tag{20}$$

The multiplier $\dot{\lambda}$ above can be calculated by use of the consistency condition $\dot{f} = 0$.

Finally, the specific constitutive equations can be obtained from equations (6), (10) and (20). In this work, the hardening variable K has the expression

$$K = -\rho_0 \frac{\partial \psi^c}{\partial \kappa} = \frac{a_1 (\kappa/\kappa_{\max}) + a_2 (\kappa/\kappa_{\max})^2}{1 + b (\kappa/\kappa_{\max})^2}, \tag{21}$$

where $\kappa_{\max}$ corresponds to the value of κ when K reaches its maximum value $K_{\max}$ and a_1, a_2, b are material parameters to be determined. The expression (21) differs from the choice in [18].

Numerical example

The present model is used in analysis of a concrete specimen with the ultimate compressive strength of $\sigma_c = 32.8$ MPa. Parameters in the inital failure surface have been determined assuming the initial tensile strength $\sigma_{t0} = 1$ MPa and compressive strength $\sigma_{c0} = 18$ MPa, equibiaxial compressive strengh $1.16\,\sigma_{c0}$ and the point on the compressive meridian $(I_1, \sqrt{J_2}) = (-5\sqrt{3}\sigma_{c0}, 4\sigma_{c0}/\sqrt{2})$. Resulting values are $A = 2.6943, B = 5.4975, k_1 = 19.0829, k_2 = 0.9982$. The hardening parameters have the values $a_1 = 85.30\,\text{MPa}, a_2 = -12.65\,\text{MPa}$, $b = 0.7032$, $K_{\max} = 42.65\,\text{MPa}$ and $\kappa_{\max} = 4.41 \times 10^{-6}$.

Fig.2a shows the results obtained by the numerical model when the material is subjected to uniaxial compression. The result is compared to the available experimental data [9]. As can be seen in the figure, the results are in good agreement with the experiments. Damage evolution is shown in Fig.2b and the typical behaviour of concrete like materials in compression can be seen, i.e. damage in the planes parallel to the loading directions is dominating. The result shows the potential of the model to simulate the splitting failure of brittle materials.

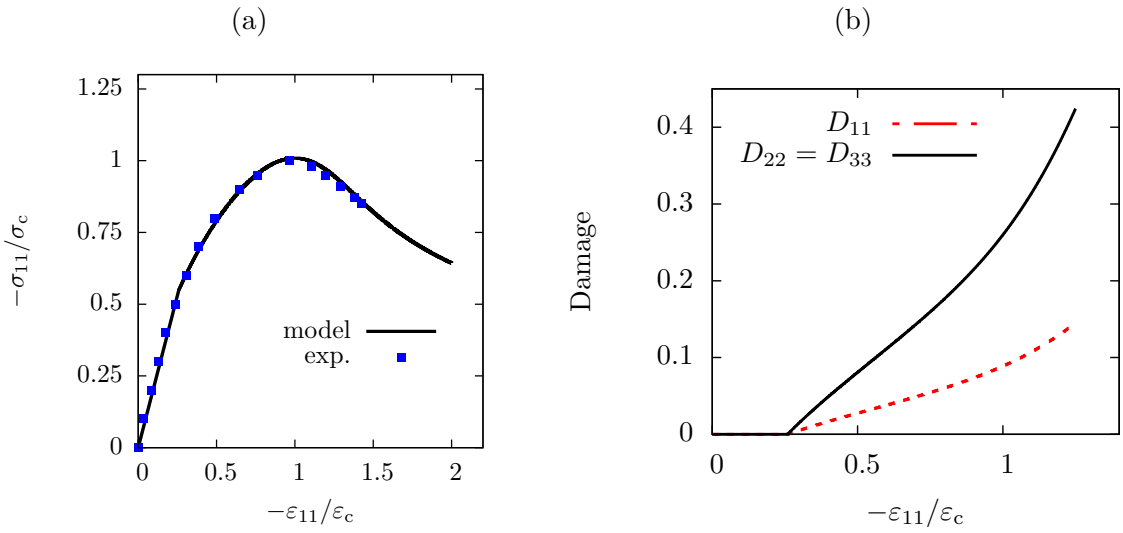

Figure 2. (a) Stress-strain diagram in uniaxial compression. Experimental data from Ref. [9]. (b) Damage evolution in uniaxial compression. Notice that damage is larger in the planes parallel to the loading direction indicating splitting failure mode.

References

[1] M. Basista. Micromechanics of damage in brittle solids. In J.J. Skrzypek and A. Ganczarski, editors, *Anisotropic Behaviour of Damaged Materials*, volume 9 of *Lecture Notes in Applied and Computational Mechanics*, pages 221–258. Springer-Verlag, 2003.

[2] U. Cicekli, G.Z. Voyiadjis, and R.K. Abu Al-Rub. A plasticity and anisotropic damage model for plain concrete. *International Journal of Plasticity*, 23:1874–1900, 2007.

[3] A. Dragon and Z. Mróz. A continuum model for plastic-brittle behavior of rock and concrete. *International Journal of Engineering Science*, 17:121–137, 1979.

[4] M. Frémond. *Non-Smooth Thermomechanics*. Springer, Berlin, 2002.

[5] P. Grassl and M. Jirásek. Damage-plastic model for concrete failure. *International Journal of Solids and Structures*, 43:7166–7196, 2006.

[6] P. Grassl, K. Lundgren, and K. Gylltoft. Concrete in compression, a plasticity theory with a novel hardening law. *International Journal of Solids and Structures*, 39:5205–5223, 2002.

[7] L. Jason, A. Huerta, G. Pijaudier-Cabot, and S. Ghavamian. An elastic plastic damage formulation for concrete: Application to elementary tests and comparison with an anisotropic damage model. *Computer Methods in Applied Mechanics and Engineering*, 195:7077–7092, 2006.

[8] L.M. Kachanov. On the creep fracture time. *Iz. An SSSR Ofd. Techn. Nauk.*, (8):26–31, 1958. (in Russian).

[9] H. Kupfer, H.K. Hilsdorf, and H. Rüsch. Behaviour of concrete under biaxial stresses. *Journal of the American Concrete Institute*, 66(8):656–666, August 1969.

[10] J. Lee and G.L. Fenves. Plastic-damage model for cyclic loading of concrete structures. *Journal of the Engineering Mechanics, ASCE*, 124(8):892–900, August 1998.

[11] P. Menétrey and K.J. Willam. A triaxial failure criterion for concrete and its generalization. *ACI Structural Journal*, 92:311–318, 1995.

[12] M.J. Mikkola and W. C. Schnobrich. Material behavior characteristics for reinforced concrete shells stressed beyond the elastic range. Technical Report 367, University of Illinois, Urbana-Champaign, 1970.

[13] G.D. Nguyen and A.M. Korsunsky. Development of an approach to constitutive modelling of concrete: Isotropic damage coupled with plasticity. *International Journal of Solids and Structures*, 45:5483–5501, 2008.

[14] N.S. Ottosen. A failure criterion for concrete. *Journal of the Engineering Mechanics, ASCE*, 103(EM4):527–535, August 1977.

[15] N.S. Ottosen. Nonlinear finite element analysis of concrete structures. Technical Report Risø-R-411, RisøNational Laboratory, DK-4000 Roskilde, Denmark, May 1980.

[16] N.S. Ottosen and M. Ristinmaa. *The Mechanics of Constitutive Modeling*. Elsevier, 2005.

[17] V.K. Papanikolaou and A.J. Kappos. Confinement-sensiive plasticity constitutive model for concrete in triaxial compression. *International Journal of Solids and Structures*, 44:7021–7048, 2007.

[18] S. Tahaei Yaghoubi, R. Kouhia, J. Hartikainen, and K. Kolari. A continuum damage model based on ottosen's four parameter failure criterion for concrete. *Journal of Structural Mechanics (Rakenteiden Mekaniikka)*, 47(2):50–66, 2014.

[19] G.Z. Voyiadjis and Z.N. Taqieddin. Elastic plastic and damage model for concrete materials: Part i-theoretical formulation. *International Journal of Structural Changes in Solids-Mechanics and Applications*, 1(1):31–59, 2009.

[20] G.Z. Voyiadjis, Z.N. Taqieddin, and P.I. Kattan. Anisotropic damage-plasticity model for concrete. *International Journal of Plasticity*, 24:1946–1965, 2008.

[21] K. Willam and E.P. Warnke. Constitutive model for the triaxial behaviour of concrete. In *IABSE Proceedings*, volume 19, pages 1–30, 1975. Seminar on Concrete Structures Subjected to Triaxial Stresses, Bergamo, Italy May 17-19, 1974.

Proceedings of the XII Finnish Mechanics Days
R. Kouhia, J. Mäkinen, S. Pajunen and T. Saksala (Eds.)

On the choice of damage variable in the continuum fatigue model based on a moving endurance surface

Timo Saksala, Sami Holopainen, and Reijo Kouhia

Tampere University of Technology
Department of Mechanical Engineering and Industrial Systems
P.O. Box 589, 33101 Tampere, Finland
timo.saksala@tut.fi, sami.holopainen@tut.fi, reijo.kouhia@tut.fi

Summary. This paper considers two different damage formulations for modelling high-cycle fatigue of materials. The underlying fatigue model is formulated within continuum mechanics framework with the concept of a moving endurance surface. Such a model has a unique feature that it allows for the concepts of fatigue limits and damage accumulation during the load history thus avoiding cycle-counting techniques. A Scalar and tensor type of damage variables are utilized with an essentially similar type of damage evolution law. The tensor damage model capable of accounting for damage induced anisotropy is based on the gradient of the endurance surface. The performance of the scalar and tensor damage formulations are compared with different multidimensional stress histories.

Key words: high-cycle fatigue modelling, isotropic damage, anisotropic damage, endurance surface, evolution equations

Introduction

Fatigue of materials under variable loads is a complicated physical process which can even result in catastrophic failure of engineering components. It is characterized by nucleation, coalescence and stable growth of cracks. Nucleation of cracks starts from stress concentrations near persistent slip bands, grain interfaces and inclusions [1, 2, 3].

In high-cycle fatigue, the macroscopic behavior of the material is primarily elastic, while in the low-cycle fatigue regime considerable macroscopic plastic deformations take place. Transition between low- and high-cycle fatigue occurs between $10^3 - 10^4$ cycles. In recent years, it has been observed that fatigue failures can occur at very high fatigue lives $10^9 - 10^{10}$, below the previously assumed fatigue limits.

In this paper only high-cycle fatigue modelling is considered. Many different approaches have been proposed to model the high-cycle fatigue behaviour which can roughly be classified into stress invariant, or average stress based and critical plane approaches. In those approaches damage accumulation is usually based on cycle-counting, which makes their use questionable under complex load histories [4, 5].

A different strategy for high-cycle fatigue modelling was proposed by Ottosen et al. [4]. In their approach, which could be classified as evolutionary, the concept of a moving endurance surface in the stress space is postulated together with a damage evolution equation. The endurance surface is expressend in terms of the second invariant of the reduced deviatoric stress tensor where the center of the surface is defined by a deviatoric back stress tensor, as is done similarly in kinematic plasticity models. Therefore, the load history is memorized by the back-stress tensor. In this model arbitrary stress states are treated in a unified manner for different loading histories, thus avoiding cycle-counting techniques.

In the present paper, different damage formulations to be used with the fatigue model by Ottosen et al. [4] are considered. Particularly, the original scalar damage formulation is compared with the proposed tensor damage model capable of accounting for damage induced anisotropy. Evolution of the tensorial damage variable is based on the normality condition for the endurance surface. Performance of the damage formulations are compared with some multidimensional stress histories.

Model formulation

Endurance surface

The continuum fatigue model developed in [4] is briefly described in the following. It is based on the assumption that a material exhibit loading condition dependent endurance limits within which no damage results under cyclic loading. Ottosen et al. [4] proposed a moving endurance surface in stress stress space to account for these limits. The endurance surface is of Drucker-Prager type as

$$\beta = \frac{1}{\sigma_{0\mathrm{e}}}\left(\bar{\sigma} + AI_1 - \sigma_{0\mathrm{e}}\right) = 0, \tag{1}$$

where $\sigma_{0\mathrm{e}}$ is the endurance limit corresponding to zero mean stress, A is a positive non-dimensional parameter, and $I_1 = \mathrm{tr}(\boldsymbol{\sigma})$. In a constant amplitude cyclic, the endurance surface reduces to the linear relation in the Haigh diagram, i.e. relation between the mean stress and the stress amplitude, see Figure 1c. Moreover, $\bar{\sigma}$ in (1) is the effective stress defined in terms of the second invariant of the reduced deviatoric stress $\boldsymbol{s} - \boldsymbol{\alpha}$, with $\boldsymbol{\alpha}$ being the back stress tensor, as

$$\bar{\sigma} = \sqrt{\tfrac{3}{2}(\boldsymbol{s} - \boldsymbol{\alpha}) : (\boldsymbol{s} - \boldsymbol{\alpha})}, \tag{2}$$

where $\boldsymbol{s} = \boldsymbol{\sigma} - \frac{1}{3}\,\mathrm{tr}(\boldsymbol{\sigma})\mathbf{I}$ is the deviatoric stress tensor, $\mathbf{I}$ stands for the identity tensor, and

$$(\boldsymbol{s} - \boldsymbol{\alpha}) : (\boldsymbol{s} - \boldsymbol{\alpha}) := \mathrm{tr}((\boldsymbol{s} - \boldsymbol{\alpha})(\boldsymbol{s} - \boldsymbol{\alpha})) \tag{3}$$

is the double dot-product. The endurance surface, $\beta = 0$, moves in the stress space driven by the back stress which memorizes the load history. Contrarily to plasticity theory, the stress states out of the endurance surface, $\beta > 0$, are allowed. Moreover, the invariant I_1 in (1) accounts for the influence of the hydrostatic stress. The final model component needed before specifying the damage formulations is the evolution law for the back stress tensor. For this end, a hardening rule similar to Ziegler's kinematic hardening rule in plasticity theory is adopted, i.e.

$$\dot{\boldsymbol{\alpha}} = C(\boldsymbol{s} - \boldsymbol{\alpha})\dot{\beta}, \tag{4}$$

where C is a non-dimensional material parameter, and the dot denotes time rate.

Damage evolution

In the original formulation by Ottosen et al. [4] a scalar damage variable is chosen to descibe the material deterioration. Evolution equation for the damage D used in [4] is

$$\dot{D} = K\exp(L\beta)\dot{\beta}, \tag{5}$$

where K and L are parameters to be calibrated by experiments. From the evolution equation (5) it can be concluded that damage only develops when the stress state is moving away from the endurance surface, that is

$$\beta \geq 0, \quad \text{and} \quad \dot{\beta} > 0. \tag{6}$$

It is also postulated that evolution for the back stress $\boldsymbol{\alpha}$, see (4), takes place when the conditions (6) are satisfied. The conditions for evolution of damage and back stress in loading and unloading are illustrated in Figure 1a and b.

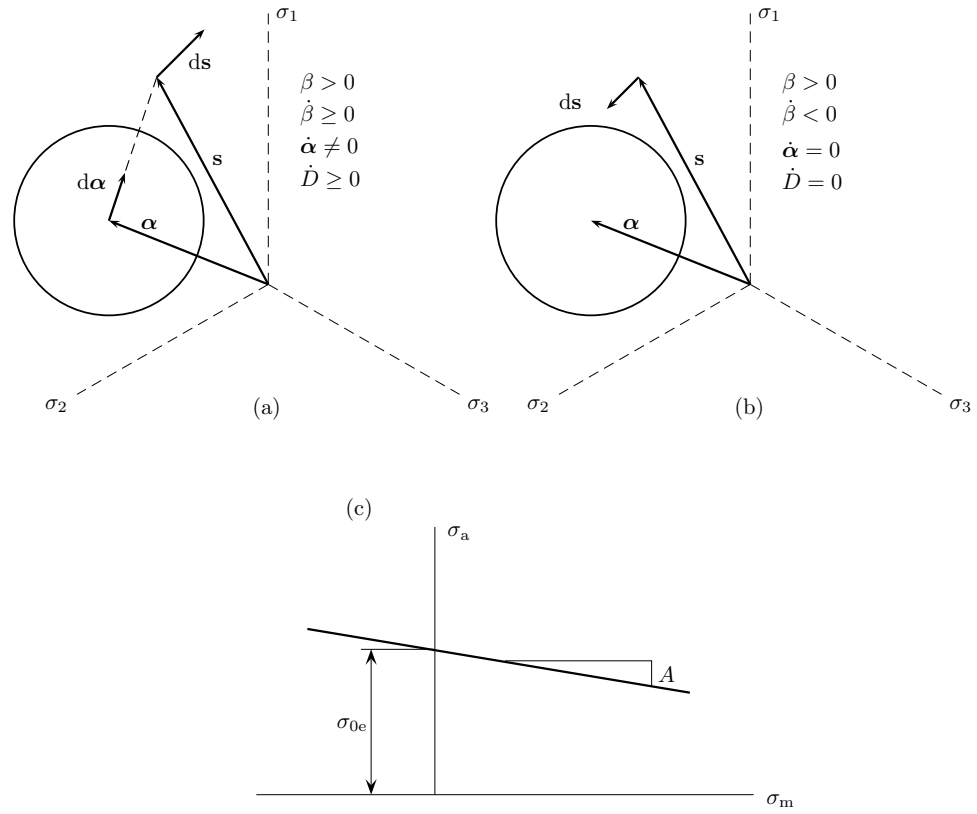

Figure 1. Illustration of damage evolution on the deviatoric plane. (a) Damage evolves only when stress moves away from the endurance surface. (b) Stress state outside the endurance surface, but damage do not evolve. (c) Illustration of the endurance surface as Haigh-diagram for constant amplitude cyclic loading.

In this paper damage is described by a second order tensor, and therefore the model can account damage induced anisotropy. The evolution law for the proposed model is chosen to be of similar form as (5):

$$\dot{\mathbf{D}} = \dot{\beta} K_{\text{aniso}} \exp\left(L_{\text{aniso}}\beta\right) \left| \frac{\partial \beta}{\partial \boldsymbol{\sigma}} \right|, \tag{7}$$

where K_{aniso} and L_{aniso} are model parameters. Since damage never decreases the absolute value is taken of the gradient $\partial\beta/\partial\boldsymbol{\sigma}$.

In order to derive a stress-strain relationship, the spesific strain energy function is postulated in the form

$$W = \tfrac{1}{2}\lambda[1 - \tfrac{1}{3}\operatorname{tr}(\mathbf{D})]\operatorname{tr}(\boldsymbol{\epsilon})^2 + \mu[\operatorname{tr}(\boldsymbol{\epsilon}^2) - \operatorname{tr}(\boldsymbol{\epsilon}^2\mathbf{D})], \tag{8}$$

where $\mathbf{D}$ is the symmetric damage tensor, and λ, μ are the Lamé parameters. The stress-strain relationship is now obtained as a derivative of the spesific strain energy function with respect to strain, i.e.

$$\boldsymbol{\sigma} = \frac{\partial W}{\partial \boldsymbol{\epsilon}} = \lambda[1 - \tfrac{1}{3}\operatorname{tr}(\mathbf{D})]\operatorname{tr}(\boldsymbol{\epsilon})\mathbf{I} + \mu(2\boldsymbol{\epsilon} - \boldsymbol{\epsilon}\mathbf{D} - \mathbf{D}\boldsymbol{\epsilon}) = \mathbf{C}_{\text{ed}} : \boldsymbol{\epsilon}. \tag{9}$$

The fourth-order material secant stiffness tensor has the form

$$\mathbf{C}_{\text{ed}} = \lambda[1 - \tfrac{1}{3}\operatorname{tr}(\mathbf{D})]\mathbf{I} \otimes \mathbf{I} + \mu(2\mathbf{I} \odot \mathbf{I} - \mathbf{I} \odot \mathbf{D} - \mathbf{D} \odot \mathbf{I}), \tag{10}$$

where $\otimes$ denotes the standard tensor product, known as the Kronecker product, and the tensor product $\odot$ is defined as in Ref. [6]:

$$(\mathbf{A} \odot \mathbf{B})_{ijkl} = \tfrac{1}{2}(A_{ik}B_{jl} + A_{il}B_{jk}). \tag{11}$$

A criterion for material failure is then provided by the requirement that the secant stiffness $\mathbf{C}_{\mathrm{ed}}$ should be positive definite. This can be checked e.g. by calculating its eigenvalues (which must be positive). The components of damage tensor $\mathbf{D}$ can also be monitored but the interpretation of final failure is then more ambiguous.

Numerical examples

Some representative numerical simulations highlighting the capabilities of the anisotropic damage formulation above are presented in this section. The isotropic model calibration is the same as in [4]. Accordingly, the parameter values (for AISI-SAE 4340 alloy steel) are: $A = 0.025, \sigma_{0\mathrm{e}} = 490\,\mathrm{MPa}, C = 1.25, K = 2.65 \times 10^{-5}, L = 14.4$. The anisotropic damage evolution law is calibrated so that it matches the prediction of the isotropic model in the case of uniaxial alternating load (of sinus form) when the mean stress is zero and stress amplitude is 600 MPa. Due to the similarity of the damage evolution laws (5) and (7), the only change in parameter values needed is that $K_{\mathrm{aniso}} = 2.32K$. Damage evolution for both damage formulations in uniaxial loading with some values of the stress amplitude and means stress are illustrated in Figure 2. In each case, the simulation is set to halt when secant stiffness $\mathbf{C}_{\mathrm{ed}}$ loses its positive definiteness. This criterion is implemented as the first normalized eigenvalue criterion $\lambda_1(t)/\lambda_1(t=0) \geq 0$ (this quantity behaves similarly as the integrity variable, i.e. $1 - D$). The model comparisons

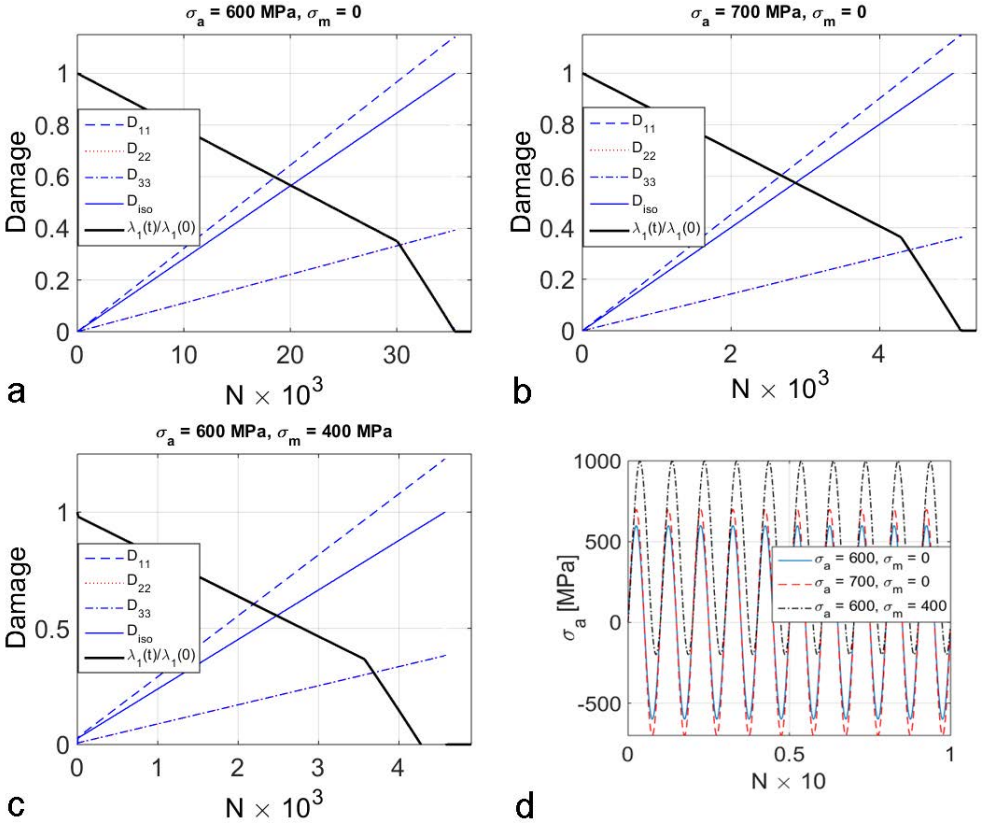

Figure 2. Damage evolution in uniaxial loading when (a) $\sigma_{\mathrm{a}} = 600$ MPa, $\sigma_{\mathrm{m}} = 0$, (b) $\sigma_{\mathrm{a}} = 700$ MPa, $\sigma_{\mathrm{m}} = 0$, (c) $\sigma_{\mathrm{a}} = 600$ MPa, $\sigma_{\mathrm{m}} = 400$ MPa, (d) and a part of load histories.

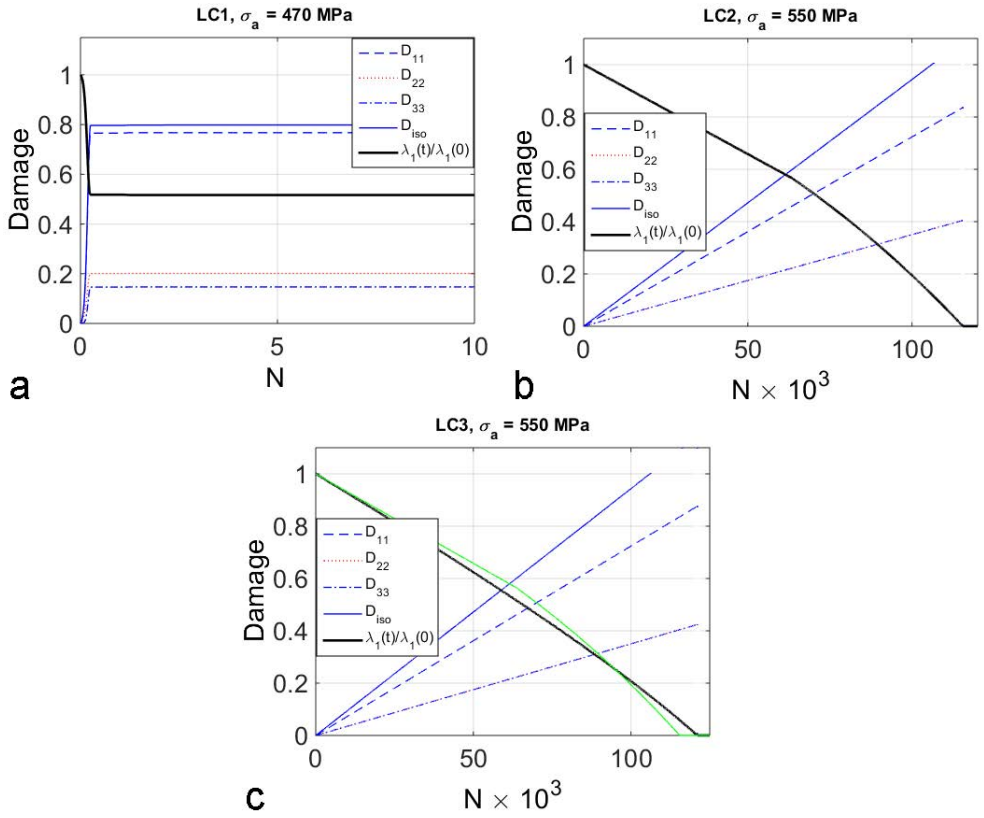

Figure 3. Damage evolution in multiaxial loading (a) for LC1 with $\sigma_{\mathrm{a}} = 470\,\mathrm{MPa}$, (b) for LC2 with $\sigma_{\mathrm{a}} = 550\,\mathrm{MPa}$, (c) for LC3 with $\sigma_{\mathrm{a}} = 550\,\mathrm{MPa}$. The green LC2 curve is shown to facilitate comparison.

show that while a good agreement is obtained between the isotropic damage model and the anisotropic one with the first eigenvalue criterion in the case the zero mean stress (Figures 2a and b), a deviation of 6% occurs when $\sigma_{\mathrm{m}} = 400\mathrm{MPa}$. As for the first three diagonal components of the damage tensor, components D_{22}, D_{33} evolve considerably despite the uni-axial loading. However, the final value of the these components is only 1/3 of that of the first component so that the model still accounts for the loading induced anisotropy. Moreover, the final value of component D_{11} exceeds 1 in each case. Notwithstanding, the model could be calibrated so that the evolution of D_{11} is identical to the evolution of isotropic damage in these load cases.

Next, multiaxial loading is considered. Namely, three special load histories leading to identical principal stress histories are tested. The first load case (LC1) has bi-axial pulsating normal stresses given by

$$\sigma_x = \sigma_{\mathrm{a}}[1 + \sin(\omega t)], \tag{12a}$$
$$\sigma_y = \sigma_{\mathrm{a}}[\sin(\omega t) - 1]. \tag{12b}$$

The second load case (LC2) has one pulsating normal stress and one pulsating shear stress as

$$\sigma_x = \sigma_{\mathrm{a}} \sin(\omega t), \tag{13a}$$
$$\tau_{xy} = \tfrac{1}{2}\sigma_{\mathrm{a}} \sin(\omega t - \pi/2). \tag{13b}$$

The third load case (LC3) has one pulsating normal stress and two pulsating shear stresses as

$$\sigma_x = \sigma_{\mathrm{a}} \sin(\omega t), \tag{14a}$$
$$\tau_{xy} = \tfrac{1}{\sqrt{8}}\sigma_{\mathrm{a}} \cos(\omega t), \tag{14b}$$
$$\tau_{yz} = -\tfrac{1}{\sqrt{8}}\sigma_{\mathrm{a}} \cos(\omega t). \tag{14c}$$

Despite the identical principal stress histories load cases LC1 and LC2 result in different endurance limits. For example, in LC1 steel 34Cr4 has endurance limit $\sigma_a = 240$ MPa while in LC2 the limit is $\sigma_a = 158$ MPa [7]. In the first test, the loading amplitude is $\sigma_a = 550$ MPa. With this amplitude, both damage formulations predicted immediate failure in LC1. Therefore, the behavior of the models is demonstrated with a lowered amplitude of $\sigma_a = 470$ MPa in LC1. The results are shown in Figure 3.

The results in Figure 3 display significant differences in the model predictions despite the fact that the loading histories have identical principal stress histories (equalling to LC1). In LC1 both models predict a huge initial jump in damage evolution after which the damage does not grow at all. The model behavior was similar with other values of stress amplitude. As for load cases LC2 and LC3, the isotropic damage model predicted identical damage evolution in them as can be observed in Figures 3b and c. In contrast, the anisotropic model with the eigenvalue criterion display a minor difference in the damage evolution so that the number cycles corresponding to failure is 115000 in LC2 and 120000 in LC3.

Conclusions

Different damage formulations in the continuum fatigue model based on a moving endurance surface by Ottosen et al. (2008) were very briefly considered in this study. The original scalar damage model was compared to a tensor damage model based on the gradient of the moving endurance surface. The latter model can account for loading induced anisotropy as was observed in the numerical simulations. According to this preliminary study, it seems that the anisotropic damage model with the eigenvalue criterion for final failure can - in contrast to the isotropic model - account for the influence of multiaxiality in load histories with identical principal stress histories. However, further studies are needed to state anything decisive on this issue.

Acknowledgements

This work has been supported by Tekes - the National Technology Agency of Finland, project SCarFace, decision number 40205/12.

References

[1] S. Suresh. *Fatigue of Materials*, Cambridge University Press, 2nd ed. 1998.

[2] V.V. Bolotin. *Mechanics of Fatigue*, CRC Mechanical Engineering Series. CRC Press, Boca Raton, 1999.

[3] D.F. Socie, G.B. Marquis. *Multiaxial Fatigue*. Society of Automotive Engineers, Inc. Warrendale, Pa., 2000.

[4] N.S. Ottosen, R. Stenstrom, M. Ristinmaa. Continuum approach to high-cycle fatigue modeling. *International Journal of Fatigue*. 30(6):996–1006, 2008.

[5] J. Lemaitre. *A Course on Damage Mechanics*, Springer-Verlag, 1990.

[6] G.A. Holzapfel. *Nonlinear Solid Mechanics. A Continuum Approach for Engineering*, John Wiley and Sons, 2001.

[7] J. Liu, H. Zenner. Fatigue limut of ductile metals under multiadial loading, in: Carpinteri, A., de Freitas, M., Spagnoli, A. (Eds.), *Biaxial/multiaxial fatigue and fracture*, Elsevier Science Ltd. and ESIS, 2003.

Proceedings of the XII Finnish Mechanics Days
R. Kouhia, J. Mäkinen, S. Pajunen and T. Saksala (Eds.)

Real-time dynamic analysis of mobile machines using semi-recursive method with sparse matrix technique

Ezral Baharudin[⋆], Asko Rouvinen[†], Pasi Korkealaakso[†], Marko K. Matikainen[⋆], Aki Mikkola[⋆]

[⋆] Lappeenranta University of Technology
Skinnarilankatu 34, 53850 Lappeenranta, Finland
e-mails: ezral.bin.baharudin@lut.fi, marko.matikainen@lut.fi, aki.mikkola@lut.fi
[†] Mevea Ltd. Laserkatu 6, 53850 Lappeenranta, Finland
e-mails: asko.rouvinen@mevea.com, pasi.korkealaakso@mevea.com

Summary. The use of modern multibody simulation techniques enables the description of complex products such as mobile machinery with a high level of detail while still solving the equations of motion in real-time. For product development, real-time simulation makes it possible to account for the machine user early on in the concept development phase. Conventionally, the system can be modeled in full matrices approach which did not consider the sparsity feature of the matrices. The numerical efficiency will decrease when the matrices are sparse and numerical approach still treated as full matrices format. In this study, the numerical procedure based on semi-recursive and augmented Lagrangian methods for real-time dynamic simulation is described. The equation of motion is imposed with the sparse matrix technique to enhance the computing efficiency. It is found that, for this specific system model using velocity transformation matrix approach in sparse format, the computing efficiency increases compared to the full matrices approach.

Key words: Multibody system dynamics, real-time simulation, sparse matrix technique, semi-recursive method, augmented Lagrangian method

Introduction

System simulation has proved to be an effective tool that is being implemented increasingly in machine development. Knowing how the dynamic behavior of a machine is affected by variations in the design variables is important and can readily be studied with a good computer simulation model. Simulation can replace some physical prototyping, and consequently, accelerate the product development cycle. To assess the performance of a machine using computerized methods, the system dynamics must be solved.

Realistic operator behavior can be taken into account by employing sophisticated real-time simulation models. In real-time simulations, the operator is actively engaged in the dynamic performance of the machinery. A real-time simulator must feel and perform like a real machine to the operator. This can be achieved only if the real-time simulation model is accurate and couples the physics from all the relevant engineering disciplines. However, these real-time models are usually case specific and tailored to specific applications. Consequently, the costs of developing these real-time simulations are often high. The problem of high cost can be alleviated using a real-time simulation approach based on the multibody system dynamics [10].

Knowing specifically type of matrices to deal with could give an advantage to write the optimal program code for numerical analysis. Conventionally, the system can be modeled in full matrices approach which did not consider the sparsity of the matrices. Increasing the number of body in the system will increase the size of matrices. Accordingly, the numerical efficiency

will decrease when the matrices are sparse and numerical approach still treated as full matrices format.

In this study, the numerical procedure based on semi-recursive and augmented Lagrangian methods for real-time dynamic simulation of multi-rigid body system is develop. The objective of this paper is to demonstrate that the sophisticated usage of sparse matrix computing approach can improve the computational efficiency real-time dynamic simulation. To this end, computer code based on the semi-recursive and augmented Lagrangian methods are written using C programming with full and sparce matrices formats. The performance of the based on full and sparce matrices formats are compared against each other.

Semi-recursive method

In the semi-recursive method, kinematic properties such as position, velocity and acceleration are developed based on the relative coordinates between neighboring bodies connected by a joint [10]. This algorithm has been used and extended by several researchers and has been generalized to improve its implementation and efficiency [2, 8].

Kinematics

Relative motion between neighboring bodies and constraints are the two main aspects of recursive kinematics used to generate the total system matrices and solve the equations of motion for the multibody system. The method uses the global position and local rotational coordinates of the center of the gravity as the generalized coordinates for formulating the equations of motion. Multibody system of two bodies inteconnected by a joint is illustrated in Figure 1.

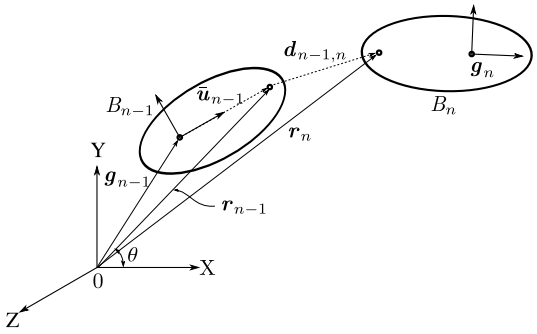

Figure 1. Description of the kinematics for recursive method.

The position of joint $\boldsymbol{r}_n$ for the body B_n can be described using kinematic of the previous body B_{n-1} in the global frame as follows

$$\boldsymbol{r}_n = \boldsymbol{g}_{n-1} + \boldsymbol{A}_{n-1}\bar{\boldsymbol{u}}_{n-1} + \boldsymbol{d}_{n-1,n} \tag{1}$$

where $\boldsymbol{g}_{n-1}$ is position vector of the center of gravity of body B_{n-1}, $\boldsymbol{A}_{n-1}$ is the rotation matrix of the body B_{n-1}, $\bar{\boldsymbol{u}}_{n-1}$ is the constant position vector in the local coordinate system and $\boldsymbol{d}_{n-1,n}$ is relative displacement vector between bodies. The velocity vector of joint $\boldsymbol{r}_n$ for the body B_n can be determined as follows

$$\dot{\boldsymbol{r}}_n = \dot{\boldsymbol{g}}_{n-1} + \tilde{\boldsymbol{\omega}}_{n-1}\bar{\boldsymbol{u}}_{n-1} + \dot{\boldsymbol{d}}_{n-1,n}, \tag{2}$$

The rotation matrix and the skew-symmetric matrix of the angular velocity vector for body B_n can be computed as:

$$\boldsymbol{A}_n = \boldsymbol{A}_{n-1}\boldsymbol{A}_{n-1,n} \tag{3}$$

$$\tilde{\boldsymbol{\omega}}_n = \tilde{\boldsymbol{\omega}}_{n-1} + \tilde{\boldsymbol{\omega}}_{n-1,n} \tag{4}$$

where $\boldsymbol{A}_{n-1,n}$ and $\tilde{\boldsymbol{\omega}}_{n-1,n}$ are the relative rotation matrix and the skew-symmetric matrix of the relative angular velocity vector.

Equations of motion

The equations of motion for the body i can be presented with respect to the centre of gravity as Newton-Euler equations as follows:

$$\underbrace{\begin{pmatrix} m_i\mathbf{I} & \mathbf{0} \\ \mathbf{0} & \boldsymbol{J_i} \end{pmatrix}}_{\boldsymbol{M_i}} \underbrace{\begin{pmatrix} \ddot{\boldsymbol{g}}_i \\ \dot{\boldsymbol{\omega}}_i \end{pmatrix}}_{\ddot{\boldsymbol{q}}_i} + \underbrace{\begin{pmatrix} \mathbf{0} \\ \tilde{\boldsymbol{\omega}}_{\boldsymbol{i}} \boldsymbol{J}_i \boldsymbol{\omega}_i \end{pmatrix}}_{\boldsymbol{Q}_i^v} = \underbrace{\begin{pmatrix} \boldsymbol{F_i} \\ \boldsymbol{T_i} \end{pmatrix}}_{\boldsymbol{Q}_i^e}. \tag{5}$$

where $\mathbf{I}$ is an identity matrix, $\boldsymbol{M}_i$ is the mass matrix, $\ddot{\boldsymbol{q}}_i$ is the vector of translationar and angular accelerations, $\boldsymbol{Q}_i^v$ accounts for the centrifugal terms and $\boldsymbol{Q}_i^e$ is the vector of the external forces $\boldsymbol{F}_i$ and torques $\boldsymbol{T}_i$. The body properties with respect to the inertia, centrifugal and external forces of the system of n bodies can be written as:

$$\boldsymbol{M} = \mathrm{diag}(\boldsymbol{M}_1, \boldsymbol{M}_2, \ldots, \boldsymbol{M}_n) \tag{6}$$

$$\ddot{\boldsymbol{q}} = [\ddot{\boldsymbol{q}}_1{}^T, \ddot{\boldsymbol{q}}_2{}^T, \ldots, \ddot{\boldsymbol{q}}_n{}^{T^T}]^T \tag{7}$$

$$\boldsymbol{Q}^v = [\boldsymbol{Q}_1^{vT}, \boldsymbol{Q}_2^{vT}, \ldots, \boldsymbol{Q}_n^{vT}]^T \tag{8}$$

$$\boldsymbol{Q}^e = [\boldsymbol{Q}_1^{eT}, \boldsymbol{Q}_2^{eT}, \ldots, \boldsymbol{Q}_n^{eT}]^T \tag{9}$$

When velocity transformation in case of the sceleronomic system $\dot{\boldsymbol{q}} = \boldsymbol{R}\dot{\boldsymbol{z}}$ is taken account and multiplying Newton-Euler equations by $\boldsymbol{R}^T$, the equations of motion can be presented as follows

$$\underbrace{\boldsymbol{R}^T\boldsymbol{M}\boldsymbol{R}}_{\boldsymbol{M}^*}\ddot{\boldsymbol{z}} = \underbrace{\boldsymbol{R}^T(\boldsymbol{Q}^e - \boldsymbol{M}\boldsymbol{c} - \boldsymbol{Q}^v)}_{\boldsymbol{Q}^*} \tag{10}$$

where in the case of sceleronomic constraints $\boldsymbol{c} = \dot{\boldsymbol{R}}\dot{\boldsymbol{z}}$. When the constraints $\boldsymbol{\Phi}$ due to the closed loop are accounted for with the penalty method, the equations of motion as function of the independet coordinates $\boldsymbol{z}$ can take form for the semi-recursive method as follows

$$(\boldsymbol{M}^* + \boldsymbol{\alpha}\boldsymbol{\Phi}_{,z}^T\boldsymbol{\Phi}_{,z})\ddot{\boldsymbol{z}} = \boldsymbol{Q}^* - \boldsymbol{\alpha}\boldsymbol{\Phi}_{,z}^T(\ddot{\boldsymbol{\Phi}} + 2\boldsymbol{\Omega}\boldsymbol{\mu}\dot{\boldsymbol{\Phi}} + \boldsymbol{\omega}^2\boldsymbol{\Phi}) \tag{11}$$

where $\boldsymbol{\alpha}$, $\boldsymbol{\Omega}$ and $\boldsymbol{\mu}$ are diagonal matrices including the penalty factors, and the vector of constraints $\boldsymbol{\Phi} = \boldsymbol{\Phi}(\boldsymbol{z}(t))$.

Velocity transformation

The multibody system can be seen as an open loop system where bodies are connected via components of the revolute and prismatic joints and/or their combinations. Figure 2 shows the H8 Logset tree harvester that is analysed in this study. Each body of the system is labeled based on the tree-structure multibody numbering. The main body of vehicle is labeled as body 0 (based body). The next bodies from based to the end are numbered in increasing order in which should meet $B_n > B_{n-1}$. This numbering is also applied for the labeling of the joints.

In the H8 logset tree harvester, each body has been numbered from 0 to 6 and each joint is represent in transformation velocity matrix notation $\boldsymbol{R}$. The values of joint variable $\boldsymbol{R}_i$ depending to the types of joints and the number of columns may vary depending to the number of degree of freedom. Below are the two types of variable joints involve in this case as proposed by Avello et al. [1] which are presented for revolute and prismatic joints as

$$\boldsymbol{R}_i^{rev} = \begin{bmatrix} \tilde{\boldsymbol{e}}_{\boldsymbol{i}}(\boldsymbol{g}_{B_n} - \boldsymbol{r}_i) \\ \boldsymbol{e}_i \end{bmatrix}; \quad \boldsymbol{R}_i^{pris} = \begin{bmatrix} \boldsymbol{e}_i \\ \mathbf{0} \end{bmatrix} \tag{12}$$

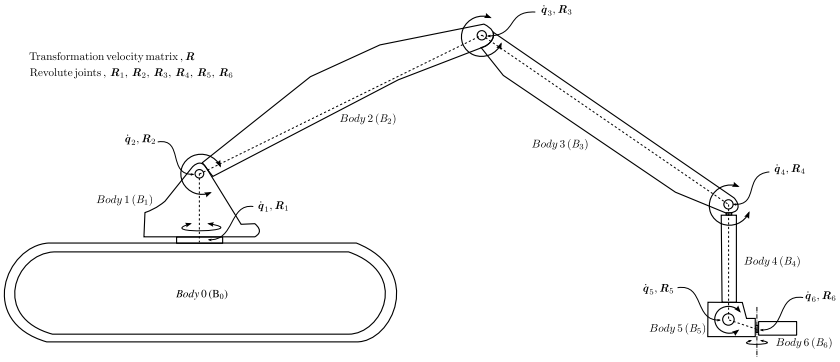

Figure 2. Description of the tree harvester

where $\boldsymbol{e}_i$ is the unit vector of joint j which point the direction of the revolute axis, $\tilde{\boldsymbol{e}}_i$ is the skew-symmetric matrix of $\boldsymbol{e}_i$ and $(\boldsymbol{g}_{B_n} - \boldsymbol{r}_i)$ is the vector points from point i in body i to the center of gravity of designated body B_n.

To get the final expression of transformation velocity matrix $\boldsymbol{R}$ for the system, all dedicated matrix $\boldsymbol{R}_i$ need to be arranged into the system level matrix that represents all joints. The rows of velocity matrix $\boldsymbol{R}$ represent the related body and the columns of velocity matrix $\boldsymbol{R}$ represent the number of degrees of freedom found in the path from body j to ground. Therefore, the system shown in Figure 2 can be arranged as

$$\boldsymbol{R} = \begin{bmatrix} \boldsymbol{R}_1 & & & & & \\ \boldsymbol{R}_1 & \boldsymbol{R}_2 & & & & \\ \boldsymbol{R}_1 & \boldsymbol{R}_2 & \boldsymbol{R}_3 & & 0 & \\ \boldsymbol{R}_1 & \boldsymbol{R}_2 & \boldsymbol{R}_3 & \boldsymbol{R}_4 & & \\ \boldsymbol{R}_1 & \boldsymbol{R}_2 & \boldsymbol{R}_3 & \boldsymbol{R}_4 & \boldsymbol{R}_5 & \\ \boldsymbol{R}_1 & \boldsymbol{R}_2 & \boldsymbol{R}_3 & \boldsymbol{R}_4 & \boldsymbol{R}_5 & \boldsymbol{R}_6 \end{bmatrix} \tag{13}$$

where $\boldsymbol{R} \in \mathbb{R}^{36\times 6}$ and as an example to obtained matrix $\boldsymbol{R}$ which corresponding to the body B_4, can be extracted from above equation as

$$\boldsymbol{R}_{B_4} = \begin{bmatrix} \boldsymbol{R}_1 & \boldsymbol{R}_2 & \boldsymbol{R}_3 & \boldsymbol{R}_4 \end{bmatrix} \tag{14}$$

where $\boldsymbol{R}_{B_4} \in \mathbb{R}^{6\times 4}$. The mass matrix of the system $\boldsymbol{M} = \mathrm{diag}(\boldsymbol{M}_1, \boldsymbol{M}_2, \ldots, \boldsymbol{M}_6)$ where mass matrix $\boldsymbol{M}_i \in \mathbb{R}^{6\times 6}$ for the body i is written as

$$\boldsymbol{M}_i = \begin{bmatrix} m_i\mathbf{I} & \mathbf{0} \\ \mathbf{0} & \boldsymbol{J}_i \end{bmatrix} \tag{15}$$

where m_i and $\boldsymbol{J}_i$ describe mass and inertia properties of body i. It can be seen from the equations of motion in section that coordinate transformation for mass matrix of the system $\boldsymbol{M}$ is employed with $\boldsymbol{R}^T\boldsymbol{M}\boldsymbol{R}$. To increase the computational efficiency, the some operations can be solved parallel as it is suggested by Jimenez et al. [7].

Augmented Lagrangian method

One possibility for solving constrained optimization problem is to use formulations based on the augmented Lagrangian methods, that can be traced back to the mid-1940's [6]. The augmented Lagrangian methods can be seen as the penalty methods that include also the Lagrangian multipliers as penalty terms to objective function. The widely used augmented Lagrangian method in real time dynamic simulation of the multibody systems is carefully explained in [3].

The method can be derived by introducing variational terms due to fictitious energies and the Lagrange multipliers as follows

$$\begin{aligned} \delta W^*_{pot} &= (\dot{\boldsymbol{\Phi}}^T_{,q}\boldsymbol{\alpha}\dot{\boldsymbol{\Phi}} - \boldsymbol{\Omega}^2\boldsymbol{\Phi}^T_{,q}\boldsymbol{\alpha}\dot{\boldsymbol{\Phi}}) \cdot \delta\boldsymbol{q} \\ \delta W^*_{kin} &= \dot{\boldsymbol{\Phi}}^T_{,q}\boldsymbol{\alpha}\dot{\boldsymbol{\Phi}}^T_{,q} \cdot \delta\boldsymbol{q} \\ \delta W^*_{dis} &= -2\boldsymbol{\alpha}\boldsymbol{\Omega}\boldsymbol{\mu}\boldsymbol{\Phi}^T_{,q}\dot{\boldsymbol{\Phi}} \cdot \delta\boldsymbol{q} \\ \delta W_{\lambda} &= \lambda\boldsymbol{\Phi}^T_{,q} \cdot \delta\boldsymbol{q} \end{aligned} \tag{16}$$

where $\boldsymbol{\alpha}$, $\boldsymbol{\Omega}$ and $\boldsymbol{\mu}$ are diagonal matrices including the penalty factors, and the vector of constraints $\boldsymbol{\Phi} = \boldsymbol{\Phi}(\boldsymbol{q})$. When equations are taken into account in Hamilton's principle, complete form of the equations of motion can be written as

$$\boldsymbol{M}\ddot{\boldsymbol{q}} = \boldsymbol{Q} - \boldsymbol{\alpha}\boldsymbol{\Phi}^T_{,q}(\ddot{\boldsymbol{\Phi}} + 2\boldsymbol{\Omega}\boldsymbol{\mu}\dot{\boldsymbol{\Phi}} + \boldsymbol{\Omega}^2\boldsymbol{\Phi}) + \boldsymbol{\Phi}^T_{,q}\boldsymbol{\lambda} \tag{17}$$

where the force vector $\boldsymbol{Q} = \boldsymbol{Q}_e - \boldsymbol{Q}_v$ and the Lagrangian multipliers $\boldsymbol{\lambda}$ can be found iteratively, see more details in [3].

Sparse matrix technique

From the equations explained previously, it can be seen that the system matrices are sparse. More than half of the matrices element for $\boldsymbol{R}$ and $\boldsymbol{M}$ are zeros. Therefore, by applying the finite element method approach into the multibody system such as sparse solver, data storage management and sparse procedure may increase the computing efficiency and optimize the memory storage.

The main engine for simulation is written in C language to obtain computationally efficent solution for real-time simulations. For sparse matrix operations, the libraries used for the engine can be seen in Figure 3. The matrices are stored in Compressed Sparse Column format which is the favorite storage format among sparse libraries. All three libraries are free libraries with GPL compatible. CSPARSE is used for direct solution of sparse linear system [4] such as matrix manipulation while UMFPACK is for solving the form of Ax = b using Unsymmetric MutiFrontal method [5]. ARPACK is a numerical library for solving large eigenvalue problem using Implicity Restarted Arnoldi Method which is fast and robust solver [9]. ARPACK need two others libraries in order to work which are Blas and SuperLU.

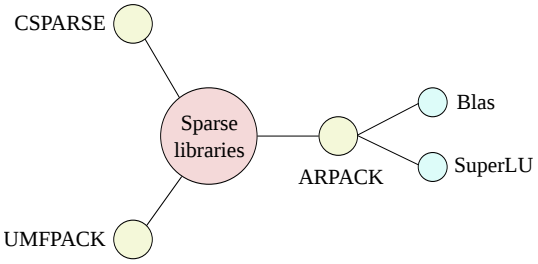

Figure 3. Included sparse libraries in the simulation engine

Numerical results and discussions

Numerical analyses introduced in this study are carried out using Mevea solver. The solver can treat the matrices with a full or sparse format. To determine the efficiency of semi-recursive and augmented Lagrangian formulation methods when using sparse matrix approach, mobile working machine (H8 Logset) is analysed. The time integration for the equations of motion is

obtained by using the explicit Runge-Kutta method of order four with a constant time step of 1.6 milliseconds.

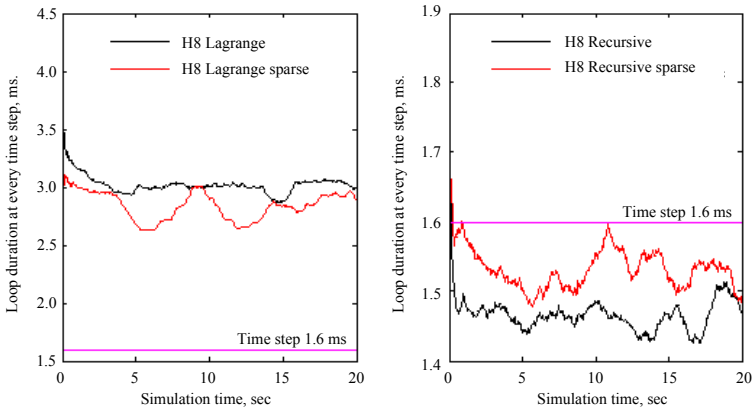

Figure 4. Loop durations at time step of the augmented Lagrangian method vs. semi-recursive method with and without sparse matrix technique. Continuous straight lines illustrate a constant step size of fourth order Runge-Kutta with respect to loop durations.

The computational efficiency for the augmented Lagrangian and semi-recursive methods with and without sparse matrix technique are illustrated in Figure 4. It can be concluded from Figure that a significant reduction of loop duration with solving the equations of motion at every time step can be reached from both methods when using the sparse matrix technique. During simulation of twenty seconds, the augmented Lagrangian method uses from 2.62-3.6 milliseconds and the semi-recursive method from 1.44 to 1.82 for the solving equations of motions at time step. Therefore, the semi-recursive method is able to solve the step with less time as compared to the augmented Lagrangian method for every loop. From the results, the implementation of the sparse matrix technique into the augmented Lagrangian method has increased the computational efficiency about 6% and decreased about 5% for the semi-recursive method. However when both methods (with sparse implementation) are compared side by side, the semi-recursive method is about 47% more efficient than the augmented Lagrangian method.

Summary and conclusion

It is shown that the implementation of the semi-recursive method with transformation velocity matrix produced a significant improvement to the computing efficiency compare to the Augmented Lagrangian method. By applying sparse matrix technique into the methods, the computing efficiency slightly increases. It should be noted that the computational efficiency is strongly case dependent. As it is known, the larger size of the system matrices increases the sparsity and therefore, more computational benefit can be gained from the use of sparse matrix technique in multibody applications. Further investigation should be done for sparse implementation in order to maximize the efficiency. In the same time, utilizing parallel computing may also improve the simulation.

References

[1] Avello, A., Jimenez, J. M., Bayo, E., and de Jalón, J. G. A simple and highly parallelizable method for real-time dynamic simulation based on velocity transformation. *Computer Methods in Applied Mechanics and Engineering 107*, 3 (1993), 313–339.

[2] Bae, D.-S., and Haug, E. J. A recursive formulation for constrained mechanical system dynamics: Part 1. open loop system. *Mechanics of Structure and Machines 15*, 3 (1987), 359–382.

[3] Bayo, E., and de Jalón, J. G. *Kinematic and Dynamic Simulation of Multibody Systems: The Real-Time Challenge*. Springer-Verlag, New York, 1993.

[4] Davis, T. A. *Direct methods for sparse linear systems*. Society for Industrial and Applied Science, Philadelphia, USA, 2006.

[5] Davis, T. A. *UMFPACK User Guide*, 2013.

[6] Gill, P. E., Murray, W., and Wright, M. H. *Practical optimization*. Academic Press Inc. [Harcourt Brace Jovanovich Publishers], London, 1981.

[7] J. M. Jimenez and A. N. Avello and J. García de Jalón and A. L. Avello. An efficient implementation of the velocity transformation method for real-time dynamics with illustrative examples. *Computational Dynamics in Multibody Systems* (1995), 15–35.

[8] Kim, S.-S., and Haug, E. J. A recursive formulation for flexible multibody dynamics. Part I: Open loop system. *Computer Methods in Applied Mechanics and Engineering 71*, 3 (1988), 293–314.

[9] Lehoucg, R. B., Sorensen, D. C., and Yang, C. *ARPACK Users' Guide: Solution of large scale eigenvalue problems with Implicity Restarted Arnoldi Methods*, 1997.

[10] P. M. Korkealaakso and A. J. Rouvinen and S. M. Moisio and J. K. Peusaari. Development of a real-time simulation environment. *Multibody System Dynamics 17*, 2–3 (2007), 177–194.

Rakenteiden Mekaniikka (Journal of Structural Mechanics)
Vol. 48, No 1, 2015, pp. 34-48
www.rmseura.tkk.fi/rmlehti

Soft body impact against aeronautical structures

Alessia Prato[1], Marco Anghileri, Andrea Milanese, Luigi M. L. Castelletti

Summary. Statistics show that impacts of soft body against aeronautical structure are not so rare events. The damage caused by the impact of hailstones or of birds can sometimes be so heavy to compromise the service life of the vehicle. Companies, research centers and universities are interested in the evaluation of the effects of this kind of events and lots of researching works have been recently developed in this field. In this paper, an overview of the last studies performed at the Laboratory for the Safety in Transports (LaST – Crash Lab.) of Politecnico of Milan are presented throughout experimental tests and numerical finite element models. The validity of the correlation results method to prevent possible heavy consequence caused by these events is shown.

Key words: crashworthiness, soft body impact, explicit finite element code, smoothed particle hydrodynamics

A. Prato, M. Anghileri, A. Milanese, L.M.L. Castelletti
Politecnico di Milano, Dip. Di Scienze e Tecnologie Aerospaziali
Via la Masa 34, 20156 Milano, Italy
alessia.prato@polimi.it

Proceedings of the XII Finnish Mechanics Days
R. Kouhia, J. Mäkinen, S. Pajunen and T. Saksala (Eds.)

Two approaches for modeling hydraulic cylinder

Antti Ylinen

Summary. In this paper the author proposes models for linear hydraulic actuator, hydraulic cylinder. The two models differ kinematically since the first model is rigid in bend whereas the second model captures the bending flexibility of the hydraulic cylinder. The derivation of the first element, truss element cylinder, is based on the equilibrium of the cylinder piston where the pressure forces are acting on the different sides of the piston. The second element, bending flexible cylinder element, however is constructed using beam elements and then deriving the coupling with the chamber pressures. Finally numerical example concerning dynamical simulation is presented where the governing equations are solved using Rosenbrock time stepping scheme.

Key words: Hydraulic cylinder, coupled problem, friction model, dynamical simulation

Introduction

Hydraulic driven working machines are a common sight in the industry today. The applications can vary from very robust excavators to precise robots like the ITER fusion reactor maintenance robot. In hydraulic systems the energy is transferred via pressurized fluid instead of using mechanical components.

Hydraulic cylinder is a linear actuator where the length of the cylinder can be changed. Using this length change we can produce movement to the mechanical system. Since the length of the hydraulic cylinder is determined by the volumes of the hydraulic fluid in the cylinder chambers we find, that the hydraulic cylinder is coupled to the hydraulic control system. This coupling is included in the hydraulic cylinder element formulations. For the solution process we utilize a monolithic approach where all state variables are solved at the same iteration.

In this work we propose two different models for the linear actuator, hydraulic cylinder. The elements are formed using the finite element method thus they are compatible with the existing framework.

Truss element cylinder

The first hydraulic cylinder is a element capable of capturing only axial effects. This current element has been presented in [9] and it is closely related to the model proposed in [2]. The element has 6 mechanical degrees of freedom, namely the translations at each end of the element. In addition the element has 3 hydraulic variables related to the cylinder chamber pressures and friction, which are now discussed.

The truss element cylinder is derived from the equilibrium equation of the cylinder piston reading

$$F_{\mathrm{c}} = p_{\mathrm{A}} A_{\mathrm{A}} - p_{\mathrm{B}} A_{\mathrm{B}} - F_{\mu}, \tag{1}$$

where the first two terms are due to the cylinder chamber pressures and the last term is the friction force. For the friction force we utilize the LuGre model introduced in [1]. The friction force introduces a new variable, bristle deflection z, to the system. The friction force is computed

using

$$F_\mu = k_0 z + k_1 \dot{z} + F_\mathrm{v} v_\mathrm{t}, \tag{2}$$

with the rate of bristle deflection written as

$$\dot{z} = v_\mathrm{t} - \frac{|v_\mathrm{t}|}{g(v_\mathrm{t})} z. \tag{3}$$

For the cylinder chamber pressures we write a simple evolution law

$$\dot{p}_\mathrm{A} = B \frac{Q_\mathrm{A} - \dot{x}_\mathrm{c} A_\mathrm{A}}{V_\mathrm{A} + x_\mathrm{c} A_\mathrm{A}} \tag{4}$$

$$\dot{p}_\mathrm{B} = B \frac{-Q_\mathrm{B} + \dot{x}_\mathrm{c} A_\mathrm{B}}{V_\mathrm{B} - x_\mathrm{c} A_\mathrm{B}} \tag{5}$$

with the inward and outward flow rates from the cylinder chambers denoted with Q_A and Q_B, respectively. Corresponding chamber areas are A_A and A_B and B is the bulk modulus for the hydraulic fluid and finally x_c is the cylinder piston position. This hydraulic cylinder element is a coupled element, since the cylinder force in Eq. (1) is a function of the chamber pressures. Equations (4),(5) and (3) are collected to a single vector denoting the rates of the hydraulic state variables for the hydraulic cylinder element as

$$\dot{\mathbf{z}} = \begin{bmatrix} \dot{p}_\mathrm{A} \\ \dot{p}_\mathrm{B} \\ \dot{z} \end{bmatrix} = \begin{bmatrix} B \dfrac{Q_\mathrm{A} - \dot{x}_\mathrm{c} A_\mathrm{A}}{V_\mathrm{A} + x_\mathrm{c} A_\mathrm{A}} \\ B \dfrac{-Q_\mathrm{B} + \dot{x}_\mathrm{c} A_\mathrm{B}}{V_\mathrm{B} - x_\mathrm{c} A_\mathrm{B}} \\ \dot{x}_\mathrm{c} - \dfrac{|\dot{x}_\mathrm{c}|}{g(\dot{x}_\mathrm{c})} z \end{bmatrix} \tag{6}$$

This equation defines the evolution law for the state variables regarding the hydraulic cylinder variables as $\dot{\mathbf{z}} = \mathbf{f}_\mathrm{cyl}$.

The internal force vector for the truss element cylinder is written with aid of the cylinder force in Eq. (1) as

$$\mathbf{f}_\mathrm{int} = F_\mathrm{c} \begin{bmatrix} \mathbf{n}_\mathrm{c} \\ -\mathbf{n}_\mathrm{c} \end{bmatrix} = -\frac{F_\mathrm{c}}{L_\mathrm{n}} \mathbf{A}\mathbf{x}, \tag{7}$$

where $\mathbf{n}_\mathrm{c}$ is the unit vector of the cylinder element and vector $\mathbf{x}$ collects the current nodal coordinates of the element. Matrix $\mathbf{A}$ is a mapping given for instance in [5].

For the solution process, the given state equations are linearized according to [9]. In the numerical example we however, consider the element to be frictionless.

Bending flexible hydraulic cylinder

The first hydraulic cylinder element is rigid in bend whereas the second hydraulic cylinder element is able to capture also bening effects. Instead of writing the equilibrium equation for the cylinder piston, we construct the cylinder lining and arm using beam elements, see Fig. 1. The beam elements are introduced in [4]. The sliding between the two cylinder members is modeled using slide-spring elements presented in [6]. The hydraulic fluid is now between nodes 1 and 2 for the A chamber and between nodes 2 and 3 for the B chamber in Fig. 1. Since the forces $\mathbf{f}_i$ are pressure induced forces, we account for the rotation of the nodes 1, 2 and 3 and define the pressure forces as follower forces.

To start, we write the pressure force vector for the A-chamber acting on nodes 1 and 2 in Fig. 1 as

$$\mathbf{f}_\mathrm{int} = \begin{bmatrix} \mathbf{f}_1 & \mathbf{0} & \mathbf{f}_2 & \mathbf{0} \end{bmatrix}^\mathrm{T}, \tag{8}$$

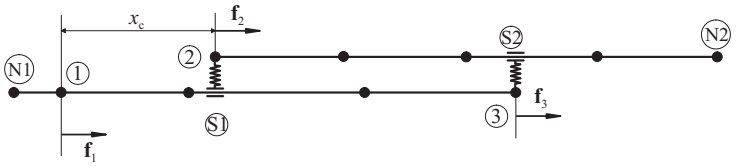

Figure 1: A bending flexible hydraulic cylinder where the members are modeled as Reissner's geometrically exact beam elements. The element is attached to the mechanical system using nodes N1 and N2.

where the forces are written

$$\mathbf{f}_1 = -p_\mathrm{A} A_\mathrm{A} \mathbf{R}_1 \mathbf{E}_\mathrm{c} \tag{9}$$

$$\mathbf{f}_2 = p_\mathrm{A} A_\mathrm{A} \mathbf{R}_2 \mathbf{E}_\mathrm{c}, \tag{10}$$

where p_A and A_A are the chamber A pressure and corresponding chamber area and $\mathbf{E}_\mathrm{c}$ is the initial direction vector for the cylinder element. The rotation matrices $\mathbf{R}_i$ are computed from the rotations of nodes 1 and 2, see Fig. 1 and [4]. The pressure forces are follower forces since they account for the rotations of the mechanical system. Similar equations follow for the B chamber of the hydraulic cylinder element. The internal force vectors given here are identified as the hydraulic state variables of the element. The state equation for the mechanical system follows from the beam elements, see [4, 6]. For the solution process the internal forces are linearized.

Time stepping

For the time stepping we utilize a semi-implicit Rosenbrock scheme suitable for stiff differential equations. Semi-implicit methods are shown to work properly for stiff differential equations and here we give presentation for the Rosenbrock type integrator, see [3]. The Rosenbrock method is based on an implicit form which is then linearized revealing the Jacobian of the system. Instead of iterative solution of the linearized equations we only take one iteration and then utilize Runge-Kutta type time stepping, see [7].

In order to utilize the Rosenbrock method, we write the equations of motion we transform the second order differential equation with two first order differential equations by substituting $\mathbf{v} = \dot{\mathbf{q}}$ thus giving for the coupled system

$$\mathbf{H} \begin{bmatrix} \dot{\mathbf{z}} \\ \dot{\mathbf{q}} \\ \dot{\mathbf{v}} \end{bmatrix} = \begin{bmatrix} \mathbf{f}_\mathrm{cyl}(\mathbf{z}, \mathbf{q}, \dot{\mathbf{q}}, t) \\ \mathbf{v} \\ \mathbf{g}(\mathbf{q}, \dot{\mathbf{q}}, \mathbf{z}, t) \end{bmatrix}, \tag{11}$$

where $\mathbf{g}$ is the exitation for the mechanical system and the matrix $\mathbf{H}$ is a coefficient matrix with diagonal components

$$\mathbf{H} = \mathrm{diag}\,(\mathbf{I}, \mathbf{I}, \mathbf{M}) \tag{12}$$

with $\mathbf{M}$ as the mass matrix. The right hand side in Eq. (11) is the unbalance of the system. We may rewrite the equation as

$$\mathbf{H}\dot{\mathbf{x}} = \mathbf{r}(t, \mathbf{x}), \tag{13}$$

which is a suitable form for time integration using the Rosenbrock scheme.

The Rosenbrock scheme grounds from diagonal IRK method with basic formula for autonomous problems, see [3]

$$\mathbf{k}_i = \Delta t\, \mathbf{r} \left(\mathbf{x}_n + \sum_{j=1}^{i-1} \alpha_{ij} \mathbf{k}_j + \alpha_{ii} \mathbf{k}_i \right) \qquad i = 1, \ldots, s, \tag{14}$$

where s defines how many stages are used. Advancing, or time stepping is then written for Runge-Kutta methods as

$$\mathbf{x}_{n+1} = \mathbf{x}_n + \sum_{i=1}^{s} b_i \mathbf{k}_i. \tag{15}$$

The form given in Eq. (14) is however, an implicit form. For the Rosenbrock method this equation is linearized and only one iteration is performed for solving the vectors $\mathbf{k}_i$, see more from [7, 3]. For this reaseon the Rosenbrock method is called semi-implicit method. The linearization process then reveals the Jacobian matrix which is computed only at the beginning of the time step, when $\mathbf{x} = \mathbf{x}_n$. Therefore only one LU-decomposition is needed for advancing one time step.

For non-autonomous systems an additional term is added to the basic form in Eq. (14) to account for the time dependency, see [3]. After the linearization the form for solving vectors $\mathbf{k}_i$ is written

$$\begin{aligned}(\mathbf{H} - \gamma \Delta t \mathbf{J})\, \mathbf{k}_i =& \Delta t \mathbf{r} \left(t_n + \alpha_i \Delta t \ , \ \mathbf{x}_n + \Delta t \sum_{j=1}^{i-1} \alpha_{ij} \mathbf{k}_j \right) \\ &+ \gamma_i \Delta t^2 \frac{\partial \mathbf{r}(t_n, \mathbf{x}_n)}{\partial t} + \Delta t \mathbf{J} \sum_{j=1}^{i-1} \gamma_{ij} \mathbf{k}_j,\end{aligned} \tag{16}$$

where $\mathbf{J}$ is the system Jacobian. This matrix is assembled from the subsystem Jacobians and coupling matrices as

$$\mathbf{J} = \begin{bmatrix} \mathbf{J}_{\mathrm{cc}} & \mathbf{J}_{\mathrm{cm}} & \mathbf{C}_{\mathrm{cm}} \\ \mathbf{0} & \mathbf{0} & \mathbf{I} \\ -\mathbf{J}_{\mathrm{mc}} & -\mathbf{K}_{\mathrm{mm}} & -\mathbf{C}_{\mathrm{mm}} \end{bmatrix}, \tag{17}$$

where

$$\mathbf{C}_{\mathrm{cm}} = -\frac{\partial \mathbf{f}_{\mathrm{cyl}}}{\partial \dot{\mathbf{q}}} \tag{18}$$

$$\mathbf{J}_{\mathrm{cm}} = -\frac{\partial \mathbf{f}_{\mathrm{cyl}}}{\partial \mathbf{q}} \tag{19}$$

$$\mathbf{J}_{\mathrm{mc}} = -\frac{\partial \mathbf{g}}{\partial \mathbf{z}}. \tag{20}$$

are the coupling matrices between the hydraulic cylinder and the mechanical system. $\mathbf{K}_{\mathrm{mm}}$ and $\mathbf{C}_{\mathrm{mm}}$ are the mechanical system stiffness and damping matrices and $\mathbf{J}_{\mathrm{cc}}$ is the Jacobian matrix for the hydraulic cylinder element written as

$$\mathbf{J}_{\mathrm{cc}} = -\frac{\partial \mathbf{f}_{\mathrm{cyl}}}{\partial \mathbf{z}} \tag{21}$$

$$\tag{22}$$

In the solution process, it is possible to use the symmetric properties of the system matrices by solving the above equations in blocks, see [5]. Coefficients α_{ij} and γ_{ij} are model parameters for two stage Rosenbrock scheme along with b_i and α_i and are given in Table 1 and as follows

$$\gamma_{ij} = \begin{bmatrix} \gamma & 0 \\ -\gamma & \gamma \end{bmatrix} \qquad \alpha_{ij} = \begin{bmatrix} 0 & 0 \\ 1/2 & 0 \end{bmatrix} \tag{23}$$

with $\gamma = 1 - 1/\sqrt{2}$, see [5, 8].

Since the Rosenbrock method does not involve iteration to reach equilibrium, it is computationally more efficient compared to Newmark scheme for instance.

Table 1: Coefficients α_i and b_i for the Rosenbrock scheme.

i	α_i	b_i
1	0	1/4
2	1/2	3/4

Numerical example

As a numerical example we introduce a lifting boom shown in Fig. 2. We set the boom initial angle to 70° and simulate an accident situation, where the boom is allowed to be in free fall for 0.5 s. The mass at the end of the boom is set to 600 kg and the structure is under gravitational load. To draw comparison, we record the boom stresses at the top edge at point D.

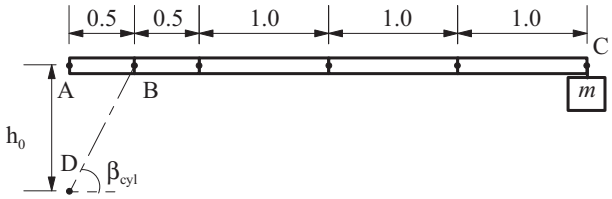

Figure 2: Boom system with an external load at the tip of the boom.

As a result we present the boom stresses at point B and they are now plotted in Fig. 3 for the truss element cylinder (TC) and for the bending flexible cylinder (BF). When the two cylinder formulations are compared with each other we find, that the bending flexible cylinder element results to lower stresses than the truss element cylinder. This is explained by the bending flexibility of the BF model. The BF model bends under the load thus allowing the mass to decelerate in longer distance. The example demonstrates that the bending accounting for the bending flexibility of the hydraulic cylinder can have and impact on the system response. In addition, in this simulation the attachment between the hydraulic cylinder and the boom system is frictionless and no moment is applied on the cylinder which would increase the bending deformations of the cylinder.

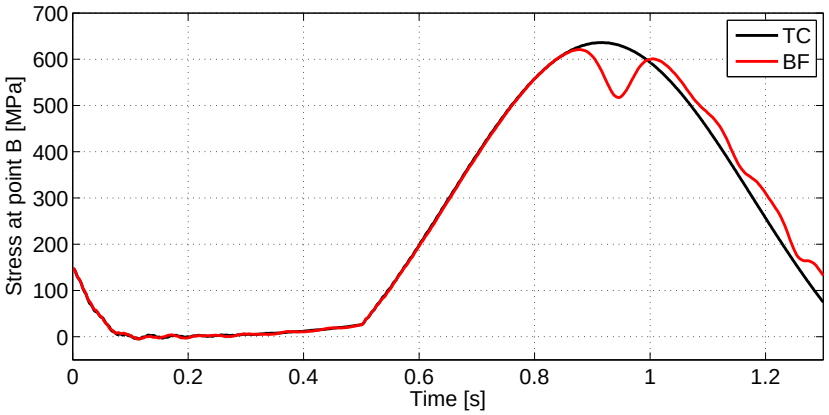

Figure 3: Boom bending stresses at the top edge of point B with the two cylinder formulation.

Conclusion

Modeling the bending flexibility of the hydraulic cylinder is not particularly useful when normal use of the cylinder is considered. However, in accident simulations, as presented in this paper, the bending flexibility changes the system response drastically. The bending flexibility is an important factor when the cylinder is long and slender and it can be susceptible for bending moments. In applications where the cylinder is not under bending the truss element cylinder is sufficient for modeling the linear actuator since it captures the coupling with the hydraulic system and is computationally more efficient.

References

[1] C. Canudas de Wit, H. Olsson, K.J. Astrom, and P. Lischinsky. New model for control of systems with friction. *IEEE Transactions on Automatic Control*, 40(3):419–425, 1995.

[2] A. Cardona and M. Géradin. Modeling of a Hydraulic Actuator in Flexible Machine Dynamics Simulation. *Mechanism and Machine Theory*, 25(2):193 – 207, 1990.

[3] E. Hairer and G. Wanner. *Solving Ordinary Differential Equations II, Stiff and Differential-Algebraic Problems*. Springer Series in Computational Mathematics 14. Springer, 1991.

[4] J. Mäkinen. Total Lagrangian Reissner's Geometrically Exact Beam Element Without Singularities. *International Journal for Numerical Methods in Engineering*, 70(9):1009–1048, 2007.

[5] H. Marjamäki and J. Mäkinen. Modelling a Telescopic Boom - the 3D Case: Part II. *Computers & Structures*, 84(29-30):2001–2015, 2006.

[6] H. Marjamäki and J. Mäkinen. Total Lagrangian Beam Element With C^1-Continuous Slide-Spring. *Computers & Structures*, 87:534–542, 2009.

[7] R. Piché. An l-stable rosenbrock method for step-by-step time integration in structural dynamics. *Computer Methods in Applied Mechanics and Engineering*, 126(3-4):343–354, 1995.

[8] L.F. Shampine and M.W. Reichelt. The matlab ode suite. *SIAM Journal on Scientific Computing*, 18(1):1–22, 1997.

[9] A. Ylinen, H. Marjamäki, and J. Mäkinen. A hydraulic cylinder model for multibody simulations. *Computers & Structures*, 138:62 – 72, 2014.

Antti Ylinen
FS Dynamics Oy
Hermiankatu 1, 33720 Tampere
antti.ylinen@fsdynamics.fi

Proceedings of the XII Finnish Mechanics Days
R. Kouhia, J. Mäkinen, S. Pajunen and T. Saksala (Eds.)

On the effect of damping on stability of non-conservative systems

Juha Jeronen[1 2] and Reijo Kouhia[2]

[(1)]University of Jyväskylä, Department of Mathematical Information Technology
P.O. Box 35, 40014 University of Jyväskylä, Finland, juha.jeronen@jyu.fi
[(2)]Tampere University of Technology, Department of Mechanical Engng and Industrial Systems
P.O. Box 589, 33101 Tampere, Finland, reijo.kouhia@tut.fi

Summary. Anomalous damping-induced destabilization is investigated in a simple, small system consisting of a double pendulum with springs. Linearized and fully non-linear results are presented.

Key words: stability, follower force, damping, two-dof model, destabilization paradox

Introduction

In 1952 Hans Ziegler reported an anomaly observed in the stability analysis of a simple double pendulum model consisting of linear springs and dampers, and loaded by a follower force at the free end [1]. Addition of small dissipative forces in the system resulted in an destabilizing effect, which is a counterintuitive result and is often called a paradox. For a system in equilibrium under the action of potential forces, the addition of dissipative forces with complete dissipation ensures asymptotic stability of the undisturbed equilibrium, as stated by the well known Kelvin's theorem [2, Page 75]. However, such a result does not exist for general non-conservative systems.

Even though the problem is more than 60 years old, and numerous investigations have been carried out on the understanding of the eigenvalue behaviour near the discontinuity at zero damping, it is not fully understood. Bolotin attributes the controversial result to the inability of the linear approximation to assess the question of stability [2, Pages 99-100], [3]. An attempt to a physical explanation is given in a rather recent paper by Sugiyama and Langthjem [4].

In this paper, behaviour of the Ziegler's pendulum with vanishing dissipation is reinvestigated by using the fully non-linear model.

Two degree-of-freedom model

A double pendulum subjected to a follower force is studied, see Fig. 1. The bars are connected to each other, and to a fixed support with an elastic spring and a linear viscous damper. In the seminal paper [1], Ziegler found that the critical load in the case of small damping can be smaller than the critical load without damping. This result, a jump in the critical load at vanishinly small damping is often called *the paradox of destabilization due to damping.*

To obtain the equations of motion, the principle of virtual work is applied:

$$\delta W_i + \delta W_e + \delta W_j = 0 \,, \tag{1}$$

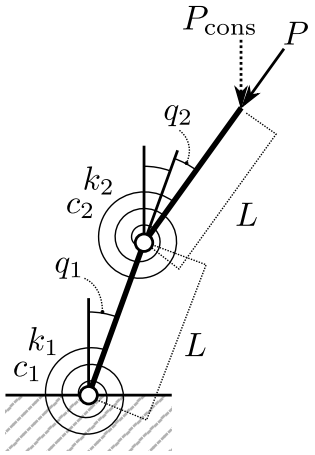

Figure 1. Problem setup.

where the internal, external and inertial parts of the virtual work have the expressions

$$\delta W_i = -\left(k_1 q_1 + c_1 \dot{q}_1\right)\delta q_1 - \left(k_2 q_2 + c_2 \dot{q}_2\right)\delta q_2 \,, \tag{2}$$

$$\delta W_e = -PL\sin(q_2)\delta q_1 \,, \tag{3}$$

$$\begin{aligned}\delta W_j = &-mL^3\left[\left(\tfrac{5}{3}+\cos(q_2)\right)\ddot{q}_1 + \left(\tfrac{1}{3}+\tfrac{1}{2}\cos(q_2)\right)\ddot{q}_2 - \sin(q_2)\dot{q}_1\dot{q}_2 - \tfrac{1}{2}\sin(q_2)(\dot{q}_2)^2\right]\delta q_1 \\ &-mL^3\left[\left(\tfrac{1}{3}+\tfrac{1}{2}\cos(q_2)\right)\ddot{q}_1 + \tfrac{1}{3}\ddot{q}_2 + \tfrac{1}{2}\sin(q_2)(\dot{q}_1)^2\right]\delta q_2 \,,\end{aligned} \tag{4}$$

where k_1, k_2 are the spring stiffnesses, c_1, c_2 the damping coefficients, L the length of one rod and P the magnitude of the follower force $\mathbf{P}$. The virtual work equation (1) can be written, as used in Ref. [6], in the form

$$(\mathbf{L} + \mathbf{Q} + \mathbf{J}) \cdot \delta\mathbf{q} = 0 \,, \tag{5}$$

where the internal, external and inertial generalized forces are

$$\begin{aligned}\mathbf{L} &= -\begin{bmatrix} k_1 q_1 + c_1 \dot{q}_1 \\ k_2 q_2 + c_2 \dot{q}_2 \end{bmatrix}, \qquad \mathbf{Q} = -PL\begin{bmatrix} \sin q_2 \\ 0 \end{bmatrix}, \\ \mathbf{J} &= -mL^3\begin{bmatrix} \left(\tfrac{5}{3}+\cos(q_2)\right)\ddot{q}_1 + \left(\tfrac{1}{3}+\tfrac{1}{2}\cos(q_2)\right)\ddot{q}_2 - \sin(q_2)\dot{q}_1\dot{q}_2 - \tfrac{1}{2}\sin(q_2)(\dot{q}_2)^2 \\ \left(\tfrac{1}{3}+\tfrac{1}{2}\cos(q_2)\right)\ddot{q}_1 + \tfrac{1}{3}\ddot{q}_2 + \tfrac{1}{2}\sin(q_2)(\dot{q}_1)^2 \end{bmatrix}.\end{aligned} \tag{6}$$

For comparison, in the conservative dead-weight loading case with $\mathbf{P}_{\text{cons}}$ (refer to Fig. 1), the corresponding external generalized force becomes (note the opposite sign)

$$\mathbf{Q}_{\text{cons}} = P_{\text{cons}} L \begin{bmatrix} \sin q_1 + \sin(q_1+q_2) \\ \sin(q_1+q_2) \end{bmatrix}.$$

Because the variation $\delta\mathbf{q}$ is arbitrary, the virtual work equation (5) results in the equations of motion

$$\mathbf{L} + \mathbf{Q} + \mathbf{J} = \mathbf{0} \,. \tag{7}$$

Equation (7) together with Eqs. (6), and proper initial conditions for $\mathbf{q}$ and $\dot{\mathbf{q}}$, completes the non-linear description for the dynamics of the considered two-rod system.

Linearization

Beside the original non-linear model, it will be useful to consider its linearization at some particular point $(\mathbf{q}_e, \dot{\mathbf{q}}_e, \ddot{\mathbf{q}}_e)$. Let us define the perturbations

$$(\mathbf{q}^*, \dot{\mathbf{q}}^*, \ddot{\mathbf{q}}^*) \equiv (\mathbf{q} - \mathbf{q}_e \,,\; \dot{\mathbf{q}} - \dot{\mathbf{q}}_e \,,\; \ddot{\mathbf{q}} - \ddot{\mathbf{q}}_e) \,, \tag{8}$$

and choose the point of linearization as an arbitrary static equilibrium point $(\mathbf{q}_e, \dot{\mathbf{q}}_e, \ddot{\mathbf{q}}_e) = (\mathbf{q}_e, 0, 0)$. Developing a multivariate Taylor series at $(\mathbf{q}_e, 0, 0)$ up to first order results in the following expressions:

$$\widehat{\mathbf{L}}(\mathbf{q}^*, \dot{\mathbf{q}}^*, \ddot{\mathbf{q}}^*) \equiv \mathbf{L}(\mathbf{q}_e, 0, 0) + \frac{\partial \mathbf{L}}{\partial \mathbf{q}}(\mathbf{q}_e, 0, 0)\, \mathbf{q}^* + \frac{\partial \mathbf{L}}{\partial \dot{\mathbf{q}}}(\mathbf{q}_e, 0, 0)\, \dot{\mathbf{q}}^* + \frac{\partial \mathbf{L}}{\partial \ddot{\mathbf{q}}}(\mathbf{q}_e, 0, 0)\, \ddot{\mathbf{q}}^* \,, \tag{9}$$

$$\widehat{\mathbf{Q}}(\mathbf{q}^*, \dot{\mathbf{q}}^*, \ddot{\mathbf{q}}^*) \equiv \mathbf{Q}(\mathbf{q}_e, 0, 0) + \frac{\partial \mathbf{Q}}{\partial \mathbf{q}}(\mathbf{q}_e, 0, 0)\, \mathbf{q}^* + \frac{\partial \mathbf{Q}}{\partial \dot{\mathbf{q}}}(\mathbf{q}_e, 0, 0)\, \dot{\mathbf{q}}^* + \frac{\partial \mathbf{Q}}{\partial \ddot{\mathbf{q}}}(\mathbf{q}_e, 0, 0)\, \ddot{\mathbf{q}}^* \,, \tag{10}$$

$$\widehat{\mathbf{J}}(\mathbf{q}^*, \dot{\mathbf{q}}^*, \ddot{\mathbf{q}}^*) \equiv \mathbf{J}(\mathbf{q}_e, 0, 0) + \frac{\partial \mathbf{J}}{\partial \mathbf{q}}(\mathbf{q}_e, 0, 0)\, \mathbf{q}^* + \frac{\partial \mathbf{J}}{\partial \dot{\mathbf{q}}}(\mathbf{q}_e, 0, 0)\, \dot{\mathbf{q}}^* + \frac{\partial \mathbf{J}}{\partial \ddot{\mathbf{q}}}(\mathbf{q}_e, 0, 0)\, \ddot{\mathbf{q}}^* \,. \tag{11}$$

The hat denotes a first-order Taylor approximation. The linearized equations of motion (7) at the specific point $(\mathbf{q}_e, 0, 0)$ have the form

$$\frac{\partial \mathbf{J}}{\partial \ddot{\mathbf{q}}}(\mathbf{q}_e, 0, 0)\, \ddot{\mathbf{q}}^* + \frac{\partial \mathbf{L}}{\partial \dot{\mathbf{q}}}(\mathbf{q}_e, 0, 0)\, \dot{\mathbf{q}}^* + \left(\frac{\partial \mathbf{L}}{\partial \mathbf{q}}(\mathbf{q}_e, 0, 0) + \frac{\partial \mathbf{Q}}{\partial \mathbf{q}}(\mathbf{q}_e, 0, 0) \right) \mathbf{q}^* = \mathbf{0} \,, \tag{12}$$

which can be written in matrix form as

$$\mathbf{M}\ddot{\mathbf{q}}^* + \mathbf{C}\dot{\mathbf{q}}^* + \mathbf{K}\mathbf{q}^* = \mathbf{0} \,, \tag{13}$$

where the stiffness, damping and mass matrices are

$$\mathbf{K} \equiv -\left(\frac{\partial \mathbf{L}}{\partial \mathbf{q}}(\mathbf{q}_e, 0, 0) + \frac{\partial \mathbf{Q}}{\partial \mathbf{q}}(\mathbf{q}_e, 0, 0) \right) \,, \quad \mathbf{C} \equiv -\frac{\partial \mathbf{L}}{\partial \dot{\mathbf{q}}}(\mathbf{q}_e, 0, 0) \,, \quad \mathbf{M} \equiv -\frac{\partial \mathbf{J}}{\partial \ddot{\mathbf{q}}}(\mathbf{q}_e, 0, 0) \,. \tag{14}$$

Evaluating the differentiations gives

$$\mathbf{K} = \begin{bmatrix} k_1 & 0 \\ 0 & k_2 \end{bmatrix} + PL \begin{bmatrix} 0 & \cos q_2 \\ 0 & 0 \end{bmatrix} \,, \quad \mathbf{C} = \begin{bmatrix} c_1 & 0 \\ 0 & c_2 \end{bmatrix} \,,$$
$$\mathbf{M} = mL^3 \begin{bmatrix} \frac{5}{3} + \cos q_2 & \frac{1}{3} + \frac{1}{2}\cos q_2 \\ \frac{1}{3} + \frac{1}{2}\cos q_2 & \frac{1}{3} \end{bmatrix} \,. \tag{15}$$

Solution of the linearized model

For simplicity the case where the two springs are identical is considered: $k_1 = k_2 \equiv k$ and $c_1 = c_2 \equiv c$. In the linearization, a natural configuration of interest is the straight upright trivial state of the system, $\mathbf{q}_e = 0$. The stiffness, damping and mass matrices are

$$\mathbf{K} = k \begin{bmatrix} 1 & 0 \\ 0 & 1 \end{bmatrix} + PL \begin{bmatrix} 0 & 1 \\ 0 & 0 \end{bmatrix} \,, \quad \mathbf{C} = c \begin{bmatrix} 1 & 0 \\ 0 & 1 \end{bmatrix} \,, \quad \mathbf{M} = \frac{1}{6} mL^3 \begin{bmatrix} 16 & 5 \\ 5 & 2 \end{bmatrix} \,. \tag{16}$$

For comparison, the stiffness matrix for the conservative dead-weight case with P_{cons} is

$$\mathbf{K}_{\text{cons}} = \begin{bmatrix} k_1 & 0 \\ 0 & k_2 \end{bmatrix} - P_{\text{cons}} L \begin{bmatrix} \cos q_1 + \cos(q_1 + q_2) & \cos(q_1 + q_2) \\ \cos(q_1 + q_2) & \cos(q_1 + q_2) \end{bmatrix} \,,$$

and on the trivial state $\mathbf{q}_e = 0$,

$$\mathbf{K}_{\text{cons}} = k \begin{bmatrix} 1 & 0 \\ 0 & 1 \end{bmatrix} - P_{\text{cons}} L \begin{bmatrix} 2 & 1 \\ 1 & 1 \end{bmatrix} \,.$$

Let us divide both sides of equation (13) by mL^3, and define the dimensionless quantities

$$t' \equiv \frac{t}{\tau} \,, \quad \beta \equiv \frac{c\tau}{mL^3} \,, \quad \gamma \equiv \frac{k\tau^2}{mL^3} \,, \quad \lambda \equiv \frac{PL}{k} \,. \tag{17}$$

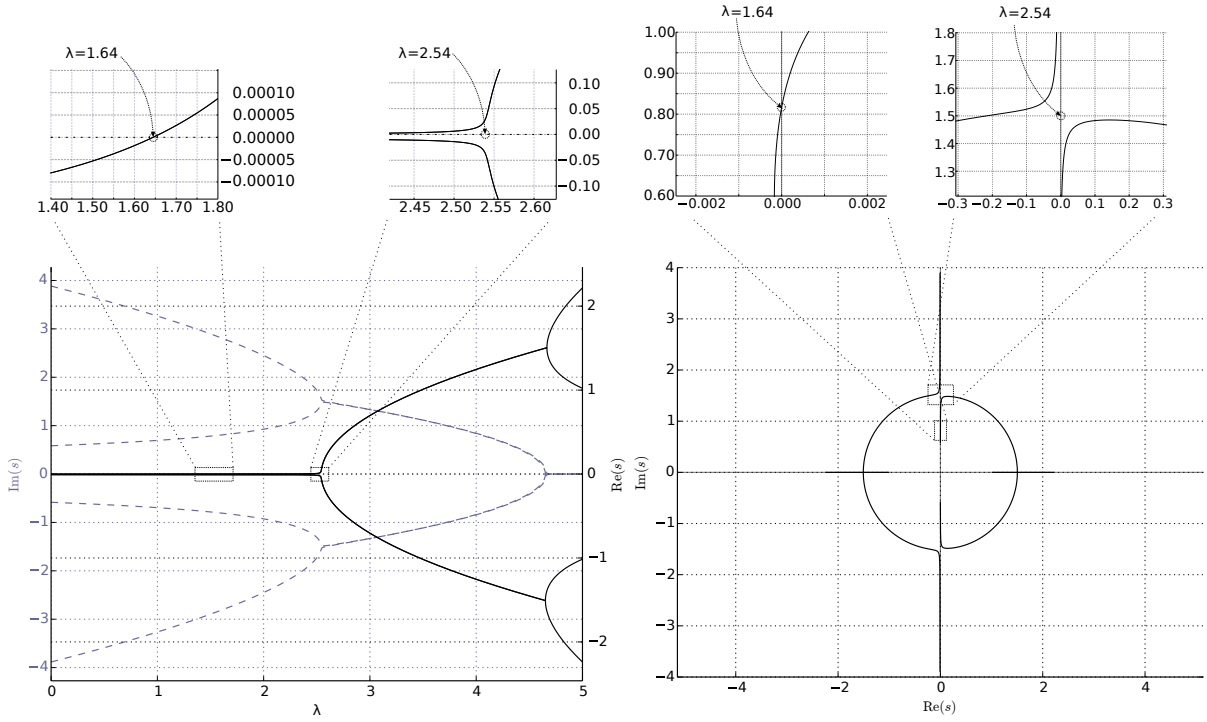

Figure 2. Solutions of the characteristic polynomial (21) for $\gamma = 1$, $\beta = 10^{-3}$. In the large left subfigure, the solid line represents $\mathrm{Re}(s)$ and the dashed line $\mathrm{Im}(s)$. The trivial equilibrium point $(q_1, q_2) = (0, 0)$ loses stability at $\lambda^{**} \approx 1.64$ in a dynamic mode (a.k.a. flutter, $\mathrm{Im}\, s \neq 0$). The bifurcation point of the undamped case, at $\lambda^{*} \approx 2.54$, is no longer a bifurcation point.

Here t' is the dimensionless time coordinate, and τ is a characteristic time (an arbitrary scaling factor). Because we are dealing with moments, in the SI system we have $[k] = \mathrm{N\,m/rad} = \mathrm{N\,m}$ and $[c] = \mathrm{N\,m\,s}$. Note also that $[m] = \mathrm{kg/m}$, the linear density of the rod material, and observe that in (13), each $\partial/\partial t$ produces a factor of $1/\tau$ when the equation is re-expressed using the dimensionless time t' (via the chain rule). The following forms are obtained for the dimensionless stiffness, damping and mass matrices:

$$\widetilde{\mathbf{K}} = \gamma \left(\begin{bmatrix} 1 & 0 \\ 0 & 1 \end{bmatrix} + \lambda \begin{bmatrix} 0 & 1 \\ 0 & 0 \end{bmatrix} \right) , \quad \widetilde{\mathbf{C}} = \beta \begin{bmatrix} 1 & 0 \\ 0 & 1 \end{bmatrix} , \quad \widetilde{\mathbf{M}} = \frac{1}{6} \begin{bmatrix} 16 & 5 \\ 5 & 2 \end{bmatrix} . \tag{18}$$

The system has three remaining parameters: β is a damping/mass ratio, γ is a stiffness/mass ratio, and λ is the loading strength relative to the reference load k/L. Thus, essentially λ may vary continuously (as a parameter), while β and γ play the role of material constants. We will perform a parametric analysis, fixing β and γ at some constant values, and examining the solutions of this system as a function of λ.

Equation (13) is a system of ordinary differential equations with constant coefficients. The standard technique is to apply the time-harmonic trial function to determine its harmonic vibrations. Inserting the trial function

$$\mathbf{q}^* = e^{s\,t'}\,\mathbf{y} \tag{19}$$

(where $\mathbf{y}$ is an eigenstate vector and s the dimensionless complex stability exponent) into the dimensionless representation of (13) and discarding the common factor $e^{s\,t'}$, the result is

$$\left(\widetilde{\mathbf{K}} + s\widetilde{\mathbf{C}} + s^2 \widetilde{\mathbf{M}} \right) \mathbf{y} = 0 \, , \tag{20}$$

which has nontrivial solutions $\mathbf{y} \not\equiv 0$ if and only if the determinant vanishes. Using (18) and (20), we construct the characteristic polynomial, which is of the fourth order in the stability

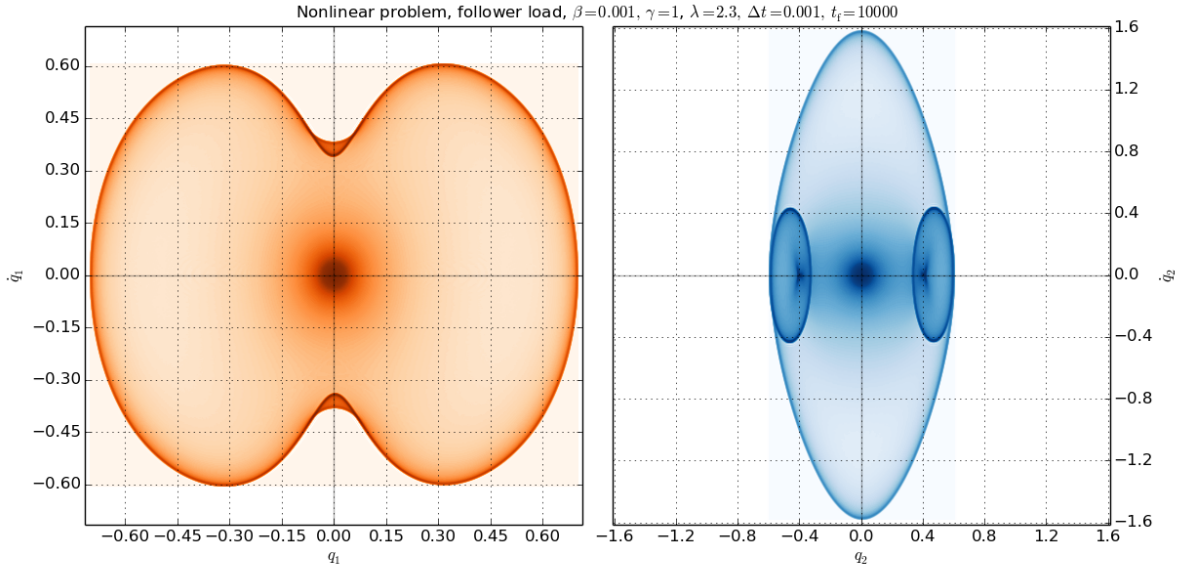

Figure 3. A solution of the non-linear system. Phase space density plots for $(q_1, \dot{q}_1)$ and $(q_2, \dot{q}_2)$ for $\gamma = 1$, $\beta = 10^{-3}$, $\lambda = 2.3$ with initial condition $(q_1, \dot{q}_1, q_2, \dot{q}_2) = (10^{-3}, 0, 10^{-3}, 0)$.

exponent s. The zeroes of this polynomial give the admissible values of the stability exponent at each point (β, γ, λ) in the parameter space. Explicitly, for the non-conservative problem it is obtained that

$$\left[\gamma + s(\beta + \frac{8}{3}s)\right]\left[\gamma + s(\beta + \frac{1}{3}s)\right] - \left[\gamma\lambda + \frac{5}{6}s^2\right]\left[\frac{5}{6}s^2\right] = 0\,. \tag{21}$$

For comparison, for the conservative (dead-weight) problem the characteristic polynomial is

$$\left[\gamma(1-2\lambda) + s(\beta + \frac{8}{3}s)\right]\left[\gamma(1-\lambda) + s(\beta + \frac{1}{3}s)\right] - \left[-\gamma\lambda + \frac{5}{6}s^2\right]\left[-\gamma\lambda + \frac{5}{6}s^2\right] = 0\,.$$

For a numerical example, let us choose $\gamma = 1$ and the range $\lambda = [0, 5]$. The solutions of the non-conservative case (21) are shown in Fig. 2. By the introduction of small damping into the model, the critical value of the load parameter has jumped down from $\lambda^* \approx 2.54$ to $\lambda^{**} \approx 1.64$; this behaviour is retained for arbitrarily small positive β. One pair of solutions crosses the imaginary axis well before the undamped bifurcation load λ^* is reached.

Solution of the non-linear model

To illustrate the behaviour of the original non-linear system, we perform direct time integration up to a prescribed end time $t'_f = 10\,000$ (with trivial time scaling, $\tau = 1\,\mathrm{s}$), choosing the load λ such that $\lambda^{**} < \lambda < \lambda^*$. By introduction of auxiliary variables for $\dot{q}_1$ and $\dot{q}_2$, the non-linear system (7) with the definitions in Eqs. (6) is reduced to the standard first-order form

$$\dot{\mathbf{w}} = f(\mathbf{w})\,, \quad \text{where } \mathbf{w} = (q_1, \dot{q}_1, q_2, \dot{q}_2)\,. \tag{22}$$

The classical implicit midpoint rule (IMR) is used to integrate the equations of motion. The integration is performed at a constant timestep, because in addition to simplicity, this leads to a property that is very useful for visualization. Consider a projection of the trajectory, where the time coordinate is projected away (discarded). The time-discretized solution forms a four-dimensional point cloud in the state space $(q_1, \dot{q}_1, q_2, \dot{q}_2)$. With a constant timestep, the local density of the point cloud is linearly proportional to the portion of total simulated time that the time-discretized system spends in that local region of the state space.

To visualize the results, the time coordinate is discarded, and the four-dimensional data is projected into two dimensions. Two physically motivated, independent projections are used; the first projection is $(q_1, \dot{q}_1)$ and the second is $(q_2, \dot{q}_2)$.

A simple kernel density estimator is applied to the resulting two-dimensional point clouds, in order to extract a discrete (raster) representation of the state space density function. Kernel density estimation is preferable over 2D histogramming, because it gives subpixel accuracy (reducing moiré artifacts), and it is not sensitive to the placement of the bin edges.

The density function has a high dynamic range, far exceeding that which is representable on a computer screen or in print. To visualize the density, a dynamic range compressor is applied before plotting. We choose the data-adaptive histogram remapping method of Larson, Rushmeier and Piatko [7], which preserves visual contrast. The resulting colour scale is neither linear nor logarithmic; instead, the colours are allocated in a data-adaptive manner in order to reveal as much structure in the data as possible. For details, see [8].

See Fig. 3 for the results. The parameters are $\beta = 10^{-3}$, $\gamma = 1$ and $\lambda = 2.3$. The shade is a monotonic function of the state space density, with darker shades indicating higher densities. The solution starts at the initial point $(q_1, \dot{q}_1, q_2, \dot{q}_2) = (10^{-3}, 0, 10^{-3}, 0)$, spirals out at first slowly (dark region near origin), and accelerates outward (shade becomes lighter). Then the non-linearity starts to have a visible effect, slowing the outward motion (shade becomes darker again) and deforming the trajectory into a more complicated shape. Eventually, the system settles onto a limit cycle (dark outer border; in the right subfigure, including the outline and the small ellipses) far away from the initial point. In this cycle, while the ranges of angles for both springs are approximately the same, the second rod has a higher maximum angular velocity.

The non-linear simulation illustrates the global meaning of the local instability of the static equilibrium at the origin for $\lambda = 2.3$, indicated by the linear analysis in Fig. 2. As is common for non-linear systems, the exponential growth of the solution norm eventually stops, and the system settles onto an attractor, which in this particular case is a limit cycle. Studying the non-linear problem parametrically, also strange attractors can be found for higher values of λ. No further static equilibria exist; by requiring $\ddot{\mathbf{q}} = \dot{\mathbf{q}} = 0$ in (7) and solving for $\mathbf{q}$, it is seen that the origin is the only static equilibrium point for the non-linear system with the follower load.

References

[1] H. Ziegler. Die Stabilitätskriterien der Elastomechanik. *Ingenieur Archiv*, **20**, 1952, 49–56.

[2] V.V. Bolotin. *Nonconservative Problems of the Theory of Elastic Stability.* Pergamon Press, 1963.

[3] V.V. Bolotin. Dynamic stability of structures. In *Nonlinear Stability of Structures*, Series CISM No 342. A.N. Kounadis and W.B. Krätzig (Eds.) Springer, 1995, 3–72.

[4] Y. Sugiyama and M.A. Langthjem. Physical mechanisms of the destabilizing effect of damping in continuous non-conservative dissipative systems. *International Journal of Non-linear Mechanics*, **42**, 2006, No 1, 132–145.

[5] Q.S. Nguyen. *Bifurcation and Stability of Dissipative Systems*, Springer-Verlag, 1993, CISM courses and lectures no. 327.

[6] Q.S. Nguyen. *Stability and Nonlinear Solid Mechanics.* John Wiley & Sons, 2000.

[7] G. Larson, H. Rushmeier and C. Piatko. Visibility Matching Tone Reproduction Operator for High Dynamic Range Scenes. *IEEE Transactions on Visualization and Computer Graphics*, **3**, 1997, 291–306.

[8] J. Jeronen. Visual contrast preserving representation of high dynamic range mathematical functions. In *Numerical methods for differential equations, optimization, and technological problems. Dedicated to Professor P. Neittaanmäki on his 60th Birthday.*, Series Computational Methods in Applied Sciences No 27. S. Repin, T. Tiihonen and T. Tuovinen (Eds.) Springer, 2013, 409–429.

Suomen XII mekaniikkapäivien esitelmät
R. Kouhia, J. Mäkinen, S. Pajunen and T. Saksala (toim.)

Numeerinen integrointi laajennetussa elementtimenetelmässä

Tom Gustafsson

Aalto-yliopiston perustieteiden korkeakoulu, Matematiikan ja systeemianalyysin laitos
PL 11100, 00076 Aalto, tom.gustafsson@aalto.fi

Tiivistelmä. Eräs suuri haaste laajennetun elementtimenetelmän soveltamisessa on tarkkojen numeeristen integrointisääntöjen puuttuminen. Tässä työssä tarkastellaan perinteiseen elementtimenetelmään perustuvissa ohjelmistoissa yleisesti käytettyjen kvadratuuripisteistöjen soveltuvuutta laajennettuun elementtimenetelmään.

Avainsanat: laajennettu elementtimenetelmä, numeerinen integrointi

Johdanto

Olkoon Ω kuvan 1 (vas.) mukainen säröytynyt alue ja (r, θ) kuvassa esitelty napakoordinaatisto. Tarkastellaan seuraavaa malliongelmaa: etsi funktio $u : \Omega \to \mathbb{R}$ siten, että

$$-\Delta u = 0, \qquad \text{alueessa } \Omega, \tag{1}$$

$$u = \sqrt{r} \sin \frac{\theta}{2}, \quad \text{reunalla } \partial\Omega. \tag{2}$$

Määritellään funktioavaruus

$$V := \left\{ w \in H^1(\Omega) \,\middle|\, w|_{\partial\Omega} = \sqrt{r} \sin \frac{\theta}{2} \right\}, \tag{3}$$

jonka avulla esitelty malliongelma voidaan kirjoittaa heikossa muodossa: etsi funktio $u \in V$ siten, että

$$\int_\Omega \nabla u \cdot \nabla v \, \mathrm{d}x = 0, \quad \forall v \in H_0^1(\Omega). \tag{4}$$

Epäsäännöllisen reunan ja asetetun reunaehdon vuoksi tehtävän (4) ratkaisu ei kuulu funktioavaruuteen $H^2(\Omega)$ [5]. Tästä huolimatta ehto $u \in H^2(\Omega)$ on säännöllisyysvaatimus täyden suppenemisnopeuden saavuttamiseksi P_1-elementtimenetelmässä [3]: etsi $u_h \in V_h := \{w \in V \,|\, w|_K \in P_1(K) \, \forall K \in \mathcal{T}_h\}$ siten, että

$$\int_\Omega \nabla u_h \cdot \nabla v_h \, \mathrm{d}x = 0, \quad \forall v_h \in V_{h,0} := \{w \in H_0^1(\Omega) \,|\, w_K \in P_1(K) \, \forall K \in \mathcal{T}_h\}, \tag{5}$$

jossa $\mathcal{T}_h$ on alueen Ω kattava säännöllinen kolmioverkko verkkoparametrilla h ja $P_1(K)$ on elementissä K määriteltyjen lineaaristen polynomien joukko. Tarkempi tarkastelu osoittaa, että tehtävän (4) ratkaisu kuuluu Sobolevin avaruuteen $H^{3/2-\epsilon}(\Omega)$, $\forall \epsilon > 0$, mikä rajoittaa tarkan ja diskreetin ratkaisun erotuksen H^1-normin kertaluokkaan $\mathcal{O}(h^{1/2})$.

Laajennetussa elementtimenetelmässä [1, 2] diskreettejä funktioavaruuksia V_h ja $V_{h,0}$ laajennetaan lausekkeen (2) kaltaisilla kantafunktioilla. Yleisesti säröjen läheisyydessä tehtävän (4) ratkaisujen tiedetään olevan muotoa $\sqrt{r} \sin \theta/2$ kun taas tässä työssä reunaehto (2) valittiin, koska tällöin tarkka ratkaisu tunnetaan. Laajentamalla diskreettejä funktioavaruuksia sopivilla kantafunktioilla saadaan H^1-virheen suppenemisnopeutta parannettua [6].

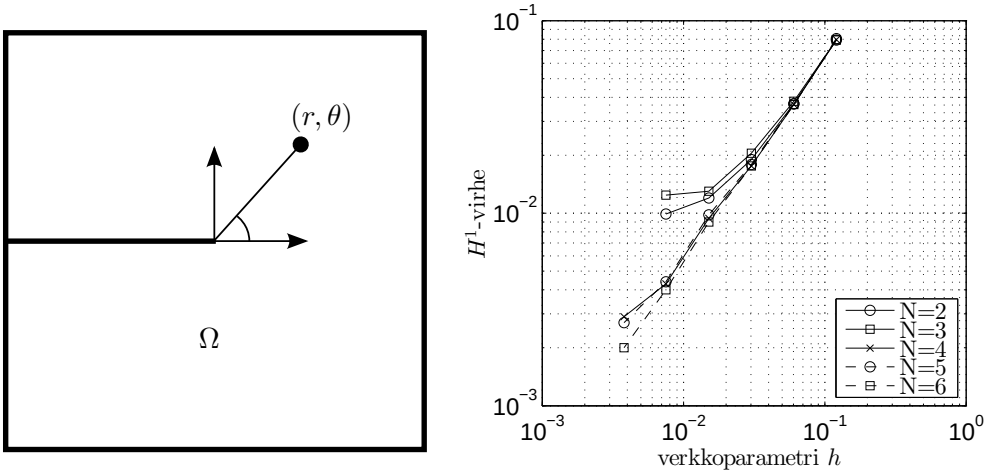

Kuva 1. (Vasen.) Tarkasteltava säröytynyt alue Ω ja napakoordinaatisto (r, θ). Paksumpi viiva kuvaa laskenta-alueen reunaa. (Oikea.) Integrointipisteiden määrän N vaikutus H^1-virheen suppenemisnopeuteen.

Integrointivirhe

Muodostettaessa laajennettuun elementtimenetelmään liittyvää matriisiyhtälöä on tarpeen laskea lisättyjen kantafunktioiden energiasisätulot itsensä ja muiden avaruuden $V_{h,0}$ kantafunktioiden kanssa [6]. Koska lisätyt kantafunktiot eivät ole polynomeja, on tarkkojen integrointisääntöjen muodostaminen haastavaa. Elementtimenetelmän toiminnan takaamiseksi tulee numeerinen integrointi lähtökohtaisesti tehdä mahdollisimman tarkasti. Koska täysin tarkka integrointi ei laajennetussa elementtimenetelmässä ole yleisessä tapauksessa mahdollista, on varmistettava, että integrointivirhe on häviävän pieni ja etteivät menetelmän ominaisuudet kuten suppenemisnopeus ja syntyvän matriisitehtävän stabiilisuus kärsi.

Kuvassa 1 (oik.) on esitelty integrointipisteiden määrän vaikutus laajennetun elementtimenetelmän H^1-virheen suppenemisnopeuteen verkkoparametrin h funktiona ratkaistaessa tehtävää (4) ja käytettäessä ns. Dunavantin integrointipisteitä [4]. Kuvasta voidaan havaita suppenemisnopeuden hidastuvan kullakin integrointipisteiden määrällä verkkoparametrin ollessa riittävän pieni.

Viitteet

[1] I. Babuška, J. M. Melenk. The partition of unity finite element method: Basic theory and applications. *Computer Methods in Applied Mechanics and Engineering*, 39:289–314, 1996. doi: 10.1016/S0045-7825(96)01087-0

[2] T. Belytschko, T. Black. Elastic crack growth in finite elements with minimal remeshing. *International Journal for Numerical Methods in Engineering*, 45(5):601–620, 1999. doi: 10.1002/(SICI)1097-0207(19990620)45:5<601::AID-NME598>3.0.CO;2-S

[3] S. C. Brenner, R. Scott. Mathematical Theory of Finite Element Methods (3rd Edition). Springer Science+Business Media, LCC. 2008. doi: 10.1007/978-0-387-75934-0

[4] D. A. Dunavant. High Degree Efficient Symmetrical Gaussian Quadrature Rules for the Triangle. *International Journal for Numerical Methods in Engineering*, 21:1129–1148, 1985. doi: 10.1002/nme.1620210612

[5] P. Grisvard. Singularities in Boundary Value Problems. Masson. 1992.

[6] T. Gustafsson, M. Juntunen, R. Stenberg. A numerical study of the extended finite element method for linear elastic fracture mechanics. *Rakenteiden Mekaniikka*, 47(3):110–126, 2014.

Proceedings of the XII Finnish Mechanics Days
R. Kouhia, J. Mäkinen, S. Pajunen and T. Saksala (Eds.)

Fatigue strength of shrink-fitted aluminium fan on steel shaft

Timo Holopainen[1], and Toni Kilpeläinen[2]

ABB Motors and Generators, P.O. Box 186, 00381 Helsinki, Finland
(1)timo.holopainen@fi.abb.com
(2)toni.kilpelainen@fi.abb.com

Summary. Large electric machines need internal cooling circuit. Fans mounted on the rotor are used to circulate the cooling air inside the motor. Aluminium is an attractive material due to low specific weight and casting an inviting manufacturing method for these fans. Internal fans must endure fatigue loading generated by the centrifugal forces and thermal cycles. The latter is particularly critical with shrink-fitted fans. This results from the different thermal expansion factors of aluminium and steel. The aim of this paper is to present the fatigue analysis of typical aluminium fan based on EN 1999-1-3.

Key words: centrifugal fan, fatigue design, thermal load

Introduction

Large electric machines need internal cooling circuit. Internal fans mounted on the rotor are often used to circulate the cooling air inside the motor enclosure. Aluminium is an attractive fan material due to the low specific weight and casting an inviting manufacturing method due to the relatively complicated fan geometry determined by the aerodynamic requirements. Figure 1 shows an example of an internal fan.

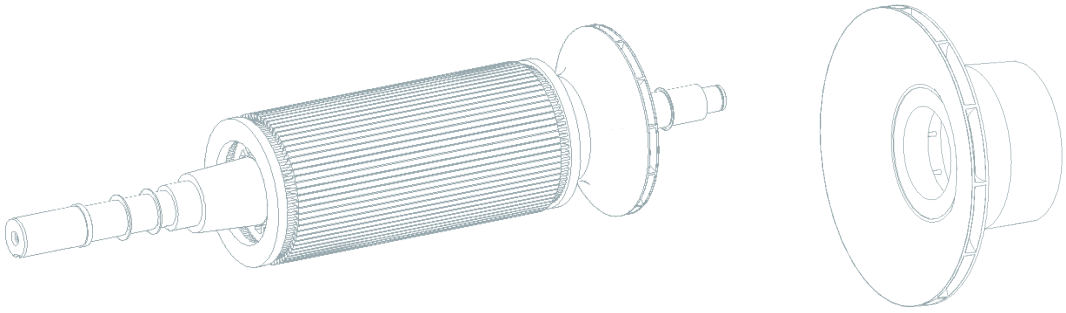

Figure 1. Assembled rotor of an electric motor with its internal fan.

The dimensioning of fans is based mainly on fatigue strenght. The fatigue loading of a fan is determined by the operation cycles including the rotational speed and temperature. There are generally two simple mounting methods for these fans: key-fitting and shrink-fitting. The

shrink-fitting has many advantages, but it leads to a more demanding fatigue design. Particularly, the thermal cycle is critical due to the different thermal expansion factors of aluminium and steel.

The aim of this paper is to present a fatigue design approach of cast aluminium fans based on EN 1999-1 [3, 4]. This approach is discussed with respect to calculation procedures and application requirements.

The paper describes first the calculation procedure based on the standards. After that, this procedure is applied for a typical fan with a key- or shrink-fitted joint. Finally, the calculation results are evaluated and the applied procedure discussed.

Calculation procedure

Design load

The design lifetime of a motor and its fan is typically 20 years. The fatigue load is generated by the cycles of centrifugal loads and thermal loads. A full load cycle of a fan for constant speed motor includes the following steps (Figure 2):

1. Zero speed in cold condition (as after mounting of the fan)
2. Rated speed in cold condition
3. Rated speed in hot condition
4. Zero speed in hot condition
5. Zero speed in cold condition

In principle, the fatigue design is based on the number of load cycles during the design lifetime. It can be assumed for instance that there are 1000 starts per year. However, it is remarkable that the full cooling down of a motor may take several days. Thus, the number of full load cycles is usually much smaller than the number of reduced load cycles (Figure 2).

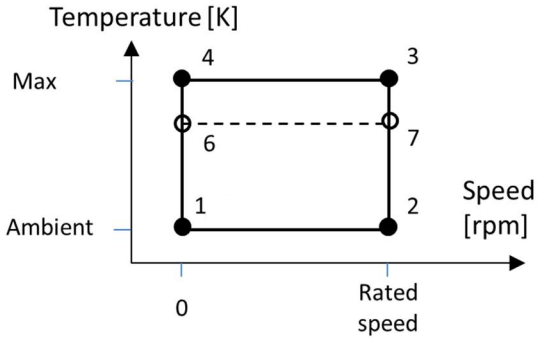

Figure 2. Schematic diagram of full load cycle (P1-P2-P3-P4-P1) and reduced load cycle (P6-P7-P3-P4).

Fatigue strength

The fatigue design relationship for aluminium constructions in the range 10^5 to $5x10^6$ cycles (with partial factors equal to 1.0) is defined by the equation [4]

$$N_i = 2 \times 10^6 \left(\frac{\Delta\sigma_c}{\Delta\sigma_i}\right)^{m_1} \quad (1)$$

where N_i is the predicted number of cycles to failure, $\Delta\sigma_c$ is the reference value of fatigue strength at 2×10^6 cycles, $\Delta\sigma_i$ is the stress range for the principal geometric stresses at the constructional detail, and m_1 is the inverse slope of the $\sigma_c - N$ curve. For cast aluminium $m_1 = 7$ and the design category is determined by the maximum diameter of the pores [4, 5]. Table 1 shows the corresponding allowable stress range for selected number of cycles. According to EN 1999-1-3 [4] Eq. (1) may by unnecessary conservative for stress cycles less than 10^5 times.

Standard EN 1999-1 [3, 4] covers six cast aluminium alloys with two casting processes: sand cast and permanent mould. It is remarkable that the fatigue strenght of these alloys is dependent only on the maximum diameter of the pores [5]. This means that the fatigue strength of aluminium casts is strongly related to the casting and quality assurance processes.

Table 1. Fatigue strenght of cast aluminium.

Detail category	Maximum pore diameter	Allowable stress range			
		N=2 000	*N*=20 000	*N*=10^5	*N*=2x10^6
71	0,2	(190,5)[1]	(137,1)	108,9	71,0
50	0,5	(134,1)	96,5	76,7	50,0
40	0,9	107,3	77,2	61,4	40,0
32	1,2	85,8	61,8	49,1	32,0
25	2,0	67,1	48,3	38,4	25,0

[1]Values in parentheses are above the yield strength of assumed base material

Stress calculations

According to EN 1999 [4] the principal geometric stress should be used for the fatigue design. In principle, the stress range between two loading conditions can be determined by calculating the difference of stress tensors and transforming this difference tensor in principal coordinates. The largest absolute value of the principal stresses of this difference tensor gives the largest stress range.

The largest stress range is not necessarily enough, because the fatigue strenght is dependent also on the stress ratio $R = \sigma_{\min}/\sigma_{\max}$ [4]. In order to get the stress ratio for critical stress ranges the principal stresses of both load conditions in critical locations must be calculated and corresponding stress ratio determined. In this paper, the critical stress ranges with stress ratios are searched as follows:

1. Critical locations are defined by the maximum and minimum principal stresses of the difference tensor of two load conditions.
2. Principal stresses with directions are determined in these locations for both load cases.
3. Algebraic differences of principal stresses are calculated by using the directional information. The largest absolute value is related to the max/min stress range. (This may induce a small error due to the alignment deviation of principal stresses)
4. Stress ratio related to the max/min stress range is calculated by using the corresponding principal stresses.

The largest stresses are usually on the surface of the structure with two non-zero principal stresses. This facilitates the “manual” procedure for finding of stress ratios. However, it must be mentioned that this approach does not necessarily yield the most critical locations due to the effect of stress ratio.

Calculation example

The example fan is designed for a 1500 kW electric motor. The fan is mounted on the shaft and is located inside the motor frame circulating the air inside the enclosure. The maximum continuous rotational speed is 3600 rpm and the maximum change of the internal air temperature is 110 K. The inner diameter of the fan hub is 210 mm. The fan material was cast aluminium with E = 70 GN/m^2, ν = 0.3, ρ = 2700 kg/m^3, and $\alpha = 23 \cdot 10^{-6}$ K^{-1}.

Key-fitted fan

The fan is fitted to the shaft with a keyway. The applied interference fit H7/m6 was chosen to balance between the stress range and the residual unbalance due to the opening interference fit. All the numerical analyses were performed by ANSYS software [1]. The material model was linear elastic. The modelling was carried out by 10 node tetra elements and the mesh density in the critical corner was modelled by 6 elements for 90 degrees [2]. Figure 3 shows the stresses in the keyway corner due to the centrifugal forces. The forces due to temperature cycle are small due to the light interference fit.

It can be mentioned that the opening of the fit due to the thermal expansion induces an unbalance of quality grade G57 for a separate fan with unpredicted direction. This is the main drawback of key-fitted fan together with the additional parts and assembly requirements.

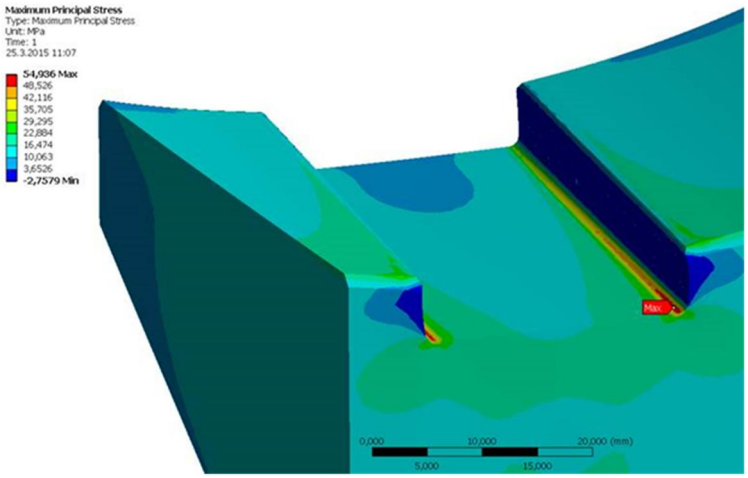

Figure 3. Maximum principal stress (54.9 MPa) in the keyway corner at 3600 rpm.

Shrink-fitted fan

The fan is fitted to the shaft with a shrink fit. A much larger interference N7/v6 is required to fix the fan to the shaft with the maximum temperature difference and rotational speed. The symmetric sector model included the slice of shaft section and fan with one radial support wing. The contact between the shaft and fan is modelled by the contact elements with friction. Figure 4 shows the maximum principal stress of then fan in the mounted condition (P1 in Figure 2)

Figure 5 shows, as an example, the maximum principal stresses for two load conditions leading to the maximum stress range (88.2 MPa) with tensile stresses.

Comparison

The maximum stress ranges were calculated between all the load conditions of full load cycle (6 in total) presented in Figure 2. Table 2 shows the stress ranges for some of the calculated cases.

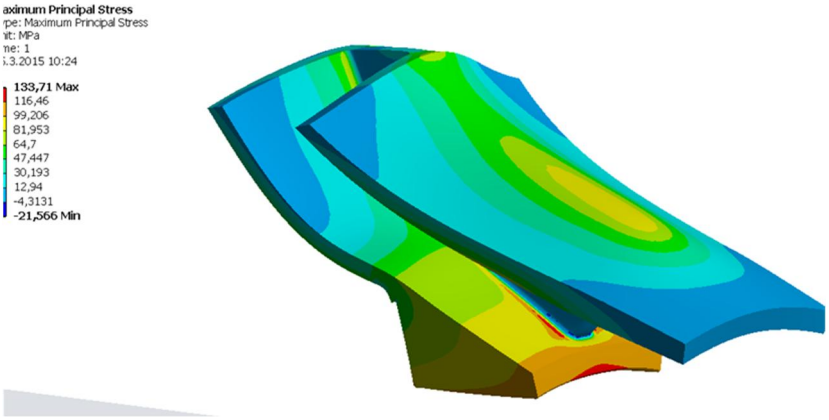

Figure 4. Maximum principal stress (134 MPa) due to shrink-fit.

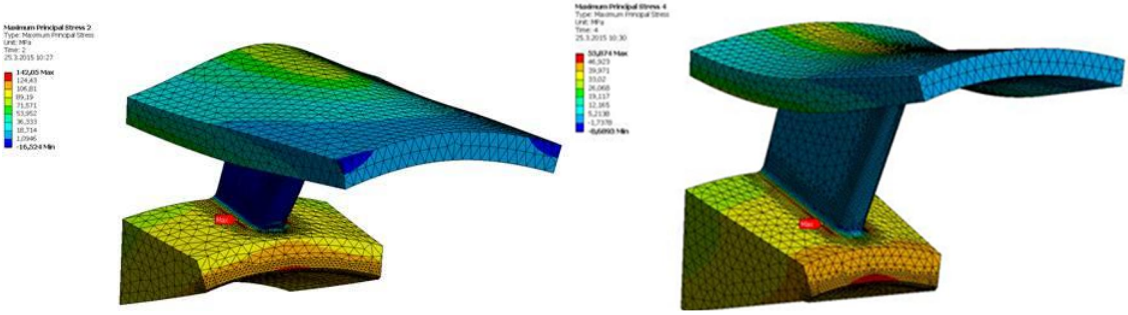

Figure 5. Maximum principal stress at 3600 rpm in cold condition (142.1 MPa) and zero speed in hot condition (53.9 MPa) in the same location and direction.

For the key-fitted case the effect of small interference fit is neglected and the stress ranges are generated purely by the centrifugal forces. The max value is obtained by choosing the location of maximum principal stress (of the stress tensor difference) and the min value by choosing the location of minimum principal stress. Some of the compressive stress ranges are unrealistically large due to the modelling details (e.g. unnecessary small fillet radius), but can be used here as qualitative values. The stress values can be compared to the yield strenght 133 MPa and the ultimate tensile strength 161 MPa of a typical material for cast parts [3].

Table 2. Maximum stress ranges of key-fitted and shrink-fitted fans between some of the load conditions presented in Figure 2.

Variable	Unit	Key fit		Shrink fit					
		P3 - P4		P1 - P3		P2 - P4		P3 - P4	
		max	min	max	min	max	min	max	min
$\Delta\sigma$	MPa	54,9	43,8	71,5	170,1	88,2	104,0	8,4	39,8
σ_{max}	MPa	54,9	0,0	133,7	-48,2	142,1	-76,3	62,2	-48,2
σ_{min}	MPa	0,0	-43,8	62,2	-218,3	53,9	-180,3	53,9	-88,0
R	-	0	-	0,47	4,53	0,38	2,36	0,87	1,82

As Table 2 shows the maximum tensile values for the shrink fitted fan are obtained in the load cycle P2-P4 and compressive values for the load cycle P1-P3. However, it is remarkable

that the load cycle P3-P4 gives relatively small stress cycles compared to the fatigue strength values of different detail categories (Table 1). It is assumed that most of the load cycles of actual fans are cumulated from the cycle P3-P4-P6-P7, which is assumed to be in most of the applications close to the load cycle P3-P4.

Discussion and conclusions

The shrink-fitted fan has several advantages compared to the key-fitted fan, e.g. the simplicity of the design and assembly with reduced residual unbalance in hot condition. The fatigue strength requirement seems to be the main challenge of shrink-fitted fan. This paper presented the calculation procedure based on EN 1999-1-3 [4].

The critical location of key-fitted fan is the corner of the key-way. A standard keyway has a rounding of the corner with a small radius. A small radius is a natural stress-raiser similar than an initial crack. The applied standard EN 1999 is based on the principal geometric stress of the actual geometry. It is open to authors how to handle the keyway corners according to this standard.

In general, it is significant that a tighter interference fit increases quickly the stresses in the keyway corner of a cold stationary motor (P1) preventing the intermediate form of the key-fitted and shrink-fitted connection. Thus, there are two qualitatively different and separate alternatives.

The shrink-fitted fan has large stress ranges in compressive side. The applied standard EN 1999 gives enhanced fatigue strength based on the stress ratio for values less than $R = +0.5$. However, as Table 2 shows, the stress ratio is positive when the maximum and minimum stress are compressive and often larger than 0.5. The authors assume that they have misunderstood the definition of stress ratio in this context.

The number of design cycles of a typical fan is order of 10 000. In addition, most of these cycles are for a hot motor (P3-P4) with clearly lower stress ranges. Thus, the dimensioning is clearly on the low-cycle fatigue range. Standard EN 1999 notes that the application of Equation (1) may be unnecessary conservative for low-cycle fatigue range and gives some alternatives for enhanced fatigue strength but not for aluminium castings.

As Table 1 shows, the fatigue strenght of aluminium castings is dependent on maximum pore size. The size of the pores is dependent on the casting methods and procedures. Small pore sizes are difficult to achieve and quality assurance and inspections are expensive procedures. Thus, the fatigue design of a simple shrink-fitted fan seems to be a very complicated task involving numerical models, expected load cycles, manufacturing practices and quality assurance.

References

[1] ANSYS Mechanical. Version 15.0, 25.3.2015. http://www.ansys.com

[2] J. Draper. *Modern metal fatigue analysis. EMAS Publishing, Warrington, UK*, 2008.

[3] EN 1999-1-1:2007. Eurocode 9: Design of aluminium structures – Part 1:1: General structural rules.

[4] EN 1999-1-3:2007. Eurocode 9: Design of aluminium structures – Part 1:3: Structures susceptible to fatigue.

[5] Q.G. Wang, C.J. Davidson, J.R. Griffiths, and P.N. Crepeau. Oxide films, pores and the fatigue lives of cast aluminium alloys. *Metallurgical and Materials Transactions B*, 37B(Dec):887-895, 2006.

Suomen XII mekaniikkapäivien esitelmät
R. Kouhia, J. Mäkinen, S. Pajunen ja T. Saksala (toim.)

Raudoitetun betonirakenteen taivutuksen mallintaminen Ansys-ohjelmalla

Jari Pietilä ja Jari Mäkinen

TTY, PL 600, 33101 TAMPERE, jari.j.pietila@tut.fi, jari.m.makinen@tut.fi

Tiivistelmä. Tässä artikkelissa käsitellään lyhyesti betonin vaurioitumisen laskennallista käyttäytymistä. Artikkelissa esitellään laskentojen lähtökohdat ja mallintamisen periaate lyhyesti, sekä analysoidaan päätulokset ja niistä havaittavissa olevat ilmiöt. Tarkempia tuloksia, analyyttista laskentaa ja halkeilua on käsitelty diplomityössä [4], mutta niitä ei käsitellä tässä artikkelissa.

Avainsanat: betoni, Ansys, Solid65, taivutus, raudoitus, murtumisenergia

Johdanto

Alun perin tutkimus liittyi aiheesta suoritettuun diplomityöhön [4], jonka lähtökohtia, laskentaa ja tuloksia selitetään artikkelissa. Työssä mallinnettiin raudoitetun betonilaatan taivutusta murtoon asti. Laskentaohjelman tuloksista pyrittiin löytämään yhteneväisyyksiä suoritettuun kokeeseen ja aiemmin suoritettuihin tutkimuksiin, sekä selittämään tuloksista havaittavissa olevia ilmiöitä.

Laskentaohjelman betonimallin toiminta

Betonin kuvaamiseen tarkoitettujen materiaalimallien triaksiaalisille vaurioitumispinnoille on olemassa neljä teoreettista vaatimusta, joiden täyttyessä mallia voidaan pitää luotettavana. Nämä vaatimukset ovat:

1. Mallin toiminta vastaa kokeellisia tuloksia.
2. Mallin parametrit ovat helposti määriteltävissä koetuloksista.
3. Vaurioitumispinnan suunta ei muutu äkillisesti.
4. Vaurioitumispinnassa ei ole epäjatkuvuuskohtia.

Ansys 14.0 käyttää Solid65-elementeillä mallinnetun betonin kuvaamiseen konstitutiivista triaksiaalista mallia [1-2], jonka kehittivät K.J. Willam ja E.P. Warnke 1970-luvulla [6]. 8-solmuiseen Solid65-elementtiin on mahdollista lisätä raudoitus, joka muuttaa sen ominaisuuksia halutussa suunnassa.

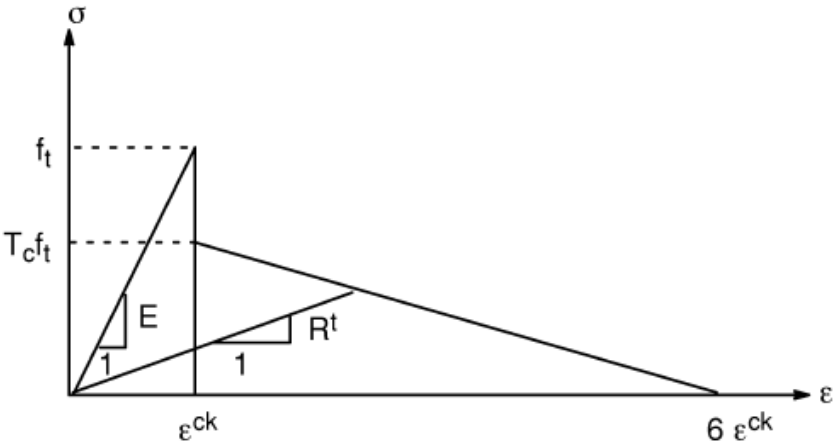

Kuva 1. Betonin jännitys-venymäkäyttäytyminen halkeilutilanteessa. [2]

Murtumishetkeä lukuun ottamatta taivutetun betonirakenteen käyttäytymiseen vaikuttaa enemmän sen veto- kuin puristusjännityksen alainen käyttäytyminen. Kun kyseessä on yksinkertainen palkkirakenteen taivutus, voidaan ajatella vetojännitystä syntyvän vain yhteen suuntaan rakenteen alapinnassa. Vetojännityksen rasittaman betonin käyttäytyminen on esitetty kuvassa 1.

Kuvasta 1 nähdään, että materiaalin käyttäytyminen on lineaarista, kunnes se saavuttaa käyttäjän asettaman vetolujuuden f_t. Tämän jälkeen jännitys laskee venymien kasvamatta käyttäjän asettaman kertoimen T_c mukaisesti. Kertoimelle T_c vaihteluväli on luonnollisesti [0,1]. Tämän jälkeen jännitys laskee lineaarisesti nollaan, niin että jännitystä ei enää ole, kun materiaali on saavuttanut kuusinkertaisen murtovenymän. Tämä skalaarikerroin ei ole säädettävissä, mutta murtovenymää voidaan säätää Hooken lain mukaisesti vetolujuuden ja kimmokertoimen avulla.

Materiaalin murtumisenergia voidaan määrittää kuvan 1 halkeamisen jälkeen kuvaajan alle jäävän pinta-alan ja karakteristisen elementtikoon tulona [5]. Koska tässä venymää syntyy vain yhteen suuntaan, voidaan karakteristinen mitta korvata elementin sen suunnan sivumittana, jossa venymää syntyy. Kun yhtälö saatetaan muotoon, jossa esiintyvät vain käyttäjän syöttämät parametrit lausumalla myös murtovenymä Hooken lain mukaan, saadaan murtumisenergiaksi

$$G_f = \frac{5T_c f_t^2 l}{2E}, \tag{1}$$

jossa T_c on käyttäjän asettama kerroin, f_t materiaalin vetolujuus, l elementin mitta vetojännityksen suunnassa ja E lineaarisen alueen kimmokerroin. Järkevä murtumisenergian arvo normaaleille betoneille on noin 40 - 140 N/m. Oleellisinta kuitenkin on, että eri FEM – malleja vertailtaessa murtumisenergian arvo tulisi olla sama. On syytä säätää enimmäkseen elementtikokoa ja kerrointa T_c, koska kimmokertoimen ja vetolujuuden väärää suuruusluokkaa olevat arvot johtavat epätodellisiin taipumiin ja toisaalta vääränaikaiseen halkeiluun.

Staattinen taivutuskoe

Ansys-laskennan lähtötietona toimi VTT:n suorittama käytännön koe [3], josta mitattiin nelipistetaivutetun betonilaatan siirtymiä sekä materiaalien muodonmuutoksia. Kuormituksen periaate on esitetty kuvassa 2.

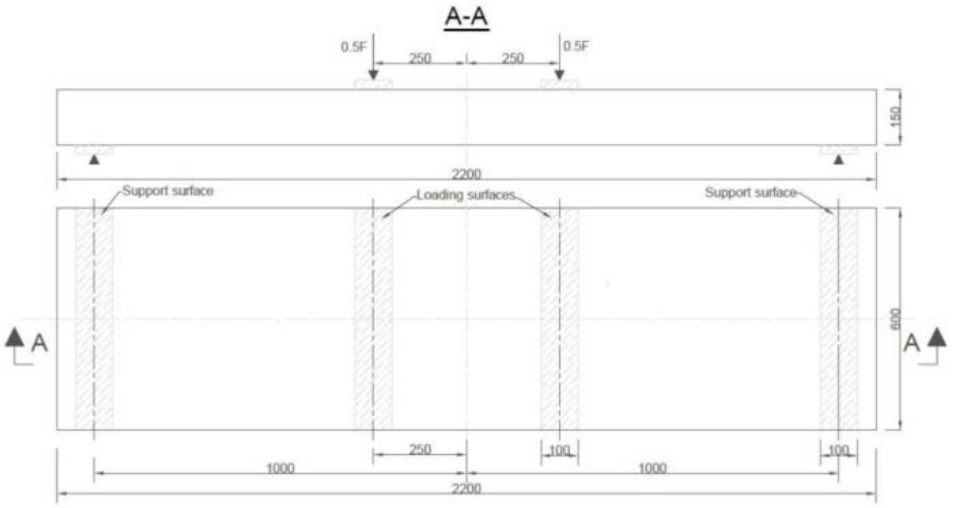

Kuva 2. Laatan mitat ja kuormitusjärjestelyt. [3]

Kuormitus tapahtui kahden kuormitussylinterin avulla. Kokonaisvoima *F* jakaantui näin tasan kahdelle kuvan 2 mukaiselle kuormituslinjalle. Laatta oli päistään vapaasti tuettu, ja sen jänneväli oli 2 m. Koe suoritettiin kaksi kertaa. Saadut voiman ja siirtymän väliset yhteydet on esitetty kuvassa 3. [3]

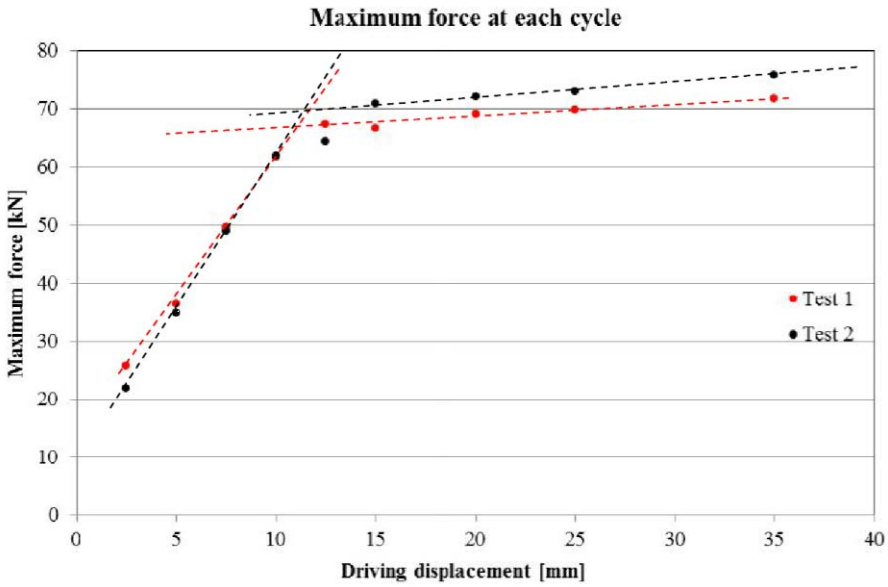

Kuva 3. VTT:n kokeen voiman ja siirtymän väliset yhteydet kahdelle suoritetulle taivutuskokeelle. [3]

Kuvasta 3 erottuu hyvin terästen myötörajan ylittyminen, joka tapahtui kokonaisvoiman F ollessa noin 66 kN. Tällöin laatan kuormituspisteen siirtymä oli noin 12 mm.

VTT:n kokeen perusteella tehtiin Ansys-laskentamalli, jonka geometria oli kokeen mukainen. Raudoituksiksi mallinnettiin taivutuksen kannalta oleelliset pääraudoitukset laatan ylä- ja alapintaan. Mallissa käytettiin 8-solmuisia Solid65-elementtejä kuvaamaan betonia. Raudoitus kuvattiin jatkuvana, jolloin elementin jäykkyysominaisuuksia muutettiin vain pääraudoituksen suunnassa raudoitetuksi halutussa elementtikerroksessa.

Laskennassa lähdettiin liikkeelle asettamalla tietty vaatimus murtumisenergialle. Murtumisenergia laskettiin kaavalla (1). Rajoituksena toimi VTT:n kokeen yhteydessä betonimateriaalista mitatut arvot vetolujuudelle f_t = 2.71 MPa ja kimmokertoimelle E = 23 000 MPa. Murtumisenergia uhkasi jäädä liian pieneksi, minkä vuoksi kertoimen T_c arvona käytettiin maksimia 1.0. Elementin mitta jänteen suunnassa oli 50 mm. Betoni yksiaksiaalinen puristuslujuus oli 41.5 MPa ja biaksiaalinen 48.1 MPa.

Kokeen raudoitus oli 5 T10 molemmissa pinnoissa. Raudoituksen keskiöetäisyys laatan pinnasta oli 25 mm. Raudoitusteräkset kuvattiin bilineaarisella jännitys-venymäyhteydellä, jonka todettiin vastaavan VTT:n kokeesta mitattua todellista yhteyttä erittäin hyvin aina venymäarvoon 3 % saakka. Myötörajaksi asetettiin 580 MPa. Murtorajaa ei asetettu, mutta laskennoissa todettiin, että rakenne murtui lopulta muilla tavoin kuin terästen katkeamisen takia. Elementtiverkko, kuormitus ja reunaehdot on esitetty kuvassa 4.

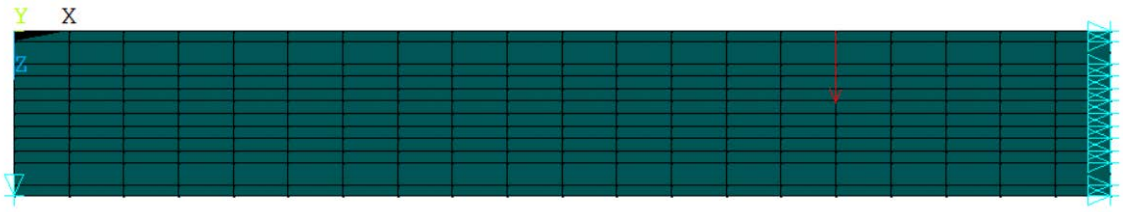

Kuva 4. Elementtiverkko, kuormitus ja reunaehdot. Uloimmat elementtikerrokset ovat raudoittamattomia. Toisiksi uloimmat ovat raudoitettuja, ja niiden etäisyys laatan pinnasta on sama kuin alkuperäisten terästen keskiöetäisyys. Elementtejä paksuuden yli oli yhteensä 12.

Laskentatulokset

Edellä esitellyn taivutuskokeen mukaista Ansys-ohjelmaan mallinnettua laattaa kuormitettiin solmuille asetetuilla pistevoimilla. Kun symmetria ja solmujen lukumäärä otettiin huomioon, vastasi kokonaiskuormitus kuvan 3 kuvaajan mukaista kokonaisvoiman arvoa. Ansyksella laskettu voiman ja siirtymän välinen yhteys sekä todellisesta kokeesta mitatut yksittäiset pisteet on esitetty kuvassa 5.

Kuvasta 5 erottuu selkeästi ensimmäisen halkeaman syntyminen rakenteeseen kuormituksen ollessa hieman yli 20 kN. Tämä saa aikaan äkillisen siirtymän kasvun halkeilun takia voimakkaasti redusoituvan taivutusvastuksen myötä. Terästen myötöraja ylittyi kuormituksen ollessa noin 72 kN, ja kuvaajan tasaantuessa 80 kN kohdalla koko

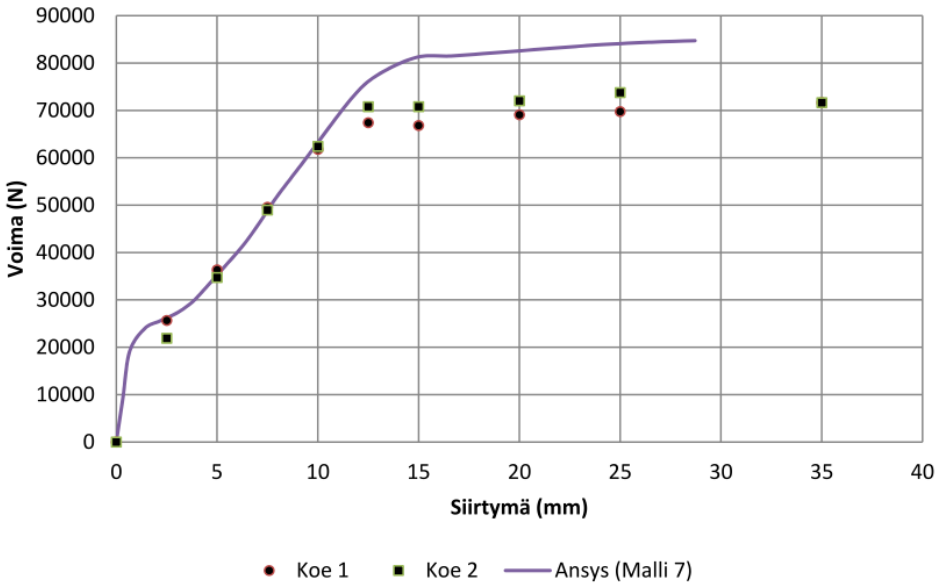

Kuva 5. Ansyksella laskettu voima-siirtymäkuvaaja, sekä todellisesta kokeesta mitatut yksittäiset arvot kummallekin laatalle.

teoreettisen maksimimomentin alueen teräkset olivat myötäneet. Myötörajan ylittyminen tapahtui Ansyksella hieman myöhemmin kuin todellisissa kokeissa, mutta kuvaajan kulmakertoimet sekä ennen että jälkeen tämän olivat samaa luokkaa.

Kuormitustapa luo vakio taivutusmomentin kuormituspisteiden väliselle alueelle. Terästen venymää mitattiin viidestä pisteestä, joista ensimmäinen (MP1) sijaitsi jännevälin puolivälissä. Seuraava piste (MP2) sijaitsi 100 mm etäisyydellä tästä, ja seuraava (MP3) taas samalla etäisyydellä edellisestä. Kuormituslinjan etäisyys jänteen puolivälistä oli 250 mm, mikä tarkoittaa, että nämä kolme mittauspistettä sijaitsivat kuormituslinjojen välisellä alueella. Kaksi mittauspistettä (MP4 ja MP5) sijaitsivat kuormituslinjalta tuelle päin. Terästen venymät edellä luetelluissa mittauspisteissä eri laatan kuormituspisteiden siirtymien arvoilla on esitetty kuvassa 6.

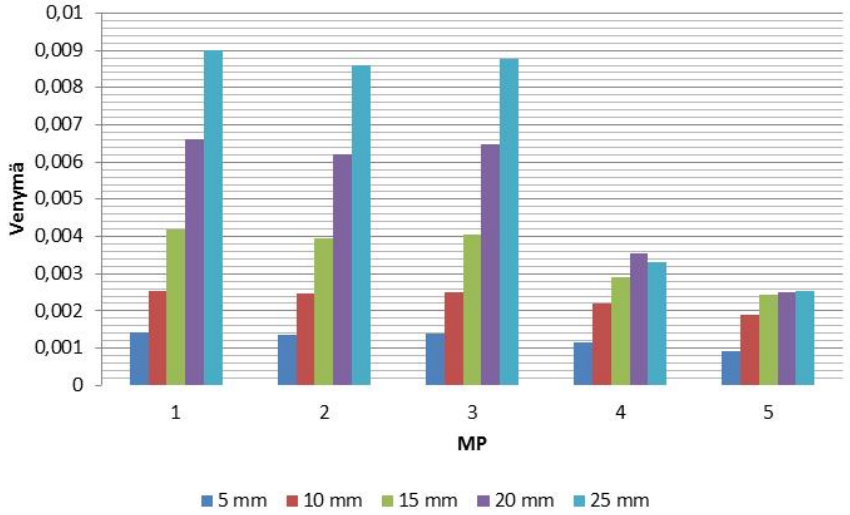

Kuva 6. Teräsvenymät eri mittauspisteissä eri siirtymien arvoilla.

Mallista ja laatoista mitattiin myös yläpinnan betonin puristumaa jännevälin keskellä. Sen arvo kuormituksen funktiona on esitetty kuvassa 7.

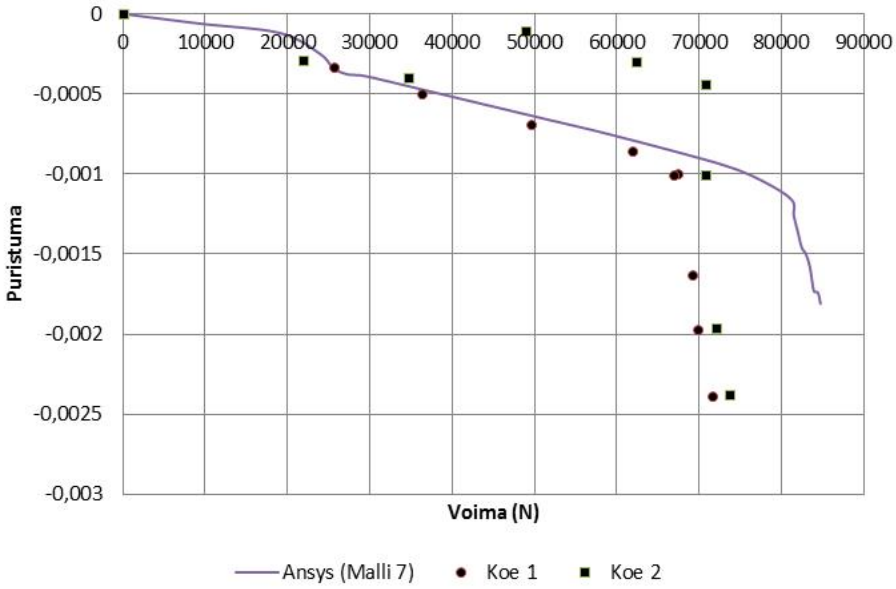

Kuva 7. Ansyksella lasketut betonin yläpinnan muodonmuutokset jännevälin keskellä, sekä todellisesta kokeesta mitatut yksittäiset arvot kummallekin laatalle.

Johtopäätökset

Tuloksia vertailemalla havaitaan, että Ansys laskee sekä siirtymiä että muodonmuutoksia varsin realisesti. Lisäksi se pystyy laskemaan rakenteessa tapahtuvien ilmiöiden, kuten betonin vetohalkeilun ja terästen myötäämisen, vaikutukset oikein. Erot tuloksissa verrattuna todelliseen käyttäytymiseen voivat johtua monesta asiasta. Betoni on todellisuudessa epähomogeeninen materiaali, jossa esiintyy monia mikrotason ilmiöitä. Laskentaohjelman materiaali on kuitenkin homogeenista. Tällöin se ei pysty esimerkiksi mallintamaan yksittäistä halkeamaa, vaan kuvaa kokonaisen elementin vaurioituneena. Tihentämällä elementtiverkkoa ottaen kuitenkin huomioon murtumisenergia, voidaan kuitenkin saada jonkinlainen käsitys myös tarkemmasta halkeilun syntymisestä.

Viitteet

[1] Ansys 14.0 Theory Reference. 4.10. Concrete.
[2] Ansys 14.0 Theory Reference 14.65. Solid65.
[3] Calonius, K., Saarenheimo, A., Tuomala, M. 2013. Research Report VTT-R-01653-13.
[4] Pietilä, J. Raudoitetun betonilaatan taivutuksen mallintaminen Ansys-ohjelmalla. Diplomityö. Tampereen teknillinen yliopisto, Rakennustekniikan laitos 2014.
[5] The International Federation for Structural Concrete. 2010. Model Code 2010.
[6] Willam, K.J., Warnke, E.P. 1974. Constitutive model for the triaxial behavior of concrete.

Proceedings of the XII Finnish Mechanics Days
R. Kouhia, J. Mäkinen, S. Pajunen and T. Saksala (Eds.)

Modelling of the web–air interaction in paper making using the unified continuum model

Tytti Saksa[1], and Johan Hoffman[2]

[(1)]Department of Mathematical Information Technology, University of Jyväskylä, P. O. Box 35, FIN-40014 University of Jyväskylä, FINLAND, tytti.saksa@jyu.fi
[(2)]School of Computer Science and Communication, Royal Institute of Technology – KTH, 10044 Stockholm, SWEDEN, jhoffman@kth.se

Summary. This presentation is concerned with dynamic behaviour of out-of-plane deformations of an axially moving web interacting with surrounding air using the unified continuum (UC) model. In this model case of fluid–structure interaction, structure is flowing instead of fluid. For a case with this type of set-up, we here apply the UC model for the first time. When studying a structure with relatively low bending stiffness, the flowing structure was found to undergo vibrations, as expected.

Key words: Modelling, Fluid-Structure Interaction, Unicorn, FEniCS

Introduction

Concerning axially moving materials, such as paper in paper making processes, the common approach is to describe the moving structure behaviour by elastic beam [7] or plate [4] models. Analysis of eigenfrequencies with respect to the structure velocity in such systems can be applied to characterizing mechanical behaviour and predicting possible losses of stability. Comparison of computational results and experimental frequencies have also been reported e.g. by Pramila [6].

In this work, the unified continuum (UC) model introduced by Hoffman et al. [3] is applied to the studied fluid-structure interaction problem. The UC model consists of conservation laws of mass and momentum, equation of phase convection and constitutive laws of stress. Here, the solid phase is described by imcompressible Neo-Hookean model and the fluid phase by Newtonian model. To avoid diffusion of the phase interface, we set the mesh velocity equal to the structure velocity in the y and z directions, assuming the structure flowing direction is aligned with the x axis. That is, the mesh points track the phase interface (Figure 1). Updating the mesh velocity in the x direction is neglected. (Compare with the general UC framework [1].)

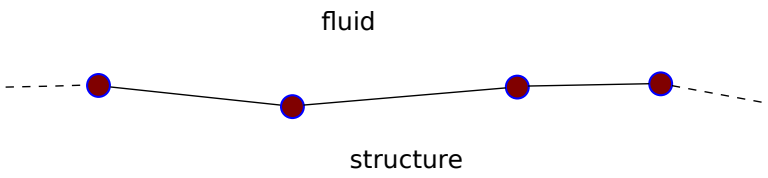

Figure 1. The mesh points track the fluid–structure interface.

Numerical considerations

In the discretization, we used unstructured tedrahedra grid. The simulations were conducted using open source tools Unicorn [1, 2], and a high performance branch of the finite element problem solving environment DOLFIN [5], both parts of the FEniCS project.

As for the boundary conditions, we set as momentum boundary conditions the in-flow and out-flow velocities for the solid phase, and pressure and density for fluid as a pinpoint at bottom corner of the outer box. For the fluid at the inner surfaces of the box, we set no slip conditions. The geometry and set-up of the problem is described in Figure 2.

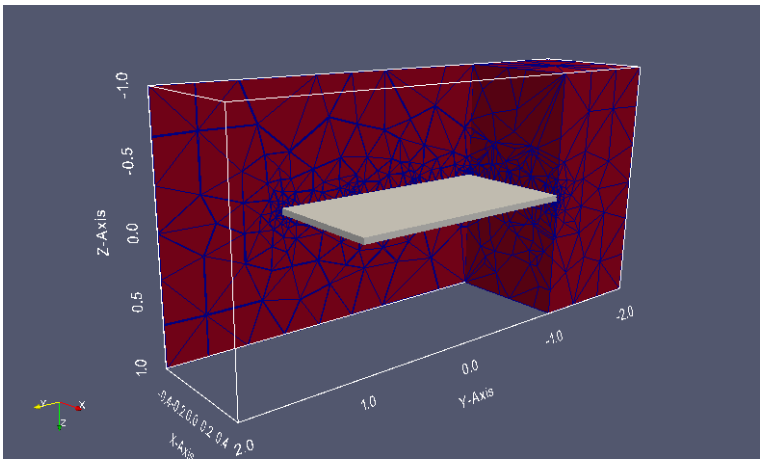

Figure 2. Model geometry for a moving structure embedded in fluid. The structure (continuum) enters the box running through the back surface ($x = -0.5$) and exits the box running through the front surface ($x = 0.5$).

In numerical simulations of accelerating the structure velocity from zero to some constant velocity (30 m/s), the structure was detected to undergo vibrations. The fluid velocity was initially zero and the velocity field for the fluid phase was generated solely from the interaction with the solid phase. The frequency of the detected vibrations was the greater the greater tension was generated by a velocity difference between the in-flow and out-flow edges.

Conclusions

Advantages of the UC approach in modelling are that we have a full three dimensional model, and thus may target a more realistic simulation. Since the mesh moves for tracking the fluid-structure interface as part of the discretization, this allows for simple and general formulation and efficient computation. Since the size of the mesh is limited by computational costs, it is a challenge to model a thin structure and keeping good quality of mesh. In this study, we have exaggerated the thickness of flowing structure.

References

[1] J. Hoffman, J. Jansson, C. Degirmenci, N. Jansson, and M. Nazarov. Unicorn: a unified continuum mechanics solver. In *Automated Solution of Differential Equations by the Finite Element Method*, volume 84 of *Lecture Notes in Computational Science and Engineering*, chapter 18. Springer, 2012.

[2] Johan Hoffman, Johan Jansson, Rodrigo Vilela de Abreu, Niyazi Cem Degirmenci, Niclas Jansson, Kaspar Müller, Murtazo Nazarov, and Jeannette Hiromi Spühler. Unicorn: Parallel

adaptive finite element simulation of turbulent flow and fluid–structure interaction for deforming domains and complex geometry. *Computers & Fluids*, 80(0):310–319, 2013. Selected contributions of the 23rd International Conference on Parallel Fluid Dynamics ParCFD2011.

[3] Johan Hoffman, Johan Jansson, and Michael Stöckli. Unified continuum modelling of fluid-structure interaction. *Mathematical models and methods in applied sciences*, 21(3):491–513, 2011.

[4] C. C. Lin. Stability and vibration characteristics of axially moving plates. *International Journal of Solids and Structures*, 34(24):3179–3190, 1997.

[5] A. Logg, G. N. Wells, and J. Hake. Dolfin: a c++/python finite element library. In *Automated Solution of Differential Equations by the Finite Element Method*, volume 84 of *Lecture Notes in Computational Science and Engineering*, chapter 10. Springer, 2012.

[6] A. Pramila. Sheet flutter and the interaction between sheet and air. *TAPPI Journal*, 69(7):70–74, 1986.

[7] J. A. Wickert and C. D. Mote. Classical vibration analysis of axially moving continua. *ASME Journal of Applied Mechanics*, 57:738–744, 1990.

Proceedings of the XII Finnish Mechanics Days
R. Kouhia, J. Mäkinen, S. Pajunen and T. Saksala (Eds.)

On kinematically inadmissible virtual displacements

Juha Paavola and Eero-Matti Salonen

School of Engineering, P.O. Box 12100, FIN-00076 Aalto, Finland
juha.paavola@aalto.fi, eero-matti.salonen@aalto.fi

Summary. The differences following from applying kinematically admissible and inadmissible virtual displacements are demonstrated in connection with a simple stretched rod example case. The reasons for using normally kinematically admissible virtual displacements become obvious. The use of post-processing to obtain reaction or constraint forces on displacement boundaries is commented on.

Keywords: mechanics education, kinematically inadmissible virtual displacements, kinematical constraints, constraint forces, SMP12

Introduction

We refer to the authoritative continuum mechanics textbook by Malvern [1, p. 237]:

> **"**A ***kinematically admissible*** displacement distribution is one satisfying any prescribed displacement boundary conditions and possessing continuous first partial derivatives in the interior of the body. Since virtual displacements to be considered are ***additional*** displacements from the equilibrium configuration, a virtual displacement component must be zero wherever the actual displacement is prescribed by the boundary conditions."

We refer additionally to the much cited mechanics textbook by Synge and Griffith [2, p. 56]:

> "We note then that virtual displacements are of two types:
> (a) virtual displacements satisfying the constraints,
> (b) virtual displacements violating the constraints."

Scanning further the literature, it seems that the mere term *virtual displacement* means usually especially in continuum mechanics the kind of displacement referred to in [1] and as (a) in [2]. In this article, we will call this kind of virtual displacement in more detail as *kinematically admissible virtual displacement*. The kind of virtual

displacement considered as (b) in [2] we will call here as *kinematically inadmissible virtual displacement.*

To be more specific, a kinematically admissible virtual displacement can be considered as the difference between two kinematically admissible displacement distributions. As the kinematically admissible displacement distributions must satisfy the displacement boundary conditions, it is seen immediately that the kinematically admissble virtual displacement must satisfy these boundary conditions with zero prescribed values. Further, the kinematically inadmissible virtual displacements will be considered as continuous as the kinematically admissible virtual displacements. The only difference is thus in continuum mechanics that the displacement boundary conditions with zero values can be violated. However, in engineering mechanics applications in general, especially in multibody dynamics, kinematical constraints other than boundary conditions appear. For instance, the motions of the subbodies in a mechanism may be constrained by pins etc. These constraints can be satisfied or not and the division between kinematically admissible and inadmissible virtual displacements must be enlarged in an obvious way.

As mentioned above, the use of kinematically admissible virtual displacements in continuuum mechanics problems is taken usually as granted. However, nothing prevents us from using alternatively kinematically inadmissible virtual displacements. This theme is considered below in connection with an extremely simple demonstration example.

A demonstration example

The problem

Let us consider a stretched uniform straight elastic rod along the x-axis in the interval $(0,l)$ under constant distributed loading per length q and by a point load P at the right-hand end. The axial displacement along the rod is denoted $u = u(x)$ and the normal force $T = T(x)$. Due to the assumed elasticity, $T = EA\mathrm{d}u/\mathrm{d}x$, where EA is the axial stiffness of the rod. The left-hand end of the rod is a displacement boundary part and the displacement boundary condition is $u(0) = \overline{u}$, where $\overline{u}$ is given. The right-hand end of the rod is a traction boundary part and the traction (force) boundary condition is $T(l) = P$.

The problem is statically determinate and the exact analytical solution is easy to find. The displacement expression is $u(x) = [q(lx - x^2/2) + Px]/EA$ and the normal force expression is $T(x) = q(l - x) + P$. The value of the reaction force (constraint force) R at the rod left-hand end (positive when acting on the rod towards right) is $R = -ql - P$.

We will solve below the present problem by the principle of virtual work to demonstrate differences between the use of kinematically admissible and inadmissible virtual displacements.

Use of kinematically admissible virtual displacements

The standard virtual work equation for the rod is

$$-\int_0^l EA\frac{\mathrm{d}u}{\mathrm{d}x}\frac{\mathrm{d}\delta u}{\mathrm{d}x}\mathrm{d}x+\int_0^l q\,\delta u\,\mathrm{d}x+P\,\delta u\,(l)=0, \tag{1}$$

where δu is a kinematically admissible virtual displacement.

We will apply the displacement finite element method to solve approximately the problem. A crude uniform two-node element mesh with the nodes 1, 2, 3 is taken. The displacement approximation is thus

$$\tilde{u}(x)=N_1(x)u_1+N_2(x)u_2+N_3(x)u_3, \tag{2}$$

where u_1, u_2, u_3 are the nodal displacements and N_1, N_2, N_3 the (global) shape functions (Figure 1).

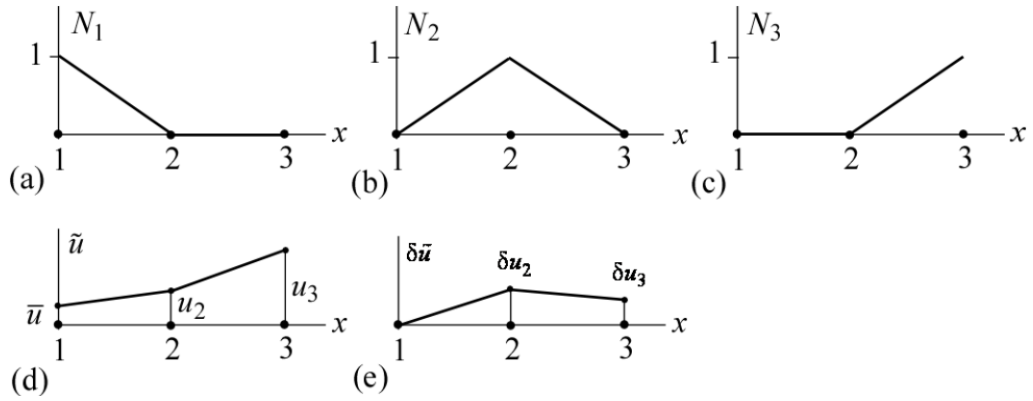

Figure 1. (a) Shape function N_1. (b) Shape function N_2. (c) Shape function N_3. (d) Schematic kinematically admissible finite element displacement approximation. (e) Kinematically admissible virtual displacements.

Proceeding in the standard way, we introduce $u_1=\bar{u}$ from the displacement boundary condition so that (2) becomes a kinematically admissible displacement distribution (Figure 1 (d)):

$$\tilde{u}(x)=N_1(x)\bar{u}+N_2(x)u_2+N_3(x)u_3. \tag{3}$$

Variation of this (or considering the difference between two representations (3) with nodal values $\bar{u}$, u_2, u_3 and $\bar{u}$, $u_2+\delta u_2$, $u_3+\delta u_3$) gives the kinematically admissible virtual displacement (Figure 1 (e))

$$\delta\tilde{u}(x)=N_2(x)\delta u_2+N_3(x)\delta u_3. \tag{4}$$

The discrete analogue of (1) is

$$-\int_0^l EA\frac{\mathrm{d}\tilde{u}}{\mathrm{d}x}\frac{\mathrm{d}\delta\tilde{u}}{\mathrm{d}x}\mathrm{d}x+\int_0^l q\,\delta\tilde{u}\,\mathrm{d}x+P\,\delta\tilde{u}\,(l)=0, \tag{5}$$

where $\tilde{u}$ and $\delta\tilde{u}$ are according to (3) and (4). As δu_2 and δu_3 are arbitrary, two discrete system equations are obtained:

$$-\int_0^l EA\left(\frac{\mathrm{d}N_1}{\mathrm{d}x}\overline{u}+\frac{\mathrm{d}N_2}{\mathrm{d}x}u_2+\frac{\mathrm{d}N_3}{\mathrm{d}x}u_3\right)\frac{\mathrm{d}N_2}{\mathrm{d}x}\mathrm{d}x+\int_0^l q\,N_2\mathrm{d}x+PN_2(l)=0\,, \tag{6}$$

$$-\int_0^l EA\left(\frac{\mathrm{d}N_1}{\mathrm{d}x}\overline{u}+\frac{\mathrm{d}N_2}{\mathrm{d}x}u_2+\frac{\mathrm{d}N_3}{\mathrm{d}x}u_3\right)\frac{\mathrm{d}N_3}{\mathrm{d}x}\mathrm{d}x+\int_0^l q\,N_3\mathrm{d}x+PN_3(l)=0\,. \tag{7}$$

Performing the details, the equations become in matrix notation as

$$\begin{bmatrix} 4\dfrac{EA}{l} & -2\dfrac{EA}{l} \\ -2\dfrac{EA}{l} & 2\dfrac{EA}{l} \end{bmatrix}\begin{Bmatrix} u_2 \\ u_3 \end{Bmatrix}=\begin{Bmatrix} \dfrac{1}{2}ql+2\dfrac{EA}{l}\overline{u} \\ \dfrac{1}{4}ql+P \end{Bmatrix}. \tag{8}$$

The solution is

$$u_2=\overline{u}+\frac{l}{EA}\left(\frac{3}{8}ql+\frac{1}{2}P\right),\quad u_3=\overline{u}+\frac{l}{EA}\left(\frac{1}{2}ql+P\right). \tag{9}$$

These nodal values coincide with the exact solution. However, between the nodes the solutions differ when q is non-zero. The approximate normal force evaluated applying (3) and formula $T=EA\mathrm{d}u/\mathrm{d}x$ is just elementwise constant and because of the crude mesh inaccurate.

Use of kinematically inadmissible virtual displacements

Using a kinematically inadmissible virtual displacement δu (meaning here that the condition $\delta u(0)=0$ is violated), the virtual work equation becomes

$$-\int_0^l EA\frac{\mathrm{d}u}{\mathrm{d}x}\frac{\mathrm{d}\delta u}{\mathrm{d}x}\mathrm{d}x+\int_0^l q\,\delta u\,\mathrm{d}x+P\,\delta u(l)+R\,\delta u(0)=0\,. \tag{10}$$

Compared to (1), the only difference is the last term on the left-hand side giving the virtual work of the unknown reaction force (constraint force) R, which is here an external force with respect to the rod.

In the finite element approximation we use the full kinematically inadmissible approximation (we do not substitute yet at this phase the relation $u_1=\overline{u}$)

$$\tilde{u}(x)=N_1(x)u_1+N_2(x)u_2+N_3(x)u_3\,. \tag{11}$$

Variation of this gives the kinematically inadmissible virtual displacement

$$\delta\tilde{u}(x)=N_1(x)\,\delta u_1+N_2(x)\,\delta u_2+N_3(x)\,\delta u_3\,. \tag{12}$$

These distributions are sketched in Figure 2.

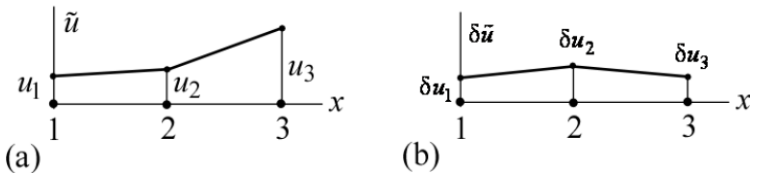

Figure 2. (a) Schematic kinematically inadmissible displacement. (b) Kinematically inadmissible virtual displacement.

When (11) and (12) are applied in (10), three system equations emerge:

$$-\int_0^l EA\left(\frac{\mathrm{d}N_1}{\mathrm{d}x}u_1+\frac{\mathrm{d}N_2}{\mathrm{d}x}u_2+\frac{\mathrm{d}N_3}{\mathrm{d}x}u_3\right)\frac{\mathrm{d}N_1}{\mathrm{d}x}\mathrm{d}x+\int_0^l q\,N_1\,\mathrm{d}x+PN_1(l)+RN_1(0)=0, \quad (13)$$

$$-\int_0^l EA\left(\frac{\mathrm{d}N_1}{\mathrm{d}x}u_1+\frac{\mathrm{d}N_2}{\mathrm{d}x}u_2+\frac{\mathrm{d}N_3}{\mathrm{d}x}u_3\right)\frac{\mathrm{d}N_2}{\mathrm{d}x}\mathrm{d}x+\int_0^l q\,N_2\,\mathrm{d}x+PN_2(l)+RN_2(0)=0, \quad (14)$$

$$-\int_0^l EA\left(\frac{\mathrm{d}N_1}{\mathrm{d}x}u_1+\frac{\mathrm{d}N_2}{\mathrm{d}x}u_2+\frac{\mathrm{d}N_3}{\mathrm{d}x}u_3\right)\frac{\mathrm{d}N_3}{\mathrm{d}x}\mathrm{d}x+\int_0^l q\,N_3\,\mathrm{d}x+PN_3(l)+RN_3(0)=0. \quad (15)$$

Now we have, however, four unknowns: u_1, u_2, u_3 and R. The missing system equation is clearly simply the kinematical constraint $u_1=\bar{u}$. Performing again the details, the system equations are found to be in matrix notations as

$$\begin{bmatrix} 2\frac{EA}{l} & -2\frac{EA}{l} & 0 & -1 \\ -2\frac{EA}{l} & 4\frac{EA}{l} & -2\frac{EA}{l} & 0 \\ 0 & -2\frac{EA}{l} & 2\frac{EA}{l} & 0 \\ 1 & 0 & 0 & 0 \end{bmatrix}\begin{Bmatrix} u_1 \\ u_2 \\ u_3 \\ R \end{Bmatrix}=\begin{Bmatrix} \frac{1}{4}ql \\ \frac{1}{2}ql \\ \frac{1}{4}ql+P \\ \bar{u} \end{Bmatrix}. \quad (16)$$

The solution is

$$u_1=\bar{u},\quad u_2=\bar{u}+\frac{l}{EA}\left(\frac{3}{8}ql+\frac{1}{2}P\right),\quad u_3=\bar{u}+\frac{l}{EA}\left(\frac{1}{2}ql+P\right),\quad R=-ql-P. \quad (17)$$

All these values coincide with the exact solution.

Concluding remarks

In the light of the demonstration example, it is quite obvious why kinematically admissible virtual displacements are in practice preferred in the finite element method applied to continuum mechanics problems. Fewer unknowns appear and the coefficient matrix in the system equations has some favourable properties: symmetry and positive definiteness (in elasticity). Using kinematically inadmissible virtual displacements, the system unknowns will be both displacement and force quantities; we have a so-called mixed formulation. In spite of this, for instance in multibody dynamics often in practice

it is found in overall more convenient to use a mixed formulation as the constraints can be awkward to satisfy in advance. Further, if say Coulomb friction is included, we have to have available the normal forces between the sliding parts of a mechanism to evaluate the contributions from friction forces, [3].

We find using the kinematically inadmissible virtual displacement formulation from the last formula (17) for the rod normal force at $x = 0$ the exact result $\tilde{T}(0) = -R = ql + P$. If $\tilde{T}(0)$ is evaluated consistently in the kinematically admissible virtual displacement formulation using expressions (3) and formula $T = EA\mathrm{d}u/\mathrm{d}x$, by the present crude mesh a quite inaccurate value

$$\tilde{T}(0) = EA\frac{\mathrm{d}\tilde{u}}{\mathrm{d}x}(0) = EA\frac{u_2 - u_1}{l/3} = \frac{9}{8}ql + \frac{3}{2}P \tag{18}$$

is obtained.

However, post-processing procedures can be employed in efforts to obtain more accurate boundary traction values on the displacement boundary. In our example case the appropriate post-processing virtual work equation would be the first equation (16) giving

$$R = 2\frac{EA}{l}u_1 - 2\frac{EA}{l}u_2 - \frac{1}{4}ql\,, \tag{19}$$

where u_1 and u_2 are known from the standard kinematically admissible formulation. Introducing $u_1 = \bar{u}$ and u_2 from (9) gives here the exact value $R = -ql - P$.

In two- and three-dimensional problems the post-processing procedures for obtaining tractions at the displacement boundaries are, however, not necessarily very practical especially if the boundaries have corners. This is obvious e.g. from [4] dealing with a similar simpler case on flux determination on temperature type boundaries in heat conduction type problems.

In multibody dynamics kinematical constraints are usually taken into account systematically by the Lagrange multiplier method. This theme will not be considered here.

References

[1] L. E. Malvern, *Introduction to the Mechanics of a Continuous Medium*, Prentice-Hall, 1969.

[2] Synge, J. L. and Griffith, B. A. (1959) *Principles of Mechanics*, 3rd edition, McGraw-Hill, New York.

[3] Salonen, E.-M. (2000). Lagrange's equations of motion and Coulomb friction, p.633-640. *VII Suomen Mekaniikkapäivät Tampereella 25-26.5.2000*, Tampere 2000.

[4] G.F. Carey, S. S. Chow and M. K. Seager. (1985) Approximate boundary-flux calculations, *Comput. Meths. Appl. Mech. Engrg*. 50 (1985) p.107-120.

Proceedings of the XII Finnish Mechanics Days
R. Kouhia, J. Mäkinen, S. Pajunen and T. Saksala (Eds.)

Generating lines of curvature coordinates for finite element modelling

Mika Malinen

CSC - IT Center for Science Ltd., P.O. Box 405, FI-02101 Espoo, Finland, mika.malinen@csc.fi

Summary. Surface parametrizations corresponding to lines of curvature coordinates provide many benefits from the viewpoint of both analysis and implementation. Nevertheless, formulations in lines of curvature coordinates are not utilized widely in practical finite element modelling, since ready representations of surfaces in this form are not usually available. Here we devise a practical method for the elementwise re-parametrization of standard surface representation in order to attain a lines of curvature parametrization which is optimally accurate with respect to the initial data supposed.

Key words: lines of curvature coordinate, surface, chart, finite element, shell

Introduction

Some applications naturally lead to handling partial differential equation (PDE) models which are defined on surfaces. Perhaps the most well-known example in the field of elasticity theory is the treatment of two-dimensional shell equations, which govern the deformation of a thin curved body using a system of curvilinear coordinates associated with the middle surface of the body. Other applications beyond the scope of traditional structural models are also described in the literature.

From the viewpoint of both computation and analysis, PDE models on smooth surfaces take usually the most appealing form when the surface is defined in terms of lines of curvature coordinates (for the basic concepts relating to lines of curvature, see [1]). In such cases each point on the surface can naturally be associated with an orthogonal system of basis vectors, providing a convenient starting point for representing vector-valued fields over the surface. Since the basis is orthogonal, the components of a vector field have then intuitive physical significance and additional tensor calculations which relate to finding the physical components of tensors are greatly simplified or even avoided [2]. Also the computations relating to the action of material models are typically simplified.

In spite of the benefits of using lines of curvature coordinates, common finite element formulations do not customarily employ such surface parametrizations, since a ready representation of the surface in this form is not usually available. Currently the most popular finite element methods utilize isoparametric formulations where the unknown field variables and geometric data are approximated by using equal-order interpolation. Still we see that many benefits could be attained if discretizations in lines of curvature coordinates were enabled by having practical methods to parameterize the model geometry in the desired way. Here we consider this parametrization problem and devise an elementwise re-parametrization method which is shown to be optimally accurate for fourth-order accurate initial data in L_2 which is supposed in the present treatment.

A simple approximation to lines of curvature representation

Let us now suppose that data is available for approximating a smooth surface $\mathcal{S} \subset \mathbf{E}^3$ via a collection of invertible transformations $\mathbf{f}_k : \hat{K} \to \mathbf{E}^3$ where $\hat{K} \subset \mathbb{R}^2$ is a simple reference domain (the reference element in the context of finite elements), such as the unit square, equipped with a system of rectangular Cartesian coordinates. In this paper, we also assume that each transformation gives $O(h^4)$ approximation of the surface location with respect to the diameter h of the coordinate patch in L_2. We note that ways to obtain these transformations are not unique but we omit the discussion of additional details in this respect.

Any part $\mathcal{S}_k = \mathbf{f}_k(\hat{K})$ of the approximate surface can now be equipped with the coordinates $\hat{x}^\alpha$ of the points of $\hat{K}$ as its curvilinear coordinates. This treatment importantly enables us to estimate the characteristics of the surface in terms of the fundamental forms. These necessary notions of differential geometry will be introduced next, while we refer to [1] for a thorough treatment of the subject.

By using the convention that Greek indices have the range {1,2} and denoting the partial differentiation with respect to the curvilinear coordinates by ∂_α, we define vector fields $\hat{\boldsymbol{a}} : \hat{K} \to \mathbb{R}^3$ by

$$\hat{\boldsymbol{a}}_\alpha = \partial_\alpha \mathbf{f}_k. \tag{1}$$

These give the covariant basis vectors of the tangent plane to the approximate surface at $\mathbf{p} = \mathbf{f}_k(\hat{\mathbf{x}})$ via their alternate descriptions defined by $\mathbf{p} \mapsto (\hat{\boldsymbol{a}}_\alpha \circ \mathbf{f}_k^{-1})(\mathbf{p})$. We also note that the contravariant basis vectors $\hat{\boldsymbol{a}}^\gamma$ of the tangent plane to the approximate surface are defined via the conditions $\hat{\boldsymbol{a}}^\alpha \cdot \hat{\boldsymbol{a}}_\beta = \delta^\alpha_\beta$, with δ^α_β the Kronecker's symbol.

The covariant components of the metric surface tensor $\hat{\boldsymbol{A}}$ (the first fundamental form) are now given by $\hat{A}_{\alpha\beta} = \hat{\boldsymbol{a}}_\alpha \cdot \hat{\boldsymbol{a}}_\beta$. The unit normal vector to the approximate surface is then obtained by

$$\hat{\boldsymbol{a}}_3 = \frac{\hat{\boldsymbol{a}}_1 \times \hat{\boldsymbol{a}}_2}{\sqrt{\hat{a}}}, \tag{2}$$

with $\hat{a}$ the determinant of the metric surface tensor. We also define $\hat{B}_{\alpha\beta} : \hat{K} \to \mathbb{R}$ by

$$\hat{B}_{\alpha\beta} = \hat{\boldsymbol{a}}_3 \cdot \partial_\alpha \hat{\boldsymbol{a}}_\beta = -\hat{\boldsymbol{a}}_\alpha \cdot \partial_\beta \hat{\boldsymbol{a}}_3 \tag{3}$$

which give the covariant components of the second fundamental form $\hat{\boldsymbol{B}}$ of the surface at $\mathbf{p} = \mathbf{f}_k(\hat{\mathbf{x}})$. Usually the definition of a PDE model also depends on the Christoffel symbols which are defined as

$$\hat{\Gamma}^\gamma_{\alpha\beta} = \partial_\beta \hat{\boldsymbol{a}}_\alpha \cdot \hat{\boldsymbol{a}}^\gamma. \tag{4}$$

The appeal of alternate surface parametrizations corresponding to lines of curvature coordinates relates to the fact that then each point on the surface can naturally be associated with an orthogonal system of surface basis vectors $\boldsymbol{a}_\alpha$. In addition to orthogonality, the defining condition for such parametrization is basically that the second fundamental form then takes a diagonal form. While it is not possible in general to find a single lines of curvature parametrization for the entire surface $\mathcal{S}$, a point on the surface generally has a neighbourhood where lines of curvature parametrization can be given (although for umbilical and planar points the choice is not unique). Here obvious candidates for such points and neighbourhoods are the mid-points $\mathbf{f}_k(\mathbf{0})$ and the parts $\mathcal{S}_k = \mathbf{f}_k(\hat{K})$.

Given a part $\mathcal{S}_k = \mathbf{f}_k(\hat{K})$, the orientation of lines of curvature coordinate curves at a point $\mathbf{p} \in \mathcal{S}_k$ can be determined by solving a simple eigenvalue problem as follows. If we describe the metric surface tensor $\hat{\boldsymbol{A}}$ and the second fundamental form $\hat{\boldsymbol{B}}$ as matrices with components $\hat{A}_{\alpha\beta}$ and $\hat{B}_{\alpha\beta}$, respectively, the product $\hat{\boldsymbol{B}}\hat{\boldsymbol{A}}^{-1}$ gives the mixed components $\hat{B}^\beta_\alpha$ of the second fundamental form. Then the principal directions $\hat{\boldsymbol{\xi}} = \hat{\xi}_\alpha \hat{\boldsymbol{a}}^\alpha$ which solve the eigenvalue problem

$$\hat{\boldsymbol{B}}\hat{\boldsymbol{A}}^{-1}\hat{\boldsymbol{\xi}} = \Lambda \hat{\boldsymbol{\xi}} \tag{5}$$

give the orientation of lines of curvature coordinate curves at $\mathbf{p} = \mathbf{f}_k(\hat{\mathbf{x}})$.

To proceed we assume that the eigenvalues Λ_α are ordered such that $|\Lambda_1| \leq |\Lambda_2|$ and define $\overline{\boldsymbol{e}}_\alpha$ to be the normalized eigenvectors $\overline{\boldsymbol{e}}_\alpha = \hat{\boldsymbol{\xi}}_\alpha / |\hat{\boldsymbol{\xi}}_\alpha|$. If the vectors $\overline{\boldsymbol{e}}_\alpha : \hat{K} \to \mathbb{R}^3$ are used to define an alternate set of covariant surface base vectors at $\mathbf{p} = \mathbf{f}_k(\hat{\mathbf{x}})$, the matrix describing the mixed components of the second fundamental form is diagonalized under the basis change. That is, if we define the matrix $\boldsymbol{Q} = (Q_{\alpha\beta}) = (q^\alpha_\beta)$ with the components $q^\alpha_\beta : \hat{K} \to \mathbb{R}$ giving the coefficients for the change of basis such that (the summation convention is used here)

$$\overline{\boldsymbol{e}}_\alpha = q^\beta_\alpha \hat{\boldsymbol{a}}_\beta, \tag{6}$$

the mixed components of the second fundamental form with respect to the basis $\overline{\boldsymbol{e}}_\alpha$ are given by

$$\overline{\boldsymbol{B}} = \boldsymbol{Q}^T \hat{\boldsymbol{B}} \boldsymbol{Q} = \mathbf{diag}(\Lambda_1, \Lambda_2). \tag{7}$$

It is noted that the eigenvalues also have geometric interpretation as principal curvatures, so that their reciprocals give the principal radii of curvature $R_\alpha = 1/\Lambda_\alpha$.

An alternate representation for the part $\mathcal{S}_k$ can now be given. To this end, we define a local coordinate system x^i by taking its origin to be at $\mathbf{f}_k(\mathbf{0})$ and by letting the orthonormal vectors $\boldsymbol{i}_\alpha = \overline{\boldsymbol{e}}_\alpha(\mathbf{0})$ and $\boldsymbol{i}_3 = \boldsymbol{i}_1 \times \boldsymbol{i}_2$ to be its covariant base vectors. The part of the approximate surface may then be described by a chart $\boldsymbol{\varphi}_k : \hat{K} \to \mathbf{E}^3$ defined as

$$\boldsymbol{\varphi}_k(\hat{\mathbf{x}}) = \mathsf{x}^1(\hat{\mathbf{x}})\boldsymbol{i}_1 + \mathsf{x}^2(\hat{\mathbf{x}})\boldsymbol{i}_2 + \hat{z}(\hat{\mathbf{x}})\boldsymbol{i}_3, \tag{8}$$

where the coordinate functions $\mathsf{x}^\alpha : \hat{K} \to \mathbb{R}$ and $\hat{z} : \hat{K} \to \mathbb{R}$ are given by

$$\begin{aligned} \mathsf{x}^\alpha(\hat{\mathbf{x}}) &= [\mathbf{f}_k(\hat{\mathbf{x}}) - \mathbf{f}_k(\mathbf{0})] \cdot \boldsymbol{i}_\alpha, \\ \hat{z}(\hat{\mathbf{x}}) &= [\mathbf{f}_k(\hat{\mathbf{x}}) - \mathbf{f}_k(\mathbf{0})] \cdot \boldsymbol{i}_3. \end{aligned} \tag{9}$$

However, assuming that $\partial_1\mathsf{x}^1\partial_2\mathsf{x}^2 - \partial_2\mathsf{x}^1\partial_1\mathsf{x}^2 \neq 0$, we may alternatively use x^α as curvilinear coordinates by employing the inverse relations $\hat{\mathbf{x}} = \mathbf{x}^{-1}(x^1, x^2)$, with $\mathbf{x}^{-1}(\cdot)$ known to be as smooth as $\mathbf{x}(\cdot)$. Thus, we may as well use a chart $\boldsymbol{\varphi}_S : S \to \mathbf{E}^3$ defined by

$$\mathbf{x} = (x^1, x^2) \mapsto \boldsymbol{\varphi}_S(\mathbf{x}) = x^1\boldsymbol{i}_1 + x^2\boldsymbol{i}_2 + z(x^1, x^2)\boldsymbol{i}_3, \tag{10}$$

where $z(x^1, x^2) = (\hat{z} \circ \mathbf{x}^{-1})(x^1, x^2)$ and $S \subset \mathbb{R}^2$ is the projection of $\mathcal{S}_k$ on the (x^1, x^2)-plane. It should be noted that S may have curved boundaries.

The chart defined by (10) can be shown to give a first-order accurate approximation to a lines of curvature coordinates parametrization to describe the part $\mathcal{S}_k$. To show this, one may consider replacing the function $(x^1, x^2) \mapsto z(x^1, x^2)$ temporarily by its Taylor polynomial approximation to see how well the defining conditions for lines of curvature coordinates are respected in the neighbourhood of the local origin $\mathbf{f}_k(\mathbf{0})$. We note that, by using the fact that the (x^1, x^2)-plane is tangent to the surface $\mathcal{S}_k$ at the origin and $(\partial_{12}z)(\mathbf{0}) = B_{12}(\mathbf{0}) = 0$, the Taylor polynomial approximation up to the third-order terms must take the form

$$\begin{aligned} z(x^1, x^2) =& 1/2A(x^1)^2 + 1/2B(x^2)^2 + 1/6D(x^1)^3 + \\ & 1/2E(x^1)^2x^2 + 1/2Fx^1(x^2)^2 + 1/6G(x^2)^3 + O(h_S^4), \end{aligned} \tag{11}$$

with h_S the diameter of S and $A = (\partial_{11}z)(\mathbf{0})$, $B = (\partial_{22}z)(\mathbf{0})$, etc. It should be noted that although the approximation (8) and the version based on (10) and (11) are basically expected to be as accurate, the latter is less useful as then the chartwise defined surface cannot be enforced to be continuous. We therefore emphasize that our intention is not to employ the Taylor polynomial approximation in the actual representation of the surface. Rather this approximation is considered just to reveal important characteristics of the representation (10).

We conclude that the simple representation of part $\mathcal{S}_k$ using the chart (10) does not correspond to an optimal selection of approximation to a lines of curvature coordinate parametrization. We note in particular that the matrix representation of the mixed components of the second fundamental form has then the expansion

$$\boldsymbol{B} = \left[\begin{array}{ll} A + Dx^1 + Ex^2 & Ex^1 + Fx^2 \\ Ex^1 + Fx^2 & B + Fx^1 + Gx^2 \end{array} \right] + O(h_S^2) \tag{12}$$

which can be considered to be diagonal around the origin only when $O(h_S)$ truncation errors are admitted. In the case of fourth-order accurate initial data in L_2, an optimal method should instead lead to $O(h_S^2)$ truncation errors. We devise an optimally accurate alternate in the next section.

A refined approximation to lines of curvature parametrization

A further examination of the chart (10) reveals a way to obtain a refined surface parametrization which respects all attributes required by lines of curvature coordinates up to neglected terms of second order. We shall describe this improved version in the following.

Let us now suppose that the domain S as defined in connection with (10) is obtained as the image $S = \boldsymbol{\phi}(K)$ where $K \subset \mathbb{R}^2$ and the mapping $\mathbf{y} \mapsto \mathbf{x} = \boldsymbol{\phi}(\mathbf{y})$ is of the form

$$\begin{array}{r} \mathbf{y} \mapsto (y^1 + \frac{1}{2}c_1(y^2)^2 + c_2 y^1 y^2 + \frac{1}{2}c_3(y^1)^2 + \frac{1}{2}c_4 y^1(y^2)^2, \\ y^2 - \frac{1}{2}c_2(y^1)^2 - c_1 y^1 y^2 + \frac{1}{2}c_5(y^2)^2 + \frac{1}{2}c_4(y^1)^2 y^2), \end{array} \tag{13}$$

with c_j constants. Assuming that $\boldsymbol{\phi}^{-1}(\mathbf{x})$ exists on S, we may then consider rewriting the representation (10) by using the chart $\boldsymbol{\varphi}_S \circ \boldsymbol{\phi} : K \to \mathbf{E}^3$ which is defined by

$$\begin{array}{r} (\boldsymbol{\varphi}_S \circ \boldsymbol{\phi})(\mathbf{y}) = [\boldsymbol{i}_1 \cdot (\boldsymbol{\phi}(\mathbf{y}) - \mathbf{o})]\boldsymbol{i}_1 + [\boldsymbol{i}_2 \cdot (\boldsymbol{\phi}(\mathbf{y}) - \mathbf{o})]\boldsymbol{i}_2 + \\ z[\boldsymbol{i}_1 \cdot (\boldsymbol{\phi}(\mathbf{y}) - \mathbf{o}), \boldsymbol{i}_2 \cdot (\boldsymbol{\phi}(\mathbf{y}) - \mathbf{o})]\boldsymbol{i}_3, \end{array} \tag{14}$$

with $\mathbf{o}$ the origin.

By employing the Taylor polynomial approximation (11), the surface basis vectors obtained via differentiation of (14) with respect to y^α are always seen to be orthogonal at least up to second-order terms (our selection of parameters will actually lead to third-order accuracy). The constants c_1 and c_2 may now be adjusted such that the matrix representation of the second fundamental form is diagonalized up to second-order terms. The constants c_3, c_4 and c_5 are not important is this aspect, as they are introduced in order to have an opportunity to adjust the behaviour of the Christoffel symbols. Using the constants in the Taylor polynomial (11), we take

$$c_3 = -c_1, \quad c_5 = c_2, \text{ and } c_4 = -AB/2, \tag{15}$$

while the constants c_1 and c_2 are defined by

$$c_1 = \frac{F}{B(1 - A/B)} \quad \text{and} \quad c_2 = \frac{E}{B(1 - A/B)}, \tag{16}$$

with $B \neq 0$ or $A \neq B$. The two exceptional cases excluded relate to cases where the surface behaves locally like a plane ($B = 0$ and, hence, also $A = 0$) or like a sphere $A = B \neq 0$.

It follows that the fields $\boldsymbol{a}_\alpha : K \to \mathbb{R}^3$, which now give the covariant base vectors of the surface at $\mathbf{p} = (\boldsymbol{\varphi}_S \circ \boldsymbol{\phi})(\mathbf{y})$ via $\mathbf{p} \mapsto (\boldsymbol{a}_\alpha \circ \boldsymbol{\phi}^{-1} \circ \boldsymbol{\varphi}_S^{-1})(\mathbf{p})$, can be expanded over K as

$$\begin{array}{l} \boldsymbol{a}_1 = [1 - c_1 y^1 + c_2 y^2 + O(h^2)]\boldsymbol{i}_1 - [c_2 y^1 + c_1 y^2 + O(h^2)]\boldsymbol{i}_2 + [Ay^1 + O(h^2)]\boldsymbol{i}_3, \\ \boldsymbol{a}_2 = [c_2 y^1 + c_1 y^2 + O(h^2)]\boldsymbol{i}_1 + [1 - c_1 y^1 + c_2 y^2 + O(h^2)]\boldsymbol{i}_2 + [By^2 + O(h^2)]\boldsymbol{i}_3, \end{array} \tag{17}$$

where h now characterizes the maximum of the diameters of S and K. As we have $\boldsymbol{a}_1 \cdot \boldsymbol{a}_2 = 0 + O(h^3)$, the matrix representation of the metric surface tensor is again diagonalized so that $\boldsymbol{A} = \mathbf{diag}(A_{11}, A_{22})$, with

$$A_{11} = A_{22} = 1 - 2c_1 y^1 + 2c_2 y^2 + O(h^2). \tag{18}$$

That is, the surface basis vectors are orthogonal but do not have the unity as their lengths. On the other hand, the unit normal vector is given by

$$\boldsymbol{a}_3 = [-Ay^1 + O(h^2)]\boldsymbol{i}_1 + [-By^2 + O(h^2)]\boldsymbol{i}_2 + [1 + O(h^2)]\boldsymbol{i}_3. \tag{19}$$

The covariant components $B_{\alpha\beta} : K \to \mathbb{R}$ of the second fundamental form are found to be

$$\begin{aligned} B_{11} &= A(1 - 2c_1 y^1 + 2c_2 y^2) + Dy^1 + Ey^2 + O(h^2), \\ B_{22} &= B(1 - 2c_1 y^1 + 2c_2 y^2) + Fy^1 + Gy^2 + O(h^2), \\ B_{12} &= B_{21} = 0 + O(h^2), \end{aligned} \tag{20}$$

so that, up to neglected terms of $O(h^2)$, the matrix of the mixed components of the second fundamental form has the eigenvalues which can be evaluated by using (18) and (20) from

$$\Lambda_\alpha = B_{\alpha\alpha}/A_{\alpha\alpha}. \tag{21}$$

If we now define the geometric Lamé parameters by

$$A_\alpha = \sqrt{A_{\alpha\alpha}}, \tag{22}$$

in the case of lines of curvature parametrization the Lamé parameters give the lengths of the surface basis vectors and are related to the Christoffel symbols via

$$\begin{aligned} \Gamma^\alpha_{\alpha\beta} &= (1/A_\alpha)\partial_\beta A_\alpha, \\ \Gamma^\beta_{\alpha\alpha} &= -(A_\alpha/A_\beta^2)\partial_\beta A_\alpha, \quad \beta \neq \alpha. \end{aligned} \tag{23}$$

The constants c_3, c_4 and c_5 have here been adjusted such that the relations (23) are satisfied up to truncation errors of $O(h^2)$. The relations (23) are thus satisfied with

$$\begin{aligned} \Gamma^1_{11} &= -c_1 + (A^2 - c_1^2 + c_2^2)y^1 + 2c_1c_2y^2 + O(h^2), \\ \Gamma^2_{11} &= -c_2 - 2c_1c_2y^1 + (AB/2 - c_1^2 + c_2^2)y^2 + O(h^2), \\ \Gamma^1_{22} &= c_1 + (AB/2 + c_1^2 - c_2^2)y^1 - 2c_1c_2y^2 + O(h^2), \\ \Gamma^2_{22} &= c_2 + 2c_1c_2y^1 + (B^2 + c_1^2 - c_2^2)y^2 + O(h^2), \\ \Gamma^1_{21} &= c_2 + 2c_1c_2y^1 + (c_1^2 - c_2^2 - AB/2)y^2 + O(h^2), \\ \Gamma^2_{21} &= -c_1 + (c_2^2 - c_1^2 - AB/2)y^1 + 2c_1c_2y^2 + O(h^2). \end{aligned} \tag{24}$$

Computational examples

To demonstrate the ability of the proposed method to produce accurate estimates of the principal directions and curvatures, we consider the following simple test case. We first create a regular $N \times N$ grid for the square domain $\omega' = [-\pi/3, \pi/3] \times [-\pi/3, \pi/3]$. We then apply a shear deformation to ω' and finally map the stretched mesh of rectangular elements to obtain an approximation to a part of cylindrical surface defined by

$$\mathcal{S} = \{\ (\sin(x' + 1/4y'), y', 1 - \cos(x' + 1/4y')) \in \mathbf{E}^3 \mid (x', y') \in \omega'\ \}. \tag{25}$$

We note that the surface $\mathcal{S}$ has now the principal radii of curvature $R_1 = 0$ and $R_2 = 1$. Nevertheless, the element edges are not aligned with the principal directions, so every element

Table 1. Computed errors for the test case.

N	$\|2H - \Lambda_1^h - \Lambda_2^h\|$	$\|A - A^h\|$	$\|\boldsymbol{e}_1 - \boldsymbol{e}_1^h\|$
3	2.3334E-01	1.0490E-01	4.2055E-02
6	6.0738E-02	2.6390E-02	1.0646E-02
12	1.5338E-02	6.6082E-03	2.6689E-03
24	3.8451E-03	1.6529E-03	6.6833E-04

in the mesh must be re-parameterized in order to obtain the desired geometry representation in lines of curvature coordinates. Additional geometric input data was also provided so that the original element data enabled an $O(h^4)$ approximation of the surface location in L_2.

The re-parametrization strategy considered in this paper has been implemented into the open source finite element software Elmer [3]. The example results of this paper were computed with this implementation. To demonstrate the accuracy of approximation to the mean curvature $H = 1/2(1/R_1 + 1/R_2)$, in Table 1 we show $\|2H - \Lambda_1^h - \Lambda_2^h\|$ where $\|\cdot\|$ denotes L^2 norm and the principal curvature approximations Λ_α^h are computed elementwise by using the equations (21), (20) and (18). We note that in this connection each domain K was approximated simply as a quadrilateral with straight edges. For reference we also show the area error $|A - A^h|$ where $A = 4(\pi/3)^2$ is the area of the exact surface $\mathcal{S}$ and the area A^h is obtained by approximating the domain K similarly and using (18) to approximate the determinant of the metric surface tensor needed in the area computation. We observe that both the mean curvature and area approximation converge quadratically as expected.

We finally demonstrate that also our computational estimates of the principal directions converge quadratically towards the right solution. To this end we compute $\|\boldsymbol{e}_1 - \boldsymbol{e}_1^h\|$ where $\boldsymbol{e}_1$ is the first principal direction for the exact surface $\mathcal{S}$ and $\boldsymbol{e}_1^h = \boldsymbol{a}_1^h/|\boldsymbol{a}_1^h|$ denotes the approximation of the first principal direction computed elementwise by using (17). The results shown for the error of the first principal direction in Table 1 are again in agreement with the quadratic rate of convergence. It should be noted that our approximation of the second fundamental form is in L^2 only, so that averaging is generally needed if unique curvature data or unique estimates for the principal directions are wanted at the element nodes.

Concluding remarks

Due to space limitations we have not been able to describe all possibilities which relate to the ideas presented here. We see interesting scenarios especially when these ideas are applied in connection with the finite element approximation of shell equations. An account on these new developments is under preparation.

References

[1] P.G. Ciarlet. *An introduction to differential geometry with applications to elasticity.* Springer, Dordrecht, the Netherlands, 2005.

[2] L.E. Malvern. *Introduction to the Mechanics of a Continuous Medium.* Prentice-Hall, Englewood Cliffs, New Jersey, 1969.

[3] Elmer finite element software homepage, `http://www.csc.fi/elmer`.

Proceedings of the XII Finnish Mechanics Days
R. Kouhia, J. Mäkinen, S. Pajunen and T. Saksala (Eds.)

Computing minimizing curves on fixed rank matrix manifolds

Alexis Fedoroff[1], Djebar Baroudi[1]

(1)Aalto University, School of Engineering, Department of Civil and Structural Engineering, PO Box 12100, FI-00076 Aalto, alexis.fedoroff@aalto.fi, dje.baroudi@gmail.com

Summary. This article demonstrates how to compute all locally length minimizing curves between two points on the Riemanninan fixed rank $n-1$ matrix manifold embedded in the $n \times n$ matrix space. As a byproduct, we obtain an algorithm that computes the numerical value of the Riemannian distance function between those two points. The proposed algorithm is verified by comparing the length minimizing curve, obtained through the minimization problem, with the corresponding geodesic, obtained through an initial value problem. As we know from the Riemannian manifold theory, the length minimizing curve and the geodesic coincide up to a re-parametrization.

Applications that could benefit from the Riemannian distance function computing algorithm are plentiful in numerical computations. In particular, an acces to a numerical pointwise approximation of a sphere with respect to the Riemannian distance function enables the extension of local sensitivity analysis from Euclidean spaces to more general metric spaces, such as Riemannian manifolds.

Key words: Riemannian manifold, fixed rank matrix manifold, length minimizig curve, geodesic, Riemannian distance function, Lie group actions, homogeneous spaces, covering map

Introduction

Continuous curves on topological spaces are mathematical objects central in many applications. One of the most common applications is the computation of the distance between two points. By definition, the distance is the minimum of the lengths of all possible continuous curves connecting the starting and ending points. For example, on the two dimensional Euclidean plane, two points A and B can be connected by an arbitrary continuous curve $f \in \mathcal{C}^0([0,1];\mathbb{R}^2)$ such that $f(0) = \mathrm{A}$ and $f(1) = \mathrm{B}$, as Figure 1a shows. Any of these curves can be smoothly transformed to any other curve fulfilling the same properties, namely having A for starting point and B for ending point. In particular, any continuous curve f can be smoothly transformed to the length minimizing curve g. On the Euclidean plane, there is only one local minimum, which is also the global minimum at the same time. However, looking at Figure 1b, one can see, that on the Euclidean plane with a hole, denoted $\mathbb{R}^2\backslash\{\mathrm{O}\}$, there are two possibilities for locally length minimizing curves: the continuous curve f , which is smoothly transformed to g, and the continuous curve f', which is smoothly transformed to g'. Both g and g' are locally length minimizing curves, but only g' is also a length minimizing curve in the global sense.

From the point of view of homotopy[1] theory, f and g "look the same" because they can be smoothly transformed from one to the other. Likewise, f' and g' look homotopically the same. Using the vocabulary of homotopy theory, $[f]$ and $[f']$ are distinct homotopy equivalence classes relative to the endpoints A and B. Homotopy equivalence classes are important objects, because they enable the enumeration of all possible topologically distinct routes from A to B. In the

[1]From Greek words *homos*: same and *topos*: place. Homotopy theory is one of the main currents in algebraic topology, [1].

example $[f]$ represents the routes that go around the point O clockwise and $[f']$ represents the routes that go counter clockwise.

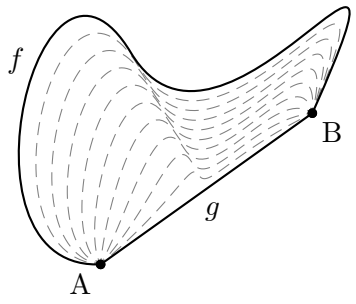

(a) A length minimizing curve on $\mathbb{R}^2$

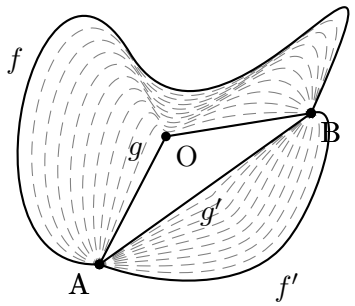

(b) A length minimizing curve on $\mathbb{R}^2\backslash\{\mathrm{O}\}$

Figure 1: Length minimizing curves from A to B

Homotopy theory tells us well how many of those equivalence classes one may expect on a given topological space, but it certainly does not give a clue how to find an explicit expression for a member of a given homotopy equivalence class. Nor does it give any algorithm to compute the representative element that has the minimal length. This is why we have to include numerical minimization algorithms in our considerations.

Notice, that one can formulate the minimization problem on the topological space $X = \mathbb{R}^2\backslash\{\mathrm{O}\}$ in the following way. Let $\{\alpha_1, \dots \alpha_k\} \subset \mathcal{C}^\infty([0,1];\mathbb{R}^2)$ be a family of smooth loops through the origin, i.e. $\alpha_i(0) = \alpha_i(1) = (0,0)$. By defining the perturbed curves $f_a, f'_a \in \mathcal{C}^k([0,1];X)$ as follows:

$$f_a(t) = f(t) + \sum_{1\leq i\leq k} a^i\,\alpha_i(t)\ , \tag{1a}$$

$$f'_a(t) = f'(t) + \sum_{1\leq i\leq k} a^i\,\alpha_i(t)\ , \tag{1b}$$

where $a = (a^1, \dots, a^k)$ is a k-tuple of real coefficients, one can define as follows the length functionals to be minimized: $\mathrm{L}(f_a) = \int_0^1 \|\frac{\mathrm{d}f_a}{\mathrm{d}t}\|\,\mathrm{d}t$ and $\mathrm{L}(f'_a) = \int_0^1 \|\frac{\mathrm{d}f'_a}{\mathrm{d}t}\|\,\mathrm{d}t$. By taking as an initial guess $a_{(0)} = (0, \dots, 0)$, one can clearly see that the minimization problem is well posed. By ensuring through an additional constraint that $f_a(t) \neq \mathrm{O}$ and $f'_a(t) \neq \mathrm{O}$ for any $t \in [0,1]$, we also ensure that an iterate of the constrained minimization algorithm does not "jump" on the wrong side of the hole. Therefore we are also expecting the following convergences for the constrained minimization problems:

$$f_{a_{(e)}} \xrightarrow[e\to\infty]{} g\ , \tag{2a}$$

$$f'_{a_{(e)}} \xrightarrow[e\to\infty]{} g'\ . \tag{2b}$$

On topological spaces more complex than the Euclidean plane, possibly with one or more holes, one proceeds exactly in the same way. In the following sections of this presentation, we shall see how one enumerates all homotopy equivalence classes of smooth curves on fixed rank matrix manifolds relative to some chosen points on the manifold. Then, these smooth curves will serve as an *initial guess* to numerical minimization problems that enable us to compute *all* locally minimizing curves connecting two given points.

Fixed rank matrix manifolds as Riemannian manifolds

When thinking of a smooth manifold, one usually thinks of a two dimensional surface in the ambient three dimensional space. Although general manifold theory give keys to cope with

spaces much more complex than that, coming back, whenever applicable, to that simple image of a "potato crisp" gives intuitive power to the reasoning.

The denomination *fixed rank matrix manifolds* implies that the embedding space is a matrix space of $m \times n$ real valued matrices, denoted $\mathbb{M}^{m\times n}$. By considering the vectorization operator $\text{vec} : \mathbb{M}^{m\times n} \to \mathbb{R}^{mn}$, which stacks the matrix columns one above the other, one can show that since the vectorization operator is an isomorphism, the matrix space is, actually, a vector space, [2]. Likewise, one can show that the set of symmetric square $n \times n$ matrices, denoted $\mathbb{M}^{\text{SYM}(n)}$, is also a vector space isomorphic to $\mathbb{R}^{n(n+1)/2}$. This is done by considering the half-vectorization operator: $\text{hvec} : \mathbb{M}^{\text{SYM}(n)} \to \mathbb{R}^{n(n+1)/2}$, which stacks from each column vector only the portion on or above the diagonal.

The set of all matrices in $\mathbb{M}^{m\times n}$ that have fixed rank, k, are denoted $\mathbb{M}_k^{m\times n}$. Recalling that up to a permutation of rows and columns, any matrix M of rank *at least* k has an full rank $k\times k$ submatrix A, one can write the following block lower-diagonal-upper matrix decomposition:

$$M = \begin{pmatrix} A & B \\ C & D \end{pmatrix} = \begin{pmatrix} I^k & 0 \\ C\,A^{-1} & I^{m-k} \end{pmatrix} \begin{pmatrix} A & 0 \\ 0 & D - C\,A^{-1}\,B \end{pmatrix} \begin{pmatrix} I^k & A^{-1}\,B \\ 0 & I^{n-k} \end{pmatrix} ,$$

where $A \in \mathbb{M}_k^{k\times k}$, $B \in \mathbb{M}^{k\times(n-k)}$, $C \in \mathbb{M}^{(m-k)\times k}$ and $D \in \mathbb{M}^{(m-k)\times(n-k)}$. Clearly, the matrix M is *exactly* of rank k if and only if the lower right submatrix in the block diagonal term vanishes, i.e. if $D - C\,A^{-1}\,B = 0$. This leads us to the definition of the smooth map $F : W \to \mathbb{M}^{(m-k)\times(n-k)}$ given by $\left(\begin{smallmatrix} A & B \\ C & D \end{smallmatrix}\right) \mapsto D - C\,A^{-1}\,B$, where $W \subset \mathbb{M}_{\geq k}^{m\times n}$ denotes the subset of all matrices of rank at least k with full rank upper left $k \times k$ submatrix. The map F is full rank everywhere on the domain of definition, which implies by the Submersion theorem, [3], that $U = F^{-1}(\{0\}) \subset \mathbb{M}_k^{m\times n}$. By considering all possible permutations of rows and columns of matrices of rank at least k one gets a smooth atlas for the set of fixed rank matrices $\mathbb{M}_k^{m\times n}$, and shows that it is a submanifold embedded in the ambient space $\mathbb{M}_{\geq k}^{m\times n}$ of matrices of rank at least k.

Consider, for illustration purposes, the set of symmetric 2×2 matrices. This set is isomorphic to the Euclidean space $\mathbb{R}^3\backslash\{O\}$ by the identification $\left(\begin{smallmatrix} a & b \\ b & d \end{smallmatrix}\right) \leftrightarrow (a, \sqrt{2}\,b, d) \in \mathbb{R}^3$. Therefore, for any $a \neq 0$, the set of rank 1 matrices is described by the parametrization $\varphi^{-1} : (a, b) \mapsto (a, \sqrt{2}\,b, b^2/a)$, as shown in Figure 2.

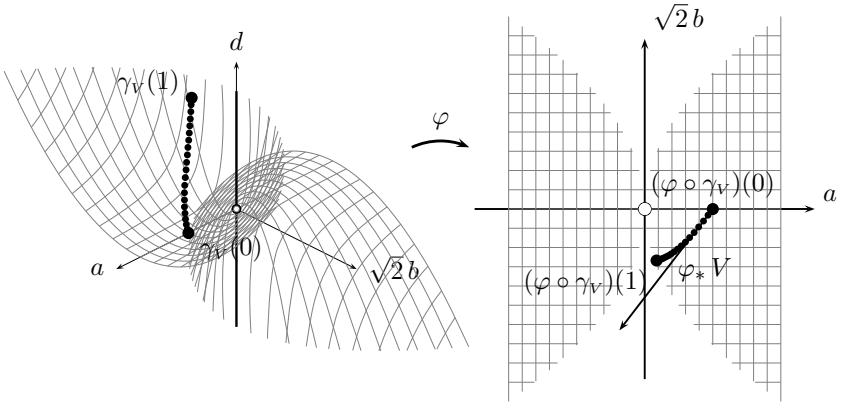

Figure 2: Example of a chart on the $\text{M}_1^{\text{SYM}(2)}$ manifold and of a geodesic $\gamma_V : [0, 1] \to \text{M}_1^{\text{SYM}(2)}$.

The map $\varphi : U \subset \mathbb{M}_1^{\text{SYM}(2)} \to \mathbb{R}^2$ defined by $\left(\begin{smallmatrix} a & b \\ b & b^2/a \end{smallmatrix}\right) \mapsto (a, b)$ is called the *chart map*, and it is defined on the domain U, which is the set of symmetric 2×2 rank 1 matrices In the general case, the chart map is defined as follows: $\left(\begin{smallmatrix} A & B \\ C & C\,A^{-1}\,B \end{smallmatrix}\right) \mapsto (\text{vec}\,A, \text{vec}\,B, \text{vec}\,C)$ and it is defined on $U = \{M \in \mathbb{M}_k^{m\times n} \ : \ (\,I^k\ 0\,)M\left(\begin{smallmatrix} I^k \\ 0 \end{smallmatrix}\right) \in \mathbb{M}_k^{k\times k}\}$.

Without going into the details, one can show how to compute the induced metric tensor with respect to the chart (U, φ), then the Riemann-Christoffel symbols, and finally, the geodesic equations that enable the formulation of an initial value problem which has a geodesic as its

solution. An illustration of a geodesic with initial point $\left(\begin{smallmatrix}1&0\\0&0\end{smallmatrix}\right)$ and an initial direction V has been drawn in Figure 2.

Fixed rank matrix manifolds as homogeneous spaces

Considering the set of fixed rank matrices as smooth manifolds endowed with a specific smooth atlas and a Riemannian metric tensor enables us to compute already a lot of things. We have shown already in the previous paragraph how to compute geodesics, which are also locally length minimizing curves, as we all know from Theorem 6.6, [4]. The theorem states, indeed, that every minimizing curve is a geodesic when given a unit speed parametrization.

Taking, for example the geodesic shown in Figure 2, one might ask the following question: is there any other length minimizing curve that connects the starting and end points? The answer is positive, but in order to be able to justify that claim, one has to show first some symmetry properties of fixed rank matrix manifolds. In [5], we have shown that the 2×2 symmetric rank 1 matrix manifold can be viewed as a cone of revolution around the axis $(\frac{1}{\sqrt{2}}, 0, \frac{1}{\sqrt{2}}) \in \mathbb{R}^3$.

This important result found in a specific case can be generalized to arbitrary fixed rank matrix manifolds using transitive Lie group actions on the fixed rank matrix manifold. Hence, we have to find a Lie group G and a left action $\theta : G \times \mathbb{M}_k^{m\times n} \to \mathbb{M}_k^{m\times n}$ that happens to be transitive. It can be shown that by using ingeniously Kronecker products and the matrix equation rule $\operatorname{vec} B\,X\,A^\intercal = A \otimes B \operatorname{vec} X$, we can come up with the following Lie group:

$$G = \left\{ \left(\left(\begin{smallmatrix} S & 0 \\ 0 & I^{n-k} \end{smallmatrix}\right) \otimes \left(\begin{smallmatrix} S & 0 \\ 0 & I^{m-k} \end{smallmatrix}\right) \right) \otimes \Big(\mathrm{SO}(n) \otimes \mathrm{SO}(m) \Big) \;:\; S \in \operatorname{diag}(\mathbb{R}_+^k) \right\} . \tag{3}$$

It follows, that the ideal candidate for a transitive Lie group action on the fixed rank matrix manifold is

$$\begin{array}{rccl} \Theta : & G \times \mathrm{M}_k^{m\times n} & \to & \mathrm{M}_k^{m\times n} \\ & (X, M) & \mapsto & \operatorname{res}^{m\times n}\left(\operatorname{res}^{mn\times mn}\left(X \operatorname{vec} I^{mn} \right) \operatorname{vec} M \right) \end{array} . \tag{4}$$

The construction of the Lie group G and of the transitive action Θ is motiveted by the singular value decomposition of a fixed rank matrix. Let $P\left(\begin{smallmatrix}\Sigma&0\\0&0\end{smallmatrix}\right)Q^\intercal = M$ be a singular value decomposition of $M \in \mathbb{M}_k^{m\times n}$ for some rotation matrices $P \in \mathrm{SO}(m)$ and $Q \in \mathrm{SO}(n)$ and a diagonal matrix $\Sigma \in \operatorname{diag}(\mathbb{R}_+^k)$. Then we construct the element in the Lie group as follows: $X = \left(\left(\begin{smallmatrix} \sqrt{\Sigma} & 0 \\ 0 & I^{n-k} \end{smallmatrix}\right) \otimes \left(\begin{smallmatrix} \sqrt{\Sigma} & 0 \\ 0 & I^{m-k} \end{smallmatrix}\right) \right) \otimes \big(Q \otimes P \big)$. The action of X on the einselement $E = \left(\begin{smallmatrix} I^k & 0 \\ 0 & 0 \end{smallmatrix}\right)$ simplifies as follows: $\Theta(X, E) = P\left(\begin{smallmatrix}\Sigma&0\\0&0\end{smallmatrix}\right)Q^\intercal = M$. Because the quantities under consideration were chosen arbitrarily, it follows that the orbit of the ection through the einselement is the entire fixed rank matrix manifold, which shows that the action is transitive, in other words that the fixed rank matrix manifold is a homogeneous G-space.

However, because the singular value decomposition is not unique, it implies that we have to identify a closed Lie subgroup of G, denoted $\mathrm{Stab}_E \subset G$ that fixes the einselement, i.e. $\Theta(\mathrm{Stab}_E, E) = E$. It can be shown that the stability subgroup has the following shape:

$$\mathrm{Stab}_E = \left\{ \Big(I^n \otimes I^m \Big) \otimes \left(\left(\begin{smallmatrix} D & 0 \\ 0 & \mathrm{SO}(n-k) \end{smallmatrix}\right) \otimes \left(\begin{smallmatrix} D & 0 \\ 0 & \mathrm{SO}(m-k) \end{smallmatrix}\right) \right) \;:\; D \in \operatorname{diag}(\pm 1, \ldots, \pm 1) \subset \mathrm{SO}(k) \right\} . \tag{5}$$

The stability subgroup of the einselement enables us to define equivalence classes on G, called left cosets, and defined as follows: $[X] = X\,\mathrm{Stab}_E = \{Y \in G \;:\; Y = X\,L \text{ for some } L \in \mathrm{Stab}_E\}$. The collection of all left cosets is called the *quotient space*. It is denoted G/Stab_E, and according to Theorem 7.5 in [3], the quotient space is a smooth manifold. In addition, it can be shown that G/Stab_E is diffeomorphic to the underlying fixed rank matrix manifold $\mathbb{M}_k^{m\times n}$.

Some computation results

A special case interests us above the others. Namely, the case of square $n \times n$ matrices of rank $n-1$. In that special case, the stability subgroup Stab_E is a finite discrete set containing

$\sum_{k=0}^{\mathrm{E}(n/2)} \binom{2\,k}{n}$ elements. Therefore the Lie group G is called a *covering space* of G/Stab_E, and $\pi : G \to G/\mathrm{Stab}_E$ the covering map. The number of elements in Stab_E equals the number of *sheets* in G hovering above G/Stab_E.

Another interesting property of the special fixed rank matrix manifold $\mathbb{M}_{n-1}^{n\times n}$ is that the Lie algebra of G, denoted $\mathfrak{g}$ is precisely the horizontal space of G/Stab_E, i.e. we have a zero dimensional vertical space precisely because the stability subgroup is a discrete set. This consideration enables us to use matrix exponentials on the quotient space, as well. Considering the following composition of the matrix exponential by the covering map, we end up constructing a discrete set of vectors in the Lie algebra that are all mapped to the same point in the quotient space.

$$\begin{array}{ccccc} \mathfrak{g} & \xrightarrow{\mathrm{mexp}} & G & \xrightarrow{\pi} & G/\mathrm{Stab}_E \\ \{V_i\} = \mathrm{mlog} \circ \pi^{-1}([X]) & \mapsto & \pi^{-1}([X]) & \mapsto & [X] \end{array} \tag{6}$$

Notice, that the corresponding one parameter subgroups $\Gamma_{V_i} : [0,1] \to G/\mathrm{Stab}_E$ defined through the matrix exponential $\Gamma_{V_i}(t) = (\pi \circ \mathrm{mexp})(t\,V_i)$ enumerate all possible homotopy equivalence classes of curves connecting the identity $[I]$ to the endpoint $[X]$. Figure 3 illustrates well this concept.

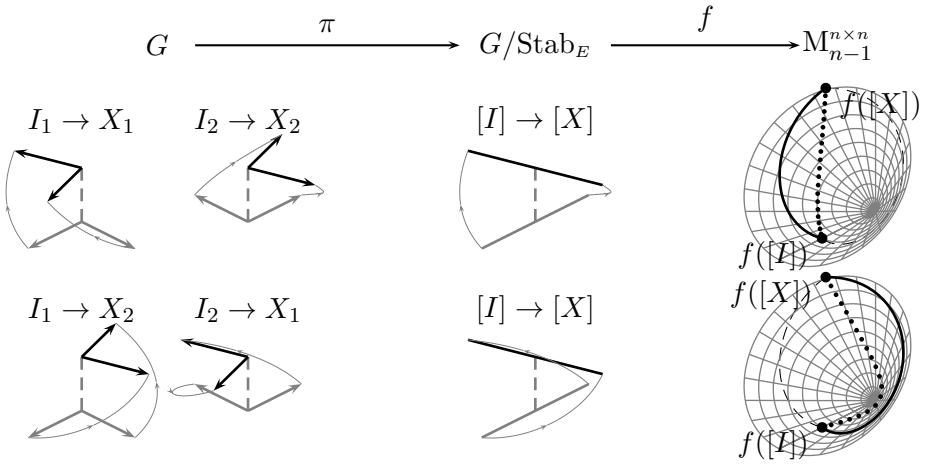

Figure 3: One parameter subgroups and minimizing curves

Coming back to our initial minimization problem, we may re-formulate our curve to be minimized by introducing sinusoidal[2] basis functions $\sin(1\,\pi\,t), \ldots, \sin(k\,\pi\,t)$ and a set of matrix valued coefficients $W_1, \ldots, W_k$ chosen from the Lie algebra $\mathfrak{g}$.

$$\Gamma_{V,W}(t) = (\pi \circ \mathrm{mexp})\big(t\,V + \sum_{1\le i\le k} W_j\,\sin(j\,\pi\,t)\big) \quad , \; V \in \mathrm{mlog} \circ \pi^{-1}([X]) \; . \tag{7}$$

Hence the functional to minimize is given as the integral $\mathrm{L}(\Gamma_{V,W}) = \int_0^1 \|\dot{\Gamma}_{V,W}\|\,\mathrm{d}t$. By denoting $\ell_i = \min_W \mathrm{L}(\Gamma_{V_i,W})$, we get a distribution of minimizing curve lengths, $\ell_1, \ell_2, \ldots$. The smallest of these values is the Riemannian distance between the starting point $f([I])$ and the ending point $f([X])$. For reference, we denote $\ell_i^0 = \mathrm{L}(\Gamma_{V_i})$, which is the length of the one parameter subgroup that serves as an initial guess in the minimization algorithm.

In Figure 4, we have drawn the output of a numerical algorithm that enumerates all one parameter subgroups that connect two given points M and N on the fixed rank matrix manifold $\mathbb{M}_3^{4\times 4}$. The corresponding Lie group G is a covering space for G/Stab_E that has 8 sheets hovering above the quotient space. As one can see from Figure 4, there is a very interesting property concerning the list of curve lengths of the one parameter subgroups, $\{\ell_1^0, \ldots, \ell_8^0\}$, and

[2]Cosinus basis functions are ruled out because the variation must vanish at the extremities.

the corresponding list of lengths of minimizing curves $\{\ell_1, \ldots, \ell_8\}$, which is that length minimization preserves the order. In other words, if we sort the one parameter subgroups suh that $\ell_1^0 \leq \cdots \leq \ell_8^0$, then we have $\ell_1 \leq \cdots \leq \ell_8$. This property seems to hold for any numerical simulation run so far.

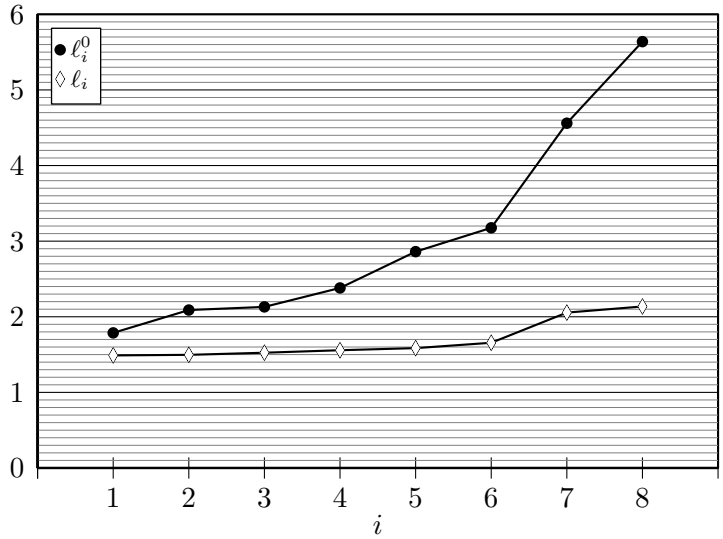

Figure 4: Enumeration of lengths of one parameter subgroups and corresponding minimizing curves

Conclusions

In this conference paper we have shown an algorithm that enumerates all homotopically distinct connecting paths between two given points on a fixed rank matrix manifold. Those connecting paths, called one parameter subgroups, serve us then as initial guesses for a minimization algorithm through which we obtain the corresponding homotopically distinct length minimizing curves. A remarkable property, that has not yet been proven formally but has strong numerical evidence, is that the minimization algorithm over a collection of one parameter subgroups is an order preserving operation with respect to the length.

References

[1] Hatcher, A. *Algebric Topology* Cambridge University Press, 2002

[2] Tapp, K. *Matrix groups* American Mathematical Society, 2005

[3] Lee, J.M. *Introduction to Smooth Manifolds* Springer, 2003

[4] Lee, J.M. *Riemannian Manifolds: An Introduction to Curvature* Springer, 1997

[5] Fedoroff, A. and Kouhia, R. Geometric approach in numerical eigenproblem analysis *Rakenteiden mekaniikka*, 45(3), 2012

Proceedings of the XII Finnish Mechanics Days
R. Kouhia, J. Mäkinen, S. Pajunen and T. Saksala (Eds.)

Surface tension problems, virtual work and minimal surfaces

Mika Reivinen[1] and Eero-Matti Salonen[1]

(1)School of Engineering, P.O. Box 12100, FIN-00076 Aalto, Finland, mika.reivinen@aalto.fi, eero-matti.salonen@aalto.fi

Summary. In this study, a formulation for the membrane form-finding treatment is presented. The treatment is based on the principle of virtual work, and it is an extension of the two-dimensional study presented in [1] to three dimensions. The essential derivations for the three-dimensional case are presented in [2]. Finally, a discrete solution method is given. The working of the discrete formulation is demonstrated by a form-finding example case.

Key words: surface tension, virtual work, tension membranes, minimal surfaces, form-finding, SMP12

Introduction

The aim of the present study is to find a proper formulation for the design of lightweight structures, especially structures having the shape of minimal surfaces. The nature produces highly optimized designs in terms of minimum weight and maximum stability and strength. Those natural designs are based on the minimization of the potential energy. Natural tension structures, such as soap-films, translates into a constant surface stress and a minimum surface area, and consequently the corresponding shapes are optimal for lightweight tension membranes. The tension membranes can be divided into two categories: surface tensioned membranes with zero pressure difference, and pneumatic structures with non-zero pressure difference.

According to the Laplace-Young equation, the surface tension σ and the mean curvature H depend on the pressure difference [2]:

$$\Delta p = -\sigma 2H = -\sigma\Big(\frac{1}{R_1} + \frac{1}{R_2}\Big), \tag{1}$$

where $1/R_1$ and $1/R_2$ are the principal curvatures. From the Laplace-Young equation it follows that in the case of zero pressure difference, also the mean curvature must vanish at every point on the surface, and consequently the tension membrane forms a minimal surface with a 'saddle' shape [3].

Problem statement

The task is to determine the position of the interface surface S bounded by s between two vapour phases (Fig. 1). The position vector $\mathbf{r}$ on S is expressed in the form

$$\mathbf{r} = \mathbf{r}(u^1, u^2), \tag{2}$$

where u^1 and u^2 are surface parameters or coordinates.

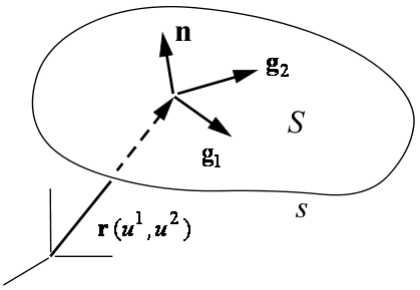

Figure 1. Interface surface S and some notations.

Virtual work

The principle of virtual work is presented here in the same way as in [1]:

$$\overline{\delta W} \equiv \overline{\delta W}^{\text{int}} + \overline{\delta W}^{\text{ext}} = 0. \tag{3}$$

Here $\overline{\delta W}^{\text{int}}$ is the virtual work of the internal forces, and $\overline{\delta W}^{\text{ext}}$ is the virtual work of the external forces. The principle of virtual work states that (3) is valid for any virtual movement of the interface. The principle of virtual work is not a variational principle in the sense that a stationarity condition of a functional is not involved. The overbar is used to emphasize thus that no variations of some quantities W are involved. Usually in the principle of virtual work the variation of the position vector of material particles are involved and the variation is called virtual displacement. Here the change in the position of the interface will be called virtual movement to indicate that the movement is not necessarily associated with a material particle.

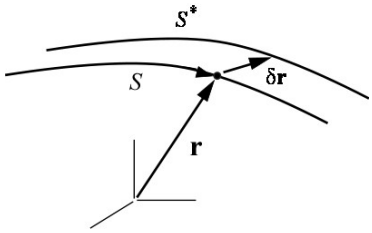

Figure 2. Surface S and a varied surface S^*

Virtual work of internal forces

Let us consider Fig. 2. Let the position vector to a generic point on the interface surface S be denoted as earlier by $\mathbf{r}(u^1, u^2)$ and let the corresponding point on a varied comparison surface S^* be given by $\mathbf{r}(u^1, u^2) + \delta\mathbf{r}(u^1, u^2)$, where $\delta\mathbf{r}$ is the virtual movement.

The expression for the virtual work of internal forces is

$$\overline{\delta W}^{\text{int}} = -\int_S \sigma\varepsilon_S \mathrm{d}S. \tag{4}$$

where σ is the surface tension and ε_S is the relative change of area of a differential surface element. The contribution of the virtual work of internal forces is derived in [2], and it can be expressed as:

$$\overline{\delta W}^{\text{int}} = -\int_{u^1,u^2} \sigma\Big[(\mathbf{n}\times\mathbf{g}_1)\cdot\frac{\partial\delta\mathbf{r}}{\partial u^2} - (\mathbf{n}\times\mathbf{g}_2)\cdot\frac{\partial\delta\mathbf{r}}{\partial u^1}\Big]\mathrm{d}u^1\mathrm{d}u^2, \tag{5}$$

where $\mathbf{n}$ is the unit normal vector to the interface S, and $\mathbf{g}_1$ and $\mathbf{g}_2$ are the covariant basis vectors (Fig. 1).

Virtual work of external forces

The external forces acting on the interface consist of the pressure difference $\Delta p\mathbf{n}$, and the corresponding contribution can be expressed as [2]:

$$\overline{\delta W}^{\text{ext}} = \int_{u^1,u^2} \sqrt{g}\Delta p\mathbf{n} \cdot \delta\mathbf{r}\mathrm{d}u^1\mathrm{d}u^2, \tag{6}$$

where quantity g is the discriminant of the covariant metric tensor $g_{\alpha\beta} = \mathbf{g}_\alpha \cdot \mathbf{g}_\beta$.

Discrete formulation

Triangular elements

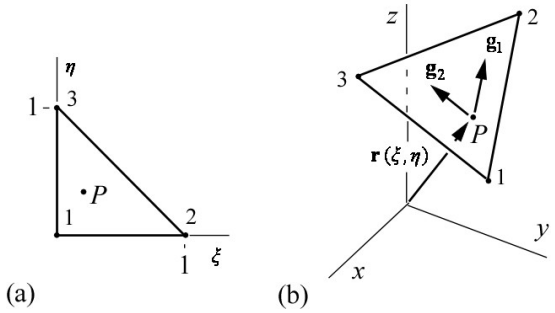

Figure 3. Mapping of a triangular element

The discrete formulation is again a rather straightforward generalization of the procedures presented in two dimensions in [1]. Instead of line or segment elements now triangular elements are used, Fig. 3. The surface coordinates have for each element the roles $u^1 = \xi$, $u^2 = \eta$, where ξ and η are dimensionless with values ranging from 0 to 1 and are called area coordinates. Fig. 3 (a) represents a so-called reference or parent element. The mapping of it to each triangular element in the surface representation is given by

$$\mathbf{r}(\xi,\eta) = x(\xi,\eta)\mathbf{i} + y(\xi,\eta)\mathbf{j} + z(\xi,\eta)\mathbf{k}, \tag{7}$$

where

$$\begin{aligned} x &= (1-\xi-\eta)x_1 + \xi x_2 + \eta x_3, \\ y &= (1-\xi-\eta)y_1 + \xi y_2 + \eta y_3, \\ z &= (1-\xi-\eta)z_1 + \xi z_2 + \eta z_3. \end{aligned} \tag{8}$$

The values x_1, x_2, ... etc. are the coordinate values of the nodes 1, 2, 3 of the element in the x, y, z-space.

Generalized forces

The virtual movement is represented by varying the position vector through the variations of the nodes. The virtual movement in the element is

$$\delta\mathbf{r}(\xi,\eta) = \delta x(\xi,\eta)\mathbf{i} + \delta y(\xi,\eta)\mathbf{j} + \delta z(\xi,\eta)\mathbf{k}, \tag{9}$$

where $\delta x = (1-\xi-\eta)\delta x_1 + \xi\delta x_2 + \eta\delta x_3$, $\delta y = (1-\xi-\eta)\delta y_1 + \xi\delta y_2 + \eta\delta y_3$, and $\delta z = (1-\xi-\eta)\delta z_1 + \xi\delta z_2 + \eta\delta z_3$. The virtual work contribution from the element obtains finally the form

$$\overline{\delta W} = X_i\delta x_i + Y_i\delta y_i + Z_i\delta z_i \tag{10}$$

where X_i, Y_i, Z_i are generalized forces, and summation convention ($i = 1, 2, 3$) is applied. The generalized forces consist similarly as the virtual work from terms corresponding to the internal and the external forces.

We do not give any detailed expressions for the generalized forces. They are obtained quite similarly as in the two-dimensional case in [1].

System equations

Also the generation and solution of the system equation goes quite similarly as in [1]. Now in general for each node of the interface model three generalized movements and forces appear.

The generalized coordinates (which might be called also generalized movements) are denoted q_i. They are defined in principle anew for the each current system configuration. Normally, we will employ three movements Δx_k, Δy_k and Δz_k for a generic node k inside the mesh. The number of movements for an individual node can also be smaller than three, especially at the boundaries.

The virtual work for the interface model (with respect to a current configuration) obtains the form

$$\overline{\delta W} = \sum_{i=1}^{N_{\mathrm{dof}}} Q_i \delta q_i, \tag{11}$$

where Q_i is the i:th generalized force corresponding to the i:th movement q_i and N_{dof} the total number of movements. The generalized forces must vanish. Thus, the system equations are

$$Q_i = 0, \qquad i = 1, ..., N_{\mathrm{dof}}. \tag{12}$$

The system equations are solved iteratively by a Newton-Raphson solution method version as in [1].

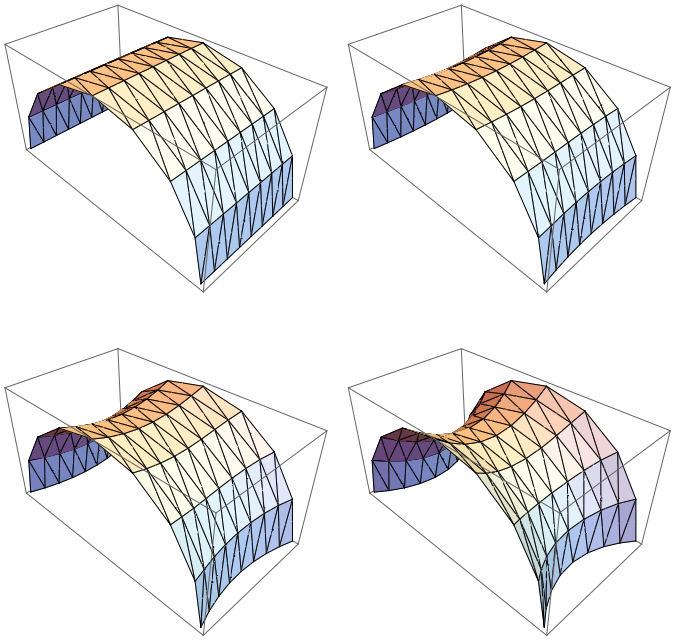

Figure 4. Initial configuration and membrane shapes after 3, 5 and 7 iterations.

Example case

As a numerical example we consider a "soap film" settled between two circular rings. The pressure difference Δp acting on the interface is zero and the surface tension σ is constant. Due to symmetry, only half of the domain is modelled. The nodes joining to the boundary rings are fixed, the nodes locating on the symmetry plane have two degrees of freedom (movements on the symmetry plane), and the rest of nodes have three degrees of freedom.

Figure 4 shows the development of the shape of soap film during the iteration. At the end of iteration, the membrane forms a minimal surface.

Conclusion

In this study, a method to determine the shape of a surface tension membrane has been developed. Our main concern has been the determination of the shape of minimal surfaces, and thus the gravity is ignored. However, the implementation of the gravity to the virtual work of external forces (6) would be straightforward.

The preliminary numerical results have been encouraging, since only few iterations to achieve the final shape of the membrane were needed. However, at the moment no comparisons considering the efficiency of the present method to corresponding methods applied to form-finding problems, for example the dynamic relaxation method [4], have not been done.

References

[1] M. Reivinen, E.M. Salonen, *Surface tension problems, virtual work and free boundary*, Proceedings of the 9th Finnish Mechanics days, Lappeenranta, 2006.

[2] M. Reivinen, E-M. Salonen, I. Todoshchenko, V.P. Vaskelainen, *Equilibrium Crystal Shapes by Virtual Work in 3D*, (in preparation), 2015.

[3] E. Kreyszig, *Differential Geometry*, Dover, 1991.

[4] B.H.V. Topping, P. Ivanyi, *Computer Aided Design of Cable Membrane Structures*, Saxe-Coburg Publications, 2007.

Proceedings of the XII Finnish Mechanics Days
R. Kouhia, J. Mäkinen, S. Pajunen and T. Saksala (Eds.)

Stochastic Finite Element Methods for Tolerance Analysis

Juho Könnö[1], Jonatan Lehtonen[2], and Harri Hakula[3]

(1)Wärtsilä Finland Oy, 65101 Vaasa, juho.konno@wartsila.com
(2)Global Boiler Works Oy, 90400 Oulu, jonatan.lehtonen@gbw.fi
(3)Aalto University, 00076 Aalto, harri.hakula@aalto.fi

Summary. This article describes a sparse grid collocation method for analysing domain uncertainty related to tolerances in machine parts. A short summary of the ideas behind the methodology are given along with some discussion of the results.

Key words: SFEM, tolerance, stochastic finite elements, reliability

Introduction

In machine design, one always has the component dimensions defined within a given tolerance. Especially for highly loaded component, even slight deviations for the ideal design geometry can have large implications on the stresses imposed on the component during operational life. To guarantee a robust design with respect to design tolerances, a robust and computationally feasible approach is needed.

A well-known standard approach is to resort to traditional Monte Carlo methods, but with increasing simulation complexity, simulating a large enough number of realizations with reasonable use of computational resources quickly becomes the limiting factor. To tackle this uncertainty quantification problem, several different stochastic methods, such as the aforementioned Monte Carlo, Galerkin and collocation methods, have been proposed.

In industrial applications one is not only limited by the methodology itself, but also by the chosen software packages and preprocessing tools, therefore intrusive Galerkin methods are less desirable. Monte Carlo and collocation methods, on the other hand, treat the FE solver as a black box. Hence they are a more readily deployable choice for industrial applications.

Model problem

In this work, we consider a simple 3D model problem which exhibits rotational symmetry, cf. Fig. 1. The parameter space for this model problem includes the radii of the two fillets and the distance between them. To this end, we adopt a collocation scheme based on a suitable choice of collocation points balanced between the solution accuracy and the number of points used. The choice of points is essential for the proper functioning of the method, for details see [1]. We call this type of solution a *sparse grid* approximation.

Another main complication is the fact that now the stochastic nature of the problem lies in the domain itself. This leads to an additional problem in combining the results from different realisations of the domain. To this end, we introduce a reference domain which is the ideal configuration of the domain, i.e. when all the tolerances are zero. Then, a conformal mapping is constructed from each 2D cross section of the realisations to the reference domain. The

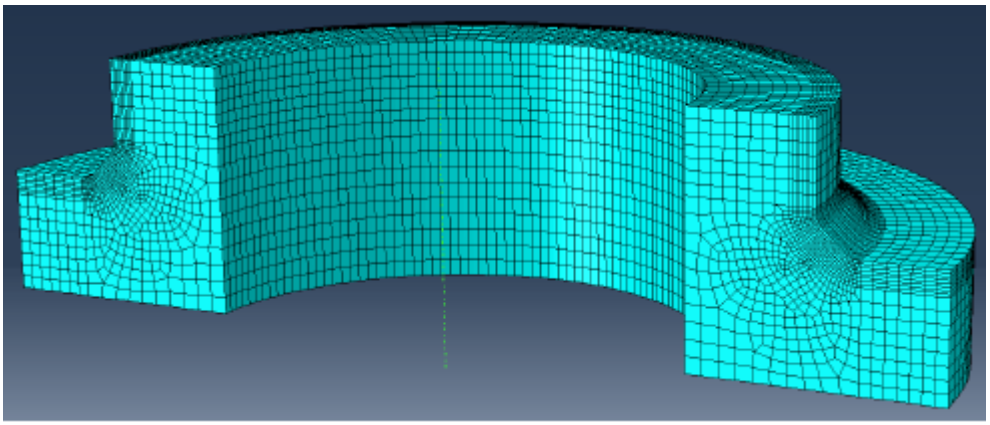

Figure 1. 3D mesh of the model problem

conformal mapping can be easily defined with the solution of two finite element solutions to a Laplace equation on the 2D domain, and hence can be readily constructed on the fly.

Results

An important conclusion of the numerical tests was that the accuracy of the finite element solution starts limiting the accuracy quite fast, thus the interpolant level can be quite low if a coarse solution is used. However, as the number of stochastic parameters increases, the benefits of a sparse grid solution become more pronounced. For example, a problem with four random variables would require 83521 FE problem evaluations with a full grid collocation method, but with a spare grid approximation one needs only 401 points to reach the same accuracy. Moreover, the method is easy to run in parallel, since the individual FE problem evaluations are independent of one another.

References

[1] J. Lehtonen Collocation method for solving stochastic elasticity problems with an uncertain domain *Master's Thesis*, Aalto University, 2015. `http://urn.fi/URN:NBN:fi:aalto-201503062021`

Proceedings of the XII Finnish Mechanics Days
R. Kouhia, J. Mäkinen, S. Pajunen and T. Saksala (Eds.)

A family of triangular shell elements

Antti H. Niemi

Department of Civil and Structural Engineering, PO Box 12100, FI-00076 AALTO, FINLAND
antti.h.niemi@aalto.fi

Summary. We introduce new type of linear triangular shell elements based on Reissner-Naghdi type shell theory. The elements incorporate five generalized degrees of freedoms per node and require the nodal normal vectors of the shell mid-surface as geometric input data. The approach enables explicit reduction of both the membrane and the transverse strains and is more transparent mathematically than the existing linear shell elements employed in industrial FEA.

Key words: shells, finite elements, locking, triangular elements

Introduction

In the finite element modelling of shell structures parametric error growth, or locking, is detected for various shell deformation types. This numerical phenomenon is harmful espcially for the standard lowest-order ($p = 1$) finite element approximation and significant mesh over-refinement is sometimes needed to compensate for the effect.

A long-standing approach to modelling of thin structures is the derivation of special low order formulations that avoid the parametric error growth. For shells, the ultimate dream element is yet to be found but there exist reduced strain formulations that work quite well on restricted class of quadrilateral meshes, at least.

In this work, we introduce and analyse a family of simple shell elements with three nodes. In particular, we compare the relative accuracy of two formulations in the family in a classical benchmark test [1] featuring different shell deformation types.

Shell theory

Let us assume that the shell body has a constant thickness t and its mid-surface is discretized using three-node triangular elements. The finite element formulations are based on a shell theory formulated in terms of local curvilinear coordinate system (x, y, ζ), where $(x, y) \in K$ are some Cartesian coordinates on each triangular element K and $\zeta \in (-t/2, t/2)$ is the coordinate along the unit normal vector $\vec{n}(x, y)$ of the shell mid-surface. The (reasonable) meshing assumption is that the elements are so small, that the assumed coordinate system can be assumed orthogonal on each element.

Kinematics

According to the standard kinematic hypothesis we assume that the displacement vector can be written in the form

$$\vec{U}(x, y, \zeta) = (u_\lambda(x, y) + \zeta\theta_\lambda(x, y))\vec{e}_\lambda(x, y) + w(x, y)\vec{n}(x, y), \tag{1}$$

where $\boldsymbol{u} = (u_1, u_2)$ are the tangential displacements of the middle surface, w is the transverse deflection, and the quantities $\boldsymbol{\theta} = (\theta_1, \theta_2)$ are the angles of rotation of the normal. The tangential displacements and the rotations follow here the tangential directions $\vec{e}_1$ and $\vec{e}_2$ along the x- and $y-$coordinate lines, respectively.

Referring to the curvilinear coordinates (x, y, ζ), the in-plane components of the linearized Green-Lagrange strain tensor can be expanded as

$$e_{\alpha\beta} \approx \varepsilon_{\alpha\beta} + \zeta\kappa_{\alpha\beta}, \quad \alpha, \beta = 1, 2, \tag{2}$$

The membrane strain tensor $\varepsilon_{\alpha\beta}$, which arises from stretching of the deformed middle surface, can be written as

$$\varepsilon_{\alpha\beta} \approx \frac{1}{2}(u_{\alpha,\beta} + u_{\beta,\alpha}) - b_{\alpha\beta}w, \tag{3}$$

where

$$b_{\alpha\beta} = -\vec{e}_\alpha \cdot \vec{n}_{,\beta}, \quad \alpha, \beta = 1, 2, \tag{4}$$

are the coefficients of the second fundamental form of the middle surface.

Introducing the cofficients of the third fundamental form of the middle surface

$$c_{\alpha\beta} = \vec{n}_{,\alpha} \cdot \vec{n}_{,\beta}, \quad \alpha, \beta = 1, 2,$$

the elastic curvature tensor $\kappa_{\alpha\beta}$, which arises from bending of the deformed middle surface, comes out as

$$\kappa_{\alpha\beta} \approx \frac{1}{2}(\theta_{\alpha,\beta} + \theta_{\beta,\alpha}) + c_{\alpha\beta}w - \frac{1}{2}(b_{\alpha\lambda}u_{\lambda,\beta} + b_{\beta\lambda}u_{\lambda,\alpha}), \quad \alpha, \beta = 1, 2 \tag{5}$$

It is possible to simplify the bending strain expressions by sacrificing their tensorial invariance. It is straightforward to verify that

$$c_{\alpha\beta} \approx b_{\alpha\lambda}b_{\lambda\beta}$$

so that we may write (5) component-wise as

$$\begin{aligned}
\kappa_{11} &\approx \underline{\theta_{1,1} + b_{12}(b_{12}w - u_{2,1})} - b_{11}\varepsilon_{11}, \\
\kappa_{22} &\approx \underline{\theta_{2,2} + b_{12}(b_{12}w - u_{1,2})} - b_{22}\varepsilon_{22}, \\
\kappa_{12} &\approx \underline{\frac{1}{2}(\theta_{1,2} + \theta_{2,1}) + \frac{b_{11}}{2}(b_{12}w - u_{1,2}) + \frac{b_{22}}{2}(b_{12}w - u_{2,1})} - \frac{b_{12}}{2}(\varepsilon_{11} + \varepsilon_{22}).
\end{aligned} \tag{6}$$

In these expressions, the contribution of the terms $b_{11}\varepsilon_{11}$, $b_{22}\varepsilon_{22}$ and $b_{12}(\varepsilon_{11} + \varepsilon_{22})$ to the maximum in-plane strains at the outer and inner surfaces of the shell is of relative order $\mathcal{O}(t/R)$ only. Therefore, the number of terms in the kinematic relations can be slightly reduced by retaining only the underlined terms in the calculations.

Finally, the transverse shear strains are defined as

$$\gamma_\alpha = 2e_{\alpha 3}. \tag{7}$$

These can be written in terms of the displacements as

$$\gamma_\alpha = \theta_\alpha + b_{\alpha\delta}u_\delta + w_{,\alpha}, \quad \alpha = 1, 2 \tag{8}$$

which completes our description of the shell kinematics.

Potential Energy Functional

The elastic strain energy functional can be written as

$$U_K(\boldsymbol{u}, w, \boldsymbol{\theta}) = \frac{1}{2}\int_K (n_{\alpha\beta}\varepsilon_{\alpha\beta} + q_\alpha\gamma_\alpha + m_{\alpha\beta}\kappa_{\alpha\beta})\, dxdy \tag{9}$$

where, assuming linearly elastic isotropic material,

$$\begin{aligned} n_{\alpha\beta} &= \frac{Et}{1-\nu^2}\left[(1-\nu)\varepsilon_{\alpha\beta} + \nu\varepsilon_{\lambda\lambda}\delta_{\alpha\beta}\right], \\ q_\alpha &= \frac{Et}{2(1+\nu)}\gamma_\alpha, \\ m_{\alpha\beta} &= \frac{Et^3}{12(1-\nu^2)}\left[(1-\nu)\kappa_{\alpha\beta} + \nu\kappa_{\lambda\lambda}\delta_{\alpha\beta}\right] \end{aligned} \tag{10}$$

correspond to the membrane forces, transverse shear forces and bending moments in static equilibrium considerations and the strains are given in terms of the displacements in (3), (8) and (5).

Similarly, the potential energy corresponding to external distributed surface forces (f_1, f_2, p) and moments (τ_1, τ_2) is

$$V_K(\boldsymbol{u}, w, \boldsymbol{\theta}) = -\int_K (f_\lambda u_\lambda + pw + \tau_\lambda\theta_\lambda)\, dxdy \tag{11}$$

and the total energy is given by the sum

$$E_K(\boldsymbol{u}, w, \boldsymbol{\theta}) = U_K(\boldsymbol{u}, w, \boldsymbol{\theta}) + V_K(\boldsymbol{u}, w, \boldsymbol{\theta}). \tag{12}$$

Finite element formulations

We assume linear triangular elements for each displacement component separately and employ a suitable skew coordinate transformation when enforcing continuity of the nodal displacements. To avoid locking when approximating bending-dominated problems, membrane and transverse shear strains must be reduced. To introduce the different methods, we denote by $\boldsymbol{F}_K = (x_K, y_K)$ the bilinear mapping of the reference triangle $\hat{K}$ onto K and by

$$\boldsymbol{J}_K = \begin{pmatrix} \dfrac{\partial x_K}{\partial \hat{x}} & \dfrac{\partial x_K}{\partial \hat{y}} \\ \dfrac{\partial y_K}{\partial \hat{x}} & \dfrac{\partial y_K}{\partial \hat{y}} \end{pmatrix}$$

the Jacobian matrix of $\boldsymbol{F}_K$. Here $(\hat{x}, \hat{y})$ are the coordinates on $\hat{K}$.

We start by defining on the reference square $\hat{K}$ the function spaces

$$\boldsymbol{S}(\hat{K}) = \{\hat{\boldsymbol{s}} = \begin{pmatrix} a + c\hat{y} \\ b + c\hat{x} \end{pmatrix} \ : \ a, b, c \in \mathbb{R}\} \tag{13}$$

and

$$\boldsymbol{M}(\hat{K}) = \{\hat{\boldsymbol{\tau}} = \begin{pmatrix} a & b \\ b & c \end{pmatrix} \ : \ a, b, c \in \mathbb{R}\} \tag{14}$$

for the reduced transverse shear strains and membrane strains, respectively. The canonical degrees of freedom associated with $\boldsymbol{S}(\hat{K})$ are

$$\hat{\boldsymbol{s}} \mapsto \int_{\hat{e}} \hat{\boldsymbol{s}}^T \hat{\boldsymbol{t}}\, d\hat{s} \text{ for every edge } \hat{e} \text{ of } \hat{K}, \tag{15}$$

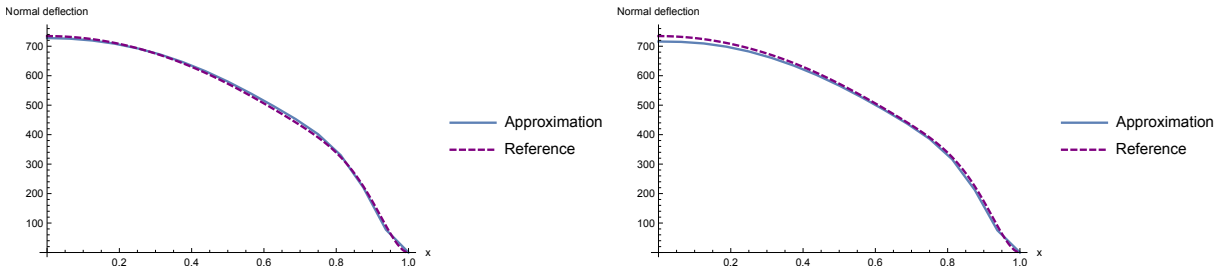

Figure 1. MITC3C vs. MITC3S in Case 1.

whereas the degrees of freedom associated with $\boldsymbol{M}(\hat{K})$ are defined as

$$\hat{\boldsymbol{\tau}} \mapsto \int_{\hat{e}} \hat{\boldsymbol{t}}^T \hat{\boldsymbol{\tau}} \hat{\boldsymbol{t}} \, d\hat{s} \text{ for every edge } \hat{e} \text{ of } \hat{K}. \tag{16}$$

The corresponding spaces associated to a general element K are then defined using covariant transformation formulas as

$$\boldsymbol{S}(K) = \{\boldsymbol{s} = \boldsymbol{J}_K^{-T} \hat{\boldsymbol{s}} \circ \boldsymbol{F}_K^{-1} = \mathcal{S}_K(\hat{\boldsymbol{s}}) \ : \ \hat{\boldsymbol{s}} \in \boldsymbol{S}(\hat{K})\} \tag{17}$$

and

$$\boldsymbol{M}(K) = \{\boldsymbol{\tau} = \boldsymbol{J}_K^{-T}(\hat{\boldsymbol{\beta}} \circ \boldsymbol{F}_K^{-1})\boldsymbol{J}_K^{-1} = \mathcal{M}_K(\hat{\boldsymbol{\tau}}) \ : \ \hat{\boldsymbol{\tau}} \in \boldsymbol{M}(\hat{K})\} \tag{18}$$

Denoting by $\boldsymbol{\Lambda}_{\hat{K}} : \boldsymbol{H}^1(\hat{K}) \to \boldsymbol{S}(\hat{K})$ and $\boldsymbol{\Pi}_{\hat{K}} : \boldsymbol{H}^1(\hat{K}) \to \boldsymbol{M}(\hat{K})$ the interpolation operators associated to the degrees of freedom (15) and (16), the corresponding projectors for a general K are defined as

$$\boldsymbol{\Pi}_K = \mathcal{M}_K \circ \boldsymbol{\Pi}_{\hat{K}} \circ \mathcal{M}_K^{-1} \text{ and } \boldsymbol{\Lambda}_K = \mathcal{S}_K \circ \boldsymbol{\Lambda}_{\hat{K}} \circ \mathcal{S}_K^{-1}$$

The transformation rule (17) guarantees that the degrees of freedom (15) and (16) are preserved on K.

We shall use the label MITC4C for the formulation for which only the transverse shear strains are projected into the space (17)

$$\boldsymbol{\gamma} \hookrightarrow \Lambda_K \boldsymbol{\gamma} \tag{19}$$

and the label MITC4S for the formulation where also the membrane strains are projected:

$$\boldsymbol{\varepsilon} \hookrightarrow \boldsymbol{\Pi}_K \boldsymbol{\varepsilon}, \quad \boldsymbol{\gamma} \hookrightarrow \Lambda_K \boldsymbol{\gamma} \tag{20}$$

when evaluating the strain energy according to (9) and (10).

Numerical results

We test the performance of the formulations in a classical benchmark test introduced in [1]. The test involves a cylindrical shell loaded by a normal pressure which is constant axially but varies trigonometrically in the axial direction. The load is self-balancing and different deformation states can be studied by varying the kinematic constraints at the ends. Fully clamped ends (Case 1) lead to a membrane-dominated deformation, free ends (Case 2) to a bending-dominated deformation and a simple support to an intermediate state.

The problem is solved on a uniform 16 by 16 triangular mesh with the two different formulations and the results are shown in Figs. 1–3. MITC3C locks in the bending-dominated case but is more accurate on the other two cases.

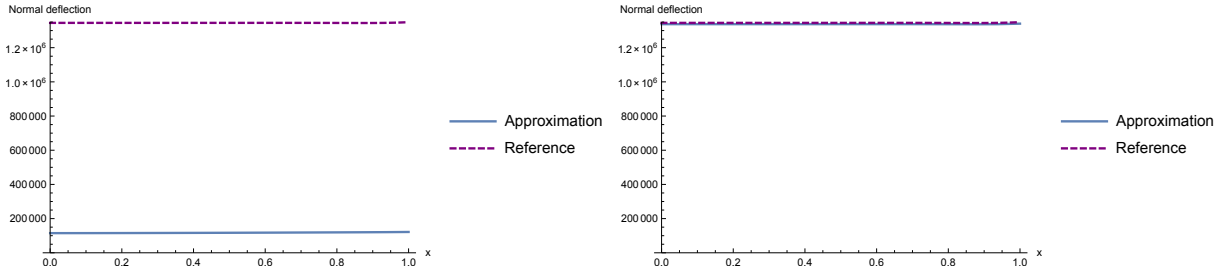

Figure 2. MITC3C vs. MITC3S in Case 2.

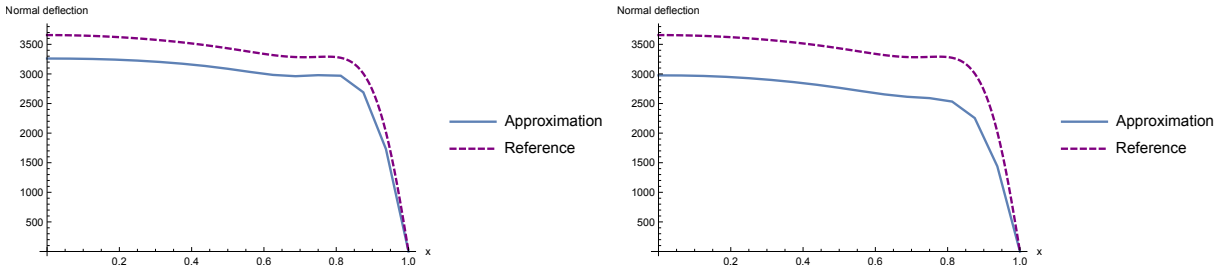

Figure 3. MITC3C vs. MITC3S in Case 3.

References

[1] Pitkäranta, J., Leino, Y., Ovaskainen, O., Piila, J. Shell deformation states and the finite element method: A benchmark study of cylindrical shells. *Computer Methods in Applied Mechanics and Engineering*, 128(1-2):81-121, 1995. doi: doi:10.1016/0045-7825(95)00870-X

Proceedings of the XII Finnish Mechanics Days
R. Kouhia, J. Mäkinen, S. Pajunen and T. Saksala (Eds.)

Exploration of different boundary conditions in the sideways falling situation in hip fracture finite element modeling

Shinya Abe[1], Antti Ylinen[2], Nathaniel NarraGirish[3], Riku Nikander[4], Jari Hyttinen[3], Reijo Kouhia[1] and Harri Sievänen[5]

[(1)]Department of Mechanical Engineering and Industrial Systems, Tampere University of Technology, P.O.Box589, FI-33101, Tampere, Finland, shinya.abe@tut.fi, reijo.kouhia@tut.fi
[(2)] FS Dynamics Finland Oy AB, Hermiankatu 1, FI-33720, Tampere, Finland, antti.ylinen@fsdynamics.fi
[(3)]Department of Electronics and Communications Engineering and BioMediTech, Tampere University of Technology, P.O.Box 692, FI-33101, Tampere, Finland, nathaniel.narragirish@tut.fi, jari.hyttinen@tut.fi
[(4)]Gerontology Research Center, Department of Health Science, University of Jyväskylä; Central Hospital of Central Finland and GeroCenter Foundation for Aging Research and Development, P.O.Box 35, FI-40014, Jyväskylä, Finland, riku.p.nikander@jyu.fi
[(5)]UKK Institute for Health Promotion Research, P.O. Box 30, FI-33501, Tampere, Finland, harri.sievanen@uta.fi

Summary. This study investigated the influence of different boundary condition settings on one sideways falling condition, an incident which often causes hip fracture in older adults. Three MRI-based FE models of a single person were created in the sideways falling condition. Results of this study showed that the presence of a fixed support at the distal end of the femoral shaft can reduce the highest stress at the fracture prone region of the femoral neck. It was also found that the location of the impact force applied can substantially alter the stress distribution pattern within the femoral neck.

Key words: finite element modeling, hip fracture, sideways falling, boundary condition

Introduction

Hip fracture is a major public health problem leading to high morbidity, mortality, and disability in older adult population. The global annual hip fracture number was estimated to 1.6 million in 2000 [7] and 7000 hip fractures were reported in Finland in 2010 [9]. Hip fractures are not only debilitating events, but also lead to substantial financial burden for societies worldwide. Its

financial burden is estimated to reach $131.5 billion by 2050 [6]. Over 90% of the hip fractures are caused by falls [5] (Figure 1).

During the two last decades, finite element (FE) method has been exploited in the hip fracture studies in order to understand the mechanism of the hip fracture. Interest has been especially in simulations where falling conditions are studied. However, literature reveals that different boundary conditions (BC) have been used in simulating even the same falling situation in terms of the fall direction. This variance in the BCs might have affected the results of FE models between studies. Recent experimental study by Choi et al. [1] addressed this issue and suggested that the BCs at the distal end of the proximal femur can influence the result. However, to the best of our knowledge, little is still known how different BCs affect the result. Therefore, the aim of this study is to elaborate this issue by creating magnetic resonance image (MRI)-based FE models of one person in one sideways falling situation with three different BCs. Specific attention was laid on following differences in the BCs; 1) presence or absence of the restrain BC such as a fixed support at the distal end of the femoral shaft, and 2) location of the impact force applied (on femoral head or on greater trochanter) (Figure 1). Mayhew et al. [10] found that the superoposterior region of the femoral neck is the hip fracture prone region due to the thin cortical bone layer. Thus, it was especially focused to study how different BC settings affect the stresses at this fracture prone region.

Materials and Methods

MR image data of proximal femur region was obtained from one adult female participant in our previous study [11]. The study protocol was approved by the Ethics Committee of the Pirkanmaa Hospital District, and a written informed consent was obtained from the participant before measurements.

The MR images were first manually segmented by delineating the periosteal and endocortical boundaries of the cortical bone using a touch panel (Wacom Tablet Clintiq 12WX, Wacom Technology Corp., Vancouver, WA.) with a medical image processing software the ITK-SNAP[16] (www.itksnap.org). The segmented bone geometry was then smoothed in MeshLab (Visual Computing Lab – ISTI – CNR, http://meshlab.sourceforge.net/) using smoothing method described by Taubin.[14] This method was chosen to avoid shrinkage of the geometry inherent in the smoothing. The smoothed proximal femur geometry consisted of cortical bone and trabecular bone, the latter denoting the inside volume of the endocortical bone layer. Thus, although the trabecular bone actually forms porous structure, the trabecular bone geometry was modeled as the non-porous homogeneous material. The smoothed proximal femur geometry was imported into SolidWorks (SolidWorks Corp., Waltham, MA.) for the 3D solid body generation.

The 3D solid body geometry of the proximal femur was imported into ANSYS 15.0 (ANSYS Inc., Houston, PA.) for the FE meshing and model analysis. A 10-noded tetrahedral finite element was used to mesh the cortical and trabecular geometries of the proximal femur. Average element edge size was set for 2mm for the entire geometry. A model consisted of approximately 190000 elements and 300000 nodes. The cortical and trabecular bone of proximal femur were modeled as homogeneous isotropic, linear elastic materials. The Young's modulus of 17GPa[4,8,13] and 1500MPa[4,13] were set for the cortical and trabecular bone, respectively. Poisson's ratio was assumed as 0.33[4,8,13] for both bone types. To simulate the sideways falling, the most commonly used force direction was chosen from the experimental studies conducted by Pinilla et al.[12] and Courtney et al.[2,3] The femoral shaft was tilted at 10° with respect to the ground and the femoral neck was internally rotated by 15°[2,3,12] (Figure1). A simulated impact force of magnitude of 5000N was applied.

In total, three FE models (A, B, and C) were created in order to address two research questions; 1) the effect of the presence or absence of the restrain BC at the distal end of the femoral shaft on the femoral neck stress distribution, and 2) the corresponding effect of location of the impact force applied (on femoral head or on greater trochanter). Figure 1 shows difference in the BCs in three FE models. Similar to the previous study conducted by Verhulp et al.[15], the impact force was equally distributed to the surface nodes of the femoral head (model A and B) /greater trochanter (model C) within 5mm layer perpendicular to the force. Also, surface nodes of the lateral side of the femoral head (model C) /greater trochanter (model A and B) in 5mm layer perpendicular to the force were restrained only in the direction of the force. For the model B, the face of the distal end was fully restrained (fixed support). The von Mises stresses were calculated from the FE models and stress distribution on the proximal femur in anterior and posterior views were plotted in order to analyze the result qualitatively.

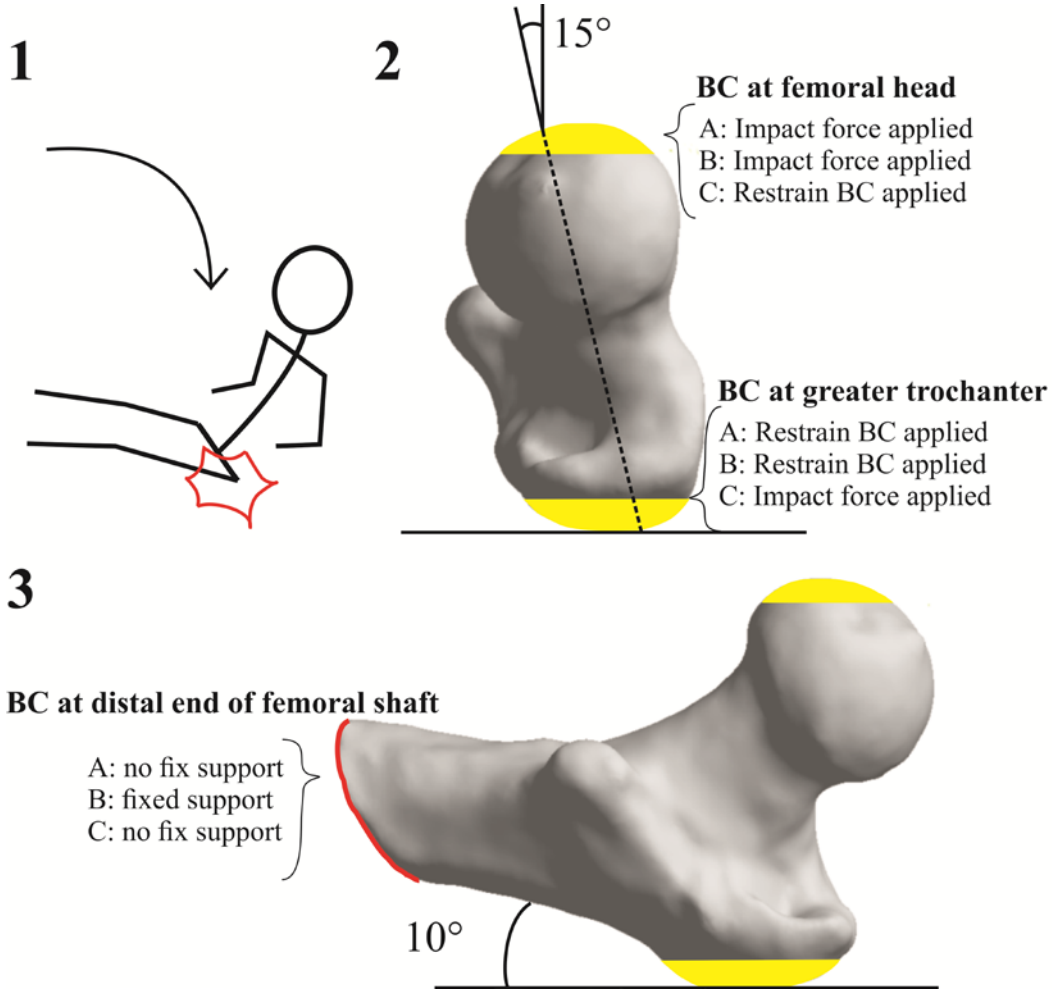

Figure 1. Sideways falling, force direction, and different BC descriptions in three models. *(1)* The sideways falling condition. *(2)* The force direction in coronal view, the BCs for model A, B, and C for the location of the impact force applied and restraining BCs. *(3)* The force direction in sagittal view and BC at the distal end of femoral shaft represented by red line which represents the face where fixed support was applied in model B. Yellow areas in the picture 2 and 3 represent the surface nodes where the BCs were applied.

Results

Stress distributions of the three models were plotted in Figure 2. By comparing the model A with the model B, the highest stresses at superoposterior region of the distal femoral neck site get decreased from 144 MPa in the model A to 110 MPa in the model B. Otherwise, the stress distributions between models A and B seemed to be quite similar. On the other hand, by comparing the model A with the model C, stress distribution pattern changed substantially. The highest 144 MPa stress at superoposterior region observed in the model A was reduced considerably down to 65 MPa in the model C. Furthermore, relatively low stress at inferoanterior region of the proximal femoral neck site in the model A (about 30 MPa) was increased drastically to about 120 MPa in the model C.

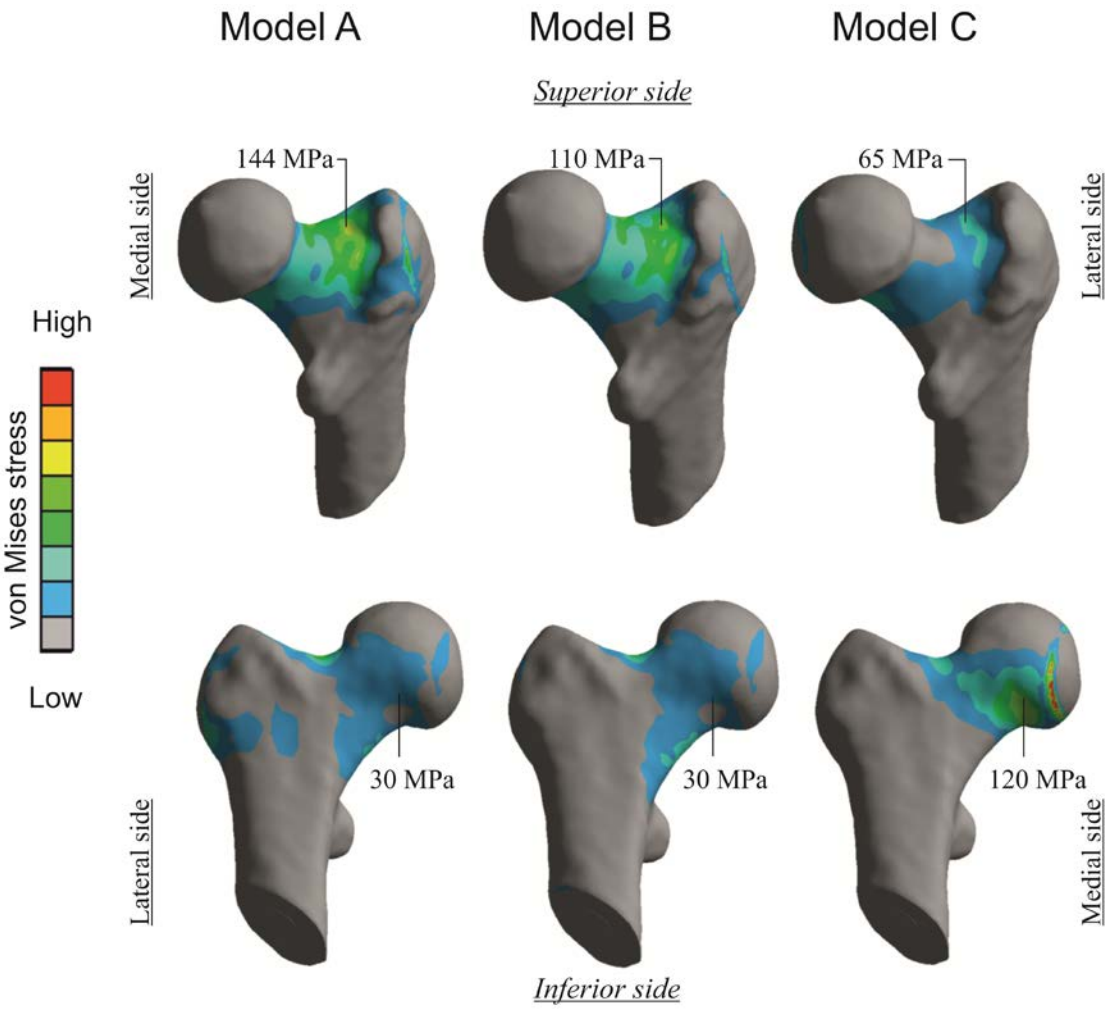

Figure 2. Stress distributions in the proximal femurs in the sideways falling condition in three models A, B, and C. Top three models are stress distributions in posterior view and are slightly rotated superiorly in order to see stress distribution at superoposterior region of the femoral neck more clearly. Lower three are stress distributions in anterior view and were also slightly rotated inferiorly in order to compare the high stress values at inferoanterior region of the proximal femoral neck site from model C with other two models' values. Vertical coloured bar on the left represents the von Mises stress magnitude.

Discussion

In this study, three proximal femur FE models of a same person were created in order to investigate how different BCs in the same sideways falling situation modify the stress distribution, especially at hip fracture prone region such as superoposterior region of the femoral neck. Results from the models A and B showed that presence of the fixed support (in model B) can reduce the highest stress at the superoposterior region. This was mostly likely attributed to decrease in bending of the femoral neck due to the fixed support at the distal end of the femoral shaft. On the other hand, the results from the models A and C showed changing the location of the impact force applied can alter the stress distribution pattern more remarkably if the distal end was not fixed. High stress region seems to shift from superoposterior region of the distal femoral neck site to inferoanterior region of the proximal femoral neck site if the impact force was applied on the greater trochanter instead of femoral head.

Boundary conditions at the distal end of the femoral shaft reflect the position of the knee at the impact from the fall. According to Choi et al. [1], absence of the restrain BCs at the distal end represents that the knee is in the air at the impact while its presence represents that the knee is in contact with ground. In the majority of the previous proximal femur FE modeling studies, the restrain BCs were applied at the distal end of the femoral shaft. In those studies, the mechanical testing was also performed for the validation of the FE models, and the distal end of the femoral shaft needed to be restrained to perform the test successfully. Thus, restrain BC was applied at the distal end to match with the mechanical test setting. The presence of the restrain BC seems to have an effect to reduce the highest stress at this fracture-prone region. This implies that the knee position in the fall may be another factor contributing to the fracture.

The impact force was commonly applied on the femoral head in the most of previous proximal femur FE studies. This was also due to the mechanical test setting. However, in the real falling situation, undoubtedly lateral side of the greater trochanter experiences the impact force. Indeed, the present study showed that stress distribution pattern changed drastically if the impact force was applied on the greater trochanter. This result questions the validity of using the femoral head as the location of the impact force applied. The result also insists that other regions in addition to the superoposterior region may have high fracture risk in a real falling situation.

In conclusion, the present FE modeling study demonstrated that difference in BCs in a same sideways falling situation can alter the stress distribution patterns. Therefore, in the future hip fracture FE modeling studies, it is necessary to give a rationale for why specific BCs were chosen and what the meaning of chosen BCs is in terms of life falling situation.

References

[1] W.J. Choi, P.A. Cripton, & S.N. Robinovitch. Effects of hip abductor muscle forces and knee boundary conditions on femoral neck stresses during simulated falls. *Osteoporos Int*, 26(1):291-301, 2015. doi: 10.1007/s00198-014-2812-4

[2] A.C. Courtney, E.F. Wachtel,, E.R. Myers, & W.C. Hayes. Effects of loading rate on strength of the proximal femur. *Calcif Tissue Int*, 55(1):53-58, 1994.

[3] A.C. Courtney, E.F. Wachtel, E.R. Myers, & W.C. Hayes. Age-related reductions in the strength of the femur tested in a fall-loading configuration. *J Bone Joint Surg Am*, 77(3):387-395, 1995.

[4] G.N. Duda, M. Heller, J. Albinger, O. Schulz, E. Schneider, & L. Claes. Influence of muscle forces on femoral strain distribution. *J Biomech*, 31(9):841-846, 1998.

[5] J.A. Grisso, J.L. Kelsey, B.L. Strom, G.Y. Chiu, G. Maislin, L.A. O'Brien, A. Hoffman, & F. Kaplan. Risk factors for falls as a cause of hip fracture in women. The Northeast Hip Fracture Study Group. *N Engl J Med*, 324(19):1326-1331, 1991.
[6] O. Johnell. The Socioeconomic Burden of Fractures: Today and in the 21st Century. *Am J Med*, 103Suppl 2A:S20-S25, 1997.
[7] O. Johnell, & J.A. Kanis. An estimate of the worldwide prevalence and disability associated with osteoporotic fractures. *Oseoporos Int*, 17(12): 1726-1733, 2006.
[8] M. Lengsfeld, J. Kaminsky, B. Merz, & R.P. Franke. Sensitivity of femoral strain pattern analyses to resultant and muscle forces at the hip joint. *Med Eng Phys*, 18(1):70-78, 1996.
[9] E. Lönnroos, I. Kiviranta, & A. Hartikainen. Hip fracture management and outcomes. *European Geriatric Medicine*, 1: 101-103, 2010.
[10] P.M. Mayhew, C.D. Thomas, J.G. Clement, N. Loveridge, T.J. Beck, W. Bonfield, C.J. Burgoyne, & J. Reeve. Relation between age, femoral neck cortical stability, and hip fracture risk. *Lancet*, 366(9480):129-135, 2005.
[11] R. Nikander, P. Kannus, P. Dastidar, M. Hannula, L. Harrison, T. Cervinka, N.G. Narra, R. Aktour, T. Arola, H. Eskola, S. Soimakallio, A. Heinonen, J. Hyttinen, & H. Sievänen. Targeted exercises against hip fragility. *Osteoporos Int*, 20(8):1321-1328, 2009. doi: 10.1007/s00198-008-0785-x
[12] T.P. Pinilla, K.C. Boardman, M.L. Bouxsein, E.R. Myers, & W.C. Hayes. Impact direction from a fall influences the failure load of the proximal femur as much as age-related bone loss. *Calcif Tissue Int*, 58(4):231-235, 1996.
[13] K. Polgár, H.S. Gill, M. Viceconti, D.W. Murray, & J.J. O'Connor. Strain distribution within the human femur due to physiological and simplified loading: finite element analysis using the muscle standardized femur model. *Proc Inst Mech Eng H*, 217(3):173-189, 2003.
[14] G. Taubin. Curve and surface smoothing without shrinkage. *Fifth International Conference on Computer Vision*; 1995 June 20-23;Cambridge Massachusetts, USA. Washington, DC, USA: *IEEE Computer Society Press*; 1995.p.852-857.
[15] E. Verhulp, B. van Rietbergen, & R. Huiskes. Load distribution in the healthy and osteoporotic human proximal femur during a fall to the side. *Bone*, 42(1):30-35, 2008.
[16] P.A. Yushkevich, J. Piven, H.C. Hazlett, R.G. Smith, S. Ho, J.C. Gee, & G. Gerig. User-guided 3D active contour segmentation of anatomical structures: significantly improved efficiency and reliability. *Neuroimage*, 31(3):1116-1128, 2006.

Suomen XII mekaniikkapäivien esitelmät
R. Kouhia, J. Mäkinen, S. Pajunen and T. Saksala (toim.)

Suunnittelutyökalu putkiristikoiden mitoitukseen ja optimointiin

Kristo Mela[1], Mikko Alinikula[2], Teemu Tiainen[1], Markku Heinisuo[1] ja Ilkka Sorsa[3]

(1)Rakennustekniikan laitos, Tampereen teknillinen yliopisto, PL 600 33101 Tampere
kristo.mela@tut.fi, teemu.tiainen@tut.fi, markku.heinisuo@tut.fi
(2)SUBNIC Oy, Pikkulinnuntie 12, 02650 Espoo, subnic@kolumbus.fi
(3)Ruukki Construction Oy, ilkka.sorsa@ruukki.com

Tiivistelmä. Tässä työssä esitellään laskennallinen työkalu teräksestä valmistettavien kattoristikoiden suunnitteluun ja optimointiin. Ohjelman tavoitteena on lyhentää merkittävästi ristikoiden suunnitteluun kuluvaa aikaa ja tuottaa rakennesuunnittelijalle taloudellisempia -jopa optimaalisia- ratkaisuja. Suunnittelija syöttää tarvittavat lähtötiedot, ja ohjelma etsii automaattisesti painon tai kokonaiskustannusten mielessä parhaan ratkaisun. Optimoinnilla määritetään sauvojen optimaaliset profiilit. Lisäksi haluttaessa voidaan optimoida uumasauvojen lukumäärää ja sijoittelua. Ohjelmaa käytetään verkkoselaimen avulla, ja optimointi sekä muu laskenta suoritetaan palvelinkoneella. Sauvojen ja liitosten kestävyyden tarkastus tehdään eurokoodin mukaisesti. Laskennan lopputuloksena saadaan siten ristikko, joka toteuttaa eurokoodin vaatimukset.

Avainsanat: Ristikon optimointi, Suunnittelutyökalu

Johdanto

Matemaattista optimointiteoriaa on sovellettu kantavien rakenteiden suunnitteluun jo yli puolen vuosisadan ajan. Tutkimusalan alkuajoista asti sauva- ja palkkirakenteet ovat olleet keskeisessä asemassa niin sovellutuskohteina kuin teoreettisten tarkastelujen perustana. Erityisesti ristikkorakenteiden optimointia on tutkittu paljon, ja keskeisimmät teoreettiset kysymykset on avattu kirjallisuudessa [7].

Lähes poikkeuksetta ristikoita käsitellään nivelpäisten sauvojen joukkona, jossa sauvojen keskilinjat kohtaavat ristikon solmupisteissä. Kuormitukset kohdistuvat vain solmupisteisiin, jolloin sauvojen ainoana rasituksena on normaalivoima. Tämä johtaa tehokkaasti ratkaistavissa oleviin optimointitehtäviin, joissa usein minimoidaan rakenteen painoa siten, että jokainen sauva kestää siihen syntyvät rasitukset eri kuormitustapauksissa.

Tässä työssä tarkastellaan teräksestä valmistettavien kattoristikoiden optimointia Eurokoodi 3:n mukaan. Tähän tehtävään edellä kuvattu malli on riittämätön. Eurokoodin mukaan paarteet tulee mallintaa jatkuvina palkkeina, joihin kohdistuvasta poikittaisesta kuormituksesta aiheutuva taivutus tulee ottaa rakenneanalyysissä huomioon. Lisäksi liitosten tarkastelussa on sovellettava ristikon tarkkaa geometriaa, jossa uumasauvojen keskilinjat eivät tyypillisesti kohtaa paarteiden keskilinjoilla. Tämä epäkeskisyys on otettava huomioon niin rakennenalyysissä kuin sauvojen ja liitosten mitoituksessa.

Eurokoodin asettamien vaatimusten lisäksi suunnittelijan on varmistettava, että valitut sauvaprofiilit löytyvät terästoimittajan valikoimasta. Tämä johtaa automaattisesti diskreettiin optimointitehtävään, jonka ratkaiseminen on tunnetusti vaikeaa. Nämä käytännön seikat johtavat siihen, että tavanomaiset optimointikirjallisuudessa esitetyt tehtävänasettelut ja ratkaisutavat

eivät ole löytäneet paikkaansa rakennesuunnittelijan työkaluvalikoimasta. Viimeaikainen tutkimus on kuitenkin osoittanut, että eurokoodin mukaiset sauvojen kestävyysehdot ja ristikon valmistukseen liittyvät tekijät voidaan liittää perinteiseen ristikkomalliin suurelta osin uudenlaisen formuloinnin avulla. Tämän tutkimuksen pohjalta Tampereen teknillisen yliopiston Metallirakentamisen tutkimuskeskus on kehittänyt Ruukki Constructionin tilauksesta rakennesuunnittelijalle soveltuvan ohjelmistotyökalun kattoristikoiden optimointiin. Työkalu on toteuttanut SUBNIC Oy. Tässä artikkelissa esitellään ohjelman pääpiirteet ja toteutus sekä siihen liittyvää taustatutkimusta. Ohjelman toimintaa havainnollistetaan esimerkkitehtävän avulla.

Optimointitehtävän formulointi

Optimoinnin lähtökohtana on tehtävänasettelu, joka ratkaisee, onko ongelma toisaalta ratkaistavissa ja toisaalta onko löydetty ratkaisu käyttökelpoinen. Tehtävän ratkaistavuuteen vaikuttavat suunnittelumuuttujien ja rajoitusehtojen lukumäärä sekä tehtävässä esiintyvien funktioiden matemaattiset ominaisuudet (esim. lineaarisuus vs. epälineaarisuus). Jotta ratkaisu olisi käyttökelpoinen, on tehtävään sisällytettävä mahdollisimman paljon rajoitusehdoiksi niitä rakenteen kestävyyteen ja valmistettavuuteen liittyviä seikkoja, jotka suunnittelijan on otettava huomioon. Jos jokin suunnittelijan kannalta oleellinen vaatimus puuttuu rajoitusehdoista, on mahdollista, että optimoinnilla saatua ratkaisua on muokattava jälkikäteen.

Ristikoiden optimoinnissa on löydettävä valmistajan valikoimasta optimaaliset profiilit ristikon sauvoille (mitoitusoptimointi). Lisäksi voidaan optimoida sauvojen ja solmujen lukumäärää sekä sauvojen sijoittelua (topologian optimointi). Kehitetyssä suunnittelutyökalussa käyttäjä voi valita joko mitoitusoptimoinnin haluamalleen ristikkotyypille, tai laskennallisesti raskaamman topologian optimoinnin, jolla päästään tavanomaisesta poikkeaviin sauvoitteluihin.

Tässä työssä optimointitehtävä perustuu ristikoille kehitettyyn ns. sekalukuformulointiin [5], jossa rakenneanalyysin yhtälöt kirjoitetaan osaksi rajoitusehtoja, ja sauvojen normaalivoimat sekä solmusiirtymät otetaan optimointiin muuttujiksi. Profiilien valinta sekä sauvojen ja solmujen olemassaolon määritys hoidetaan binäärimuuttujilla. Formuloinnin yleisessä muodossa rajoitusehtoihin kuuluvat sauvojen lujuuden ja stabiilisuuden vaatimukset eurokoodin mukaan, sekä topologian optimoinnissa ongelmia tuottanut ristikon kinemaattisen stabiilisuuden vaatimus. Kuormitukset voivat olla solmuihin kohdistuvia pistekuormia tai jakautuneita viivakuormia, jotka muunnetaan ekvivalenttisiksi solmuvoimiksi. Kohdefunktiona on oletusarvoisesti ristikon paino. Formulointi johtaa lineaariseen sekalukutehtävään (*mixed-integer linear programming*), josta tulee kuormitustapausten, profiilivaihtoehtojen ja ristikon sauvojen lukumäärän kasvaessa nopeasti suuri. Tehtävälle voidaan kuitenkin löytää jopa globaali optimi, sillä viime aikoina sekalukutehtävien ratkaisuohjelmat ovat kehittyneet voimakkaasti [1].

Kattoristikoita varten formulointia on laajennettu sisältämään edellä kuvailtuja eurokoodista peräisin olevia ehtoja mahdollisuuksien mukaan siten, että tehtävä säilyy lineaarisena.

Paarteiden taivutus otetaan huomioon arvioimalla jokaisen yläpaarteen sauvan taivutusmomentiksi $M_{\mathrm{Ed}} = qL^2/10$, missä q on sauvaan vaikuttava tasainen kuorma ja L on sauvan pituus. Tätä momentin vakioarvoa käyttäen saadaan tehtävään sisällytettyä Eurokoodi 3:n momentin ja normaalivoiman yhteisvaikutuskaavat [2, kohdat 6.2.9.1 ja 6.3.3]. Alapaarteella $M_{\mathrm{Ed}} = qL^2/20$.

Liitosten kestävyyden tarkastaminen ei sisälly rajoitusehtoihin. Sen sijaan lineaariseen tehtävänasetteluun saadaan liitoksen sauvojen sivusuhteille määritetyt ehdot [3, Taulukko 7.8].

Topologian optimoinnissa on varmistettava, että liitosten sauvoittelu on eurokoodin mukainen. Binäärimuuttujia koskevin rajoitusehdoin voidaan pakottaa liitokset K-, KT-, tai N-tyyppisiksi. Lisäksi liitoksen vierekkäisten uumasauvojen välinen kulma on oltava hitsattavuuden vuoksi vähintään 30°. Topologian optimoinnissa estetään myös risteävät uumasauvat.

KT-liitoksissa vertikaali sijoitetaan vedettyyn diagonaaliin. Näin menetellen liitoksen epäkeskisyys saadaan huomattavasti pienemmäksi kuin jos vertikaali tulisi diagonaalien väliin. Tällöin on kuitenkin varmistettava, että vertikaalin ulkomitat eivät ylitä diagonaalien ulkomittoja, ts.

että vertikaali todella saadaan kiinnitettyä diagonaalin pintaan.

Painon lisäksi kohdefunktioksi voidaan valita ristikon kokonaiskustannukset. Tätä varten on kehitetty erityinen kustannuslaskentatyökalu, joka pohjautuu aiempaan tutkimukseen [4]. Kustannustiedot perustuvat todelliseen valmistusprosessiin. Myös kustannusfunktio on mahdollista esittää binäärimuuttujien lineaarisena funktiona.

Suunnittelutyökalun toiminta

Käyttäjän näkökulma

Ohjelman lähtökohtana on, että käyttäjän ei tarvitse tuntea optimointiteoriaa lainkaan. Optimointi tuodaan luontevaksi osaksi suunnittelutyötä siten, että käyttäjä kokoaa tehtävää samaan tapaan kuin hän valmistelisi ristikkoa rakenneanalyysiä varten. Rakenteen analysoinnin sijaan suoritetaan optimointi, jonka etenemistä käyttäjä voi seurata ruudulta.

Optimointia varten käyttäjä siis antaa joukon ristikon lähtötietoja, joihon kuuluvat mm. jänneväli, ristikon korkeus, yläpaarteen kaltevuus, kuormitukset sekä paarteissa ja uumasauvoissa käytetyt teräslaadut. Näiden tietojen lisäksi käyttäjä voi valita haluamansa ristikkotyypin (K-, KT- tai N-ristikko) tai antaa ohjelman etsiä optimaalinen sauvoittelu topologian optimoinnin keinoin. Valittavissa olevien profiilien valikoima sisältää SSAB:n neliöputket.

Ohjelmaa käytetään verkkoselaimen avulla (kuva 1). Käyttäjä kirjautuu järjestelmään tunnuksineen ja asettaa optimointiin tarvittavat lähtötiedot. Varsinainen laskenta tehdään palvelinkoneella. Käyttäjän ei siis tarvitse asentaa mitään ohjelmia omalle koneelleen käyttääkseen suunnitelutyökalua.

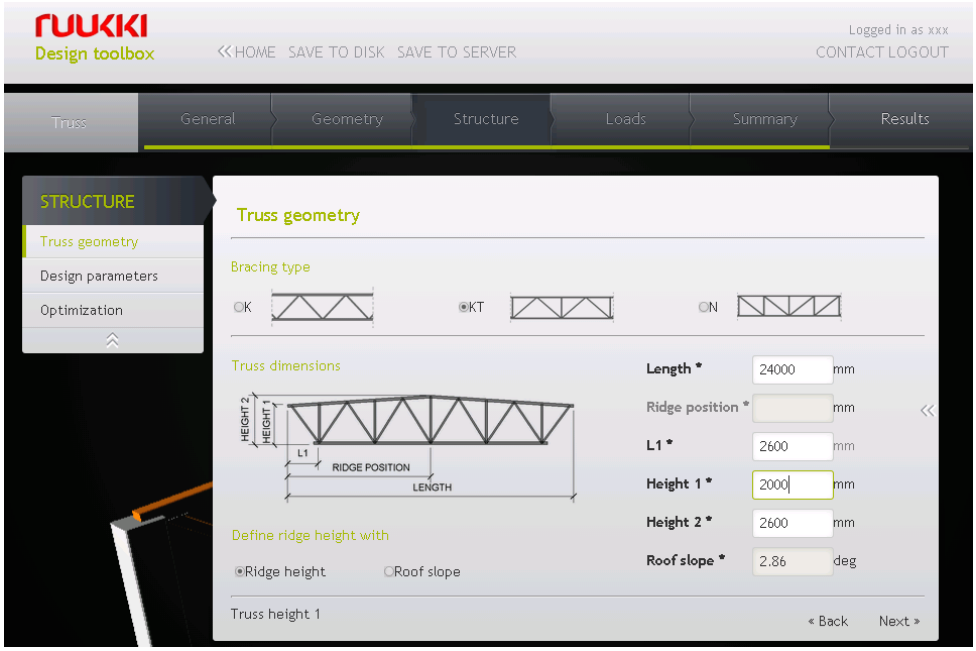

Kuva 1: Suunnittelutyökalun käyttöliittymä. Lähtötietojen antaminen etenee suoraviivaisesti vaiheittain.

Tekninen toteutus

Ohjelman sisäinen rakenne on esitetty kuvassa 2. Käyttäjän antamien tietojen pohjalta luodaan optimointia varten ns. perusrakenne, joka sisältää kaikki mahdolliset sauvat ja solmut. Perusrakenteen pohjalta aloitetaan joko topologian optimointi tai mitoitusoptimointi, jos käyttäjä on valinnut ristikkotyypin.

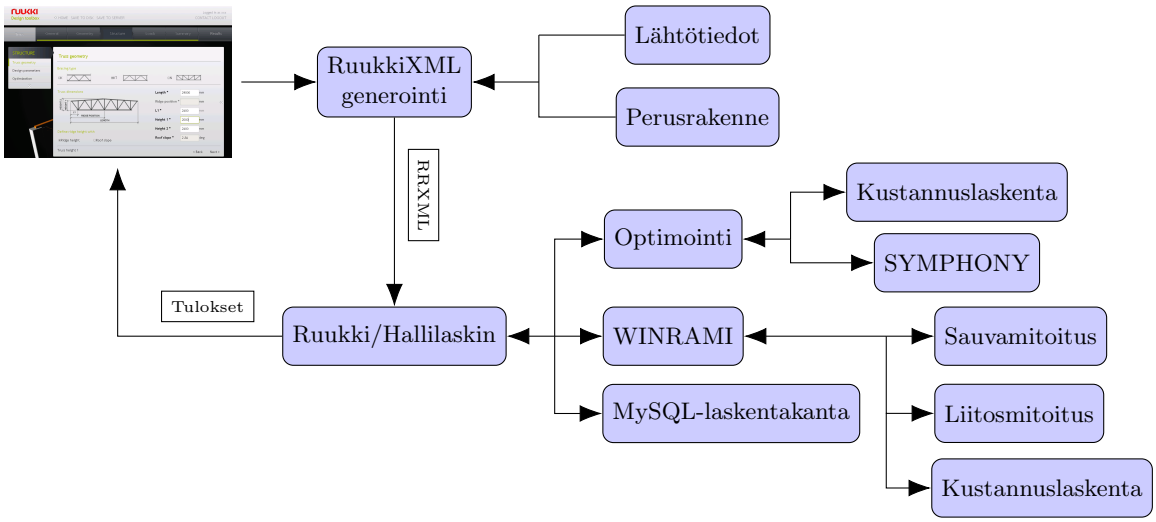

Kuva 2: Suunnittelutyökalun sisäinen rakenne. Nuolet kuvaavat tiedonsiirtoa ohjelman osien välillä.

Perusrakenteen tiedot tallennetaan rakenteisena dokumenttina XML-muodossa. Tämä dokumentti kytkeytyy yleisempään hallirakennuksiin soveltuvaan laskentaohjelmaan, joka hallinnoi optimointia ja muuta rakenteeseen liittyvää laskentaa. Tämä ohjelma myös välittää tulokset takaisin käyttäjälle.

Perusrakenteen XML-kuvauksen pohjalta generoidaan tarvittava määrä optimointiobjekteja, joissa määritellään ratkaistavat optimointitehtävät. Yhdestä perusrakenteesta voidaan generoida useita optimointitehtäviä valitsemalla vain osa sauvoista mukaan optimointiin. Näin menetelläänkin esimerkiksi mitoitusoptimoinnissa, jossa käyttäjä on valinnut ristikkotyypin.

Muodostetut optimointitehtävät ratkaistaan valitulla optimointiohjelmalla. Tässä käytetään avoimen lähdekoodin ohjelmaa SYMPHONY (versio 5.5.7) [6]. Perusrakenteen pohjalta muodostetaan optimointitehtävän kerroinmatriisit ja -vektorit, jotka viedään rajapintaa käyttäen SYMPHONY:lle. Toteutus on tehty siten, että optimointiohjelma voidaan myöhemmin vaihtaa.

Kun kaikki optimointiajot on suoritettu, halliohjelma laskee kullekin optimointiobjektille kohdefunktion arvon. Jatkokäsittelyyn valitaan se objekti, joka tuottaa parhaan arvon kohdefunktiolle. Valitulta objektilta kerätään tämän jälkeen tarvittavat tiedot WINRAMI-mallin pystyttämistä varten.

WINRAMI:n avulla tarkastetaan vielä, että ristikko todella toteuttaa eurokoodin vaatimukset. Laskentamallissa paarteet ovat jatkuvia palkkeja, joihin uumasauvat kiinnittyvät nivelellisesti. Liitoksia käsitellään omina objekteinaan. Niiden geometria muodostetaan siten, että epäkeskisyydet minimoituvat.

Kun rakenne on mallinnettu, lasketaan voimasuureet ja tarkastetaan sauvojen ja liitosten kestävyys. Koska nyt liitokset ovat mukana, voi käydä niin, että joidenkin sauvojen kestävyys ei riitä. Tällöin sauvan profiilia kasvatetaan seinämänpaksuutta lisäämällä. Jos profiileja joudutaan muuttamaan, lasketaan voimasuureet uudelleen. Vastaavasti, jos liitosten kestävyysrajat ylittyvät, muokataan mallia. Murtumistavasta riippuen liitokseen voidaan lisätä vahvikelevyjä, tai uumasauvojen seinämänpaksuutta kasvattaa. Muokkailujen jälkeen voimasuureet lasketaan uudelleen kuten edellä.

Jos käyttäjä on määritellyt ristikolle paloluokan lasketaan seuraavaksi sauvojen kriittiset lämpötilat palosuojausta varten.

Viimeisenä laskentavaiheena lasketaan lopullisen ristikon kokonaiskustannus käyttäjän kustannusmäärittelyn mukaan kustannuslaskimien liittymien avulla.

WINRAMI:sta noudetaan mallin tiedot WINRAMI:n tarjoaman liittymän avulla tuloksien palauttamista varten ja lopuksi WINRAMI-malli tallennetaan serverille.

Optimointien tulokset kootaan MySQL-tietokantaan, josta voidaan myöhemmin hakea erilaisia laskentatietoja ja mm. laskennassa generoituja WINRAMI-malleja. Eri ajoissa kertynyttä tietoa voidaan myöhemmin hyödyntää monin tavoin. Esimerkiksi, jos havaitaan, että optimoitavaksi on tulossa tietyillä lähtötiedoilla varustettu ristikko, joka on jo aiemmin optimoitu, saadaan tulos suoraan poimittua tietokannasta.

Esimerkki

Ristikkotyökalun käyttöä havainnollistetaan esimerkin avulla. Tarkasteltavana on 24 m jännevälin harjaristikko, jonka geometria on esitetty kuvassa 3. Ristikkoa kuormittavat oman painon lisäksi kattorakenteen paino ($0.8\,\mathrm{kN/m^2}$), lumi (arvo maassa $2.5\,\mathrm{kN/m^2}$) ja tuuli ($0.6\,\mathrm{kN/m^2}$). Rakennuksen kehäjako on 5 m. Näistä kuormista muodostetaan kuormitusyhdistelyt eurokoodin mukaisesti. Kaikkiaan yhdistelyjä tulee 8 kappaletta, joista optimointiin valikoituu kaksi (symmetrinen ja epäsymmetrinen lumikuorma). WINRAMI:ssa tarkastetaan optimoinnin jälkeen, että sauvojen ja liitosten kestävyydet toteutuvat kaikissa 8:ssa kuormitusyhdistelyssä.

Kaikille sauvoille käytetään terästä S420, ja profiilivalikoimaksi otetaan Ruukin neliöputket, jotka kuuluvat poikkileikkausluokkiin 1 tai 2.

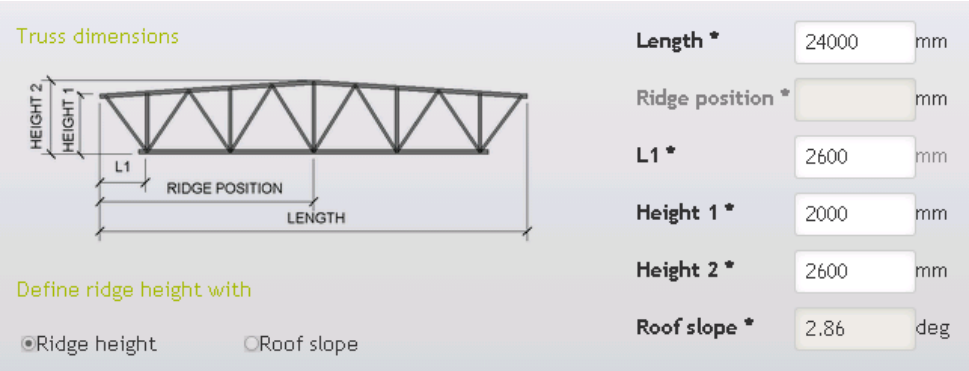

Kuva 3: Esimerkin ristikon geometriatiedot.

Optimoinnilla haetaan minimipainoratkaisua. Ristikko voi olla K- tai KT-tyyppinen. Kaikkaan suoritetaan neljä mitoitusoptimointitehtävää, kaksi kummallekin ristikkotyypille. Molemmille tyypeille on tarjolla ”harva” ja ”tiheä” topologia, joissa K- tai KT-liitosten lukumäärä muuttuu. Ristikko pakotetaan symmetriseksi harjakohdan suhteen.

Ohjelma suorittaa neljä mitoitusoptimointia ja WINRAMI-tarkastuksen parhaalle ristikolle yhteensä 85 sekunnissa. Minimipainoksi saadaan 1180 kg. Yläpaarteen käyttöaste on 99.0 %, ja alapaarteen käyttöasteeksi saadaan 92.2 %. Uumasauvojen käyttöasteet vaihtelevat 22 % ja 75 % välillä. Keskimmäisen vertikaalin käyttöasteeksi jää 2.0 %. Liitoksissa päästään enimmillään 94.4 % käyttöasteeseen. Tuen sekä alapaarteen ensimmäistä liitosta on vahvistettu paarteen pintaan hitsattavalla levyllä. Ohjelma antaa ristikon kustannuksiksi 2158 €. Ristikon topologia on esitetty kuvassa 4a.

Kun minimoitavaksi suureeksi valitaan ristikon kustannukset, suorittaa ohjelma optimoinnit ja WINRAMI-tarkastuksen 95 sekunnissa. Nyt kustannuksiksi saadaan 2106 €, ja ristikon paino on 1332 kg. Minimipainoristikkoon nähden kustannukset ovat 2.4 % pienemmät, ja painoa on 11.4 % enemmän. Tähän on syynä se, että minimikustannusristikossa on vähemmän uumasauvoja (kuva 4b), jolloin työkustannukset pienentyvät selvästi. Toisaalta yläpaarteen profiilikoon kasvattaminen on johtanut painon nousuun. Tulokset osoittavat, että ristikkorakenteissa kannattaa pyrkiä kokonaiskustannusten minimointiin painon minimoinnin sijaan, kun valmistusprosessi on hyvin tunnettu.

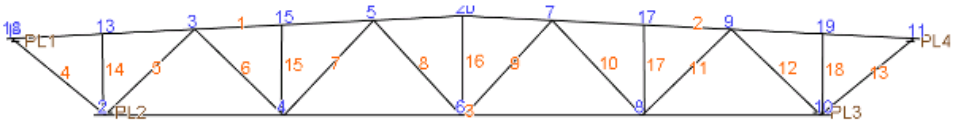

(a) Minimipainoristikko.

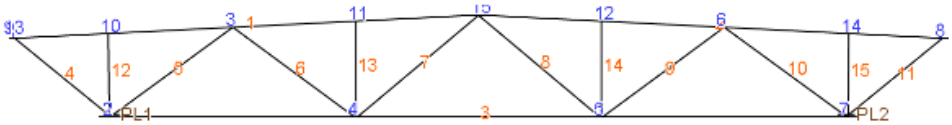

(b) Minimikustannusristikko.

Kuva 4: Optimaaliset ristikot.

Johtopäätökset

Tässä työssä esitetty suunnittelutyökalu on seurausta pitkäjänteisestä perustutkimuksesta ja avarakatseisesta näkemyksestä tuoda optimointi rakennesuunnittelijan päivittäiseen käyttöön. Liittämällä insinööriosaaminen matemaattiseen optimointiteoriaan on mahdollista kehittää helppokäyttöisiä ja tehokkaita välineitä, joilla suunnittelutyön osittaisen automatisoinnin seurauksena päästään nopeammin aiempaa parempiin tuloksiin.

Optimoitavan kohteen erityispiirteiden tuntemisen kautta voidaan täydentää optimoinnissa käytetyn tehtävänasettelun puutteita. Esimerkiksi tässä esitellyssä ohjelmistossa liitosten kestävyys ei sisältynyt optimointiin, joten mahdollinen liitosten kestävyyden ylittyminen hoidettiin jälkikäsittelynä vahvikelevyjen ja profiilien seinämänvahvuuksien kasvattamisen avulla. Näin optimoinnista saadaan hyvin käyttökelpoinen työkalu, vaikka tehtävänasettelusta puuttuisikin joitain suunnittelunäkökulmia.

Ohjelman jatkokehitys voidaan esimerkiksi suunnata laskennan nopeuttamiseen rinnakkaislaskennan avulla. Tämän on tärkeää erityisesti topologian optimoinnissa, joka on laskennallisesti huomattavasti mitoitusoptimointia raskaampaa. Toisaalta työkalun taustalla olevaa tehtävänasettelua voidaan täydentää siten, että jälkikäsittelyn tarve vähenee. Erityisesti liitosten kestävyyden tarkastelu olisi syytä saada jo optimointivaiheessa laskentaan mukaan.

Viitteet

[1] R. Bixby and E. Rothberg. Progress in computational mixed integer programming – a look back from the other side of the tipping point. *Mathematical Programming*, 149:37–41, 2007.

[2] CEN. *Eurocode 3: Design of Steel Structures. Part 1-1: General rules and rules for buildings.* CEN, 2005.

[3] CEN. *Eurocode 3: Design of Steel Structures. Part 1-8: Design of joints.* CEN, 2005.

[4] J. Haapio. *Feature-Based Costing Method for Skeletal Steel Structures Based on the Process Approach.* PhD thesis, Tampere University of Technology, 2012.

[5] K. Mela. *Mixed Variable Formulations for Truss Topology Optimization.* PhD thesis, Tampere University of Technology, 2013.

[6] T. Ralphs, M. Güzelsoy, and A. Mahajan. Symphony 5.5.0 user's manual. `http://www.coin-or.org/SYMPHONY/doc/SYMPHONY-5.5.0-Manual.pdf`, 2013.

[7] G. Rozvany, M. Bendsøe, and U. Kirsch. Layout optimization of structures. *Applied Mechanics Review*, 48(2):41–119, 1995.

Proceedings of the XII Finnish Mechanics Days
R. Kouhia, J. Mäkinen, S. Pajunen and T. Saksala (Eds.)

Surrogate-based optimization of airfoil using open source software

Aku Karvinen

VTT Technical Research Centre of Finland LTD, P.O. Box 1000, FI-02044 VTT, Finland, aku.karvinen@vtt.fi

Summary. Surrogate optimization is utilized in the case of a drag minimization of the airfoil when the minimum lift is given as a constraint. As the surrogate, a polynomial response surface computed using linear least squares regression method is used. Sampling points needed for the response surface are generated using latin hypercube samples. Optimization of the surrogate objective function is done using a conjugate gradient optimization method. As an optimization software, DAKOTA is utilized, whereas, the objective function is calculated using a computational fluid dynamics software OpenFOAM. Computational domain is constructed using Salome-platform. All used software are published as open source and free of license fees. Results show that the usage of the surrogate makes method robust and hence usable for the industrial CFD cases. The number of needed objective function evaluation is quite high, but substantially lower than in the genetic algorithms.

Key words: optimization, computational fluid dynamics, Dakota, Salome, OpenFOAM

Introduction

There are two types of optimization methods for nonlinear unconstrained or constrained optimization problems, namely gradient-based and non-gradient based methods. Former includes for example traditional conjugate gradient method [8], whereas, the latter consists of for example methods based on the genetic algorithms [11].

Due to non-smooth nature resulted from the ubiquitous numerical error originated from the coarseness of the grid and due to expensiveness of the simulation of the objective function, traditional optimization methods are difficult to utilize in the computational fluid dynamics (CFD) [12]. One promising class of methods is surrogate-based optimization methods in which the objective function is replaced by simpler surrogate function [4][1].

In this study, surrogate optimization is utilized in the case of a drag minimization of an airfoil when the minimum lift is given as an inequality constraint. As the surrogate, a polynomial response surface (quadratic in this study) computed using linear least squares regression method is used. Sampling points needed for the response surface are generated using latin hypercube samples [3]. Optimization of the surrogate objective function is done using a conjugate gradient optimization method. As an optimization software, DAKOTA [2] (The Design Analysis Kit for Optimization and Terascale Applications) is utilized, whereas, the objective function is calculated using a computational fluid dynamics software OpenFOAM (Open Field Operation And Manipulation) [9]. Computational mesh is constructed using snappyHexMesh which is part of the OpenFOAM distribution. Computational domain is constructed using Salome-platform [10]. All used software are published as open source and free of license fees.

[1]Usually in literature, "surrogate based optimization" means methods in which actual CFD model is replaced with the surrogate.

Main objectives of the study are not to develop new optimization methods but

- Demonstrate how open source software Dakota [2], Salome [10] and OpenFOAM [9] can be coupled together to optimize computational fluid flow system.
- Demonstrate how artificial local minimum extreme problem (caused by the insufficient grid resolution) can be overcome using surrogate based optimization.

The ultimate goal is the industrial size CFD case where methods used in the academic word such as the grid morphing cannot be used. Hence, the grid is completely reconstructed every time new objective function is calculated. This causes also grid topology to change which results in before mentioned difficulties with the artificial local minimum (or maximum).

Because the aim of the study is to investigate the possibilities of the open source software in the CFD optimization and the demonstration of the coupling of the software, some crucial stages of CFD simulation are omitted, for example grid independency test.

Theory

The optimization procedure in the software coupling level is given in Figure 1. Dakota [2] manages optimization procedure and runs software needed in function evaluation phase (CFD phase) and given to Dakota as a simulation script file. The simulation script file consists of all the commands needed in CFD simulation (pre-processing, solution, post-processing etc.). In addition, there are two files needed to run Dakota. The first is dakota.in file in which all the optimization parameters are given. The second one is the dprepro Perl file which is the utility that inserts values from Dakota parameters file into a simulation input file and is part of Dakota distribution.

Dakota sends design variables (three in this study) to the Salome [10] which makes the computational domain and saves it as .stl-files. After that, snappyHexMesh produces the computational mesh. OpenFOAM [9] solves the CFD case and saves value of the objective function (drag in this study) in the result file. In addition, results needed in the nonlinear constraints are saved (lift in this study). Also some .vtk files are saved for the post-processing purposes.

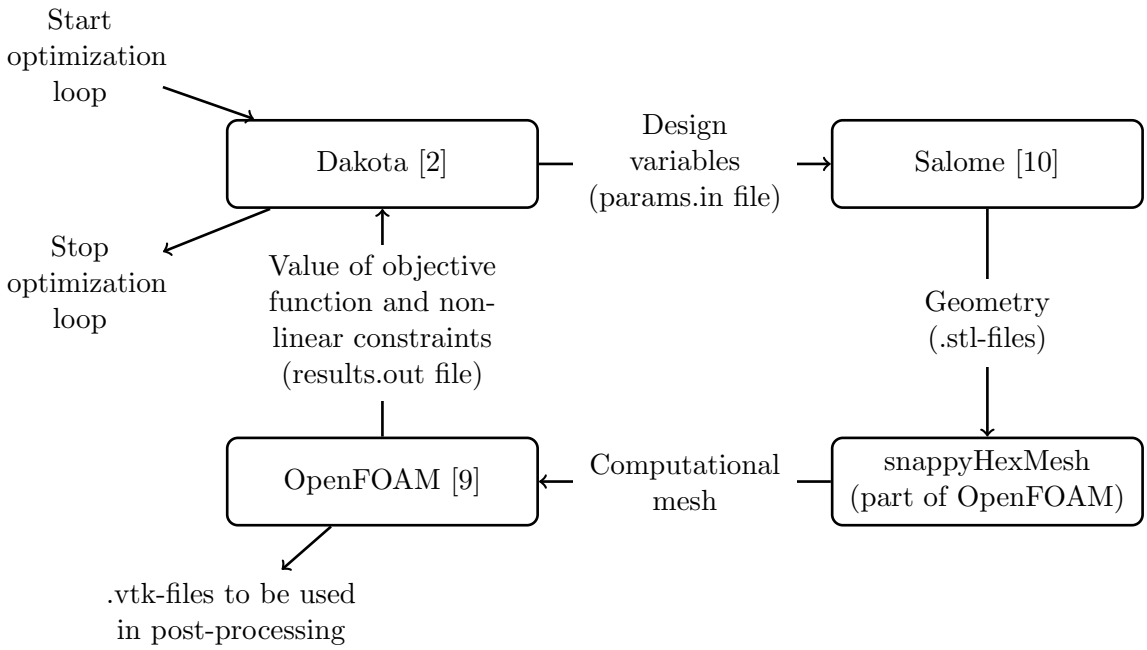

Figure 1. Optimization procedure.

Optimization (Dakota)

Actual optimization is done in several stages, which are:

1. Simulate CFD case in the sampling points (three per design variables = 27 in this study) generated using latin hypercube samples [3] and chosen inside the trust region in which the surrogate is believed to represent the actual objective function fairly well.
2. Generate the surrogate of the actual objective function using simulated CFD results and the linear least squares regression method.
3. Optimize the surrogate using the conjugate gradient method.
4. Compare the values of the objective function obtained using the surrogate and the actual function at the optimal point of the surrogate and based on the accuracy:
   - If the accuracy is poor, reduce the trust region and reject the optimization step.
   - If the accuracy is marginal, reduce the trust region but accept the step.
   - If the accuracy is satisfactory, retain the trust region and accept the step.
   - If the accuracy is excellent, enlarge the the trust region and accept the step.
5. Investigate if the optimum is found. If not, go to step 1., if yes, stop.

Comptuational fluid dynamics (OpenFOAM)

Gorverning equations (Reynolds averaged Navier Stokes equations, RANS) of incompressible steady state turbulent fluid flow are

$$\frac{\partial U_i}{\partial x_i} = 0, \tag{1}$$

where U_i is the time averaged x_i component of the velocity and x_i is the spatial coordinate and

$$U_j \frac{\partial U_i}{\partial x_j} = -\frac{1}{\rho}\frac{\partial P}{\partial x_i} + \nu \frac{\partial^2 U_i}{\partial x_j \partial x_j} + \frac{\partial}{\partial x_j}\left(-\overline{u_i' u_j'}\right), \tag{2}$$

where P is the time averaged pressure and ν is the kinematic viscosity. u_i' is the flucuation part of the velocity and overline denotes the time averaging.

The last term of the equation (2) includes Reynolds stresses, $\overline{u_i' u_j'}$, which represents the transport of momentum by the turbulence and cannot be neglected. The term should be modeled using additional equations in order to close the equation system.

SST k-ω turbulence model

In the SST (shear-stress transport) k-ω model [5], there are equations for the turbulent kinetic energy, k, and for the turbulent specific dissipation rate, ω. They are as follows

$$\frac{\partial k}{\partial t} + U_j \frac{\partial k}{\partial x_j} = \frac{\partial}{\partial x_j}\left[\left(\nu + \alpha_k \nu_\mathrm{t}\right)\frac{\partial k}{\partial x_j}\right] + \tilde{G}_k - Y_k \tag{3}$$

and

$$\frac{\partial \omega}{\partial t} + U_j \frac{\partial \omega}{\partial x_j} = \frac{\partial}{\partial x_j}\left[\left(\nu + \alpha_\omega \nu_\mathrm{t}\right)\frac{\partial \omega}{\partial x_j}\right] + G_\omega - Y_\omega + D_\omega, \tag{4}$$

where $\alpha_k = F_1(\alpha_{k1} - \alpha_{k2}) + \alpha_{k2}$ and $\alpha_\omega = F_1(\alpha_{\omega 1} - \alpha_{\omega 2}) + \alpha_{\omega 2}$, in which α_{k1} is the inner and α_{k2} is the outer inverse turbulent Prandtl number of turbulent kinetic energy, respectively. The constants $\alpha_{\omega 1}$ and $\alpha_{\omega 2}$ are the inner and the outer inverse Prandtl number of turbulent specific dissipation rate, respectively. Blending function[2]

$$F_1 = \tanh\left\{\min\left\{\min\left[\max\left(\frac{\sqrt{k}}{\beta^* \omega y}, \frac{500\nu}{y^2\omega}\right), \frac{4\alpha_{\omega 2} k}{\mathrm{CD}_{k\omega}^{+} y^2}\right], 10\right\}^4\right\}, \tag{5}$$

[2]The limiter which limits the blending functions smaller than 10 and 100 are not included in [5], but implemented in OpenFOAM in order to stabilize iteration.

where y is the distance to the nearest wall and[3]

$$\mathrm{CD}_{k\omega}^{+} = \max\left(\mathrm{CD}_{k\omega}, 10^{-10}\right), \text{ where } \mathrm{CD}_{k\omega} = 2\alpha_{\omega 2}\frac{1}{\omega}\frac{\partial k}{\partial x_j}\frac{\partial \omega}{\partial x_j}. \tag{6}$$

Kinematic turbulent viscosity is computed as follows

$$\nu_\mathrm{t} = \frac{a_1 k}{\max(a_1\omega, \sqrt{2}b_1 S F_2)}, \tag{7}$$

where the second blending function

$$F_2 = \tanh\left\{\min\left[\max\left(\frac{2\sqrt{k}}{\beta^*\omega y}, \frac{500\nu}{y^2\omega}\right), 100\right]^2\right\}. \tag{8}$$

The production of turbulent kinetic energy due to mean velocity gradients, $G_k = \nu_\mathrm{t} S^2$, is limited as follows

$$\tilde{G}_k = \min(G_k, c_1\beta^* k\omega). \tag{9}$$

The production of ω is computed as follows

$$G_\omega = \frac{\gamma}{\nu_\mathrm{t}}\tilde{G}_k, \tag{10}$$

where $\gamma = F_1(\gamma_1 - \gamma_2) + \gamma_2$.

The dissipation of the turbulent kinetic energy and dissipation of ω are computed as follows

$$Y_k = \beta^* k\omega \text{ and } Y_\omega = \beta\omega^2, \tag{11}$$

where $\beta = F_1(\beta_1 - \beta_2) + \beta_2$.

The additional term D_ω in Equation (4) brings into the model features from the standard k-ε model and is computed using

$$D_\omega = 2(1 - F_1)\alpha_{\omega 2}\frac{1}{\omega}\frac{\partial k}{\partial x_j}\frac{\partial \omega}{\partial x_j}. \tag{12}$$

The constants get following values:

$$\alpha_{k1} = 0.85034;\ \alpha_{k2} = 1.0;\ \alpha_{\omega 1} = 0.5;\ \alpha_{\omega 2} = 0.85616$$
$$\beta_1 = 0.075;\ \beta_2 = 0.0828;\ \beta^* = 0.09$$
$$\gamma_1 = 0.5532;\ \gamma_2 = 0.4403;\ a_1 = 0.31;\ b_1 = 1.0;\ c_1 = 10.0$$

It should be noted that the implementation differs in respect of boundary layer treatment from the original model proposed in [5]. Actual implementation follows closely [6][4].

Case

The case chosen as a demonstration case is shown with the dashed line in Figure 2. Velocity is fixed to the value $U = 30\,\mathrm{m/s}$. This yields Reynolds number based on the chord line $\mathrm{Re} = 3\,000\,000$. There are three design variables which are y_top, y_bottom and y_tail. The allowable ranges of the variables are indicated by the arrows in the figure. The airfoil is constructed from the three circular arc, therefore, only three points are needed to fix the shape of the upper and

[3]The limit value proposed in [5] was 10^{-20}.

[4]Unfortunately this paper is very difficult to get. Therefore, in this study the method is captured from the source code of OpenFOAM.

lower part of the foil. x coordinates of the top and the bottom points are fixed and are both $x = 0.5\,\mathrm{m}$. x coordinate of the tail is fixed as $x = 1.0\,\mathrm{m}$. Initially, the design variables get the values: $y_{\mathrm{top}} = 0.03\,\mathrm{m}$, $y_{\mathrm{bottom}} = -0.07\,\mathrm{m}$ and $y_{\mathrm{tail}} = -0.15\,\mathrm{m}$ which yields the drag coefficient $C_d = 0.0424$ and the lift $C_\ell = 1.37$[5].

Optimization problem can be given as:

$$\text{minimize } C_{\mathrm{d}} \tag{13}$$

$$\text{subject to } C_\ell \geq 1.0 \tag{14}$$

$$0.001\,\mathrm{m} \leq y_{\mathrm{top}} \leq 0.15\,\mathrm{m} \tag{15}$$

$$-0.15\,\mathrm{m} \leq y_{\mathrm{bottom}} \leq -0.001\,\mathrm{m} \tag{16}$$

$$-0.3\,\mathrm{m} \leq y_{\mathrm{tail}} \leq 0.3\,\mathrm{m} \tag{17}$$

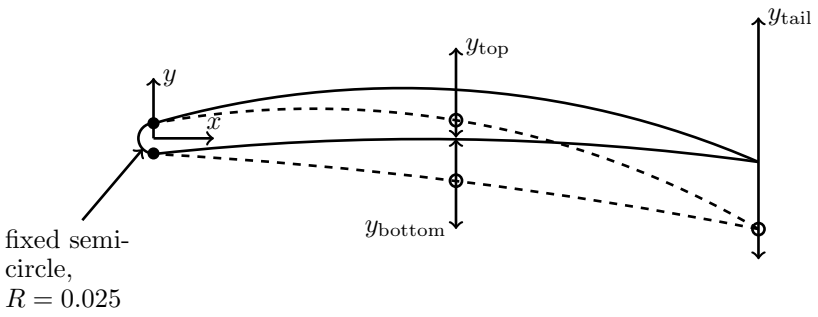

Figure 2. Initial (dashed line) and optimal (solid line) geometry. Filled circles indicate fixed points, open circles indicate free to move points. Arrows in design variables indicate allowable range of values.

Results and conclusions

Evolvement of the design variables, the drag and the lift are shown in Figures 3, 4 and 5. The optimal geometry is given as solid line in Figure 2. In the CFD case, there are approximately 285,000 cells. Using 8-core computer, one function evaluation took approximately 500 s from which about 20% went into mesh generation, about 75% into CFD solution and 5% into communication. One optimization cycle consists of 28 (27 for the surrogate construction and one for the trust region size check) function evaluations, hence, whole optimization took about 40 h.

It is interest to note that this case would be a good candidate for the multiobjective optimization [1], but in this study only single parameter is used as a objective function and other candidate, i.e. lift, has been handled via inequality constraint.

Optimum is found to be:

$$C_{\mathrm{d}} = 0.0157$$

$$C_\ell = 1.00$$

$$y_{\mathrm{top}} = 0.0807\,\mathrm{m}$$

$$y_{\mathrm{bottom}} = -0.001\,\mathrm{m}$$

$$y_{\mathrm{tail}} = -0.0391\,\mathrm{m}$$

Results show that the usage of the surrogate makes method robust (compared to traditional gradient based methods) and hence usable for the industrial CFD cases. This is mainly due to smoothness of the surrogate function. Without the surrogate, numerical error associated to the coarseness of the grid makes exploitation of the gradient-based methods very difficult. Number of needed objective function evaluation is still high, but lower than in the genetic algorithms.

[5]Coeffients are calculated using reference values for the density $\rho = 1.2\,\mathrm{kg/m^3}$ and for the area $A = 1.0\,\mathrm{m}$ (in 2D case dimension of area is meter). In the airfoil, it is customary to use the planform area as a reference area.

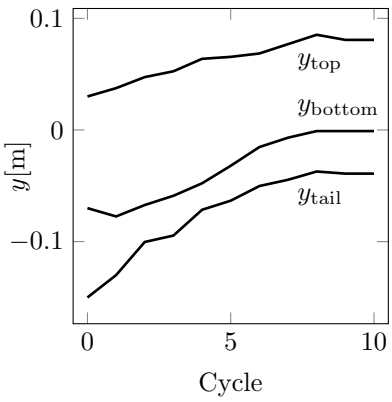

Figure 3. Design variables.

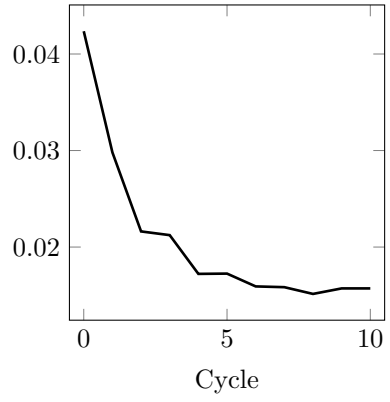

Figure 4. Drag coefficient C_d.

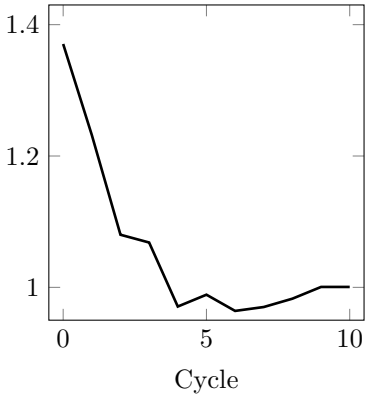

Figure 5. Lift coefficient C_ℓ.

Acknowledges

This work was supported by the SIMPRO (Computational methods in mechanical engineering product development) project funded by Tekes (the Finnish Funding Agency for Technology and Innovation).

References

[1] J. Branke, K. Deb, K. Miettinen and K. Slowiński (Eds.). *Multiobjective Optimization*, Springer, 2008. doi: 10.1007/978-3-540-88908-3

[2] Dakota. Retrieved January 18, 2015, from `dakota.sandia.gov`

[3] R. L. Iman and M. J. Shortencarier. *A FORTRAN 77 Program and User's Guide for the Generation of Latin Hypercube and Random Samples for Use with Computer Models*, Sandia National Laboratories, 1984.

[4] S. Koziel and L. Leifsson (Eds.). *Surrogate-Based Modeling and Optimization, Applications in Engineering*, Springer, 2013. doi: 10.1007/978-1-4614-7551-4

[5] F. R. Menter. Two-Equation Eddy-Viscosity Turbulence Models for Engineering Applications. *AIAA Journal*, 32:1598–1605, 1994. doi: 10.2514/3.12149

[6] F. Menter and T. Esch. Elements of Industrial Heat Transfer Prediction. *16th Brazilian Congress of Mechanical Engineering (COBEM)*, Brazilian, 2001.

[7] S. G. Nash and A. Sofer. *Linear and Nonlinear Programming*, McGraw-Hill International Editions, 1996.

[8] J. Nocedal and S. J. Wright. *Numerical Optimization*, Springer, 2006. doi: 10.1007/978-0-387-40065-5

[9] OpenFOAM. Retrieved January 18, 2015, from `www.openfoam.org`

[10] Salome-platform. Retrieved January 18, 2015, from `www.salome-platform.org`

[11] S. N. Sivanandam and S. N. Deepa. *Introduction to Genetic Algorithms*, Springer, 2008. doi: 10.1007/978-3-540-73190-0

[12] D. Thévenin and G. Janiga (Eds.). *Optimization and Computational Fluid Dynamics*, Springer, 2008. doi: 10.1007/978-3-540-72153-6

Proceedings of the XII Finnish Mechanics Days
R. Kouhia, J. Mäkinen, S. Pajunen and T. Saksala (Eds.)

Dynamic analysis of higher-order shear deformable beams within gradient elasticity

Saba Tahaei Yaghoubi[1], S. Mahmoud Mousavi[1], and Juha Paavola[1]

[(1)]Department of Civil and Structural Engineering, Aalto University, Box 12100, FI 00076 Aalto, Finland, saba.tahaei@aalto.fi, mahmoud.mousavi@aalto.fi, juha.paavola@aalto.fi

Summary. A third order shear deformable beam is formulated based on strain and velocity gradient theory. The governing equations and boundary conditions are obtained by using Hamilton's principle. Static and kinetic length scales are introduced to capture the size effect. The developed model, depicts the influence of the velocity gradients on the governing equations, initial and boundary conditions of the third-order shear deformable theory and can be simplified to Timoshenko and Euler-Bernoulli beam theories [8].

Key words: shear deformable beam, strain gradient, velocity gradient, variational approach

Introduction

Micro scale beams are widely used in micro electro mechanical systems and devices such as in sensors and resonators. Thus, the accurate prediction of their behavior under different loading conditions is of great importance. It is well-known that the classical continuum theories have certain deficiencies in determining materials elastic fields in ultra small scales, where the size effect cannot be negligible. Therefore, such theories are not adequate for interpreting the behavior of micro or nano sized beams and higher order continuum theories such as gradient elasticity theory are applied. In gradient elasticity theory, the equations of classical elasticity are extended with additional higher-order spatial derivatives of strains, stresses and/or accelerations and entering new material constants into the formulation of classical continuum theory enables one to interpret the materials behavior in micro/ nano scales. A complete gradient elasticity theory should include gradients of strain in the generalized strain energy as well as velocity gradients in the generalized kinetic energy.

Several authors investigated the behavior of Euler-Bernoulli, Timoshenko or higher-order shear deformable micro and nanobeams via gradient theory (e.g. [4], [5], [7], [9]). However, in most of the studies, velocity gradients are neglected in the formulation of the generalized kinetic energy.

In a recent study [8], a third order Reddy beam is studied in the framework of strain gradient theory where the generalized strain energy including strain and strain gradients, together with the generalized kinetic energy including velocity and velocity gradients are considered.

Variational formulation of the gradient elasticity theory

In strain gradient elasticity, the strain energy U_t in a region Ω occupied by the elastically deformed isotropic material (at time t) is given by [3]

$$U_t = \frac{1}{2}\int_\Omega (u_{i,j}\sigma_{ij} + u_{i,jk}\tau_{ijk})\mathrm{d}v, \quad i,j,k \in \{x,y,z\} \tag{1}$$

where u_i denotes the displacement components, comma represents the partial derivative and the Cauchy-like stress tensor σ_{ij} and double-stress tensor τ_{ijk} for an isotropic material are

$$\sigma_{ij} = \lambda\delta_{ij}\varepsilon_{mm} + 2\mu\varepsilon_{ij}, \tag{2}$$

$$\tau_{ijk} = l_{\mathrm{s}}^2\left(\lambda\delta_{ij}\varepsilon_{mm,k} + 2\mu\varepsilon_{ij,k}\right) = l_{\mathrm{s}}^2\sigma_{ij,k}. \tag{3}$$

In equations (2) and (3), λ and μ denote the Lamé constants, δ_{ij} are the components of the unit second-order tensor (i.e., Kronecker delta), l_{s} is internal length scale related to the strain gradient and ε_{ij} denotes the infinitesimal elastic strain components as

$$\varepsilon_{ij} = \varepsilon_{ji} = \frac{1}{2}\left(u_{j,i} + u_{i,j}\right). \tag{4}$$

The variation of the strain energy takes the form

$$\delta U_t = \int_\Omega (\delta u_{i,j}\sigma_{ij} + \delta u_{i,jk}\tau_{ijk})\mathrm{d}v. \tag{5}$$

According to Mindlin (1964) [3], the kinetic energy K_t in a region Ω occupied by the elastically deformed material (at time t) is

$$K_t = \frac{1}{2}\int_\Omega \rho\left(u_{i,t}u_{i,t} + l_{\mathrm{k}}^2 u_{i,jt}u_{i,jt}\right)\mathrm{d}v. \tag{6}$$

where ρ is the mass density, l_{k} is internal length regarding the velocity gradient, and "$_{,t}$" denotes the time derivative. The variation of the kinetic energy reduces to

$$\delta K_t = \int_\Omega \rho\left(u_{i,t}\delta u_{i,t} + l_{\mathrm{k}}^2 u_{i,jt}\delta u_{i,jt}\right)\mathrm{d}v. \tag{7}$$

According to Hamilton's principle

$$\int_0^t \left[\delta K_t - \delta U_t + \delta W_t\right]\mathrm{d}t = 0. \tag{8}$$

where δW_t is the variation of external work. The governing equations and boundary conditions can be obtained by applying equation (8) together with equations (5), (7) and the fundamental lemma of the calculus of variation.

Reddy third-order beam theory within strain and velocity gradient theory [8]

Consider a beam with a rectangular cross-section of height h and width b (figure (1)). The beam is made of homogenous and isotropic material and is subjected to a lateral load $t_y(x)$ on its upper surface. According to the Reddy beam theory ([1], [2], [6]), the displacements of the beam are

$$\begin{aligned} u_x\left(x,y,t\right) &= y\beta\left(x,t\right) - \alpha y^3\left(\beta + w_{,x}\right)\left(x,t\right) \\ u_y\left(x,y,t\right) &= w\left(x,t\right) \end{aligned} \tag{9}$$

where

$$\alpha = \frac{4}{3h^2} \tag{10}$$

and u_x and u_y denote the displacements along the coordinates x and y, respectively. In equation (9), w represents the deflection of a point on the mid-plane and β denotes the rotation of the beam cross section. Nonzero components of the stress and strain tensor which are obtained

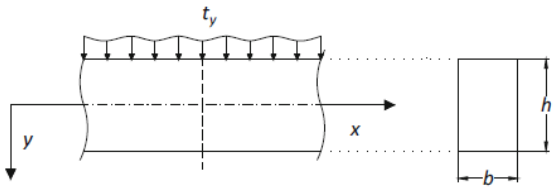

Figure 1. Beam with rectangular cross section subjected to lateral load $t_y(x)$.

using equations (2), (3), (4) and (9) are substituted in equation (5), which leads to

$$\begin{aligned}\delta U_t = \int_0^L \{&M_{xx}\delta\beta_{,x} - \alpha P_{xx}\left(\delta\beta_{,x} + \delta w_{,xx}\right) + \left(Q_{xx} - 3\alpha R_{xx}\right)\left(\delta\beta + \delta w_{,x}\right)\\ &+ l_{\mathrm{s}}^2 M_{xx,x}\delta\beta_{,xx} - l_{\mathrm{s}}^2\alpha P_{xx,x}\left(\delta\beta_{,xx} + \delta w_{,xxx}\right) + l_{\mathrm{s}}^2\left(Q_{xx,x} - 3\alpha R_{xx,x}\right)\left(\delta\beta_{,x} + \delta w_{,xx}\right)\\ &+ l_{\mathrm{s}}^2\bar{N}_{xx}\delta\beta_{,x} - 3l_{\mathrm{s}}^2\alpha\bar{S}_{xx}\left(\delta\beta_{,x} + \delta w_{,xx}\right) - 6l_{\mathrm{s}}^2\alpha\bar{T}_{xx}\left(\delta\beta + \delta w_{,x}\right)\}\mathrm{d}x.\end{aligned} \tag{11}$$

In equation (11), L is the length of the beam and the general bending moments and shear forces are defined as

$$\begin{aligned}M_{xx} := \int_A \sigma_{xx} y \mathrm{d}A,\ P_{xx} := \int_A \sigma_{xx} y^3 dA,\ Q_{xx} := \int_A \sigma_{xy}\mathrm{d}A,\ R_{xx} := \int_A \sigma_{xy} y^2 \mathrm{d}A,\\ \bar{N}_{xx} := \int_A \sigma_{xx,y}\mathrm{d}A,\ \bar{S}_{xx} := \int_A \sigma_{xx,y} y^2 \mathrm{d}A,\ \bar{T}_{xx} := \int_A \sigma_{xy,y} y \mathrm{d}A,\end{aligned} \tag{12}$$

where A represents the cross section area of the beam. The general bending moments and shear force in terms of deflection can be written as

$$\begin{aligned}M_{xx} = \hat{D}_{xx}\beta_{,x} - \alpha F_{xx} w_{,xx},\ \ P_{xx} = \hat{F}_{xx}\beta_{,x} - \alpha H_{xx} w_{,xx},\ Q_{xx} = \hat{A}_{xy}\left(\beta + w_{,x}\right),\ R_{xx} = \hat{D}_{xy}\left(\beta + w_{,x}\right),\\ \bar{N}_{xx} = \hat{A}_{xx}\beta_{,x} - 3\alpha D_{xx} w_{,xx},\ \bar{S}_{xx} = \hat{D}_{xx}\beta_{,x} - 3\alpha F_{xx} w_{,xx},\ \bar{T}_{xx} = -6\alpha D_{xy}\left(\beta + w_{,x}\right)\end{aligned} \tag{13}$$

where

$$\left(A_{xx}, D_{xx}, F_{xx}, H_{xx}\right) = \int_A \left(1, y^2, y^4, y^6\right) E dA,\ \left(A_{xy}, D_{xy}, F_{xy}\right) = \int_A \left(1, y^2, y^4\right) G \mathrm{d}A \tag{14}$$

and

$$\hat{D}_{xx} = D_{xx} - \alpha F_{xx}, \hat{F}_{xx} = F_{xx} - \alpha H_{xx}, \hat{A}_{xy} = A_{xy} - 3\alpha D_{xy}, \hat{A}_{xx} = A_{xx} - 3\alpha D_{xx}, \hat{D}_{xy} = D_{xy} - 3\alpha F_{xy}. \tag{15}$$

In equation (14), E and G denote elastic and shear moduli respectively. Applying Green's theorem to equation (11) results in

$$\begin{aligned}\delta U_t = &\int_0^L \left[-\hat{M}_{xx,x} + \hat{Q}_{xx} + l_{\mathrm{s}}^2\left(\hat{M}_{xx,xxx} - \hat{Q}_{xx,xx} - \hat{N}_{xx,x} - 6\alpha\bar{T}_{xx}\right)\right]\delta\beta\mathrm{d}x\\ &+ \int_0^L \left[-\alpha P_{xx,xx} - \hat{Q}_{xx,x} + l_s^2\left(\alpha P_{xx,xxxx} - \hat{Q}_{xx,xxx} - 3\alpha\bar{S}_{xx,xx} + 6\alpha\bar{T}_{xx,x}\right)\right]\delta w\mathrm{d}x\\ &+ \left[\hat{M}_{xx} + l_s^2\left(-\hat{M}_{xx,xx} + \hat{Q}_{xx,x} + \hat{N}_{xx}\right)\right]\delta\beta|_0^L + l_s^2\hat{M}_{xx,x}\beta_{,x}|_0^L\\ &+ \left[\alpha P_{xx,x} + \hat{Q}_{xx} + l_{\mathrm{s}}^2\left(-\alpha P_{xx,xxx} - \hat{Q}_{xx,xx} + 3\alpha\bar{S}_{xx,x} - 6\alpha\bar{T}_{xx}\right)\right]\delta w|_0^L\\ &+ \left[-\alpha P_{xx} + l_{\mathrm{s}}^2\left(\alpha P_{xx,xx} + \hat{Q}_{xx,x} - 3\alpha\bar{S}_{xx}\right)\right]\delta w_{,x}|_0^L - l_{\mathrm{s}}^2\alpha P_{xx,x}\delta w_{,xx}|_0^L,\end{aligned} \tag{16}$$

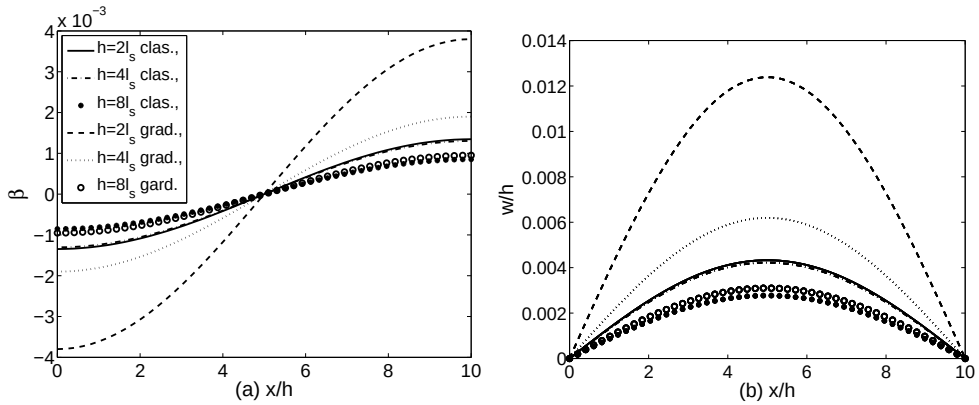

Figure 2. Variations of (a) rotation β and (b) normalized deflection w/h of a simply supported Reddy beam with length x/h for three different beam sizes, compared to the classical model, $b = 2h, L = 10h$.

where

$$\hat{M}_{xx} = M_{xx} - \alpha P_{xx},\ \hat{Q}_{xx} = Q_{xx} - 3\alpha R_{xx},\ \hat{N}_{xx} = \bar{N}_{xx} - 3\alpha \bar{S}_{xx}. \tag{17}$$

Assuming that the transverse load $t_y(x)$ acts on the centroidal axis of the beam, the variation of the external work takes the form

$$\delta W = \int_0^L t_y \delta w \mathrm{d}x. \tag{18}$$

Substitution of equation (9) into the variation of the kinetic energy (7), using Green's theorem and Hamilton's principle (8) and applying fundamental lemma of calculus of variation will readily result in the governing motion equations and boundary conditions. With the aid of equations (13) and (17) the governing equations can be written in terms of deflection as

$$\begin{aligned}
&-\left(\bar{D}_{xx}\beta_{,x} - \alpha\hat{F}_{xx}w_{,xx}\right)_{,x} + \bar{A}_{xy}\left(w_{,x}+\beta\right) + l_{\mathrm{s}}^2\left(\bar{D}_{xx}\beta_{,x} - \alpha\hat{F}_{xx}w_{,xx}\right)_{,xxx} \\
&- l_{\mathrm{s}}^2\left(\bar{A}_{xy}\left(w_{,x}+\beta\right)\right)_{,xx} - l_{\mathrm{s}}^2\left(\bar{A}_{xx}\beta_{,x} + 3\alpha\left(3\alpha F_{xx} - D_{xx}\right)w_{,xx}\right)_{,x} + 36\alpha^2 l_{\mathrm{s}}^2 D_{xy}\left(w_{,x}+\beta\right) \\
&= -\rho\left(I + \alpha^2 H - 2\alpha F\right)\beta_{,tt} - \rho\left(\alpha^2 H - \alpha F\right)w_{,xtt} - \rho l_{\mathrm{k}}^2\left(A + 9\alpha^2 F - 6\alpha I\right)\beta_{,tt} \\
&- \rho l_{\mathrm{k}}^2\left(9\alpha^2 F - 3\alpha I\right)w_{,xtt} + \rho l_{\mathrm{k}}^2\left(I + \alpha^2 H - 2\alpha F\right)\beta_{,xxtt} + \rho l_{\mathrm{k}}^2\left(\alpha^2 H - \alpha F\right)w_{,xxxtt},
\end{aligned} \tag{19}$$

$$\begin{aligned}
&-\alpha\left(\hat{F}_{xx}\beta_{,x} - \alpha H_{xx}w_{,xx}\right)_{,xx} - \left(\bar{A}_{xy}\left(w_{,x}+\beta\right)\right)_{,x} + l_{\mathrm{s}}^2\alpha\left(\hat{F}_{xx}\beta_{,x} - \alpha H_{xx}w_{,xx}\right)_{,xxxx} \\
&+ l_{\mathrm{s}}^2\left(\bar{A}_{xy}\left(w_{,x}+\beta\right)\right)_{,xxx} - 3\alpha l_{\mathrm{s}}^2\left(\hat{D}_{xx}\beta_{,x} - 3\alpha F_{xx}w_{,xx}\right)_{,xx} - 36\alpha^2 l_{\mathrm{s}}^2\left(D_{xy}\left(w_{,x}+\beta\right)\right)_{,x} - t_y \\
&= \rho\alpha^2 H w_{,xxtt} + \rho\left(\alpha^2 H - \alpha F\right)\beta_{,xtt} - \rho A w_{,tt} - \rho l_{\mathrm{k}}^2\alpha^2 H w_{,xxxxtt} \\
&\rho l_{\mathrm{k}}^2\left(9\alpha^2 F - 3\alpha I\right)\beta_{,xtt} + \rho l_{\mathrm{k}}^2\left(A + 9\alpha^2 F\right)w_{,xxtt} - \rho l_{\mathrm{k}}^2\left(\alpha^2 H - \alpha F\right)\beta_{,xxxtt},
\end{aligned} \tag{20}$$

where

$$(I, F, H) = \int_A \left(y^2, y^4, y^6\right)\mathrm{d}A. \tag{21}$$

Moreover; the boundary conditions at both ends of the beam are obtained as

$$
\begin{array}{l}
\left\{\begin{array}{l}\hat{M}_{xx}+l_{\mathrm{s}}^{2}\left(-\hat{M}_{xx,xx}+\hat{Q}_{xx,x}+\hat{N}_{xx}\right)\\ +\rho l_{\mathrm{k}}^{2}\left(I+\alpha^{2}H-2\alpha F\right)\beta_{,xtt}+\rho l_{\mathrm{k}}^{2}\left(\alpha^{2}H-\alpha F\right)w_{,xxtt}=0\end{array}\right\}\quad \text{or}\quad \delta\beta=0\\
\left\{l_{\mathrm{s}}^{2}\hat{M}_{xx,x}=0\right\}\quad \text{or}\quad \delta\beta_{,x}=0\\
\left\{\begin{array}{l}\alpha P_{xx,x}+\hat{Q}_{xx}+l_{\mathrm{s}}^{2}\left(-\alpha P_{xx,xxx}-\hat{Q}_{xx,xx}+3\alpha\bar{S}_{xx,x}-6\alpha\bar{T}_{xx}\right)\\ +\rho\alpha^{2}Hw_{,xtt}+\rho\left(\alpha^{2}H-\alpha F\right)\beta_{,tt}-\rho l_{k}^{2}\left(\alpha^{2}H-\alpha F\right)\beta_{,xxtt}\\ -\rho l_{\mathrm{k}}^{2}\alpha^{2}Hw_{,xxxtt}+\rho l_{\mathrm{k}}^{2}\left(9\alpha^{2}F-3\alpha I\right)\beta_{,tt}+\rho l_{\mathrm{k}}^{2}\left(A+9\alpha^{2}F\right)w_{,xtt}=0\end{array}\right\}\quad \text{or}\quad \delta w=0\\
\left\{-\alpha P_{xx}+l_{\mathrm{s}}^{2}\left(\alpha P_{xx,xx}+\hat{Q}_{xx,x}-3\alpha\bar{S}_{xx}\right)+\rho l_{\mathrm{k}}^{2}\left(\alpha^{2}H-\alpha F\right)\beta_{,xtt}+\rho l_{\mathrm{k}}^{2}\alpha^{2}Hw_{,xxtt}=0\right\}\quad \text{or}\quad \delta w_{,x}=0\\
\left\{-l_{\mathrm{s}}^{2}\alpha P_{xx,x}=0\right\}\quad \text{or}\quad \delta w_{,xx}=0
\end{array}
\tag{22}
$$

The appropriate boundary conditions for the beam will be selected among the conditions of equation (22). Clearly, by setting l_{s} and l_{k} the classical governing equations and boundary conditions for Reddy beam are obtained.
$w(x,t)$ and $\beta(x,t)$ can be determined by solving the governing equations (19) and (20) subject to proper boundary conditions specified from equation (22). To illustrate the size effect, normalized deflection and rotation of a simply supported Reddy beam are determined for three different beam sizes and compared to the classical Reddy beam model (figure (2)) The beam is subjected to load $t_y(x) = q\sin(\frac{\pi x}{L})$, $q = 1$ N/m and assumed to be made of an epoxy with material properties $E = 1.44$ GPa, $l_{\mathrm{s}} = 17.6\ \mu$m, $\rho = 1.22$ kg/m^3. It is observed that for or a beam with a larger size, the difference between the classical and strain gradient theories vanishes.

Conclusion

Reddy third-order beam model is formulated in the framework of velocity and strain gradient theory. The generalized kinetic energy including velocity and velocity gradients is considered. Within a variational approach, the governing differential equations and boundary conditions are obtained. The generalized kinetic energy contributes to additional terms in the governing equations as well as the initial and boundary conditions.

References

[1] W.B. Bickford. A consistent higher order beam theory. In *Developments in Theoretical and Applied Mechanics*, volume 11, pages 137–150, 1982.

[2] M. Levinson. A new rectangular beam theory. *Journal of Sound and Vibration*, 74:81–87, 1981. URL `http://dx.doi.org/10.1016/0022-460X(81)90493-4`.

[3] R.D. Mindlin. Micro-structure in linear elasticity. *Archive for Rational Mechanics and Analysis*, 16:51–78, 1964. URL `http://dx.doi.org/10.1007/BF00248490`.

[4] S. Papargyri-Beskou, D. Polyzos, and D. E. Beskos. Dynamic analysis of gradient elastic flexural beams. *Structural Engineering and Mechanics*, 15:705–716, 2003. URL `http://dx.doi.org/10.12989/sem.2003.15.6.705`.

[5] S. Ramezani. A microscale geometrically non-linear Timoshenko beam model based on strain gradient elasticity theory. *International Journal of Non-linear Mechanics*, 47:863–873, 2012. URL `http://dx.doi.org/10.1016/j.ijnonlinmec.2012.05.003`.

[6] J.N. Reddy. A simple higher-order theory for laminated composite plates. *Journal of Applied Mechanics*, 51:745–752, 1984. URL `http://dx.doi.org/10.1115%2f1.3167719`.

[7] B. Wang, J. Zhao, and S. Zhou. A microscale Timoshenko beam model based on strain gradient elasticity theory. *European Journal of Mechanics-A/Solids*, 29:591–599, 2010. URL http://dx.doi.org/10.1016/j.euromechsol.2009.12.005.

[8] S.T. Yaghoubi, S.M. Mousavi, and J. Paavola. Strain and velocity gradient theory for higher-order shear deformable beams. *Archive of Applied Mechanics*, in press. URL http://dx.doi.org/10.1007/s00419-015-0997-4.

[9] B. Zhang, Y. He, D. Liu, Z. Gan, and L. Shen. A novel size-dependent functionally graded curved mircobeam model based on the strain gradient elasticity theory. *Composite Structures*, 106:374–392, 2013. URL http://dx.doi.org/10.1016/j.compstruct.2013.06.025.

Proceedings of the XII Finnish Mechanics Days
R. Kouhia, J. Mäkinen, S. Pajunen and T. Saksala (Eds.)

Effective radia of threaded bars in bending

J.Freund[1] and K.Kantola[2]

(1)Aalto University, P.O.BOX 14300, FI-00076 AALTO, jouni.freund@aalto.fi
(2)Aalto University, P.O.BOX 14300, FI-00076 AALTO, kari.kantola@aalto.fi

Summary. A computational homogenization method for finding the shear and torsion correction factors of the elastic Timoshenko beam model is suggested. The method is based on concepts of precise and rough models and matching of the virtual work expressions of the models on a RVE (Representative Volume Element). As an example, the shear and torsion correction factors for an open annular cross-section are compared to the values in literature. Application on a threaded bar indicates that the effective radius in bending is close to the minor radius of ISO 261 standard metric screw.

Key words: Computational homogenization, Timoshenko beam model, shear correction factor

Introduction

The standard Timoshenko beam model assumes that the cross-sections of the beam move as rigid bodies in deformation. This is a well-known source for modelling error in the constitutive equation e.g. due to the warping effect. The methods for reducing the modeling error are based on solving a beam problem under less restrictive assumptions than used in the standard model as discussed e.g. in [1], [2], and [3]. Shear and torsion correction factors of literature are just a convenient way to quantify the difference between the standard constitutive equation and the effective constitutive equation obtained by a precise model.

A two-scale computational homogenization method is suggested for derivation of the effective constitutive equation. The idea is to match the virtual work expressions of the precise and rough models on a RVE (Representative Volume Element) under periodicity assumption of the solution in the axial direction of beam. The direct outcome of calculations is the effective constitutive equation of the beam model considered as the rough model. In practice, finite element method is needed for finding the solution to linear elasticity equations used as the precise model. The method assumes that the length of the beam element used as the RVE is small compared to the length of the beam. In addition, the RVE is assumed not to be located near the boundaries, if warping of the cross-section is constrained there.

Standard constitutive equation

Timoshenko beam model assumes that the cross-sections move as rigid bodies in deformation and normal stress components in the thin directions are negligible i.e.

$$\vec{u}_r = \vec{u}_0 + \vec{\theta}_0 \times \vec{\rho}\,, \tag{1}$$

$$\sigma_{xx} = \sigma_{yy} = 0\,, \tag{2}$$

in which translation $\vec{u}_0(z)$ and rotation $\vec{\theta}_0(z)$ of a cross section are associated with the particle $x = y = 0$ of the material coordinate system and $\vec{\rho}(x,y) = x\vec{i} + y\vec{j}$ is the relative position vector. Above, the $z-$axis is taken to be aligned with the axis of the slender prismatic domain occupied by the beam. The linear strain expression

$$\vec{\varepsilon}_r = \frac{1}{2}\vec{k}(\vec{\varepsilon} + \vec{\kappa} \times \vec{\rho}) + \frac{1}{2}(\vec{\varepsilon} + \vec{\kappa} \times \vec{\rho})\vec{k} \tag{3}$$

obtained from the kinematic assumption in Equation (1) depends on the strain measures of the Timoshenko beam model $\vec{\varepsilon} = \vec{u}' + \vec{k} \times \vec{\theta}$ and $\vec{\kappa} = \vec{\theta}'$ in which the prime denotes derivative with respect to the axial coordinate. The role of the kinetic assumption in Equation (2) is to reduce the tendency for a too stiff behavior due to the kinematic assumption in Equation (1).

The standard constitutive equation follows from material model, assumptions above, and the stress-resultant definition of the beam model

$$\begin{Bmatrix} \vec{F} \\ \vec{M} \end{Bmatrix} = \lim_{\Delta L \to 0} \frac{1}{\Delta L} \int_{\Omega} \begin{Bmatrix} \vec{\sigma} \\ \vec{\rho} \times \vec{\sigma} \end{Bmatrix} dV\,, \tag{4}$$

where $\vec{\sigma} = \vec{k} \cdot \vec{\sigma}$ and the integral is over the cross-section. The definition above, using a beam element $\Omega \subset \mathbb{R}^3$ (RVE) of length ΔL and centered at z, is chosen to match the expression to appear later. In terms of the strain measures $\vec{\varepsilon}$ and $\vec{\kappa}$, Equation (4) takes the form

$$\begin{Bmatrix} \vec{F} \\ \vec{M} \end{Bmatrix} = \begin{bmatrix} \vec{A} & \vec{C} \\ \vec{C}_{\mathrm{c}} & \vec{B} \end{bmatrix} \cdot \begin{Bmatrix} \vec{\varepsilon} \\ \vec{\kappa} \end{Bmatrix}. \tag{5}$$

in which the elements $\vec{A}$, $\vec{B}$ and $\vec{C}$ of the matrix depend on the geometry of the cross-section, position of the material coordinate system, and material properties.

The standard constitutive equation, derived in this manner, is known to be particularly poor in torsion of open thin walled cross-sections. The well-known improvements, e.g. in terms of shear and torsion correction factors, are based on improved prediction of stress in equation (4).

Computational homogenization

Derivation of the more accurate constitutive equation uses the concepts of precise and rough models and computational homogenization on a RVE with variational equation

$$\delta W + \delta \int_{\Omega} \vec{\lambda}_r \cdot (\vec{u} - \vec{u}_r) dV = \delta W_r\,. \tag{6}$$

Here, the rough model corresponds to the Timoshenko beam model, classical linear 3D elasticity to the detailed model, and the domain Ω occupied by the RVE is a beam section of length ΔL .Virtual work expressions of the rough and precise models are given by

$$\delta W_r = -\Delta L(\delta\vec{\varepsilon}\cdot\vec{F} + \delta\vec{\kappa}\cdot\vec{M}), \tag{7}$$

$$\delta W = -\int_\Omega \delta\ddot{\varepsilon}_c : \ddot{\sigma} dV . \tag{8}$$

In expression (7), $\vec{\varepsilon}$ and $\vec{\kappa}$ are taken to be constants inside the RVE. In expression (8), $\ddot{\sigma}$ and $\ddot{\varepsilon}$ are the symmetric Cauchy stress and the linear symmetric strain, respectively. Expressions take into account only the internal forces so that gravity etc. are omitted.

Displacement $\vec{u}$ of the detailed model is divided into two parts

$$\vec{u} = \vec{u}_r + \Delta\vec{u} \tag{9}$$

in which $\vec{u}_r$ is given in Equation (1) and $\Delta\vec{u}$ is the remainder displacement. The second term on the left hand side of Equation (6), where $\vec{u}_r$ and $\vec{\lambda}_r$ belong to the same set of functions, is one way to express the uniqueness of the decomposition. Additionally, remainder displacement $\Delta\vec{u}$ is subjected to ΔL -periodicity in the direction of the $z-$axis i.e. to condition

$$\Delta\vec{u}(x,y,z-\frac{1}{2}\Delta L) = \Delta\vec{u}(x,y,z+\frac{1}{2}\Delta L). \tag{10}$$

More detailed discussion on the kinematic and kinetic conditions to be satisfied in computational homogenization is available e.g. in [3].

Effective constitutive equation

In the constitutive equation application, variational equation (6) is used to find the rough model representation of the virtual work expression of the detailed model and thereby the improved relationship between the rough model strain and stress measures. To be precise, the goal is to find $\Delta\vec{u}\in U(\Omega)$, $\vec{\lambda}_r \in U_r(\Omega)$, $\vec{F}\in\mathbb{R}^3$, and $\vec{M}\in\mathbb{R}^3$ satisfying the variational equation (6) for all $\delta\Delta\vec{u}\in U(\Omega)$, $\delta\vec{\lambda}_r \in U_r(\Omega)$, $\delta\vec{\varepsilon}\in\mathbb{R}^3$, and $\delta\vec{\kappa}\in\mathbb{R}^3$.

In the first step, strain measures $\vec{\varepsilon}$ and $\vec{\kappa}$ are considered as given so that the variations $\delta\vec{\varepsilon}=0$ and $\delta\vec{\kappa}=0$. Then, Equation (6) simplifies to the standard elasticity problem giving as its solution the remainder displacement $\Delta\vec{u}$ as function of $\vec{\varepsilon}$ and $\vec{\kappa}$. In the second step, $\Delta\vec{u}$ is taken to be given from the first step so that $\delta\Delta\vec{u}=0$. As $\vec{\varepsilon}$ and $\vec{\kappa}$ are constants in the RVE and $\delta\ddot{\varepsilon}=\delta\ddot{\varepsilon}_r$ when $\delta\Delta\vec{u}=0$, equation (6), expression (7) and (8), and strain in equation (3) give the solution

$$\begin{Bmatrix}\vec{F}\\ \vec{M}\end{Bmatrix} = \frac{1}{\Delta L}\int_\Omega \begin{Bmatrix}\vec{\sigma}\\ \vec{\rho}\times\vec{\sigma}\end{Bmatrix} dV \tag{11}$$

to the stress resultants. Above, $\vec{\sigma}=\vec{k}\cdot\ddot{\sigma}$ is the stress vector corresponding to the detailed model. As the stress given by the first step is linear in the strain measures $\vec{\varepsilon}$ and $\vec{\kappa}$, the final outcome can be expressed in the same form as the standard constitutive equation (5) with modified expression of $\vec{A}$, $\vec{B}$, and $\vec{C}$.

In the application examples, finite element method based on a continuous approximation to $\Delta\vec{u}$ and equation (6) is used to find an approximate solution to the remainder displacement. In practice, the elasticity problem is solved 6 times corresponding to the 6 components of $\vec{\varepsilon}$ and $\vec{\kappa}$. Thereafter, stress of the detailed model is integrated over the RVE according to expression in Equation (11) to obtain the matrix elements $\vec{\vec{A}}$, $\vec{\vec{B}}$, and $\vec{\vec{C}}$ of the effective constitutive equation.

Annular cross-section application

An open or closed annular cross-section can be taken as a basic benchmark case due to the symmetry and results in literature [2]. For a closed case, the standard constitutive equation is acceptable. However, if the cross-section is cut to the centerpoint to make it open as shown in Figure 1, the standard constitutive equation is a very poor choice. Computational homogenization gives the expressions

$$\vec{\vec{A}} = \kappa_1 GA\vec{i}\vec{i} + \kappa_2 GA\vec{j}\vec{j} + EA\vec{k}\vec{k}\,, \tag{12}$$

$$\vec{\vec{B}} = EI(\vec{i}\vec{i} + \vec{j}\vec{j}) + \kappa_3 2GI\vec{k}\vec{k}\,, \tag{13}$$

$$\vec{\vec{C}} = G\sqrt{2AI}\,\kappa_4 \vec{i}\vec{k}\,, \tag{14}$$

in which the correction factors $\kappa_1 \ldots \kappa_4$ are given in Table 1 as functions of thickness ratio $\alpha = t/D$. The zero and second moments of the area A and I are according to the standard theory (where $\kappa_1 = \kappa_2 = \kappa_3 = 1$ and $\kappa_4 = 0$). Shear in the $x-$direction and torsion are connected in the effective constitutive equation, whereas the connection does not exist in the standard constitutive equation.

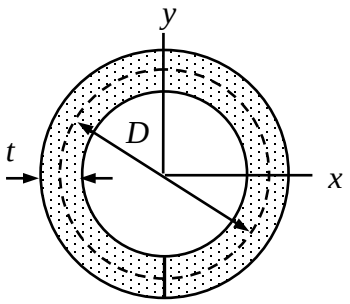

Figure 1. Open annular cross-section.

The values of κ_2 in Table 1 coincide with the shear correction factors of a closed annulus and agree well agree well with the values given in [2] for $\alpha = 1$ and $\alpha = 1/20$. It is noteworthy that the values e.g. in [2] depend on the Poisson's ratio, whereas the shear correction factors of Table 1 do not depend on the Poisson's ratio.

With an annular cross-section, any ΔL defines a RVE. Therefore the outcome does not depend on ΔL or the shape of the end surface (need not to be planar). It is also possible to consider the limit case $\Delta L \to 0$ or assume that the remainder displacement does not depend on the axial coordinate i.e. $\partial\Delta\vec{u}/\partial z = 0$. This simplifies calculation as the linear elasticity problem boils down into a 2D case.

Table 1. Correction factors for an open annular cross-section as functions of $\alpha = t / D$.

α	κ_1	κ_2	κ_3	κ_4
1	0.451	**0.857**	0.750	-0.294
3/4	0.328	**0.812**	0.741	-0.325
1/2	0.238	**0.682**	0.722	-0.338
1/4	0.184	**0.551**	0.688	-0.336
1/10	0.169	**0.508**	0.671	-0.334
1/16	0.168	**0.503**	0.668	-0.336
1/20	0.167	**0.502**	0.667	-0.333
1/32	0.167	**0.501**	0.667	-0.333

Threaded bar application

In the threaded bar application, size ΔL of the RVE cannot be chosen freely but it is rather given by the geometry of the beam. Figure 2 shows the nominal geometry of the ISO 261 standard metric screw defined by the major diameter D and pitch P. Pitch represents also the length scale of the geometry in the direction of the $z-$axis so that $\Delta L = i\,P \quad i \in \mathbb{Z}$. Root radius r has minimum value and the maximum value depending on the minor diameter d.

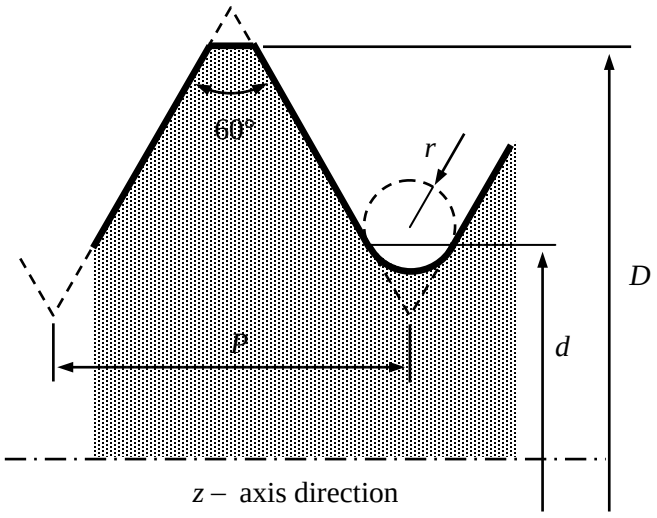

Figure 2. Geometry of ISO 261 standard metric screw

In the present case, it is convenient to use a circular cross-section of nominal diameter D in the calculation of the standard/reference constitutive equation. Using the area A and second moment I based on that selection, computational homogenization gives

$$\vec{\vec{A}} = \kappa_1 GA(\vec{i}\vec{i} + \vec{j}\vec{j}) + \kappa_2 EA\vec{k}\vec{k}\,, \tag{15}$$

$$\vec{\vec{B}} = \kappa_3 EI(\vec{i}\vec{i} + \vec{j}\vec{j}) + \kappa_4 2GI\vec{k}\vec{k}\,, \tag{16}$$

$$\vec{\vec{C}} = \kappa_5\sqrt{GAEI}(\vec{i}\vec{i} + \vec{j}\vec{j}) + \kappa_6\sqrt{2GAEI}\vec{k}\vec{k}\,, \tag{17}$$

in which $\kappa_1 = 0.648$, $\kappa_2 = 0.689$, $\kappa_3 = 0.474$, $\kappa_4 = 0.487$, $\kappa_5 = 0.001$, and $\kappa_6 = -0.002$. The geometrical parameters used in the calculations were $D = 8\,\text{mm}$ and $P = 1.25\,\text{mm}$ giving the minor diameter value $d = 6.65\,\text{mm}$. The effective radius of bending deformation mode $d_{\text{eff}} = 6.64\,\text{mm}$, giving the bending rigidity of the effective constitutive equation when applied in the standard constitutive equation, is close to the minor diameter d even when the rounding radius is close to its maximum value. The finding, showing that the thread part does not contribute much to the bending rigidity, was verified by a three point bending test that gave an even smaller value $d_{\text{exp}} = 6.45\,\text{mm}$.

Conclusions

Computational homogenization with Equation (6) has various applications of which finding the shear and bending correction of the Timoshenko beam model is just one example. The present method is based on matching of the virtual work expression of the precise and rough models on a RVE. To get a constitutive equation of the same for as the standard one, rough model strain measures were chosen to be constants. Then, a more precise constitutive equation follows, when the stress according to the standard model is replaced by more accurate one in the definition of the stress resultants of the Timoshenko beam model.

The conditions for finding the effective constitutive equation of the Timoshenko beam model vary in literature. Clearly, matching of two models based on vibration properties, deflection at some point or virtual work expressions may give somewhat different results. Here, the goal was to improve the constitutive equation, which is the main source for the modelling error.

Threaded bar application indicates that an effective constitutive equation can be derived in a consistent manner also when the beam cross-section geometry is periodic in the direction of the beam axis. Then, the constitutive equation describes the relationship between the beam model stress and strain measures in average sense.

References

[1] S.B. Dong, C. Alpdogan and E. Taciroglu. Much ado about shear correction factors in Timoshenko beam theory. *Int. J. Solids Struct*., 47:1651–1665, 2010.

[2] R. El Fatmi and H. Zenzri, A numerical method for the exact elastic beam theory: applications to homogeneous and composite beams. *Int. J. Solids Struct.*, 41: 2521–2537, 2004.

[3] J. Freund, A. Karakoç, J. Sjölund. Computational homogenization of regular cellular material according to classical elasticity, *Mechanics of Materials*, 78:56–65, 2014.

Proceedings of the XII Finnish Mechanics Days
R. Kouhia, J. Mäkinen, S. Pajunen and T. Saksala (Eds.)

Warping of a tubular mat

Ilkka Pöllänen[1], Timo Björk[2], and Heikki Martikka[3]

(1)LUT , PL 20, 53851 Lappeenranta , ilkka.pollanen@lut.fi
(2)LUT, PL 20, 53851 Lappeenranta , timo.bjork@lut.fi
(3)Himtech Oy, Ollintie 4, 54100 Joutseno, heikki.martikka@pp.inet.fi

Summary: This study is part of a larger research of heat transfer platens also called thermal mats which are important components in large industrial boilers. The focus is on the problem of their vibration and fatigue of the welded joints. The warping stiffness is an important local stress riser on the mat. The warping stresses are calculated with an analytical approach. The results are compared with numerical analyses based on FEA and simple experimental tests. The initial results are satisfactory and the analytical models are utilized in similar industrial components.

Key words: primary warping, secondary warping, torsion, bimoment, tubular mat

Introduction

The objects of this study are tubular mats called platens and their branch joints which are used widely for heat transfer from combustion gas to steam in tubes. They are essential in industry and in bio structures. Here the focus is on analysing a basic component consisting of only two tubes interconnected connected with a fin and rigidly attached to the wall. Since the tubes are often slender the transversely bending dynamic vibrations are excited easily. Also torsional and warping stresses are important. The joint stresses can be obtained by several methods. The effects of bending loads on platens are discussed by Martikka and Pöllänen [1] using orthotropic plate modelling and by Martikka and Pöllänen [2] using beam modelling. These papers are based on dynamic modelling as by Rao [3] and Boresi [4]. It is known that the applied torque is composed as sum of Saint Venant and warping torques as discussed by Rees [5]. The effect of torsional vibrations can be considered by FEM [6]. The dynamic torsional vibrations are studied using a simple model of two tubes joined by a fin or a flange. Lagrangian dynamics is used to get dynamical equations of motion and dynamic fatiguing stresses as their response. Dynamic torque is applied to this system to get Eigen frequency and stress response. The warping stresses will be calculated. The models of this study are utilized in similar industrial components.

Design goals

The design goals in this study are parts of larger goals. The function of the platens in a typical boiler is to transfer combustion heat to steam in the tubes. All vibrations are damaging to the platens and structures. One goal of the design of platens is to prevent vibration by controlling loads, consisting of the combustion gas flow (which may excite galloping), soot blow lance jet loads, unstable vibrations caused by fluid flow in tubes and sound cavity vibrations.

The detailed goal is to redesign the tube joints of the platens to prevent fatigue fractures due to these loads. The focus in this study is on dynamic vibrations of the platens including warping.

The studied structure

The aim in this section is to give an overview of the structure. A typical joint is shown in figure 1. Free body models are shown in figure 2.

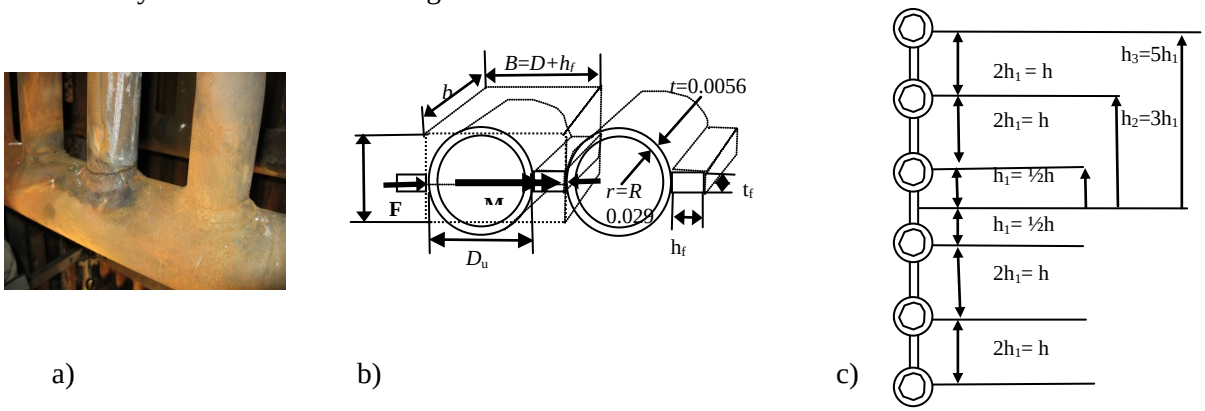

Figure 1. Welded tube joint used in heat exchangers. a) Joint with fatigue cracks, b) Basic element of a tube- fin- tube geometry, c) typical cross section of a platen with N= 6 tubes

The bending stiffness of the orthotropic plates is needed for use in surrogate beam models. In figure 1b typical dimensions of common boiler tubing are shown. The platen is an orthotropic plate.Tube mean radius r_m=0.029m, tube wall t = 0.0056, fin height h_f =0.0245, fin thickness t_f = 0.006

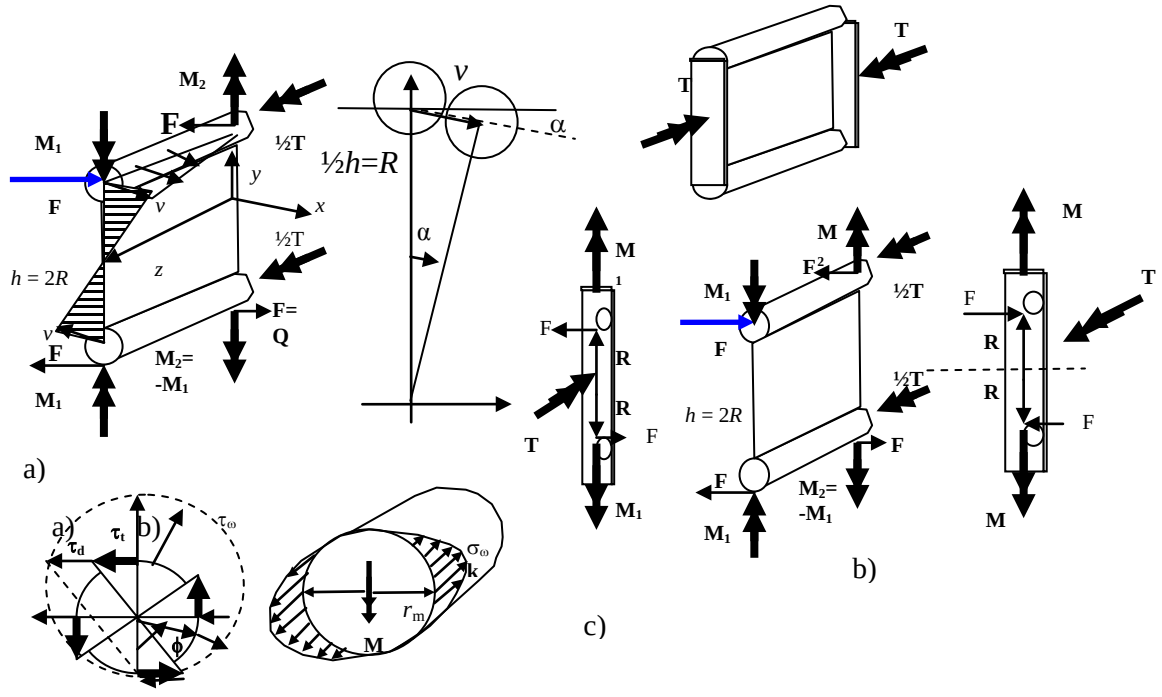

Figure 2. Miniplaten modelling a) Torsional loading , b) Free body models, c) Distribution of stresses , τ_t is torsional shear stress , τ_d is direct stress, τ_ω is warping shear stress and the warping bending stresses is $\sigma_\omega \hat{\mathbf{k}} = f(\omega)\omega\hat{\mathbf{k}}$

Equation of motion and its solution

The equation of motion for the maximal torsional tube displacement v is

$$J\ddot{v} + Kv = \tfrac{1}{R}\left(T_m + T_a \sin \Omega t\right) = \tfrac{1}{R}T\left(t\right) \tag{1}$$

Here J is mass moment of inertia of around the axis of rotation calculated using an assumed shape function, K is stiffness coefficient and $T(t)$ is the load torque excitation.
The solution is the sum of various displacement components

$$v = v_h + v_p = v_h + v_{p1} + v_{p2} = v = a \sin \omega t + b \cos \omega t + v_{p1} + v_{p2} \tag{2}$$

Where
v_h = solution of the homogeneous equations, v_p = solution of the particular equation
v_{p1} is the constant part , v_{p2} is the time dependent part
The lowest Eigen frequency ω and the excitation Ω and the ratio p are

$$\omega = \sqrt{\frac{K}{J}}, \quad \Omega = p\omega, \quad p = \frac{\Omega}{\omega} \tag{3}$$

The total particular response is

$$v_p = v_{p1} + v_{p2} = \frac{\frac{1}{2}T_m}{K} + \frac{1}{\omega^2}\frac{1}{1-p^2} \bullet \frac{\frac{1}{R}T_a}{J} \sin p\omega t \tag{4}$$

Results of Dynamical Simulations

The stiffness coefficient K is derived from the total strain energy U stored in the structure as the sum of three energies, U_f = torsional energy of one flange plate , the energies of two tubes are U_b = bending energy and U_t = torsional energy of one tube. The total energy stored as a surrogate spring of the spring constant K

$$U = U_f + 2\left(U_b + U_t\right) = \tfrac{1}{2}K \cdot v^2 = \left[k_f + 2k_b + 2k_{tt}\right]\tfrac{1}{2}v^2, \quad K = k_f + 2k_b + 2k_{tt} \tag{5}$$

k_f = 75000, $k_b = 4 \cdot 10^7$, k_{tt} = 0.017 .The dynamical parameters are $K = 8.37 \cdot 10^7$, J = 6.1
The lowest Eigen frequency by the analytic model corresponds to mode 4 of FEM [6].

$$f_{anal} = \frac{1}{2\pi}\sqrt{\frac{K}{J}} = 590Hz, \quad f_{\mathrm{FEM}} = 468Hz, \quad for \bmod e4 \tag{6}$$

The analytical results are qualitatively satisfactory considering many simplifications and approximations

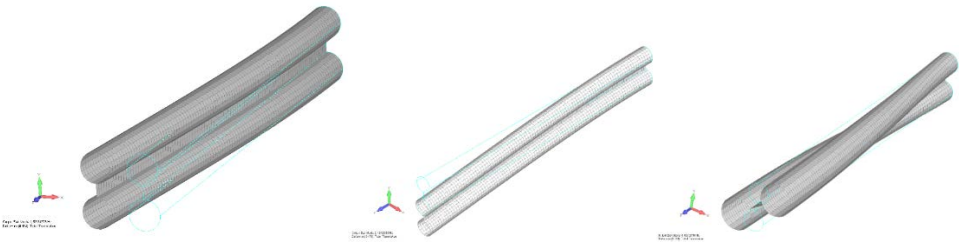

Figure 3. FEM model of the basic platen modules, mode shapes and Eigen frequencies.

Sideways cantilever vibration mode 1 f_{FEM} = 56 Hz. ,vertical cantilever vibration mode 2 f_{FEM} = 124 Hz, , mode 4 f_{FEM} = 468 Hz analytical f = 590 Hz for the same mode. [6].

Stresses by the dynamical model

The aim in this section is to estimate the warping stresses. Mises stress is useful for fatigue calculations. The shear stress acts in different direction and may be added vectorally. Here Mises stress is calculated assuming that shear stresses act at the same location in same direction also so that they can be added directly. For fatigue analysis the mean and amplitude Mises stresses may be calculated.

$$\sigma_{eq} = \left[\sigma_b{}^2 + 3(\tau_t + \tau_d)^2\right]^{\frac{1}{2}} \tag{7}$$

Here the bending stress, the direct shear stress and the torsional shear stress are

$$\sigma_b = \frac{6Er_{\mathrm{m}}}{l^2}v = A_b v, \quad \tau_d = \frac{3E}{2r}\left(\frac{r_{\mathrm{m}}}{l}\right)^3, \tau_t = \frac{Gr_{\mathrm{m}}}{Rl} \tag{8}$$

Torque at the end of the beam

The aim in this section is to first find the torque at the end of the beam and then find out the normal warping stress and the shear warping stress

The solution of a beam under torque with warping is discussed in several textbooks such as Boresi [4]. One end is fixed at z = 0 and the load torque T acts at the $z = l$ end of the beam. It has two components, T_{d} is the Saint-Venant torque and T_{ω} is the torque due to restraint of warping.

$$T(z) = T_d(z) + T_\omega(z) \tag{9}$$

T_{d} may include the flange and the tubes.

At the fixed end z = 0 with long beams the warping torque is small relative to the Saint-Venant moment

$$B(z) = -T(t)\frac{\sinh k(l-z)}{k\cosh kl}, \quad M_\omega = -\frac{dB(z)}{dz} = -B'(z) \tag{10}$$

Large platen model with several tubes

This model is shown in figure 1c.

$$k^2 = \frac{G}{E}\frac{I_{vN}}{J_{\omega N}}, \quad I_{vN} = N\left[\tfrac{1}{3}t_f{}^3 h_f + 2\pi r_m{}^3 t\right], \quad J_{\omega N} = \tfrac{1}{2}h^2 J_{ztube}\left[1 + 3^2 + 5^2 + (2N-1)^2\right] \tag{11}$$

The omega function at height h_{i} is distance from the mid plane to tube centres. For the larger model the outermost tube $n = N/2 = 8/2 = 4$

$$\begin{aligned} &\omega_i = h_i r_m \sin\varphi, \quad h_1 = \tfrac{1}{2}h = R, \quad h_i = (2\cdot i - 1)R, \\ &\omega_n = h_n \cdot r_m \sin\varphi = (2n-1)\tfrac{1}{2}h \cdot r_m \sin\varphi \end{aligned} \tag{12}$$

Stresses by the warping model

The aim in this section is to find the normal warping stress and the shear warping stress.

Normal warping stress

The stresses for tube number n = 1…i.....½N at height h_n from the mid line of the platen are considered. Normal stress at the top at angle $\phi = \pi$ is zero

$$\sigma_{\omega n}(\varphi=\pi) = T(t)\frac{\sinh kl}{k\cosh kl}\bullet\frac{(2n-1)\cdot\frac{1}{2}h\cdot r_m\sin(\varphi)\big|_{\varphi=\pi}}{\frac{1}{2}h^2 J_{ztube}\left[1^2+3^2+5^2+(2N-1)^2\right]}=0 \tag{13}$$

Normal stress at the side is maximal at

$$\sigma_{\omega n} = B(z)\frac{\omega(s)}{J_{\omega N}}\to\max\Rightarrow\sigma_{\omega n}(\phi=\tfrac{1}{2}\pi)=T(t)\frac{\sinh kl}{k\cosh kl}\bullet\frac{(2n-1)\cdot\frac{1}{2}h\cdot r_m\sin(\psi)\big|_{\psi=\pi/2}}{\frac{1}{2}h^2 J_{ztube}\left[1^2+3^2+5^2+(2N-1)^2\right]} \tag{14}$$

Normal stress at the first tube i = 1 is maximum at angle $\phi = \pi/2$ since it is proportional to the omega function

$$\omega_1 = h_1\cdot r_m\sin\varphi\to h_1\cdot r_m\sin\tfrac{1}{2}\pi \tag{15}$$

The normal stress maximum is at z= 0 and angle $\varphi = 0.5\,\pi$

$$\sigma_{\omega 1} = B(z)\frac{\omega_1(s)}{J_{\omega 1}}\to\max\Rightarrow\quad\sigma_{\omega 1}=T(t)\frac{\sinh kl}{k\cosh kl}\bullet\frac{1\cdot\frac{1}{2}hr_m}{\frac{1}{2}h^2 J_{ztube}\left[1^2+0\right]}=0.27MPa \tag{16}$$

Shear warping stress at top tubes of the platen

Shear stress is maximal at the top of the tube i_{th} number N at angle $\varphi=\pi$, figure 1c ,2c. The shear stress and its parameters, torque T and S function are

$$\tau_{\omega N}(\phi) = -B'(z)\frac{S_{\omega N}}{J_{\omega N}t}\Rightarrow\max,\quad -B'(z)\big|_{z=l}=T(t),\quad S_{\omega N}(\phi)=\int_0^s\omega t ds\Rightarrow t{r_m}^2 h_N\left[1-\cos\varphi\right]_{\varphi=\pi} \tag{17}$$

The shear stress depends on angle coordinate ϕ, figure 2c. Thus shear stress at the side is half the shear stress at the top

$$\tau_{\omega N}(\phi)=T(t)\frac{t{r_m}^2 h_N\left[1-\cos\phi\right]_{\varphi=\pi}}{J_{\omega N}t},\ r=r_m\Rightarrow\tau_{\omega N}(\tfrac{1}{2}\pi)=\tfrac{1}{2}\tau_{\omega N}(\pi) \tag{18}$$

Shear warping stress at the first tube of the platen

Shear stress at the first tube at the upper line is maximum at the top and half of it at the sides of the tube, N=1

$$S_{\omega 1,\max}=\int_0^s\omega t ds = t{r_m}^2 h_1\left[1-\cos\phi\right]_{\varphi=\pi} \tag{19}$$

Here the warping stress for the first tube N= 1 is. Stresses are illustrated in figure 1c

$$\tau_{\omega N}(\varphi) = -B'(z)\frac{S_{\omega N}}{J_{\omega N} t} \Rightarrow N = 1 \Rightarrow \tau_{\omega 1} = T(t)\frac{tr_m{}^2 h_1[1-\cos\phi]}{J_{\omega 1} t}$$
$$\tau_{\omega 1 \max}\frac{1-\cos\phi}{1-\cos\pi} = 0...0.48MPa, \tau_{\omega 1 \max} = 0.48MPa \quad (20)$$

Results

The dynamical loading produced normal bending and warping bending stresses

$$\sigma_b = 4.1MPa, \quad \sigma_{\omega 1} = 0.27MPa \quad (21)$$

Their ratio is 0.27/4.1 is small as should be for a slender long beam
The shear stresses are maximal at the top of the beam

$$\tau_{\max} = \tau_d + \tau_t = 0.12 + 0.17 = 0.29MPa, \quad \tau_{\omega 1 \max} = 0.48MPa \quad (22)$$

Conclusions

This study is motivated by the need to develop methodology to increase the useful lifetimes of heat transfer components. For this reason a simplified basic model of two tubes joined with a fin are used. In this study the emphasis is to obtain stresses, which are needed for fatigue design. Reasonable prediction for the dynamical behaviour of the mini platen was obtained using assumed mode shapes and Lagrangian dynamics.

Warping modelling of a beam under torque gave the lowest Eigen frequency which was higher than given by FEM. The difference was due to use of an approximate model for the shape function.

The warping stresses were reasonable. They will be compared to model FEM results and to results obtained with a LUT laboratory test apparatus. This information will be published in another report.

References

[1] Martikka, I.Pöllänen. (2013). Use of orthotropic Plate Model Dynamics to Design for Endurance of Heat Transfer Plates. *Mechanical Engineering Research* , Vol 3, No.2 2013,ISSN 1927-0607 E-ISSN1927-0615, pp.28-2,,.doi:10.5539/mer.v3n2p28, URL:http://dx.doi.org/10.5539/mer.v3n2p28

[2] H.Martikka, I.Pöllänen. (2013). Beam Dynamics Design using Analytic Methods For Optimizing Heat Transfer Plates Dynamics Behavior, *Mechanical Engineering Research* , Vol 4, No.1; 2014,ISSN 1927-0607 E-ISSN 1927-0615, doi:10.5539/mer.v4n1p12, URL:http://dx.doi.org/10.5539/mer.v4p12,

[3] S.R.Rao, *Vibration of Continuous systems*.(2007).John Wiley. ISBN-13 978 -0-471-77171-5

[4] A.Boresi, R. Schmidt, O.Sidebottom.(1993) .*Advanced mechanics of materials*, John Wiley, ISBN 0-471-60009-1

[5] D.W.A.Rees . (2000). *Mechanics of Solids and structures*, Imperial College Press, ISBN: 1-86094-217-2 , Singapore

[6] NX Nastran for FEMAP solver .Version11.0.0.

Proceedings of the XII Finnish Mechanics Days
R. Kouhia, J. Mäkinen, S. Pajunen and T. Saksala (Eds.)

2D FEM-DEM simulations on ice-structure interaction process in shallow water

Riikka Häsä[1], Arttu Polojärvi[1,2], and Jukka Tuhkuri[1,2]

[1]Aalto University, School of Engineering, Department of Applied Mechanics
P.O. Box 14300, FI-00076 Aalto, Finland, riikka.hasa@aalto.fi
[2]Sustainable Arctic Marine and Coastal Technology (SAMCoT), Centre for Research-based Innovation (CRI), Norwegian University of Science and Technology, Trondheim, Norway

Summary. In this paper we use 2D finite-discrete element method (FEM-DEM) to model ice-structure interaction process in shallow water. In the simulations we modelled the intact ice sheet, its failure into ice blocks, and the contacts between the ice blocks, ice sheet, structure and the sea floor. We varied the depth of the water in front of the structure. Here we present preliminary results on the ice loads applied on the structure and describe the simulated ice-structure-sea floor interaction process.

Key words: ice mechanics, ice loads, 2D FEM-DEM

Introduction

Understanding ice mechanics and defining ice loads is essential when designing off-shore structures for seas where freezing or permanent sea ice occur. These structures, including bridges, lighthouses, wind turbines and offshore facilities, are subjected to ice loads when moving ice pushes against them due to prevailing wind conditions and ocean currents. Some of these structures are built in relatively shallow water, where the sea floor affects the loading process. An example of such structures are the ice barriers that are used to protect ports from moving ice.

Here we concentrate on two-dimensional combined finite-discrete element method (FEM-DEM) modelling of ice rubbling process against an inclined structure, such as ice barrier, in shallow water. First we describe our simulations briefly. Then we present typical force records, discuss the maximum force values, and describe the ice behavior during the so-called peak load events. We conclude our paper by some remarks on future work on the topic. It should be noticed that all of the results of this paper are from ongoing work and as such are preliminary.

Simulations

We used the 2D FEM-DEM model, which is described in detail and earlier used to model ice-structure interaction in [4, 5, 2, 3]. The ice sheet is modelled using visco-elastic Timoshenko beam elements, which may fail through a cohesive failure process after chosen stress criterion is reached. The contact forces between the blocks are calculated using an elastic-viscous-plastic normal force model and an incremental Coulomb tangential force model [1]. The simulation code was developed at Aalto University and has its DEM part based on [1]. The model is able to capture the ice-structure interaction processes: in [4, 5] the model was validated by comparing its results to laboratory and full scale measurements reported in [6] and [7].

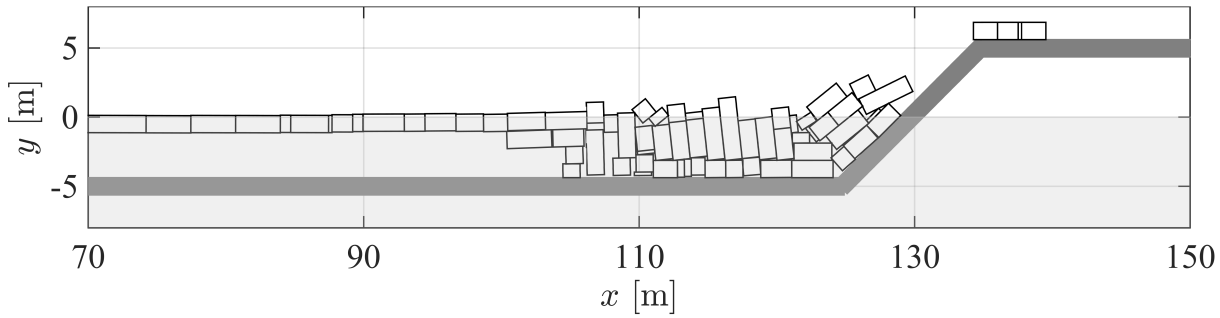

Figure 1. A simulation of an ice-structure interaction process in the case of shallow water. The ice sheet is pushed from the left towards the structure and breaks into ice blocks of various sizes. Water is shown in light gray. The figure does not show the whole simulation domain.

In the ice-structure-bottom interaction simulations, a floating continuous ice sheet is pushed against an inclined structure as illustrated by Figure 1. During the simulation, an initially intact ice sheet fails into ice blocks, which can then interact with each other, the structure, and the bottom during the later simulation. The structure was assumed to be infinitely rigid and it extended five meters above the water level. The top of the structure was a flat surface where the rubble could accumulate when the so-called overtopping occured. The simulation continued until 250 m of ice was pushed against the structure.

Table 1 shows the main simulation parameters. The ice properties in the simulations are mostly based on Timco and Weeks [8]. We varied the bottom depth D and ice thickness h as shown by the table. The simulations were ran with D/h ratios $4 \ldots 30$. Repeated simulations with the same D and h were run with only small variation in the effective modulus E of the ice sheet (normal contact stifness k_n always had the same value as E). This could be done, since the model we used is sensitive to changes in effective modulus E as shown in [2]. Thus slight variation in E leads to the solution following a different path and to changes in the interaction process details. Number of repeated simulations in this paper varied from three to five depending on the case.

Table 1. Main paramaters used in the simulations. Structure height is measured from the waterline. Abbreviations in the table: eff.=effective, fri.=friction, coe.=coefficient, struct.=structure, cont.=contact, and nor.=normal.

Parameter		Unit	Value	Parameter		Unit	Value
Ice thickness	h	m	$0.5, 1.25$	Ice-ice fri.coe.	μ_{ii}	-	0.3
Eff. modulus	E	GPa	3.98...4.02	Ice-struct. fri.coe.	μ_{is}	-	0.1
Poisson's ratio	ν	-	0.3	Cont. nor. stiffness	k_{ne}	GPa	3.98...4.02
Ice density	ρ_i	kgm^{-3}	900	Plastic limit	σ_p	MPa	2.0
Tensile strength	σ_f	kPa	600	Inclination angle	α	$^\circ$	45
Shear strength	τ_f	kPa	600	Struct. height	h_s	m	5
Fracture energy	G_f	Jm^{-2}	12	Time step	Δt	s	$2.0 \cdot 10^{-5}$
Water density	ρ_w	kgm^{-3}	1010	Ice sheet vel.	v_p	ms^{-1}	0.05
Water depth	D	m	$5, 10, 15$	Element length	L_0	m	0.25
				Drag coe.	d_c	-	2.0

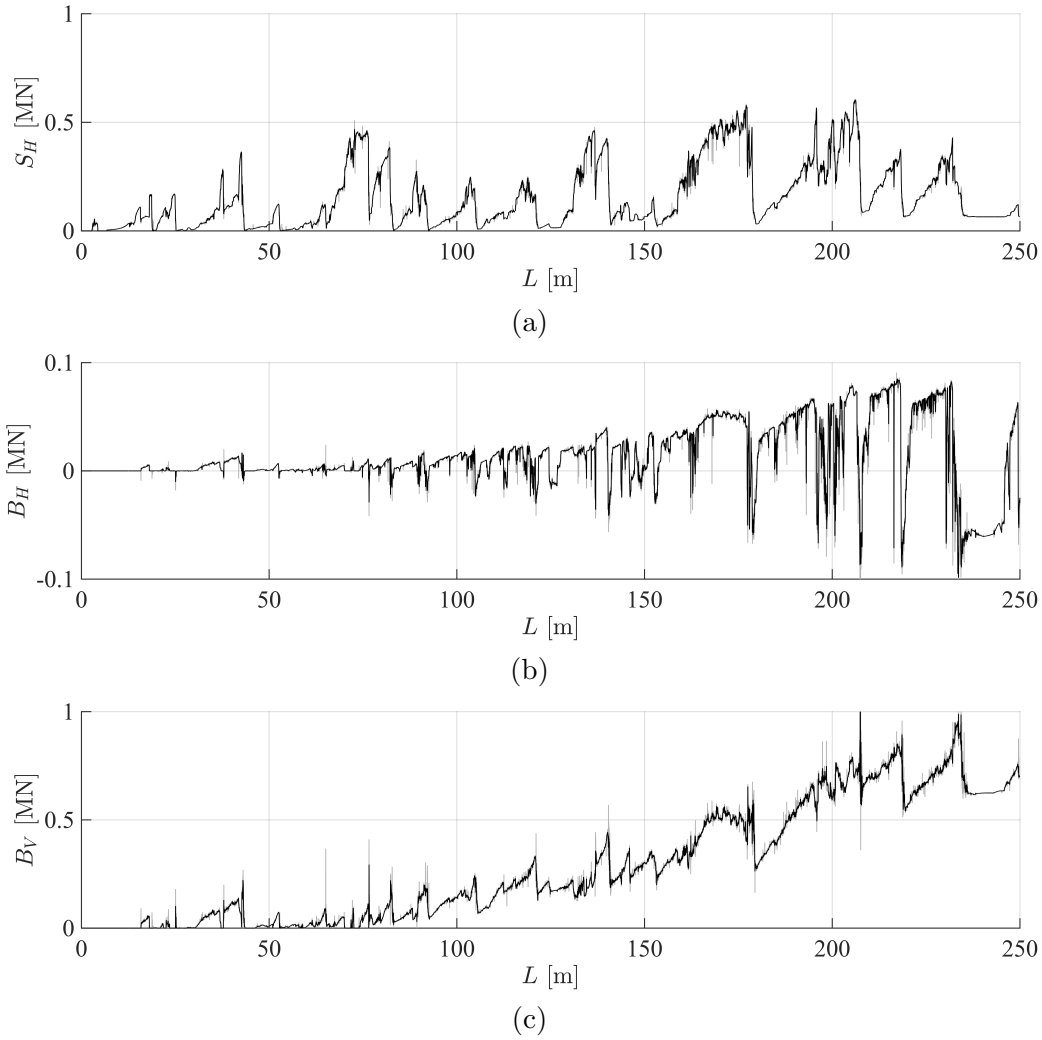

Figure 2. Typical horizontal force-displacement records from the simulations: (a) horizontal force S_H on the inclined part of the structure, (b) horizontal force B_H at the bottom, and (c) vertical force B_V at the bottom. The data is from simulations with water depth $H = 5$ m and ice thickness $h = 1.25$ m. Positive direction for the horizontal force is towards the structure for horizontal force and downwards for the vertical force. The figures show raw data in gray and filtered data in black.

Preliminary results and analysis

Force-displacement records

Figure 2 a-c give typical force records from the simulations with water depth $D = 5$ m and ice thickness $h = 1.25$ m ($D/h = 4$). Figure 2 a and b show, respectively, the horizontal load S_H applied on the structure and B_H on the bottom, and Figure 2 c the vertical force B_V applied on the bottom. All figures have the force plotted against the length L of the ice pushed against the structure. We filtered the data as illustrated by the graphs to remove potential peaks due to impact loads and instead focused on the peaks that had somewhat longer duration. We used Matlab medfilt function with window size three in filtering similarly to [2].

Figure 2 a illustrates how S_H typically showed several successive peak load events: a force is building up towards a peak value and then abruptly drops. Comparison of Figure 2 a and b show, that simultaneously with the drops in S_H values, B_H showed drops in its values. The sign of B_H changes due to a change in the direction of the frictional force at the bottom. This on the other hand changes when the direction of the motion of the ice in contact with the bottom changes. Most of the time B_H applied to the bottom has a positive sign, which means that the

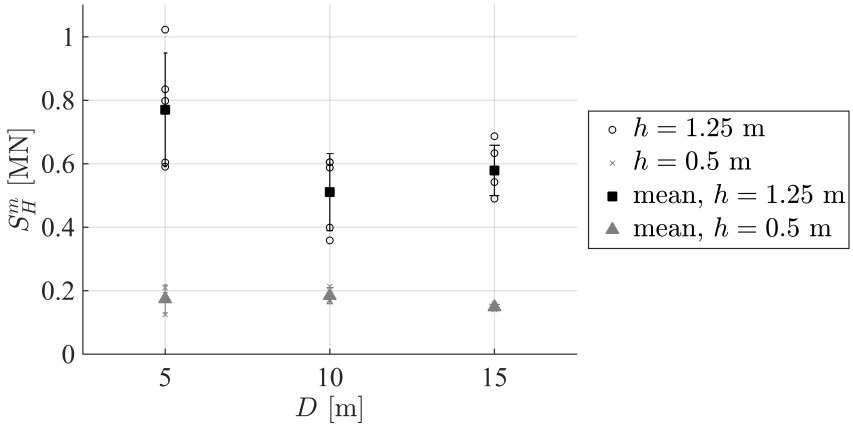

Figure 3. Maximum horizontal load S_H^m values on the inclined part of the structure. The figure shows the S_H^m values from all simulations with their means and standard deviations. The data was filtered as indicated by Figure 2 before extracting the S_H^m values.

friction is resisting the ice motion towards the structure (the sign of the frictional force acting on the ice blocks in contact with the bottom has the opposite sign). The absolute values of B_H when the peaks of S_H occurred were approximately from 10 to 15 % of the peaks.

The vertical bottom force B_V in Figure 2 c is seen to show an increasing trend throughout the simulation. This was often the case in the simulations with $D = 5$ m and $h = 1.25$ m. The increase was due to increase in the rubble mass in front of the structure and in contact with the bottom. Similar increasing trend can be in fact seen in the absolute values of B_H in Figure 2 b. This would be expected based on Coulomb friction: frictional force on the bottom increases together with the normal force applied on it. We did not observe similar increasing trend in B_V with deeper water, since in these cases the ice rubble was only rarely in contact with the bottom.

We extracted the maximum horizontal structure load S_H^m from the filtered $S_H - L$ records of each simulation. This quantity was chosen as it is often of first engineering interest. Figure 3 presents the S_H^m values from the simulations of this paper. The figure gives S_H^m values for both ice thickness h values as a function of water depth D. The figure shows that h strongly affects the S_H^m values as simulations with $h = 1.25$ m yielded roughly three, up to four, times higher S_H^m values than the simulations with $h = 0.5$ m. On the other hand the effect of D is not so clear. The S_H^m values in the case of $D = 5$ m and $h = 1.25$ m ($D/h = 4$) are approximately one third higher than in other cases with $h = 1.25$ m, whereas the simulations with $h = 0.5$ m yield approximately equal S_H^m values regardless of D. The data and the standard deviations in Figure 3 indicate, that the scatter in S_H^m values with $h = 1.25$ m is large, whereas with $h = 0.5$ m, the repeated simulations yielded S_H^m values showing fairly small variation.

Mechanics of the peak load events

Our initial analysis suggests that the peak load events in general corresponded to the so-called ride-up events. This is in line with observations in [5]. In a ride-up event, the ice is pushed upwards along the inclined part of the structure. To demonstrate one of these ride-up events, a close up of $S_H - L$ record in Figure 2, in the proximity of an occurrence of a peak load, is given in Figure 4. Further, Figure 4 shows three snapshots that correspond to the instances (1)-(3) of the close-up of the $S_H - L$ record.

At (1) of Figure 4 the rubble is shown at the onset of load build up. It can be observed that the rubble is in contact with the structure, but there is no ride-up. At the peak load, on the

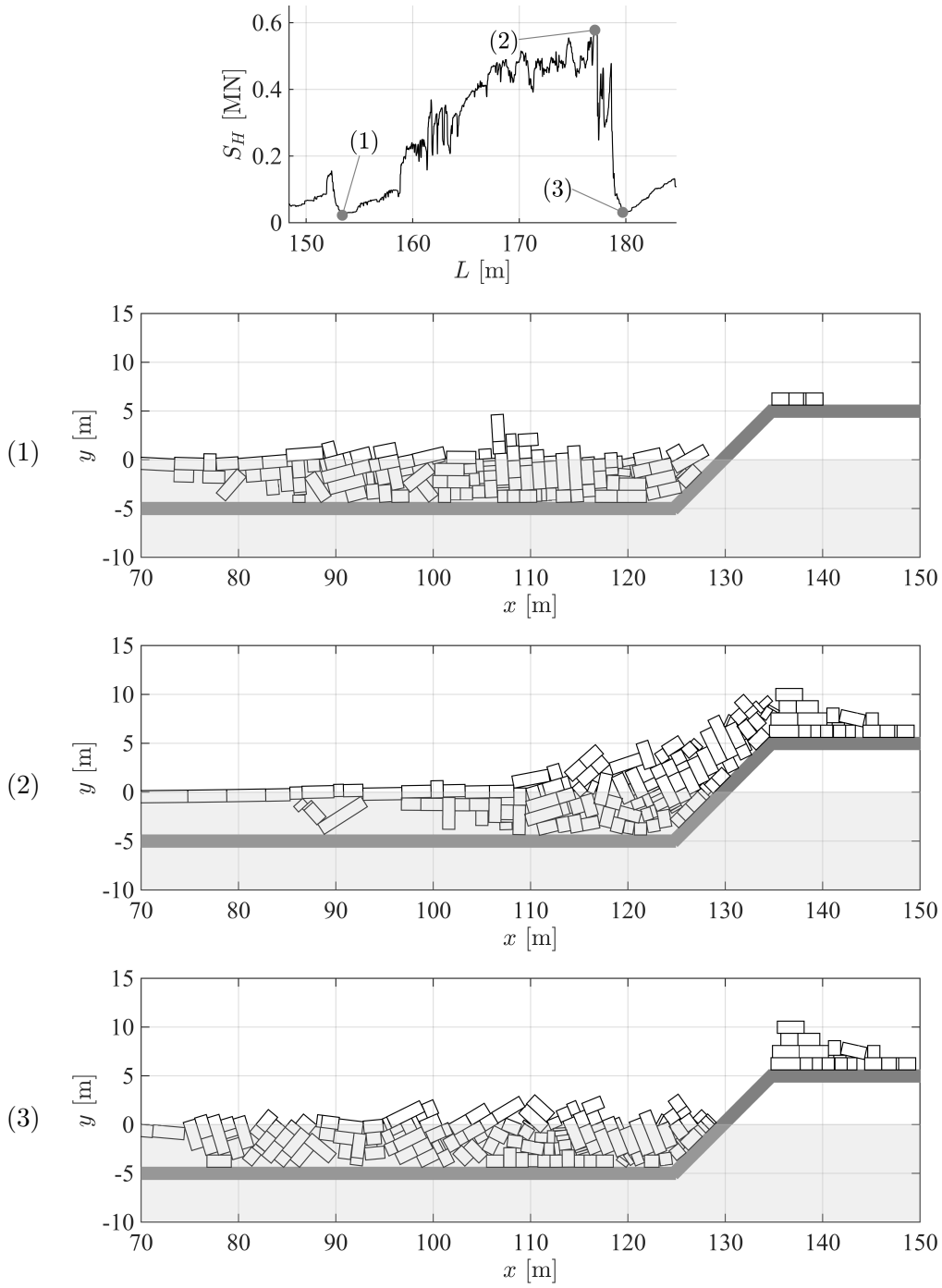

Figure 4. A close-up of a $S_H - L$ record and snapshots from a simulation illustrating the behavior of the ice rubble during a peak load event: (1) on the onset of load build up, (2) at peak load, and (3) after the load drop following the peak force. The numbers (1)-(3) refer to instances indicated in the force record of the event. The snapshots are from simulations with water depth $H = 5$ m and ice thickness $h = 1.25$ m Water is shown in light gray. The snapshots do not show the whole simulation domain.

other hand, large volume of rubble is being pushed by the ice sheet and slides upwards along the structure as snapshot (2) shows. The load then drops as the rubble slides down the structure at the end of the event, as has occurred at (3). The peak load event of the snapshots leads to an increase in the volume of the overtopped ice (ice on top of the structure) as the comparison of the snapshots (1) and (3) shows.

Conclusions

We introduced some preliminary results from our simulations on ice-structure interaction in shallow water. Next we wish to understand how the water depth to ice thickness ratio affects rubble pile features and other phenomena such as rubble ride-up along the wall and its accumulation on top of the structure. We will also look into the rubble pile evolution. The most interesting rubble pile features are the dimensions of the pile during and at the end of the simulation, and the amount of rubble accumulated on top of the structure.

Acknowledgements

AP and JT wish to acknowledge the support from the Research Council of Norway through the Centre for Research-based Innovation SAMCoT and the support from all SAMCoT partners.

References

[1] Hopkins, M. (1992). Numerical simulation of systems of multitudinous polygonal blocks. Technical Report 92-22, Cold Regions Research and Engineering Laboratory, CRREL. 69 p.

[2] Paavilainen, J. and Tuhkuri, J. (2012). Parameter effects on simulated ice rubbling forces on a wide sloping structure. *Cold Regions Science and Technology*, 81:1 – 10.

[3] Paavilainen, J. and Tuhkuri, J. (2013). Pressure distributions and force chains during simulated ice rubbling against sloped structures. *Cold Regions Science and Technology*, 85:157 – 174.

[4] Paavilainen, J., Tuhkuri, J., and Polojärvi, A. (2009). 2D combined finite–discrete element method to model multi-fracture of beam structures. *Engineering Computations*, 26(6):578–598.

[5] Paavilainen, J., Tuhkuri, J., and Polojärvi, A. (2011). 2D numerical simulations of ice rubble formation process against an inclined structure. *Cold Regions Science and Technology*, 68(1-2):20–34.

[6] Saarela, S. (2000). Description of the pile-up process of an ice sheet against an inclined plate. Master's thesis, Helsinki University of Technology, Department of Mechanical Engineering.

[7] Timco, G. and Johnston, M. (2003). Ice loads on the molikpaq in the canadian beafourt sea. *Cold Regions Science and Technology*, 37:51–68.

[8] Timco, G. and Weeks, W. (2010). A review of the engineering properties of sea ice. *Cold Regions Science and Technology*, 60(2):107–129.

Proceedings of the XII Finnish Mechanics Days
R. Kouhia, J. Mäkinen, S. Pajunen and T. Saksala (Eds.)

Why simulate ice rubble shear box tests?

Arttu Polojärvi[1,2], Jukka Tuhkuri[1,2], and Anna Pustogvar[2]

[1]Aalto University, School of Engineering, Department of Applied Mechanics
P.O. Box 14300, FI-00076 Aalto, Finland, arttu.polojarvi@aalto.fi
[2]Sustainable Arctic Marine and Coastal Technology (SAMCoT), Centre for Research-based Innovation (CRI), Norwegian University of Science and Technology, Trondheim, Norway

Summary. This paper describes simulations of laboratory scale direct shear box experiments on ice rubble. The modeled experiments were pseudo 2D and we used 2D discrete element method (DEM) to model them. We show that our simulations can be used to describe the experiments with good accuracy. Then we highlight the effect of shear box wall induced force chains, which cause high loads measured during a shear box test.

Key words: ice rubble, discrete element method, simulations

Introduction

There is an urgent and increasing need for a better understanding on ice loads. The need is partly caused by a demand for clean energy resources, such as offshore wind energy, on regions with ice covered seas, and by an increase in off-shore operations on ice covered seas. These operations are due to the demand for efficient transport routes, such as the Northern Searoute, and due to the exploitation of natural resources in the Arctic. A common cause for high ice loads are ice ridges. The underwater part of the ridge, called the keel, can be extensive in volume and thus cause high loads. The keel of a first year ridge is mostly comprised of a more or less loose pile of ice blocks. We study this type of ice rubble in this paper.

We analyze the direct shear box tests illustrated in Figure 1 a. A typical direct shear box test has an ice rubble specimen placed in a box, and a part of the shear box is moved with some velocity $\dot{\delta}$ while the shear load S required for the motion is recorded. We recently performed a set of shear box tests [13] and simulated them using two-dimensional discrete element method (DEM). In DEM, the ice rubble is modeled block by block as discontinuous material, and it is the interaction of these blocks through contact forces that results into rubble deformation. DEM was pioneered by [1] and has been used in ice mechanics earlier by e.g. [5, 4, 10, 11, 8, 9, 7].

Here we look into interpreting shear box test results. The rubble behaviour and resistance in a direct shear box test is often described in terms of Mohr-Coulomb material model. The relation between the shear resistance τ and the so-called confining pressure σ (see Figure 1 a) in this model is given by

$$\tau = \sigma \tan \varphi + c, \tag{1}$$

where c and ϕ are the cohesion and friction angle of the material, respectively. Typically τ is assumed to act on a shear plane (see dashed line in Figure 1 a) that has an area A (note that $A = A(\delta)$ due to the motion of the box). With this assumption, τ is simply derived from the $S - \delta$ records from

$$\tau(\delta) = \frac{S(\delta)}{A(\delta)}. \tag{2}$$

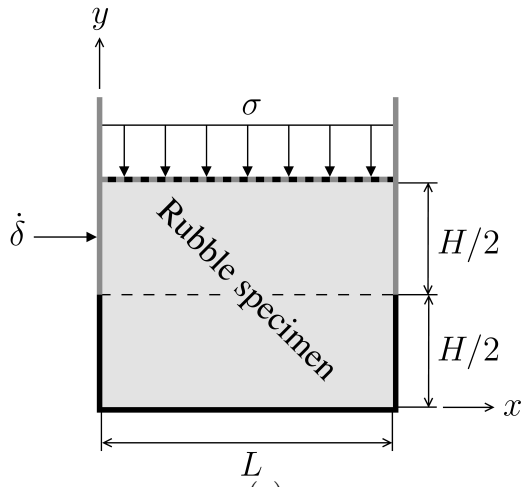

(a)

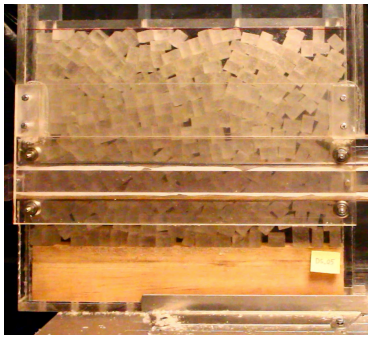

(b)

Figure 1. Direct shear box experiment set up: (a) gives a sketch with symbols used here and (b) a photo from an experiment. A box with a length L and height H has its upper half of the box (shown in gray) moved right with velocity $\dot{\delta}$. Confining pressure σ is applied to the rubble by a cover (indicated in (a) by black and gray dashed line). Cover may rotate and translate in vertical direction freely. The shear plane, as assumed in Equation 2, is shown in (a) with dashed line.

We first show that our simulations models the problem well. Then we discuss the simulations and highlight the physical phenomena force records of the experiments. We show that the maximum loads in the experiments were caused by the force chains, which are not accounted for by simplifications included into Equation 1 and 2. The force chains were fairly easy to observe in the simulations, whereas observing them in an experiment can be challenging. The work we present here is based on [12].

Simulations of the experiments

Our two-dimensional discrete element method (DEM) simulations are largely based on the models described in detail in [4] and [8]. In the model, the contact forces between the blocks are calculated using an elastic-viscous-plastic normal force model and an incremental Mohr-Coulomb tangential force model. The normal forces in contact are always compressive for a block, thus no freeze bonds between the blocks are modelled. The block fracture is neither simulated but this is not a limitation: no block breakage was observed in the experiments. The main parameters used in the simulations are given in Table 1.

Figure 1 b shows a photo of the experimental set up, which we describe in detail in [13]. The

Table 1. Most important paramaters used in the simulations. Abbreviations in the table: fri.coe.=friction coefficient, nor.=normal, tan.=tangential, and cont.=contact.

Parameter		Unit	Value	Parameter		Unit	Value
Ice-ice fri.coe.	μ	-	0.5	Rubble length	L	m	0.6
Ice-wall fri.coe.	-	-	0.3	Rubble height	H	m	0.4
Cont. stiffness nor.	-	Pa	$4.0 \cdot 10^8$	Shearing velocity	$\dot{\delta}$	ms^{-1}	0.02
Cont. stiffness tan.	-	Pa	$1.5 \cdot 10^8$	Confining pressure	σ	kPa	5.76, 11.03
Plastic limit	-	Pa	$2.0 \cdot 10^6$	Small block size	-	m×m	0.02×0.03
				Large block size	-	m×m	0.04×0.06

shear box used in the experiments was made out of Plexiglas and had a length $L = 0.6$ m and height $H = 0.4$ m as Figure 1 a shows. Since the box was only 0.04 m wide, the experiments could be considered pseudo two-dimensional. The cover was free to rotate and move in vertical direction yielding to approximately constant σ throughout an experiment. Dead weights was placed on top of the rubble to apply desired confining pressure σ onto the rubble: σ values 5.76 kPa and 11.03 kPa, respectively referred to as low and high σ, were used. The velocity of the box motion was set up to 0.02 ms^{-1}. We used displacement interval $\delta \approx 0 \ldots 0.14$ m similarly to our experiments in [13]. Two different types of rubble were used: one consisting of small (0.02 m $\times$ 0.03 m) blocks and the other consisting of large (0.04 m $\times$ 0.06 m) blocks.

Validation of our simulations

We first validated our simulations by comparing their results to the experimental results. The shear force-box displacement ($S - \delta$) are shown in Figures 2 a-d or simulations and experiments. The figures show how the simulations and the experiments showed similar features: commonly S first increased with high $\partial S/\partial\delta$ rate towards its mean value $\bar{S}$, and then varied substantially and showed peak load events, which are here defined as being distinct load peaks followed by abrupt drops. The exact details of the S records depended on rubble configuration, which were not identical between the experiments and the simulations. Increase in σ and block size led to more prominent peak load events in the simulations and the experiments. In addition to $S - \delta$ records, the figures show the mean values $\bar{S}$ of shear force in each experiment and simulation. The mean and the maximum S values both increased with an increase in σ and in block size and were in fair agreement in the experiments and simulations. We present a more thorough validation in [12].

Findings from the simulations

Our simulations showed that the rubble behaved like a typical granular material: the forces within the rubble were transmitted through chains of highly loaded particles, or force chains, while most of the blocks were only lightly loaded. In the simulations these can be straightforwardly illustrated by using a particle stress tensor $\boldsymbol{\sigma}^*$ as (see e.g. [2, 6])

$$\sigma^*_{ij} = \frac{1}{A} \sum_{c=1}^{n} f^c_i r^c_j. \tag{3}$$

In this definition A is the area of a block, n the number of contacts on a block, and f^c_i and r^c_j are the components of the contact force $\mathbf{f}^c = f^c_x\mathbf{i} + f^c_y\mathbf{j}$ and the so-called branch vector $\hat{\mathbf{r}}^c = r^c_x\mathbf{i} + r^c_y\mathbf{j}$, respectively. Here $\hat{\mathbf{r}}^c$ is defined to be the unit vector having the direction of a vector from the centroid of a block to the point of application of contact force c acting on it. The minor principal value σ^*_2 (here the negative sign indicates compression) of the symmetric part of $\boldsymbol{\sigma}^*$ and the corresponding principal direction can be used to illustrate the main compressive load and its direction for a block.

Figures 3 illustrate typical force chain networks and their change in the simulations. The figures are from three stages of two simulations: (1) as S increases towards a peak load, (2) close to a peak load, and (3) after a peak load. The figures show the normalized values $\hat{\sigma}^*_2$ of minor principal stresses with the corresponding direction for each block. Here the $\hat{\sigma}^*_2$ values are normalized by the maximum value of σ^*_2 at stage (2) of each simulation. The $\hat{\sigma}^*_2$ values and directions are only shown for blocks having σ^*_2 value less (higher compression) than mean value of σ^*_2 at stage (2).

The snapshots in Figures 3 from stage (2) clearly show that the force chains and the boundary conditions of the experiment are closely related to the peak load events: a chain of blocks transmits high loads from the upper part of the left wall, on which the S was measured, to the

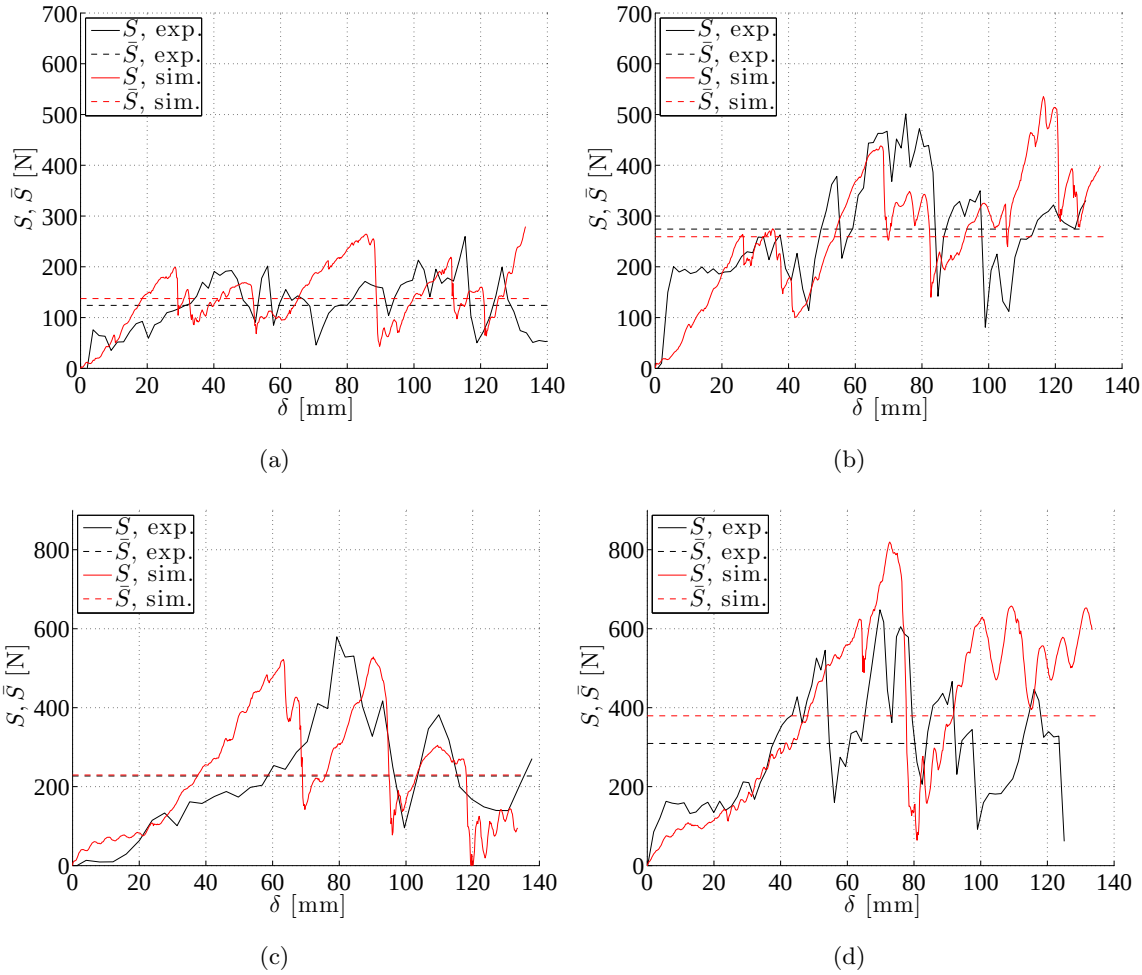

Figure 2. Typical shear force-displacement ($S - \delta$) records from experiments (exp.) and corresponding simulations (sim.): small blocks with confining pressures (a) $\sigma = 5.76$ kPa and (b) $\sigma = 11.03$ kPa and large blocks with (c) $\sigma = 5.76$ kPa and (d) $\sigma = 11.03$ kPa. The figure also shows the mean shear force $\bar{S}$ for each experiment and simulation.

fixed lower part of the right wall. These force chains usually vanished abruptly together with a drop in S, as the snapshots from stage (3) indicate. For example, the simulation on the right column of Figure 3 at stage (3) does not have any blocks with $\hat{\sigma}_2^*$ values higher than the mean $\hat{\sigma}_2^*$ at the peak load event of stage (2).

This simulation-based observation implies that caution should be used when interpreting data from the shear box experiments: the measured maximum loads are related to the force chains and the boundary conditions of the experiments. If the force chains are not accounted for correctly, rubble properties derived from the results, for example material parameters for a Mohr-Coulomb model, are dependent on the experimental set-up. The so-called shape interlocking component [3, 5] included into the shear load of a direct shear box experiment, may be very high and related to force chains.

Conclusions

We performed direct shear box experiments in laboratory scale and simulated them with discrete element method. We validated the simulations and used them for a study on the rubble behavior in the experiments. This showed the strength of the simulations: simulations clearly show how force chains were generated within the ice rubble during a test and cause a sequence of peak shear load events (see Figures 3). More details on our work on this topic can be found from [12].

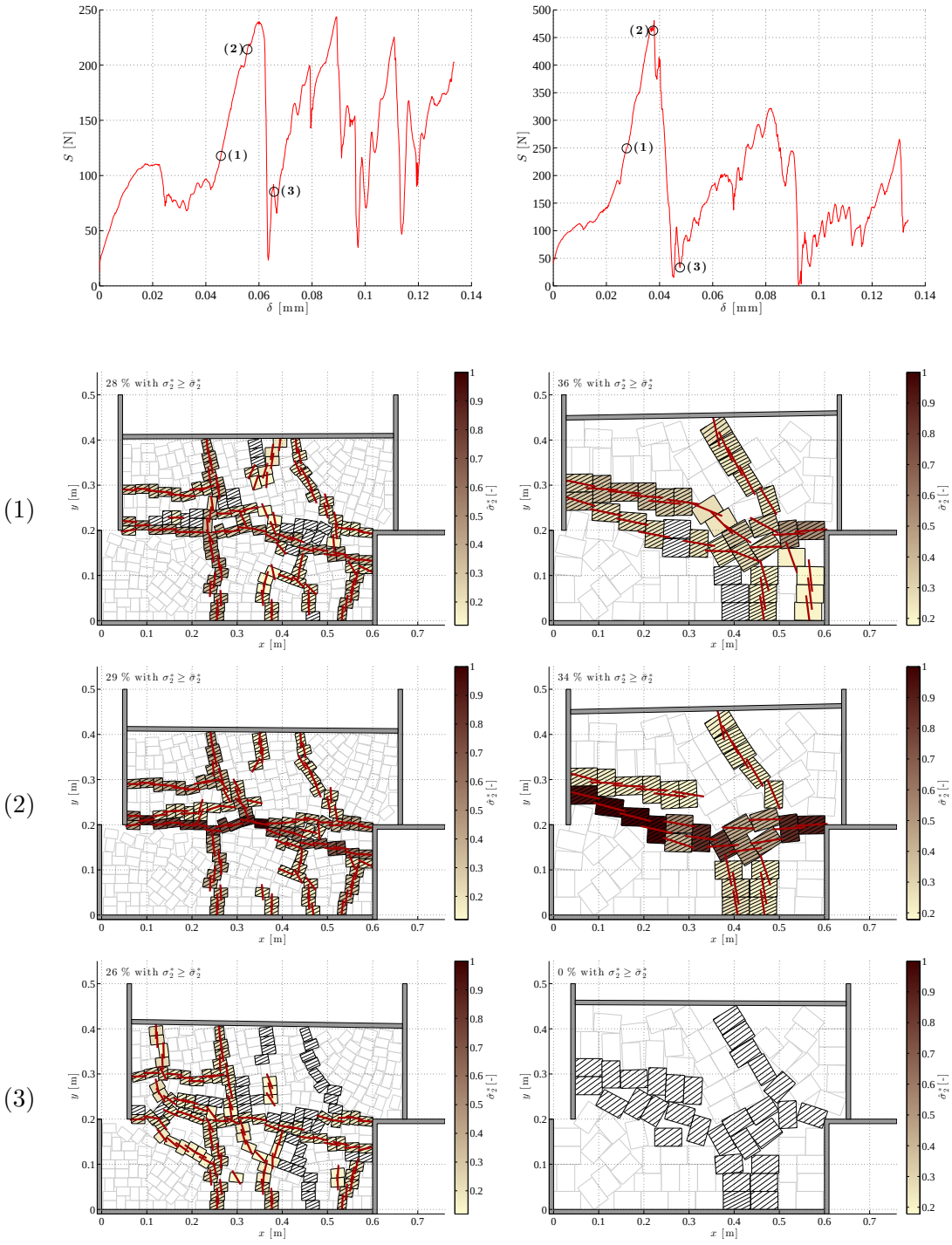

Figure 3. The shear force-displacement $S-\delta$ records and normalized principal particle stresses $\hat{\sigma}_2^*$ with their directions indicated in two simulations on three stages (1)-(3): left (right) column shows a simulation with small (large) blocks. The confining stress was high in these cases. Only the blocks with $\hat{\sigma}_2^*$ higher than the mean value of $\hat{\sigma}_2^*$ within the rubble at stage (2) are colored. In addition blocks having $\hat{\sigma}_2^*$ higher than its mean value at stage (2) have slanted line pattern. The blocks with The $S-\delta$ records indicate stages (1)-(3) shown in each column by numbers.

Acknowledgements

We wish to acknowledge the support from the Research Council of Norway through the Centre for Research-based Innovation SAMCoT and the support from all SAMCoT partners.

References

[1] Cundall, P. and Strack, O. (1979). A discrete numerical model for granular assemblies. *Géotechnique*, 29(1):47–65.

[2] Cundall, P. and Strack, O. (1983). Modeling of microscopic mechanisms in granular material. In Jenkins, J. and Satake, M., editors, *Mechanics of Granular Materials: New Models and Constitutive Relations*, Studies in Applied Mechanics 7, pages 137–149. Elsevier.

[3] Ettema, R. and Urroz, G. E. (1989). On internal friction and cohesion in unconsolidated ice rubble. *Cold Regions Science and Technology*, 16(3):237–247.

[4] Hopkins, M. (1992). Numerical simulation of systems of multitudinous polygonal blocks. Technical Report 92-22, Cold Regions Research and Engineering Laboratory, CRREL. 69 p.

[5] Hopkins, M. and Hibler III, W. D. (1991). On the shear strength of geophysical scale ice rubble. *Cold Regions Science and Technology*, 19(2):201–212.

[6] Luding, S. (1997). Stress distribution in static two-dimensional granular model media in the absence of friction. *Physical Review E - Statistical Physics, Plasmas, Fluids, and Related Interdisciplinary Topics*, 55(4):4720–4729.

[7] Paavilainen, J. and Tuhkuri, J. (2013). Pressure distributions and force chains during simulated ice rubbling against sloped structures. *Cold Regions Science and Technology*, 85:157 – 174.

[8] Paavilainen, J., Tuhkuri, J., and Polojärvi, A. (2009). 2D combined finite–discrete element method to model multi-fracture of beam structures. *Engineering Computations*, 26(6):578–598.

[9] Paavilainen, J., Tuhkuri, J., and Polojärvi, A. (2011). 2D numerical simulations of ice rubble formation process against an inclined structure. *Cold Regions Science and Technology*, 68(1-2):20–34.

[10] Polojärvi, A. and Tuhkuri, J. (2009). 3D discrete numerical modelling of ridge keel punch through tests. *Cold Regions Science and Technology*, 56(1):18–29.

[11] Polojärvi, A., Tuhkuri, J., and Korkalo, O. (2012). Comparison and analysis of experimental and virtual laboratory scale punch through tests. *Cold Regions Science and Technology*, 81:11–25.

[12] Polojärvi, A., Tuhkuri, J., and Pustogvar, A. DEM simulations of direct shear box experiments of ice rubble: Force chains and peak loads. *Accepted for publication in Cold Regions Science and Technology.*

[13] Pustogvar, A., Høyland, K. V., Polojärvi, A., and Bueide, I. M. (2014). Laboratory scale direct shear box experiments on ice rubble: the effect of block to box size ratio. In *Proceedings of OMAE14, 33th International Conference On Offshore Mechanics and Artcic Engineering.*

Suomen XII mekaniikkapäivien esitelmät
R. Kouhia, J. Mäkinen, S. Pajunen and T. Saksala (toim.)

A review on a peak ice load data from 2D combined finite-discrete element method simulations

Janne Ranta[1,2], Jukka Tuhkuri[1,2] and Arttu Polojärvi[1,2]

(1) Aalto University, School of Engineering, Department of Applied Mechanics, P.O. Box 14300, FI-00076 Aalto, Finland, janne.ranta@aalto.fi
(2) Sustainable Arctic Marine and Coastal Technology (SAMCoT), Centre for Research-based Innovation (CRI), Norwegian University of Science and Technology, Trondheim, Norway

Summary. In this paper, a peak ice load data from 2D combined finite-discrete element simulations is reviewed. The paper gives simple examples on how the effects of model parameters on peak ice loads can be studied. Results also highlight that there is a need to use statistical methods to describe the data in its full extent.

Keywords: Ice-structure interaction, Peak ice loads, Combined finite-discrete element method

Introduction

Reliable ice load calculation is a complex task. One of the sources of complexity is the ice rubble formation that in many cases, especially with wide structures, occurs in front of the structure [10]. This rubble and its deformation may change the failure process of the ice sheet and affect ice loads in many ways [5, 9, 10]. Different tools are available for calculating ice loads. Some analytical methods have been reviewed in [8]. Numerical models, however, are more general and they are capable to produce more realistic and profound information about ice-structure interaction processes.

Ice-structure interaction processes consist of discrete events and they are stochastic [2, 4]. Thus, a natural way of studying ice loads is to use discrete models. Previously discrete approaches in some forms have been utilized e.g. in [1, 3, 11]. Recently a two-dimensional combined finite discrete element method (2D FEM-DEM) approach has been developed and validated in [6] and further utilized in [7] for instance.

Measured and simulated ice loads are scattered and therefore statistical methods need to be used in studying them. In this paper, this problematic is demonstrated by few examples based on peak ice load observations from 207 2D FEM-DEM simulations. The same data has been previously considered and analysed from a different point of view in [9]. First in this paper, the 2D FEM-DEM simulations and peak ice load extraction are explained. Then the results from simulations are shown and shortly discussed. Finally the paper is ended with conclusions.

Simulations

In the simulations, a floating and initially continuous ice sheet was moving with a constant velocity of 0.05 m/s against a sloping rigid structure (see Figure 1). During the process, the ice sheet was broken apart into smaller ice blocks. The ice sheet was formed with discrete elements that were connected to each other with Timoshenko beam elements. Beam elements were used firstly to model the elasticity and secondly to model cohesive softening and fracturing of the

ice. Discrete elements were used to treat interactions between different parts of the system, e.g. contacts between ice blocks and contacts between the ice and the structure. More detailed description of the model is given in [6]. Parameters used in the simulations are summarized in Table 1. Eight model parameters were varied in 207 simulations as indicated in the table.

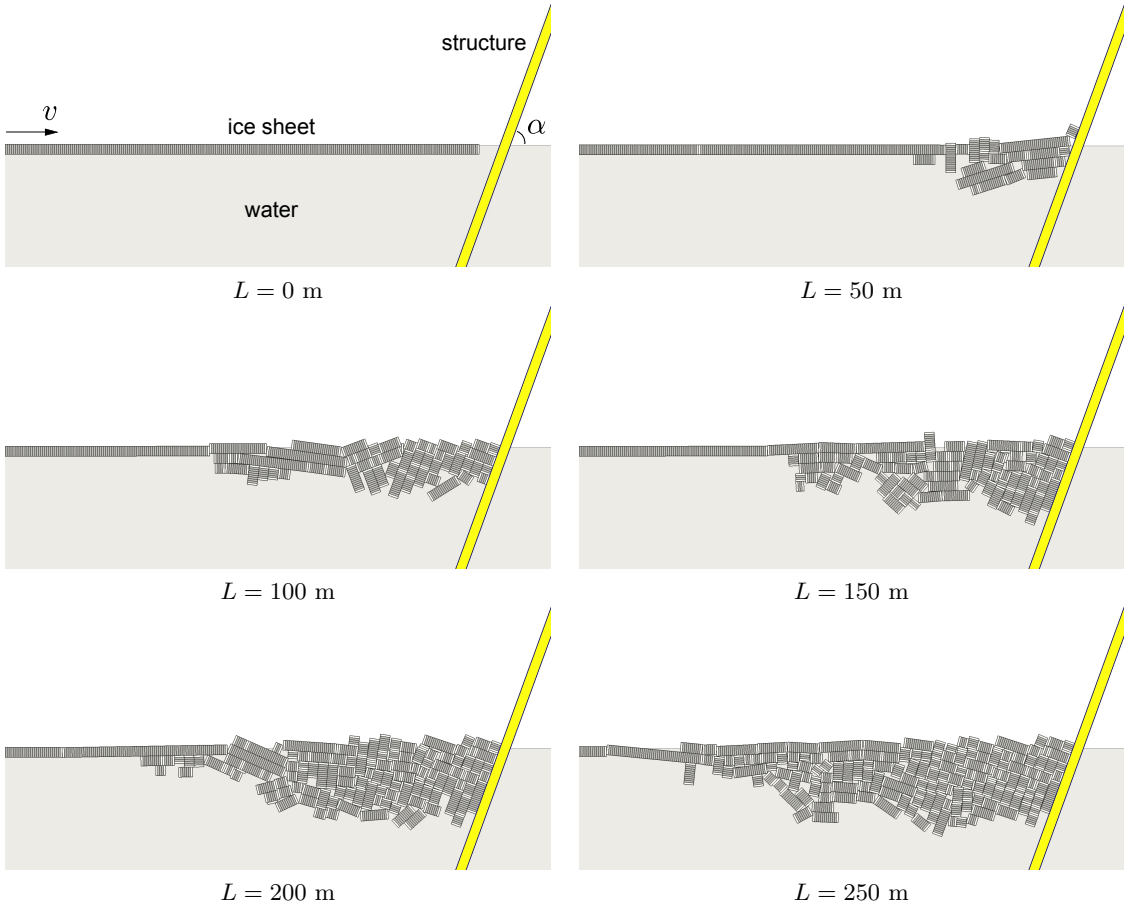

Figure 1: Snapshots from a simulation with $h = 1.25$ m and $\alpha = 70°$. The amount of pushed ice L [m] is used to identify the process stage.

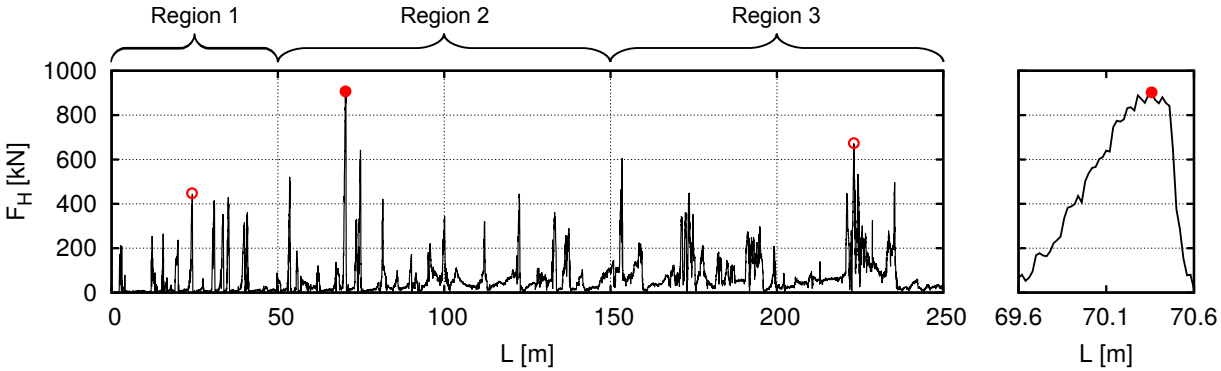

Figure 2: A typical ice load record from a 2D FEM-DEM simulation. Extracted peak ice loads are highlighted with red circles. The close-up on the right highlights the data during the global peak ice load observation. Regions 1, 2 and 3 are explained in the text.

A typical horizontal ice load F_{H} record from a simulation is shown in Figure 2. Ice load records were divided into three subregions based on certain amount of pushed ice L. These

subregions cover initial (0 m $\leq L <$ 50 m), middle (50 m $\leq L <$ 150 m) and end parts (150 m $\leq L \leq$ 250 m) of simulations. Thus, three separate peak ice load values were obtained from each simulated ice load history. In this way, we were able to study how the accumulated ice rubble in front of the structure affected peak ice loads.

Table 1: Summary of simulation parameters. Varied parameters are emphasized with an asterisk symbol ($*$).

	Parameter	Symbol	Unit	Value(s)
General	Gravitational acceleration	g	m/s^2	9.81
	Ice sheet velocity	v	m/s	0.05
	Drag coefficient	d_c		2.0
Ice sheet	Thickness*	h	m	0.25-1.50
	Effective modulus*	E	GPa	2.5-5.0
	Poisson's ratio	ν		0.3
	Density	ρ_i	kg/m^3	900
	Tensile strength*	σ_f	kPa	200-600
	Shear strength*	τ_f	kPa	195-600
Contact	Plastic limit*	σ_p	MPa	1.0, 2.0
	Ice-ice friction coefficient*	μ_{ii}		0.1-1.0
	Ice-structure friction coefficient*	μ_{is}		0.05-0.35
Water	Density	ρ_w	kg/m^3	1010
Structure	Slope angle*	α	°	20-70

Results and discussion

Figures 3 and 4 display the simulated peak ice load data with respect to the ice thickness h and the slope angle α respectively. Based on earlier observations in [9] these two quantities have been chosen for this study as an interesting parameters. In figures 3 and 4, the data from regions 1, 2 and 3 are separated with different type of markers and small horizontal offsets. In addition, linear fits were added for descriptions of "averaged" effects.

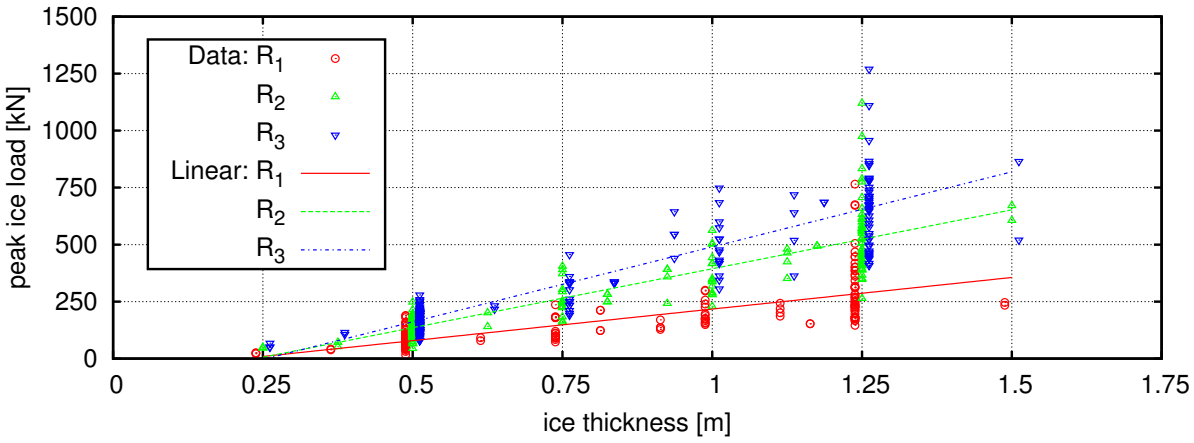

Figure 3: Simulated peak ice loads and corresponding linear fits for Regions 1–3. Peak ice loads are plotted against the ice thickness h.

The data in Figure 3 suggests that peak ice loads depend strongly on the ice thickness h. The slope of the linear regression line is approximately 280 kN/m in case of Region 1 and 660 kN/m in case of Region 3. Hence, another prominent effect is that the dependency on the ice thickness strengthens when the process evolves from Region 1 towards Region 3. Notice that

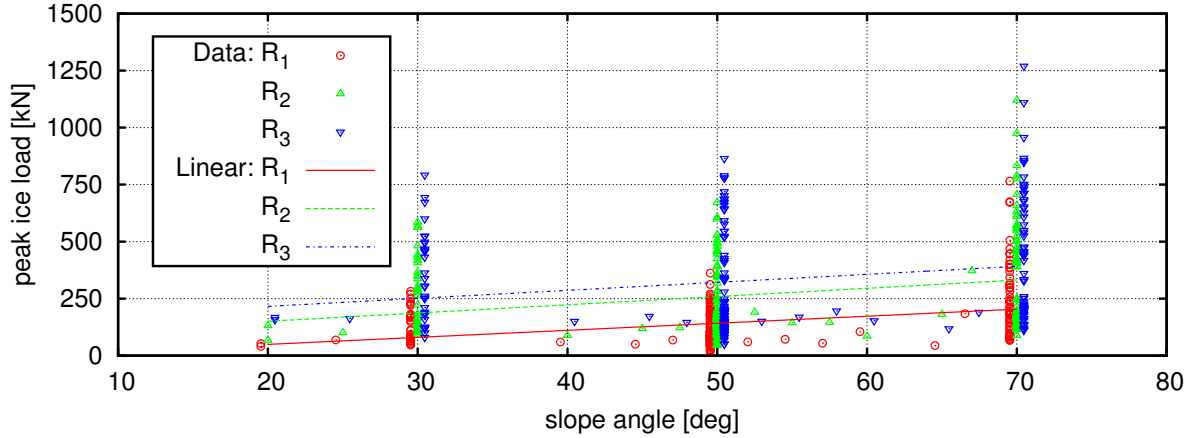

Figure 4: Simulated peak ice loads and corresponding linear fits for Regions 1–3. Peak ice loads are plotted against the slope angle α.

660 kN/m is more than twice as much as 280 kN/m.

A bit surprisingly the data in Figure 4 suggests that peak ice loads do not depend strongly on the slope angle α. The slope of the linear regression line is approximately 3 kN/° in case of Region 1 and 3.5 kN/° in case of Region 2. This time, the effect of the process and the ice rubble accumulation can be clearly seen as the linear regression line translates in vertical direction when the process evolves from Region 1 towards Region 3.

Because of large scatter in the data, regression lines in figures 3 and 4 do not provide good estimates for the most extreme peak ice load observations. This highlights a need to study statistical properties of the data, e.g. peak ice load distributions, in more detail. Numerical simulations can be greatly utilized to obtain required data and samples. Main advantages of these 2D FEM-DEM simulations, for instance, are the full control on all model parameters and the ability to run long-term processes to reach extensive ice rubble formations. For reference, it is good to recognize that from practical reasons the ice thickness is often the only measured ice parameter in full-scale experiments.

Conclusions

In this paper, peak ice load results from 207 combined finite discrete element method simulations were concisely reviewed. The outcome of the paper is summarized in following conclusions:

- Based on the used data, simulated peak ice loads depend strongly on the ice thickness h and only a little on the slope angle α.
- The ice rubble accumulation clearly have an effect on peak ice loads and thus the full ice-structure interaction process need to be considered in peak ice load calculation.
- Because of large scatter in observed peak ice loads, a more detailed statistical analysis is required to describe the data in its full extent.
- The 2D FEM-DEM approach is an applicable way to provide data for ice load estimation due to full control over model parameters and with ability to run long-term processes to reach extensive ice rubble formations.

ACKNOWLEDGEMENTS

The authors wish to acknowledge the support from the Research Council of Norway through the Centre for Research-based Innovation SAMCoT and the support from all SAMCoT partners.

References

[1] Barker, A. and Croasdale, K. Numerical modelling of ice interaction with rubble mound berms in the Caspian Sea. *in: IAHR 04 Proceedings of the 17th International Symposium on Ice*, Saint Petersburg, Russia, 257–264, 2004.

[2] Daley, C.G., Tuhkuri, J. and Riska, K. The role of discrete failures in local ice loads. *Cold Regions Science and Technology*, 27:197–211, 1998.

[3] Hopkins, M. Numerical Simulation of Systems of Multitudinous Polygonal Blocks. *Cold Regions Research and Engineering Laboratory (CRREL)*, Technical Report 92-22, 69 p., 1992.

[4] Jordaan, I.J. Mechanics of ice-structure interaction. *Engineering Fracture Mechanics*, 68:1923–1960, 2001.

[5] Määttänen, M. Ice sheet failure against an inclined wall. *in: IAHR 86 Proceedings of the 8th International Symposium on Ice*, Iowa City, U.S.A., 149–158, 1986.

[6] Paavilainen, J., Tuhkuri, J. and Polojärvi, A. 2D Combined finite-discrete element method to model multi-fracture of beam structures. *Engineering Computations*, 26(6):578–598, 2009.

[7] Paavilainen, J., Tuhkuri, J. and Polojärvi, A. Parameter effects on simulated ice rubbling forces on a wide sloping structure. *Cold Regions Science and Technology*, 81:1–10, 2012.

[8] Palmer, A., Croasdale, K. Arctic Offshore Engineering. World Scientific, 357 p., ISBN 978-981-4368-77-3, 2013.

[9] Ranta, J., Tuhkuri, J. and Polojärvi, A. Statistical reconstruction of peak ice load data based on 2D combined finite-discrete element method simulations of ice interactions against inclined wall. *in: IAHR 2014 Proceedings of the 22nd International Symposium on Ice*, Singapore, 2014.

[10] Timco, G. and Johnston, M. Ice loads on the Molikpaq in the Canadian Beafourt Sea. *Cold Regions Science and Technology*, 37:51–68, 2003.

[11] Williams, J.R., Mustoe, G.G.W. and Worgan, K. Force transfer and behavior of rubble piles, *in: IAHR 86 Proceedings of the 8th International Symposium on Ice*, Iowa City, U.S.A., 615–626, 1986.

Suomen XII mekaniikkapäivien esitelmät
R. Kouhia, J. Mäkinen, S. Pajunen and T. Saksala (toim.)

Cauchy-Navierin yhtälö ja kvaternioanalyysi

Heikki Orelma

Matematiikan laitos, Tampereen teknillinen yliopisto
Korkeakoulunkatu 10, 33720 Tampere

Tiivistelmä. Tässä katsauksessa esitetään perinteiselle vektorilaskennalle vaihtoehtoinen tapa esittää Cauchy-Navierin yhtälö kvaternioanalyysin avulla.

Avainsanat: Kvaterniot, Cauchy-Navierin yhtälö

Johdanto

Tässä kirjoituksessa tarkastellaan kvaternioanalyysiä ja sen soveltamista Cauchy-Navierin yhtälön ratkaisemiseen. Tarkastelemme vain yhtä tiettyä reuna-arvo -ongelmaa, eikä näin lyhyt teksti voi luonnollisestikkaan olla kovin täydellinen. Kirjoitus onkin laadittu enemmänkin tiekartaksi asiasta kiinnostuneille, jossa esitellään keskeiset ideat ja annetaan kirjallisuusviitteet, josta yksityiskohtia ja lisätietoa voi alkaa etsiä. Perusteoriaa kvaternioista ja analyysistä löytyy Klaus Gürlebeckin ja Wolfgang Sprößigin monografioista [1, 2] ja viimeisimpiä tutkimustuloksia löytyy esimerkiksi Sebastian Bockin väitöskirjasta [3]. Nämä lähteet auttavat alkuun ja viimeisimpiä tutkimusartillekeita löytyy esimerkiksi edellä mainitun väitöskirjan lähdeluettelosta.

Kvaterniot

Tarkastellaan kolmiulotteisen avaruuden $\mathbb{R}^3$ kantavektoreita i, j ja k. Perinteisessä vektorilaskennassa avaruuden pisteet esitetään näiden lineaarikombinaationa $\mathbf{x} = xi + yj + zj$. Tämä notaatio mahdollistaa kaiken perinteisen "ristin ja pisteen"matematiikan muodostamisen ilman, että kiinnitämme mitään huomiota symboleiden i, j ja k sisältöön. Irlantilainen matemaatikko William Rowan Hamilton ryhtyi miettimään 1800-luvulla, voitaisiinko edellä oleville vektoreille määritellä tulo kompleksilukujen tapaan. Huomautettakoon tässä, että ristitulo ei ole ominaisuuksitaan riittävä, kompleksilukutulon tapaisen tulon määrittelemiseksi vektoreille $\mathbf{x}$. Hamiltonin oivallus oli määritellä vektoreiden i, j ja k välille tulo, asettamalla

$$i^2 = j^2 = k^2 = ijk = -1.$$

Hamiltonin huomio oli, että pyrittäessä pitämään kiinni tulon assosiatiivisuutta, on pakko ottaa kantavektoriksi mukaan myös skalaari 1. Tällä tulolla varustettu kanta-alkoiden $\{1, i, j, k\}$ generoimaa algebraa kutsutaan *kvaternioalgebraksi* ja merkitään $\mathbb{H}$. Lisäksi edellä olevista laskusäännöistä seuraa kantavektoreiden antikommutatiivisuus, eli $ij = -ji$, $ik = -kj$ jne. Mielivaltainen alkio $q \in \mathbb{H}$ on siis muotoa

$$q = t + xi + yj + zj,$$

ja kvaternioita voidaankin pitää kompleksilukujen luonnollisena yleistyksenä. Kvaternioalgebrassa $\mathbb{H}$ on voimassa samat laskusäännöt kuin kompleksiluvuilla poislukien se, ettei kommutatiivisuus ole voimassa[1]. Kvaterniot on yleensä tapana esittää skalaari- ja vektoriosien summana

$$q = t + \mathbf{x}.$$

Määritellään kvaternion reaaliosa asettamalla $\mathrm{Re}(q) = t$ ja imaginaari- tai vektoriosa $\mathrm{Im}(q) = \mathbf{x}$. Kompleksikonjugoinnin tapaan määritellään konjugaatti asettamalla

$$\overline{q} = t - \mathbf{x},$$

jolloin normi voidaan määritellä

$$|q|^2 = q\overline{q} = \overline{q}q = t^2 + x^2 + y^2 + z^2.$$

Jos $q \neq 0$, saadaan normin määritelmästä vasta-alkion kaava

$$q^{-1} = \frac{\overline{q}}{|q|^2},$$

joka siis toteuttaa $qq^{-1} = q^{-1}q = 1$. Jos $p = s + \mathbf{y}$ on toinen kvaternio, saadaan tulolle esitys

$$qp = ts - \mathbf{x} \cdot \mathbf{y} + t\mathbf{y} + s\mathbf{x} + \mathbf{x} \times \mathbf{y}.$$

Tästä nähdään, että vektoriosien tulo on $\mathbf{xy} = -\mathbf{x} \cdot \mathbf{y} + \mathbf{x} \times \mathbf{y}$.

Differentiaali- ja integraaliperaattoreita

Reaalifunktioiden funktioluokat laajenevat kvaternioarvoisille funktioille olettamalla ominaisuudet komponenttifunktioille. Olkoon siis $f : \Omega \to \mathbb{H}$ dervoituva funktio avoimessa joukossa $\Omega \subset \mathbb{R}^3$, eli $f = f_0 + f_1 i + f_2 j + f_3 k$, missä $f_\alpha : \Omega \to \mathbb{R}$ on reaaliarvoinen derivoituva funktio, kun $\alpha = 0, 1, 2, 3$. Kvaternioarvoista differentiaalioperaattoria

$$D = i\partial_x + j\partial_y + k\partial_z$$

kutsutaan *Diracin operaattoriksi* tai *yleistetyksi Cauchy-Riemannin operaattoriksi*. On helppo todeta, että Df voidaan kirjoittaa muodossa

$$Df = -\operatorname{div} \mathbf{f} + \nabla f_0 + \operatorname{rot} \mathbf{f}, \tag{1}$$

kun $f = f_0 + \mathbf{f}$. Huomaamme, että reaalifunktioilla $\nabla f_0 = Df_0$ ja vektoriarvoisilla funktioille $\operatorname{div} \mathbf{f} = D \cdot \mathbf{f}$ ja $\operatorname{rot} \mathbf{f} = D \times \mathbf{f}$. Jos $Df = 0$ avoimessa joukossa $\Omega \subset \mathbb{R}^3$, kutsutaan funktiota f (*vasemmalta*) *monogeeniseksi* joukossa Ω. Koska kvaternioiden tulo ei ole kommutatiivinen, pitää Diracin operaattorin operointia tarkastella myös oikealta. Näin ollen, jos siis[2] $fD = 0$ avoimessa joukossa $\Omega \subset \mathbb{R}^3$, kutsutaan funktiota f *oikealta monogeeniseksi* joukossa Ω. Diracin operaattorin tärkein ominaisuus on se, että se on Laplacen operaattorin negatiivinen neliö, eli on voimassa

$$D^2 = -\Delta,$$

missä $\Delta = \partial_x^2 + \partial_y^2 + \partial_z^2$. Tämä kaava takaa monogeenisten funktioiden olemassaolon, sillä jos $h : \Omega \to \mathbb{R}$ on harmoninen funktio, eli $\Delta h = 0$, niin tällöin $f = Dh$ on monogeeninen. Eräs esimerkki monogeenisestä funktiosta on ns. Cauchyn ydin

$$E(\mathbf{x}) = -\frac{1}{4\pi} \frac{\mathbf{x}}{|\mathbf{x}|^2},$$

[1] Tämä nähdään helposti esim. $(1 + i)j = j + ij = j + k \neq j - k = j + ji = j(1 + i)$.
[2] Merkintä tarkoittaa $fD = \partial_x f i + \partial_y f j + \partial_z f k$.

joka on monogeninen, kun $\mathbf{x} \neq \mathbf{0}$. Tarkastellaan seuraavaksi yhtälöä $Df = g$ joukossa Ω, kun funktio g on annettu. Tämän ratkaisemiseksi tarvitaan seuraavia integraalioperaatoreita. Oletetaan, että joukon reuna $\partial\Omega$ on riittävän säännöllinen integroimista varten. Olkoon nyt ν joukon $\partial\Omega$ yksikköulkonormaali. Operaattoria

$$F_{\partial\Omega} f(\mathbf{x}) = \int_{\partial\Omega} E(\mathbf{x}-\mathbf{y})\nu(\mathbf{y})f(\mathbf{y})dS_{\mathbf{y}}$$

kutsutaan *Cauchy-Bitsadze -operaattoriksi* ja (singulaarista integraali)operaattoria

$$T_\Omega f(\mathbf{x}) = -\int_\Omega E(\mathbf{x}-\mathbf{y})f(\mathbf{y})dV_{\mathbf{y}}$$

puolestaan *Teodorescu-muunnokseksi*. On suoraviivainen lasku (katso [1]) osoittaa, että Teodorescu-muunnos on Diracin operaattorin oikea käänteisoperaattori, eli

$$DT_\Omega f(\mathbf{x}) = f(\mathbf{x}),$$

kun $\mathbf{x} \in \Omega$. Kaikkia yllä mainittuja operaattoreita yhdistää seuraava identiteetti (katso todistus [1]).

Lause 1 (Borel-Pompeiun kaava) *Jos $f : \Omega \to \mathbb{H}$ on derivoituva joukossa $\mathbb{R}^3$, niin*

$$F_{\partial\Omega} f(\mathbf{x}) + T_\Omega(Df(\mathbf{x})) = \begin{cases} f(\mathbf{x}), & \text{kun } \mathbf{x} \in \Omega, \\ 0, & \text{kun } \mathbf{x} \notin \Omega. \end{cases}$$

Joukossa Ω Borel-Pompeiun kaava voidaan kirjoittaa operaattorimuodossa

$$F_{\partial\Omega} + T_\Omega D = I.$$

Tilanteessa, jossa f on monogeeninen, eli $Df = 0$, Borel-Pompeiun kaava tuottaa Cauchyn integraalikaavan

$$f(\mathbf{x}) = F_{\partial\Omega} f(\mathbf{x}) = \int_{\partial\Omega} E(\mathbf{x}-\mathbf{y})\nu(\mathbf{y})f(\mathbf{y})dS_{\mathbf{y}},$$

joka on suora kompleksianalyysin Cauchyn kaavan yleistys. Borel-Pompeiun kaavan avulla voidaan myös ratkaista reuna-arvo -ongelma

$$\begin{cases} Df = g & \text{joukossa } \Omega, \\ g = 0 & \text{reunalla } \partial\Omega, \end{cases} \tag{2}$$

jonka ratkaisuksi saadaan $f = T_\Omega g$, kunhan g oletetaan riittävän säännölliseksi.

Avaruuden $L^2_{\mathbb{H}}(\Omega)$ jako

Tarkastellaan seuraavaksi reuna-arvo -ongelmien ratkaisemisessa tarvittavia funktioavaruuksia. Funktioavaruus $L^2_{\mathbb{H}}(\Omega)$ koostuu vektorimuuttujan funktioista $f = f_0 + f_1 i + f_2 j + f_3 k$, joiden kertoimet[3] $f_\alpha \in L^2(\Omega)$. Funktiolla $h : \Omega \to \mathbb{R}$ on *heikko derivaatta* joukossa $\Omega \subset \mathbb{R}^3$ muuttujan x suhteen, jos on olemassa funktio g siten, että

$$\int_\Omega g(\mathbf{x})\varphi(\mathbf{x})dV = -\int_\Omega h(\mathbf{x})\partial_x\varphi(\mathbf{x})dV$$

[3]Palautetaan mieliin, että $g \in L^2(\Omega)$, jos ja vain jos $\int_\Omega |g(\mathbf{x})|^2 dV < \infty$.

jokaisella $\varphi \in C_0^\infty(\Omega)$. Tällöin merkitään $\partial_x h = g$. Vastaavasti määritellään heikot derivaatat $\partial_y h$ ja $\partial_z h$. Heikkojen derivaattojen avulla määritellään Sobolev-avaruus

$$W_2^1(\Omega) = \{h \in L^2(\Omega) : \partial_x h, \partial_y h, \partial_z h \in L^2(\Omega)\}$$

ja kvaternioarvoisille funktioille

$$W_{2,\mathbb{H}}^1(\Omega) = \{f = f_0 + f_1 i + f_2 j + f_3 k : f_\alpha \in W_2^1(\Omega)\}.$$

Reuna-arvo -ongelmien kannalta tärkeätä ovat ne Sobolevin avaruuden funktiot, joiden arvo reunalla on nolla. Merkitään näitä funktioita

$$\dot{W}_{2,\mathbb{H}}^1(\Omega) = \{f \in W_{2,\mathbb{H}}^1(\Omega) : f = 0 \text{ reunalla } \partial\Omega\}.$$

Olkoon $Ru = r_0 u_0 + r_1 u_1 i + r_2 u_2 j + r_3 u_3 k$ kvaternio-operaattori, jossa komponenttifunktiot $r_\alpha > 0$ ovat derivoituvia. Määritellään tällä operaattorilla painotettu sisätulo avaruuteen $L_{\mathbb{H}}^2(\Omega)$ asettamalla

$$(f, g)_R = \int_\Omega \overline{R^{-1} f} R^{-1} g \, dV.$$

Sisätulon arvot eivät ole välttämättä reaaliarvoisia, mutta $(f, f)_R \geq 0$. Avaruudelle $L_{\mathbb{H}}^2(\Omega)$ saadaan dekompositio (katso todistus [1])

$$L_{\mathbb{H}}^2(\Omega) = (R\mathrm{Ker}(D) \cap L_{\mathbb{H}}^2(\Omega)) \oplus_R D\dot{W}_{2,\mathbb{H}}^1(\Omega),$$

missä $\mathrm{Ker}(D) = \{f : \Omega \to \mathbb{H} : Df = 0\}$ on monogeenisten funktioiden joukko ja suora summa on laskettu sisätulon $(\cdot, \cdot)_R$ suhteen. Näin ollen jokaista $f \in L_{\mathbb{H}}^2(\Omega)$ kohden löytyy funktiot $g, h : \Omega \to \mathbb{H}$, joille

$$f = Rg + Dh,$$

missä g on monogeeninen ja joka määrää f:n reuna-arvot. Määritellään nyt projektiot $P_R : L_{\mathbb{H}}^2(\Omega) \to R\mathrm{Ker}(D) \cap L_{\mathbb{H}}^2(\Omega)$ asettamalla $P_R f = Rg$ ja $Q_R = I - P_R : L_{\mathbb{H}}^2(\Omega) \to D\dot{W}_{2,\mathbb{H}}^1(\Omega)$ asettamalla $Q_R f = Dh$.

Cauchy-Navierin yhtälö

Tarkastellaan nyt lineaariseen elastisuusteoriaan liittyvää reuna-arvo -ongelmaa

$$\begin{cases} \mu \Delta \mathbf{u} + (\mu + \lambda) \nabla \operatorname{div} \mathbf{u} = -\mathbf{f}, & \text{joukossa } \Omega, \\ \mathbf{u} = \mathbf{0}, & \text{reunalla } \partial\Omega, \end{cases}$$

missä Lamén vakiolle asetetaan rajoitukset $\mu > 0$ ja $2\mu + \lambda > 0$. Lisätään superpositioperiaatteen nojalla ongelmaan reuna-arvo -ongelma $\Delta u_0 = -f_0$, $u_0 = 0$ reunalla, jolloin saadaan käyttämällä edellisissä kappaleissa esiteltyjä kaavoja

$$\begin{cases} -\mu D^2 u - (\mu + \lambda) D \operatorname{Re} Du = -f, & \text{joukossa } \Omega, \\ u = 0, & \text{reunalla } \partial\Omega, \end{cases}$$

missä $\operatorname{Re} Du = -\operatorname{div} \mathbf{u}$ kaavan (1) nojalla. Nyt ylempi yhtälö saadaan muotoon

$$-D(\mu Du + (\mu + \lambda) \operatorname{Re} Du) = -f$$

Ryhmitellään sulkeiden sisällä olevan operaattorin termejä, saadaan

$$\begin{aligned} \mu Du + (\mu + \lambda) \operatorname{Re} Du &= \mu \operatorname{Re} Du + \mu \operatorname{Im} Du + (\mu + \lambda) \operatorname{Re} Du \\ &= (2\mu + \lambda) \operatorname{Re} Du + \mu \operatorname{Im} Du. \end{aligned}$$

Määritellään nyt operaatori $Mq = (2\mu + \lambda)\,\mathrm{Re}(q) + \mu\,\mathrm{Im}(q)$. Tällöin saadaan $\mu Du + (\mu + \lambda)\,\mathrm{Re}\,Du = MDu$ ja alkuperäinen reuna-arvo -ongelma muotoon

$$\begin{cases} DMDu = f, & \text{joukossa } \Omega, \\ u = 0, & \text{reunalla } \partial\Omega. \end{cases}$$

Tämä ongelma voidaan ratkaista kvaterinoanalyysin keinoin. Operoidaan yhtälöön puolittain T_Ω:lla ja sovelletaan Borel-Pompeiun kaavaa $T_\Omega D = -F_{\partial\Omega} + I$, jolloin saadaan

$$-F_{\partial\Omega}MDu + MDu = T_\Omega f.$$

Koska $M^{-1}q = \frac{1}{2\mu+\lambda}\,\mathrm{Re}(q) + \frac{1}{\mu}\,\mathrm{Im}(q)$ saadaan yhtälö muotoon

$$-M^{-1}F_{\partial\Omega}MDu + Du = M^{-1}T_\Omega f. \tag{3}$$

Jos nyt

$$M^{-1}T_\Omega f \in L^2_{\mathbb{H}}(\Omega) = (M^{-1}\mathrm{Ker}(D) \cap L^2_{\mathbb{H}}(\Omega)) \oplus_{M^{-1}} D\dot{W}^1_{2,\mathbb{H}}(\Omega)$$

on olemassa $u \in \dot{W}^1_{2,\mathbb{H}}(\Omega)$, joka toteuttaa yhtälön[4]. Operoimalla yhtälöön (3) puolittain projektiolla $Q_{M^{-1}}$, saadaan $Du = Q_{M^{-1}}M^{-1}T_\Omega f$. Koska termin Du reuna-arvot ovat nollia saadaan, kuten ongelmassa (2), yhtälön *ratkaisuksi*

$$u = T_\Omega Q_{M^{-1}}M^{-1}T_\Omega f.$$

Alkuperäisen ongelman ratkaisu saadaan tästä poimimalla vektoriosa.

Viitteet

[1] K. Gürlebeck, W. Sprößig, *Quaternionic Analysis and Elliptic Boundary Value Problems*, Birkhäuser, Basel, 1990

[2] K. Gürlebeck, K. Habetha, W. Sprößig, *Funktionentheorie in der Ebene und im Raum*, Grundstudium Mathematik, Birkhäuser Verlag, Basel, 2006.

[3] S. Bock, *Über funktionentheoretische Methoden in der räumlichen Elastizitätstheorie,* PhD thesis, Bauhaus-University, Weimar, (url: http://e-pub.uni-weimar.de/frontdoor.php?sourceopus=1503), 2009.

[4] Sillä $-M^{-1}F_{\partial\Omega}MDu \in M^{-1}\mathrm{Ker}(D) \cap L^2_{\mathbb{H}}(\Omega)$ ja $Du \in D\dot{W}^1_{2,\mathbb{H}}(\Omega)$.

Proceedings of the XII Finnish Mechanics Days
R. Kouhia, J. Mäkinen, S. Pajunen and T. Saksala (Eds.)

Transpositions and duals of high-order tensors. On theory and applications in mechanics

Sami Holopainen

Tampere University of Technology, P.O.Box 589, 33 101 Tampere, Sami.Holopainen@tut.fi

Summary. The transpositions and duals of a tensor have numerous applications in many fields of mechanics. They are needed for calculation of a tensor norm, for the definition of pull-backs and push-forwards, and in connection with tensor symmetrizations. Considering the literature of mechanics, the transpose of a bilinear map or a second order tensor is well-defined whereas the duals and transpositions of higher order tensors have remained abstract. The main goal of this work is to demonstrate the difference between the transpositions and duals of high order tensors and show the influence of that difference on real-life applications.

Key words: Tensor transpositions, duals, symmetries

Introduction

The transpositions and duals of tensors have significance in mechanics. Examples can be found in nonlinear continuum mechanics [1], in finite elasto-plasticity [2, 3], and in micro-mechanics [4, 5]. Two mainstreams can actually be identified from the literature: classical tensor algebra on inner product spaces and tensor analysis on manifolds, [1, 6]. The derivations of those concepts differ since in the classical approach the identification of both dual and primary vector spaces is performed a priori whereas the different forms of tensors in tensor analysis on manifolds are clearly identified by the explicit use of a metric. Based on tensor analysis on manifolds, the scalar and the inner product become clearly distinguished and can be used to define the duals and the transpositions, respectively, [7, 6]. Depending on the order of the tensor under consideration, various number of duals and transpositions can be defined. Within the framework adopted, also symmetries of higher order tensors are determined on a systematic manner involving their closed-form representations. An important example is the fourth order tangent stiffness tensor which is of practical value in numerical solution methods. The paper closes with the conclusions and implications for both theory and practice.

Introduction of second order tensors on tangent spaces

Let $\mathcal{P}_0$ and $\mathcal{P}$ be the placements of a manifold and let $T_{\mathbf{X}}\mathcal{P}_0$ and $T_{\mathbf{x}}\mathcal{P}$ be tangent spaces at the points $\mathbf{X} \in \mathcal{P}_0$ and $\mathbf{x} \in \mathcal{P}$, respectively. The natural bases on $T_{\mathbf{X}}\mathcal{P}_0$ and $T_{\mathbf{x}}\mathcal{P}$ are termed $\{\mathbf{G}_A,\ A = 1, 2, 3\}$ and $\{\mathbf{g}_a,\ a = 1, 2, 3\}$, respectively. Similarly, the corresponding dual bases of the cotangent spaces $T^*_{\mathbf{X}}\mathcal{P}_0$ and $T^*_{\mathbf{x}}\mathcal{P}$ are $\{\mathfrak{G}^A,\ A = 1, 2, 3\}$ and $\{\mathfrak{g}^a,\ a = 1, 2, 3\}$, respectively.

The so-called reciprocal bases $\{\mathbf{G}^B\}$ and $\{\mathbf{g}^b\}$ to $\{\mathbf{G}_A\}$ and $\{\mathbf{g}_a\}$ are defined by the inner product as

$$\mathbf{G}_A \cdot \mathbf{G}^B = \delta^B_A, \quad \text{and} \quad \mathbf{g}_a \cdot \mathbf{g}^b = \delta^b_a, \tag{1}$$

where δ^B_A and δ^b_a are Kronecker's delta symbols [6]. With the notation $G_{AB} := \mathbf{G}_A \cdot \mathbf{G}_B$ and $G^{AB} := \mathbf{G}^A \cdot \mathbf{G}^B$, and analogously for g_{ab} and g^{ab}, one can deduce the linear relations between

the reciprocal base-vectors and the base-vectors as being

$$\begin{aligned} \mathbf{G}^A &= G^{AB}\mathbf{G}_B, \quad \mathbf{g}^a = g^{ab}\mathbf{g}_b, \\ \mathbf{G}_A &= G_{AB}\mathbf{G}^B, \quad \mathbf{g}_a = g_{ab}\mathbf{g}^b. \end{aligned} \tag{2}$$

The corresponding dual bases $\{\mathfrak{G}^A\}$ and $\{\mathfrak{g}^a\}$ of the dual spaces $T^*_{\mathbf{X}}\mathcal{P}_0$ and $T^*_{\mathbf{x}}\mathcal{P}$, respectively, are defined as

$$(\mathfrak{G}^A, \mathbf{G}_B)_{\mathfrak{V}} = \delta^A_B, \quad (\mathfrak{g}^a, \mathbf{g}_b)_{\mathfrak{W}} = \delta^a_b, \tag{3}$$

where the bracket, $(\ ,\ )$, expresses the dual pairing, also termed the scalar product [6]. The relations between the dual and the reciprocal base-vectors are given by

$$\mathfrak{G}^A = \mathbf{G}\mathbf{G}^A =: (\mathbf{G}^A)^\flat, \quad \mathfrak{g}^a = \mathbf{g}\mathbf{g}^a =: (\mathbf{g}^a)^\flat, \tag{4}$$

or the dual vectors $\mathfrak{G}^A$ and $\mathfrak{g}^a$ equal to the covectors associated to $\mathbf{G}^A$ and $\mathbf{g}^a$, respectively. The bilinear tangent map, such as the deformation gradient in continuum mechanics, is defined locally as a two-point tensor, [6],

$$\mathbf{F} = F^a_{\cdot A}\mathbf{g}_a \boxtimes \mathfrak{G}^A \in Lin(T_{\mathbf{X}}\mathcal{P}_0; T_{\mathbf{x}}\mathcal{P}). \tag{5}$$

Definition 1 *The adjoint or the dual* $\mathbf{F}^* \in Lin(T^*_{\mathbf{x}}\mathcal{P}; T^*_{\mathbf{X}}\mathcal{P}_0)$ *of* $\mathbf{F}$ *is defined by means of the dual pairing as*

$$(\mathbf{F}^*\mathfrak{f}, \mathbf{a})_{T_{\mathbf{X}}\mathcal{P}_0} = (\mathfrak{f}, \mathbf{F}\mathbf{a})_{T_{\mathbf{x}}\mathcal{P}} \in \mathbb{R} \quad \forall \mathbf{a} \in T_{\mathbf{X}}\mathcal{P}_0, \mathfrak{f} \in T^*_{\mathbf{x}}\mathcal{P}.$$

Since the inner product is only defined between the objects existing on the same space, the transposed map instead of the dual is provided.

Definition 2 *The transpose of a two-point tensor* $\mathbf{F} \in Lin\big(T_{\mathbf{X}}\mathcal{P}_0; T_{\mathbf{x}}\mathcal{P}\big)$ *is defined as*

$$\mathbf{F}^T\mathbf{a} \cdot \mathbf{b} = \mathbf{a} \cdot \mathbf{F}\mathbf{b}, \quad \forall\, \mathbf{a} \in T_{\mathbf{x}}\mathcal{P},\ \mathbf{b} \in T_{\mathbf{X}}\mathcal{P}_0.$$

Based on Defs. 1 and 2, one can write

$$\mathbf{F}^T\mathbf{a} \cdot \mathbf{b} := (\mathbf{G}\mathbf{F}^T\mathbf{a}, \mathbf{b})_{T_{\mathbf{X}}\mathcal{P}_0} = (\mathbf{g}\mathbf{a}, \mathbf{F}\mathbf{b})_{T_{\mathbf{x}}\mathcal{P}} = (\mathbf{F}^*\mathbf{g}\mathbf{a}, \mathbf{b})_{T_{\mathbf{X}}\mathcal{P}_0}, \tag{6}$$

cf. [6] for more detailed account. The result (6) gives the relation between the transposed and the dual map, i.e.

$$\mathbf{F}^T = \mathbf{G}^{-1}\mathbf{F}^*\mathbf{g} \in Lin(T_{\mathbf{x}}\mathcal{P}; T_{\mathbf{X}}\mathcal{P}_0), \quad \forall \mathbf{F} \in Lin(T_{\mathbf{X}}\mathcal{P}_0; T_{\mathbf{x}}\mathcal{P}).$$

Duals and transpositions of high order tensors

In the following, the set of linear maps between tangent or vector spaces is denoted by *Lin* or more precisely by Lin_{k}, $\mathrm{k} \in \{2, (3), 4, ..., 2m \,|\, \text{order of a tensor}\}$ if no need for specification exists. Similarly, the set of invertible and symmetric maps is denoted by $Inv_k \subset Lin_k$ and $Sym_k \subset Lin_k$, respectively. Since tensors are understood as being invariant quantities, absolute notation will be employed. The generalized scalar and inner product needed in the definition of the duals and transpositions, respectively, are demonstrated in the subsequent Section by using their specific form for fourth order tensors.

Definition 3 *Let there be* $\mathbf{V}, \mathcal{W} \in Lin_m$ *and* $\mathcal{C} \in Lin_{2m}$*. The duals of* $\mathcal{C}$*, denoted by* $\mathcal{C}^*$*,* $\mathcal{C}^\star$ *and* ${}^\star\mathcal{C}$*, are defined as follows:*

$$\begin{aligned} (\mathcal{C}(\mathbf{V}), \mathfrak{W}) := \mathcal{W}\mathcal{C}\mathbf{V} &= \mathbf{V}\mathcal{C}^*\mathcal{W} \in \mathbb{R} \quad \textit{(major) dual of } \mathcal{C}, \\ \mathcal{W}\mathcal{C}\mathbf{V} &= \mathcal{W}^*\,{}^\star\mathcal{C}\mathbf{V} = \mathcal{W}\mathcal{C}^\star\mathbf{V}^* \in \mathbb{R} \quad \textit{left and right minor dual of } \mathcal{C}, \\ \mathcal{W}\mathcal{C}\mathbf{V} &= \mathbf{V}^*\,{}^\star(\mathcal{C}^*)\mathcal{W} = \mathbf{V}(\mathcal{C}^*)^\star\mathcal{W}^* \in \mathbb{R} \quad \textit{left and right minor dual of } \mathcal{C}^*. \end{aligned}$$

Definition 4 *Let there be* $\mathbf{V},\mathbf{W}\in Lin_m$ *and* $\mathcal{C}\in Lin_{2m}$*. The transpositions of* $\mathcal{C}$*, denoted by* $\mathcal{C}^T$*,* $\mathcal{C}^t$ *and* ${}^t\mathcal{C}$*, are defined as follows:*

$$\mathbf{W}\bullet\mathcal{C}\mathbf{V}=\mathbf{V}\bullet\mathcal{C}^T\mathbf{W}\in\mathbb{R}\quad \textit{major transposition or the transpose of } \mathcal{C},$$
$$\mathbf{W}\bullet\mathcal{C}\mathbf{V}=\mathbf{W}^T\bullet{}^t\mathcal{C}\mathbf{V}=\mathbf{W}\bullet\mathcal{C}^t\mathbf{V}^T\in\mathbb{R}\quad \textit{left and right minor transposition of } \mathcal{C},$$
$$\mathbf{W}\bullet\mathcal{C}\mathbf{V}=\mathbf{V}^T\bullet{}^t(\mathcal{C}^T)\mathbf{W}=\mathbf{V}\bullet(\mathcal{C}^T)^t\mathbf{W}^T\in\mathbb{R}\ \textit{left and right minor transposition of } \mathcal{C}^T$$

where the notation $\bullet$ *denotes the generalized inner product.*

Let there be $\mathcal{C}\in Lin_{2m}$. Based on 3 and 4, the following identities apply to the duals and the transpositions, [8]:

$$(\mathcal{C}^*)^T=(\mathcal{C}^T)^*,\quad (\mathcal{C}^\star)^T={}^\star(\mathcal{C}^T),\quad ({}^\star\mathcal{C})^T=(\mathcal{C}^T)^\star,\quad (\mathcal{C}^*)^t=({}^t\mathcal{C})^*,$$
$${}^t(\mathcal{C}^*)=(\mathcal{C}^t)^*,\quad (\mathcal{C}^\star)^t=(\mathcal{C}^t)^\star,\quad {}^\star(\mathcal{C}^t)=({}^\star\mathcal{C})^t,\quad ({}^t\mathcal{C})^\star={}^t(\mathcal{C}^\star),\quad {}^\star({}^t\mathcal{C}^t)^\star={}^t({}^\star\mathcal{C}^\star)^t.$$

The duals and transpositions of fourth order tensors

The duals and the transpositions of different tensor products are defined to be consistent with the contractions being employed. For subsequent considerations, the two tensor products termed "$\boxtimes$" and "$\odot$", and the double contraction ":" are defined. The tensor product "$\boxtimes$" is known as the Kronecker product, whereas the tensor product "$\odot$" is defined and frequently employed in continuum mechanics.

Definition 5 *The double contraction between a fourth and a second order tensor is a four-linear map* $Lin_4\times Lin_2\to Lin_2$*, and between two second order tensors it is defined as* $Lin_2\times Lin_2\to\mathbb{R}$*, i.e.*

$$(\mathbf{A}\boxtimes\mathbf{B}:\mathbf{v}_1\boxtimes\mathfrak{w}_1):\mathfrak{w}_2\boxtimes\mathbf{v}_2=(\mathfrak{w}_2,\mathbf{A}\mathbf{v}_1)(\mathfrak{w}_1,\mathbf{B}\mathbf{v}_2),$$
$$(\mathbf{A}\odot\mathbf{B}:\mathfrak{w}_1\boxtimes\mathbf{v}_2):\mathfrak{w}_2\boxtimes\mathbf{v}_1=(\mathfrak{w}_2,\mathbf{A}\mathbf{v}_1)(\mathfrak{w}_1,\mathbf{B}\mathbf{v}_2)$$

holds.

If the double contraction is calculated on the basis of the inner products, it is termed the double-dot product, denoted by "$:$".

Theorem 6 *Let* $\mathbf{A},\mathbf{B}\in Lin_2$ *be second order tensors. The duals of the decomposable tensors (with respect to the double contractions)* $\mathbf{A}\boxtimes\mathbf{B}\in Lin_4$ *and* $\mathbf{A}\odot\mathbf{B}\in Lin_4$ *are given by*

$$(\mathbf{A}\boxtimes\mathbf{B})^*=\mathbf{A}^*\boxtimes\mathbf{B}^*,\quad {}^\star(\mathbf{A}\boxtimes\mathbf{B})^\star=\mathbf{B}^*\boxtimes\mathbf{A}^*,\quad (\mathbf{A}\odot\mathbf{B})^*=\mathbf{B}\odot\mathbf{A},$$
$$(\mathbf{A}\odot\mathbf{B})^\star=\mathbf{A}\odot\mathbf{B}^*,\quad {}^\star(\mathbf{A}\odot\mathbf{B})={}^*\mathbf{A}\odot\mathbf{B},\quad {}^\star(\mathbf{A}\odot\mathbf{B})^\star=\mathbf{A}^*\odot\mathbf{B}^*.$$

Proof. Without loss of generality, let there be $\mathbf{A},\mathbf{B}\in Lin(T_{\mathbf{X}}\mathcal{P}_0;T_{\mathbf{x}}\mathcal{P})$, $\mathbf{v}_1,\mathbf{v}_2\in T_{\mathbf{X}}\mathcal{P}_0$, and $\mathfrak{w}_1,\mathfrak{w}_2\in T^*_{\mathbf{x}}\mathcal{P}$. Then $\mathbf{A}\boxtimes\mathbf{B}$, $\mathbf{A}\odot\mathbf{B}\in Lin(T^*_{\mathbf{x}}\mathcal{P}\times T_{\mathbf{X}}\mathcal{P}_0\times T^*_{\mathbf{x}}\mathcal{P}\times T_{\mathbf{X}}\mathcal{P}_0;\mathbb{R})$. Application of Def. 5 for the duals results in

$$(\mathbf{A}\boxtimes\mathbf{B}:\mathbf{v}_1\boxtimes\mathfrak{w}_1):\mathfrak{w}_2\boxtimes\mathbf{v}_2=(\mathfrak{w}_2,\mathbf{A}\mathbf{v}_1)(\mathfrak{w}_1,\mathbf{B}\mathbf{v}_2)=(\mathbf{v}_1,\mathbf{A}^*\mathfrak{w}_2)(\mathbf{v}_2,\mathbf{B}^*\mathfrak{w}_1)=$$
$$(\mathbf{A}^*\boxtimes\mathbf{B}^*:\mathfrak{w}_2\boxtimes\mathbf{v}_2):\mathbf{v}_1\boxtimes\mathfrak{w}_1=:((\mathbf{A}\boxtimes\mathbf{B})^*:\mathfrak{w}_2\boxtimes\mathbf{v}_2):\mathbf{v}_1\boxtimes\mathfrak{w}_1,$$
$$(\mathbf{A}\odot\mathbf{B}:\mathfrak{w}_1\boxtimes\mathbf{v}_2):\mathfrak{w}_2\boxtimes\mathbf{v}_1=(\mathfrak{w}_2,\mathbf{A}\mathbf{v}_1)(\mathfrak{w}_1,\mathbf{B}\mathbf{v}_2)=(\mathfrak{w}_1,\mathbf{B}\mathbf{v}_2)(\mathfrak{w}_2,\mathbf{A}\mathbf{v}_1)=$$
$$(\mathbf{B}\odot\mathbf{A}:\mathfrak{w}_2\boxtimes\mathbf{v}_1):\mathfrak{w}_1\boxtimes\mathbf{v}_2=:((\mathbf{A}\odot\mathbf{B})^*:\mathfrak{w}_2\boxtimes\mathbf{v}_1):\mathfrak{w}_1\boxtimes\mathbf{v}_2,$$

etc. □

Figure 1: Domain and range of the four-linear map (isomorphism) $\mathcal{C} \in Lin(T^*_{\mathbf{x}}\mathcal{P} \times T_{\mathbf{X}}\mathcal{P}_0 \times T^*_{\mathbf{x}}\mathcal{P} \times T_{\mathbf{X}}\mathcal{P}_0; \mathbb{R})$ and the commutative diagram for the dual, transpose and metrics (taken from [8]).

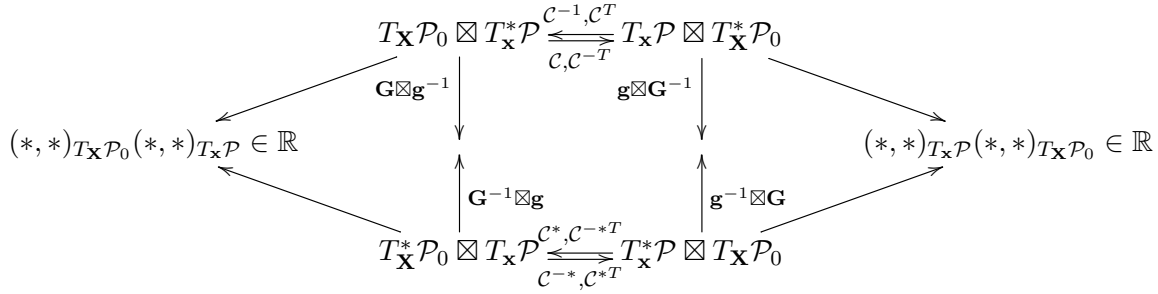

Theorem 7 *Let* $\mathbf{A}, \mathbf{B} \in Lin_2$ *be second order tensors. The transpositions of the decomposable tensors* (*with respect to the double-dot products*) $\mathbf{A} \boxtimes \mathbf{B} \in Lin_4$ *and* $\mathbf{A} \boxdot \mathbf{B} \in Lin_4$ *are given by*

$$(\mathbf{A} \boxtimes \mathbf{B})^T = \mathbf{A}^T \boxtimes \mathbf{B}^T, \quad {}^t(\mathbf{A} \boxtimes \mathbf{B})^t = \mathbf{B}^T \boxtimes \mathbf{A}^T, \quad (\mathbf{A} \boxdot \mathbf{B})^T = \mathbf{B}^{*T} \boxdot \mathbf{A}^{*T},$$
$$(\mathbf{A} \boxdot \mathbf{B})^t = \mathbf{A} \boxdot \mathbf{B}^T, \quad {}^t(\mathbf{A} \boxdot \mathbf{B}) = \mathbf{A}^T \boxdot \mathbf{B}, \quad {}^t(\mathbf{A} \boxdot \mathbf{B})^t = \mathbf{A}^T \boxdot \mathbf{B}^T.$$

Proof. Let there be $\mathbf{A}, \mathbf{B} \in Lin(T_{\mathbf{X}}\mathcal{P}_0; T_{\mathbf{x}}\mathcal{P})$, $\mathbf{v}_1 \in T_{\mathbf{X}}\mathcal{P}_0$, $\mathfrak{v}_2 \in T^*_{\mathbf{X}}\mathcal{P}_0$, $\mathfrak{w}_1 \in T^*_{\mathbf{x}}\mathcal{P}$, and $\mathbf{w}_2 \in T_{\mathbf{x}}\mathcal{P}$. Based on Def. 4 the transpose $(\mathbf{A} \boxdot \mathbf{B})^T$ is obtained by

$$(\mathbf{A} \boxdot \mathbf{B} : \mathfrak{w}_1 \boxtimes \mathbf{v}_1) \mathbf{:} \mathbf{w}_2 \boxtimes \mathfrak{v}_2 = (\mathbf{w}_2 \cdot \mathbf{A} \cdot \mathfrak{v}_2)(\mathfrak{w}_1, \mathbf{B}\mathbf{v}_1) = (\mathfrak{w}_1 \cdot \mathbf{B}^{*T} \cdot \mathbf{v}_1)(\mathbf{w}_2, \mathbf{A}^{*T}\mathfrak{v}_2) =$$
$$(\mathbf{B}^{*T} \boxdot \mathbf{A}^{*T} : \mathbf{w}_2 \boxtimes \mathfrak{v}_2) \mathbf{:} \mathfrak{w}_1 \boxtimes \mathbf{v}_1 =: ((\mathbf{A} \boxdot \mathbf{B})^T : \mathbf{w}_2 \boxtimes \mathfrak{v}_2) \mathbf{:} \mathfrak{w}_1 \boxtimes \mathbf{v}_1 \quad \text{etc.} \quad \square$$

Explicit representations of the transpositions on tangent spaces

Since the duals and the transpositions are both tensorial operations, they were defined using absolute notation, cf. Defs. 3 and 4. Calculation of the transpositions, however, depends on the metric of the metric tensor spaces being involved.

Corollary 8 *Suppose that* $\mathcal{C} \in Lin(T^*_{\mathbf{X}}\mathcal{P}_0 \times T_{\mathbf{X}}\mathcal{P}_0 \times T^*_{\mathbf{X}}\mathcal{P}_0 \times T_{\mathbf{X}}\mathcal{P}_0; \mathbb{R})$. *The transpositions of* $\mathcal{C}$ *are given by*

$$\begin{aligned}
\mathcal{C}^T &= \mathbf{G}^{-1} \boxtimes \mathbf{G} : \mathcal{C}^* : \mathbf{G} \boxtimes \mathbf{G}^{-1}, \\
\mathcal{C}^t &= \mathcal{C} : (\mathbf{G}^{-1} \boxtimes \mathbf{G})^\star, \\
{}^t\mathcal{C} &= {}^\star\big(\mathbf{G} \boxtimes \mathbf{G}^{-1}\big) : \mathcal{C}, \\
{}^t\mathcal{C}^t &= {}^\star(\mathbf{G} \boxtimes \mathbf{G}^{-1}) : \mathcal{C} : (\mathbf{G}^{-1} \boxtimes \mathbf{G})^\star, \\
{}^t(\mathcal{C}^T) &= (\mathcal{C}^t)^T = {}^\star(\mathcal{C}^*) : \mathbf{G} \boxtimes \mathbf{G}^{-1}, \\
(\mathcal{C}^T)^t &= ({}^t\mathcal{C})^T = (\mathbf{G}^{-1} \boxtimes \mathbf{G}) : (\mathcal{C}^*)^\star,
\end{aligned}$$

i.e. the transpositions lie on the same space $Lin(T^*_{\mathbf{X}}\mathcal{P}_0 \times T_{\mathbf{X}}\mathcal{P}_0 \times T^*_{\mathbf{X}}\mathcal{P}_0 \times T_{\mathbf{X}}\mathcal{P}_0; \mathbb{R})$.

Proof. See [8].

Fig. 1 shows the commutative diagram for the dual and transpose of a four-linear map. It can be concluded that the transposed map operates from the actual primary tensor space into the original primary tensor space and the dual transposed map operates from the original dual

tensor space into the actual dual tensor space. The original tensor and its dual operate vice versa.

Example 9 *In state-of-the-art models for polymer materials, the symmetric Kirchhoff stress in its mixed form $\tau \in Sym(T_{\mathbf{x}}\mathcal{P}; T_{\mathbf{x}}\mathcal{P})$ is defined as*

$$\tau^{\natural} := 2\mu(\ln \mathbf{v}^e)^{dev} + \kappa trace(\ln \mathbf{v}^e)\mathbf{i} = 2\mu(\mathbf{i} \boxtimes \mathbf{i} + \frac{3\kappa + 2\mu}{6\mu}\mathbf{i} \boxdot \mathbf{i}) : \ln \mathbf{v}^e =: \mathcal{L}^e : \ln \mathbf{v}^e \tag{7}$$

where $(\ln \mathbf{v}^e)^{dev} := \ln \mathbf{v}^e - \frac{1}{3}trace(\ln \mathbf{v}^e)\mathbf{i}$ denotes the deviatoric component of the elastic stretch tensor $\mathbf{v}^e$, and μ and κ are the elastic constitutive parameters, [5]. In contrast to the mixed form (7)*, the kinetic, stress-like quantities are often given in the contravariant form while the kinematic quantities are given in the covariant form. Using* (2) *and* (4)*, yields the Kirchhoff stress*

$$\begin{aligned} \tau = \tau^{\natural}\mathbf{g}^{-1} &:= 2\mu\mathbf{g}^{-1}(\ln \mathbf{v}^e)^{dev}\mathbf{g}^{-1} + \kappa trace(\mathbf{g}^{-1}\ln \mathbf{v}^e)\mathbf{g}^{-1} \\ &= 2\mu(\mathbf{g}^{-1} \boxtimes \mathbf{g}^{-1} + \frac{3\kappa + 2\mu}{6\mu}\mathbf{g}^{-1} \boxdot \mathbf{g}^{-1}) : \ln \mathbf{v}^e =: \mathcal{L}^e : \ln \mathbf{v}^e \in Sym(T^*_{\mathbf{x}}\mathcal{P}; T_{\mathbf{x}}\mathcal{P}), \end{aligned} \tag{8}$$

which is in the contravariant form depending on the contravariant metric $\mathbf{g}^{-1}$ under consideration.

In an implicit finite element solution process, the stress-strain relation needs to be linearized. Using the correct transformations, see e.g. [8], the second Piola-Kirchhoff stress is defined as $\mathbf{S} := \mathbf{F}^{-1}\tau\mathbf{F}^{-*} \in Sym(T^*_{\mathbf{X}}\mathcal{P}_0; T_{\mathbf{X}}\mathcal{P}_0)$ and its work-conjugate Cauchy-Green deformation tensor as $\mathbf{C} := \mathbf{F}^*\mathbf{g}\mathbf{F} \in Sym(T_{\mathbf{X}}\mathcal{P}_0; T^*_{\mathbf{X}}\mathcal{P}_0)$. Then,

$$\begin{aligned} \mathcal{C} :=& 2\frac{d\mathbf{S}}{d\mathbf{C}} = {}'(\mathbf{F}^{-1} \boxtimes \mathbf{F}^{-*})' : \frac{d\tau}{d\mathbf{F}} : (\mathbf{g}^{-1}\mathbf{F}^{-*} \boxtimes \mathbf{I})' - 2\,{}'(\mathbf{S} \boxtimes \mathbf{C}^{-1})' \\ &\in Lin(T^*_{\mathbf{X}}\mathcal{P}_0 \times T^*_{\mathbf{X}}\mathcal{P}_0 \times T^*_{\mathbf{X}}\mathcal{P}_0 \times T^*_{\mathbf{X}}\mathcal{P}_0; \mathbb{R}) \end{aligned} \tag{9}$$

where $\mathbf{I}$ is the identity. The details how to obtain the derivative $d\tau/d\mathbf{F}$ which is consistent with the integration algorithm employed can be found e.g. from [3]. In (9)*, the left, right, and their coupled sub-symmetrization, denoted by*

$${}'(\bullet) = \frac{1}{2}((\bullet) + {}^{\star}(\bullet)), \quad (\bullet)' = \frac{1}{2}((\bullet) + (\bullet)^{\star}), \quad {}'(\bullet)' = \frac{1}{4}((\bullet) + (\bullet)^{\star} + {}^{\star}(\bullet) + {}^{\star}(\bullet)^{\star}), \tag{10}$$

were introduced. The left sub-symmetry results from the symmetry of the stress $\mathbf{S}$, whereas the differentiation with respect to the symmetric strain $\mathbf{C}$ results in the right sub-symmetry of $\mathcal{C}$. However, the major symmetry of $\mathcal{C}$ does not explicitly appear. The Lagrangian form (9) *can be pushed forward to the spatial configuration which yields*

$$\mathfrak{c} := \frac{d\tau}{d\mathbf{F}} : (\mathbf{g}^{-1} \boxtimes \mathbf{F})' - 2'(\tau \boxtimes \mathbf{g}^{-1})' \in Lin(T^*_{\mathbf{x}}\mathcal{P} \times T^*_{\mathbf{x}}\mathcal{P} \times T^*_{\mathbf{x}}\mathcal{P} \times T^*_{\mathbf{x}}\mathcal{P}; \mathbb{R}), \tag{11}$$

see e.g. [8] for more detailed account. According to the classical approach (tensor calculus on inner-products spaces), the metric in Eqs. (9) *and* (11) *would be considered as identity, i.e.*

$$\begin{aligned} \mathcal{C} &= {}'(\mathbf{F}^{-1} \boxtimes \mathbf{F}^{-T})' : \frac{d\tau}{d\mathbf{F}} : (\mathbf{F}^{-T} \boxtimes \mathbf{I})' - 2\,{}'(\mathbf{S} \boxtimes \mathbf{C}^{-1})', \\ \mathfrak{c} &= \frac{d\tau}{d\mathbf{F}} : (\mathbf{i} \boxtimes \mathbf{F})' - 2'(\tau \boxtimes \mathbf{i})'. \end{aligned} \tag{12}$$

Comparison of Eqs. (9) and (11) with Eq. (12) reveals an important outcome. An advantage of Eqs. (9) and (11) is their applicability over different sub-spaces, whereas the results in (12) can be applied only on the sub-space under consideration. In other words, it is not clear how Eqs. (9) and (11) could be obtained if only the results in Eq. (12) would be at hand. Moreover, different forms of a tensor cannot be identified in the classical approach either. A consequence is that important transformations, such as pull-back and push-forward, become ambiguous.

References

[1] P. Haupt and Ch. Tsakmakis. On the application of duals variables in continuum mechanics. *Continuum Mechanics and Thermodynamics*, 1:165–196, 1989.

[2] O. Kintzel. *Modeling of Elasto-plastic Material Behavior and Ductile Micropore Damage of Metallic Materials at Large Deformations.* Shaker-Verlag: Aachen, 2007.

[3] C. Miehe, E. Stein, and W. Wagner. Associative multiplicative elasto-plasticity: Formulation and aspects of the numerical implementation including stability analysis. *Comp. Struct.*, 52: 969–978, 1994.

[4] S. Nemat-Nasser and M. Hori. *Micromechanics - Overall Properties of Heterogenous Solids.* North-Holland: Amsterdam, 1993.

[5] P. D. Wu and E. van der Giessen. On improved network models for rubber elasticity and their applications to orientation hardening in glassy polymers. *J. Mech. Phys. Solids*, 41(3): 427–456, 1993.

[6] H. Stumpf and U. Hoppe. The application of tensor algebra on manifolds to nonlinear continuum mechanics-invited survey artile. *Z. Angew. Math. Mech (ZAMM)*, 77:327–339, 1997.

[7] E. van der Giessen and F. G. Kollmann. On mathematical aspects of dual variables in continuum mechanics. part 1: Mathematical principles. *Z. Angew. Math. Mech. (ZAMM)*, 76:447–462, 1996.

[8] S. Holopainen. Representations of m-linear functions on tensor spaces. Duals and transpositions with applications in continuum mechanics. *Mathematics and Mechanics of Solids*, 19: 168–192, 2014.

Proceedings of the XII Finnish Mechanics Days
R. Kouhia, J. Mäkinen, S. Pajunen and T. Saksala (Eds.)

Guaranteed and computable error estimates of Uzawa iteration method for a class of Bingham fluids

Marjaana Nokka and Sergey Repin

University of Jyväskylä, Finland, marjaana.nokka@jyu.fi

Summary. This presentation is concerned with fully guaranteed and computable bounds of errors generated by Uzawa type methods for variational problems in the theory of visco-plastic fluids. The respective estimates have two forms. The first form contains global constants (such as the constant in the Friedrichs inequality for the respective domain), and the second one is based upon decomposition of the domain into a collection of subdomains and uses local constants associated with subdomains.

Suomen XII mekaniikkapäivien esitelmät
R. Kouhia, J. Mäkinen, S. Pajunen ja T. Saksala (toim.)

Finger and toe photoplethysmographic pulse waveform analysis with means of logarithmic transformation

Matti Huotari[1], Kari Määttä[2], Juha Röning[1]

(1) Computer Science and Engineering, University of OULU, POBox 4500, 90014 OULU UNIVERSITY, FINLAND, firstname.surname@ee.oulu.fi
(2) Electronics Laboratory, University of OULU, 90014 OULU UNIVERSITY, FINLAND, POBox 4500, firstname.surname@ee.oulu.fi

Abstract. A new method for a measurement and analysis cardiovascular health has to offer new information for clinical doctors. The received information has to be repeatable and reproducible before routine clinical studies will begin. We have developed a photoplethysmographic system for PPG waveforms which are measured repeatable way in consecutive recordings as well as reproducible in longer time recording intervals. Temporal values of the signal components are studied in order to define the invariants of the signals by means of envelope construction. Furthermore, due to the sensitivity of waveform measurements, any bodily movements cause error in the correctness of the results. After measurements in supine position the arterial pulse waveform analysis (PWA) is a valid and very reliable technique. The main goal for this study is the verification and validation of the noninvasive method for arterial elasticity assessment.

Key words: arterial elasticity index, pulse waveform decomposition, photoplethysmography

Introduction

Arteriosclerosis is a common vascular disorder among older people, but its negative impacts on young people are much greater than on the elderly people. Early arterial aging has become the most common and important issue in clinical research. Arterial elasticity (AE) has proved to be a direct indicator for cardiovascular diseases (CVD). That's why accurate measurements and analysis of the blood vessel properties are important for better characterization of both arterial and venous diseases and the development of reliable computational models. Many non-invasive measurement methods for direct and indirect arterial pulse waveform have been proposed, such as the use of ultrasonic transducers (arterial and venous wall thickness and pulse wave velocity (PWV)), photoplethysmograms (PPG, volume PW) and mechanical sensors (pressure PW) [1, 2]. Ultrasonography and pulse wave velocity (PWV) tests are the main diagnostic methods in clinics to assess the degree of arteriosclerosis or atherosclerosis. Because atherosclerosis occurs as calcifications of vessels, it may obstruct the ultrasound beam but optically vessels can be measured. Sometimes ultrasound cannot differentiate between a blood vessel and other tissue. There is a few methods to record the healthiness of blood vessels. These methods can give new

insights into the physiology and before pathophysiological processes in the central and especially peripheral circulatory system.

In photoplethysmographic (PPG) measurements, both the systolic and diastolic pulse waveform have the peak and trough inside of the upper and lower envelopes. Before envelope calculation the signal is smoothed for 25 points window (1 kHz sample frequency). After the envelopes removal it is possible to calculate, e.g., pulse waveform decomposition, spectral functions, correlations, Lissajous' patterns, respiratory rate, heart rate, autonomic and vascular activity, both vasoconstriction. We study the representation of PPG pulse waveform decomposition based on a lognormal function form and a finite Gaussian basis in the pulse waveform analysis (PWA). The Gaussian basis is received simply by taking logarithm of the time axis on the normalized pulse waveform. The Levenberg-Marquardt algorithm is much applied for the solution of nonlinear least-squares curve fitting and estimation problems. This iteration algorithm works faster on the Gaussian basis function compared with the linear pulse waveform, being 50-200 times faster giving the exact same results. The found pulse and its features can be specifically called. Namely, a pulse waveform can be decomposed into a percussion, tidal, dicrotic, repercussion, and retidal wave. Arterial pulse decomposition refers to dividing a measured pulse wave into a set of mentioned constituent pulse waves and thus makes a complex pulse wave transmission phenomenon understood more easily. Pulse wave decomposition (PWD) has been successfully used in PPG pulse wave analysis and ECG signal analysis, but also in image processing. It has potential needed to draw a clear distinction of contributions made by constituent pulses, in this case by the five constituents. However, however, there are no internationally recognized standards for clinical PPG measurement. Processing of the PPG pulse waveform series is as follows:

Generate the upper and lower envelopes to connect the maxima and minima respectively. The upper envelope u(t) and lower envelope v(t) of the PPG signals x(t). Then we subtract the upper envelope u(t) from the x(t) and taking the absolute value of the original PPG signal. The PPG signal is then inverted so that it correlates positively with blood volume. For normalization between $[0, \dots, 1]$ we determine the new upper envelope u(t) for the new signal x(t). By this new envelope u(t) we divide the signal x(t) which is now between 0 and 1 from its minimum to its maximum. Each true signal s_i is also connected with the corresponding noise n_i. The true signals can be due to the blood volume change (1), respiratory rate (2), vasomotor activity (3), autonomic activity (4), vasoconstrictor (5), thermoregulation (6), which can be together combined as so-called Traube Hering Mayer (THM) waves. These waves give a steady signal that changes very slowly. These waves are in part caused by different mechanisms, and that they provide different information about arterial properties at central and peripheral sites. As in the equation (1), these waves are simply summed up

$$x(t) = s_i(t) + n_i(t),\ i = 1, \dots, 6 \tag{1}$$

Because the behavior of arteries is a function of the dynamic characteristics of the circulatory system, the analysis of arterial pulse waveform gives information also on the arterial elasticity. The drift phenomenon of the PPG signal causes inaccuracy for assessing arterial stiffness if not properly processed. Therefore, we used a signal process method, known as the pulse waveform decomposition (PWD) with curve fitting. The finger PPG pulse wave can be decomposed a signal set of five components which can be called basis functions. However, the PPG method suffers from interference and distortion such as baseline wander, mains-line interference, and random spikes or other such artifacts. The baseline wander is removed by the envelopes, light, and mains-line power interference by the phase sensitive detection (PSD) electronics in measurements.

Materials and methodology

The PPG pulse waveforms analyzed in this study were obtained from volunteer subjects in supine position. Data were collected with approval of each person tested with informed consent. The results of this volunteer study was carried out on healthy individuals, where PPG device was used to measure the pulse waveforms at least 300 sec from left index finger and second toe to monitor peripheral perfusion after 10 min rest. The PPG pulse waveform with its envelope signals from the radial artery are captured using a lab made PPG device connected with USB measurement card to a personal computer. The measurement software is Signal Express (National Instruments). Signal processing was realized with OriginLab (Microcalc) software for envelopes and the pulse waveform decomposition. The pulse waveforms from the radial artery were captured using two laboratory made probes, which contain two pulse oximeter sensors based on two different wavelengths of LED light (640 nm & 920 nm) to capture the pulsations with its baseline and single pulses. Photon envelope represents a space area along which most photons travel from the LED to the photodetector through the measured tissue. The received signal is processed by the phase sensitive detector (PSD) electronics. In the finger PPG pulse waveform it is possible to find percussion, tidal, dicrotic, repercussion, and retidal peaks in the off-line signal processing. These peaks are identified by the software and the intervals between these components are calculated to find out the Arterial Elasticity Index (AEI), a useful tool for assessing noninvasively the status of the vascular but also autonomic nervous system.

Results and discussion

PPG recordings were obtained from all the volunteers throughout the study, and also PCG (phonocardiography) were used as a timing reference for the PPG signals. PPG signal processing as an example is applied as follows. Figure 1 shows the draw and smoothed finger PPG (left) and the upper and lower envelopes of the corresponding PPG.

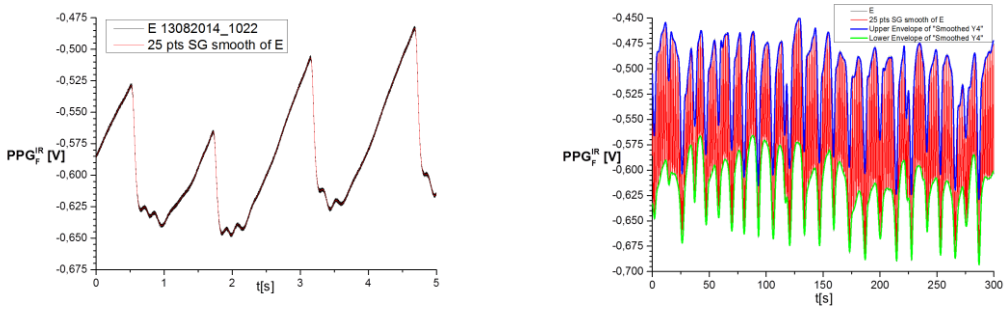

Figs. 1. The original infrared finger PPG (black), its smoothed 25 points curve (red) (left), and the upper (blue) and lower (green) envelope (right) for 300 s (31 male person).

Figure 2 shows the normalized PPG envelope wave (left) for 300 s and the normalized PPG pulse waves for 5 s from the Figure 1 (right). PPG signals contain the three peaks indicating a specific elastic structure of the PPG waveform measured from a young person. In Figure 3 it is shown the corresponding infrared toe PPG recording (black), its smoothed 25 points curve (red) (left), and the normalized toe envelope signal (right) for 300 s (31 male person, Figure 1). Both the finger and toe envelopes contain the similar "peaks" resulting the respiration rate.

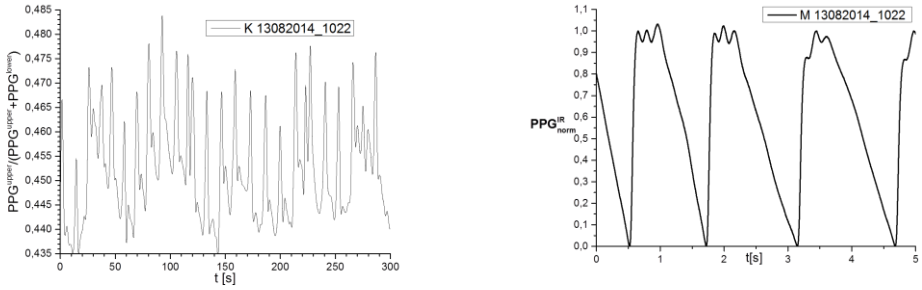

Figs. 2. The normalized PPG envelope wave (left) for 300 s, and the normalized PPG pulse waves for 5 s from the Figure 1 (right).

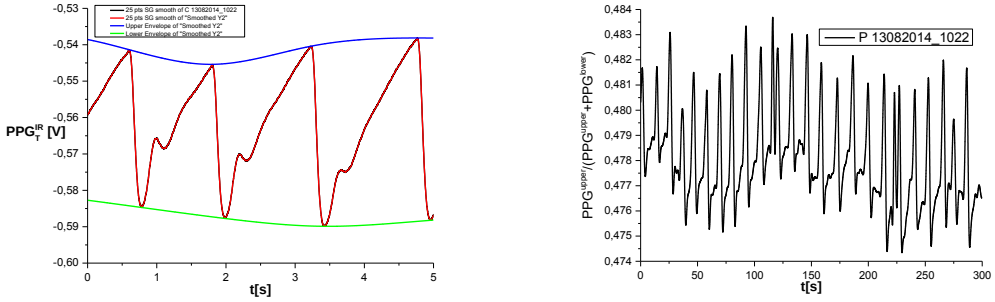

Figs. 3. The infrared toe PPG (black), its smoothed 25 points curve (red) (left), and the normalized toe envelope signal (right) for 300 s (31 male person, Figure 1).

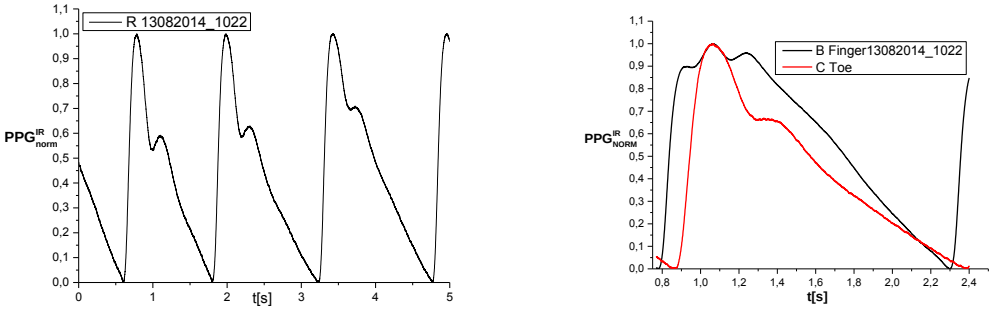

Figs. 4. The toe PPG pulse wave (left) for 5 s, and the finger (black) and toe PPG (red) (right).

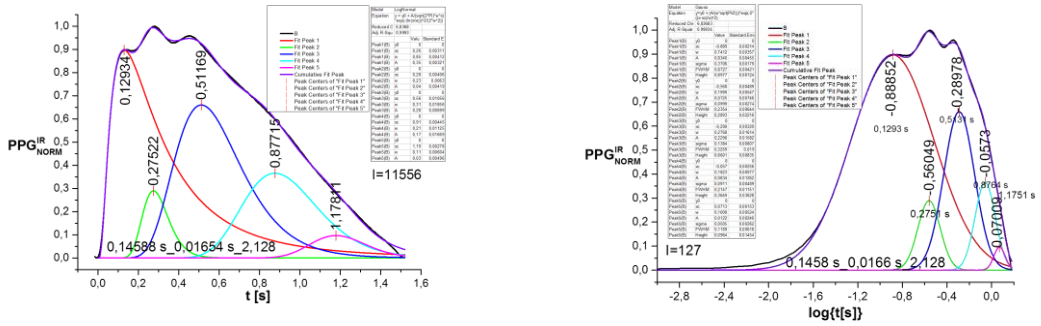

Figure 5. The decomposed PPG pulse waveform (left), and the corresponding PPG in the logarithmic scale (right). PPG (black) contains percussion (red), tidal (green), dicrotic (blue), repercussion (cyan), retidal (magneta), and composed wave (violet). In the both case the decomposition time values are the same, however, in the linear scale 11556 iterations are needed whereas only 127 in the logarithmic case. Arterial elasticity index=2.128 in each case.

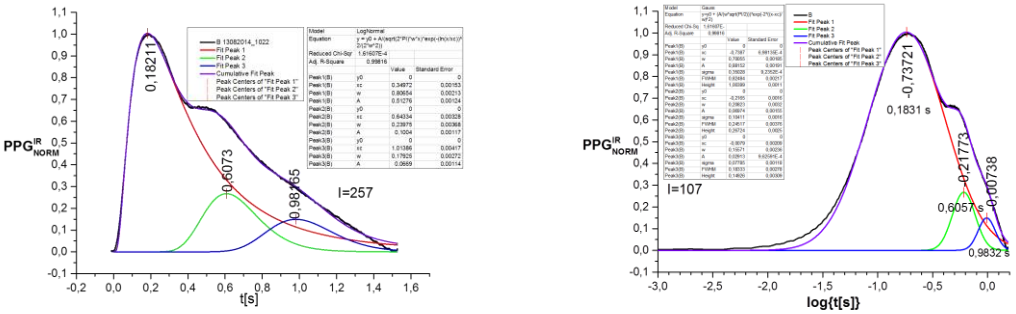

Figure 6. The decomposed toe PPG pulse waveform and the corresponding PPG in the logarithmic scale. In the both case the decomposition time values are almost the same, however, in the linear scale 257 iterations are needed whereas 107 in the logarithmic case, but only three waves are needed in the curve fitting, respectively.

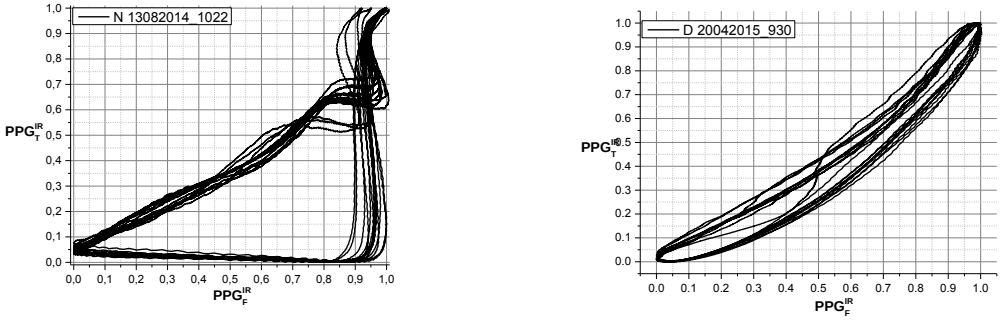

Figure 7. The normalized finger PPG pulses vs the normalized toe PPG pulses, e.g., the Lissajous pattern for the young male (31 y) (left), and the corresponding pattern for a person over 65 years (right).

Lissajous pattern provides information about the basic mechanical properties of the material, e.g., arterial wall elasticity, with a linear response being hypothetically an ellipsoid. However, in biomedical applications the Lissajous' patterns analysis are more complex and not easily interpreted. The pattern contains both the upper and lower peripheral arterial elasticity. PPG signal data collection is underway in the clinical settings.

References

[1] V. G. Almeida et al, "Machine Learning Techniques for Arterial Pressure Waveform Analysis," J. Pers. Med., 2, 82-101, 2013.

[2] M. Baruch et al., "Pulse Decomposition Analysis of the digital arterial pulse during hemorrhage simulation," Nonlinear Biomedical Physics 2011, 5:1, 4(8), 2012.

Proceedings of the XII Finnish Mechanics Days
R. Kouhia, J. Mäkinen, S. Pajunen and T. Saksala (Eds.)

A model for anisotropic magnetostriction

Anouar Belahcen[1], Reijo Kouhia[2], Paavo Rasilo[1], and Matti Ristinmaa[3]

[1]Aalto University, Department of Electrical Engineering and Automation
P.O. Box 13000, FI-00076 Aalto, Finland
[2]Tampere University of Technology, Department of Mechanical Engng and Industrial Systems
P.O. Box 589, 3FI-3101 Tampere, Finland
[3]Lund University, Division of Solid Mechanics, P.O. Box 118, SE-22100 Lund, Sweden
anouar.belahcen@aalto.fi, reijo.kouhia@tut.fi, paavo.rasilo@aalto.fi, matti.ristinmaa@solid.lth.se

Summary. In this paper, a coupled magnetoelastic model for isotropic ferromagnetic materials commonly used in electrical machines is presented. The constitutive equations are written on the basis of the total energy in which the right Cauchy-Green strain tensor and the Lagrangian form of the magnetic field strength are used as the basic state variables.

Key words: magnetostriction, anisotropy, integrity basis, total energy function

Introduction

In transformers and rotating electrical machines magnetostriction is known to generate vibrations and acoustic noise. Electrical steel used in these machines is known to behave anisotropically. In this paper a model for anisotropic magnetostriction is developed. The model is based on the formulation introduced by Dorfmann and Ogden [1, 2, 3] utilizing the concept of "total energy function".

Lagrangian fields

In magnetoelastostatics the three basic magnetic variables are the magnetic field $\boldsymbol{H}$, the magnetic induction $\boldsymbol{B}$ and the magnetization $\boldsymbol{M}$. The fields $\boldsymbol{H}$ and $\boldsymbol{B}$ are considered as the primary fields and $\boldsymbol{M}$ only as an auxiliary field [4], which can be defined in terms of $\boldsymbol{H}$ and $\boldsymbol{B}$.

In electromagnetics it is customary to work with the Eulerian frame, so the field $\boldsymbol{H}$ and $\boldsymbol{B}$ are related to the current configuration. To model anisotropic behaviour where the material orientation is important, the material description of motion is preferable and the Lagrangian forms of the primary magnetic fields are

$$\boldsymbol{H}_{\mathrm{L}} \equiv \boldsymbol{F}^T \boldsymbol{H}, \qquad \text{and} \qquad \boldsymbol{B}_{\mathrm{L}} \equiv J\boldsymbol{F}^{-1}\boldsymbol{B}, \tag{1}$$

where $\boldsymbol{F}$ is the deformation gradient and $J = \det \boldsymbol{F}$. For further details see [1, 2, 3].

Constitutive equations

General form

Denoting the complementary form of the total energy function as $\Omega^*(\boldsymbol{F}, \boldsymbol{H}_{\mathrm{L}})$, and using the standard Coleman-Noll procedure, the total stress $\boldsymbol{\tau}$ and the magnetic induction $\boldsymbol{B}$ can be

obtained from equations

$$\boldsymbol{\tau} = J^{-1}\boldsymbol{F}\frac{\partial\Omega^*}{\partial\boldsymbol{F}}, \qquad \boldsymbol{B} = -J^{-1}\boldsymbol{F}\frac{\partial\Omega^*}{\partial\boldsymbol{H}_{\mathrm{L}}}. \tag{2}$$

The function $\Omega^*(\boldsymbol{F}, \boldsymbol{H}_{\mathrm{L}})$ is a partial Legendre transform of the total energy function $\Omega(\boldsymbol{F}, \boldsymbol{B}_{\mathrm{L}})$, i.e.

$$\Omega^*(\boldsymbol{F}, \boldsymbol{H}_{\mathrm{L}}) = \Omega(\boldsymbol{F}, \boldsymbol{B}_{\mathrm{L}}) - \boldsymbol{H}_{\mathrm{L}}\cdot\boldsymbol{B}_{\mathrm{L}}. \tag{3}$$

The total energy function Ω is related to the Helmholtz free energy per unit mass ψ as

$$\Omega \equiv \rho_0\Phi + \tfrac{1}{2}\mu_0^{-1}J\boldsymbol{B}\cdot\boldsymbol{B}, \qquad \text{where} \qquad \Phi(\boldsymbol{F}, \boldsymbol{B}_{\mathrm{L}}) \equiv \psi(\boldsymbol{F}, J^{-1}\boldsymbol{F}\boldsymbol{B}_{\mathrm{L}}) \tag{4}$$

in which ρ_0, μ_0 are the density in the reference configuration and the magnetic permeability in vacuum, respectively.

Intregrity basis

For modelling ansiotropic magnetostriction, it has been chosen that the energy function depends on the right Cauchy-Green deformation tensor $\boldsymbol{C} = \boldsymbol{F}^T\boldsymbol{F}$, the Lagrangian magnetic field $\boldsymbol{H}_{\mathrm{L}}$ and two direction vectors $\boldsymbol{a}_1$ and $\boldsymbol{a}_2$, not necessarily orthogonal to each other. Integrity basis of a scalar function depending of a symmetric second order tensor and three vectors consist of the following 21 invariants [5]:

$$\begin{aligned}
&I_1 = \operatorname{tr}\boldsymbol{C}, && I_2 = \tfrac{1}{2}[(\operatorname{tr}\boldsymbol{C})^2 - \operatorname{tr}\boldsymbol{C}^2], && I_3 = \det\boldsymbol{C}, && I_4 = \boldsymbol{H}\cdot\boldsymbol{H}, && I_5 = \boldsymbol{H}\cdot\boldsymbol{a}_1,\\
&I_6 = \boldsymbol{H}\cdot\boldsymbol{a}_2, && I_7 = \boldsymbol{a}_1\cdot\boldsymbol{a}_2, && I_8 = \boldsymbol{H}\cdot\boldsymbol{C}\boldsymbol{H}, && I_9 = \boldsymbol{a}_1\cdot\boldsymbol{C}\boldsymbol{a}_1, && I_{10} = \boldsymbol{a}_2\cdot\boldsymbol{C}\boldsymbol{a}_2,\\
&I_{11} = \boldsymbol{H}\cdot\boldsymbol{C}\boldsymbol{a}_1, && I_{12} = \boldsymbol{H}\cdot\boldsymbol{C}\boldsymbol{a}_2, && I_{13} = \boldsymbol{a}_1\cdot\boldsymbol{C}\boldsymbol{a}_2, && I_{14} = \boldsymbol{H}\cdot\boldsymbol{C}^2\boldsymbol{H}, && I_{15} = \boldsymbol{a}_1\cdot\boldsymbol{C}^2\boldsymbol{a}_1,\\
&I_{16} = \boldsymbol{a}_2\cdot\boldsymbol{C}^2\boldsymbol{a}_2, && I_{17} = \boldsymbol{H}\cdot\boldsymbol{C}^2\boldsymbol{a}_1, && I_{18} = \boldsymbol{H}\cdot\boldsymbol{C}^2\boldsymbol{a}_2, && I_{19} = \boldsymbol{a}_1\cdot\boldsymbol{C}^2\boldsymbol{a}_2, && I_{20} = \boldsymbol{a}_1\cdot\boldsymbol{a}_1,\\
&I_{21} = \boldsymbol{a}_2\cdot\boldsymbol{a}_2.
\end{aligned} \tag{5}$$

Since $\boldsymbol{a}_1$ and $\boldsymbol{a}_2$ are unit vectors, i.e. $\boldsymbol{a}_1\cdot\boldsymbol{a}_1 = \boldsymbol{a}_2\cdot\boldsymbol{a}_2 = 1$, there are only 19 invariants in the anisotropic magnetoelastic model.

Total stress tensor and magnetic induction

From equations (2) expressions to the total stress tensor $\boldsymbol{\tau}$ and the magnetic induction vector $\boldsymbol{B}$ are

$$\boldsymbol{\tau} = J^{-1}\boldsymbol{F}\sum_{k=1}^{19}\frac{\partial\Omega^*}{\partial I_k}\frac{\partial I_k}{\partial\boldsymbol{F}}, \tag{6}$$

$$\boldsymbol{B} = -J^{-1}\boldsymbol{F}\sum_{k=1}^{19}\frac{\partial\Omega^*}{\partial I_k}\frac{\partial I_k}{\partial\boldsymbol{H}_{\mathrm{L}}}. \tag{7}$$

Evaluation of the derivatives $\partial\Omega^*/\partial\boldsymbol{F}$ and $\partial\Omega^*/\partial\boldsymbol{H}_{\mathrm{L}}$ gives

$$\begin{aligned}
\boldsymbol{\tau} =& J^{-1}[2\boldsymbol{b}\Omega_1^* + 2(I_1\boldsymbol{b} - \boldsymbol{b}^2)\Omega_2^* + 2I_3\Omega_3^* + 2\boldsymbol{b}\boldsymbol{H}\otimes\boldsymbol{b}\boldsymbol{H}\Omega_8^* + 2\boldsymbol{F}\boldsymbol{a}_1\otimes\boldsymbol{F}\boldsymbol{a}_1\Omega_9^* +\\
&+ 2\boldsymbol{F}\boldsymbol{a}_2\otimes\boldsymbol{F}\boldsymbol{a}_2\Omega_{10}^* + (\boldsymbol{F}\boldsymbol{a}_1\otimes\boldsymbol{b}\boldsymbol{H} + \boldsymbol{b}\boldsymbol{H}\otimes\boldsymbol{F}\boldsymbol{a}_1)\Omega_{12}^* + (\boldsymbol{F}\boldsymbol{a}_2\otimes\boldsymbol{b}\boldsymbol{H} + \boldsymbol{b}\boldsymbol{H}\otimes\boldsymbol{F}\boldsymbol{a}_2)\Omega_{13}^* +\\
&+ 2(\boldsymbol{b}\boldsymbol{H}\otimes\boldsymbol{b}^2\boldsymbol{H} + \boldsymbol{b}^2\boldsymbol{H}\otimes\boldsymbol{b}\boldsymbol{H})\Omega_{14}^* + (\boldsymbol{F}\boldsymbol{a}_1\otimes\boldsymbol{b}\boldsymbol{F}\boldsymbol{a}_1 + \boldsymbol{b}\boldsymbol{F}\boldsymbol{a}_1\otimes\boldsymbol{F}\boldsymbol{a}_1)\Omega_{15}^* +\\
&+ (\boldsymbol{F}\boldsymbol{a}_2\otimes\boldsymbol{b}\boldsymbol{F}\boldsymbol{a}_2 + \boldsymbol{b}\boldsymbol{F}\boldsymbol{a}_2\otimes\boldsymbol{F}\boldsymbol{a}_2)\Omega_{16}^* + 2(\boldsymbol{b}\boldsymbol{H}\otimes\boldsymbol{b}\boldsymbol{F}\boldsymbol{a}_1 + \boldsymbol{b}\boldsymbol{F}\boldsymbol{a}_1\otimes\boldsymbol{b}\boldsymbol{H})\Omega_{17}^* +\\
&+ 2(\boldsymbol{b}\boldsymbol{H}\otimes\boldsymbol{b}\boldsymbol{F}\boldsymbol{a}_2 + \boldsymbol{b}\boldsymbol{F}\boldsymbol{a}_2\otimes\boldsymbol{b}\boldsymbol{H})\Omega_{18}^* +\\
&+ (\boldsymbol{F}\boldsymbol{a}_1\otimes\boldsymbol{b}\boldsymbol{F}\boldsymbol{a}_2 + \boldsymbol{b}\boldsymbol{F}\boldsymbol{a}_1\otimes\boldsymbol{F}\boldsymbol{a}_2 + \boldsymbol{F}\boldsymbol{a}_2\otimes\boldsymbol{b}\boldsymbol{F}\boldsymbol{a}_1 + \boldsymbol{b}\boldsymbol{F}\boldsymbol{a}_2\otimes\boldsymbol{F}\boldsymbol{a}_1)\Omega_{19}^*],
\end{aligned} \tag{8}$$

$$\begin{aligned}
\boldsymbol{B} =& -J^{-1}(2\boldsymbol{b}\boldsymbol{H}\Omega_4^* + \boldsymbol{F}\boldsymbol{a}_1\Omega_5^* + \boldsymbol{F}\boldsymbol{a}_2\Omega_6^* + 2\boldsymbol{b}\boldsymbol{H}\Omega_8^* + \boldsymbol{b}\boldsymbol{F}\boldsymbol{a}_1\Omega_{11}^* + \boldsymbol{b}\boldsymbol{F}\boldsymbol{a}_2\Omega_{12}^* +\\
&+ 2\boldsymbol{b}^3\boldsymbol{H}\Omega_{14}^* + \boldsymbol{b}^2\boldsymbol{F}\boldsymbol{a}_1\Omega_{17}^* + \boldsymbol{b}^2\boldsymbol{F}\boldsymbol{a}_2\Omega_{18}^*),
\end{aligned} \tag{9}$$

where $\boldsymbol{b} = \boldsymbol{F}\boldsymbol{F}^T$ is the left Cauchy-Green deformation tensor, the notation Ω_i^* denotes the derivative $\Omega_i^* = \partial\Omega^*/\partial I_i$ and $\otimes$ is the standard tensor product. The specific form of the total energy function is now to be determined based on experimental evidence.

References

[1] A. Dorfmann and R.W. Ogden. Nonlinear magnetoelastic deformation of elastomers. *Acta Mechanica*, 167:13–28, 2004.

[2] A. Dorfmann and R.W. Ogden. Nonlinear magnetoelastic deformations. *Quarterly Journal of Mechanics and Applied Mathematics*, 57:599–622, 2004.

[3] A. Dorfmann and R.W. Ogden. Some problems in nonlinear magnetoelasticity. *Zeitschrift für Angewandte Mathematik und Physik*, 56:718–745, 2005.

[4] A. Kovetz. *Electromagnetic Theory*. Oxford University Press, 2000.

[5] A.J.M. Spencer. Theory of invariants. In A.C. Eringen, editor, *Continuum Physics*, volume 1, pages 239–353. Academic Press, 1971.

Suomen XII mekaniikkapäivien esitelmät
R. Kouhia, J. Mäkinen, S. Pajunen ja T. Saksala (toim.)

Teräsbetonikuorielementin mitoitus murtorajatilassa optimointitehtävänä

Pentti Varpasuo[1], Lauri Jaamala [2]

(1) Fortum Power and Heat Oy, POB 100, FI-00048 FORTUM, Finland,
pentti.varpasuo@fortum.com
(2)ÅF-Consult Ltd, Bertel Jungin aukio 9, FI-02600 Espoo, Finland,
Lauri.Jaamala@afconsult.com

Tiivistelmä. Tässä artikkelissa esitetään menetelmä, jolla voidaan mitoittaa kuorielementin ortogonaaliset pääteräkset ja leikkaushaat murtorajatilassa. Menetelmän erityisenä vaatimuksena on pääterästen mitoituksen toimivuus mille tahansa mielivaltaiselle normaalivoiman ja taivutusmomentin yhdistelmälle. Mitoitusmenetelmä perustuu hyvin tunnettuun ja yleisesti käytettyyn teräsbetonisen poikkileikkauksen voimatasapainomitoitukseen ja se huomioi Rakennusmääräyskokoelma B4: n asettamat vaatimukset rakenteen mitoituksessa. Laskentamenetelmä ei huomioi rakenteen mahdollisia stabiiliusongelmia, ns. 2. kertaluvun vaikutuksia. Näin ollen ohuiden, mahdollisesti nurjahtavien kuorirakenteiden mitoitukseen menetelmä ei sovellu.

Avainsanat: kuorielementti, murtorajatila, pääteräkset, normaalivoima, taivutusmomentti.

Johdanto

Tässä artikkelissa esitetään mitoitusmenetelmä [1], jolla kyetään mitoittamaan paikalla valettuja teräsbetonikuorirakenteita. Mitoituksen vaatimukset on määritetty seuraavasti:
-Mitoituksen tulee tapahtua Rakennusmääräyskokoelma B4: n [2] vaatimusten mukaisesti.
-Mitoitus tulee kyetä tekemään tehokkaasti myös suurille ja vaativille rakenteille.
-Menetelmän tulee mitoittaa ortogonaaliset pääteräkset sekä leikkaushaat kuorielementin teräsbetonipoikkileikkaukselle.
-Mitoituksen tulee toimia mille tahansa mielivaltaiselle poikkileikkauksen kuormitukselle.

Lähtötiedot

Teräsbetonirakenteiden terästyksiä mitoitettaessa ovat rakenteiden ulkomitat yleensä tiedossa. Nämä rakenteiden ulkomitat suunnittelija on valinnut kokemuksen tuomalla asiantuntemuksella sopiviksi huomioiden kuormitukset sekä muut rakenteen kelpoisuuteen vaikuttavat seikat. Mitoitettavista rakenteista tiedetään kaikki muu, paitsi niihin sijoitettavat teräsmäärät. Suojabetonipaksuudet suunnittelija saa normeista ja suojabetonipaksuuksien ollessa tiedossa

tiedetään myös terästen sijainti. Kuvassa 1 on esitetty teräsbetonipoikkileikkauksen mitoitukseen liittyvät geometriset suureet.

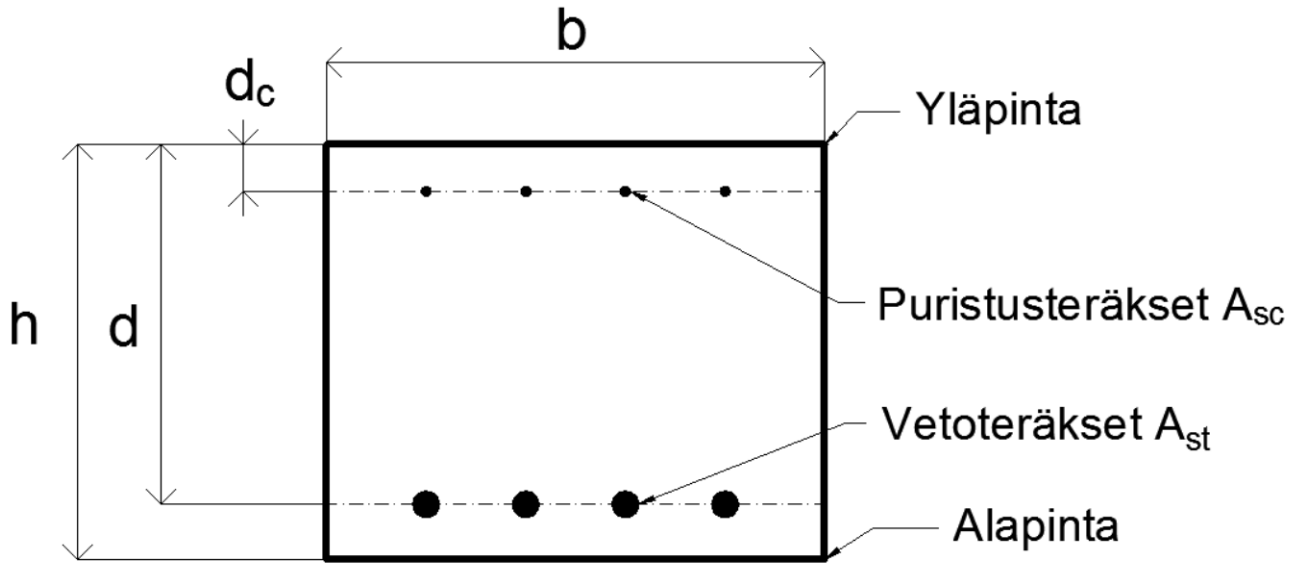

Kuva 1. Teräsbetonipoikkileikkauksen mitoitukseen liittyvät geometriset suureet

Mitoitusvoimasuureet elementtimenetelmästä

Teräsbetonipoikkileikkauksen mitoitusvoimasuureet saadaan elementtimenetelmällä suoritetusta lineaarisesta elastisesta analyysistä isotrooppisilla materiaaliominaisuuksilla. Tämä menettelytapa on yleisesti hyväksytty ja laajassa käytössä. Mitoitusvoimasuureet lasketaan elementtimenetelmällä alkeiskuormitustapauksittain. Alkeiskuormitustapausten mitoitusvoimasuureet yhdistellään mitoituksessa varmuuskertoimilla kuormitusyhdistelyiksi. Elementtimenetelmästä saadaan raudoitteiden mitoittamista varten elementtikohtaiset mitoitusvoimasuureet. Jokaiselle elementille mitoitetaan elementtikohtainen raudoitus. Pääteräksien mitoittamista varten tarvitaan kummallekin raudoitesuunnalle (x-ja y-suunnille) mitoittava momentti ja normaalivoima. Kuorielementti antaa pääteräksien mitoitukseen voimat Fx, Fy ja Fxy sekä momentit Mx, My ja Mxy. Leikkaushakojen mitoitusvoimiksi saadaan kuorielementiltä pystysuuntaiset leikkausvoimat Vx ja Vy. Kuvasta 2 ilmenee voimien merkkisääntö ja elementin yläpinnan ja alapinnan määrittely. Elementin yläpinta on elementin paikallisen koordinaatiston Xe-Ye-Ze positiivisen Ze – akselin puoleinen pinta Positiiviset momentit Mx-ja My-suunnissa aiheuttavat elementin alapintaan vetoa ja yläpintaan puristusta. Positiiviset normaalivoimat Fx ja Fy aiheuttavat vetoa elementin keskipinnan suunnassa ja negatiiviset normaalivoimat vastaavasti puristusta. Mitoitusvoimasuureina käytetään voimasuureita elementin keskipisteessä.

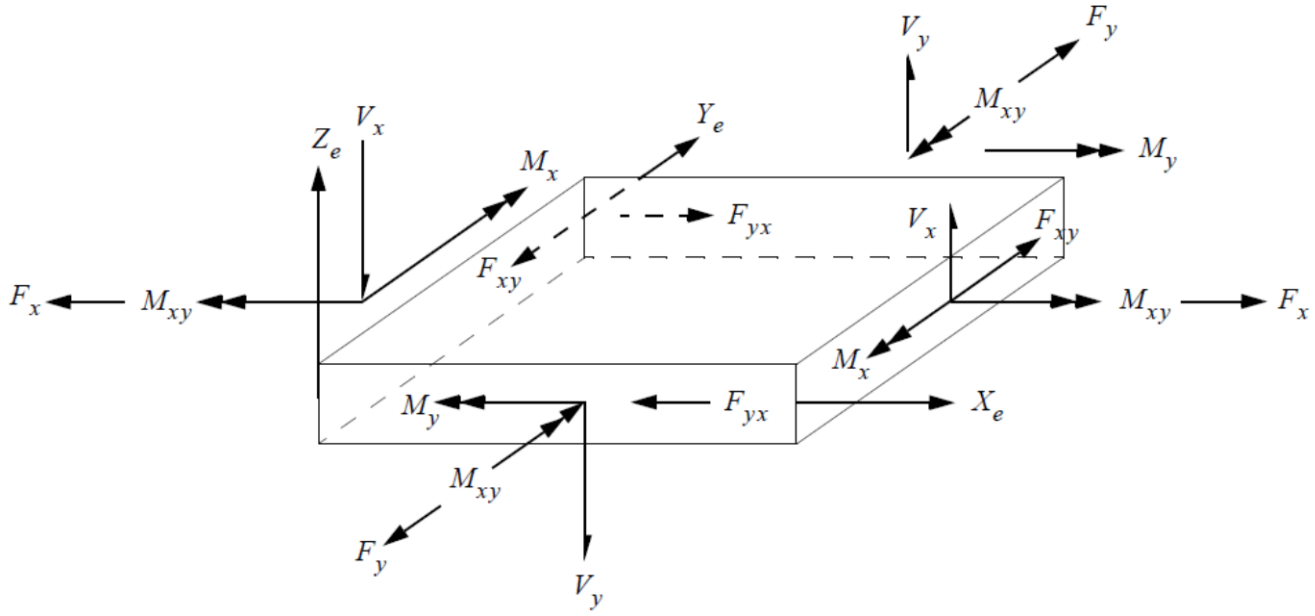

Kuva 2. Elementtimenetelmäanalyysista saatavat mitoitusvoimasuureet

Poikkileikkauksen mitoitus optimointitehtävänä [3]

Teräsbetonisen poikkileikkauksen mitoittaminen perustuu voimatasapainon aikaansaamiseen ulkoisten kuormien ja sisäisten vastustavien voimien välille. Teräsbetonipoikkileikkauksen voimien kehittymistä betonin puristusblokissa ja teräksissä on tutkittu monilla käytännön kuormituskokeilla. Kuormituskokeiden tuloksena teräsbetonipoikkileikkauksen käyttäytyminen ja voimien kehittyminen tunnetaan hyvin. Yleiset teräsbetonin mitoitusoletukset kuten puristusblokin ideaalinen toiminta ja betonin jäykkä-plastinen materiaalioletus ovat luotettavia ja riittävän tarkkoja oletuksia, jotka perustuvat kuormituskokeiden havaintoihin. Teräsbetonipoikkileikkaus mitoitetaan siten että poikkileikkauksen sisäiset voimat voivat kehittyä tasapainoon rakenteen ulkoisten kuormituksien kanssa. Pääteräkset mitoitetaan tasapainoon momenttikuormalle ja normaalivoimalle. Pääteräksiä mitoitettaessa on käytössä kaksi tasapainoyhtälöä.

$$F_c + F_{Asc} + F_{Ast} + N_d = 0 \quad (1)$$

$$F_c \cdot (d - 0.5 \cdot k_x \cdot x) + F_{Asc} \cdot (d - dc) + M_d = 0 \quad (2)$$

Yhtälöissä (1) ja (2) on käytetty seuraavia merkintöjä:
F_c = Betonin puristusblokin resultanttivoima [N]
F_{Asc} = Puristusterästen resultanttivoima [N]
F_{Ast} = Vetoterästen resultanttivoima [N]
N_d = Mitoittava normaalivoima [N]
M_d = Mitoittava momenttivoima [Nm]

k_x = Puristusblokin suhteellinen korkeus
x = Neutraaliakselin etäisyys poikkileikkauksen yläpinnasta [m]
d = Vetoterästen etäisyys poikkileikkauksen yläpinnasta [m]
d_c = Puristusterästen etäisyys poikkileikkauksen yläpinnasta [m]
Mitoitettaessa teräsbetonirakennetta ovat tuntemattomina vetoterästen määrä A_{st} ja puristusterästen määrä A_{sc}. Tämän lisäksi tuntemattomana on poikkileikkauksen neutraaliakselin sijainti x (kuva 3). Neutraaliakselin sijainti tarvitaan betonin puristusblokin korkeuden $k_x \cdot x$ määrittämiseen. Tuntemattomia on kolme, ja ratkaistavia yhtälöitä kaksi.

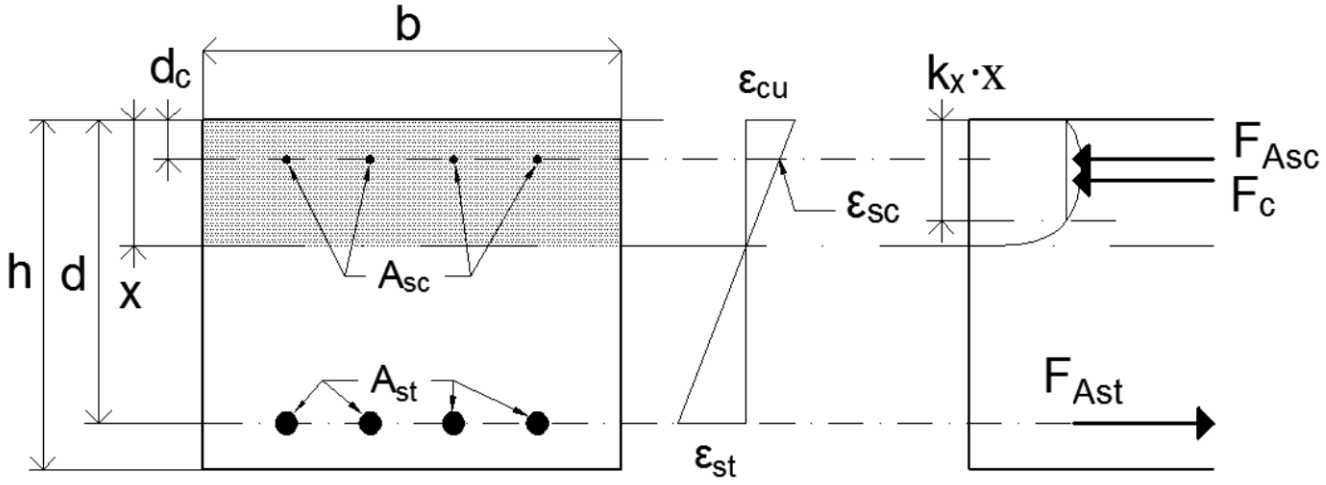

Kuva 3. Poikkileikkauksen geometria, muodonmuutoskuvio ja sisäiset voimat

Kyseessä on siis optimointiongelma. Kuinka valita raudoitepinta-alat A_{st} ja A_{sc} sekä neutraaliakselin sijainti x, jotta tasapainoyhtälöt toteutuvat ja ratkaisu on paras mahdollinen? Parhaana mahdollisena ratkaisuna voidaan pitää esimerkiksi pienintä teräsmenekkiä. Pienin teräsmenekki saavutetaan minimoimalla kokonaisteräspinta-alaa. Ongelman matemaattinen esitysmuoto on seuraava:

$$\min [A_{sTot}(N_d, M_d, \Phi, f_{cd}, f_{yd}, b, h, d, d_c, x)] \quad (3)$$

Yhtälössä (3) Φ = poikkileikkauksen tutkittavan rajatilan muodonmuutosjakauman aiheuttama käyristys ja A_{sTot} = Yhteenlaskettu kokonaisteräspinta poikkileikkauksen ala- ja yläpinnassa. Yhtälön (3) minimiä haetaan seuraavien epäyhtälöiden rajoittamassa avaruudessa:

$$A_{st} \geq 0,\ A_{sc} \geq 0 \text{ ja } x \text{ sijaitsee välillä } -\infty \leq x \leq +\infty \quad (4)$$

Ratkaisualgoritmin käytännön toteutus

Laskenta-algoritmeissa jotka halutaan yleispäteviksi, kaikissa tilanteissa toimiviksi proseduureiksi, numeeriset ongelmat aiheuttavat suurimman työmäärän. Tässä artikkelissa on tarkoituksena esittää menetelmä jolla kyetään mitoittamaan teräsbetonipoikkileikkaus mille tahansa mielivaltaiselle kuormitusyhdistelmälle. Edellä esitetty laskentateoria ei sellaisenaan toimi yleispätevänä mitoitusmenetelmänä. Mitoitus sisältää singulaarisuuspisteitä, joita edellä

esitelty laskentateoria ei ota huomioon. Ongelmia aiheuttaa myös optimoinnissa käytettävä peitemenetelmä, eli koko sallitun avaruuden yli kulkeminen. Laskentatehon säilyttämiseksi, tulisi raudoitemääriä laskea mahdollisimman harvoilla neutraaliakselin sijainnin pisteillä. Mitä harvemmilla neutraaliakselin sijainneilla optimia tutkitaan, sitä suurempi on mahdollisuus että käypää optimia ei löydy. Algoritmissa joudutaan tämän takia käyttämään ns. suodattimia jotka löytävät toleranssien puitteissa aluksi ei käypien ratkaisujen joukosta tarkentavilla iteraatioden avulla haettavan käyvän ratkaisun. Käytetyistä suodattimista esitetään seuraavassa esimerkkejä. Tärkein käytetty suodatin on normaalivoiman sijaintisuodatin, joka toimii seuraavasti: Suodattimessa kuormitusta tutkitaan epäkeskisenä normaalivoimana N_d. Jos kuormittava normaalivoima on esimerkiksi tuhatkertainen mitoitusmomenttiin nähden, voidaan ajatella poikkileikkauksen olevan puhtaan normaalivoiman kuormittavana eli normaalivoima on keskinen. Suodattimien avulla hakuavaruus jaetaan seuraavasti nimettyihin ala-avaruuksiin: 1) Kuormittamaton poikkileikkaus; 2) Kauttaaltaan vedetty poikkileikkaus; 3) Kauttaaltaan puristettu poikkileikkaus; 4) Neutraaliakseli sijaitsee vetoterästen painopisteessä; 5) Poikkileikkaus puhtaassa taivutuksessa; 6) Neutraaliakseli poikkileikkauksen sisällä pois lukien tapaukset 4) ja 5).

Sovellusesimerkki: Merikosken vesivoimalaitoksen tuloputken spiraali

Kuvassa 4 on esitetty elementtimalli Merikosken vesivoimalaitoksen vesiteistä.

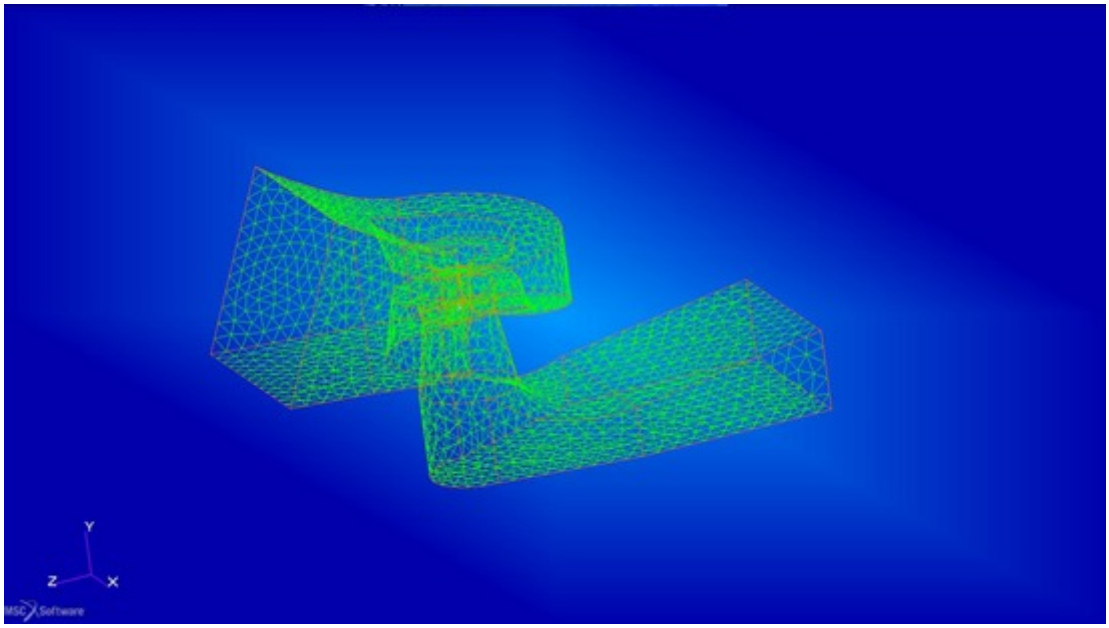

Kuva 4. Merikosken vesivoimalaitoksen vesiteitten elementtimalli

Seuraavassa kuvassa 5 on esitetty spiraalin takaseinän (180 astetta) sisäpinnan tarvittava pystysuuntainen raudoitusmäärä neliömillimetreinä seinän leveysmetriä kohti pikasulun hydrostaattisen paineen (16 metriä vesipatsasta) ja oman painon kuormitusyhdistelmälle.

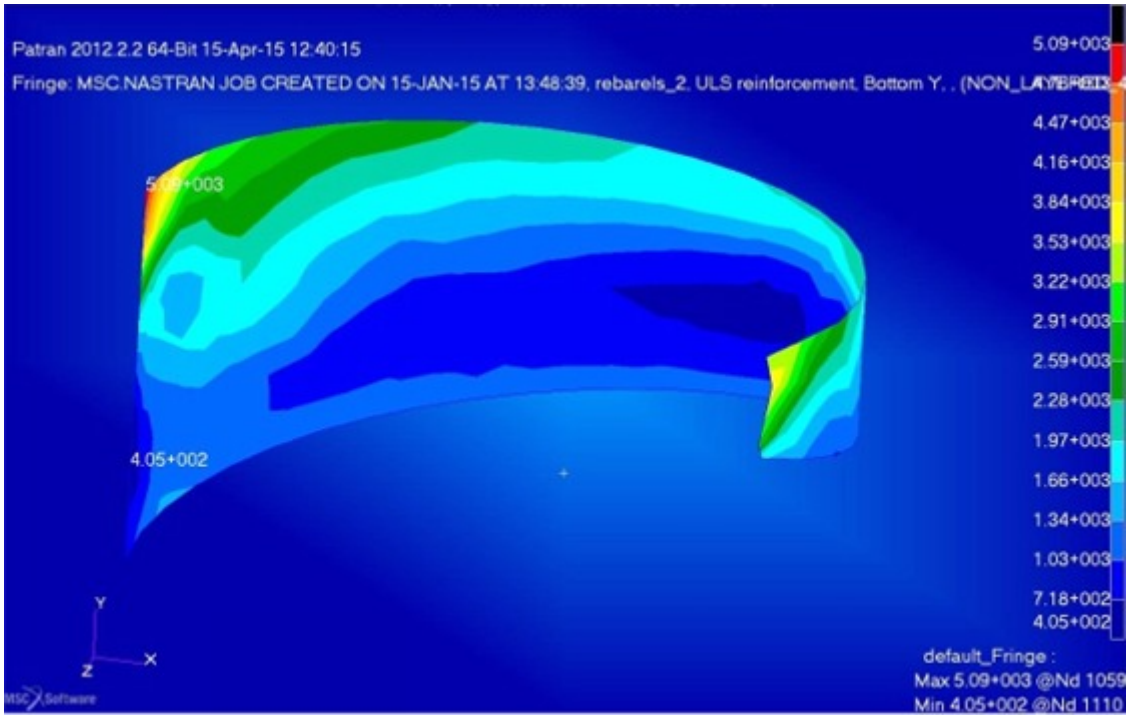

Kuva 5. Merikosken vesivoimalaitoksen tuloputken spiraalin takaseinän (180 astetta) sisäpinnan tarvittava pystysuuntainen raudoitusmäärä murtorajatilassa neliömillimetreinä seinän leveysmetriä kohti pikasulun hydrostaattisen paineen (16 metriä vesipatsasta) ja oman painon kuormitusyhdistelmälle

Yhteenveto

Tässä artikkelissa esitettiin menetelmä teräsbetonipoikkileikkauksen murtorajatilan mitoittamiseen murtorajatilassa. Mitoitusteorian taustalla oleva optimointi-lähtöinen ratkaisutapa osoittautui tehokkaaksi. Kehitetyn menetelmän toimivuus varmistettiin useilla numeerisilla testeillä. Testituloksia verrattiin perinteisillä mitoitusmenetelmillä saatuihin ratkaisuihin ja tulokset olivat yhteneviä. Mitoitusmenetelmä toimii jälkikäsittelijänä elementtimenetelmä-ohjelmistolle [4].

Viitteet

[1] Lauri Jaamala , Tasomaisen teräsbetonipoikkileikkauksen automatisoitu mitoitus murtorajatilassa, Diplomityö, Oulun Yliopisto, Joulukuu 2014.
[2] RakMKB4 (2005) Rakennusmääräyskokoelma B4, Betonirakenteet, Ohjeet 2005, Ympäristöministeriö.
[3] Hernández-Montes E, Gil-Martín L M, Pasadas-Fernández M & Aschheim M (2008) Theorem of optimal reinforcement for reinforced concrete cross sections, Structural and Multidisciplinary Optimization, Vol. 36: 509-521
[4] MD/MSC Nastran 2010 – Getting Started with MD Nastran User’s Guide, 250 p.

Proceedings of the XII Finnish Mechanics Days
R. Kouhia, J. Mäkinen, S. Pajunen and T. Saksala (Eds.)

An experimental and numerical study of the dynamic Brazilian disc test on Kuru granite

Ahmad Mardoukhi[1], Timo Saksala[2], Mikko Hokka[1], and Veli-Tapani Kuokkala[1]

[(1)]Department of Materials Science, Tampere University of Technology, P.O. Box 589, FI-33101, Tampere, Finland, ahmad.mardoukhi@tut.fi, mikko.hokka@tut.fi, veli-tapani.kuokkala@tut.fi
[(2)]Department of Mechanical Engineering and Industrial Systems, Tampere University of Technology, P.O. Box 589, FI-33101, Tampere, Finland, timo.saksala@tut.fi

Summary. This paper deals with numerical modeling of the dynamic tensile strength of Kuru granite and corresponding experiments with the dynamic Brazilian Disc (BD) tests using the Split Hopkinson Pressure Bar apparatus (SHPB). It was found that the indirect tensile strength of the Kuru granite increased from the static value of 13 MPa to 36 MPa when the impact velocity reached 20 m/s. A numerical method was developed for simulations of these tests. The method includes a material model based on the rate-dependent isotropic compliance damage and embedded discontinuity concepts for rock and an FEM based explicit time marching technique for simulating the dynamics of the SHPB apparatus. Simulation results are in decent agreement with the experiments.

Key words: Dynamic Brazilian disc test, Split Hopkinson Pressure Bar, FEM, rock fracture

Introduction

The tensile strength of brittle materials, such as rock and concrete, is usually much lower than their compressive strength (up to 30 times). Moreover, while both strengths display significant loading rate hardening effects, this effect is especially pronounced with the tensile strength. Therefore, a numerical model aiming at a realistic prediction of the rock behaviour under dynamic loading conditions should take the loading (strain) rate sensitivity into account. The dynamic tensile strength of rock can be indirectly measured using the Split Hopkinson Pressure Bar (SHPB) apparatus with the so-called Brazilian Disc (BD) specimens [1].

This paper presents some preliminary results of an on-going project at TUT, the purpose of which is to provide experimental data on the dynamic tensile strength and failure modes of the granite rocks. The data can be used, for example, for (dynamic) calibration and validation of rock material models. This paper also presents a numerical model based on a viscodamage and an embedded discontinuity models originally developed in [2]. The numerical simulations of the failure mode and the dynamic tensile strength are compared to the experimental results. High speed photography and Digital Image Correlation were used to analyse the experimental results and to provide still-shots with the deformation field of the deforming BD specimen.

Experimental setup

The principle of the SHPB test apparatus with the Brazilian Disc sample is shown schematically in Figure 1.

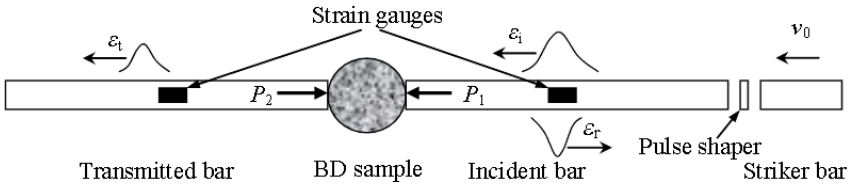

Figure 1. Schematic picture of the SHPB setup for the dynamic BD test.

The striker bar impacts the free end of the incident bar generating a compressive stress wave (incident pulse), which travels through the incident bar and the BD sample, causing its diametrical splitting. The incident, transmitted, and reflected pulse strains, ε_i, ε_t, ε_r, are measured as a function of time using the strain gages indicated in Figure 1. Moreover, a pulse shaper of relatively soft material (copper, rubber) is used to improve the dynamic stress equilibrium by increasing the rise time of the incident stress pulse. The indirect tensile strength of the specimen can be calculated, based on the elasticity solution of the quasi-static problem, as

$$\sigma_T = 2P / \pi LD \tag{1}$$

where P is the force acting on the specimen with the length L and diameter D. The dynamic forces acting on the incident and transmitted sides of the BD specimen are calculated using Equations (2) [1]

$$P_1 = A_b E_b (\varepsilon_i + \varepsilon_r), \quad P_2 = A_b E_b \varepsilon_t \tag{2}$$

where A_b and E_b are the cross-sectional area and Young's modulus of the bars. When good stress equilibrium is reached, the forces P_1 and P_2 are equal, but P_2 typically has fewer oscillations, and is therefore more often used for calculations of the indirect tensile strength with Eq. (1).
Two Photron SA-X2 high speed cameras were used to record the deformation and fracture of the samples. A speckle pattern was applied on the surface of the samples since the natural pattern of the rock surface does not provide a very strong contrast for the Digital Image Correlation algorithm. Images were recorded at 160 kfps and the size of image was 256×176 pixels. These images were analyzed with the LaVision StrainMaster (DaVis) 3D-DIC software. A circular mask was used to limit the outer edges of the samples outside the analyzed region. Analyzing the images were carried out by comparing the images to the first (reference) image using a step size of 9 pixels and a subset size of 25 pixels.

Material model for rock fracture

The material model for the rock fracture is based on a combination of isotropic rate-dependent damage model and an embedded discontinuity model. The model briefly described here is described in more details in ref. [2]. The isotropic rate-dependent compliance damage model is chosen for description of the nonlinear pre-peak hardening process. For the present purposes, such a model is defined by

$$\bar{\phi}(\boldsymbol{\sigma},\bar{\kappa},\dot{\bar{\kappa}}) = \sqrt{\boldsymbol{\sigma}_+ : \mathbf{D}_\mathrm{e} : \boldsymbol{\sigma}_+} - \tfrac{1}{\sqrt{E}}(\sigma_\mathrm{t} + \bar{q}(\bar{\kappa},\dot{\bar{\kappa}})), \quad \bar{q}(\bar{\kappa},\dot{\bar{\kappa}}) = \bar{h}\,\bar{\kappa} + \bar{s}\,\dot{\bar{\kappa}}$$
$$\bar{h} = \bar{g}\sigma_\mathrm{t}\exp(-\bar{g}\bar{\kappa}), \quad \dot{\mathbf{D}} = \tfrac{\dot{\bar{\lambda}}}{\|\boldsymbol{\sigma}\|_{\mathbf{D}_\mathrm{e}}}\mathbf{D}_\mathrm{e}, \quad \dot{\bar{\kappa}} = -\dot{\bar{\lambda}}\tfrac{\partial\bar{\phi}}{\partial\bar{q}} \tag{3}$$

where $\bar{\phi}$ is the viscodamage loading function, $\boldsymbol{\sigma}_+$ is the positive part of the stress tensor, σ_t is the elastic limit stress, **D** is the compliance tensor obtained from the initial compliance tensor $\mathbf{D}_\mathrm{e} = \mathbf{E}_0^{-1}$ ($\mathbf{E}_0$ is the undamaged stiffness tensor), while $\bar{\kappa}, \dot{\bar{\kappa}}$ are the internal variable and its rate, respectively, $\dot{\bar{\lambda}}$ is the viscodamage increment, and $\bar{q}$ is the hardening variable. Moreover, $\bar{h}, \bar{s}$ are the hardening and viscosity modulus, respectively, and $\bar{g}$ is a parameter controlling the initial slope of the hardening curve. The inverse compliance tensor, $\mathbf{E}_d$, is the damaged stiffness modulus.

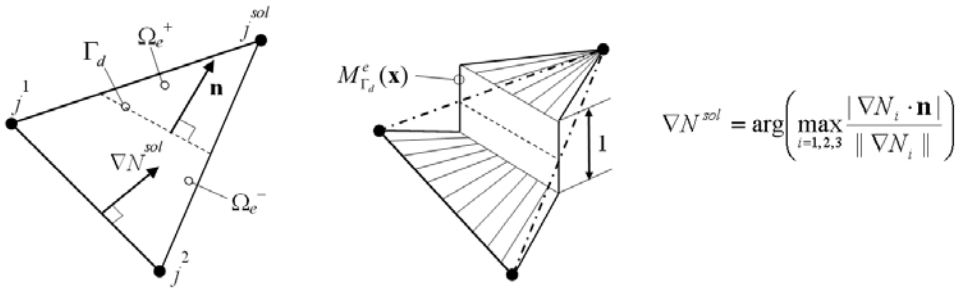

Figure 2. CST element with a discontinuity line Γ_d (left), and function M_{Γ_d} (right).

The embedded discontinuity part of the model describes the post peak softening process leading to final failure of the material. It is based on the decomposition of the displacement field into a regular part and the displacement jump due to a crack. When a body in $\mathbf{R}^2$ is discretized with CST elements (see Figure 2), the displacement and strain fields can be written as

$$\mathbf{u}(\mathbf{x}) = N_i\mathbf{u}_i^e + M^e_{\Gamma_d}\boldsymbol{\alpha}_d, \quad M^e_{\Gamma_d} = H_{\Gamma_d}(\mathbf{x}) - N^{sol}(\mathbf{x})$$
$$\boldsymbol{\varepsilon}(\mathbf{x}) = (\nabla N_i \otimes \mathbf{u}_i^e)^{sym} - (\nabla N^{sol}(\mathbf{x}) \otimes \boldsymbol{\alpha}_d)^{sym} + \delta_{\Gamma_d}(\mathbf{n} \otimes \boldsymbol{\alpha}_d)^{sym} \tag{4}$$

where the displacement jump is denoted by $\boldsymbol{\alpha}_d$, while N_i and $\mathbf{u}_i^e$ are the standard interpolation functions and nodal displacements (with summation on repeated indices), respectively. Moreover, H_Γ is the Heaviside function, and δ_Γ is the Dirac delta function. The solitary node j^{sol} is chosen so that the node n and ∇N^{sol} are as parallel as possible. This is achieved by the criterion in Figure 2. For the details of the FE implementation of Equation (4), see ref. [2].

A bi-surface discontinuity model accounting for mode I and II fracture types developed in ref. [2] reads

$$\phi_\mathrm{t}(\mathbf{t}_{\Gamma_d}, \kappa, \dot{\kappa}) = \mathbf{n}\cdot\mathbf{t}_{\Gamma_d} - (\sigma_\mathrm{t} + q(\kappa,\dot{\kappa})), \quad \phi_\mathrm{s}(\mathbf{t}_{\Gamma_d}, \kappa, \dot{\kappa}) = \left|\mathbf{m}\cdot\mathbf{t}_{\Gamma_d}\right| - (\sigma_\mathrm{s} + \tfrac{\sigma_\mathrm{s}}{\sigma_\mathrm{t}}q(\kappa,\dot{\kappa}))$$
$$\dot{\boldsymbol{\alpha}}_\mathrm{d} = \dot{\boldsymbol{\alpha}}_\mathrm{I} + \dot{\boldsymbol{\alpha}}_\mathrm{II} = \dot{\lambda}_\mathrm{t}\frac{\partial\phi_\mathrm{t}}{\partial\mathbf{t}_{\Gamma_d}} + \dot{\lambda}_\mathrm{s}\frac{\partial\phi_\mathrm{s}}{\partial\mathbf{t}_{\Gamma_d}}, \quad \dot{\kappa} = \dot{\lambda}_\mathrm{t}\frac{\partial\phi_\mathrm{t}}{\partial q} + \dot{\lambda}_\mathrm{s}\frac{\partial\phi_\mathrm{s}}{\partial q} \tag{5}$$
$$\mathbf{t}_{\Gamma_d} = \mathbf{n}\cdot\mathbf{E} : \left(\nabla^s\bar{\mathbf{u}} - (\nabla N^{sol} \otimes \boldsymbol{\alpha}_d)^{sym}\right) = \mathbf{n}\cdot\boldsymbol{\sigma}$$

where **n** and **m** are the unit normal and tangent vectors for the crack surface, $\boldsymbol{\sigma}$ is the bulk stress, and while σ_t and σ_s are the elastic limits in tension and shear, respectively. Moreover, $\kappa, \dot{\kappa}$ are the internal variable and its rate related to the softening law for discontinuity, while $\dot{\lambda}_t, \dot{\lambda}_s$ are the crack opening and sliding increments. An exponential softening law is assumed as $q = h\kappa + s\dot{\kappa}$ with $h = -g\sigma_t \exp(-g\kappa)$. Finally, $g = \sigma_t/G_{Ic}$ where G_{Ic} is the mode I fracture energy. The displacement jump can be solved by the standard return mapping of computational plasticity as shown in ref. [2].

Fixed crack concept is adopted, i.e. **n** remains the same after introducing a discontinuity in an element. A crack is embedded perpendicular to the first principal direction into an element when the criterion $\varepsilon_{deqv} \geq \varepsilon_{dlim}$ is met. Here, the equivalent damage strain $\varepsilon_{deqv} = \sqrt{\boldsymbol{\varepsilon}_d^+ : \boldsymbol{\varepsilon}_d^+}$ is defined with $\boldsymbol{\varepsilon}_d = (\mathbf{D} - \mathbf{D}_e) : \boldsymbol{\sigma}$ (damage strain), while $\boldsymbol{\varepsilon}_d^+$ is the positive part of it, and ε_{dlim} is the limit of the damage strain.

In order to have continuous response upon transition from the continuum model to the discontinuity model, the hardening variable q and the parameter controlling the post peak slope, g above, are set as $q(\kappa, \dot{\kappa}) = \bar{q}(\bar{\kappa}, \dot{\bar{\kappa}})$, $g = \sigma_{tdyn}/G_{Icdyn}$ where $\sigma_{tdyn} = \sigma_t + \bar{q}(\bar{\kappa}, \dot{\bar{\kappa}})$ is the dynamic tensile strength, and G_{Icdyn} is the dynamic mode I fracture energy.

SHPB simulation model

The SHPB test setup with the BD sample of rock illustrated in Figure 1 is modelled as follows: the incident and transmitted bars are modelled with standard 2-node bar elements. The incident pulse is modelled as an external stress pulse, $\sigma_i(t)$, applied to the end of the incident bar. The contacts between the BD sample and the incident and transmitted bars are modelled in a standard manner by imposing contact constraints between the bar end nodes and the edge nodes of the discretized BD sample. The contact constraints are imposed with the forward increment Lagrange multiplier method and the explicit modified Euler time integrator is employed in solving the response of the system in time.

Numerical simulations and experimental results

The following set of material properties and model parameters were used in the simulations: E = 60 GPa, ν = 0.2, ρ = 2600 kg/m^3, σ_t = 8 MPa, σ_s = 16 MPa, G_{Ic} = 100 N/m, $G_{Icdyn} = 10G_{Ic}$, ε_{dlim} = 5.5E-5, g = 80 1/m, $\bar{s} = 0.04$ MPa · s/m and s = 0.001 MPa·s/m. The simulations are carried out in 2D (plane stress conditions) with a mesh consisting of 3616 CST elements. Due to the limited page count of this paper, only the results for the impact speed of v = 10 m/s are presented in Figure 3.

Figure 4 show the stress vs. time for the tests with impact speeds of 10m/s and 20m/s. The increase of the impact speed from 10m/s to 20 m/s results in an increase of the dynamic strength of the rock by 13%. The DIC analysis shows that the fracture of the samples initiates closer to the incident bar contact point. Point (a) on the Figure shows the starts of the loading and (b) indicates the moment just before reaching the maximum stress. The corresponding images taken by high speed-cameras are shown in Figure 5. These images are overlaid with strain maps in Y-directional Lagrange strain maps (vertical, perpendicular to loading). The first two images show uniform strain over the surface of the sample and the first strain localization does not appear until few microseconds before the strength of the rock starts to decrease. This implies that the fracture starts from inside of the sample and not on the surface. As the fracture propagates, it appears on the strain map as well (Figure 5c). This is followed by a rapid propagation of the

crack (Figure 5 d and e) and the test is finished by crushing of the sample at contact points with stress bars. Engineering strain in the direction perpendicular to loading before the fracture was measured placing a virtual strain gage on the centre of the BD samples. The maximum strains prior to the fracture for the tests with impact speeds of 10 and 20 m/s are 0.46% and 0.62%.

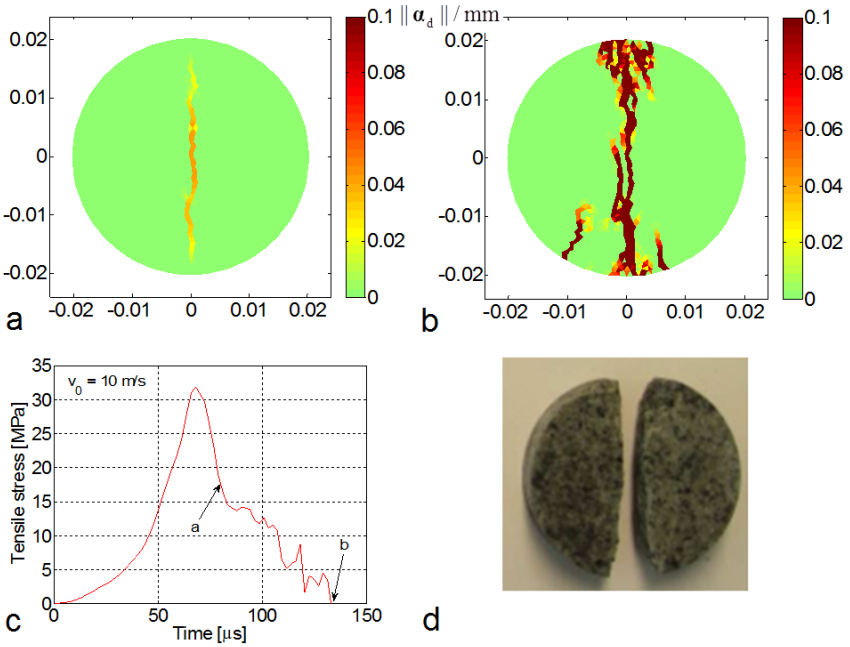

Figure 3. Simulation results: propagation of the fracture at t = 80 µs (a), t = 135 µs, tensile stress as a function of time (c), and experimental failure mode (d).

The simulated and experimental tensile strengths (Figures 3c and 4) have a good agreement. The simulated failure is the typical axial splitting observed also in the experiments (Figure 3b and d)

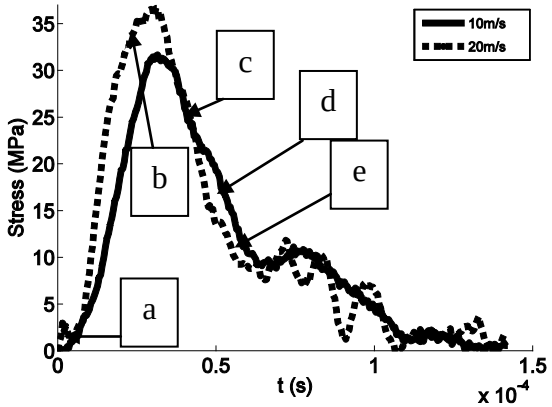

Figure 4. Tensile strength as a function of time.

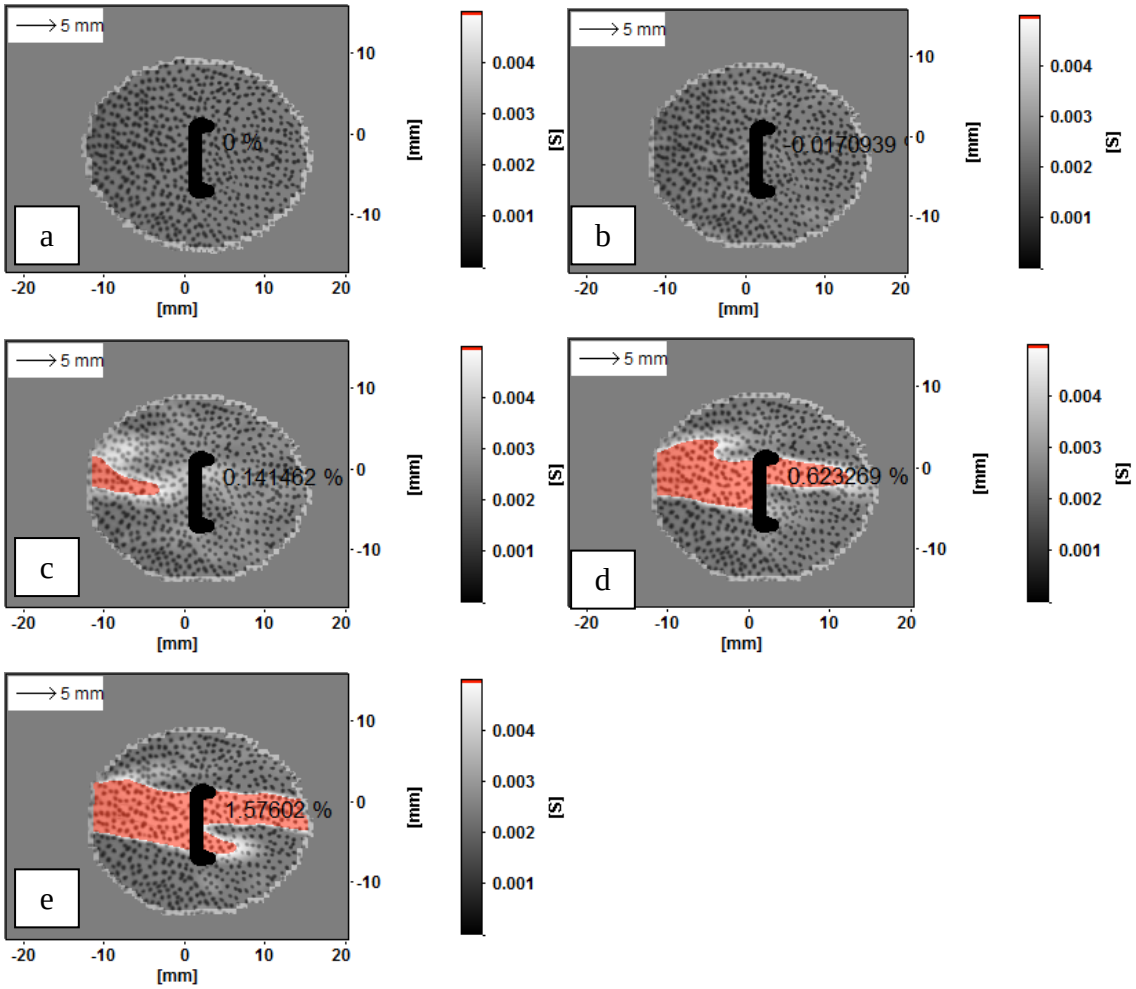

Figure 5. DIC images obtained during the dynamic deformation of the test with impact speed of 20m/s. a) t = 0μs b) t = 12.5 c) t = 43.75μs d) t = 50μs e) t = 56.25μs.

Conclusions

Numerical and experimental testing of the Kuru Gray granite was carried out. The simulated and experimental results show a reasonable match before and after the maximum stress. The DIC results also show that the final fracture initiates below the surface before becoming visible on the surface. The DIC analysis can provide useful information for both model verification and material characterization.

References

[1] Q.Z. Wang, W. Li, X.L. Song, A Method for Testing Dynamic Tensile Strength and Elastic Modulus of Rock Materials Using SHPB, *Pure and Applied Geophysics*, 163(5-6):1091-1100, 2006.

[2] T. Saksala, D. Brancherie, I. Harari, A. Ibrahimbegovic. Combined continuum damage-embedded discontinuity model for explicit dynamic fracture analyses of quasi-brittle materials. *International Journal for Numerical Methods in Engineering* 2015; 101:230-250.

Proceedings of the XII Finnish Mechanics Days
R. Kouhia, J. Mäkinen, S. Pajunen and T. Saksala (Eds.)

Wind-tunnel testing of Helsinki Olympic Stadium new roof

Risto Kiviluoma

Aalto University, P.O.Box 12100, 00076 Aalto, risto.kiviluoma@aalto.fi

Summary. This paper discusses wind-tunnel testing done for the structural engineering of the planned new roof structure of the Helsinki Olympic Stadium. In the plan, all spectator stands will be covered by wing-like slender structure, whose wind-induced vibrations, wind-induced fatigue and dynamic wind loads are of special interest. The new roof will have shape and structure closely like the existing roof of the East spectator stands completed 2005. Although wind-tunnel testing results of this existing roof are available, the new roof can possibly make such changes to aerodynamics that new testing was considered important. This also make possible to apply two enhanced testing techniques; namely net-pressure measurements of time-dependant pressure fluctuations and high-frequency force-balance measurements. The purpose of this paper is to describe these and the related results in detail.

Key words: wind-tunnel testing, boundary-layer wind tunnels, wind loads, high-frequency force-balance measurements, stadium structures

Introduction

Helsinki Olympic Stadium is one of the national landmarks of Finland, and was originally build for the cancelled Olympics 1940. The stadium was completely modernized in 1990–1994 and also renovated just before the 2005 World Championships in Athletics. One of the major change was a new roof for the East spectator stands. The roof was designed as slender wing-like architecture giving a challenge to structural engineers to cope with wind-induced vibration and to reliable predict reaction loads to old structures. To this end, the author conducted 2004 comprehensive wind-tunnel testing program for determining equivalent static wind loads, wind-induced vibration response and stress-cycle count for wind-induced fatigue analysis. A major new renovation is planned to start 2016, in which rest of the spectator places will be covered with a similar type of roof. The wind-tunnel testing for the new roof was done 2014-2015 (Fig. 1) by the author New testing technique were added to the program, namely time-dependent net-pressure measurements through the roof using miniature pressure taps; and high-frequency force balance (HFFB) measurements of the scale model constraint forces and moments.

The present type of testing is generally done in boundary-layer wind-tunnel (BLWT), where turbulence is generated in the flow that cope to be similar with the real wind. BLWT testing technique was originally put forward since 1960's in the engineering of skyscrapers [1], and are in the last decade also applied in Finland in this context [2]. In typical test, the scale model of

the structure will be used, where also the surrounding topography and structures are included. Thus, the scale model size will be determined by the size of the wind-tunnel working section that is in most tunnels is around 2…5 m in width or more. Although the scale model is big, the test objects are usually relative small in size, typically less than half meter.

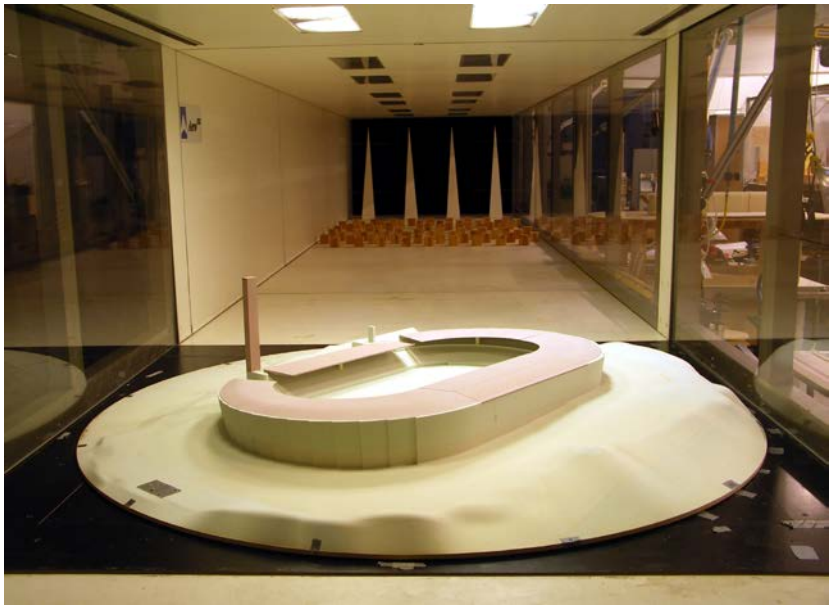

Figure 1. Overview of the test object and the test setup in boundary-layer wind tunnel of the Aalto University. Geometric scale of the model is 1:160 (photo the author).

The fundamental scaling law that determines the measurement of time-dependant quantities is the time scaling given by

$$\left(\frac{tV}{L}\right)_P = \left(\frac{tV}{L}\right)_M, \tag{1}$$

where t = time; V = wind speed; L = geometric dimension; and the subscripts P and M denote the full scale (real structure) and the wind tunnel model, respectively. Eq. (1) also characterises the eddy size, or other length-scale measure, of turbulence. Time taken by an eddy of size L passing an observation point at rest is given by

$$t = \frac{L}{V}. \tag{2}$$

Thus, if in testing one is interested to capture impact of eddies of size 0.01 m in flow speed of 10 m/s, one need sampling rate of order 1000 samples per second and more. On the other hand, if the testing flow speed is decreased sampling rate could be decreased, but on the hand, the load (pressure, force or moment) to be identified will be smaller making them more difficult to measure precisely. For this reason, pressure measurement are often done with the maximum flow speed available at the wind tunnel and the scale model can resist without vibration and damage. HFFB-testing approaches utilizes the frequency-domain methods through the scaling law related to non-dimensional form of spectral densities

$$\left[\frac{fS_i(f)}{\sigma_i^2}\right]_P = \left[\frac{fS_i(f)}{\sigma_i^2}\right]_M, \tag{3}$$

where f = frequency; $S_i(f)$ = spectral density of a time-dependant quantity i and σ_i^2 = variance of the quantity i. In practice, spectral densities are most often determined by software algorithms employing the Fast-Fourier Transform technique. HFFB-based vibration assessment requires load spectral density being measured and extracted with a stiff scale model. In addition to being stiff, the HFFB scale-model is designed as as lightweight as possible to push its own natural frequency high: in order to avoid its own resonant vibration and dynamic amplification factor to influence the measurement results.

To fulfil Eq. (3) the turbulence spectral density should be similar in a wind tunnel. This is done using the long floor (Fig. 1) of typical BLWT that generate a boundary layer which is adjusted similar to natural wind at the site by changing size and location of roughness blocks on the floor. In the testing, the flow speed and turbulence then varies with height and it being measured and confirmed before the testing. This is generally done by using the hot-wire sensor technique. The similarity of local turbulence caused by nearby objects are made similar by just reproducing the geometry faithfully in the scale model.

It could be observed that the definition of reference wind speed is important in comparing the wind-tunnel-test results to the results based design standard approaches. Most design standard use short duration wind speed peak values (1 s or 3 s gust) as bases to determine the wind velocity pressure and the wind load. To reach consistent reliability-level in design, the wind tunnel testing should basically use the same definition. For example, the Eurocode defines gust wind velocity inherently through the equation

$$V_g = \sqrt{1+7I_v}\, V_m \tag{4}$$

where V_g = gust wind speed, I_v = turbulence intensity and V_{m} = mean wind velocity. Both I_v and V_m varies with height and roughness of the topography. Turbulence intensity denotes the standard deviation of wind speed fluctuation respect to mean wind velocity by the definition

$$I_v = \frac{\sigma_V}{V_m}, \tag{5}$$

where σ_V = standard deviations of the wind velocity. This standard deviations is measured through continues wind speed measurements with high sampling frequency: in experiments of natural wind around 1…40 Hz over one hour; and in wind-tunnel testing around 1 kHz over around 30...60 s. Being non-dimensional quantity and contributing the results I_v should be the same in the testing than in the full scale. If the height profiles of V_m and I_v are similar in testing, then the turbulence is often assumed similar also, and the scaling law of Eq. (3) is being assumed fulfilled. In the most precise assessments however, wind tunnel turbulence is often found to lack low frequency content (slow wind speed fluctuations) that contributes the I_v measured in natural wind.

Measurement of time-dependant net-pressures

Pressures transducers were mounted at 2.5 mm diameter holes drilled through the roof structure. The front sensing-end of the transducers was mounted on the top surface. The rear end, transmitting the reference pressure, was mounted on the bottom surface. On those points were transducer length exceed the roof thickness, a short pneumatic tube was used to move the underneath measurement point exactly on the bottom surface. This setup allowed net pressure

across the roof being measured directly. Total 45 points were measured that were distributed on the south end of the stadium (Fig. 2).

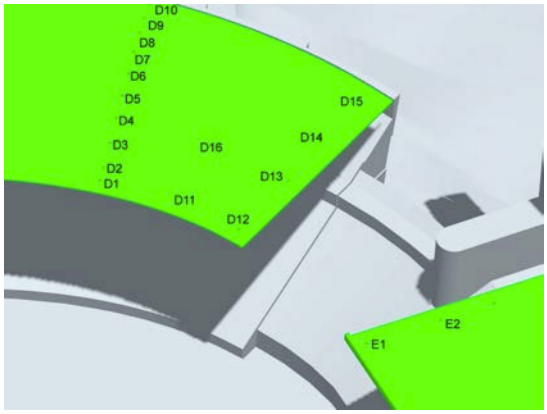

Figure 2. Example of transducer locations at the South-West roof block.

Sampling rate of the 2.5 kHz was used with mean flow speed 16 m/s at the roof level. As all wind directions were measured using angle increment 10^{o}, total 1620 data series were recorded, each containing data for 30 s (= 75'000 numbers). In text format, this was 1.7 gigabytes of data that eventually needed some software-automation to be efficiently processed.

Typical measurement result is illustrated in Fig. 3 and processed results in Fig. 4. Result to report include the mean value; the standard deviation; and the positive and negative extreme values. The extremes are obtained through moving averaging corresponding to 1 s full-scale values. Because extreme values are basically random quantities they could be extracted by two methods: 1) just recording maxima within covering sufficient long time-period in full scale, or 2) by statistical sense fitting the presumed probability distribution to the tests results, and picking up the results with desired confidence level (as peak factor to the standard deviation). The approach 1) was used in the present case. In approach 2) on the suction side amplitudes appear to be the Weibull-distributed and at the pressure side the Normal-distributed [1].

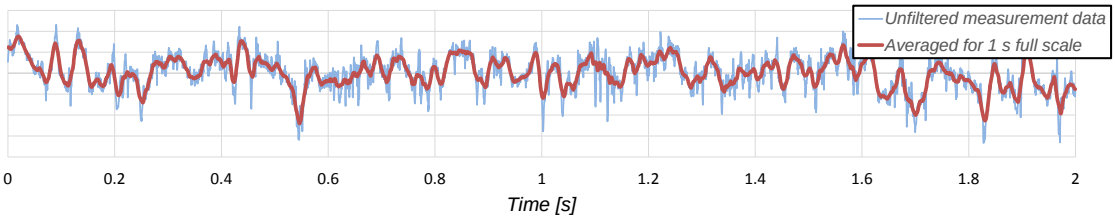

Figure 3. Two second extract for raw measurement data.

It was found out that the biggest 1 s net pressures in 50 y return period storm are of order 3.0…3.9 kN/m^2, and occur in the leading edge of the roof. For comparison, related peak velocity pressures outside the stadium, at roof level, were computed to be 0.8…1.2 kN/m^2 depending on the wind direction.

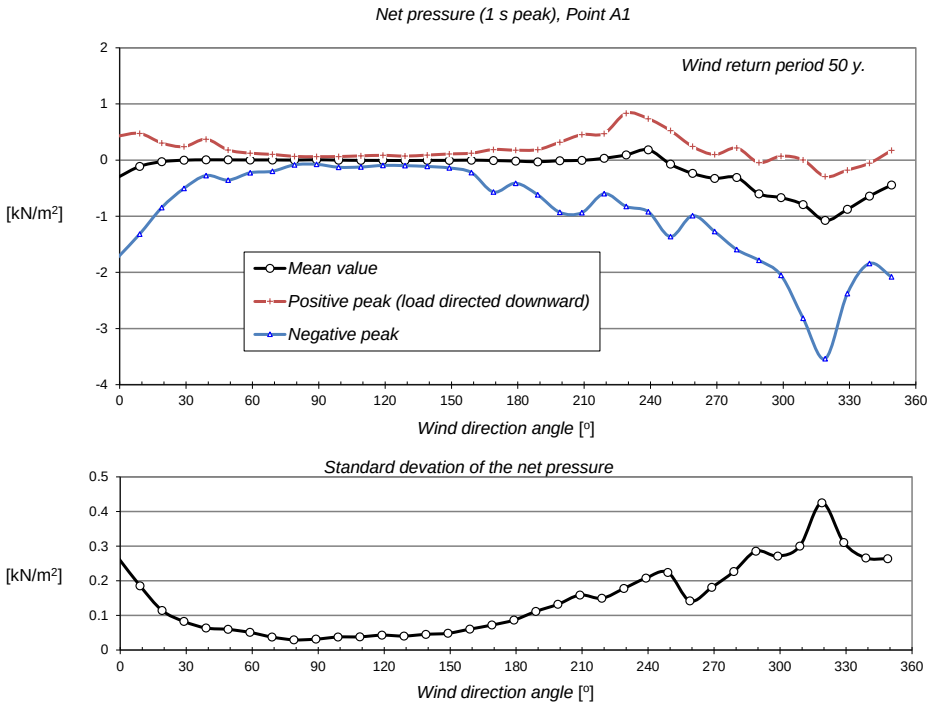

Figure 4. Typical processed result of pressure measurements for full scale structure.

It is generally important to consider electrical noise in the measurements, as the peak values are related to very short averaging in the experiments. In the present case, the time scaling imply that some 30 consecutive numbers (over the period of 0.012 s) could be averaged to obtain 1 s full-scale peak value. In the present case, the noise was not an issue, and the spectral density analysis of the data indicate that the results are usable up to 900…1250 Hz depending on the tap location, i.e. pressure level being measured.

HFFB Testing

HFFB testing was conducted to get more detailed information of resultant load reactions, especially on horizontal direction, and to get data for vibration assessment and fatigue stress cycle count. South-East segment of the roof, which correspond the planned moving joints of the structure, were instrumented with custom force balance system (Fig. 5). Main aim in the balance design was to measure horizontal load as accurate as possible as it small compering to vertical load, but yet important in structural engineering. Example of extracted spectral densities is shown in Fig. 6. Here, with the used flow speed and geometric scale the model natural frequencies in range f_M = 100…200 determines the resonances with full-scale natural frequencies of order f_P = 1…2 Hz in 50 y return period wind. Drag coefficient for horizontal load was found to be to be of order 0.15; and the peak horizontal and vertical acceleration in full scale of order 0.5 m/s^2 and 5 m/s^2 in 50 y return period wind, respectively.

In the present case, factory made miniature force-balance modules were used, that are electrically sealed in both the sensing unit and the cables. Electrical noise was not found to be an issue. The calibration of the HFFB is tedious, as in practice the stiffness of the test object and the supports along the non-sensing directions distorts the theoretical calibration. Here, the theoretical calibration refers to rigid body equilibrium that can be computed from the geometry and the factory calibration constants of the force-balance modules.

a) b)

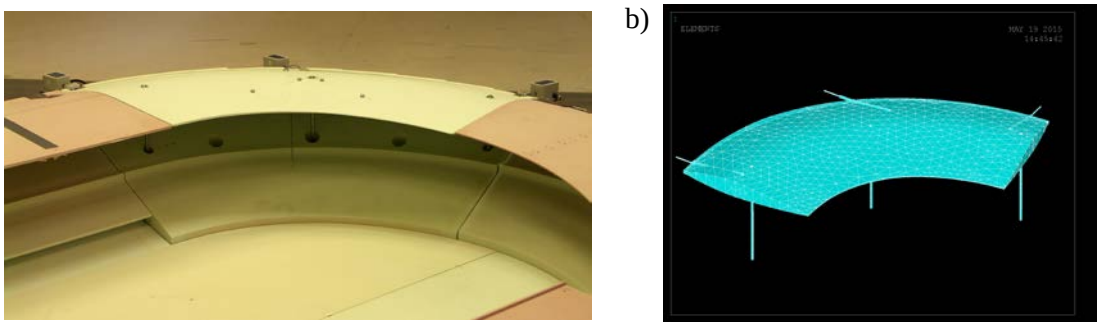

Figure 5. a) HFFB setup, and b) FEM model used in design of the balance system.

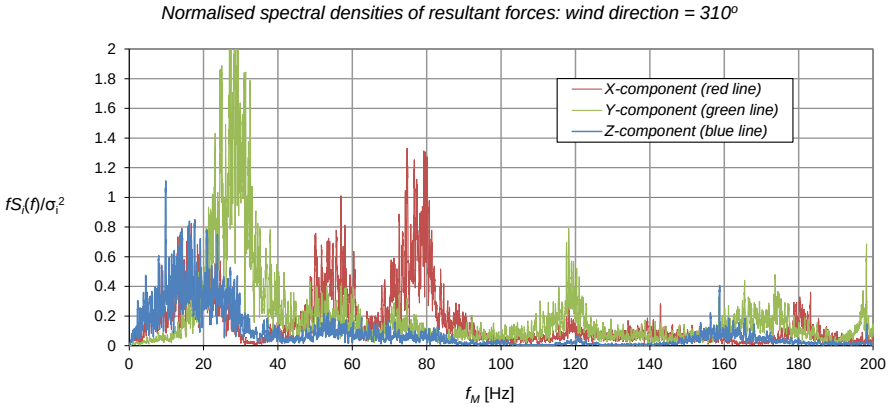

Figure 6. Example of measured normalised spectral densities of resultant loads.

Conclusions

Wind-tunnel testing done for the Helsinki Olympic Stadium new roof is presented concentrating on net-pressure measurements and HFFB techniques. The results can be characterised to be within expectations from the earlier tests done for the East roof. The results are mainly important for the structural engineering of the project. They do have also some research significance, as the structural engineer of the project performed computational fluid dynamics (CFD) simulation using mutually the same 3D geometry and the same assumptions of the wind and turbulence environment outside the stadium. As the goal of the both was to predict wind loads for structural engineering, the studies conducted allow better understanding of the phenomena and limitations involved, and hopefully lead to a proposal how turbulence needs to be taken into account in CFD analysis to get consistent results.

References

[1] *Tall building design criteria and loading, Vol. CL*. Council of Tall Buildings & Urban Habitat, American Society of Civil Engineers, New York 1980, Chapter CL-3 pp. 145-248.

[2] R. Kiviluoma. Problematic in formulation of wind loads on buildings. *Rakenteiden Mekaniikka* (Journal of Structural Mechanics) **42**(2009)1, pp. 48..60.

Proceedings of the XII Finnish Mechanics Days
R. Kouhia, J. Mäkinen, S. Pajunen and T. Saksala (Eds.)

X-ray tomographic method for measuring 3D deformation and liquid content in swelling materials

Tero Harjupatana, Jarno Alaraudanjoki and Markku Kataja

University of Jyväskylä, Department of Physics, tero.t.harjupatana@jyu.fi

Summary. A non-invasive method for measuring the three-dimensional displacement field and liquid content distribution in a wetting and swelling material using X-ray tomographic imaging is introduced. The method is demonstrated here in monitoring the evolution of 3D deformation and water content distributions in cylindrical samples of swelling clay material wetted in a constant total volume. The measurements were carried out using a high-resolution microtomographic device (SkyScan 1172) and image voxel size 24 μm. The results obtained are repeatable and appear qualitatively correct and plausible. They are useful *e.g.* in validating models involving transport of water and the resulting deformation of swelling materials. The method is potentially applicable also in other materials and processes involving liquid transport and deformation.

Key words: X-ray tomography, liquid content, liquid transport, deformation, bentonite, swelling, wetting.

Introduction

The dynamics of liquid transport and deformation in processes involving wetting or drying of solid materials such as soils, building materials, foods and various biological materials [1, 2, 3, 4] can be quite complicated. Theoretical approaches based on first principles towards modelling these processes tend to become tedious, and phenomenological input is often required. Measuring the total liquid content and the global deformation of a wetting/drying material sample is rather straightforward by conventional gravimetric and morphological methods [5, 6]. At least rough local information can be obtained by destructive segmenting of the sample. Various modalities of tomography and other non-destructive methods have been used for measuring the local three-dimensional liquid content distribution [7, 8, 9, 10] or the local deformation of material samples in various mechanical conditions [11, 12]. However, few efforts appears to have been made towards simultaneous non-destructive measurement of the evolution of both the liquid content and the local deformation field of a material sample during wetting or drying process. Availability of such a measurement method would be potentially useful for experimental research of processes involving liquid transport and the resulting deformation, and for development and validation of theoretical models of such processes.

In this work, we introduce a method based on X-ray microtomography for non-destructive simultaneous measurement of three dimensional distribution of local liquid content and displacement field of a wetted material. The method is applied here in monitoring the wetting-swelling behaviour of bentonite clay samples enclosed in a sample chamber of constant total volume.

Methods

X-ray tomography

With X-ray tomography, the spatial distribution of the linear X-ray attenuation coefficient (LAC) in the sample is obtained [13]. In a typical X-ray tomographic imaging procedure, of the order of one thousand X-ray projection images of the sample are taken from different directions by rotating the sample in the X-ray beam. The three-dimensional distribution of LAC is then reconstructed from the projection images by a computer. The data is conveniently represented as a three-dimensional gray-scale image (stack of two-dimensional cross-sectional images) allowing not only visualization but also quantitative study of the internal structure of many heterogeneous materials. The gray-scale 'voxel' values in such an image are linearly correlated with the actual LAC value in the sample. In a case of monochromatic X-ray beam, the gray-scale value (or the LAC) is furthermore linearly correlated with partial densities of materials present in the sample so for the solid-liquid system the gray-scale value is

$$G = C + \alpha_s \cdot \rho_s + \alpha_l \cdot \rho_l \tag{1}$$

where C, α_s and α_l are constants depending on materials and settings used. For a polychromatic X-ray source (*e.g.* X-ray tube), linearity in Eq. 1 may not hold exactly due to beam hardening artifact. However, this artifact can be corrected at the reconstruction stage which seems to work well for the purposes of this study. There are usually many other artifacts present in images such as ring artifacts, cone-beam artifacts and noise. Those can be reduced by optimizing scanning settings or performing specific corrections in reconstruction software.

The X-ray microtomographic device used in the present work was SkyScan 1172 desktop scanner (Fig. 1) which has a microfocus X-ray tube with maximum operating voltage of 100 kV and maximum power of 10 W. The minimum pixel size is 0.7 μm but for the purposes of the present study the device was used in a reduced resolution mode with image size 1000 x 524 pixels of size 24 μm.

Experimental set-up and samples

Cylindrical bentonite samples of diameter 17 mm and height 10 mm were made by compacting a weighed amount of bentonite powder (MP Biomedicals Bentonite) in a mould into a predetermined mean solid phase partial density (1.2 – 1.5 g/cm^3), and placed in a sample holder (see Fig. 1). In order to facilitate deformation measurement, hollow glass microspheres of diameter 100 μm were mixed with the bentonite powder to act as inert tracer particles in the otherwise quite homogeneous material. During the experiment, the sample was held in approximately constant volume in a plastic (PEEK) tube and between cylindrical end-pieces. The end-pieces include wetting and venting channels, and glass sintered plates that allow liquid flow in the sample through the lower end surface, and escape of air through the upper surface. The experiment was started by taking a reference state tomographic image of the non-wetted sample and after that, the wetting (simulated groundwater) of the sample was initiated. The wetting was periodically interrupted and the sample holder with the partially saturated sample weighed, scanned in the tomographic device, weighed again and reconnected to liquid supply to resume wetting. The scanning time was about 45 minutes, and the total time required for each scanning-weighing interval was about an hour. The procedure was repeated typically 10 times until the sample was completely saturated in about 1–2 weeks total time.

Deformation analysis

The local displacement of the solid phase caused by swelling can, in principle, be found by comparing the tomographic images of the reference state and each of the partially wetted states of the sample, provided that both images contain enough tractable details. The displacement

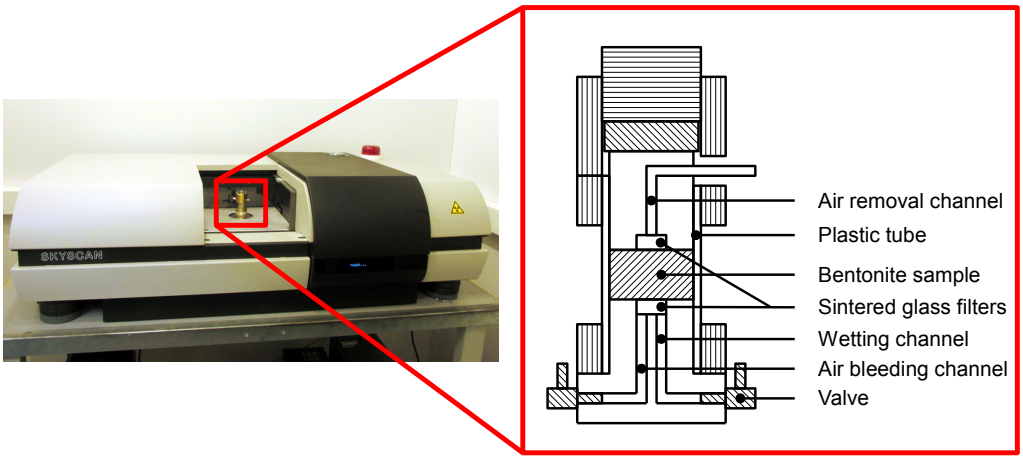

Figure 1. Microtomographic device (SkyScan 1172) and schematic cross-sectional view of the sample holder.

vectors are determined in a three-dimensional grid defined in the reference state image. At every point of that grid, a reference subimage is compared with subimages extracted from the deformed image at the vicinity of the grid point. The minimum for the sum of the squares of the difference in voxel values then defines the measured displacement for that particular grid point. Sub-pixel accuracy is further achieved by fitting second order polynomial function to the minimum.

In order to test the deformation analysis algorithm, a cylindrical sample was made of two-component liquid rubber material doped with glass tracer particles similarly to the bentonite samples. The rubber sample was placed in a material testing stage that allows tomographic imaging of the material under compression or tension. A reference tomographic image of the sample was taken at zero load. The sample was then compressed axially inducing deformation into a barrel-like shape, and imaged again in this configuration. The subimage matching algorithm was used to calculate the displacement field between the unloaded reference state and the deformed state. The experimental result was compared with a numerical solution for the same set-up obtained by COMSOL software indicating very close qualitative and quantitative agreement.

Liquid content distribution

The unknown coefficients (C, α_s and α_l) in the Eq. 1 can be evaluated from measurements of additional calibration samples made by varying solid and liquid densities. The reference tomographic image gives the initial density of the solid material if the possible liquid content in the reference state is known (measurable and assumed to be constant here). The change in solid density between wetted and reference state can be calculated from the measured displacement field and therefore the solid density distribution is known in the wetted state. The remaining unknown quantity, *i.e.* the liquid density ρ_l can then be calculated from in Eq. 1.

The tomographic liquid content analysis method discussed above was compared with results from a straightforward gravimetric analysis of subsamples obtained by slicing a partially wetted (22 h) test sample. After CT method, the sample was carefully cut horizontally into 10 slices of thickness about 1 mm. The liquid content of each slice was determined gravimetrically using oven drying at 105 °C. The results obtained from the gravimetric measurement and from the tomographic imaging method indicate reasonably good correspondence between the two results in regions well inside the sample.

Results

The X-ray tomographic imaging and image analysis methods described above yield three-dimensional displacement field and liquid content distributions in the material sample at selected times during the slow wetting process. Typical examples of such results averaged over the azimuthal angle for a bentonite sample wetted in the sample holder chamber are visualized in Fig. 2. The results on displacement distributions obtained by the X-ray tomographic analysis appear consistent and repeatable in the entire sample region. The water transport mechanism resembles diffusion which is characteristic for the bentonite. The time evolution of the displacement field seems to be complicated which indicates that the swelling of the bentonite is complex phenomenon.

The most important source of error in the deformation analysis are the spurious displacement vector values that occasionally appear as a result of false local minima found by the image correlation algorithm. Those do not seem to have significant contribution to azimuthally averaged results. Another experimental issue affecting the accuracy of liquid content measurement is the incomplete stability of the X-ray source and detector. For accurate results, very good stability is required during each individual scan and between the scans during the experiment. Although, lacking an applicable reference method, quantitative assessment of absolute errors of both the local displacement and the total local liquid content analysis is not feasible, the overall confidence level of the results is reflected by the deformation and wetting test cases.

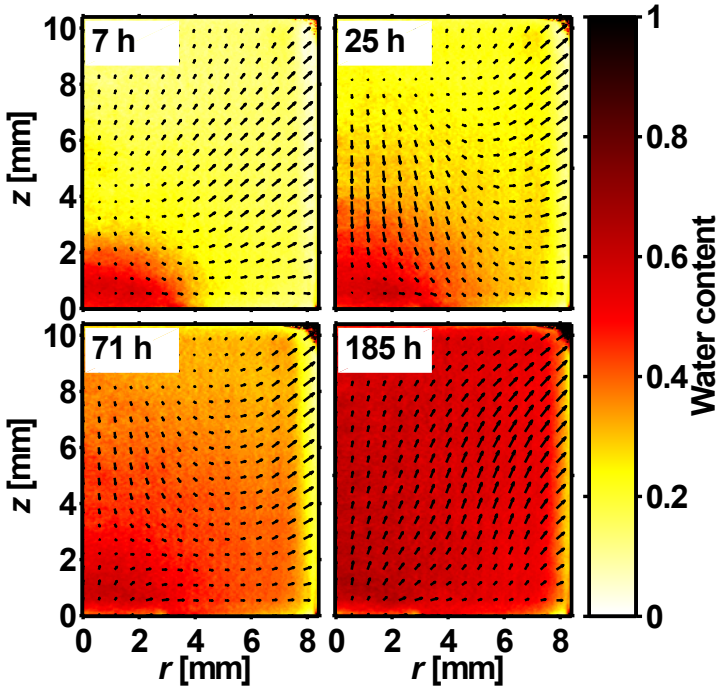

Figure 2. Azimuthally averaged displacement field (scaled by a factor of 5) and water content (ρ_l/ρ_s) in a bentonite sample measured at four different times during wetting.

Conclusions

A method for simultaneous non-intrusive analysis of three-dimensional deformation and liquid transport in solid, wetting material, based on X-ray tomographic imaging has been introduced. The analysis is based on comparing the tomographic images of the reference state and of a wetted and deformed state. The displacement field is obtained by a straightforward image correlation method. This requires that a sufficient amount of local detail, identifiable in the two images, are

found in both states, and that the imaging resolution is sufficient for revealing the deformations. In addition, liquid transport in the material should be slow enough such that the sample can be considered approximately stationary during a single tomographic scan. The deformation analysis was successfully compared with numerical solution for a rubber test sample under axial compression. The liquid content analysis was compared with gravimetric results from axially wetted and sliced cylindrical bentonite samples. The results showed relatively good accuracy in the interior parts of the sample. The method requires calibration with samples of known solid and liquid partial densities. The plausible sources of errors in the method are related to conical X-ray beam geometry, false displacements found by deformation analysis algorithm and instabilities in tomographic device. While the primary motivation and field of application in this work has been the study of the hydromechanical properties and swelling of bentonite clay, the developed method is potentially applicable in also other materials and processes involving liquid transport and deformation.

References

[1] P. Moldrup, T. Olesen, T. Komatsu, P. Schjønning, and D. E. Rolston. Tortuosity, diffusivity, and permeability in the soil liquid and gaseous phases. *Soil Science Society of America Journal*, 65(3):613–623, 2001.

[2] J. Carmeliet and S. Roels. Determination of the isothermal moisture transport properties of porous building materials. *Journal of Building Physics*, 24(3):183–210, 2001.

[3] I. S. Saguy, A. Marabi, and R. Wallach. New approach to model rehydration of dry food particulates utilizing principles of liquid transport in porous media. *Trends in Food Science & Technology*, 16(11):495–506, 2005.

[4] F. C. Meinzer. Co-ordination of vapour and liquid phase water transport properties in plants. *Plant, Cell & Environment*, 25(2):265–274, 2002.

[5] C. M. K. Gardner, D. Robinson, K. Blyth, and J. D. Cooper. *Soil water content. In Soil and environmental analysis: Physical methods.* CRC Press, 2000.

[6] J.-J. Orteu. 3-D computer vision in experimental mechanics. *Optics and Lasers in Engineering*, 47(3):282–291, 2009.

[7] K.-H. Herrmann, A. Pohlmeier, D. Gembris, and H. Vereecken. Three-dimensional imaging of pore water diffusion and motion in porous media by nuclear magnetic resonance imaging. *Journal of Hydrology*, 267(3):244–257, 2002.

[8] W. Aregawi, T. Defraeye, S. Saneinejad, P. Vontobel, E. Lehmann, J. Carmeliet, D. Derome, P. Verboven and B. Nicolai. Dehydration of apple tissue: Intercomparison of neutron tomography with numerical modelling. *International Journal of Heat and Mass Transfer*, 67:173–182, 2013.

[9] M. Mukhlisin, A. Saputra, A. El-Shafie, and M. R. Taha. Measurement of dynamic soil water content based on electrochemical capacitance tomography. *International Journal of Electrochemical Science*, 7(6), 2012.

[10] J. A. Huisman, S. S. Hubbard, J. D. Redman, and A. P. Annan. Measuring soil water content with ground penetrating radar. *Vadose zone journal*, 2(4):476–491, 2003.

[11] S. Peth, J. Nellesen, G. Fischer, and R. Horn. Non-invasive 3D analysis of local soil deformation under mechanical and hydraulic stresses by μCT and digital image correlation. *Soil and Tillage Research*, 111(1):3–18, 2010.

[12] H. Bart-Smith, A.-F. Bastawros, D. R. Mumm, A. G. Evans, D. J. Sypeck, and H. N. G. Wadley. Compressive deformation and yielding mechanisms in cellular Al alloys determined using X-ray tomography and surface strain mapping. *Acta Materialia*, 46(10):3583–3592, 1998.

[13] S. R. Stock. *Microcomputed tomography: methodology and applications.* CRC press, 2008.

Rakenteiden Mekaniikka
Vol. 48, No 1, 2015, s. 18-33
www.rmseura.tkk.fi/rmlehti

Betonisten ratapölkkyjen väsytyskuormituskokeet

Tommi Rantala, Olli Kerokoski ja Antti Nurmikolu

Tiivistelmä. Väsytyskuormituskokeissa kuormitettiin käyttämättömiä suomalaisia betonisia ratapölkkyjä B97 ja BP99. Kuormituskokeiden tarkoituksena oli selvittää ratapölkkyjen väsymisominaisuuksia ja väsymisen vaikutusta ratapölkyn jäykkyyteen. Lisäksi tutkimuksessa arvioitiin halkeaman merkitystä. Kuormitustasot valittiin siten, että väsymisen merkitystä todellisessa käyttötilanteessa voitiin arvioida. Kuormituskokeista johdettu väsymisraja ja laskennallinen halkeilukestävyys ovat selvästi suurempia kuin kenttäkokeissa mitatut rasitukset. Raiteessa sijaitsevien ratapölkkyjen murtuminen liikennekuormituksessa väsymisen vaikutuksesta on siis hyvin epätodennäköistä.

Avainsanat: betoniratapölkky, kuormituskoe, väsyminen

Tommi Rantala, Olli Kerokoski, Antti Nurmikolu
Tampereen teknillinen yliopisto,
PL 600, 33101 Tampere
tommi.rantala@tut.fi, olli.kerokoski@tut.fi, antti.nurmikolu@tut.fi

Proceedings of the XII Finnish Mechanics Days
R. Kouhia, J. Mäkinen, S. Pajunen and T. Saksala (Eds.)

Seismic analysis of a liquid-filled shell structure

Jussi-Pekka Matilainen[1] and Jari Puttonen[1]

[(1)]Aalto University, School of Engineering, Department of Civil and Structural Engineering, PO Box 12100, FI – 00076 Aalto, jussi-pekka.matilainen@outlook.com, jari.puttonen@aalto.fi

Summary. The purpose of this study is to introduce a numerical technique for analysing a liquid-filled shell structure under earthquake ground motions. Prescriptions of the EN 1998 to the representation of earthquake ground motion as accelerograms are explained. Accelerograms representing the ground motion are generated by matching recorded accelerograms to a response spectrum and, alternatively, artificial accelerograms are generated for reference. For the numerical simulations, structures are treated with traditional Lagrangian formulation while the liquid is represented by arbitrary Lagrangian-Eulerian (ALE) formulation. Governing equations of the ALE formulation are introduced. An industrial-sized liquid-filled tower subjected to both the matched and artificial accelerograms is analysed. Horizontal deflections of both the liquid-filled and empty towers due to accelerograms are determined. As a result of this study, information is gained from both the effect of ground motion selection process and liquid fill on the structural response of the tower. This study demonstrates that the fluid-structure interaction significantly affects the dynamic behaviour of a structure during a seismic event.

Key words: EN 1998, earthquake ground motions, arbitrary Lagrangian-Eulerian, ALE, fluid-structure interaction, FSI

Introduction

The European seismic design code EN 1998 [1] introduces two different methods for the selection of earthquake ground motions. First, a set of earthquake events are selected from the Pacific Earthquake Engineering Research Center (PEER) [2] Ground Motion Database based on surface-wave magnitude (M_s) and shear-wave velocity ($v_{s,30}$). The natural accelerograms are matched to the elastic response spectrum in order to fulfil the spectrum-compatibility requirements and scaled to the design ground acceleration, a_g, in order to correspond the desired seismic zone. Second, artificial earthquake accelerograms are generated for reference.

For problems with both fluids and solids, Eulerian formulation is used for the fluid part and Lagrangian formulation for the structure part, and a coupling algorithm known as Euler-Lagrange coupling is employed between them. Since the Eulerian mesh is stationary, it must be large enough to enclose the entire fluid domain of interest. In order to optimize the Eulerian mesh, advantage may be taken of arbitrary Lagrangian-Eulerian (ALE) formulation in which the Eulerian mesh moves in an arbitrary manner.

A numerical simulation for the liquid-filled shell structure under earthquake ground motions is carried out with Abaqus/Explicit [3], which is an explicit dynamics finite element program.

Selection of earthquake ground motion records

EN 1998 prescriptions

Within the scope of EN 1998 the earthquake ground motion at a given point of the ground surface is presented by an elastic ground acceleration response spectrum. However, the description of the seismic motion may be made by using artificial and recorded or manipulated accelerograms [4]. According to the EN 1998, the sets of accelerograms that are selected must satisfy the following criteria:

1. The mean of the zero period spectral response acceleration values has to be higher than the value a_gS for the site in question, where a_g is the design ground acceleration and S is the soil factor.
2. The mean of the 5 % damped elastic spectrum that is calculated from all time histories should be no less than 90 % of the corresponding value of the 5 % damped elastic response spectrum, in the range of periods between $0.2T_1$ and $2T_1$, where T_1 is the fundamental period of the structure in the direction where the accelerogram is applied.
3. A minimum of three accelerograms has to be selected in each set. When three different accelerograms are used, the structural demand is determined from the most unfavourable value that occurs from the corresponding dynamic analyses. On the other hand, in case that at least seven different records are used, the design value of the action can be derived from the average of the response quantities that result from all the analyses.

In this study, it is assumed that the site of interest is located on an area of high seismicity (M_s>5.5) which imposes the use of Type 1 spectrum for horizontal ground motions. In addition, it is assumed that the reference peak ground acceleration on type A ground, a_{gR}, corresponding to the seismic zone is set to 0.40g and the underground conditions correspond to the ground type B. An importance factor γ_I equal to 1.0 is assigned, resulting in a design ground acceleration on type A ground $a_g=\gamma_I a_{gR}$. Based on this information, the elastic horizontal (S_e) response spectrum prescribed in EN 1998 is established for 5 % viscous damping as a function of the vibration period of linear single-degree-of-freedom system (T).

Recorded accelerograms

Based on the assumed site of interest in this study, PEER Ground Motion Database was queried to find seven earthquake events with M_s>5.5 and 360 m/s $\leq v_{s,30} \leq$ 800 m/s that best match the Type 1 horizontal elastic response spectrum for a class B site. The selected earthquake events, along with their NGA numbers, dates, recording stations, distances of the recording stations to the rupture planes (R_{rup}) and seismogenetic parameters (M_s, $v_{s,30}$) are listed in Table 1.

After the selection of earthquake events from the database, accelerograms are matched to the elastic horizontal spectrum and scaled to the design value a_g=0.40g with the SeismoMatch [5] software, which uses the wavelets algorithm. Comparison of the difference between the matched horizontal spectra and the elastic horizontal spectrum is shown in Figure 1.

Artificial accelerograms

In addition, the SeismoArtif [5] program is employed for the generation of seven artificial accelerograms compatible with the horizontal response spectrum.

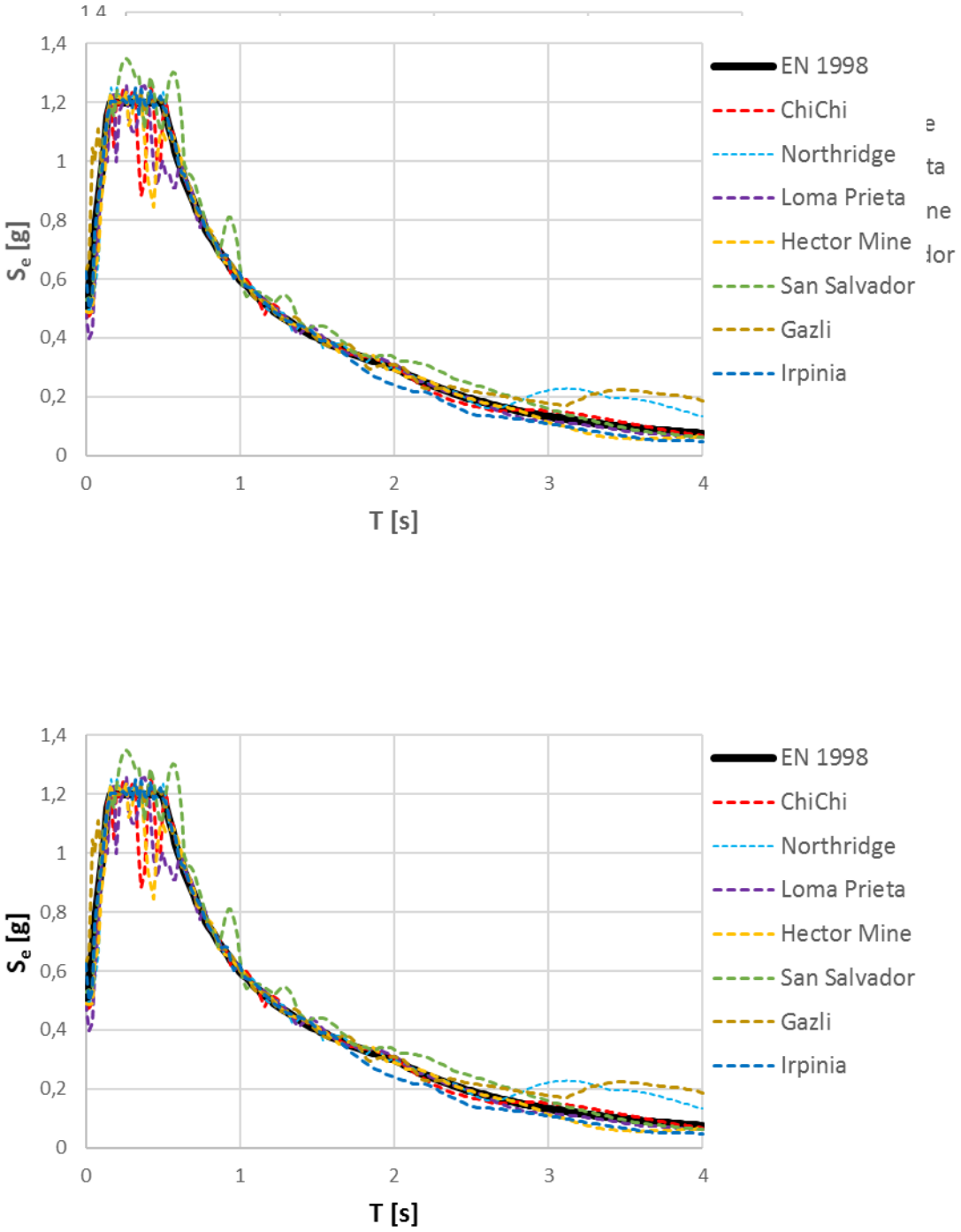

Figure 1. Comparison of the horizontal matched acceleration spectra to the elastic horizontal spectrum, EW-direction (East-West).

Arbitrary Lagrangian-Eulerian and Euler-Lagrange coupling

Governing equations of the ALE formulation

Governing equations of the ALE formulation are based on conservation laws which are a group of fundamental equations of continuum mechanics that must always be satisfied by physical systems. The conservation laws relevant to the ALE formulation are the mass, momentum and energy conservation. [6]

Adopting the notation used by Benson [7], the spatial coordinates of a point are denoted $\bar{\boldsymbol{x}}$, velocity of the material is $\bar{\boldsymbol{u}}$, velocity of the reference coordinates is $\bar{\boldsymbol{v}}$, and their difference, the convective velocity, is $\bar{\boldsymbol{w}} = \bar{\boldsymbol{u}} - \bar{\boldsymbol{v}}$. Both the material and reference coordinate velocities, $\bar{\boldsymbol{u}}$ and $\bar{\boldsymbol{v}}$, are expressed with respect to the spatial coordinates. In addition, the Cauchy stress is denoted $[\boldsymbol{\sigma}]$ and specific body force is $\bar{\boldsymbol{b}}$ while the state variables ρ and e denote the density and internal energy per unit mass, respectively. The superscript r is added to the state variables ρ and e or material time derivative $\bar{\boldsymbol{u}}$ when they are expressed as a function of the reference coordinates.

The governing equations for mass, momentum and energy, respectively, are given by equations (1) to (3) as

$$\frac{\partial \rho^r}{\partial t} = -\rho \frac{\partial u_i}{\partial x_i} - w_i \frac{\partial \rho}{\partial x_i} \tag{1}$$

$$\rho \frac{\partial u_i^r}{\partial t} = \frac{\partial \sigma_{ij}}{\partial x_j} + \rho b_i - \rho w_j \frac{\partial u_i}{\partial x_j} \tag{2}$$

$$\rho \frac{\partial e^r}{\partial t} = \sigma_{ij} \frac{\partial u_i}{\partial x_j} + \rho b_i u_i - \rho w_j \frac{\partial e}{\partial x_j} \tag{3}$$

Governing equations of the ALE formulation are solved by a method known as operator splitting which breaks the partial differential equations into a series of simpler ones that are solved sequentially. In this approach, the computation of ALE equations is divided into two phases for each time step. First, the solution is advanced in time by a Lagrangian step in which the mesh moves with the material. In this step, the changes in velocity and internal energy due to the internal and external forces are calculated. The second step, called Eulerian step, computed the transport of mass, energy and momentum across element boundaries. During the Eulerian step, the mesh that was displaced in the Lagrangian step is remapped back to its arbitrary position. There is no time step associated with the Eulerian step. In the Lagrangian step, velocity of the reference coordinate system $\bar{\boldsymbol{v}}$ equals the material velocity $\bar{\boldsymbol{u}}$, resulting in $\bar{\boldsymbol{w}} = 0$ and mass is automatically conserved. Thus, the governing equations (1) to (3) in the Lagrangian step simplify to

$$\rho \frac{\partial u_i}{\partial t} = \frac{\partial \sigma_{ij}}{\partial x_j} + \rho u_i \tag{4}$$

$$\rho \frac{\partial e}{\partial t} = \sigma_{ij} \frac{\partial u_i}{\partial x_j} + \rho b_i u_i \tag{5}$$

In the Eulerian step, Van Leer transport algorithm is used in transporting the state variables.

Seismic analysis of a liquid-filled shell structure

Applicability of the ALE formulation and Euler-Lagrange coupling is put to an industrial level test by analysing a liquid-filled tower under earthquake accelerograms.

The tower is made of concrete with a density of 2500 kg/m^3, elastic modulus of 30 GPa and Poisson's ratio of 0.2. Isotropic linear elastic material model is used to represent the concrete. The tower has a radius of 3.125 m at the bottom and a radius of 6.250 m at the top. Shaft of the tower is 42 m high while the total height is 60 m and the wall thickness 0.4 m. The tower is filled up to a height of 54 m and the Mie-Grüneisen equation of state with a bulk modulus of 2.2 GPa is used to represent the water. Viscosity is not taken into account. Masses of the empty tower and the liquid are 1093 and 3030 tonne, resulting in a total mass of 4123 tonne.

Arbitrary Lagrangian-Eulerian (ALE) formulation is employed to represent the water domain which follows motion of the tower as a rigid body. Three-dimensional, 8-node Eulerian elements of type EC3D8R are used to model the water. The tower, on the other hand, is modelled with 4-noded, quadrilateral shell elements of type S4R. Finally, the bottom plate is modelled with rigid shell elements of type R3D4.

The rotational degrees of freedom are constrained at the tower base, thus enabling the acceleration in the orthogonal directions. A vertical field of 1.0 g is applied to give a realistic hydrostatic pressure in the water. In order to enforce Euler-Lagrange coupling, the Lagrangian mesh for the tower, the Lagrangian mesh for the tower structure is embedded in the ALE mesh for the fluid. The finite element model of the liquid-filled tower is shown in Figure 2.

Dynamic time-history analyses are conducted under both the matched and artificial accelerograms with 0.40 g peak acceleration. As response parameters, time-histories of the horizontal deflections are recorded up to 20 s in order to evaluate the effect of liquid-fill and record selection process on the results.

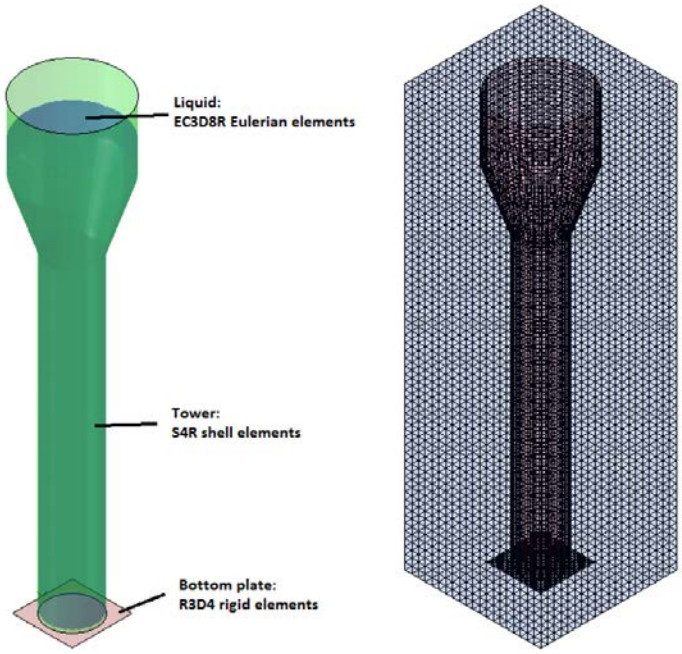

Figure 2. Finite element model of the liquid-filled tower.

Conclusion

A numerical technique for analyzing a liquid-filled shell structure subject to earthquake ground motions is presented in this study. Selection process of accelerograms representing the seismic ground motion according to EN 1998 is introduced. Suitable earthquake events are chosen from the PEER database, matched spectrum-compatible and scaled to the desired level of ground acceleration. Artificial accelerograms are generated for reference.

ALE formulation of the finite element method is used for the fluid domain while traditional Lagrangian formulation is used for the structure domain. Coupling between the fluid and structure domains is achieved through Euler-Lagrange coupling algorithm. The governing equations of the ALE formulation are introduced.

Earthquake accelerograms and ALE formulation are applied to simulate the effect of fluid-structure interaction on the structural response for a liquid-filled shell structure. This study demonstrates that ALE formulation is a convenient tool for analysing dynamic FSI problems in a single model for real-sized complex structures.

References

[1] CEN, 2004. *Eurocode 8: Design of structures for earthquake resistance – Part 1: General rules, seismic actions and rules for buildin*gs. Brussels: Comitè Europèen de Normalisation.

[2] PEER, 2015. *Pacific Earthquake Engineering Research Center: NGA Database*. http://ngawest2.berkeley.edu/

[3] Abaqus, 2012. *Version 6.12 Documentation*. Providence, RI, USA: Dassault Systèmes Simulia Corp.

[4] Solomos, G., Pinto, A. & Dimova, S, 2008. *A Review of the Seismic Hazard Zonation in National Building Codes in the Context of Eurocode 8*. Luxembourg: European Commission.

[5] Seismosoft, 2013. *Earthquake engineering solutions*. http://seismosoft.com/en/HomePage.aspx

[6] Belytschko, T., Liu, W. K. & Moran B., 2000. *Nonlinear Finite Elements for Continuia and Structures*. Baffins Lane. Chichester, West Sussex PO19 1UD, England: John Wiley & Sons Ltd.

[7] Benson, D. J., 2010. Introduction to Arbitrary Lagrangian-Eulerian in Finite Elements Methods. In: M. Souli & D. J. Benson, eds. *Arbitrary Lagrangian-Eulerian and Fluid-Structure Interaction: Numerical Simulation.* Hoboken, NJ 07030, USA: John Wiley & Sons, Inc, pp. 1-50.

Rakenteiden Mekaniikka (Journal of Structural Mechanics)
Vol. 48, No 1, 2015, pp. 1-17
www.rmseura.tkk.fi/rmlehti.fi

Performance-based seismic optimization design

Qimao Liu and Juha Paavola

Summary. Performance-based engineering is to design, evaluate and construct, as economically as possible, the engineering facilities that can meet the uncertain future demands of owner-users and natural hazards. The performance-based design is believed to be the promising method in earthquake engineering, wind engineering and fire engineering. The paper takes the performance-based seismic optimization design as an example to describe the philosophy of the performance-based design method. First, the basic concepts of performance-based seismic design are introduced. Second, how to quantify the uncertain future hazard levels, i.e., to obtain the future demand diagrams, is presented. Third, how to quantify the capability of the structures to resist the future hazard, i.e., to achieve the capability diagram, is in detail. Fourth, how to evaluate the performance of the structures at different future hazard levels, i.e., to catch the performance points, is described. Finally, the optimization modelling is proposed for the performance-based design. The performance-based design of steel frame is demonstrated. The limitations of the current performance-based seismic design method are also discussed.

Key words: performance-based design, earthquake engineering, capability diagram, demand diagrams, performance points

Qimao Liu and Juha Paavola
Aalto University
Department of Civil and Structural Engineering
P.O. Box 12100
00076 Aalto, Finland
qimao.liu@aalto.fi, juha.paavola@aalto.fi

Rakenteiden Mekaniikka (Journal of Structural Mechanics)
Vol. 48, No 1, 2015, pp. 83-98
www.rmseura.tkk.fi/rmlehti/

Shear bands in soft clays: strain-softening behavior in finite element method

Marco D'Ignazio and Tim Länsivaara

Summary. Strain-softening behavior of soft sensitive clays is very often neglected in geotechnical design. During undrained loading, such materials show a dramatic loss of strength after the peak stress, until residual strength is reached at large strain. As a consequence, local failure occurs and plastic strains localize in a shear band. Shear band modeling in Finite Element Method requires a regularization technique to overcome mesh dependency. NGI-ADPSoft2 model is able to simulate the post-peak softening behavior of sensitive clays. In this study, the influence of strain softening on the stability of sensitive clay slopes is studied using the NGI-ADPSoft2 model. The analyses are conducted using the finite element software PLAXIS 2D AE. The advantages of using a strain-softening soil model are discussed.

Key words: strain-softening, shear band, FEM, sensitive clays, PLAXIS

Marco D'Ignazio, Tim Länsivaara
Tampere University of Technology, Tampere, Finland
P.O. Box 600, FI-33101, Tampere, Finland
marco.dignazio@tut.fi; tim.lansivaara@tut.fi

Proceedings of the XII Finnish Mechanics Days
R. Kouhia, J. Mäkinen, S. Pajunen and T. Saksala (Eds.)

Changes of pore water pressure in clay during consolidation

Samuli Laaksonen[1], Osmo Korhonen, Mirva Koskinen[2], Leena Korkiala-Tanttu[3], Matti Lojander[3] and Monica Löfman[3]

(1)Ramboll Finland Oy, PL 25, Säterinkatu 6 FI-02601 Espoo, Finland,
samuli.laaksonen@ramboll.fi
osmo.e.korhonen@gmail.com
(2)City of Helsinki, mirva.koskinen@hel.fi
(3)Aalto University School of Engineering, leena.korkiala-tanttu@aalto.fi,
matti.lojander@aalto.fi, monica.lofman@aalto.fi

Summary. Settlement of clay is a combination of several processes. The applied load causes excess pore water pressure in clay. Usually the largest part of settlement is called (primary) consolidation settlement, which is caused by pore water flowing out of clay. At the same time also the creep of soil structure (secondary consolidation) occurs. In this paper a model for calculating simultaneous primary and secondary settlements is represented. Model is derived from Darcy's law applied to measured pore water pressure data. Parameters can be determined by using a modified oedometer apparatus.

Key words: consolidation, clay, pore water pressure, oedometer test

Introduction

Applying load causes excess pore water pressure. Draining of pore water from clay layer leads to decrease in volume known as primary consolidation. However, not only draining of pore water but also changes in soil skeleton cause volume decrease and thus settlement. This process is called secondary consolidation or creep. In geotechnical engineering, rate of settlement (primary settlement) of a structure founded on clay (or other cohesive soil) is generally calculated using either Terzaghi's [10] or Janbu's [5] theory of consolidation. Terzaghi's theory of consolidation is based on pore water pressure –equation, which describes changing of pore water pressure u as a function of time t and depth z.

Changes of pore water pressure are usually described by partial differential equations (PDE). Almost all partial differential equations governing diffusion contain only first order term of time, thus only the rate of increasing of pore water pressure u is included. The simplest is Equation 1 which was first introduced in geomechanics by Terzaghi in the 1920's [10].

$$\frac{\partial u}{\partial t} = c_v \frac{\partial^2 u}{\partial z^2}. \quad (1)$$

Janbu's [5] theory of consolidation is based on distribution of remaining degree of deformation. Terzaghi's and Janbu's theories lead to the identical solution in one-dimensional flow- and deformation conditions which take place in oedometer test. Various assumptions limit applications of the two theories. The main assumptions in Terzaghi's one-dimensional theory of consolidation are: (i) the soil is homogeneous and fully saturated, (ii) solid particles and water are incompressible, (iii) compression and flow are one-dimensional, (iv) strains are small, (v) Darcy's law is valid, (vi) the coefficient of permeability and the coefficient of volume compressibility remain constant and (vii) there is a unique relationship between void ratio and effective stress [9].

Oedometer test

Standard oedometer test

For almost 100 years oedometer tests have been used for the determination of calculation parameters for settlement analysis for structures constructed on clay (cohesive soil). Oedometer test is carried out on a cylindrical test specimen that is confined laterally by a rigid ring [3]. In incrementally loaded standard oedometer test only height of the sample and time are measured in several ($\geq$7) load increments. Typically the load increments are doubled once a day. In order to help the interpretation of parameters and to reduce the effect of sample disturbance it is recommended to include unloading and reloading cycles. Thus the duration of the test can be 2-3 weeks.

Pore water pressure oedometer test

In the pore water pressure oedometer not only height of the sample (H) and time (t) are measured but also pore water pressure (u) from the bottom of the sample. Thus drainage occurs only upwards and primary consolidation takes four times longer than in a standard test, because time for primary consolidation is dependent on the second power of drainage path. Minimizing the duration of the test would require choosing load increments corresponding to the stress increase caused by the structure. In this paper only pore water pressure at the bottom of the sample is used: The distribution of pore water pressure inside the sample is not needed in this study.

The development of the pore water pressure during different load increments is represented in Figure 1. After the loading the pore water pressure increases until it reaches its maximum value after few minutes. In all consolidation models, however, it is assumed that the pore water pressure reaches its maximum value immediately after the loading. Furthermore, the pore water pressure does not reach the applied load ($\Delta\sigma_1$) as it is assumed in classical soil mechanics. During the increase of pore water pressure remarkable part of primary consolidation occurs (Figure 2). In Figure 2 also Brinch-Hansen's [2] formula representing Terzaghi's theory of consolidation is fitted to observations, which indicates that Terzaghi's theory can be applied and pure secondary consolidation starts after 5-6 hours.

As seen in Figure 2, the pore water pressure has a peak value in the early stage of the consolidation. This is caused by two processes: first the pore water pressure rapidly increases to match the applied load and then at the same time the pore water pressure decreases due to water flowing out of the sample.

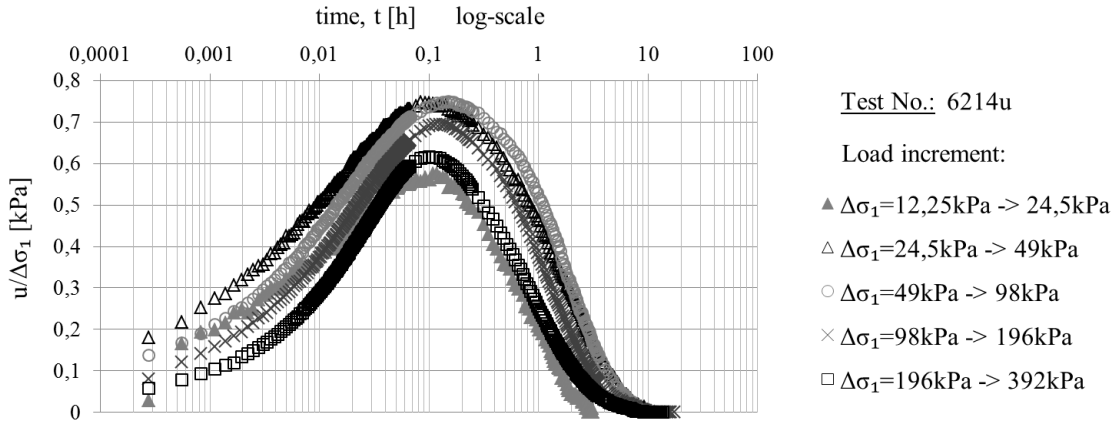

Figure 1. Observed pore water pressure in oedometer test of HUT-Clay. [8]

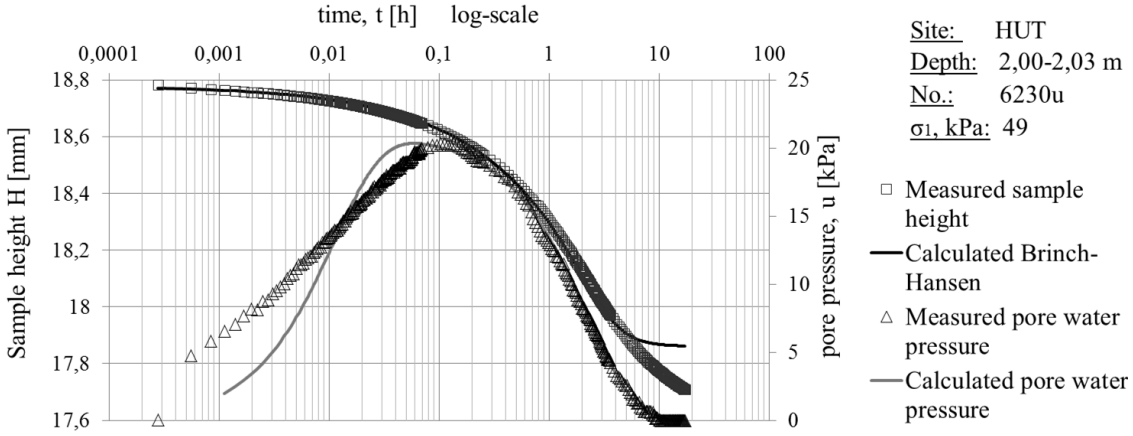

Figure 2. Time-dependent behaviour of HUT-Clay in oedometer test. [8]

Separation of primary and secondary settlements

Secondary consolidation (creep) is supposed to start immediately after loading, even before pore water pressure reaches its maximum value. That is obvious near the upper part of the sample where drainage is arranged through the porous stone. The primary and secondary consolidation can be separated from each other by deriving Darcy's law by replacing the hydraulic gradient with pore water pressure. In this method the decrease of water permeability can also be taken into account.

There are several time-settlement functions which are based on a simple first order differential equations. Usually there are two parameters to be solved, and they depend on the boundary conditions. Primary settlement can be calculated with Equation 2:

$$s_{pri}=\mathrm{k}\int u(t)dt\,, \tag{2}$$

where s_{pri} is primary settlement. In Equation 2 parameter k describes changes in rate of settlement v with respect to u

Some theories of consolidation include two damping factors acting simultaneously (one for primary consolidation and one for creep). Especially Kondner's solution [6], [7] is very

powerful in practice, when for example one has to predict future settlements from measured data in structures.

Solution of Equation 1 contains only one term of decreasing pore water pressure *u* with time *t*. Thus there cannot be any peak values of pore water pressure. The changes of pore water pressure u can be calculated using a modified version of Equation 1, which includes better all processes during the loading:

$$\frac{\partial^2 u}{\partial t^2} + \alpha_1 \frac{\partial u}{\partial t} + \alpha_2 u = c_v \frac{\partial^2 u}{\partial z^2}, \tag{3}$$

where α_1, α_2 and c_v are parameters and *z* is depth. If distribution of u with respect to the variable *z* is not taken into account, the solution for u(t) with peak value u_0 is

$$u(t) = -u_0 e^{\lambda_1 t} + u_0 e^{\lambda_2 t}, \tag{4}$$

and the solution of *u* with respect to the variables *z* and *t* is

$$u(z,t) = \frac{(-u_0 e^{\lambda_1 t} + u_0 e^{\lambda_2 t}) \cdot e^{(-z^2/4c_v t)}}{\sqrt{2\pi c_v t}}, \tag{5}$$

where λ_1 and λ_2 are the roots of characteristic equation of Equation 3 (left side) and u_0 is the peak value pore water pressure (,which in ideal case is the applied load).

If Equation 2 is assumed to represent primary settlement only, it is possible to predict the creep parameter(s) since the remaining settlement is supposed to be only creep. The creep parameters can be the determined either by subtracting calculated primary settlement values from observed total settlement or by fitting the observed data to creep function (as has been done here).

The primary settlement can be calculated with Equation 2. In Equation 2 the (graphical) integral of *u(t)* can be obtained directly from measured data. The parameter k is different for increasing and decreasing pore water pressures (k_1, k_2). The k values can be obtained from measured rate of settlement and pore water pressure as represented in Figure 3. At first, a line parallel to rate of settlement at the end of the load increment is drawn from origin (step 1). Next, the line is cut at the point of peak value of pore water pressure u_0 (step 2). Finally, a line parallel to rate of settlement before the peak value is drawn (step 3). The rate of settlement at the beginning of the load increment cannot be used as Darcy's law is not valid at such low, increasing *u* values. The slope of first line gives the k_2 value for settlement caused by decreasing *u* and the slope of other line gives the k_1 value for settlement caused by increasing *u*.

Total settlement of the sample in oedometer test is the sum of primary settlement (Equation 2) and creep settlement defined by the creep function (s_{cr}):

$$s_{tot} = s_{pri} + s_{cr} = k \int u(t)dt + s_{cr,f}\left(1 - e^{\lambda_3 t}\right) = s_{inc,f}\left(1 - e^{\lambda_1 t}\right) + s_{dec,f}\left(1 - e^{\lambda_2 t}\right) + s_{cr,f}\left(1 - e^{\lambda_3 t}\right), \tag{6}$$

where s_{tot} = total settlement, s_{cr} = creep (settlement), $s_{inc,f}$ and $s_{dec,f}$ are final values of primary settlements (increasing and decreasing respectively) and $s_{cr,f}$ is final value of creep. The parameters of Equation 6 are determined by by fitting the observed data of *s*, *u* and *t* to

Equations 2, 4 and 6. Thus primary settlement can be calculated by using either Equation 2 or Equation 6 (if creep has been calculated).

Calculated primary settlements (u increasing and u decreasing), calculated creep settlement and both calculated and observed total settlement are represented in Figure 4. The primary settlements have been determined with Function 2 as described earlier. Creep parameters have been calculated with fitting the observed data to the creep function at the time when pore water pressure is 0 or constant (when settlement is solely caused by creep). The creep function used represents theory of consolidation by Gibson & Lo [4]. It is also possible to calculate creep settlement by subtracting calculated primary settlement values from observed total settlement values. Calculated total settlement is the sum of calculated primary settlement and creep.

Pore water pressure calculated with Equation 4 is represented in Figure 2. The parameters (λ_1 and λ_2) are the same as in Equation 6.

List of parameters of Equations 4 and 6 is shown in Table 1.

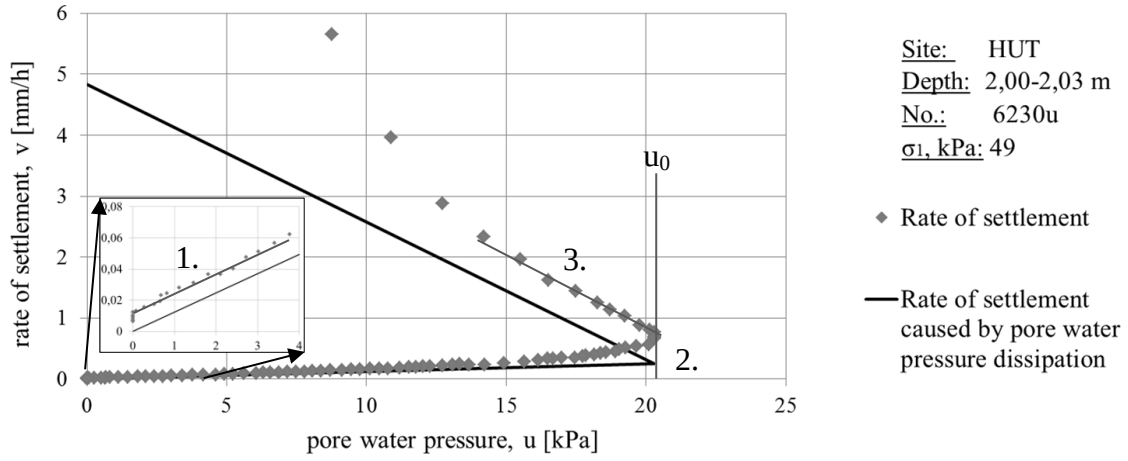

Figure 3. Pore water pressure versus rate of settlement of HUT-Clay in oedometer test. [8]

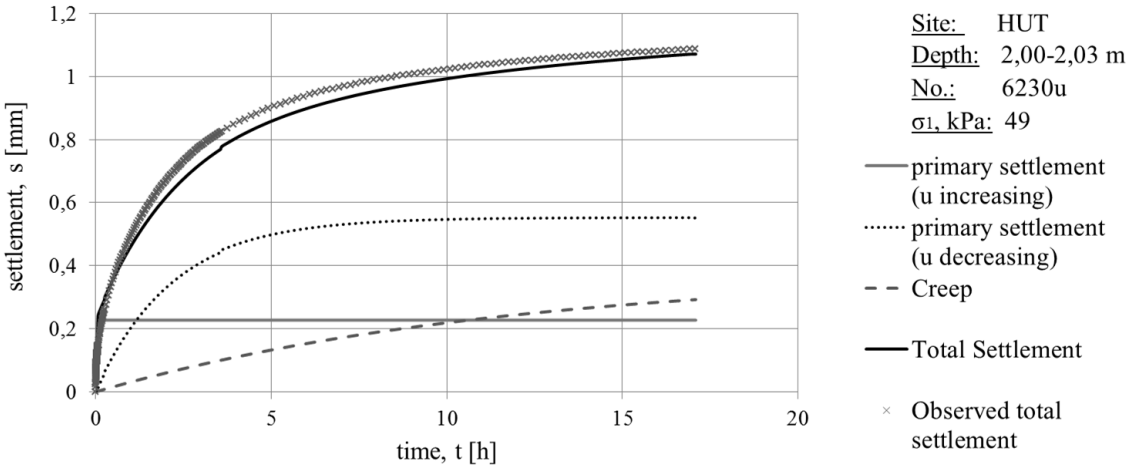

Figure 4. Observed and calculated settlements of HUT-Clay in pore pressure oedometer test.

Table 1. List of pore water pressure and settlement parameters. HUT-clay. Test number 6230u.

s_{inc} (mm)	s_{dec} (mm)	s_{cr} (mm)	u_0 (kPa)	λ_1 (1/h)	λ_2 (1/h)	λ_3 (1/h)	k_1 ((mm/h)/kPa)	k_2 ((mm/h)/kPa)
0,18	0,53	0,38	21	-90	-0,45	-0,086	0,217	0,02

Conclusion

The observations show that the time-settlement behaviour of HUT-Clay from Otaniemi is separated to primary and secondary phases from the very beginning of the test. This behaviour can be calculated with a combined settlement model Equation 6.

The development of the modelling is based on the measured pore water pressure of an undisturbed sample tested with pore water pressure oedometer. The model is derived from Darcy's law.

All the parameters are derived from one oedometer test results. In this article the parameters for one load increment are determined from 24 hours load increment. The duration of load increment shall be determined in each case based on measured pore water pressure, which is dependent on the permeability of clay and also the height of the sample.

In the future the development of the calculation model continues. This development will be based on the experiments with different soils. Test procedure shall also be developed.

References

[1] L. Barden, Consolidation of Clay with Non-Linear Viscosity. Geotechnique 15 (1965)4 p. 345-362

[2] J. Brinch-Hansen, A model law for simultaneous primary and secondary consolidation. Proc. 5. Int. Conf. Soil Mech. Found. Eng., Vol. 1. Paris 1961. p. 133-136.

[3] prEN ISO/TS 17892-5:en. Geotechnical investigation and testing. Laboratory testing of soil. Part 5: Incremental loading oedometer test, June 2014, DRAFT

[4] R. E. Gibson & K.Y Lo, A Theory of Consolidation for Soils Exhibiting Secondary Consolidation. NGI, Nr 41. Oslo 1961. p. 1-16.

[5] N. Janbu, Grunnlag i Geoteknikk. Trondheim 1970. 426p.

[6] R.L Kondner, Hyperbolic stress-strain response of cohesive soils. Journal of the soil mechanics and foundation division. ASCE, 89(1). p. 115-143.

[7] K.-H. Korhonen, Heikosti kantavan maapohjan konsolidoituminen.. Valtion Teknillinen Tutkimuskeskus, Rakennus- ja Yhdyskuntatekniikka, Julkaisu 19. Espoo 1977. 72p.

[8] S. Laaksonen, Saven muodonmuutosominasuuksien määritysmenetelmien ja –laitteistojen kehittäminnen. MSc. thesis. Aalto University. School of Engineering. 2014. 81p.

[9] D.W Taylor, Fundamentals of soil mechanics. New York 1948. 700p.

[10] K. V. Terzaghi, Erdbaumechanik auf Bodenphysikalischer Grundlage. Leipzig & Wien 1925. 399p.

Rakenteiden Mekaniikka
Vol. 48, Nro 1, 2015, s. 49-67
www.rmseura.tkk.fi/rmlehti

Rautatiekiskon sivukuluneisuuden vaikutusten mallintaminen

Tiia-Riikka Loponen, Pekka Salmenperä, Antti Nurmikolu ja Jari Mäkinen

Tiivistelmä. Tässä artikkelissa käsitellään rautatiekiskon sivukuluneisuuden vaikutusta rautatiekaluston kulkuun. Kiskon sivukuluminen kasvattaa raideleveyttä, jolloin myös raidevälys kasvaa. Raidevälys säätelee laippakosketuksen syntyä, ja raidevälyksen kasvaminen mahdollistaa pyöräkerralle, eli akselin yhdistämille pyörille, suuremman sivuttaissuuntaisen liikkeen. Artikkelissa tutkitaan kiskon sivukuluneisuuden vaikutusta kaluston kulkuominaisuuksiin ja rataan kohdistuviin rasituksiin erityisesti mallinnuksen ja simulointien avulla. Mallinnus toteutetaan yhdellä kalustotyypillä: Ex-matkustajavaunulla, joka on yksikerroksinen IC-vaunu. Sivukuluneisuuden vaikutusta kaluston kulkuun tarkastellaan eri kuluneisuusasteen omaavien kiskoprofiilien avulla. Kiskoprofiileiksi on valittu kulumaton kiskoprofiili, lievästi kulunut kiskoprofiili, voimakkaasti kulunut kiskoprofiili ja erittäin voimakkaasti kulunut kiskoprofiili. Mallinnus tehdään suoralla ja kaarteissa, ja kaarretarkastelussa huomioidaan erilaiset kaarresäteet. Vaihdealueet on rajattu tämän tarkastelun ulkopuolelle. Simulointien avulla saadaan selville, että kiskon sivukuluneisuudella ei ole merkittävää negatiivista vaikutusta kaluston kulkuun ja rataan kohdistuvaan rasitukseen.

Avainsanat: liikkuva kalusto, kiskon sivukuluminen, pyörä-kisko-kontakti, simulointi, kalustomallinnus, monikappaledynamiikka

Tiia-Riikka Loponen, Pekka Salmenperä, Antti Nurmikolu, Jari Mäkinen
Rakennustekniikan laitos
Tampereen teknillinen yliopisto
PL 600, 33101 Tampere
tiia.loponen@tut.fi

Proceedings of the XII Finnish Mechanics Days
R. Kouhia, J. Mäkinen, S. Pajunen and T. Saksala (Eds.)

On the direct solution of critical equilibrium states

Anders Eriksson[1], Reijo Kouhia[2], Jari Mäkinen[3]

[1]KTH Mechanics, Osquars backe 18, SE-10044 Stockholm, Sweden
[2]Dep. of Mechanical Engineering and Industrial Design, Tampere University of Technology
P.O. Box 589, FI-33101 Tampere, Finland
[3] Department of Civil Engineering, Tampere University of Technology
P.O. Box 589, FI-33101 Tampere, Finland
anderi@kth.se, reijo.kouhia@tut.fi, jari.m.makinen@tut.fi

Summary. Determination of a critical point is the primary problem in structural stability analysis. Mathematically it means solution of a non-linear eigenvalue problem together with the equilibrium equations. Several techniques exist to compute the critical equilibrium states and the corresponding modes. In this paper direct algorithms to solve the critical equilibrium state are discussed and a hybrid algorithm is proposed, which hopefully has enlarged domain of convergence.

Key words: computational stability analysis, finite element method, critical points, eigenvalue problem, non-linear systems

Introduction

Proper stability analysis of structures, or other systems in various physical disciplines, requires the computation of the critical point and its sensitivity analysis, which in structural stability analysis is called as imperfection sensitivity analysis. In practice, the stability analysis is most often performed with the following two-step procedure. First, the linearized stability eigenvalue problem is computed, where the linearization is performed with respect to the unloaded, undeformed state. Second, a full non-linear analysis is performed, with an imperfect structure through some continuation (path-following) algorithm. The imperfection is usually taken as a combination of the lowest critical modes. Success of such an approach is very much depending on the proper choice of the perturbation. In most commercial finite element (FE) codes, this is the only possible approach for stability analysis.

The non-linear stability eigenvalue problem consists of solving the equilibrium equations simultaneously with the criticality condition. The first appearance of this idea seems to be from 1973 by Keener and Keller [1]. In their approach the criticality condition is augmented as an eigenvalue equation. Similar approaches have been used also in Refs. [2, 3, 4, 5]. Another approach uses a scalar equation indicating the criticality [6, 7] or expansion to a higher order polynomial eigenvalue problem [8, 9]. In the context of parametric investigations of instability behavior, several methods for defining and handling criticality have been discussed in [10, 11].

Stability eigenvalue problem

The problem of finding a critical point along an equilibrium path can be stated as: find the critical values of $\boldsymbol{q}, \lambda$ and the corresponding eigenvector $\boldsymbol{\phi}$ such that

$$\begin{cases} \boldsymbol{f}(\boldsymbol{q},\lambda) &= \boldsymbol{0} \\ \boldsymbol{f}'(\boldsymbol{q},\lambda)\boldsymbol{\phi} &= \boldsymbol{0} \end{cases} \tag{1}$$

where $\boldsymbol{f}$ is a vector defining the equilibrium equations and $\boldsymbol{f}'$ denotes the Gateaux derivative (Jacobian matrix) with respect to the state variables $\boldsymbol{q}$, i.e. the stiffness matrix. At the critical point the equilibrium equations $(1)_1$ has to be satisfied together with the criticality condition $(1)_2$, which states the zero stiffness in the direction of the critical eigenmode $\boldsymbol{\phi}$. Such a system is considered in Refs. [3, 12, 5].

The equilibrium equation $(1)_1$ constitutes the balance of internal forces $\boldsymbol{r}$ and external loads $\boldsymbol{p}$, which is usually parameterized by a single variable λ, the load parameter, defining the intensity of the load vector:

$$\boldsymbol{f}(\boldsymbol{q}, \lambda) \equiv \boldsymbol{r}(\boldsymbol{q}) - \lambda \boldsymbol{p}_{\mathrm{r}}(\boldsymbol{q}). \tag{2}$$

If the loads do not depend on the deformations, like in dead-weight loading, the reference load vector $\boldsymbol{p}_{\mathrm{r}}$ is independent of the displacement field $\boldsymbol{q}$. A more general case, with $\boldsymbol{p} = \boldsymbol{p}(\lambda, \boldsymbol{q})$ is an obvious expansion of the above expressions. A discussion on different loading control variables, and their effects on stability conclusions is given in [13].

The system (1) consists of $2n+1$ unknowns, the displacement vector $\boldsymbol{q}$, the eigenmode $\boldsymbol{\phi}$ and the load parameter value λ at the critical state. Since the eigenvector $\boldsymbol{\phi}$ is defined uniquely up to a constant, a normalizing condition can be added to the system (1). In addition, some stabilizing conditions might also be needed. In general, the full augmented system can be written as

$$\boldsymbol{g}(\boldsymbol{q}, \boldsymbol{\phi}, \boldsymbol{\lambda}) = \begin{cases} \hat{\boldsymbol{f}}(\boldsymbol{q}, \boldsymbol{\lambda}) \equiv \boldsymbol{f}(\boldsymbol{q}, \lambda) + \boldsymbol{f}_0(\boldsymbol{q}, \boldsymbol{\lambda}) = \boldsymbol{0} \\ \boldsymbol{h}(\boldsymbol{q}, \boldsymbol{\phi}, \boldsymbol{\lambda}) \equiv \boldsymbol{f}'(\boldsymbol{q}, \boldsymbol{\lambda})\boldsymbol{\phi} + \boldsymbol{h}_0(\boldsymbol{\phi}, \boldsymbol{\lambda}) = \boldsymbol{0} \\ \boldsymbol{c}(\boldsymbol{q}, \boldsymbol{\phi}, \boldsymbol{\lambda}) = \boldsymbol{0}, \end{cases} \tag{3}$$

where $\boldsymbol{\lambda}$ is a vector of control and auxiliary parameters and $\boldsymbol{c}$ is a vector of constraint or stabilizing equations: the dimension of these vectors is $p \geq 1$. The additional functions $\boldsymbol{f}_0$ and $\boldsymbol{h}_0$ are chosen such that $\boldsymbol{f}_0 = \boldsymbol{h}_0 = \boldsymbol{0}$ at the solution point. A Newton step for the approximate solution of (2) can thereby be written as

$$\begin{bmatrix} \boldsymbol{K}_f & \boldsymbol{0} & \boldsymbol{P} \\ \boldsymbol{Z} & \boldsymbol{K}_h & \boldsymbol{N} \\ \boldsymbol{C}_q & \boldsymbol{C}_\phi & \boldsymbol{C}_\lambda \end{bmatrix} \begin{Bmatrix} \delta\boldsymbol{q} \\ \delta\boldsymbol{\phi} \\ \delta\boldsymbol{\lambda} \end{Bmatrix} = - \begin{Bmatrix} \hat{\boldsymbol{f}} \\ \boldsymbol{h} \\ \boldsymbol{c} \end{Bmatrix}, \tag{4}$$

where

$$\boldsymbol{Z} = \left[\boldsymbol{f}'\boldsymbol{\phi}\right]', \quad \boldsymbol{C}_q = \boldsymbol{c}' = \frac{\partial \boldsymbol{c}}{\partial \boldsymbol{q}}, \quad \boldsymbol{C}_\phi = \frac{\partial \boldsymbol{c}}{\partial \boldsymbol{\phi}}, \quad \boldsymbol{C}_\lambda = \frac{\partial \boldsymbol{c}}{\partial \boldsymbol{\lambda}}. \tag{5}$$

$$\boldsymbol{K}_f = \boldsymbol{K} + \boldsymbol{f}_0', \quad \boldsymbol{K}_h = \boldsymbol{K} + \frac{\partial \boldsymbol{h}_0}{\partial \boldsymbol{\phi}}, \quad \boldsymbol{P} = \frac{\partial \boldsymbol{f}}{\partial \boldsymbol{\lambda}} \quad \text{and} \quad \boldsymbol{N} = \frac{\partial \boldsymbol{h}}{\partial \boldsymbol{\lambda}} \tag{6}$$

Computation of the matrix $\boldsymbol{Z}$ requires second order derivatives of the residual. In the literature, these are usually obtained by numerical differentiation. For the geometrically exact Reissner's beam model, an analytical derivation of the $\boldsymbol{Z}$-matrix is given in [14].

For the eigenvector normalization different constraint equations can be used, [5, 14, 15].

The system (4) is usually solved by a block elimination scheme together with direct linear solvers. Utilization of iterative linear solvers has been discussed in [15].

The key problem in solving the extended system (3) with the Newton's method starting from the unloaded undeformed equilibrium state is that the Newton's method is only locally convergent. Therefore the domain of attraction can be small and it is likely that the initial state does not belong to it.

Hybrid algorithm

A simple way to circumvent the problem related to the small convergence domain is to use a continuation algorithm to get closer to the domain of attraction of the extended system. A single "continuation step algorithm" for critical point computation could be constructed in the following way.

1. Compute a crude approximation to the lowest critical load and the corresponding eigenvector.

2. Use that point as a starting point of the orthogonal trajectory method [16, 17, 18] to get a nearby point on the equilibrium path.

3. From the computed equilibrium state, use the extended system (3) for computing the critical point.

It is believed that such an algorithm is more robust, but not computationally more demanding than the pure direct procedure.

References

[1] Keener, J. & Keller, H. Perturbed bifurcation theory. *Archive for Rational Mechanics and Analysis* **50**, 159–175 (1973).

[2] Keener, J. Perturbed bifurcation theory at multiple eigenvalues. *Archive for Rational Mechanics and Analysis* **56**, 348–366 (1974).

[3] Seydel, R. Numerical computation of branch points in nonlinear equations. *Numerische Mathematik* **33**, 339–352 (1979).

[4] Wriggers, P., Wagner, W. & Miehe, C. A quadratically convergent procedure for the calculation of stability points in finite element analysis. *Computer Methods in Applied Mechanics and Engineering* **70**, 329–347 (1988).

[5] Wriggers, P. & Simo, J. A general procedure for the direct computation of turning and bifurcation problems. *International Journal for Numerical Methods in Engineering* **30**, 155–176 (1990).

[6] Abbot, J. An efficient algorithm for the determination of certain bifurcation points. *Journal Computational and Applied Mathematics* **4**, 19–27 (1987).

[7] Battini, J.-M., Pacoste, C. & Eriksson, A. Improved minimal augmentation procedure for the direct computation of critical points. *Computer Methods in Applied Mechanics and Engineering* **192**, 2169–2185 (2003).

[8] Huitfeldt, J. & Ruhe, A. A new algorithm for numerical path following applied to an example from hydrodynamic flow. *SIAM Journal on Scientific and Statistical Computing* **11**, 1181–1192 (1990).

[9] Huitfeldt, J. Nonlinear eigenvalue problems - prediction of bifurcation points and branch switching. Tech. Rep. 17, Department of Computer Sciences, Chalmers University of technology (1991).

[10] Eriksson, A. Fold lines for sensitivity analyses in structural instability. *Computer Methods in Applied Mechanics and Engineering* **114**, 77–101 (1994).

[11] Eriksson, A. Structural instability analyses based on generalised path-following. *Computer Methods in Applied Mechanics and Engineering* **156**, 45–74 (1998).

[12] Werner, B. & Spence, A. The computation of symmetry-breaking bifurcation points. *SIAM Journal on Numerical Analysis* **21**, 388–399 (1984).

[13] Eriksson, A. & Nordmark, A. Instability of hyper-elastic balloon-shaped space membranes under pressure loads. *Computer Methods in Applied Mechanics and Engineering* **237–240**, 118–129 (2012).

[14] Mäkinen, J., Kouhia, R., Fedoroff, A. & Marjamäki, H. Direct computation of critical equilibrium states for spatial beams and frames. *International Journal for Numerical Methods in Engineering* **89**, 135–153 (2012).

[15] Kouhia, R., Tůma, M., Mäkinen, J., Fedoroff, A. & Marjamäki, H. Implementation of a direct procedure for critical point computations using preconditioned iterative solvers. *Computers and Structures* **108–109**, 110–117 (2012).

[16] Haselgrove, C. The solution of non-linear equations and of differential equations with two point boundary conditions. *Computer Journal* **4**, 225–259 (1961).

[17] Fried, I. Orthogonal trajectory accession to the equilibrium curve. *Computer Methods in Applied Mechanics and Engineering* **47**, 283–297 (1984).

[18] Allgower, E. & Georg, K. *Numerical Continuation Methods - An Introduction* (Springer-Verlag, 1990).

Suomen XII mekaniikkapäivien esitelmät
R. Kouhia, J. Mäkinen, S. Pajunen ja T. Saksala (toim.)

Menetelmä lentokoneen ohjausservon sisäisen vuodon havaitsemiseksi

Jouko Laitinen

Tampereen teknillinen yliopisto, Kone- ja tuotantotekniikan laitos
PL 589, 33101 Tampere, jouko.laitinen@tut.fi

Tiivistelmä. Lentokoneen ohjausservon sisäistä vuotoa, eli esimerkiksi hydraulisylinterin vuotoa männän tiivisteiden ohi, on vaikea havaita. Vuodosta seuraa servon nopeuden ja voiman menetystä, jolla varsinkin lentokoneessa voi olla vakavat seuraukset. Tällaisesta vuodosta ei ole näkyvissä ulkoisia merkkejä, eikä vuodosta johtuvaa voiman ja nopeuden menetystä normaalikäytössä välttämättä huomaa. Kuitenkin suurta voimaa tai nopeutta vaativissa lentoliikkeissä ohjausservon riittämätön suorituskyky voi aiheuttaa tilanteen, jossa ohjainpinnan aerodynaamiset voimat eivät riitä pitämään lentokonetta ohjaajan hallinnassa.

Tässä julkaisussa esitellään menetelmä lentokoneen korkeusvakaajan servon sisäisen vuodon havaitsemiseksi. Menetelmä perustuu lentokoneen järjestelmien tuottaman prosessidatan tulkintaan ja analysointiin. Datasta voidaan laskea ohjainpinnan saranamomentti, eli ohjainpinnan liikuttamiseen vaadittavan vääntömomentin suuruus kulloisessakin korkeudessa, nopeudessa ja lentotilassa. Laskettua saranamomenttia verrataan ohjauspinnan asennon virheeseen, eli ohjauspinnan komentosignaalin ja saavutetun asennon väliseen eroon. Mikäli virhe on huomattava tilanteissa joissa ohjauspinnan vääntömomentin tarve ei ole suuri, on syytä epäillä ohjauspinnan servon sisäistä vuotoa.

Avainsanat: ohjausservo, hydraulisylinteri, sisäinen vuoto

Johdanto

Hornet F/A-18 lentokoneen korkeusvakaimen (stabilaattorin) komentosignaali (Pitchcommand) ja kummankin korkeusvakaimen asento (Left stab position, Right stab position) rekisteröidään 20Hz:n taajuudella, eli 20 kertaa sekunnissa. Korkeusvakaimien servojen asentotietoja tutkittiin laskemalla kuinka paljon korkeusvakaimien asennot poikkeavat komentosignaalin arvosta. Kun korkeusvakaimen servojen laskettuja komento-asentoeroarvoja (korkeusvakaimen komennon ja saavutetun asennon ero) verrattiin, huomattiin että niissä on suuria eroja lennon eri vaiheissa.

Ihannetapauksessa komento-asentoeron arvo on nolla, eli vakaimen asento vastaa sille annettua käskyä. Käytännössä komento-asentoeroarvo poikkeaa enemmän tai vähemmän nollasta ja on joko negatiivinen tai positiivinen. Arvon poikkeaminen nollasta tarkoittaa virhettä, eli sitä ettei korkeusvakain pysty täysin toteuttamaan ohjauskäskyä.

Aluksi arveltiin suurten poikkeamien tarkoittavan sitä, että stabilaattorin servo on viallinen. Kun useilta lennoilta kerättyä dataa vertailtiin, huomattiin, että lennoilla, joilla oli käytetty paljon suuria ja nopeita ohjainpoikkeutuksia (esim. taitolento), myös komento-asentoeroarvot olivat suuret.

Koska komento-asentoerosta ei voida suoraan päätellä ohjainservon kuntoa, asiaa tutkittiin vertaamalla komento-asentoeroa ohjaimen kääntämiseen tarvittavan voiman suuruuteen. Ohjaimen kääntämiseen tarvittava voima, tarkemmin sanottuna saranamomentti, voidaan laskea ohjainpinnan mitoista ja lentokoneen nopeudesta, korkeudesta ja ohjainpinnan saranamomenttikertoimesta. Saranamomenttikerrointa ei voitu suoraan laskea, vaan se täytyi selvittää tuulitunnelikokeiden perusteella piirretyistä kuvaajista. Saranamomenttikertoimeen vaikuttaa lentokoneen kohtauskulma, ohjainpinnan poikkeutuskulma ja sivuluisu, joka oletettiin tässä tarkastelussa nollaksi.

Ajatuksena tässä tarkastelussa on se, että kun tarvitaan suurta voimaa ohjainpinnan kääntämiseen, voidaan hyväksyä suurempi virhe. Jos taas voiman tarve on pieni, mutta virhe on suuri, kyseessä saattaa olla ohjainservon tai hydraulijärjestelmän vika.

Tarkastelun kohteeksi otettiin lento, jolla koneen järjestelmä antoi varoituksen oikean korkeusvakaajan servon viasta, jolloin voitiin olla varmoja, että kyseessä oli varmasti servon toimintahäiriö.

Kyseinen lento oli koelento, jonka aikana koneen oikea moottori sammutettiin ja käynnistettiin uudelleen. Ohjainservon toimintaa tarkasteltiin kahdessa kohtaa lentoa: ensimmäiseksi kohdaksi valittiin kohta huomattavasti ennen häiriötä ja jossa molemmat moottorit ovat käynnissä, toiseksi kohta juuri ennen toimintahäiriötä ja jossa oikea moottori oli sammutettu. Syy, miksi toinen tarkastelukohta oli juuri ennen häiriötä, eikä sen aikana, johtui siitä, että haluttiin nähdä, voidaanko lähestyvä häiriö havaita ennakolta.

Saranamomentin laskeminen

Ohjainpinnan saranamomentti laskemiseksi tarvitaan kuvassa 1 esitettyjä arvoja ohjainpinnasta. Saranamomentti laskettiin yhtälöillä (1) ja (2). Laskentaa voitiin yksinkertaistaa korvaamalla yhtälössä olevat ohjainpinnan fyysiset mitat kertoimella yksi, koska tarkastelun kohteena on saranamomentin suhteellinen arvo (ohjainpinnan koko ei muutu, kun saranamomentin arvoja lasketaan lennon eri pisteissä) [1].

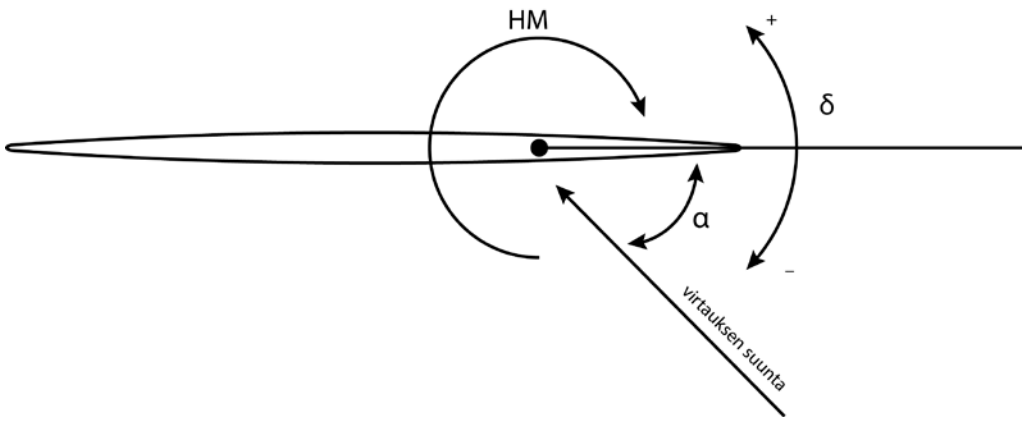

Kuva 1. Ohjainpinnan kulmat α = kohtauskulma virtaukseen nähden, δ = ohjainpinnan poikkeutuskulma. HM = saranamomentin suunta ohjainpinnan sarana-akselin suhteen.

$$HM = 0.5\rho V^2 C_M S_e \overline{c_e} \quad (1)$$

Yhtälössä (1) termin $0.5\rho V^2$ kertoimet ρ = ilman tiheys ja V = nopeus saadaan koneen lentoarvojen rekisteröinnistä. Kertoimet S_e = ohjainpinnan pinta-ala ja c_e = ohjainpinnan jänne asetetaan ykkösiksi, koska tarkastellaan keskenään samanlaisten ohjainpintojen saranamomentteja.

$$C_M = C_{h_0} + C_{h_\alpha}\alpha_h + C_{h_{\delta_e}}\delta_e \quad (2)$$

Yhtälössä (1) esiintyvä saranamomenttikerroin C_M lasketaan yhtälöstä (2). Ohjainpinnan ominaisuuksia eri lentotiloissa kuvaavia kertoimia C_{h_0}, C_{h_α} ja $C_{h_{\delta_e}}$ ei ole saatavilla, vaan saranamomenttikertoimen C_M arvo selvitettiin koelentojen perusteella tehdystä kuvaajasta, kuva 2 [2] [3].

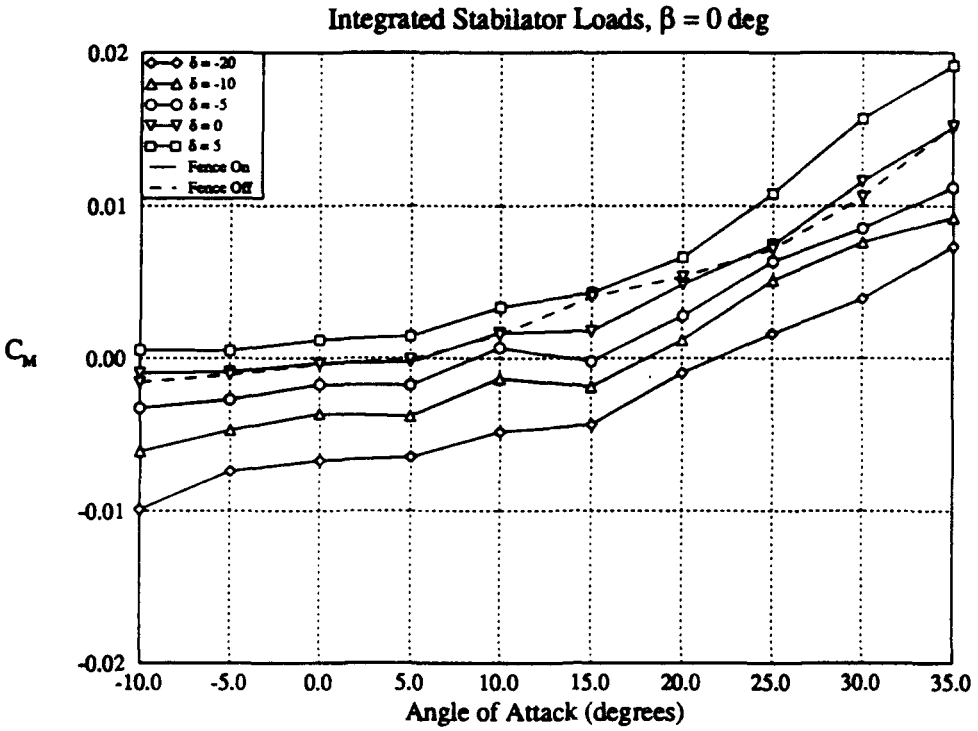

Kuva 2. Saranamomenttikertoimen arvot tuulitunnelikokeiden perusteella laaditussa kuvaajassa. Pystyakselilla saranamomenttikertoimen arvo, vaaka-akselilla koneen kohtauskulma. Eri käyrät kuvaavat saramomenttikertoimen muutosta ohjainpinnan eri poikkeutuskulmilla [3].

Komento-asentoeron vertaaminen ohjaimen saranamomenttiin

Komento-asentoeron eli halutun ja saavutetun ohjaimen asennon eli virheen suuruutta verrattiin kulloisessakin lentotilassa tarvittavan saranamomentin suuruuteen. Vertailu tehtiin jakamalla virheen suuruus saranamomentin lasketulla arvolla ja normeeraamalla tulos. Jotta tuloksista voitiin piirtää frekvenssikuvaaja, laskennan tulokset jaettiin 50 luokkaan.

Kuvassa 3 ja 5 on kuvattu vasemman ja kuvassa 4 ja 6 oikean korkeusvakaajan servon komentoasentoeron ja saranamomentin suhteen jakaumaa. Kun suhde on pieni (jakauma painottuu lähelle nollaa), tarkoittaa se, että vaikka tarvittava saranamomentti on suuri, virhe on silti pieni. Päinvastaisessa tapauksessa (suhde on suuri) virhe on suuri, vaikka tarvittava saranamomentti on pieni. Kuvissa vaaka-akselilla virheen ja saranamomentin suhde $\Delta\delta / HM$ kasvaa oikealle, pystyakselilta voidaan lukea kunkin luokan on suhteellinen osuus koko joukosta.

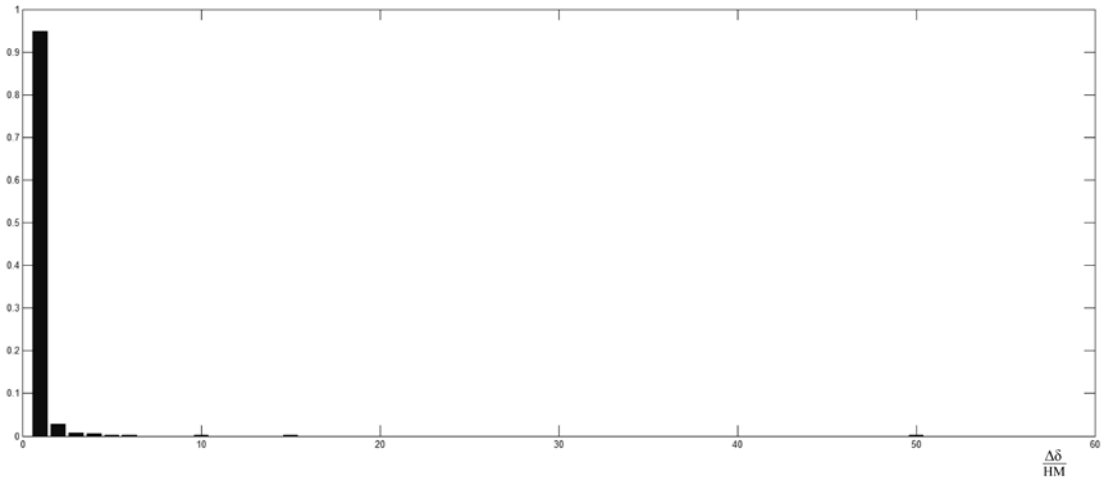

Kuva 3. Vasemman korkeusvakaajan servon komentoasentoeron ja saranamomentin suhteen jakauma ennen häiriötä. Pääosa arvoista, noin 95 %, on lähellä nollaa, vaikka osa on nollasta poikkeavia.

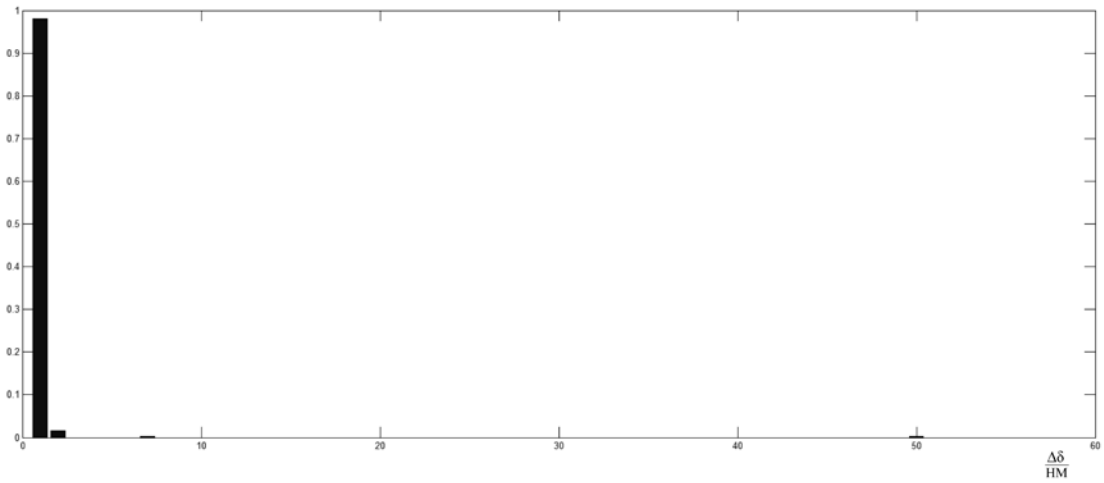

Kuva 4. Oikean korkeusvakaajan servon komentoasentoeron ja saranamomentin suhteen jakauma ennen häiriötä. Miltei kaikki arvot ovat lähellä nollaa.

Kuvien 3 ja 4 mukaan kummakin, oikean ja vasemman, ohjausservon toiminta oli normaalia kun molemmat moottorit olivat käynnissä. Vaikka koneella tehtiin voimakasta liikehdintää, molempien servojen virheen ja tarvittavan saranamomentin suhde oli pieni, lähellä nollaa. Tämä tarkoittaa, että vaikka ohjausservo eikä ohjainpinta saavuttanut haluttua asentoa, se voidaan hyväksyä, jos lentotila on sellainen, että ohjainpinnan liikuttaminen vaatii suurta voimaa. Tällaisessa tilanteessa ohjausservon suorituskyky tulee vastaan vaikka servo ei olisikaan viallinen.

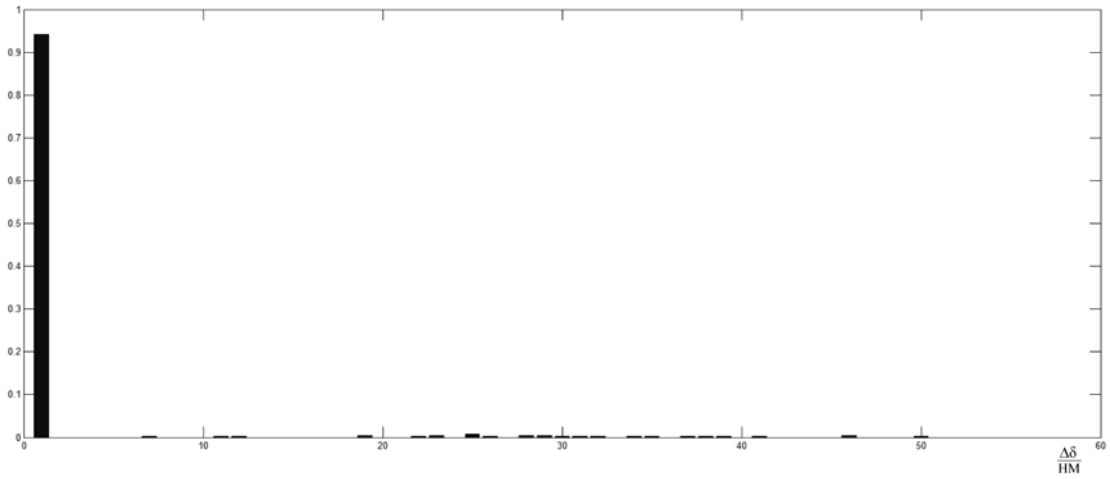

Kuva 5. Vasemman korkeusvakaajan servon komentoasentoeron ja saranamomentin suhteen jakauma juuri ennen vikailmoitusta. Pääosa arvoista, noin 94 %, on lähellä nollaa, vaikka osa on nollasta poikkeavia.

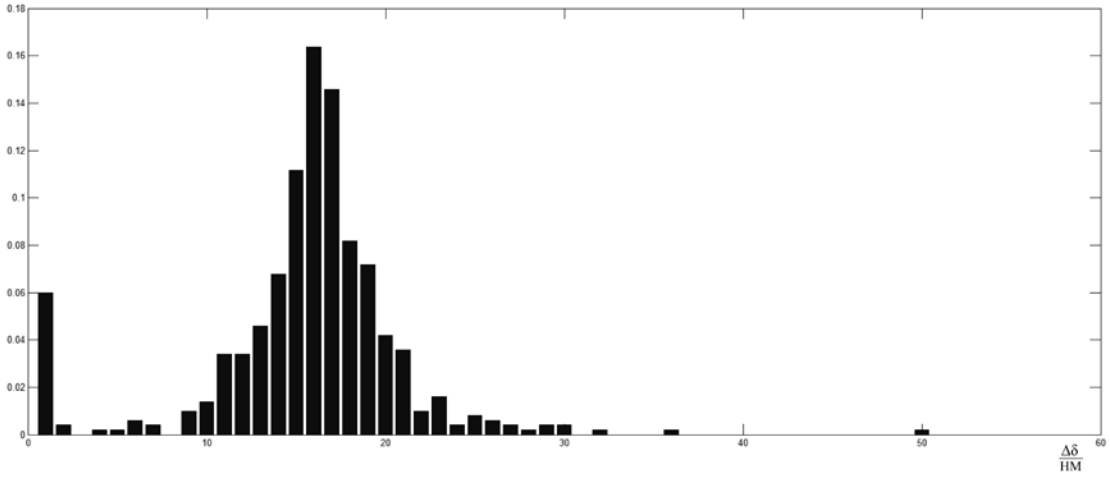

Kuva 6. Oikean korkeusvakaajan servon komentoasentoeron ja saranamomentin suhteen jakauma juuri ennen vikailmoitusta. Jakauma on suurelta osalta oikealla, mikä tarkoittaa sitä, että servon suorituskyky on puutteellinen.

Kuvista 5 ja 6 voidaan nähdä, että oikean ohjausservon toiminnassa on vikaa. Kuvassa komentoasentoeron ja saranamomentin suhteen jakauma on selvästi oikealle painottunut, mikä tarkoittaa sitä, että vaikka tarvittava saranamomentti on pieni, ohjainpinnan asentovirhe on suuri. Tällaisessa tilanteessa ohjausservon suorituskyky ei riitä välttämättä normaalissakaan lentotilassa.

Yhteenveto

Tarkastelun tuloksista voidaan päätellä, että korkeusperäsinservon vikaantuminen on mahdollista havaita tallennetusta peräsinservo- ja lentoarvodatasta peräsimen voimantarvetta tutkimalla. Tämän mahdollistaa koneen aerodynamiikasta saatava tutkimustieto ja lentoarvodataa analysoimalla saatavat lentoarvotiedot sekä ohjainten komento- ja asentotiedot. Nyt tehdyssä tarkastelussa havaintojen syy voi olla myös hydraulijärjestelmässä, koska toinen moottori oli sammutettu ja hydraulipaineen tuotto näin ollen mahdollisesti pienempää kuin molempien moottoreiden toimiessa. Oli syy sitten hydraulijärjestelmässä tai peräsinservossa, tulokset osoittavat, että peräsinservon toimintakyky oli kyseisessä tapauksessa rajoittunut. Jos peräsinservon vikatapauksissa hydraulijärjestelmän vika voidaan sulkea pois dataa analysoimalla, vika voidaan kohdistaa varmemmin peräsinservon toimintaan.

Viitteet

[1] M. Mulder. Aerodynamic Hinge Moment Coefficient Estimation Using Automatic Fly-By-Wire Control Inputs. AIAA Modelling and Simulation Technologies Conference, 10 - 13 August 2009, Chicago, Illinois

[2] Candida D. An Evaluation Technique for an F/A-18 Aircraft Loads Model Using F/A- 18 Systems Research Aircraft Flight Data. National Aeronautics and Space Administration,Washington DC, 2000.

[3] L.D: MacLaren, Low-speed pressure distribution measurements over the aft-fuselage, fins and stabilators of a 1/9 scale F/A-18 wind tunnel model. Research Report 9, Aeronautical Research Laboratory, Melbourne, Victoria, Australia, 1993. http://www.dtic.mil/dtic/tr/fulltext/u2/a274870.pdf

Rakenteiden Mekaniikka (Journal of Structural Mechanics)
Vol. 48, No 1, 2015, pp. 68-82
www.rmseura.tkk.fi/rmlehti/

Heat release caused by the smouldering combustion of the binder of rockwool

Perttu Leppänen[1], Manuela Neri and Jari Mäkinen

Summary. Recently, numerous fires have started in Finland around roof penetrations of metal chimneys. One reason for the fires is the smouldering combustion of the binder of rockwool used at the roof penetrations of metal chimneys. The charring of the binder produces heat which can increase the temperature in the penetration to over 100 °C. Tests which were performed on rockwool demonstrate the heat release.

Key words: smouldering combustion, heat release

Perttu Leppänen, Jari Mäkinen
Department of Civil Engineering
Tampere University of Technology
P.O. Box 600, 33101 Tampere
perttu.leppanen@tut.fi, jari.m.makinen@tut.fi

Manuela Neri
Department of Industrial and Mechanical Engineering
Universita Degli Studi di Brescia
Via Branze 38, 25123 Brescia Italy
m.neri001@unibs.it

Proceedings of the XII Finnish Mechanics Days
R. Kouhia, J. Mäkinen, S. Pajunen and T. Saksala (Eds.)

Orthotropic constitutive model for steel fibre reinforced concrete: linear-elastic state and bases for the failure

Marika Eik[1],[2], Heiko Herrmann[2], and Jari Puttonen[1]

[(1)]Aalto University, Department of Civil and Structural Engineering, Rakentajanaukio 4 A, 02150 Espoo, Otaniemi, Finland, marika.eik@aalto.fi
[(2)]Centre for Nonlinear Studies, Institute of Cybernetics at Tallinn University of Technology, Akadeemia tee 21, 12618 Tallinn, Estonia

Summary. Steel fibre reinforced concrete (SFRC) is a highly promising building material offering durable structures alongside with the minimisation of steel consumption and construction time. Though, its reliable application in civil engineering requires a deeper study due to complex material properties defining its failure and related to volumetric dispersion of fibres, and a bond between the fibres and concrete. The different fibre alignments in concrete matrix lead to anisotropic behaviour, which specifies the tensile strength and the crack intensity of the composite. SFRC crack initiation and development, and failure depend on the strength of the bond and interaction between the steel fibres and concrete. The present paper focuses on the modelling of SFRC linear-elastic state considering and evaluating the orientation distribution of fibres. In addition, the bases of SFRC failure are introduced.

Key words: steel fibre reinforced concrete, fibre orientation, constitutive equation, bond strength

Introduction

A strong interest in fibre reinforced cement-based composites (FRCC) currently appearing in many countries can be explained by the increasing concern of construction industry on obtaining effective solutions by more durable concrete structures and structural parts. The reduction of steel consumption as, for example, to satisfy the serviceability limit state (SLS) with reinforced concrete structures involving crack width control, as well as the minimisation of time and labour required for placing the reinforcement bars become extremely significant. A possible solution would be the use of steel fibre reinforced concrete (SFRC), which is a highly promising building material. The use of steel fibres may allow to replace the secondary or minimum reinforcement by steel fibres thus reducing the steel consumption. In addition, the use of steel fibres leads to a significant reduction of construction time by avoiding reinforcement placing phase, as well as to less dependence on skilled labour. Although, compared to the traditional reinforcing solutions, the reliable use of SFRC in civil engineering requires a deeper study as the production of the composite may be reasonable to move from the construction site to the concrete factory.

SFRC is made by mixing of a fresh concrete mass with various combinations of steel fibres: either with only one type of fibres or with a mix of different types of fibres (different lengths and geometry). The present research is concentrated on the study of concrete reinforced with hooked-end steel fibres, figure 1. The steel fibres reinforce concrete matrix increasing its tensile strength, crack resistance, and fracture toughness. One of the most important properties of SFRC is the ability to control crack opening, which is due to volumetric dispersion of fibres and bond between the steel fibres and concrete. However, the volumetric dispersion of fibres leads to anisotropic material properties, which depend on the orientation distribution of fibres in concrete matrix. Thereby, the modelling and the quantification of the spatial orientation

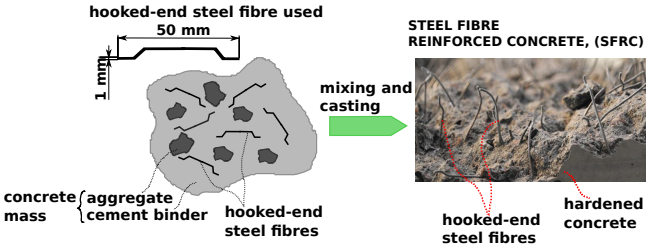

Figure 1. Concrete reinforced with hooked-end steel fibres. The dimensions of hooked-end steel fibres used.

distribution of fibres is a starting point for the development of material model for SFRC. At the same time, one of the key aspects in crack initiation and development, and, further, in failure state of SFRC is the strength of the bond and interaction between the steel fibres and concrete. In this paper we are focusing on modelling of SFRC linear-elastic behaviour considering and evaluating the orientation distribution of fibres.

Assumptions for linear-elastic material model of SFRC

The concrete matrix surrounding steel fibres has a brittle failure in tension. A typical volume percentage (concentration) of fibres, for example, in elevated floor slabs is $1\% - 2\%$ per cubic meter of concrete. Increasing the amount of fibres may, in some cases, not be economically reasonable since the amount of ordinary reinforcement varies between $1.25\% - 1.5\%$. A high concentration of fibres usually causes clumping since only up to 2% of steel fibres can be incorporated into fresh concrete mass using conventional practice of concreting with modern super-plasticizers [1]. The fibres can provide an effective reinforcement if their contents is in between $2\% - 6\%$ [1]. In general, if the volume percentage of fibres stays below 2%, the functionality of fibres is limited in controlling the opening of cracks, and the failure is brittle and may appear by the propagation of a single crack. The described brittle failure mode was also noticed in the tested full-size floor slabs used in the study [2, 3]. Based on the bending test, the load-deformation curves exhibited brittle failure of four out of six slabs. The behaviour of four slabs was linear in the first loading stage, i.e. the formation of the first crack, and dropped sharply after the achievement of the peak load indicating a drastic opening of the first crack. Thereby, the linear-elastic state was selected to the first step in modelling of SFRC material properties.

The tensile strength as well as the cracking intensity of SFRC depends on the alignment of fibres. The problem to solve within the study was to measure the fibre orientation from the test-samples extracted from the full-size floor slabs. The results of measurements showed that the fibre orientation distributions vary in three dimensions [2, 3, 4]. This fact supported the assumption about the anisotropic behaviour of SFRC and indicated the necessity of a theory capable to model the spatial material properties of SFRC.

Orthotropic liner-elastic model for SFRC

To define the orientation of a fibre in space, the spherical polar coordinate system was employed: the inclination θ and in-plane ϕ angles. It was assumed that the effective elasticity of SFRC should include two terms: concrete matrix contributing isotropically and short steel fibres influencing anisotropicly. The meso-scale for the representative volume element (RVE) of SFRC was chosen based on the measured fibre orientation distributions in the tested floor-slabs. The measurements revealed that the orientation of fibres varies in three-dimensions and has a local character within the structural element [3].

The modelling started by assuming a hyperelastic material, where the first differentiation of the strain-energy density function W produces the 2^{nd} Piola-Kirchhoff stress tensor, S_{ij}, and the

second differential gives the 4^{th} order elasticity tensor, C_{ijkl} [5]. The advantage of the described approach is the symmetry of the 2^{nd} Piola-Kirchhoff stress tensor, and a minor and major symmetries of the 4^{th} order elasticity tensor. The anisotropic influence of fibres is modelled by the orthotropic model with three principal material directions. The structural tensors $\{\mathbf{L}^i\}_{i=1,2,3}$ are employed for specifying the orthotropic material symmetry [6].

The strain-energy density function for the orthotropic material can be represented as a function of its principal traces–isotropic tensor function, where the arguments include the structural tensors [6, 7, 8, 9]. The strain-energy density function for an isotropic case can be obtained from the orthotropic one since the direction dependent structural tensors are vanishing. Considering only the second-order terms in the isotropic tensor function for the orthotropic material symmetry, the orthotropic elastic material with three symmetry axes can be defined as the combination of mixed traces, such as:

$$\hat{W}^{(2)}_{E,\mathrm{ortho}}(\mathbf{E},\mathbf{L}^i) = \frac{1}{2}\sum_{i,j=1}^{3}\gamma^{ij}\,\mathrm{tr}(\mathbf{E}\mathbf{L}^i)\,\mathrm{tr}(\mathbf{E}\mathbf{L}^j) + \sum_{i,j\neq i}^{3} G^{ij}\,\mathrm{tr}(\mathbf{E}\mathbf{L}^i\mathbf{E}\mathbf{L}^j)\ , \tag{1}$$

where $\mathbf{E}$ is the *Lagrangian* strain tensor. The latter model presents the orthotropic St. Venant-Kirchhoff material [7]. The further differentiation leads to the orthotropic 2^{nd} Piola-Kirchhoff stress tensor [5]:

$$\mathbf{S}_{E,\mathrm{ortho}} = \frac{\partial}{\partial\mathbf{E}}\hat{W}^{(2)}_{E,\mathrm{ortho}}(\mathbf{E},\mathbf{L}^i) = \sum_{i,j=1}^{3}\gamma^{ij}\,\mathrm{tr}(\mathbf{E}\mathbf{L}^j)\mathbf{L}^i + 2\sum_{i,j\neq i}^{3} G^{ij}\mathbf{L}^i\mathbf{E}\mathbf{L}^j\ , \tag{2}$$

which is linear with respect to $\mathbf{E}$. The eqs. (1, 2) include Lamé constants γ^{ij}, G^{ij}, which are given in terms of Young's modulus Y and Poisson's ratio ν. They are direction dependent referring to material symmetry axes and planes, respectively. As it was noted, for an isotropic material the structural tensors in eqs. (1, 2) are vanishing and the elasticity constants become equal for all directions, i.e. $\gamma = \gamma^{ij},\ G = G^{ij}$.

The structural tensors and the direction dependent elasticity constants in eqs. (1, 2) for the case of SFRC are created utilising the orientation state of fibres, which is evaluated by the orientation tensors, $O_{\mu_1\ldots\mu_l}$, and the orientation distribution function (ODF), $f(\mathbf{n})$, where $\mathbf{n}$ is a unit vector representing the orientation of a rod-like particle in space [10, 11].

The symmetric orientation tensors are calculated as the l-order outer products of the vector $\mathbf{n}$ with itself, $n_{\mu_1}\otimes\ldots\otimes n_{\mu_l}$, and then integrating the result with the ODF. The symmetric irreducible part–traceless, $\overline{n_{\mu_1}\otimes\ldots\otimes n_{\mu_l}}$, of the l-order orientation tensor called as the l-order alignment tensor, $A_{\mu_1\ldots\mu_l}$, can reconstruct the ODF [10, 11]. The ODF is given on a unit sphere, S^2, and belong to square-integrable functions and thus can be decomposed into the series of main spherical harmonics, where the alignment tensors are acting as the expansion coefficients and the symmetric irreducible tensors, $\overline{n_{\mu_1}\otimes\ldots\otimes n_{\mu_l}}$, calculated considering all possible directions of a rod-like particle on a unite sphere, i.e. $\mathbf{n}\in(\theta,\phi), \theta\in[0°,180°], \phi\in[0°,360°]$ and forming the complete orthonormal basis, act as main spherical functions [10, 12, 13, 14], such as:

$$f(\mathbf{n}) \;=\; A_0\cdot 1 + \sum_{l=1}^{\mathbb{N}}(2l-1)!!A_{\mu_1\ldots\mu_l}\ \overline{n_{\mu_1}\otimes\ldots\otimes n_{\mu_l}}\ , \tag{3}$$

where A_0 represents the zero harmonic and $A_{\mu_1\ldots\mu_l}$ are the harmonics (alignment tensors) approximating the deviation of the original function $f(\mathbf{n})$ from its mean value, and they read as:

$$A_0 \;=\; \frac{1}{4\pi}\oint_{S^2} f(\mathbf{n})\cdot 1\cdot \mathrm{d}^2 n\ , \tag{4}$$

$$A_{\mu_1\ldots\mu_l} \;=\; \frac{1}{4\pi}\frac{(2l+1)}{l!}\oint_{S^2} f(\mathbf{n})\cdot\ \overline{n_{\mu_1}\otimes\ldots\otimes n_{\mu_l}}\ \cdot\mathrm{d}^2 n\ , \tag{5}$$

where $l!$ is the factorial and $(2l-1)!!$ denotes the double factorial. It is worth to note, that if the expansion coefficients (ATs) in a complete orthonormal basis are known, then the original function $f(\mathbf{n})$ can also be considered as known [14].

In the study the 2^{nd} order alignment tensor is used to define the material symmetry axes of one meso-volume element of SFRC. The structural tensors $\{\mathbf{L}^i\}_{i=1,2,3}$ are calculated employing the normalised eigenvectors $\mathbf{d}^1, \mathbf{d}^2, \mathbf{d}^3$ of the 2^{nd} order alignment tensor thus representing the symmetry axes of SFRC and modelling the orthotropic influence of fibres. The orientation distribution function $f(\mathbf{n})$ is utilised to estimate the contribution of fibres in the directions of the eigenvectors thus defining the orthotropic meso-elasticity constants of the composite, i.e. γ^{ij}, G^{ij}. The latter is implemented by transforming the elasticity of an individual fibre in its local coordinates and defined by the Young's modules in its longer axis into the symmetry axes defined by the $\mathbf{d}^1, \mathbf{d}^2, \mathbf{d}^3$ and then weighting with the ODF of fibres.

Hereinafter, it is assumed that $\frac{\partial}{\partial x} \approx \frac{\partial}{\partial X}$, which allows to use the linearised hyperelasticity for the case of SFRC meaning that $\mathbf{E} \approx \boldsymbol{\varepsilon}$. In addition, a complete bond between the steel fibres and concrete is expected. The orthotropic linear-elastic material model for one meso-volume element of SFRC is developed by the superposition of the isotropic and orthotropic St. Venant-Kirchhoff models, as follows:

$$\mathbf{S}^{(c)} = \underbrace{V^{(m)}\left(\gamma \mathbf{I}\,\mathrm{tr}(\boldsymbol{\varepsilon}^{(c)}) + 2G\boldsymbol{\varepsilon}^{(c)}\right)}_{\text{concrete, isotropic}} + \underbrace{V^{(f)}\left(\sum_{i,j=1}^{3}\gamma^{ij}\,\mathrm{tr}(\boldsymbol{\varepsilon}^{(c)}\mathbf{L}^j)\mathbf{L}^i + 2\sum_{i,j\neq i}^{3} G^{ij}\mathbf{L}^i\boldsymbol{\varepsilon}^{(c)}\mathbf{L}^j\right)}_{\text{fibres, orthotropic}} . \quad (6)$$

The differentiation of eq. (6) gives the orientation-weighted orthotropic meso-elasticity of the composite, which reads as:

$$^{<4>}\mathbf{C}^{(c)} = \underbrace{V^{(m)}\left(\gamma \mathbf{I}\otimes\mathbf{I} + 2G\,{}^{<4>}\mathbf{I}^S\right)}_{\text{concrete, isotropic}} + \underbrace{V^{(f)}\left(\sum_{i,j}^{3}\gamma^{ij}\mathbf{L}^i\otimes\mathbf{L}^j + \sum_{i,j\neq i}^{3} 2G^{ij}(\mathbf{L}^i\tilde{\otimes}\mathbf{L}^j)^S\right)}_{\text{fibres, orthotropic}} . \quad (7)$$

During the study the 2^{nd} order alignment tensors were calculated based on fibre orientation distribution measurements from test samples [2, 4]. This enabled to reconstruct the ODFs of fibres and calculate the respective orientation-weighted orthotropic meso-elasticities [15, 16].

Discussion: bases for the failure

The developed orthotropic linear-elastic model for SFRC can be extended to cover the failure state, which would mean the involvement of a failure function. The advantage of such a material model is that it will enable to simulate and analyse the load-bearing capacity of SFRC members. The failure function should include bond strength characteristics, such as: adhesion and mechanical anchorage (in case of deformed fibres). Whereas the mechanical anchorage is important in post-cracking behaviour, the adhesion is essential for gradual debonding of fibres and, as a consequence, the crack initiation and development of cracking. The adhesion is relevant for the micro-cracking state, when the steel fibres have their best performance delaying the micro-crack opening [17]. The adhesion layer–interfacial transition zone (ITZ)–is forming between the fibre, cement paste and aggregate [18, 19], figure 2. The quality of the adhesion is influenced by the microstructure of the ITZ, which is rather inhomogeneous and considerably differs from the bulk concrete matrix. In the formation of the ITZ the hydration of cement (clinker, clay) and aggregate mixture have major roles [1]. The mechanical and physical properties of the ITZ involving its porosity, thickness, extent, continuity or discontinuity, and activation when stress is applied are the subjects still requiring further research [1, 19, 20]. The outcome of the study devoted to the quantification of the mechanical and physical properties of ITZ will lead to the formulation of a damage function, and thus it will be developed an improved orthotropic material model for

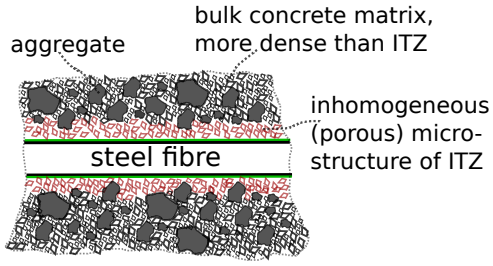

Figure 2. Representation of adhesion layer–interfacial transition zone (ITZ)–around a fibre.

SFRC.

Conclusion

The orthotropic linear-elastic material model developed for SFRC can be successfully tested employing numerical computation methods. The material model has a continuous formulation, which makes it attractive for implementing to the finite element programs. The results of computer simulations with different fibre orientation distributions will improve understanding the effect of fibre orientation under different stress conditions.

The further option in material modelling is its extension to cover the failure regime, which will enable the evaluation of load-bearing capacity of SFRC members. SFRC failure mechanism is largely determined by the physical and mechanical properties of the interaction between the steel fibres and concrete matrix. The physio-chemical adhesion plays an important role in crack width control while the mechanical anchoring is relevant for post-cracking behaviour. The quantitative and qualitative evaluation of the bond strength characteristics in SFRC will strengthen the reliability of SFRC in load-bearing structures.

References

[1] A. Bentur and S. Mindess. *Fibre Reinforced Cementitious Composites*. Taylor & Francis, 2nd edition, 2007.

[2] M. Eik, K. Lõhmus, M. Tigasson, M. Listak, J. Puttonen, and H. Herrmann. DC-conductivity testing combined with photometry for measuring fibre orientations in SFRC. *Journal of Materials Science*, 48(10):3745–3759, 2013. DOI: 10.1007/s10853-013-7174-3.

[3] M. Eik. *Orientation of short steel fibres in concrete: measuring and modelling*. PhD thesis, Aalto University School of Engineering, 2014. URL `http://urn.fi/URN:ISBN:978-952-60-5592-3`.

[4] J.-P. Suuronen, A. Kallonen, M. Eik, J. Puttonen, R. Serimaa, and H. Herrmann. Analysis of short fibres orientation in steel fibre-reinforced concrete (sfrc) by x-ray tomography. *Journal of Materials Science*, 48(3):1358–1367, 2013. DOI: 10.1007/s10853-012-6882-4.

[5] C. Truesdell and W. Noll. *The Non-Linear Field Theories of Mechanics, Encyclopedia of Physics*. Springer-Verlag, 1965.

[6] M. Itskov. *Tensor Algebra and Tensor Analysis for Engineers With Applications to Continuum Mechanics*. Springer, 2009.

[7] M. Itskov and N. Aksel. A class of orthotropic and transversely isotropic hyperelastic constitutive models based on a polyconvex strain energy function. *International Journal of Solids and Structures*, 41(14):3833 – 3848, 2004. DOI: 10.1016/j.ijsolstr.2004.02.027.

[8] A.J.M. Spencer and R.S. Rivlin. Isotropic integrity bases for vectors and second-order tensors. *Archive for Rational Mechanics and Analysis*, 9(1):45–63, 1962. DOI: http://dx.doi.org/10.1007/BF00253332.

[9] P. P. Teodorescu and N. A. Nicorovici. *Applications of the theory of groups in mechanics and physics*, volume 140 of *Fundamental Theories of Physics*. Springer Netherlands, 2004. DOI: http://dx.doi.org/10.1007/978-1-4020-2047-6.

[10] W. Muschik, C. Papenfuss, and H. Ehrentraut. *Concepts of Continuum Thermodynamics*. Kielce University of Technology, Technische Universität Berlin, 1996.

[11] S. G. Advani and C. L. Tucker III. The use of tensors to describe and predict fiber orientation in short fiber composites. 31(8):751–784, 1987. DOI: 10.1122/1.549945.

[12] H. Ehrentraut and W. Muschik. On Symmetric irreducible tensors in d-dimensions. *ARI - An International Journal for Physical and Engineering Sciences*, 51:149–159, 1998. DOI: 10.1007/s007770050048.

[13] H. Herrmann and M. Eik. Some comments on the theory of short fibre reinforced material. *Proceedings of the Estonian Academy of Sciences*, 60(3):179–183, 2011. DOI: 10.3176/proc.2011.3.06.

[14] J.M Neiman and L.S Sugaipova. *(Spherical functions and their application)*. (Moscow State University of Geodesy and Cartography), 2005. URL `http://vm.miigaik.ru/kollektiv_kafedr/preppages/neiman_um/`.

[15] H. Herrmann, M. Eik, V. Berg, and J. Puttonen. Phenomenological and numerical modelling of short fibre reinforced cementitious composites. *Meccanica*, 49(8):1985–2000, 2014. DOI: 10.1007/s11012-014-0001-3.

[16] M. Eik, J. Puttonen, and H. Herrmann. An orthotropic material model for steel fibre reinforced concrete based on the orientation distribution of fibres. *Composite Structures*, 121(0):324 – 336, 2015. DOI: http://dx.doi.org/10.1016/j.compstruct.2014.11.018.

[17] Jong-Pil Won, Byung-Tak Hong, Su-Jin Lee, and Se Jin Choi. Bonding properties of amorphous micro-steel fibre-reinforced cementitious composites. *Composite Structures*, 102 (0):101 – 109, 2013. DOI: http://dx.doi.org/10.1016/j.compstruct.2013.02.015.

[18] I. Löfgren. *Fibre-reinforced Concrete for Industrial Construction–a fracture mechanics approach to material testing and structural analysis*. PhD thesis, Chalmers University of Technology, 2005.

[19] S. F. Lee. Sample preparation technique on interfacial transition zone of steel fiber reinforced mortar. *Concrete Research Letters*, 4(4):696–715, 2014.

[20] T. N. S. Htut. *Fracture processes in steel fibre reinforced concrete*. PhD thesis, Civil & Environmental Engineering, Faculty of Engineering, UNSW, 2010. URL `http://handle.unsw.edu.au/1959.4/45521`.

Suomen XII mekaniikkapäivien esitelmät
R. Kouhia, J. Mäkinen, S. Pajunen ja T. Saksala (toim.)

Wood compression model for radial compression of earlywood and latewood

Carolina Moilanen[1], Tomas Björkqvist[2] and Pentti Saarenrinne[1]

[(1)]Tampere University of Technology Department of Mechanical Engineering and Industrial Systems, P.O. box 589, 33101 Tampere, Finland, carolina.moilanen@tut.fi, pentti.saarenrinne@tut.fi
[(2)]Tampere University of Technology Department of Automation Science and Engineering, P.O. box 692, 33101 Tampere, Finland, tomas.bjorkqvist@tut.fi

Abstract. The goal of the current research is to develop a novel wood material model for optimization of the mechanical pulping process. The novel material model will be based on the earlywood and latewood compression models presented in this paper. Spruce samples were subjected to dynamic and quasi-static radial compression at 20-135°C. An image-based full-field strain measurement method was employed. The in-plane strain components were calculated with 4-node quadrilateral elements and numerical integration. Earlywood was modelled by a linear model defined in three parts. Hooke's law was used for latewood. High strain rate compression models for earlywood and latewood are presented.

Keywords: wood compression model, dynamic, quasi-static, earlywood, latewood

Introduction

Wood compression behaviour should be taken into account when designing the mechanical pulping process and machinery. The most common raw material for mechanical pulping in the Nordic countries is Norway spruce (*Pieca abies*). A characteristic feature of Norway spruce is the distinct differences in mechanical properties inside the annual ring. During compression, earlywood lumen can be completely collapsed while there is no visible change to the latewood fibres. A compression model that takes the contribution of earlywood and latewood into account is therefore needed. Wood is an anisotropic material. If the sample is small and cut far enough from the centre of the three, the properties can be considered orthotropic. The planes of symmetry are radial, tangential and longitudinal (or axial). The stiffness and strength are greatest in the longitudinal direction of the tree [1].

No wood model suitable for mechanical pulping simulations was found. Most wood models are limited to elastic compression or do not take earlywood and latewood contributions into account. Elastic earlywood and latewood compression is taken into account in the models presented in [2] and [3]. The model presented in [4] is not limited to elastic compression but does not take earlywood and latewood contributions into account.

Previous research in the field has shown that strain-rate, temperature and moisture content have major impact on the wood compression behaviour [5, 6]. This means, that in order to use the results in mechanical pulping, the measurements need to be conducted on wet wood at high strain rate and high temperature. High strain-rate measurements of wood compression have been conducted previously but none that analyses earlywood and latewood properties. Previous research on earlywood and latewood has been conducted at quasi-static and medium strain rate conditions and mainly room temperature. One of the most important findings was that earlywood is anisotropic while latewood can be considered isotropic [7]. The strain amplitudes in earlywood were more than twice as large as in latewood [8, 9]. The location of maximum strain is located about one fourth into the annual ring [8, 10]. The Young's modulus measured of Norway spruce with moisture content 7 % is for earlywood 744 MPa in the radial direction and 210 MPa in the tangential direction. The Young's modulus for latewood is 1230 MPa in the radial direction and 1250 MPa in the tangential direction [11]. There is no difference in softening temperature for earlywood and latewood [12].

In this paper, the conducted measurements are presented first and then the simple compression model. Only the results for the high strain rate measurements are presented in the results section. The overall results and future work are summarized in the discussion section.

Materials and methods

Extensive high strain rate and quasi-static radial compression measurements have been carried out on native and mechanically pre-fatigued Norway spruce samples. The high strain rate measurements were conducted in the encapsulated split-Hopkinson pressure bar (ESHD) with the possibility to control ambient temperature and pressure presented by Holmgren [3]. The average strain rate for the ESHD measurements was in the range 700-1200 s^{-1}. The quasi-static measurements were conducted in an Instron E1000 tensile testing machine (TTM) that can apply forces up to 1000 N. The TTM measurements were carried out both at room temperature and at elevated temperatures. The TTM measurements were conducted both in air (20°C) and submerged in water (20°C and 80°C). The complete measurement program is presented in Table 1.

Table 1: Number of samples measured at different temperatures and with different loading devices.

Temperature (°C)	Native	Pre-fatigued	Loading
20	4 + 8	4 + 8	ESHD + TTM
80	4	4	TTM
100	4	4	ESHD
135	4	4	ESHD

The Norway spruce samples in the high strain rate measurements were 11.2 - 11.9 mm in the longitudinal direction, 11.3 - 12.1 mm in the tangential direction and 5.4 - 6.5 mm in the radial direction. Two different sample sizes were used in the quasi static measurements: cubes with the side 5.0 ± 0.8 mm and cubes with the side 12.0 ± 0.8 mm. The moisture content of the samples was approximately 30 %, which corresponds to fibre saturation where the cell walls are moist but there is no free water in the lumen. Part of the samples was pre-fatigued by 20 000 strain pulses at 500 Hz in a device described in [13]. This pre-fatigue treatment can be considered to be intensive.

The wood samples were imaged during the compression trials. High speed photography was required for the high strain rate measurements. An image based full field strain measurement was used, where the in-plane strain components were calculated with 4-node quadrilateral elements and numerical integration. Average earlywood and latewood contributions were identified from the full field data. The image based analysis method is described in [14].

Three regions can be identified in the stress-strain curve for wood: an elastic region, a plateau region and a densification region. The high strain rate measurements showed the elastic and plateau regions well. The initial densification region is seen in all quasi-static measurements but only in the room temperature measurements at high strain rate. The earlywood stress-strain curve showed the same characteristics as average wood while latewood showed only the elastic region.

Compression model

Previous wood compression models that take the contributions of earlywood and latewood into account are limited to elastic compression. Our goal is to develop a wood compression model for large plastic deformations with earlywood and latewood contributions taken into account. This work has been started by defining separate models for earlywood and latewood compression. More work is needed to combine these to a wood compression model.

Latewood was assumed to follow Hooke's law, whereas earlywood was modelled by a simple linear model defined in three parts, giving the 5 parameter model in Equation 1

$$\sigma_{EW} = \begin{cases} E_1\varepsilon_{EW} & \varepsilon_{EW} \le \varepsilon_1 \\ E_1\varepsilon_1 + E_2(\varepsilon_{EW} - \varepsilon_1) & \varepsilon_1 < \varepsilon_{EW} \le \varepsilon_2 \\ E_1\varepsilon_1 + E_2(\varepsilon_2 - \varepsilon_1) + E_3(\varepsilon_{EW} - \varepsilon_2) & \varepsilon_{EW} > \varepsilon_2 \end{cases}, \quad (1)$$

where E_1, E_2, E_3, ε_1 and ε_2 are material parameters and ε_{EW} is strain in earlywood. E_1 approximately corresponds to the Young's modulus and ε_1 the yield limit. The densification limit ε_2 was expected to be of the order 0.5 as seen in [15, 16]. The model was reduced to a two part model for the measurements that did not reach the densification region. The material parameters were optimized by the least squares method in Matlab for all four parallel experiments at once.

Results

Only high strain rate measurements have been analysed so far. The results measured at 20°C and 135°C are presented in [17]. The measured stress-strain curves are compared to the model at different temperatures for earlywood in Figure 1 and latewood in Figure 2.

The densification region was barely reached in the measurements at room temperature in Figure 1a and not at all at 100°C and 135°C in Figures 1b and 1c. At elevated temperatures, the maximum stress is reduced due to wood softening. The optimized material parameters and sum of squared differences (SSD) are presented in Table 2.

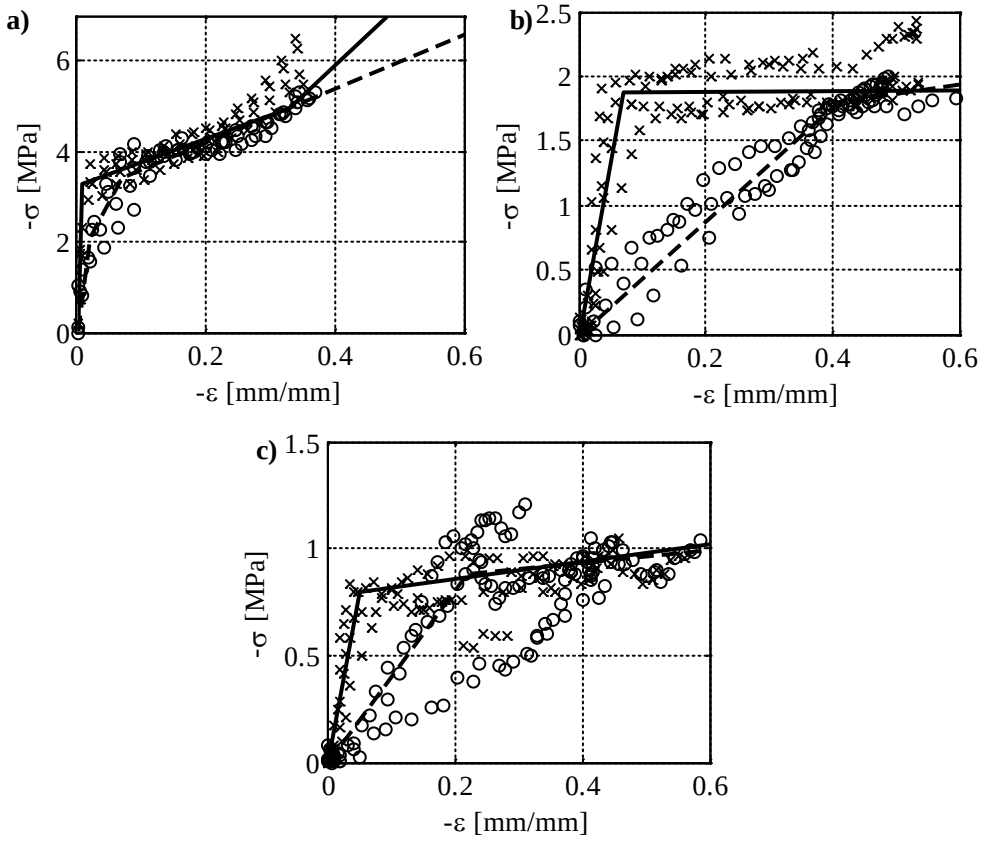

Figure 1. Measured earlywood stress-strain curves (x for native and o for pre-fatigued wood) compared to model (solid line for native and dashed line for pre-fatigued wood) at a) 20°C, b) 100°C and c) 135°C, note that the scale varies on the σ-axes.

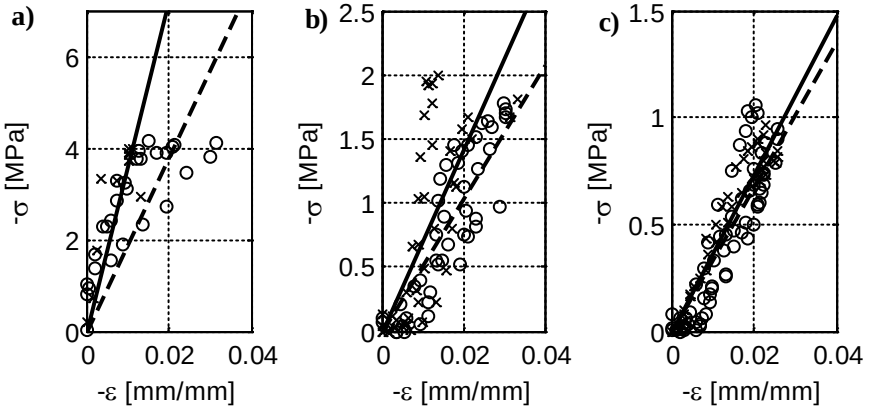

Figure 2. Measured latewood stress-strain curves (x for native and o for pre-fatigued wood) compared to model (solid line for native and dashed line for pre-fatigued wood) at a) 20°C, b) 100°C and c) 135°C, note that the scale varies on the σ-axes and that the maximum strain is smaller than in Figure 1.

Table 2. High strain rate material parameters for all temperatures, where Nat is native wood and Fat pre-fatigued wood.

	ε_1 mm/mm	ε_2 mm/mm	E_1 MPa	E_2 MPa	E_3 MPa	E_{LW} MPa	SSD_{EW} MPa	SSD_{LW} MPa
Nat 20°C	-0,009	-0,33	367	5	13	355	6.0	18.6
Fat 20°C	-0,021	-0,07	100	27	6	190	7.4	37.5
Nat 100°C	-0,07	-	26	0,03	-	72	15.1	10.9
Fat 100°C	-0,41	-	4	0,7	-	52	2.1	3.8
Nat 135°C	-0,05	-	16	0,4	-	37	1.4	0.5
Fat 135°C	-0,22	-	4	0,3	-	34	3.9	1.6

Discussion

Simple compression models for earlywood and latewood have been fitted to high strain rate measurement data at various temperatures. The models agreed well with the measurement data, indicating the applicability of the chosen simple models for earlywood and latewood compression. The fit of the model for native wood at 20°C is reduced significantly when the parameters are rounded. Figure 1 is plotted with rounded values, four decimals for native wood at 20°C and according to Table 2 for the other measurements.

The slope of the plateau region was approximately the same for pre-fatigued and native earlywood; E_3 for fatigued wood was almost the same as E_2 for native wood at room temperature. There was not enough data for reliable results in the earlywood densification region. The major effect of the pre-fatigue treatment for earlywood was in the elastic region, E_1 was reduced 73-85 % by the pre-fatigue treatment. The stress strain curve for pre-fatigued earlywood at 20°C had four regions: an elastic region, a region where the pre-fatigued fibres collapse, a plateau region and a densification region. The plateau region and the densification region were combined in the optimized results.

Increase of temperature reduced the E_1 stiffness of earlywood more than pre-fatigue treatment. The increase of temperature from 20°C to 100°C reduced E_1 by 93 % for native earlywood and 96% for pre-fatigued earlywood. The increase from 100°C to 135°C reduced the stiffness E_1 for native earlywood further by 38 %. The increase from 100°C to 135°C did not affect E_1 for pre-fatigued earlywood.

The pre-fatigue treatment reduced the latewood stiffness E_{LW} by 48 % at 20°C, 28 % at 100°C and only 8 % at 135°C. The increase of temperature affected also latewood stiffness more than the pre-fatigue treatment. The increase of temperature from 20°C to 100°C reduced the stiffness by 78 % for native latewood and 73 % for pre-fatigued latewood. The increase from 100°C to 135°C reduced the stiffness by 49 % for native latewood and 35 % for pre-fatigued latewood.

The presented work is a good base to build the wood compression model on. Future work will focus on combining high strain rate and quasi-static measurements to make dynamic compression models and to combine the earlywood and latewood models.

Acknowledgements

The Academy of Finland is acknowledged for the funding under Decision number 140462. The authors are also grateful for the cooperation with Birgitta Engberg, Staffan Nyström and Max Lundström at Mid Sweden University for the high strain rate measurements, Professor Mikko

Alava and his researchers Juha Koivisto, Amandine Miksic and Markus Ovaska at Aalto University for the quasi-static measurements and with Lauri Salminen for the pre-fatigue treatment of the wood samples.

References

[1] L. J. Gibson, M. F. Ashby. *Cellular solids structure and properties.* Cambridge University Press, Cambridge, 1997.

[2] C. S. Moden. A two-phase annual ring model of transverse anisotropy in softwoods. *Composites Sci Technol*, 68(14): 3020-3026, 2008.

[3] S. Koponen, T. Toratti, P. Kanerva. Modelling elastic and shrinkage properties of wood based on cell structure. *Wood Sci Technol*, 25(1): 25-32, 1991. doi: 10.1007/BF00195554

[4] C. Adalian, P. Morlier. A model for the behaviour of wood under dynamic multiaxial compression. *Compos Sci Technol*, 61(3): 403-408, 2001. doi: 10.1016/S0266-3538(00)00109-3

[5] S. Widehammar. Stress-strain relationships for spruce wood: Influence of strain rate, moisture content and loading direction. *Exp Mech*, 44(1): 44-48, 2004.

[6] A. Uhmeier, L. Salmén. Influence of strain rate and temperature on the radial compression behavior of wet spruce. *J Eng Mater Technol Trans ASME*, 118(3): 289-294, 1996.

[7] J. B. Boutelje. The Relationship of Structure to Transverse Anisotropy in Wood with Reference to Shrinkage and Elasticity. *Holzforschung*, 16(2): 33-46, 1962.

[8] L. O. Jernkvist, F. Thuvander. Experimental determination of stiffness variation across growth rings in Picea abies. *Holzforschung*, 55(3): 309-317, 2001. doi: 10.1515/HF.2001.051

[9] M. Eder, K. Jungnikl, I. Burgert. A close-up view of wood structure and properties across a growth ring of Norway spruce (Picea abies [L] Karst.). *Trees Struct Funct*, 23(1): 79-84, 2009. doi: 10.1007/s00468-008-0256-1

[10] B. I. Hassel, C. S. Modén, L. A. Berglund. Functional gradient effects explain the low transverse shear modulus in spruce - Full-field strain data and a micromechanics model. *Compos Sci Technol*, 69(14): 2491-2496, 2009. doi: 10.1016/j.compscitech.2009.06.025

[11] F. Farruggia, P. Perré. Microscopic tensile tests in the transverse plane of earlywood and latewood parts of spruce. *Wood Sci Technol*, 34(2): 65-82, 2000.

[12] M. Wennerblom, A-M. Olsson, L. Salmén. Softening properties of early wood and latewood of spruce. *Nord Pulp Pap Res J*, 11(4): 279-280, 1996.

[13] A. Salmi, L. Salminen, E. Hæggström. Quantifying fatigue generated in high strain rate cyclic loading of Norway spruce. *J Appl Phys*, 106(10) doi:10.1063/1.3257176

[14] C. S. Moilanen, P. Saarenrinne, B. A. Engberg, T. Björkqvist. Image based stress and strain measurement of wood in the split-Hopkinson pressure bar. *Meas Sci Tech*, submitted, 2015.

[15] K. N. Law, B. V. Kokta, C. Mao. Compression properties of wood and fibre failures. *J Pulp Pap Sci*, 32(4): 224-230, 2006.

[16] L. Salmén, J. F. Dumail, A. Uhmeier. Compression behaviour of wood in relation to mechanical pulping. *Proceedings of the International Mechanical Pulping Conferrence*,June 9-13, 1997.

[17] C. S. Moilanen, T. Björkqvist, B. A. Engberg, L. I. Salminen, P. Saarenrinne. High strain rate radial compression of Norway spruce earlywood and latewood. *Cellulose*, to be submitted, 2015.

Proceedings of the XII Finnish Mechanics Days
R. Kouhia, J. Mäkinen, S. Pajunen and T. Saksala (Eds.)

Modeling asymmetric cyclic plastic hysteresis of nodular cast iron materials

Joona Vaara and Juho Könnö

Wärtsilä Finland Oy, Järvikatu 2-4 65101 Vaasa
joona.vaara@wartsila.com, juho.konno@wartsila.com

Summary. A set of constitutive equations described by Seifert et al. for modeling cast iron behavior are tested on Wärtsilä's experimental data of nodular cast iron. The model is based on phenomenological classical unified viscoplastic framework. Emphasis of the paper is on modeling the observed stress-strain hysteresis asymmetry. The Gurson-Needleman-Tvergaard porous plastic model combined with Mori-Tanaka model for spherical voids looks initially promising for this task. The model had to be extended with a porosity-independent asymmetry mechanism, asymmetric backstress, to match the experimental data.

Key words: nodular cast iron, asymmetric hysteresis

Introduction

The present paper concerns cyclic plastic experimental observations and constitutive equations capable of describing nodular cast iron materials. The temperature behavior of nodular cast iron is quite similar from grade to grade, but over the measurement range from 23 to 450 °C the behavior is quite complex. At 250 °C a significant inverse strain rate sensitivity is observed. In [1], the classical unified viscoplastic framework was extended to cover dynamic and static strain aging phenomena. The stress-strain hysteresis was observed to be slightly asymmetric as well.

Thermomechanical behavior of nodular cast iron was studied in [2] where the classical unified viscoplastic framework was adopted with Gurson-Tveergaard-Needleman (GTN) porous plastic yield criterion and Mori-Tanaka model for spherical voids in which effective elastic parameters are affected by the porosity.

The main objective of this paper is the modeling of the asymmetric hysteresis in the classical unified viscoplastic framework.

The main experimental observations

The typical observed asymmetry in nodular cast iron stress-strain hysteresis is shown in Figure 1 with the numerical elastic modulus E and hardening modulus K at the strain reversal points. The material is EN-GJS-500-7 at 450 °C. Trying to fit a symmetric model causes the model to overshoot at the compressive side and undershoot at the tension side. The numeric values for elastic and hardening moduli are gathered in Table 1.

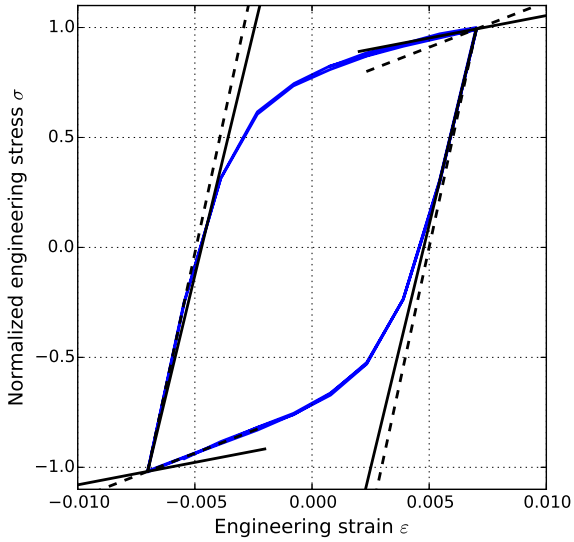

Figure 1: Typical nodular cast iron asymmetry. Solid line and dashed line denote the quantities at tension and compression stress reversal points, respectively.

Table 1: Elastic and hardening moduli at tension and compression stress reversals.

E [MPa]		K [MPa]	
compression	tension	compression	tension
165000	148000	13800	6800

Constitutive framework

Following [2], the stress evolution for isothermal, small strain, additive strain decomposition and non-rotating framework can be written as

$$\dot{\boldsymbol{\sigma}} = \mathcal{C}^* : \left(\dot{\boldsymbol{\epsilon}}^{el}\right) + \frac{\partial \mathcal{C}^*}{\partial f}\dot{f} : \mathcal{C}^{*-1} : \boldsymbol{\sigma}, \tag{1}$$

in which $\mathcal{C}^*$ is effective elasticity tensor and f is porosity caused by the graphite inclusions. The effective elasticity tensor is defined as

$$\mathcal{C}^* = K^* \boldsymbol{I} \otimes \boldsymbol{I} + 2G^* \left(\mathcal{I} - \frac{1}{3}\boldsymbol{I} \otimes \boldsymbol{I}\right) \tag{2}$$

where the effective bulk and shear modulus are

$$K^* = K\left(1 - \frac{f}{1 - \frac{3K}{3K+4G}(1-f)}\right) \quad \text{and} \quad G^* = G\left(1 - \frac{f}{1 - \frac{6(K+2G)}{5(3K+4G)}(1-f)}\right). \tag{3}$$

The Gurson-Tvergaard-Needleman (GTN) yield criterion has succesfully been used for modeling monotonic ductile failure of porous materials. The derivation is based on a spherical void in a spherical ideally plastic matrix volume element

$$F = \left(\frac{J_2}{\sigma_M}\right)^2 + 2q_1 f \cosh\left(q_2 \frac{I_1}{2\sigma_M}\right) - \left(1 + q_3 f^2\right), \tag{4}$$

J_2 is the second invariant of the deviatoric stress tensor, I_1 is the first invariant of the stress tensor, σ_M is the current flow stress of the matrix material and q_1, q_2 and q_3 are parameters. Tvergaard proposed values $q_1 = 1.5$, $q_2 = 1.0$ and $q_3 = q_1^2$ which shall be used here as well.

Evolution of the porosity is split in two parts: growth of existing voids and nucleation of voids. The growth is defined as

$$\dot{f}_{gr} = (1 - f)\,\mathrm{tr}\,(\dot{\boldsymbol{\epsilon}}^{vp})\,. \tag{5}$$

Two models have been proposed for the nucleation. Both of the models are based on normal distribution function and the first one uses inelastic strains as the evolution driving force

$$\dot{f}_{nucl} = \frac{f_N}{s_N\sqrt{2\pi}} \exp\left(-\frac{1}{2}\left(\frac{\mathrm{tr}\,(\boldsymbol{\epsilon}^{vp}) - \epsilon_N}{s_N}\right)^2\right) \mathrm{tr}\,(\dot{\boldsymbol{\epsilon}}^{vp}) \tag{6}$$

which was designed to describe void nucleation at larger strains. Lower strain nucleation model is controlled by the hydrostatic stress σ_m

$$\dot{f}_{nucl} = \frac{f_N}{s_N\sqrt{2\pi}} \exp\left(-\frac{1}{2}\left(\frac{\sigma_m - \sigma_N}{s_N}\right)^2\right) \dot{\sigma}_m, \tag{7}$$

in which σ_N, ϵ_N, s_N and f_N are model parameters. These models are the basis of modeling the asymmetry of the cyclic plastic hysteresis. The total evolution of porosity is then

$$\dot{f} = \dot{f}_{gr} + \dot{f}_{nucl}. \tag{8}$$

Kinematic hardening is defined as a sum of symmetric non-linear backstresses $\boldsymbol{X}_i$

$$\boldsymbol{X} = (1 - f)\sum_{i=1}^{N} \underbrace{\frac{2}{3} C_i \boldsymbol{\alpha}_i}_{=\boldsymbol{X}_i}\,. \tag{9}$$

The plastic flow direction $\frac{\partial F}{\partial \boldsymbol{\sigma}}$ is denoted as $\boldsymbol{n}$ in equation (10). Here the evolution of underlying variable $\boldsymbol{\alpha}_i$ is defined as

$$\dot{\boldsymbol{\alpha}}_i = \dot{p}\,(\boldsymbol{n} - D_i\boldsymbol{\alpha}_i)\,, \tag{10}$$

with $\dot{p}$ being the plastic rate norm

$$\dot{p} = \sqrt{\frac{2}{3}\dot{\boldsymbol{\epsilon}}^{vp} : \dot{\boldsymbol{\epsilon}}^{vp}}. \tag{11}$$

With addition of the backstresses into equation (4) the stress tensor has to be translated with the backstress

$$F\,(\boldsymbol{\sigma}) \to F\,(\boldsymbol{\sigma} - \boldsymbol{X})\,. \tag{12}$$

The associated inelastic strain rate is defined as

$$\dot{\boldsymbol{\epsilon}}^{vp} = \dot{\lambda}\frac{\partial F}{\partial \boldsymbol{\sigma}}. \tag{13}$$

The matrix material viscoplasticity is modeled using a Norton type power-law formulation

$$\dot{\lambda}_M = \left(\frac{\sigma_M - R}{M}\right)^n, \tag{14}$$

in which M and n are viscoplasticity model parameters and R is the isotropic hardening parameter which is considered constant here. The macroscopic viscoplasticity is obtained by assuming the equivalence of microscopic and macroscopic inelastic work

$$(\boldsymbol{\sigma} - \boldsymbol{X}) : \dot{\boldsymbol{\epsilon}}^{vp} = (1 - f)\,\sigma_M\dot{\lambda}_M. \tag{15}$$

Finally, the current flow stress of the matrix material is solved from the consistency condition

$$\dot{F} = \frac{\partial F}{\partial \boldsymbol{\sigma}} : \dot{\boldsymbol{\sigma}} + \frac{\partial F}{\partial \boldsymbol{X}} : \dot{\boldsymbol{X}} + \frac{\partial F}{\partial \sigma_M}\dot{\sigma}_M + \frac{\partial F}{\partial f}\dot{f} = 0. \tag{16}$$

In the numerical simulations the author observed that the model worked better using rate-independent consistency condition $F = 0$ instead of (16). If the asymmetry provided by porosity and Gurson yield criterion are not enough, one can introduce an asymmetric kinematic hardening model [3], which was used to describe grey cast iron

$$\dot{\boldsymbol{X}}_i = C_i^* \dot{p} \left(\boldsymbol{n} - \frac{3}{2}\frac{D_i^*}{C_i^*}\boldsymbol{X}_i \right), \tag{17}$$

in which the parameters (C_i^*, D_i^*) are switched between tensile values (C_i^t, D_i^t) and compressive values (C_i^c, D_i^c) at set $\mathrm{tr}\,(\boldsymbol{\sigma})$ value. This would add an additional, porosity-independent, asymmetry mechanism.

Modeling hysteresis asymmetry

A 1D-version of the model was implemented in an implicit Euler integration scheme. The objective was to test whether the porosity evolution equations (5), (6) and (7) are enough to describe the observed asymmetry. The model fitting strategy is listed below

1. Set Young's modulus E to the observed mean value of the compression and tension values.
2. Set viscoplasticity parameters arbitrarily $M = 100$ and $n = 10$ as we lack data to fit them. The study could have been made using a rate-independent version of the material model as well.
3. Fit kinematic hardening variables C_i and D_i with symmetric model and fixed porosity $f = 0$ and $f_N = 0$ (von Mises yield criterion).
4. Fit initial porosity f and porosity evolution with isotropic hardening R being available for changes as well.
5. Introduce the asymmetric kinematic hardening model if needed.

Fitting the porosity evolution laws is a more difficult task. A seemingly good fit can be achieved with many sets of parameters and one cannot claim to have found the best set of parameters and this is typically why using optimization has to be limited to smaller bits or weighted in a clever way. One could look at the observed Young's moduli and try to fit the porosity evolution to that. The Gurson yield criterion (4) as well as the backstresses (9) are also connected to the porosity evolution. The strain driven law (6) with a zero mean value gives a stable porosity hysteresis where the backstresses are reduced when going to tension and increased when going to compression, which corresponds well to the observed hardening modulus behavior. Porosity stays unchanged in the elastic region with the strain driven nucleation law, so that the elastic region size is increased after compression and reduced after tension, which also corresponds well to the observed behavior. Porosity increase also accelerates further evolution of porosity due to the pressure dependent part of the yield function (4) being linearly dependent on porosity. Thus with increasing porosity the plastic deformation becomes more volumetric.

The hydrostatic stress driven nucleation law (7) could be a bit controversial. It is active even in the elastic region and thus the size of the elastic region would be reduced after compression and increased after tension, which is contradictory to the observations. On the other hand, if one sets the mean value heavily to the plastic region combined with a small standard deviation

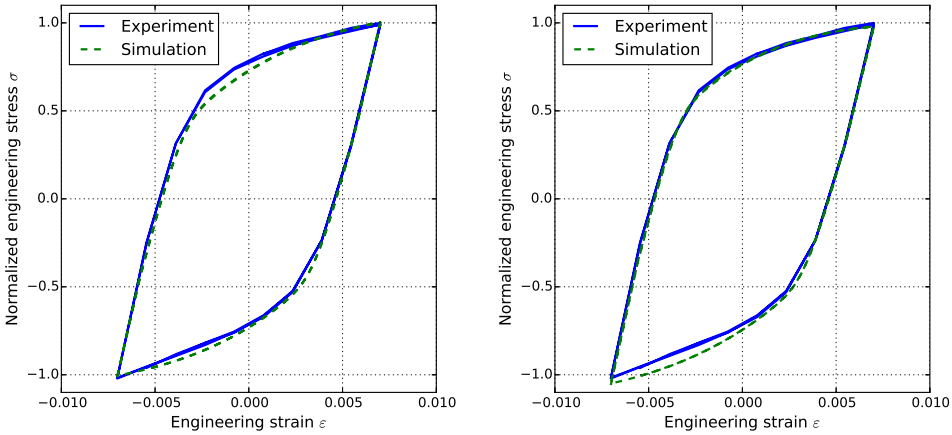

(a) Symmetric von Mises model fit.

(b) Strain nucleation law fit.

Figure 2

the size variation of the elastic region should be neglected. This nucleation law could be used to enhance the backstress-porosity interaction at either the tensile or the compressive end.

In [4] Seifert et al. used the strain driven nucleation law for EN-GJS-700 with parameters $f_N = 0.04$, $s_N = 0.001$, $\varepsilon_N = 0$ and initial porosity $f(0) = 0.02$. They also used a bilinear effective porosity in the Gurson yield criterion to model accelerated damage evolution above critical porosity due to the interaction of graphite inclusions and the coalescence of voids.

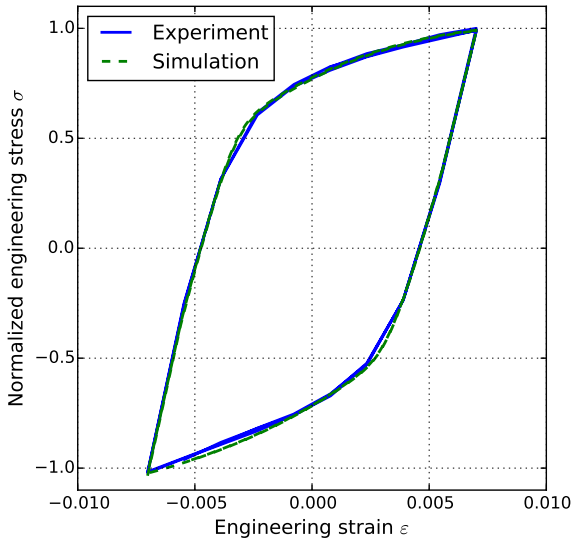

Figure 3: Strain nucleation and asymmetric kinematic hardening.

Both the size of elastic region as well as the effective elastic modulus are close to linear with respect to porosity and a variation of approximately 0.05 would be needed to model the observed Young's modulus asymmetry. Slightly larger variation would be needed for the observed asymmetry of the size of the elastic. Thus an effective porosity can be introduced in (4) which linearly scales the porosity value $f^* = kf$.

In Figure 2b the strain driven nucleation law was fit to the measurements and the result looks promising. The backstress shape follows the measured values much better as well as the observed Young's modulus asymmetry is captured. Slight overshoot remains at the compressive side. Introducing the hydrostatic stress driven nucleation law (6) would not help the situation. The asymmetric kinematic hardening was introduced to one of the backstresses for 10% difference to the slope variable C and the resulting fit can be seen in Figure 3.

As a conclusion, the porous plastic Gurson model combined with the Mori-Tanaka effective elasticity seems to be a good foundation for modeling the nodular cast iron asymmetry. Porosity is linked to everything which is a beneficial considering that there are less parameters. However, in this case it was required to introduce another asymmetry-mechanism independent of the porosity.

References

[1] J.-L. Chaboche, A. Gaubert, P. Kanouté, A. Longuet, F. Azzouz and M. Mazière. Viscoplastic constitutive equations of combustion chamber materials including cyclic hardening and dynamic strain aging, *International Journal of Plasticity*, 46:1–22, 2013.

[2] T. Seifert and H. Riedel. Mechanism-based thermomechanical fatigue life prediction of cast iron. Part I: Models, *International Journal of Fatigue*, 32:1358–1367, 2010.

[3] B.L. Josetson, U. Stigh and H.E. Hjelm. A Nonlinear Kinematic Hardening Model for Elastoplastic Deformations in Grey Cast Iron, *Journal of Engineering Materials and Technology*, 117:145–149, 1995.

[4] T. Seifert and H. Riedel. Mechanism-based thermomechanical fatigue life prediction of cast iron. Part II: Comparison of model predictions with experiments, *International Journal of Fatigue*, 32:1368–1377, 2010.

Proceedings of the XII Finnish Mechanics Days
R. Kouhia, J. Mäkinen, S. Pajunen and T. Saksala (Eds.)

Isogeometric analysis of gradient-elastic rods and 2D gradient-elastic dynamic problems

Viacheslav Balobanov, Jarkko Niiranen, Sergei Khakalo, Bahram Hosseini

Aalto university, P.O. Box 12100, 00076 Aalto
viacheslav.balobanov@aalto.fi, jarkko.niiranen@aalto.fi, sergei.khakalo@aalto.fi

Summary. In the present contribution, isogeometric methods are used to analyse statics and dynamics of rod and 2D problems based on gradient elasticity. Typically, the aim of the generalized theories of elasticity is to provide length scale parameters taking into account the effect of the microstructure of the material on its mechanical behaviour. The current models, in particular, include one length scale parameter enriching the classical constitutive equations and resulting in fourth order partial differential equations instead of the corresponding second order ones based on the classical elasticity. In our approach, the solvability of the problems is first formulated in a Sobolev space setting and then the problem is implemented by utilizing an isogeometric NURBS based discretization. Computational results of the current approach cover different boundary condition types and are compared to analytical solutions or other type of reference solutions such as standard finite element approximations.

Key words: isogeometric analysis, gradient elasticity theory, rod problem, 2D plane strain problem

Introduction

With the development of mechanics of microstructures it has become clear that classical linear theory of elasticity is not capable to describe multi-scale phenomena as effects of meso-scale, micro-scale or nano-scale in primarily macro-scale problems. A lot of improvements of classical elasticity theory have been done in order to explain such effects. One of the first significant contributions was done by Mindlin [3]. The simplest possible variant of his gradient elasticity theory implies the existence of an additional term in the definition of the potential energy density $\hat{W}$:

$$\hat{W} = \frac{1}{2}\boldsymbol{\sigma} \cdot\cdot \boldsymbol{\varepsilon} + \frac{1}{2} g^2 \nabla\boldsymbol{\sigma} \cdots \nabla\boldsymbol{\varepsilon}, \tag{1}$$

where $\boldsymbol{\varepsilon}$ is the classical strain tensor, $\boldsymbol{\sigma}$ – the classical Cauchy stress tensor and g is the gradient coefficient with dimension of length.

Equations of motion within a framework of the gradient elasticity theory are the partial differential equations with high order derivatives and they can be solved analytically only in the simplest cases. It is convenient to use isogeometric analysis (IGA) in order to obtain the solution of such equations. IGA can be considered as the "next generation" of the finite-element methods family. It has been under development at a quick rate during last 10 years. The main difference between classical FEM and IGA is using of non-uniform rational B-splines (NURBS) as basis functions instead of Lagrange polynomial (or some special basis function like Hermit polynomial for the beam elements) of the classical FEM. There are a lot of advantages of IGA methods, but in context of gradient elasticity the most useful one is that it provides C^{p-1} continuity across the elements boundaries.

Governing equations

Static equation of rod

Consider a straight prismatic rod of constant cross section A and length L under a static distributed load p and a displacement u along longitudinal axis x. According to [4], the governing equilibrium equation of this rod can be written as follows:

$$AE(u'' - g^2 u^{(4)}) + p = 0. \tag{2}$$

As one can see the gradient theory brings into existence an additional micro-structural term $g^2 u^{(4)}$ containing the fourth derivative of u with respect to x. For $g = 0$ this term vanishes and equation (2) reduces to the classical case.

Dynamic equation of rod

In order to predict wave propagation in rod of gradient-elastic material it is necessary to solve next equation below:

$$Eu'' - g^2 Eu^{(4)} = \rho\ddot{u} - \rho h^2 \ddot{u}'', \tag{3}$$

with ρ mass density, $\ddot{u}$ second derivative with respect to time t. Besides the micro-structural term there is additional micro-inertia term $\rho h^2 \ddot{u}''$ in the right-hand side of the equation (3) with h denoting the micro-inertia parameter, second used gradient elasticity constant.

Dynamic equation of 2D problem

In this paper, the dynamic 2D problem means the vibrations of a plate in the plane strain state. Following designations are used: displacements $\boldsymbol{u} = u\boldsymbol{e}_x + v\boldsymbol{e}_y$ and 2D nabla-operator $\nabla = \boldsymbol{e}_x \frac{\partial}{\partial x} + \boldsymbol{e}_y \frac{\partial}{\partial y}$. According to [5]

$$(1 - g^2\nabla^2)(\mu\nabla^2 \boldsymbol{u} + (\lambda + \mu)\nabla\nabla \cdot \boldsymbol{u}) = \rho(\ddot{\boldsymbol{u}} - h^2\nabla^2\ddot{\boldsymbol{u}}). \tag{4}$$

Numerical results

Problems described in the previous section can be solved by using numerical methods. Isogeometric analysis (IGA) has been used for this purpose. NURBS basis functions are the rational extension of polynomial B-spline functions. For 1D case B-spline basis functions can be written as follows:

$$\begin{gathered} N_{i,p}(\xi) = \frac{\xi - \xi_i}{\xi_{i+p} - \xi_i} N_{i,p-1}(\xi) + \frac{\xi_{i+p+1} - \xi}{\xi_{i+p+1} - \xi_{i+1}} N_{i+1,p-1}(\xi) \quad for \quad p = 1, 2, 3, ... \\ N_{i,0}(\xi) = \begin{cases} 1 & \text{if } \xi_i \le \xi \le \xi_{i+1}; \\ 0 & \text{otherwise.} \end{cases} \end{gathered} \tag{5}$$

Corresponding NURBS basis functions is presented below:

$$R_i^p(\xi) = \frac{N_{i,p}(\xi) w_i}{\sum_{\hat{i}=1}^{n} N_{\hat{i},p}(\xi) w_{\hat{i}}}, \tag{6}$$

with $1 \le i \le n$, n is the number of NURBS and p it the polynomial degree. For more details see [1].

Numerical results for some simple benchmark problems are given below. For verification of solution results convergence curves have been obtained for different polynomial degrees(figure 1).

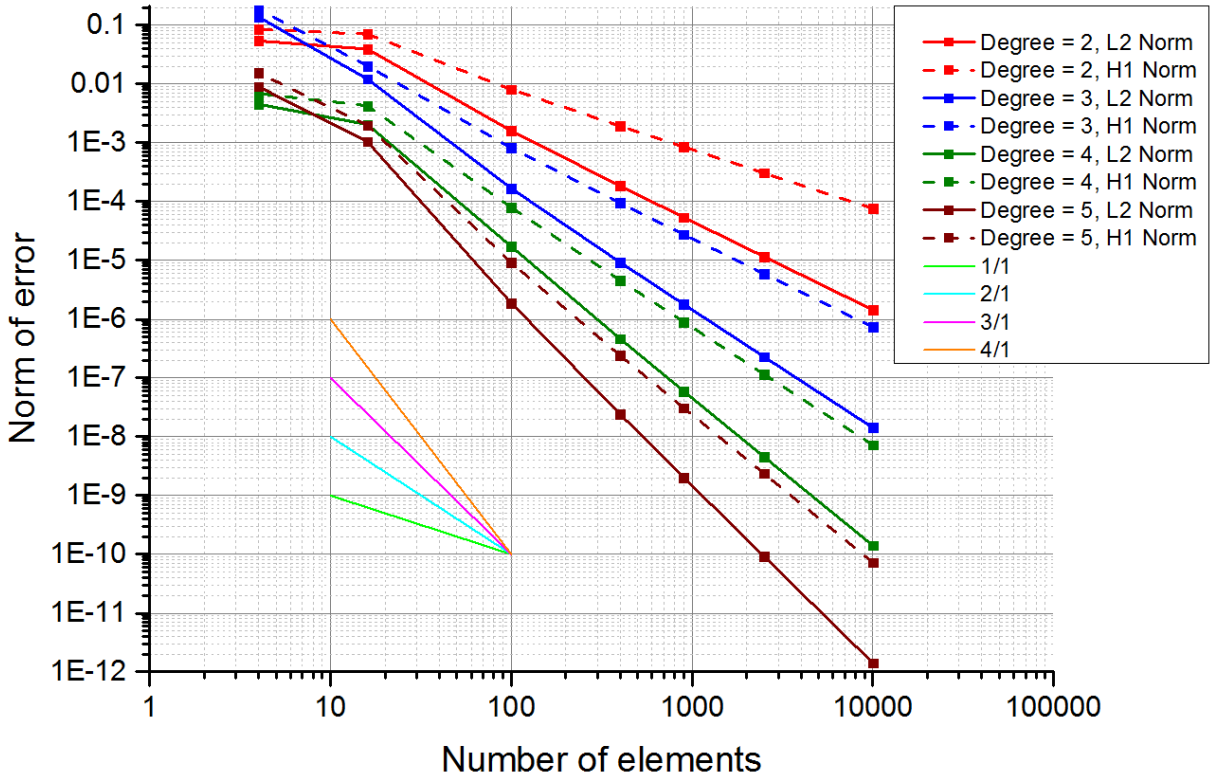

Figure 1. Convergence curves using different order NURBS basis functions.

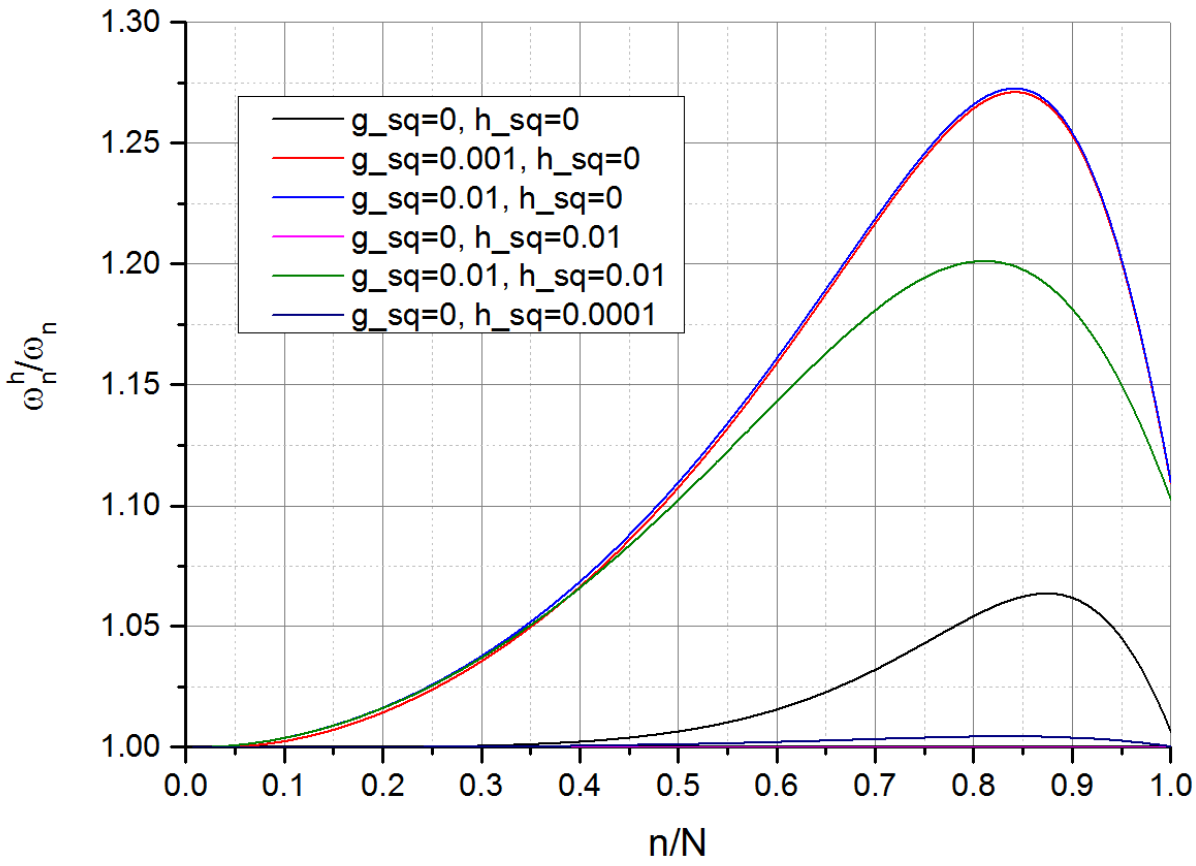

Figure 2. Normalized discrete spectra using different gradient elasticity parameters.

Results of eigenvalue analysis of rod fixed on both ends are presented on Figure 2. The analyses have been carried out using $N = 128$ degrees-of-freedom. g_sq and h_sq designate squares of gradient coefficients g and h resp. $\frac{\omega_n^h}{\omega_n}$ is the ratio of numerical obtained eigen frequency to exact eigen frequency of number n.

For more solution results of rod and 2D-problems see [2].

References

[1] J.A. Cottrell, T.J.R. Hughes, Y. Bazilevs. *Isogeometric analysis: toward integration of CAD and FEA*. John Wiley & Sons Ltd, Chichester, United Kingdom, 2009.

[2] J. Niiranen, S. Khakalo, V. Balobanov, B. Hosseini. Isogeometric static and dynamic analysis of gradient-elastic rod and plane strain problems. *In preparation.*

[3] R.D. Mindlin. Micro-structure in linear elasticity. *Archive for Rational Mechanics and Analysis*, 16(1):51-78, 1964.

[4] S. Papargyri-Beskou, A.E. Giannakopoulos, D.E. Beskos. Static analysis of gradient elastic bars, beams, plates and shells. *The Open Mechanics Journal*, 4:65-73, 2010.

[5] S. Papargyri-Beskou, D. Polyzos, D.E. Beskos. Wave dispersion in gradient elastic solids and structures: A unified treatment. *International Journal of Solids and Structures*, 46:3751-3759, 2009.

Proceedings of the XII Finnish Mechanics Days
R. Kouhia, J. Mäkinen, S. Pajunen and T. Saksala (Eds.)

Isogeometric static and dynamic analysis of gradient-elastic plane strain problems

Sergei Khakalo, Jarkko Niiranen, Viacheslav Balobanov, and Bahram Hosseini

Aalto University, PO Box 12100, 00076 AALTO,
sergei.khakalo@aalto.fi, jarkko.niiranen@aalto.fi, viacheslav.balobanov@aalto.fi,
bahram.hosseini@aalto.fi

Summary. In the present contribution, isogeometric methods are used to analyse statics and dynamics of the plane strain problems based on gradient-elasticity. Typically, the aim of the generalized theories of elasticity is to provide length scale parameters taking into account the effect of the microstructure of the material on its mechanical behaviour. The current models, in particular, include one length scale parameter enriching the classical constitutive equations and resulting in fourth order partial differential equations instead of the corresponding second order ones based on the classical elasticity. In our approach, the solvability of the problems is first formulated in a Sobolev space setting and then the problem is implemented by utilizing an isogeometric NURBS based discretization. Computational results of the current approach cover different boundary condition types and are compared to analytical solutions or other type of reference solutions such as standard finite element approximations. Numerical results are achieved by implementing the isogeometric methods into a commercial software Abaqus.

Key words: isogeometric analysis, plane strain problem, gradient-elasticity, Abaqus

Introduction

For centuries, classical continuum theories, such as theories of linear or nonlinear elasticity and plasticity, have been widely used in various fields of science and engineering for modeling, analyzing and predicting the behaviour of solids and structures. The ability of classical continuum theories for describing multi-scale phenomena, as effects of meso-scale, micro-scale or nano-scale in primarily macro-scale problems, is very limited, however. On the other hand, small-scale phenomena in micro-scale, or even nano-scale, structures have been modelled by using classical theories.

One of the main motivations for further development of single-scale continuum mechanics has been the fact that theories and computational methods for studying small scale phenomena, such as molecular dymanics, are often inefficient in many applications eventually ruled by macro-scale conservations laws. Therefore, classical theories have been extended in different ways towards multi-scale capabilities – still preserving the most characteristic advantages of their homogenizing nature.

The origins of generalized continuum theories can be traced back to the 1850s, while the first major revival took place in 1960s. The second major revival in 1980s and 1990s was focusing on simplified models taking into account only few high-order terms with corresponding additional material parameters from the original generalized theories (see [1] for an overview and references).

In this contribution, the static and dynamic gradient-elastic [2, 3, 4] plane strain problems are studied by applying isogeometric [5] finite element analysis.

Gradient-elastic plane stress and strain problems

Within the first strain gradient elasticity the equation of motion of the generilized continua can be written as follows [6]

$$(1 - g^2\Delta)[\mu\Delta\boldsymbol{u} + (\lambda + \mu)\nabla\nabla \cdot \boldsymbol{u}] + \boldsymbol{f} = \rho(\ddot{\boldsymbol{u}} - h^2\Delta\ddot{\boldsymbol{u}}), \tag{1}$$

where $\boldsymbol{u}$ is the displacement vector, $\boldsymbol{f}$ is the density of the body forces, λ and μ are the Lame parameters, ρ is the material volume density, g^2 and h^2 are the micro-structural and the micro-inertia parameters, respectively. For the linear elastic isotropic material Cauchy $\boldsymbol{\tau}$ stress tensor can be written as

$$\boldsymbol{\tau} = 2\mu\boldsymbol{\varepsilon} + \lambda tr(\boldsymbol{\varepsilon})\boldsymbol{I}, \tag{2}$$

where the strain tensor $\boldsymbol{\varepsilon}$ is taken as

$$\boldsymbol{\varepsilon} = \frac{1}{2}(\nabla\boldsymbol{u} + \boldsymbol{u}\nabla). \tag{3}$$

Double ${}^3\boldsymbol{\mu}$ and total $\boldsymbol{\sigma}$ stress tensors are introduced as follows

$${}^3\boldsymbol{\mu} = g^2\nabla\boldsymbol{\tau}, \tag{4}$$

$$\boldsymbol{\sigma} = \boldsymbol{\tau} - g^2\Delta\boldsymbol{\tau}. \tag{5}$$

After certain assumptions regarding dimension reduction the above equations and formulae are used for the static and dynamic analysis of the gradient-elastic plane stress and strain problems.

Numerical results

Let us consider a rectangular plane $\Omega = (0, L) \times (0, L) \subset \mathbb{R}^2$ in the following field of the volume forces

$$\boldsymbol{f} = f_x\boldsymbol{e}_x + f_y\boldsymbol{e}_y, \tag{6}$$

where

$$f_x(x, y) = 4\frac{\pi^2}{L^2}\sin(2\pi\frac{x}{L})[(2\mu + \lambda)(1 + 4\pi^2\frac{g^2}{L^2}) - 2\mu\cos(2\pi\frac{y}{L})(1 + 8\pi^2\frac{g^2}{L^2})], \tag{7}$$

$$f_y(x, y) = 4\frac{\pi^2}{L^2}\sin(2\pi\frac{y}{L})[-(2\mu + \lambda)(1 + 4\pi^2\frac{g^2}{L^2}) + 2\mu\cos(2\pi\frac{x}{L})(1 + 8\pi^2\frac{g^2}{L^2})]. \tag{8}$$

The boundary conditions are taken as follows

$$\boldsymbol{u} = 0 \text{ on } \partial\Omega, \tag{9}$$

$$\frac{\partial\tau_{yy}}{\partial y} = 0 \text{ and } \frac{\partial\tau_{xy}}{\partial y} = 0 \text{ on } y = 0,\ y = L, \tag{10}$$

$$\frac{\partial\tau_{xx}}{\partial x} = 0 \text{ and } \frac{\partial\tau_{xy}}{\partial x} = 0 \text{ on } x = 0,\ x = L. \tag{11}$$

The analytical solution of the static gradient-elastic equation

$$(1 - g^2\Delta)[\mu\Delta\boldsymbol{u} + (\lambda + \mu)\nabla\nabla \cdot \boldsymbol{u}] + \boldsymbol{f} = 0 \text{ in } \Omega \tag{12}$$

with boundary conditions above is the following $\boldsymbol{u} = u_x\boldsymbol{e}_x + u_y\boldsymbol{e}_y$, where

$$u_x(x, y) = \sin(2\pi\frac{x}{L})(1 - \cos(2\pi\frac{y}{L})), \tag{13}$$

$$u_y(x, y) = \sin(2\pi\frac{y}{L})(-1 + \cos(2\pi\frac{x}{L})). \tag{14}$$

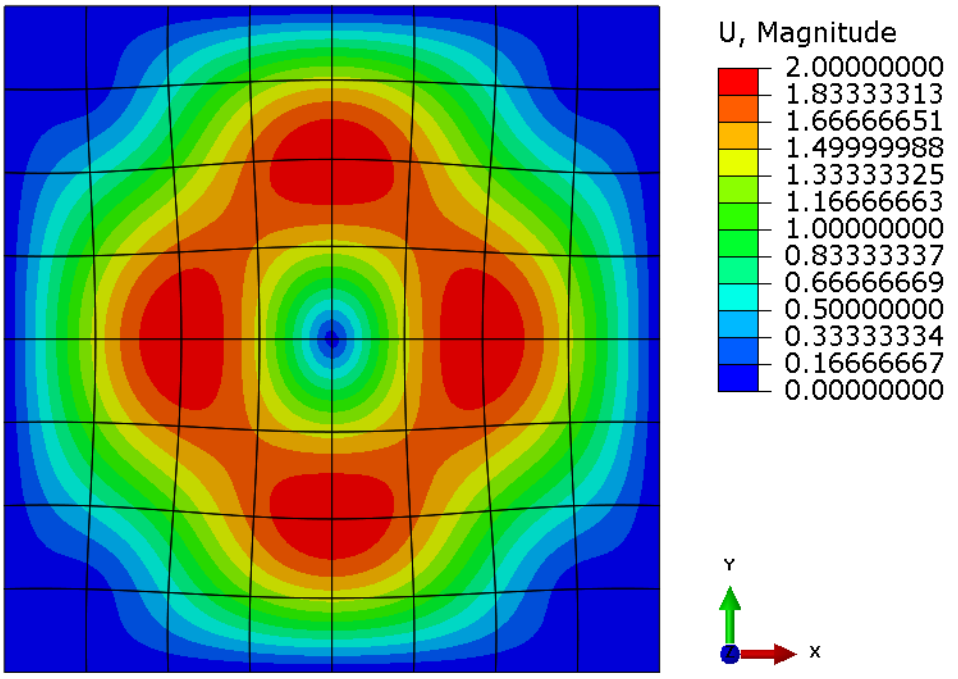

Figure 1. The magnitude of the displacement field distribution

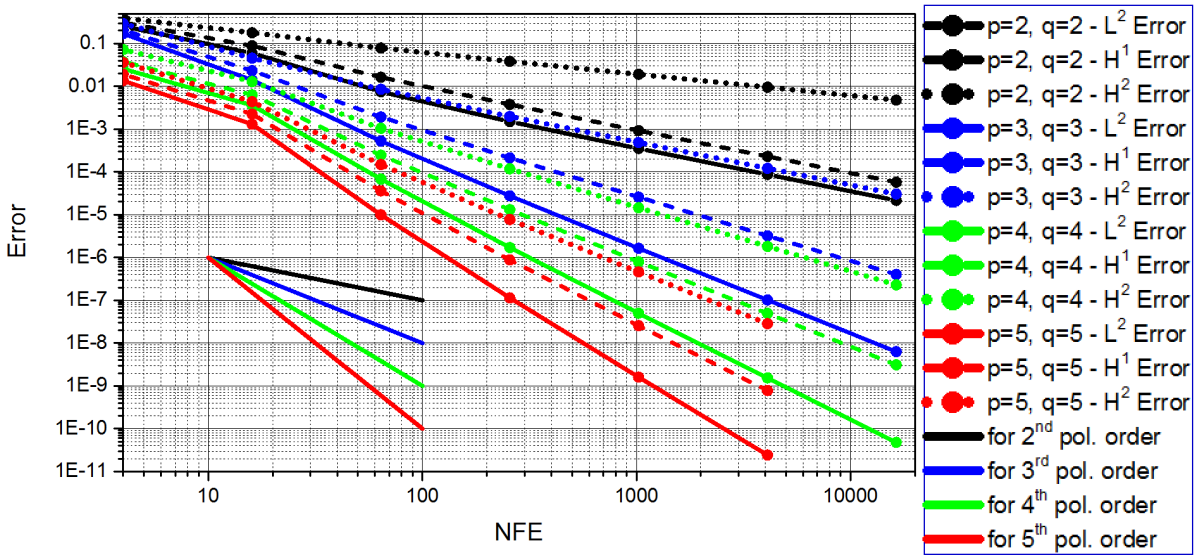

Figure 2. Relative error curves with respect to $L^2(\Omega)$, $H^1(\Omega)$ and $H^2(\Omega)$ norms

The numerical results was obtained in Abaqus using Users Subroutines. This tool allows us to modify the finite element formulation for implementing the isogeometric method and use the Abaqus as a solver and a Post-Processor. In Figure 1 is shown the magnitude of the displacement field distribution. Domain was divided into 64 elements and the NURBS basis functions of order five was taken with C^4 continuity across the element boundaries. The curves of the relative solution error with respect to $L^2(\Omega)$, $H^1(\Omega)$ and $H^2(\Omega)$ norms are shown in Figure 2.

The benchmark problems such as the gradient-elastic solution of the Lame problem with 1 and 2 materials and the gradient-elastic solution of the MEMS specimen tension can be found in [3].

References

[1] Harm Askes, Elias C. Aifantis. Gradient elasticity in statics and dynamics: An overview of formulations, length scale identification procedures, finite element implementations and new results. *International Journal of Solids and Structures* 48 (2011)

[2] S. Papargyri-Beskou, A.E. Giannakopoulos, D.E. Beskos. Static analysis of gradient elastic bars, beams, plates and shells. *The Open Mechanics Journal*, 4:65-73, 2010

[3] J. Niiranen, S. Khakalo, V. Balobanov, B. Hosseini. Isogeometric static and dynamic analysis of gradient-elastic rod and plane strain problems. *In preparation*

[4] P. Fischer, M. Klassen, J. Mergheim, P. Steinmann, R. Muller. Isogeometric analysis of 2D gradient elasticity. *Computational Mechanics*, 47:325-334, 2011

[5] T.J.R. Hughes, J.A. Cottrell, Y. Bazilevs. Isogeometric analysis: CAD, finite elements, NURBS, exact geometry and mesh refinement. *Computer Methods in Applied Mechanics and Engineering*, 194:4135-4195, 2005

[6] S. Papargyri-Beskou, D. Polyzos, D.E. Beskos. Wave dispersion in gradient elastic solids and structures: A unified treatment. *International Journal of Solids and Structures* 46 (2009)

Proceedings of the XII Finnish Mechanics Days
R. Kouhia, J. Mäkinen, S. Pajunen and T. Saksala (Eds.)

Thermo-Hygro-Mechanics (THM) in the frame of the Finnish connection

Andras Szekeres
Dept. Applied Mechanics, Budapest University of Technology and Economics
Research Group for Dynamics of Machines and Vehicles, Hungarian Academy of Sciences, szekeres@mm.bme.hu

Summary. The presentation deals with the newest results on THM, based mainly on [1,2]. Our THM investigation started ca. 20 years ago in Oulu during my visiting professorship and researchership there in the Laboratory of Mechanics. That is the reason of the large No. of the co-authors from Oulu. One of the nice back-bones of the co-operation is the Fenno-Ugric Days of Mechanics (FUDoM), started in 1995 and celebrated the 6th one in 2013 [3,4,5]. Also the Thermal Stresses (TS) Congresses give a useful summary on the results of the THM and on the schools formed around them [6,7]. A good summary on the co-operation was the Helsinki presentation [8]. A short overview on the results will be displayed based on the above mentioned papers.

References

[1] Szekeres A: Thermo-Hygro-Elasticity, Entry in the Encyclopedia of Thermal Stresses, Springer, 2014, p.5918-5924.
[2] Szekeres A: Cross-Coupled Heat and Moisture Transport: Part 1 - Theory, J. Thermal Stresses, 35: 248-268, 2012. Part 2 - Application in Mechanics, Part 3 – Application in Engineering, co-author Fekete B, (being prepared).
[3] Koivurova H, Szekeres A:Theoretical and Experimental Investigation on the Diffusivities of Composites, Periodica Polytechnica, Ser Mech Eng 41 (2):151-161, 1997.
[4] Szekeres A, Pramila A, Heller R: Theory and Practice of THM Tailoring of FRCs, Some Results on Diffusivities. Proc. of 4th Int.Conf. Composite Engineering, Hawaii, 6-12 July, 1997.
[5] Szekeres A, Pramila A: Heat and Moisturein Solids: Dynamical Sorption with MIcrocracks, EUROMECH 436, Tallinn, 29 May-1 June, 2002.
[6] Szekeres A, Elesztos P, Enikov E: Thermal Stresses (TS), Thermomechanics (TM), Thermo-Hygro-Mechanics (THM), TS 2009 Congr. June 1-4, 2009, Urbana-Champaign, USA.

[7] Szekeres A, Fekete B: Thermo-Hygro-Mechanics (THM) and Engineering - Framed by the Thermal Stresses Congs. TS 2013 Congr. May 31-June 4, 2013, Nanjing, China.
[8] Szekeres A, Pramila A: THM Tailoring of FRC Materials and Structures - Theory and Application in Mechanical Engineering, Seminar in the Inst. of Mechanics, HUT, 22 Nov, 2002, Otaniemi.

Author index

XII Finnish Mechanics Days – Sponsors

A-INSINÖÖRIT

EDR™ MEDESO

ETiMADEN
AB ETiPRODUCTS OY

FEMdata

PRESSUS Oy

RAMBØLL

ril

VERTEX SYSTEMS

Federation of Finnish Learned Societies

RAKENNUTTAMINEN · RAKENNESUUNNITTELU ·
INFRASUUNNITTELU · KALLIO- JA YMPÄRISTÖSUUNNITTELU

www.ains.fi

A-INSINÖÖRIT

EDR™ MEDESO
Perfect engineering

ANSYS®

How is the airflow affected if you change the design?

Rent a wind tunnel.
Or try something new.

ANSYS simulation software and services

For more information, please contact
Jani Ojala, +358 50 3599 002
jani.ojala@edrmedeso.com

AB ETIPRODUCTS OY: COMPANY PRESENTATION

Ab Etiproducts Oy was founded in 1982 in Helsinki, and is a subsidiary of the Turkish state owned company EtiMaden G.M, who is the world leading provider of boron products. Etiproducts' mission is to be the leading market provider of Turkish boron products in our exclusivity territory, and to supply the best quality of boron products to our customers.

Our business exclusivity territory has expanded throughout the years, and consists of the Nordic countries, Baltic member stated, Poland, Ukraine, Germany and recently Sub-Saharan African Countries. To succeed in our mission, we have a established an effective logistic network, with warehouses in Finland, Sweden, Latvia, Poland and South- Africa, which allows us to serve our customers in the best possible way.

HOW BORATES ARE USED IN METALLURGY?

Borates are used in the production of steel and non-ferrous metals, amorphous metals, welding fluxes, alloys, rare earth magnets and plating compounds. Boron is generally used in Metallurgy (such as in abrasives, cutting tools, magnets and soldering) for the following purposes;

- ✓ to reduce melting temperature (thus to lower the energy consumed)
- ✓ to increase fluidity (as a fluxing agent)
- ✓ to increase strength (hardenability) of the steel
- ✓ to reduce the corrosion of the refractory material in the furnace

Boron is also used in the production of pure, strong metals to remove the oxygen and nitrogen that is either dissolved in the metal or chemically bound to it. In steel and non-ferrous metal production, borates act as a flux during the smelting operation helping to dissolve metallic oxide impurities which are then removed in the slag.

FEMdata

FEM -programs for:

Piping (EN, ASME)

Steel structures (EC3)

General structures

Support and user training

Ukkohauentie11-13 B
02170 Espoo, Finland
358-9-420 8855
eero.torkkeli@femdata.inet.fi

Mekaniikan ja lujuusopin oppikirjoja

www.pressus.fi

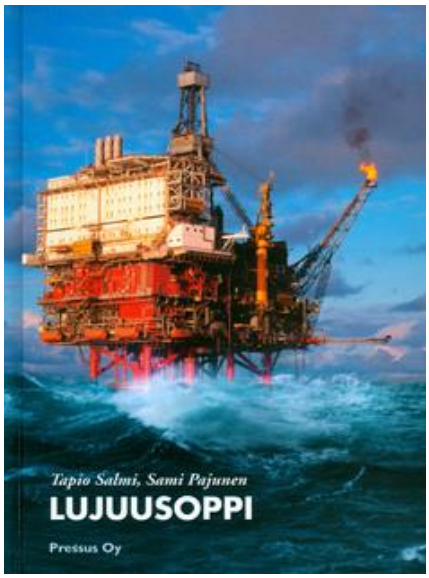

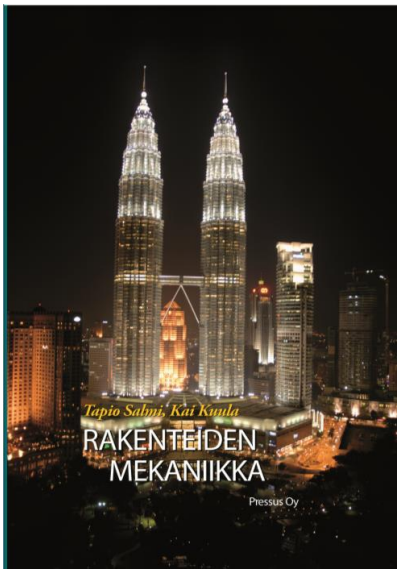

Salmi, Statiikka, 2014, 400 sivua	38 €
Salmi, Virtanen, Dynamiikka, 2006, 480 sivua	32 €
Salmi, Pajunen, Lujuusoppi, 2010, 464 sivua	38 €
Salmi, Virtanen, Materiaalien mekaniikka, 2008, 413 sivua	38 €
Salmi, Kuula, Rakenteiden mekaniikka, 2012, 464 sivua	38 €
Salmi, Teknillisen mekaniikan perusteet, 2006, 464 sivua	32 €

Hinnat sisältävät alv:n (10 %). Postituskulut 4 € /lähetys.

Lisätietoja kirjoista ja tilaukset verkkosivulta www.pressus.fi tai suoraan sähköpostilla tapio.salmi@pressus.fi.

PRESSUS Oy
Ritalankatu 35 B
33400 TAMPERE
puh 050-3071682
www.pressus.fi
tapio.salmi@pressus.fi

Suomen Rakennusinsinöörien Liitto RIL ry tuottaa ajankohtaista ja korkeatasoista eri käyttötarkoituksiin soveltuvaa ammattikirjallisuutta. Julkaisutoimintamme luo edellytykset rakennusalan asiantuntijoiden ja opiskelijoiden ammattitaidon kehittämiseen ja ylläpitoon.

Ammattilainen!

RILin uudet julkaisut sinulle

RIL 269-2015
Rakennusten rakenteellisen turvallisuuden tarkastusohje

RIL 255-1-2014
Rakennusfysiikka I
Rakennusfysikaalinen suunnittelu ja tutkimukset

RIL 226-2014
Urakkaohjeen asema ja laadinta

RIL 245-2014
Pienet savupiiput

RIL 265-2014
Uusiutuvien lähienergioiden käyttö rakennuksissa

RIL 263-2014
Kaivanto-ohje

RIL 266-2014
Kalliopultitusohje

RIL 262-2014
Taitava kuntarakennuttaja

RIL 229-1-2013 ja RIL 229-2-2013
Rakennesuunnittelun asiakirjaohje
Tekstiosa ja Mallipiirustukset ja -laskelmat

Eurokoodit-julkaisut

Tulossa:
RIL 268-2015
Jatkuvan sortuman estäminen

Julkaisuja saatavissa myös eKirjoina
ks. www.ril.fi/kirjakauppa > eKirjat

Julkaisutilaukset ja lisätietoja:
jaana.henell@ril.fi tai www.ril.fi/kirjakauppa

Ril.fi

Flow

Koneenrakentajan uusi workflow –

Vertex Flow

Vertex Flow:lla saat tuotetiedot koko organisaation ja sidosryhmien käyttöön. Hyödynnä suunnittelussa syntyvä tuotetieto tehokkaasti tuotannossa, ostotoiminnoissa, myynnissä ja varaosaliiketoiminnoissa.

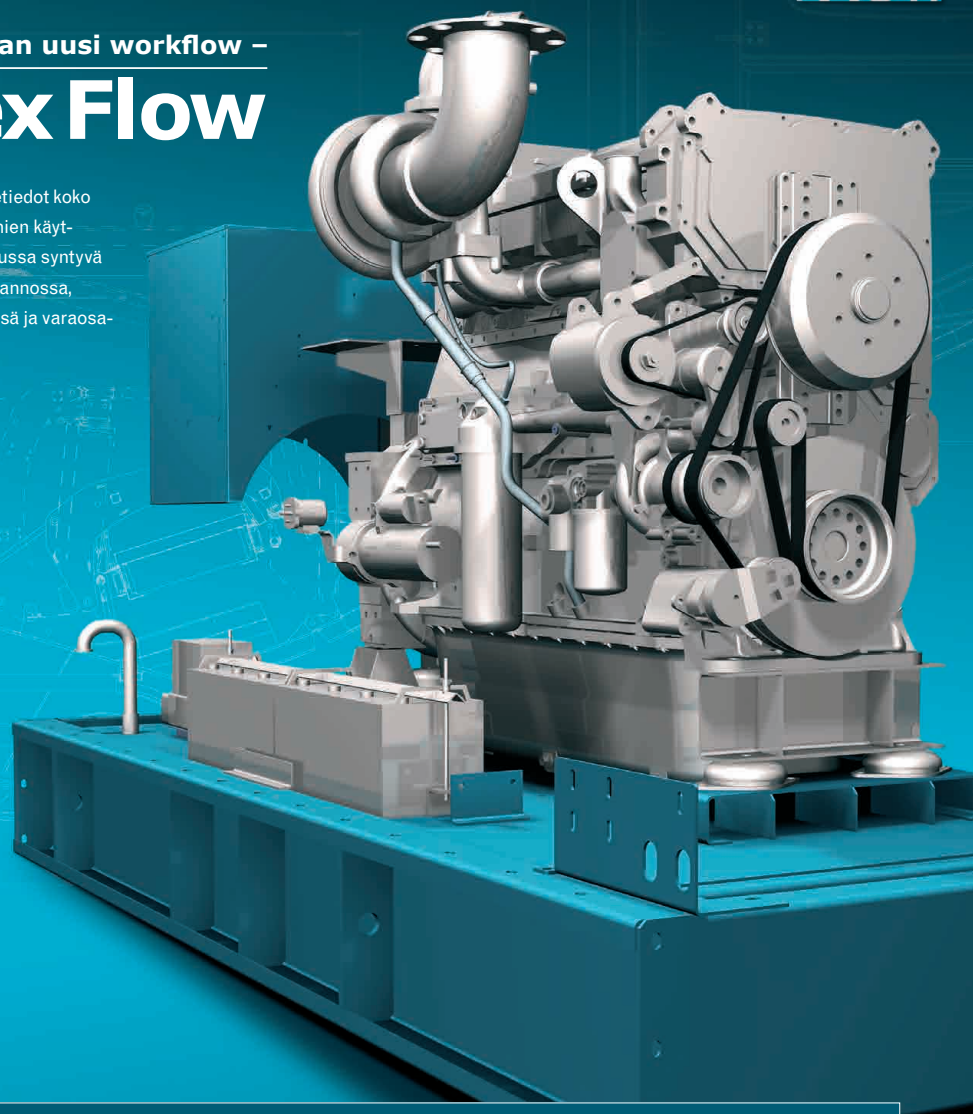

Suomessa kehitetyt
teollisuuden ohjelmistoratkaisut

Vertex Systems Oy kehittää ja toteuttaa kotimaisia toimialakohtaisia suunnittelun ja tiedonhallinnan ohjelmistoratkaisuja teollisuudelle.

Flow-yhteensopivat suunnitteluohjelmat

G4	G4 Plant	G4PI	ED	HD
Vertex G4 Koneensuunnittelu	**Vertex G4Plant** Laitossuunnittelu	**Vertex G4PI** PI-kaaviosuunnittelu	**Vertex ED** Sähkösuunnittelu	**Vertex HD** Hydrauliikkasuunnittelu

www.vertex.fi

VERTEX SYSTEMS

Esitykset - Presentations Torstai - Thursday 4.6.2015

Plenary I 9:00-10:10

- A stabilized, meshless method for the simulation of strongly coupled fluids and nonlinear solids, Ignacio Romero Technical University of Madrid, Spain
- Finite Elements on Non-Linear Manifolds of Rotations or Complete Motion - Relationships between Objectivity, Helicoidal Interpolation and Fixed-Pole Approach, Gordan Jelenic, University of Rijeka, Croatia

Session 1A: Structural Engineering - Rakennetekniikka (EFFF) 10:40-12:00

- The effects of initial moisture on damp problems of a timber framed wall construction – a numerical approach, Filip Fedorik, Mikko Malaska,University of Oulu, Finland
- Numeerisen virtauslaskennan käyttö tuulikuormien määrittämisessä, Juha Soini, Jussi Jalkanen,Sweco Rakennetekniikka,
- Teräsristikon paarteiden liitoksen vapaan välin leikkausvoiman arviointi, Teemu Tiainen, Markku Heinisuo,TTY
- Seismiset analyysimenetelmät rakennesuunnittelussa, Jyri Tuori, Jussi Jalkanen, Sweco Rakennetekniikka Oy

Session 1B: Fracture & Damage Mechanics (English) 10:40-12:00

- Nonsingular fracture mechanics within generalized continua, S. Mahmoud Mousavi, Juha Paavola, Aalto University, Finland
- Continuum damage mechanics without the variable damage D, Kari Santaoja, Aalto-yliopisto, Finland
- An anisotropic continuum damage model for concrete, Saba Tahaei Yaghoubi[1], Juha Hartikainen[1], Kari Kolari[2], Reijo Kouhia[3],[1]Aalto University; [2]VTT; [3]TUT
- On the choice of damage variable in the continuum fatigue model based on a moving endurance surface, Timo Juhani Saksala, Sami Holopainen, Reijo Kouhia, TUT

Session 2A: Multibody Dynamics (English) 13:00-14:20

- Real-time dynamic analysis of mobile machines using semi- recursive method with sparse matrix technique, Ezral Baharudin[1], Asko Rouvinen[2], Pasi Korkealaakso[2], Marko Matikainen[1], Aki Mikkola[1], [1]LUT; [2]Mevea Ltd
- Soft body impact against aeronautical structures, Alessia Prato, Marco Anghileri, Andrea Milanese, Luigi Castelletti, Politecnico di Milano, Italy
- Two approaches for modeling hydraulic cylinder, Antti Ylinen,FS Dynamics Oy Ab, Finland
- On the effect of damping on stability of non-conservative systems, Juha Jeronen[1,2], Reijo Kouhia[21]University of Jyväskylä; [2]TUT

Session 2B: Numeeriset menetelmät - Numerical Methods (Finnish) 13:00-14:20

- Numeerinen integrointi laajennetussa elementtimenetelmässä, Tom Gustafsson, Aalto University, Finland;
- Fatigue strength of shrink-fitted aluminium fan on steel shaft, Timo Pekka Holopainen, Toni Kilpeläinen, ABB Oy, Finland
- Raudoitetun betonirakenteen taivutuksen mallintaminen Ansys-ohjelmalla, Jari Juhani Pietilä, Jari Mäkinen, TTY
- Modelling of the web--air interaction in paper making using the unified continuum model, Tytti Saksa[1], Johan Hoffman[2] [1]University of Jyväskylä, Finland; [2]Royal Institute of Technology - KTH

Session 2C: Theoretical Mechanics - Teoreettinen mekaniikka (EEEF) 13:00-14:20

- On kinematically inadmissible virtual displacements, Eero-Matti Salonen, Juha Paavola, Aalto University, Finland;
- Generating lines of curvature coordinates for finite element modelling, Mika Malinen, CSC - IT Center for Science, Finland
- Computing minimizing curves on fixed rank matrix manifolds, Alexis Fedoroff, Djebar Baroudi, Aalto, Finland
- Surface tension problems, virtual work and minimal surfaces, Mika Reivinen, Eero-Matti Salonen, Aalto University, Finland;

Session 3A: Finite Element Methods (English) 14:50 15:50

- Stochastic finite element methods for tolerance analysis, Juho Könnö[1], Jonatan Lehtonen[2], Harri Hakula[31]Wärtsilä Finland Oy, Finland; [2]Global Boiler Works Oy, Finland; [3]Aalto University, Finland
- A family of triangular shell elements, Antti H. Niemi, Aalto University, Finland
- Exploration of different boundary conditions in the sideways falling situation in hip fracture finite element modelling, Shinya Abe[1], Nathaniel Girish Narra[1], Riku Nikander[2], Jari Hyttinen[1], Reijo Kouhia[1], Harri Sievänen[3],[1]Tampere University of Technology, [2]University of Jyväskylä, [3]UKK Institute, Finland;

Session 3B: Optimointi - Optimization (Finnish) 14:50 15:50

- Suunnittelutyökalu putkiristikoiden mitoitukseen ja optimointiin, Kristo Mela[1], Mikko Alinikula[2], Teemu Tiainen[1], Markku Heinisuo[1], Ilkka Sorsa[3] [1]Tampere University of Technology, Finland; [2]SUBNIC Oy, Finland; [3]Ruukki Construction Oy, Finland;
- Surrogate-based optimization of airfoil using open source software, Aku Karvinen, VTT, Finland

Session 3C: Beam Theory - Palkkiteoria (EEF) 14:50 15:50

- Dynamic analysis of higher-order shear deformable beams within gradient elasticity, Saba Tahaei Yaghoubi, S. Mahmoud Mousavi, Juha Paavola,Aalto University, Finland
- Effective radia of threaded bars in bending, Jouni Tapani Freund, Kari Kantola, Aalto university, Finland;
- Dynamical warping of tube branch welded joints, Ilkka Pöllänen[2], Timo Björk[3], Heikki Ilmari Martikka[1] [1]Himtech Oy, Finland; [2]SAV Oy; [3]LUT

Plenary II 15:50-17:00

- (All kinds of) instabilities in structural membranes, Anders Eriksson, KTH, Sweden
- Challenges of Climatic Changes for Coastal Engineering, Tarmo Soomere,Tallinn University of Technology, Estonia

Esitykset - Presentations Perjantai - Friday 5.6.2015

Session 4A: Ice Mechanics - Jäämekaniikka (EFF) 9:00-10:00

- 2D FEM-DEM simulations on ice-structure interaction process in shallow water, Riikka Häsä[1], Arttu Polojärvi[1,2], Jukka Tuhkuri[1,2], [1]Aalto University, Finland; [2]Norwegian University of Science and Technology, Norway;
- Why simulate ice rubble shear box tests?,Arttu Sakari Polojärvi[1,2], Jukka Tuhkuri[1,2], Anna Pustogvar[2] [1]Aalto University; [2]University of Science and Technology, Norway;
- A review on a peak ice load data from 2D combined finite discrete element method simulations, Janne Ranta, Jukka Tuhkuri, Arttu Polojärvi, Aalto University, Finland

Session 4B: Matemaattiset menetelmät - Mathematical Methods (FFF) 9:00-10:00

- Cauchy-Navierin yhtälö ja kvaternioanalyysi, Heikki Orelma, TTY, Finland
- Transpositions and duals of high-order tensors. On theory and applications in mechanics, Sami Holopainen, TUT, Finland
- Guaranteed and computable error estimates of Uzawa iteration method for a class of Bingham fluids, Marjaana Nokka[1], Sergey Repin[1,2] ,[1]University of Jyväskylä, Finland; [2]St. Petersburg State Polytechnical University, Russia

Session 4C: Models and Analyses (EEF) 9:00-10:00

- Finger and toe photoplethysmographic pulse waveform analysis with means of logarithmic transformation, Matti Huotari, Kari Määttä, Juha Röning, University of Oulu, Finland
- A model for anisotropic magnetostriction, Anouar Belahcen[1], Reijo Kouhia[2], Paavo Rasilo[1], Matti Ristinmaa[3], [1]Aalto University; [2]Tampere University of Technology, Finland; [3]Lund University, Sweden
- Teräsbetonikuorielementin mitoitus murtorajatilassa optimointitehtävänä, Pentti Varpasuo[1], Lauri Jaamala[2], [1]Fortum Power and Heat Oy, Finland; [2]AF-Consult Ltd, Finland

Session 5A: Experimental Mechanics - Kokeellinen mekaniikka (EEEF) 10:30-12:00

- An experimental and numerical study of the dynamic Brazilian disc test on Kuru granite, Ahmad Mardoukhi, Timo Saksala, Mikko Hokka, Veli-Tapani Kuokkala, Tampere University of Technology, Finland
- Wind-tunnel testing of Helsinki Olympic Stadium new roof, Risto Olavi Kiviluoma, Aalto University, Finland
- X-ray tomographic method for measuring 3D deformation and liquid content in swelling materials, Tero Harjupatana, Jarno Alaraudanjoki, Markku Kataja, University of Jyväskylä, Finland
- Betonisten ratapölkkyjen väsytyskuormituskokeet, Tommi Rantala, Olli Kerokoski, Antti Nurmikolu, TUT, Finland

Session 5B: Seismic & Soil Mechanics (EEEF)) 10:30-12:00

- Seismic analysis of a liquid-filled shell structure, Jussi-Pekka Matilainen, Jari Puttonen, Aalto University, Finland
- Performance-based seismic optimization design, Qimao Liu, Juha Paavola, Aalto University, Finland
- Shear bands in soft clays: strain-softening behavior in finite element method, Marco D'Ignazio, Tim Länsivaara, TUT, Finland
- Changes of pore water pressure in clay during consolidation, Samuli Laaksonen[1], Osmo Korhonen[4], Mirva Koskinen[2], Leena Korkiala-Tanttu[3], Matti Lojander[3], Monica Löfman[3], [1]Ramboll Finland Oy; [2]City of Helsinki; [3]Aalto University, Finland; [4]

Session 5C: Mallintaminen - Modelling (Finnish)) 10:30-12:00

- Rautatiekiskon sivukuluneisuuden vaikutusten mallintaminen, Tiia-Riikka Loponen, Pekka Salmenperä, Antti Nurmikolu, Jari Mäkinen, TTY
- On the direct solution of critical equilibrium states, Anders Eriksson[2], Reijo Kouhia[1], Jari Mäkinen[1], [1]TUT, Finland; [2]KTH Mechanics, Sweden
- Menetelmä lentokoneen ohjausservon sisäisen vuodon havaitsemiseksi, Jouko Laitinen, TUT, Finland
- Heat release caused by the smouldering combustion of the binder of rockwool, Perttu Leppänen[1], Manuela Neri[2], Jari Mäkinen[1], [1]TUT; [2]Universita Degli Studi di Brescia, Italy

Session 6A: Material models - Materiaalimallit (EFF) 13:00-14:00

- Orthotropic constitutive model for steel fibre reinforced concrete: linear-elastic state and bases for the failure, Marika Eik[1,2], Heiko Herrmann[2], Jari Puttonen[1], [1]Aalto University, Finland; [2]Tallinn University of Technology, Estonia
- Wood compression model for radial compression of earlywood and latewood, Carolina Sofia Moilanen, Tomas Björkqvist, Pentti Saarenrinne, TUT, Finland
- Modeling asymmetric cyclic plastic hysteresis of nodular cast iron materials, Joona Kalevi Vaara, Juho Könnö, Wärtsilä Finland Oy, Finland

Session 6B: Isogeometric Analysis (English) 13:00-14:00

- Isogeometric analysis of gradient-elastic rods and 2D gradient-elastic dynamic problems, Viacheslav Balobanov, Jarkko Niiranen, Sergei Khakalo, Bahram Hosseini, Aalto University, Finland
- Isogeometric Static and Dynamic Analysis of Gradient-Elastic Plane Strain Problems, Sergei Khakalo, Jarkko Niiranen, Viacheslav Balobanov, Bahram Hosseini, Aalto University, Finland
- Thermo-Hygro-Mechanics (THM) in the frame of the Finnish connection, Andras Szekeres, Budapest University of Technology and Economics, Hungary

Torstai - Thursday, 4.6.2015

8:45-9:00	**Avaus - Opening** Location: **Konsu**		
9:00-10:10	**Plenary I** Location: **Konsu** Chair: **Martti Mikkola**		
10:10-10:40	**Kahvi - Coffee** Location: **Konsu**		
10:40-12:00	**1A: Structural Engineering - Rakennetekniikka (EFFF)** Chair: **Kristo Mela**	**1B: Fracture & Damage Mechanics (English)** Chair: **Jouni Freund**	
12:00-13:00	**Lounas – Lunch**		
13:00-14:20	**2A: Multibody Dynamics (English)** Chair: **Marko Matikainen**	**2B: Numeeriset menetelmät - Numerical Methods (Finnish)** Chair: **Timo Saksala**	**2C: Theoretical Mechanics - Teoreettinen mekaniikka (EEEF)** Chair: **Kari Santaoja**
14:20-14:50	**Kahvi - Coffee** Location: **Konsu**		
14:50-15:50	**3A: Finite Element Methods (English)** Chair: **Rolf Stenberg**	**3B: Optimointi - Optimization (Finnish)** Chair: **Jussi Jalkanen**	**3C: Beam Theory - Palkkiteoria (EEF)** Chair: **Arttu Polojärvi**
15:50-17:00	**Plenary II** Location: **Konsu** Chair: **Juha Paavola**		

Perjantai - Friday, 5.6.2015

9:00-10:00	**4A: Ice Mechanics - Jäämekaniikka (EFF)** Chair: **Jukka Tuhkuri**	**4B: Matemaattiset menetelmät - Mathematical Methods (Finnish)** Chair: **Juha Jeronen**	**4C: Models and Analyses (EEF)** Chair: **Baroudi Djebar**
10:00-10:30	**Kahvi - Coffee** Location: **Konsu**		
10:30-12:00	**5A: Experimental Mechanics - Kokeellinen mekaniikka (EEEF)** Chair: **Mikko Hokka**	**5B: Seismic & Soil Mechanics (EEEF)** Chair: **Pentti Varpasuo**	**5C: Mallintaminen - Modelling (Finnish)** Chair: **Jari Mäkinen**
12:00-13:00	**Lounas - Lunch**		
13:00-14:00	**6A: Material models - Materiaalimallit (EFF)** Chair: **Juho Könnö**	**6B: Isogeometric Analysis (English)** Chair: **Antti H. Niemi**	
14:00-14:30	**Kahvi - Coffee** Location: **Konsu**		
14:30-15:00	**Loppusanat - Ending** Location: **Konsu**		

Plenaries in **Konsu 3rd** floor
A Sessions in **Väinö Voionmaa, 8th** floor
B Sessions in **Yrjö Mäkelin, 6th** floor
C Sessions in **Unto Kanerva, 6th** floor
Lunches in **Theatre foyer, P** floor

RAKENTEIDEN MEKANIIKAN SEURA R.Y.
FINNISH ASSOCIATION FOR STRUCTURAL MECHANICS

ISBN 978-952-93-5608-9 (printed)
ISBN 978-952-93-5609-6 (PDF)